Experimental Study of Vertically Vibrated Granular Matter: Patterns and Segregation

A Thesis
Submitted for the Degree of
Doctor of Philosophy

by

Mohammed Istafaul Haque Ansari

Engineering Mechanics Unit
Jawaharlal Nehru Centre for Advanced Scientific Research
(A Deemed University)
Bangalore – 560 064

MAY 2016

My family

DECLARATION

I hereby declare that the matter embodied in the thesis entitled "**Experimental Study of Vertically Vibrated Granular Matter: Patterns and Segregation**" is the result of investigations carried out by me at the Engineering Mechanics Unit, Jawaharlal Nehru Centre for Advanced Scientific Research, Bangalore, India under the supervision of **Prof. Meheboob Alam** and that it has not been submitted elsewhere for the award of any degree or diploma.

This work forms a part of the Research Project titled "Dynamics and patterns in granular fluid: Theory and experiment" of Prof. Meheboob Alam, funded by the Department of Atomic Energy, Government of India (Sanction No. 2010/21/06-BRNS).

In keeping with the general practice in reporting scientific observations, due acknowledgment has been made whenever the work described is based on the findings of other investigators.

Mohammed Istafaul Haque Ansari

CERTIFICATE

I hereby certify that the matter embodied in this thesis entitled "**Experimental Study of Vertically Vibrated Granular Matter: Patterns and Segregation**" has been carried out by **Mr. Mohammed Istafaul Haque Ansari** at the Engineering Mechanics Unit, Jawaharlal Nehru Centre for Advanced Scientific Research, Bangalore, India under my supervision and that it has not been submitted elsewhere for the award of any degree or diploma.

Prof. Meheboob Alam
(Research Supervisor)

Acknowledgements

First and foremost, I would like to express my deep sense of thanks and gratitude to my research supervisor and mentor Prof. Meheboob Alam for teaching me all about research, for giving me a golden opportunity to work on this experimental project. His dedication and keen interest above all his overwhelming attitude to help his students had been solely and mainly responsible for completing my thesis. His timely advice, meticulous scrutiny and scientific approach have helped me to a very great extent in accomplishing this task. I gratefully acknowldege the funding disbursed by the Department of Atomic Energy, Government of India to carry out this experimental investigation.

I owe a deep sense of gratitude to Prof. K. R. Sreenivas for teaching me a course during MS (Engg.) and guiding me in the course project. I am grateful for his prompt inspirations which supported me morally. I thank all the professors of EMU, Prof. S. M. Deshpande, Prof. Santosh Ansumali, Prof. Ganesh Subramanian, Prof. Rama Govindarajan for teaching me various courses. My thanks goes to Prof. Kameswara Rao (IISc, Instrumentation and Applied Physics Dept.) and Prof. Chandra Sekhar (IISc, Electrical Engg. Dept.) for giving me courses in IISc. I would also like to thank my engineering college professors who encouraged me to strive for academic and research career. My unfeigned thanks to Prof. Roddam Narasimha and Prof. Shobhana Narasimhan for their kind suggestions.

I sincerely thank Mr. Krishnoji Rao for fabricating the experimental setup and the related accessories, and Mr. Raghavendra, Mr. Venkateshulu (Jost Engg. Ltd.), and Mr. Ramakrishna (Data Physics Private Ltd.) for exhaustive demonstration sessions of the shaker system.

I thank my labmate Sunil for helping me in PIV analysis and Ronak, Deepthi for their help in codes. I thank my other lab mates Priyanka , Saikat, Reddy, Ramkrishna, Achal, Nandu, Unni for their help. I thank Siddharth, Shashank, Vybhav, Rafiuddin and Nakul for their help. My deep sense of gratitude goes to Dr. Subba Rao and Dr. Archana for their kind help and suggestions during my stay in JNCASR.

There are many individuals who have supported me directly or indirectly in my educational pursuits. I am grateful for the kind and overwhelming support of my parents, siblings and relatives. Thanks for inspiring me to pursue my career and educational goals. Both of you are excellent role models and mentors for our family. I am heartfully thankful to my wife for her strong moral support and her company.

Abstract

This thesis explores the dynamical behavior of granular materials via experiments in a vertically vibrated granular bed. Experiments are designed with the primary objective to understand the pattern formation dynamics that manifests in a vertically-vibrated container filled with mono-disperse spherical particles as well as binary mixtures of equal sized spherical particles of different materials. While the aesthetically pleasing shapes and the novel phase-coexistence of these patterns have generated curiosity, the question of underlying mechanism for their genesis, in addition to their dynamics, must be addressed from a theoretical point of view in future. In this thesis, we report, for the first time, (i) a variety of "phase-coexisting" patterns having different spatial and temporal order, a novel "Ratcheting/Oscillatory" cluster, and the related phase diagrams in vibrated binary mixtures, (ii) a novel unsteady dynamics of the so-called "density-inverted" Leidenfrost state and (iii) the micro-structural signatures of the transition from the "bouncing-bed" to the Leidenfrost state. All these new experimental results are awaiting theoretical explanations.

The first set of experiments was performed on a mono-disperse system of glass, as well as, steel particles of diameter $d = 1.0\ mm$, confined in a quasi-two-dimensional rectangular Plexiglas container. The various control parameters involved in such experiments are: (i) the shaking acceleration/ intensity ($\Gamma = A\omega^2/g$, where A is the shaking amplitude, $\omega = 2\pi f$ is the angular frequency of shaking, and g is the gravitational acceleration), (ii) the particle filling depth at rest ($F = h_0/d$, where h_0 is the bed height at rest), and (iii) the aspect ratio of the container L_x/h_0. The experiments were carried out by increasing the shaking intensity (Γ) via frequency ramping at a linear rate of 0.01 Hz/sec, while maintaining a constant shaking amplitude (A/d). The evolution of patterns has been monitored by varying the filling depth ($F = h_0/d$, where h_0 is the height of the bed at rest) of the particles in the system, and subsequently a phase diagram is constructed in (Γ, F)-plane. Various patterns observed in the system are: (i) the bouncing bed (BB), (ii) the sub-harmonic waves ($f/4$ spikes and $f/2$ undulatory Waves), (iii) the Leidenfrost state (LS), (iv) the bulk convective/recirculating motion and (v) a gas-like state. All these patterns were found to be present in both glass- as well as in steel-particle bed. The phase diagram of steel and glass particles looks qualitatively similar, except the realization of an interesting transition "$Gas \rightarrow Convection$" in the case of glass-particle bed. One more notable difference of the glass-bed from the steel-bed is the suppression and emergence of Spikes at lower and higher filling depths, respectively. To study the effect of frequency ramping rates on the onset of patterns, and in turn on the phase diagram, we performed experiments at various rates and found the phase diagram to be qualitatively similar with slight quantitative differences on the Γ-onset for the patterns. The collective motion of the particles in the patterned states is analyzed with the aid of coarse-grained velocity fields

obtained via PIV (particle image velocimetry) technique. The aspect ratio of the container has been varied in order to examine the onset/suppression of different patterns. The aspect ratio also affects the number of convection rolls emerging in the system. To study the impact of shaking amplitude (A/d) on these dynamical patterns, experiments have also been conducted for two layer depths of $F = 3$ and 6 with different shaking amplitudes, leading to the construction of phase diagrams in $(\Gamma, A/d)$-plane.

The second set of experiments on the monodisperse granular system has been carried out considering a purely 'two-dimensional' (i.e. a mono-layer of spheres along the depth of the container) system under vertical vibration. The primary objective of this set of 2D-experiments is to characterize the origin of the Leidenfrost State and the related micro-structural signatures as it transitions from the BB-state. Experiments have been conducted considering various filling depths with glass beads of diameter $d = 2mm$, wherein two phases, namely, the Bouncing Bed (BB) and the Leidenfrost State (LS), have been observed. The onset of these states have been summarized as a phase diagram in $(\Gamma, A/d)$-plane and an empirical expression of the critical shaking intensity (Γ_{crit}) for the transition from BB to LS, has been derived. The critical shaking intensity Γ_{crit} is found to be exponentially dependent on the particle loading depth (F) as well as shaking amplitude (A/d). The characteristics and distinguishing features of these states have been studied with the help of their mean-fields, namely, the density and temperature profiles along the vertical direction. A study of the micro-structures of various regions identified in the LS as well as in the crystal-packed BB has been accomplished by calculating (i) the radial distribution function (RDF) and (ii) the radial-angular distribution function (RADF). A novel unsteadiness of the interface (between the dilute and dense layers) and the top surface of the bed has also been uncovered, wherein the interface as well as the top surface are found to oscillate sinusoidally, with the oscillation frequency closely matching that of the external shaking. The robustness of the 'synchronized' oscillation of the Leidenfrost state has been further verified by carrying out additional experiments with 5.0 mm diameter glass beads as well as those in a quasi-two-dimensional container. Lastly, the onset of convection has also been reported in our 'mono-layer' two-dimensional system by confining the beads in a container of larger length. A phase diagram has been prepared that depicts the additional transition of LS to convection exhibiting a pair of rolls, which eventually melts to a one-roll system and finally to a gas-like state with increasing shaking intensity. The latter transition, from convection to a gas-like state, was never reported in earlier studies.

A substantial part of this dissertation has been devoted to the study of binary granular mixtures subjected to vertical harmonic oscillations. The various mixtures considered constitute equimolar proportion of equal sized spherical particles (diameter $d = 1.0$ mm) of (i) steel and glass (density ratio, $\rho_s/\rho_g = 3.06$), (ii) brass and glass ($\rho_b/\rho_g = 3.46$) and (iii) brass and steel ($\rho_b/\rho_s = 1.13$). The first two types of mixtures have a significant disparity in the density of particles, while the third mixture behaves almost akin to a monodisperse system presumably due to its slight density contrast. In mixtures with large density-contrasts, our experiments unveiled a variety of segregation-driven phase coexisting patterns wherein a gas-like phase can coexist with a liquid-like phase separated along the horizontal direction – this type of 'horizontal' segregation, induced along the length of the container in the horizontal direction, was never

reported in the literature on vertically vibrated granular mixtures. The coexisting phases are found to exhibit (i) different spatial order as well as different temporal symmetry (for example, in case of "f/2" undulatory waves that coexist with a 'disordered' gas), and (ii) different spatial order but having the same temporal symmetry, for example, in the case of the Leidenfrost state coexisting with a gas. In all these patterns, the gaseous region is always found to be dominated by heavier particles, while the lighter particle-rich regions existing in a solid-like or liquid-like state. A plausible theoretical explanation for the genesis of such patterns has been furnished by invoking the well-known fact of non-equipartition of granular energy between two types of inelastic particles having different masses.

One more phenomenon observed in these experiments is of particular interest: the appearance of an "oscillating/ratcheting" cluster that coexists with a gas. The cluster is found to spontaneously drift along the horizontal direction from one end of the container to the other end. The associated drift velocity is about 1% of the maximum velocity of the shaker.

In addition to the mixture experiments that were performed considering equimolar proportion of two types of particles, a thorough study of the effect of variation of species number fraction on the onset/suppression of the patterns and on the related phase diagrams has also been carried out. One of the important findings of this study is the control of convection patterns by adding a small amount of heavier (or lighter) particles in an otherwise monodisperse system. With this technique, one can control the number of convection rolls emerging in the system and can transit from a convection-state to a "partial" convection state (i.e. the convection rolls coexisting with a Leidenfrost State along the horizontal direction) and subsequently to a "complete" Leidenfrost State and vice versa. We also observed an hysteresis in the onset of these segregation-driven patterns while up-sweeping and down-sweeping experiments carried out at atmospheric pressure. The same experiments carried out in a sealed-contained with variable pressure showed that the amount of hysteresis decreases as one reduces the pressure inside the container leading to its total suppression at low vacuum settings. A plausible explanation of such hysteresis has been proposed based on the theory of viscous drag experienced by two type of particles. Furthermore, the effects of increasing shaking amplitude (A/d) on the pattern formation dynamics have also been examined by focussing on two layer-depths of $F = 3$ and 6 with an equimolar mixture. In contrast to steel-glass and brass-glass particle mixtures, the mixture of steel and brass particles, however, does not lead to segregation-induced patterns, suggesting that this system behaves similar to a monodisperse case. This is presumably due to the small density difference between steel and brass particles ($\rho_b/\rho_s = 1.13$).

Contents

Chapter 1

Introduction

1.1 General aspects of granular materials

A granular material is an aggreate of macroscopic dicrete, solid particles dispersed in vacuum or an insterstitial fluid. The terms granular materials, bulk solids and particulate solids are used interchangeably in the literature. They are ubiquitous in our daily life, nature and of huge importance in industrial processes (Jaeger & Nagel 1992; Jaeger *et al.* 1996*b*). Example of such materials include sand, gravel, food grains, seeds, sugar, coal, cement and pharmaceuticals. They range from particles of sizes of a few hundred microns such as in powders to huge ice bergs, asteroids and planetary rings. The granular matter is a system of interest to many disciplines such as engineering, geology, material science, physics and biology. Since researchers have initiated to theoretically describe granular materials, this field has attracted mathematicians and computer scientists, opening up many possibilities for the development of new theories and large-scale computer simulations to model granular phenomena and to compare these with the results of physical experiments (Ristow 2000).

The direct interaction of particles plays an important role in the flow behaviour of granular materials, and the energy dissipation and momentum transfer occurs only when the particles come in contact with each other or the wall confining them. Granular materials are unique in that they can exhibit all the three states of matter: gas, liquid, and solid. A highly fluidized system of particles have been succesfully modeled in analogy to a molecular gas (Haff 1983; Jenkins & Savage 1983). However, a major difference between a molecular gas and a granular gas is that, unlike gas molecules, the solid particles collide inelastically, dissipating energy. Thus, a granular gas can rapidly achieve a "dead state" having a zero temperature, if energy is not continuously injected into the system through external forcing.

Granular materials can flow like a liquid from a vessel but the mass flow rate is approximately independent of the height of material above the discharge orifice; this feature accounts for the use of hourglasses containing sand as clocks a few centuries ago. Furthermore, when granuar material is poured into a container, the assembly conforms, in a bulk sense, to the shape of the container. They can sustain shear stresses at rest like solids as in the case of slope of a sandpile. In a sandpile the inclination of the free surface of the heap to the horizontal is not arbitrary but decided primarily by the angle of repose.

For an assembly of non-cohesive particles, the solid-like behavior is limited only to compressive loads. When subjected to tensile-loads, particles come apart. However, the assemblies of cohesive-particles can resist a limited tensile load. Another unusual result of material granularity is that the force-transmission is anisotropic. Forces are transmitted along particle contacts and can form long *force chains* (Jaeger & Nagel 1992).

1.2 Granular Materials: Motivation of Study

Understanding the governing laws of granular materials is of huge technological and industrial importance. A wide variety of substances used in industry are routinely handled in the form of granules (Bridgewater 1995), for example cement, pills and cereals. The most common method of moving industrial granular materials is gravity feed. Grain elevators, silos, hopper cars, and coal chutes, all rely on the force of gravity to move materials. A related variant is the rotating drum, which is used to crush, mix, segregate and agglomerate material. Finally, the vibrational forcing is used to convey, mix, segregate and pack materials. Understanding the static, dynamic and flow properties of these materials is crucial for their storage and processing. It is interesting to note that the total yearly production of granular materials is enormous, reaching approximately ten million metric tons and consuming roughly 10% of all the energy produced on the planet (Duran 2000). Hence, any advancement in understanding the physics of such materials is bound to have a major economic benefit.

Granular processes consisting of large-scale flows of particulate solids are also widespread in geology (Iverson 1997). These are central to the fluidisation of soil by the shaking of violent earthquakes, debris flows and landslides, rock and snow avalanches in mountain slopes, pyroclastic flows and motion of sand dunes. All of these can do immense property damage as well as fatalities. FEMA (Federal Emergency Management Agency) assesses that land-slides alone result in an annual loss of $1.5 billion and 25 fatalities in the United States (FEMA, 1996). Thus, there is a dire need not only to understand the underlying triggering mechanisms but also to be able to predict the actual size and evolution of such events.

The study of granular materials has a long tradition amongst engineers and geologists who have tended to approach problems in an ad hoc way with practical experience playing a greater role than the understanding of physics. Over the last decade, significant interest has arisen in the physics community and modern ideas from nonequilibrium statistical mechanics and pattern formation are now being used with some success in the description of some aspects of granular phenomena. Nevertheless, a firm mathematical formulation of granular media remains aloof and may well require new theoretical ideas beyond those of standard statistical mechanics, hydrodynamics or traditional solid mechanics (Jaeger *et al.* 1996*b*; Kadanoff 1992). Also, recent developments of well controlled precision experiments have yielded a variety of new and intriguing phenomena and motivated a wealth of further research.

1.3 Dry Granular Media

In "dry" granular media, the constituent particles of granular materials interact with each other and with any boundaries via dissipative collisional and contact forces. A fraction of the kinetic energy of the colliding particles is lost after each collision and the coefficient of restitution, ϵ, is generally employed to describe the collision dynamics,

$$\epsilon = \frac{u_{1f} - u_{2f}}{u_{2i} - u_{1i}}, \tag{1.1}$$

where u_{ji} and u_{jf} are the initial and final normal velocity for the jth particle, respectively. A collision is elastic if $\epsilon = 1$ (energy of the particles remain conserved) and perfectly inelastic if $\epsilon = 0$, i.e., the two particle involved stick together after a collision. Energy can also be lost by rubbing and sliding of particles over each other, characterized by a coefficient of friction, μ. The thermal energy of a particle is approximately 18 order of magnitude smaller than the potential energy needed to lift one typical grain over another in a gravitational field. Therefore, the Brownian motion is insignificant in the collective behaviour and the grains attain a *dead* state once they come to rest. Hence, the dissipation of energy in inter-particle contacts and collisions requires that energy must be continuously inputted into the system to instigate or maintain motion.

The granular materials for which the effects of interstitial fluids are negligible for the particle dynamics are known as *dry granular materials*. For dry granular media, the dominant interactions are inelastic collisions and friction, which are short-range and non-cohesive. A requirement for this condition is that the grains are large enough (typically $\gtrsim 250\mu m$) and that the viscosity of the surrounding fluid is negligibly small. Under these constraints, liquid bridging (capillary) forces, van der Waals forces, viscous forces and electrostatic forces can be neglected and, as discussed above, the mechanical properties of the material are governed only by the momentum transfer during collisions or frictional contacts between grains. In contrast, the aggregates of particles of size within $1\mu m$ and $100\mu m$ are known as *powders* for which the cohesive effects due to the interstitial fluid can no longer be neglected. In this thesis, we have dealt with the system of dry granular material.

1.4 Early Developments

Early research into granular materials is directly applicable and goes back at least to Charles-Augustin de Coulomb, whose law of friction was originally stated for granular materials (Rhodes 1997). The first published studies on shaken granular media are due to Chladni (1787) who observed that sand sprinkled on the surface of a horizontal vibrating plate migrated to displacement nodes inducing a wide range of patterns on the layer's surface. Faraday (1831) showed that these patterns were due to induced motions of the air surrounding the vibrating plate.

In 1885, Reynolds (Reynolds 1885, 1886) noted that a deformation of an ensemble of particles, for example through shearing, can induce an increase in the volume of the packing. This Reynold's dilatancy occurs because the particles in a compacted state are interlocked and therefore do not have the freedom to move around one another. When stressed, a lever motion occurs between neighboring particles, which produces a bulk expansion of the material. On the other hand, when a granular material starts in a very loose state it may initially compact instead of dilating under shear. Reynold's dilatancy is a common feature of soils and sands studied by geotechnical engineers, and is a part of the broader topic of soil mechanics.

Static configurations of granular media were first studied by Janssen (1895) who investigated the dependence of the pressure, P , at the bottom of a container filled with granular material, on the filling level. For a container full of liquid, P is proportional to the height of the filling level. If granular material is used instead, P increases with height but eventually saturates above a critical value of the filling height. In addressing the question of the mechanism behind this

reduced mass, Janssen realised that the weight of the granular ensemble is partially redirected towards the container's walls thereby supporting the material through frictional contacts.

1.5 Recent Developments

The legacy of the early work by Coulomb, Faraday, Reynolds and Janssen was then promoted by the majority of physicists throughout the 20th century. Research in granular media became an important engineering topic, in particular soil mechanics (Terzaghi 1943). A remarkable work by Bagnold (1954) laid the foundations for the research on sand transport by wind in his influential book "*The Physics of Blown Sand and Desert Dunes*". In this book, he gave a detailed presentation of the behaviour of wind driven sand and put forward an explanation for the formation of small and large scale structures such as surface ripples and dunes, respectively. Renewed interest within the physics community on granular materials began in 1987 with the publication of an interesting paper by (Bak *et al.* 1987) on self-organised criticality (SOC) where a sand pile was used as the canonical model system. They argued that as the angle of the free surface of the pile was increased, the pile would maintain an average slope by generating avalanches characterised by a 1/f power spectra. In physics, the self-organized criticality (SOC) is a property of (classes of) dynamical systems that have a critical point as an attractor. Their macroscopic behaviour thus displays the spatial and/or temporal scale-invariance characteristics of the critical point of a phase transition, but without the need to tune control parameters to precise values. Despite this result having been refuted by a number of experiments (Jaeger *et al.* 1989), Bak's work vigorously renewed interest in the behaviour of granular materials.

Since 1987, a large number of detailed experimental developments have revealed a multitude of fascinating phenomena, which along with challenging attempts to formulate appropriate theoretical models, have also conferred an active and dynamic sense to the study of granular media. An extensive discussion of recent investigations can be found in the review articles by Jaeger & Nagel (1992); Jaeger *et al.* (1996*b*,*a*) and Shinbrot & Muzzio (2000, 2001).

The granular media are usually classified into three categories depending upon the macroscopic flow velocity: rapid flows, dense flows and static packings. These regimes will be discussed in following subsections.

1.5.1 Rapid Granular Flows

In rapid granular flows, the system is said to be in a fluidized gas-like state such that the constituent particles are highly agitated and adequately apart from each other. In modern granular parlance such a flow is often referred as granular *gases*. Researchers have achieved some amount of success to theoretically model such flow regime by applying ideas from kinetic theory of inelastic granular gases (Campbell 1990; Goldhirsch 2003; Brilliantov & Pöschel 2004; Pöschel & Luding 2001). Due to the dissipative collisions, the equilibrium state in granular gases does not exist and the steady state or steady flow of granular particles can be retained only if it is driven externally. In this sense, the granular gases are intrinsically out of equilibrium and quite different from molecular gases. Following the kinetic theory approach, the study of interactions in a large aggregate of particles can be carried out in a statistical mechanical sense to characterise

its macroscopic flow behaviour. Such thoeretical approach was developed by Savage & Jeffrey (1981); Jenkins & Savage (1983); Jenkins & Richman (1984) who built models following the classic work on non-uniform molecular gases by Chapman & Cowling (1952). We know that the kinetic theory of molecular gases predicts the transport coefficients starting from the Enskog-Boltzmann equation. The Chapman-Enskog method, Sonine polynomials expansion and Grad expansion are successful tools to evaluate the distribution functions and the transport coefficients, and it is realized that kinetic theory successfully bridges the gap between the microscopic and the macroscopic properties of molecular gases. Although the employment of kinetic theory to granular gases involves several problems, for example, the lack of scale separation, the long range correlations, etc (Goldhirsch 2003), yet the granular hydrodynamic equations derived by the kinetic theory of granular gases well describe the dynamics of rapid granular flows. The basic assumption in applying kinetic theory to granular gases is that statistical properties of granular gases are mainly determined by the binary collisions of particles and collisions accompanying more than three particles are too rare to be neglected. This assumption pertains to the density of granular gases, the time duration of a collision, and the rigidity of granular particles. To satisfy this assumption the density of the system should be low enough. The time duration of each collision is also crucial, because the long time duration causes to invite other particles to have multibody collision. The duration time depends on the hardness of particles, the harder particles will have less collision time. Alike, the standard kinetic theory of molecular gases, wherein the Boltzmann equation is employed to derive Navier-Stokes-like continuum set of equations, in rapid granular flows (granular gases) too these continuum equations have been derived, though there is a presence of an additional term that describes the overall energy loss due to inelastic collisions (Jenkins & Savage 1983). The kinetic theory models have been successfully applied to experiments on vertically vibrated granular bed (Bizon *et al.* 1999; Shukla *et al.* 2014) and to the quantitative description of shocks in a supersonic steady granular flow past a stationary wedge (Rericha *et al.* 2002). Nevertheless, the homogeneous solutions of the granular hydrodynamic equations are unstable due to the inbuilt dissipative collisions. For example, the shear band in the granular shear flow (Alam & Nott 1998; Saitoh & Hayakawa 2007; Tan & Goldhirsch 1997), *cluster* formation in the *homogeneous* cooling state (Aranson & Tsimring 2006; Goldhirsch & Zanetti 1993; Brilliantov & Pöschel 2004) and the emergence of convection rolls in thin oscillated granular layer (Aranson & Tsimring 2006). The growth of such type of instabilities in the system can be expected by the *linear stability analysis* (Alam & Nott 1997, 1998). These instabilities have been studied in more recent work via *weekly nonlinear theory* (Saitoh & Hayakawa 2011; Shukla & Alam 2009, 2011*b*,*a*; Alam & Shukla 2013; Shukla & Alam 2013).

1.5.2 Quasi-static Slowly Creeping Granular Flows

When particles do not have sufficient relative speed to withstand the imposed pressure, either by an externally imposed compressive stress or due to the weight of grains, these particles tend to collapse into a dense state of slow creeping. This regime of slowly creeping particles is often termed “quasi-static” in the sense that particles are always in static equilibrium, supported by direct contacts with multiple neighbor particles while creeping around each other. In this regime, the inertia of individual particles plays an insignificant role in the flow dynamics. Slow geological

flows Mandl (1988) is a good example in which particles throughout the entire granular packing move in the quasi-static regime. Quasi-static and rapid flows can even coexist in granular flows that are highly inhomogeneous, such as flow in industrial blenders (Forterre & Pouliquen 2008; Moakher *et al.* 2000; Ottino & Khakhar 2001). Quasi-static granular flows exhibits a wealth of phenomena, such as long-term evolution and history dependence. Such type of behaviors are also found in many other glassy or nearly jammed granular systems. A common way to experimentally study the evolution of quasi-static flows is to continuously shear it and then probe the dense granular packings. The contact forces at the lower boundary of a slowly sheared dense granular packing have been measured by Miller *et al.* (1996), wherein they found that the fluctuation spectrum of local contact forces is invariant over a wide range of driving velocity. This finding demonstrates the quasi-static nature of the creeping flow, i.e., the particles are almost always in static equilibrium. An MRI technique has been used by Mueth *et al.* (2000) to study the flow dynamics of particles in a several particle-diameters thick sheared layer, and determined the internal mass flow with sub-particle-size spatial resolution. The effect of particle layering on the mass flow field has been suggested.

A static sand pile is a common example of quasi-static granular packing. Janssen (1895) studied this regime focussing on the stress distribution along force chains. These force chains have been observed by Dantu (1967) in an ensemble of birefringent cylinders and visualised through crossed polarisers. A more recent experimental approach has been adopted by Geng *et al.* (2001), wherein they presented detailed investigations of the force chain network and its fluctuations in a granular pile. One of the fascinating aspects of the granular pile is the observation of a pressure dip at its centre, as reported by Brockbank *et al.* (1997). Nevertheless, they observed that this dip can be suppressed on increasing the particle diameter to three times. Another remarkable feature of granular piles is that their properties depend strongly on the method of its preparation. The local pressure at the bottom of container can have a dip or a maxima at the centre of pile, depending upon whether the pile has been prepared by *pouring* method or by stacking horizontal layers, respectively (Vanel *et al.* 1999).

1.5.3 Dense Granular Flows

In between these two regimes of rapid and quasi-static flows, there exists a dense liquid regime where particle inertia becomes important although a contact network still exists (Pouliquen & Chevoir 2002; MiDi 2004; Forterre & Pouliquen 2008). In these dense granular flows the motion of the particles is restricted because of the high volume fractions involved and the forces are transmitted through a percolating network of particle contacts. These flows do not follow the kinetic theory assumption of instantaneous binary collision, since contact during a collision lasts for a significant amount of time and furthermore, more than two particles can collide at a particular instant. Even though a number of experimental, numerical and theoretical investigations have been performed (Pouliquen & Chevoir 2002; MiDi 2004), this "liquid" regime still lacks correct constitutive equations and their rheology is still incompletely apprehended. The lack of a proper unified theory about this regime had provided an impetus to scientists towards many experimental, numerical and theoretical works. Different flow configurations have been investigated, that includes annular shear cells (Miller *et al.* 1996), vertical chutes

(Nedderman & Laohakul 1980), inclined planes (Gray *et al.* 2003), rotating drums (Gray 2001) and heaps (Liu *et al.* 1991).

Savage & Hutter (1989) proposed an avalanche theory for such dense flows, which was further developed by Gray (2001). Savage & Hutter (1989) in their theory considered that the avalanche is a shallow incompressible Mohr-Coulomb (inviscid) material that stream down a rigid impervious surface inclined at an angle θ to the horizontal. The leading-order mass and momentum equations were integrated through the avalanche depth to obtain a one-dimensional theory along the flow direction. This continuum theory accurately emulated various features observed in experiments; for example shock waves, dead zones and particle-free regions that form when a thin surface avalanche of granular material flows around a fixed obstacle or encounter a change in the bed topography (Tai *et al.* 2001; Gray *et al.* 2003).

1.6 Pattern Formation in Vibrated Granular Layer

In granular flows, particles dissipate energy on collision, so to make the flow happen additional energy needs to be injected into the system continuously through any external force field, such as gravity, by applying shear stress at boundaries as in Couette flow, or by vibrating the material. Of particular interest is the application of vibration to granular materials due to various practical reasons. In industrial settings, equipments that are commonly used to handle and transport materials such as food grains, pharmaceuticals and powders, utilize vibration. The equipments which use vibration includes conveyor belts, hoppers, sorting tables and fluidized bed reactors. The natural settings where vibration of granular materials comes into picture are avalanches, earthquakes and landslides. Therefore, the study of response of granular materials when subjected to external vibrations can help to avoid design failures in extreme conditions. Furthermore, performing table top experiments on granular materials in a laboratory is nowadays feasible, with the advancement of vibration technology. Many interesting patterns can be observed when the granular materials are subjected to periodic vibration. Depending on the whole set of parameters; amplitude and frequency of the vibration, shapes and sizes of the grains, size of the container, depth of the bed and direction of vibration forcing, a plethora of unexpected and fascinating patterns and textures can be realized (Melo *et al.* 1994, 1995; Metcalf *et al.* 1997; Umbanhowar *et al.* 1996). We will review the literature on pattern formation in the granular bed for various scenarios of external forcing: vertical and horizontal vibration.

1.6.1 Vertically Vibrated Bed

Granular bed exhibits a variety of rich and interesting phenomena when subjected to external oscillations in the vertical direction. The first detailed study of vibrated bed of particles was done by Chladni (Chladni 1787). He observed that when sand particles are kept on a vibrating plate they form heaps corresponding to the vibration anti-nodes. Later on, Faraday in his pioneering work (Faraday 1831) examined these patterns and found that particles move in convection pattern within the heap. The particles avalanche down the free surface of heap, enter back into the bed from the base and reach the peak of the heap again to repeat this cycle. He also discovered various types of surface wave patterns in a shallow layer of vibrating grains. An

important observation made by Bachmann (1940) and later investigated by Kroll (1954) is that the behavior of the bed significantly depends on its depth. Bachmann (1940) reported that when the depth of the particle bed is less than about six particle diameters, particles bump around randomly as in a fluidized bed. Nevertheless, when the depth is greater than six particle layers, the whole bed moves coherently akin a single plastic body. The pattern formation scenario in vertically vibrated granular bed have been studied experimentally, later on by various researchers (Melo *et al.* 1994, 1995; Clément *et al.* 1996; Metcalf *et al.* 1997; Douady *et al.* 1989; Edwards & Fauve 1994; Umbanhowar & Swinney 2000; Sano *et al.* 1999; Bizon *et al.* 1998; Ugawa & Sano 2002; Umbanhowar *et al.* 1996; Carrillo *et al.* 2008; Pöschel *et al.* 2000; Renard *et al.* 2001; Luding *et al.* 1996; Luding 1997 a; Aoki & Akiyama 1996; Bizon *et al.* 1999; Sano 2005, 2010).

Recent experiments by Eshuis *et al.* (2007) in a deep bed have unveiled various types of patterns depending on the shaking intensity (i.e. the dimensionless acceleration of shaking scaled by gravitational acceleration, Γ) and the layer height (F) at rest. For $\Gamma \leq 1$ the granular bed moves like a solid bed without getting detached from the bottom plate since the input energy is smaller than the potential energy of the particles, and this gives birth to a bouncing-bed state at $\Gamma > 1$ wherein the particles move collectively with the sinusoidal motion of the shaker. The bouncing bed becomes unstable beyond a critical value of $\Gamma \approx 5$, giving rise to a period-2 or $f/2$ (where f is the frequency of the shaker) subharmonic wave via a period-doubling bifurcation (Douady *et al.* 1989; Eshuis *et al.* 2007). Higher-order (period-4, i.e. $f/4$) subharmonic waves (Aoki & Akiyama 1996; Ansari & Alam 2013) have also been discovered; other related patterns are Faraday waves and oscillons (Umbanhowar *et al.* 1996), kinks (Douady *et al.* 1989; Melo *et al.* 1995), clustering (Olafsen & Urbach 1998), heaping (Clément *et al.* 1992), density inversion (Lan & Rosato 1997) or the granular Leidenfrost state (Meerson *et al.* 2003; Eshuis *et al.* 2005) and convection (Wildman *et al.* 2001; Eshuis *et al.* 2007).

Among these, "kinks" and "oscillons" are particularly intriguing patterns. They are spatially localized structures and are related to high Reynolds number nonlinear dynamics. A "kink" is a region of particles bed between two sections that oscillate out-of-phase. Each "kink" is sorrounded by two convective cells, wherein particles move down at the kink and shoot up on either side of it. These features were first realized by Douady *et al.* (1989) and have also been reported later on experimentally by Melo *et al.* (1995) and Wassgren *et al.* (1996). "Oscillons" are stable two-dimensional localised excitations which have the tendency to assemble into molecular and crystalline structures, appearing in a hysteretic way at the boundary between "stripes" and "squares" patterns. They are small, circularly symmetric structures that oscillate at a frequency $f/2$ (f is the shaking frequency), i.e., during one cycle it is a peak; and on the next cycle it is a valley (Umbanhowar *et al.* 1996).

The above patterns have also attracted many researchers employing numerical approaches (Bizon *et al.* 1998; Clément & Labous 2000; Lan & Rosato 1995*a*; Luding *et al.* 1994*b*; Metha & Luck 1990; Rothman 1990; Shattuck *et al.* 1999; Tsimring & Aranson 1997; Carrillo *et al.* 2008; Pöschel *et al.* 2000; Renard *et al.* 2001; Luding *et al.* 1996; Luding 1997 a; Bizon *et al.* 1999; Goddard & Didwania 2009). Carrillo *et al.* (2008) studied these subharmonic instabilities in a vertically vibrated granular layer and found that above a certain Γ, a periodic wave-like pattern appears with a frequency $f/2$. Although, the condition $\Gamma > 1$ is not necessary for pattern

formation (Pöschel *et al.* 2000; Renard *et al.* 2001), experimental observations revealed the onset of pattern formation for $\Gamma \gtrsim 4$. These waves were reproduced in quantitative agreement with numerical MD simulations by Luding *et al.* (1996) and Luding (1997 a) and they were also obtained from a linear stability analysis of an oscillating granular layer, modeled as an isothermal incompressible fluid with vanishing surface tension (Bizon *et al.* 1999). Most of this thesis work revolves around this subject of *pattern formation* in vertically vibrated monodisperse as well as bidisperse granular system.

1.6.2 Horizontally Vibrated Bed

Horizontally driven granular flow is also of interest because both horizontal and vertical vibrations are commonly used in industries as an aid to mixing, demixing and transporting granular materials. Soil liquefaction during earthquakes is a general and catastrophic phenomenon concomitant with horizontal shaking. Granular materials on horizontal shaking exhibit various types of instabilities: solid-fluid phase transition (Ristow *et al.* 1997; Ristow 1997), spontaneous pattern formation in shallow layers (Strassburger *et al.* 1996), convection (Tennakoon *et al.* 1999; Medved *et al.* 1999, 2000; Salueña *et al.* 1999; Salueña & Pöschel 2000), and repeated periodic swelling of the shaken layer surface, wherein the frequency of the surface oscillations are found to be decoupled from the drive frequency (Rosenkranz & Pöschel 1997). Horizontally vibrated granular materials have been studied numerically employing cellular automata (Strassburger *et al.* 1996) and MD simuation (Ristow *et al.* 1997; Ristow 1997; Iwashita *et al.* 1988; Liffman *et al.* 1997; Salueña *et al.* 1997*a*,*b*, 1998, 1999). The experiemental studies on horizontal shaking include the works of Evesque (1992),Tennakoon *et al.* (1999)Medved *et al.* (1999); Metcalfe *et al.* (2002). Evesque (1992) demostrated that the physics of sand pile and the emergence of convection rolls is mostly governed by friction of walls and dilatancy of the bed; this implies that sand-pile mechanics is quite sensitive to rotations of the principal stress axis and hence the convection pattern evolution depends on the boundary conditions. Medved *et al.* (1999) reported that the shape and number of convection rolls is primarily determined by the roughness of the container walls and its dimensions. Metcalfe *et al.* (2002) presented a series of experiments and a comparison with the MD simulations, wherein they focussed on the transition between the “fluid” and “solid” states of granular materials under horizontal shaking.

The emergence of convective motion in granular materials subjected to horizontal vibrations is studied less in comparison to convection induced by vertical vibrations, wherein we can find a plethora of experimental, theoretical and numerical references. The structure of convective cells in horizontally shaken containers is complex having convective motion in the direction both parallel as well as perpendicular to the external forcing (Tennakoon *et al.* 1999); on the contrary the convection pattern in vertically shaken containers is relatively lucid, wherein particles stream shoots up at certain horizontal locations along the container length and rain down alongside the vertical walls. Furthermore, MD simulations of vertically shaken granular matter are successful to reproduce most of the features of convection faithfully; however in case of horizontal shaking simulation studies are inconsistent with experimental observations, wherein experiments shows a downward motion of the particles alongside the vertical walls (Tennakoon *et al.* 1999; Rosenkranz & Pöschel 1997; Pöschel & Rosenkranz 1998), while simulation reports counter-rotating rolls on

the surface of the bed (Liffman *et al.* 1997).

1.7 Particle Segregation

One of the intriguing behavior of granular mixtures of particles having different sizes and/or densities is the segregation phenomenon, wherein an originally uniform mixture can demix into its constituent species under various flow conditions (Duran 2000; Ristow 2000; Mullin 2002). Difference in rigidity and surface properties of the particles such as roughness, may also lead to segregation (Williams 1976*b*; Bridgewater 1993). Interestingly, segregation always happens under a properly tuned set of flow parameters which are non-trivial to predict. Shinbrot & Muzzio (2000),Ottino & Khakhar (2000),Kudrolli (2004) have dealt with the various issues involved in granular segregation, in their reviews.

Although various researchers have devoted their tireless effort in understanding the mechanism involved for the origin of segregation phenomenon since more than a half century, yet it is not a well deciphered topic. Apart from posing several fundamental questions from a theoretical point of view, research on segregation phenomenon is direly needed due to its direct applications in industrial settings. The demixing of particles having different physical properties is an ubiquitous process witnessed in various areas such as material science, geophysics and almost all branches of engineering, i.e., involving production of food, drugs, detergents, cosmetics, ceramics, and so on (Fan *et al.* 1990). Handling of mixtures can lead to undesired separation which can be a nuisance. A crucial scenario is the manufacturing of pharmaceutical pills which invloves mixing of a number of chemical powders and a mere 1% mal-mixing can lead to drastic consequences. Segregation can be induced by many processes such as vibration, shearing, rotation and fluidization (Williams 1976*a*; Bridgewater 1976).

The spatial distribution and dynamics of segregation of granular mixtures seem to depend on a number of factors besides size and density differences, including the pressure of the interstitial air, shape of boundaries and particle velocity. Since the parameter space of such a system spans wide range, a lot of research still needs to be done.

We will review in detail the various geometries commonly employed to study segregation phenomenon. A very widespread technique to achieve segregation in granular mixture is through vertical vibration, wherein one can realize the so-called *Brazil-Nut Effect* (Williams 1963). In a binary mixture of classical immiscible fluids, the lighter fluid is observed to be layered on the top due to Archimede's principle. However, in vibrated granular bed one can witness the reverse behavior. Fig. 1.1 demonstrates the motion of a large heavy intruder placed at the bottom of smaller grains. On vibrating the column in vertical direction, the intruder will mostly rise to the surface, where it remains thereafter (Rosato *et al.* 1987; Jullien *et al.* 1992; Duran *et al.* 1993; Dippel & Luding 1995). An equally probable scenario which arouses one's curiosity is the sinking of a large particle (that has a lower density than the sorrounding bed of fine grains) to the bottom of the bed, when subjected to vibration (Shinbrot & Muzzio 1998). These phenomena have been referred to as *reverse buoyancy*. An extension of the problem with a single large intruder is the case of segregation of an initially homogeneous mixture of large and small particles having equal or comparable volume fraction (Hsiau & Yu 1997). Hong *et al.* (2001) observed an opposite behavior to that of *Brazil-Nut Effect* which they named *Reverse Brazil-Nut*

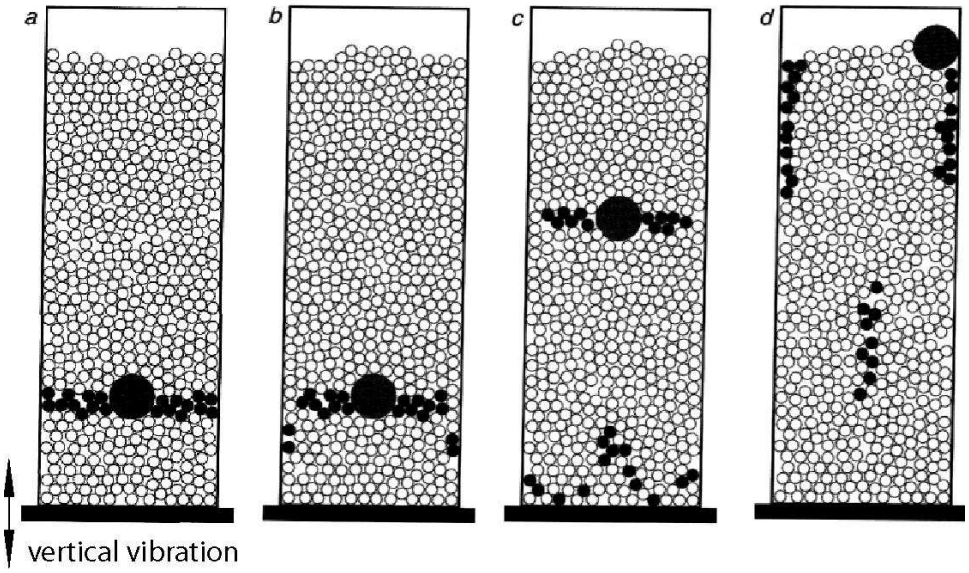

Figure 1.1: **The Brazil-Nut Effect**. A large heavy intruder is shown submerged in an aggregate of small particles in (a). As the column is vibrated the intruder raises to the surface. The other three snapshots display the sequential intermediate vertical location of the intruder, until it reaches to the top in (d). A layer of black small particles has been introduced in the bed to aid visualization of the convective motion that may set up due to vibration. Figure has been taken from Knight *et al.* (1993).

Effect, wherein the large particle, if sufficiently heavy, could sink to the bottom. They presented a simple relation between the size and density ratios that predicts the crossover from BNE to the RBNE , based on the theory of competition between the percolation effect and the condensation of hard spheres. Later on, Jenkins & Yoon (2002) and Trujillo *et al.* (2003); Alam *et al.* (2006) bolstered this theory by etablishing a similar criterion employing kinetic theory for a binary mixture in gravitational field.

Furthermore, Möbius *et al.* (2001) found that ambient air pressure plays a crucial role in determing the dynamics and spatial distributions of the finally segregated state. They reported that the time required for a large particle to rise to the surface of the bed depends non-monotonically on both the background air pressure and the density ratio of the two particles. Later on, Burtally *et al.* (2002) performed similar type of experiments on vertically vibrated mixture of fine and equal sized bronze and glass particles. They observed a variety of segregated states depending upon the amplitude and frequency of vibration. At lower frequencies and moderate shaking amplitude, a sharp separation was formed between upper heavier bronze-rich region and lower glass-rich region. At higher frequencies, the bronze-rich layer is found to be sandwiched between two glass-rich layers. A variety of other oscillatory regimes of periodic tilting were also found. They also reported that segregation was not found in either case: when the air pressure falls below a certain value or if the base plate was made porous to allow flow of air through it. Burtally *et al.* (2002) hypothesized that this type of segregation in their system is due to the differential viscous drag experienced by the two types of particles.

The dynamics of segregation in granular mixtures driven by horizontal vibration has been a relatively unexplored field (Betat *et al.* 1998; Kudrolli 2004). A few studies of horizontally shaken deep layers have been performed, wherein complex convective motion, both on the surface

(a) 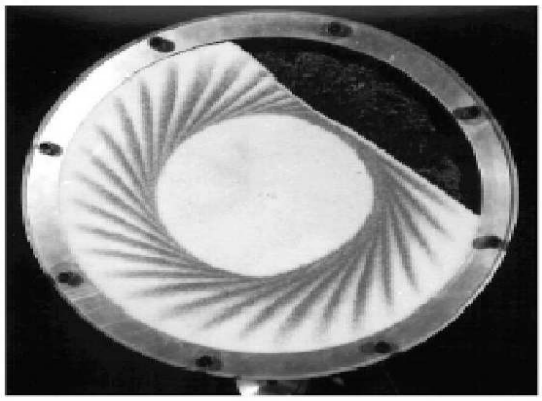 (b) 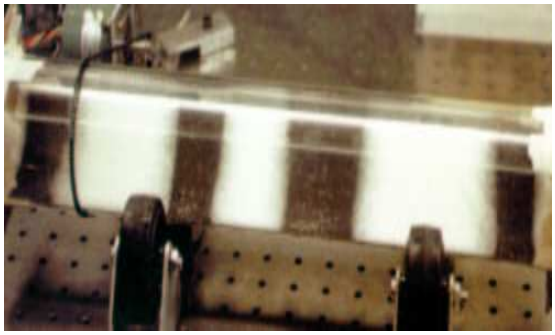

Figure 1.2: **(a) Radial segregation in a rotating drum.** The large sugar particles are white in color and the small iron spheres are greyish. Snapshot has been taken from Gray & Hutter (1997). **(b) Axial segregation bands in a long rotating drum for a mixture of white salt and black sand.** Snapshot has been taken from Choo *et al.* (1997).

as well as in the bulk, was observed (Painter & Behringer 2000; Metcalfe *et al.* 2002). Due to the setup of these convective currents, RBNE can be induced in the system (Liffman *et al.* 2000), wherein larger particles in a sea of smaller ones can sink to the bottom of a horizontally shaken container. A particularly interesting theoretical and numerical study on granular segregation has been performed by Fierro *et al.* (2003). They studied a binary mixture of hard-spheres, with different sizes, on a three-dimensional lattice using Monte Carlo simulations. The two types of spheres were dispersed on a cubic lattice and initially prepared in a random loose stable pack. Under vertical vibrations their model succesfully reproduced both BNE as well as RBNE. In case of horizontal vibrations, Fierro *et al.* (2003) observed the formation of segregation structures reminiscent of those found by Mullin (2000).

Now, we will recapitulate the literature on segregation occuring in rotating drums filled with granular mixtures. Rotating drum flows span diverse research areas, encompassing physics of granular media, hydrodynamics of suspensions and pure liquid flows (Seiden & Thomas 2011). During the last decade, numerous manuscripts dealing with the granular flow in a rotating horizontal drum and spherical tumbler have been published. This indeed has contributed our awareness of related subjects such as avalanches and segregation in granules. Apart from the importance of rotating horiozntal drum geometry in the development of basic physics, it has a salubrious contribution in industrial settings. Rotary drums are used as kilns, mixers, dryers and granulators where segregation of granular particles is often the cause of process and product defects. Rotary drums are also used for wood debarking in paper-making industries.

The granular flow in the rotary horiozontal drum constitute two regions: a major part of the drum remains occupied with particles undergoing a soild body rotation and moving upwards alongwith the drum wall, and a thin fluidized layer existing on the surface avalanching downwards. Rotation of a mixture of different size and/or density particles in a horiozontal drum often exhibits two types of segregation depending upon the aspect ratio (L/D, where L and D are axial length and diameter) of the drum: *radial segregation* that occurs across the cross-section of a short cylinder (L is much smaller than D) and *axial segregation* occuring in a long cylinder (L is much larger than D). In radial segregation, the small (or high density)

particles concentrate in the central core while the large (or low density) particles migrate and gather close to the periphery of the cylinder (Donald & Roseman 1962; Henein *et al.* 1985; Nityanand *et al.* 1986; Alonso *et al.* 1991; Ristow 1994; Cantelaube & Bideau 1995; Khakhar *et al.* 1997; Dury & Ristow 1997; Prigozhin & Kalman 1998; Eskin & Kalman 2000; Thomas 2000). A typical segregation pattern of this configuration is displayed in Fig. 1.2(a), after one period of rotation of a mixture of large sugar particles and small iron spheres. Nityanand *et al.* (1986) demonstrated that this radial segregation pattern in a mixture of different sized particles can even reverse at high angular speeds, i.e., larger particles migrate towards the core while smaller particles concentrate on the periphery of the cylinder. More recent experiments by Thomas (2000) also confirmed this *reverse segregation*, in addition to the finding of a novel *double segregation*. The *double segregation* has been particularly observed in mixtures with few large particles, wherein large particles can concentrate at any radial location depending on the size ratio. Such type of sergregation has also been observed by Dolgunin & Ukolov (1995) and Thomas (2000) in chute flow experiments of mixtures.

In *axial segregation*, an initially homogeneous binary mixture when rotated in a long thin drum at high speed, segregates in axial bands; whereas at lower speeds the same two species may remain mixed (Hill & Kakalios 1995). An example showing such *axial segregation* has been displayed in Fig. 1.2(b). It is noteworthy that *axial segregation* occurs on much longer time scales, in contrary to *radial segregation*. The phenomena of *axial segregation* was reported long back (Donald & Roseman 1962), though the emergence of the bands (Nakagawa 1994) and its stability (Choo *et al.* 1997) are still matters of debate.

1.8 Thesis Outline

This thesis has been partitioned into six chapters.

A description of the experimental setup and its working principle has been given in Chapter 2. The monitoring of the vibration and operating the shaker system is discussed in detail. The control electronics involved and the software employed to generate the desired vibration profiles has been emphasized. The precise control parameters such as the frequency ramping rate, filling depth of the granular mixture, aspect ratio of the container and the setting up of the initial conditions are descibed. The design features and material used for the manufacturing of the container and head expander has been elucidated. Spherical particles of specific materials have been used as granules; their specification and the size distribution has been detailed. The procedure to carry out the experiments, visualization, imaging and image post-processing techniques are then discussed. The software used for obtaining velocity fields of the patterns via *Particle Image Velocimetry* and the related parameters used has been explicated. The method to detect and link particles in each frame of the image sequence has also been explained; this particle positioning and tracking is employed to determine the granular temperature and microstructure of the system.

Chapter 3 deals with the study of pattern formation dynamics in a vibrated quasi-two-dimensional monodisperse granular system of both glass as well as steel particles (having diameter $d = 1.0\ mm$). Phase diagrams have been constructed in (Γ, F)-plane, depicting the unfolding

of various patterns with increasing filling depth (F). Experiments have been performed at different frequency ramping rates to investigate its impact on the phase diagrams of the patterns. PIV has been employed to obtain the velocity field for each type of pattern. Attention has been focussed on determining the structure and number of convection rolls with the help of their density contours and PIV fields. Experiments are also performed with a smaller length container to consider the effect of its varying length on the onset and emergence of number of convection rolls and other patterns in the system. Some additional set of experiments have been conducted with monodisperse steel particles of smaller size ($d = 0.5\ mm$) to carry out a comparative study of pattern evolution with larger particles. Although, most of the experiments have been performed at constant shaking amplitude $A/d = 3$, we have also checked the effects of changing shaking amplitude on the threshold of these dynamical patterns, and thence on the phase diagrams in $(\Gamma, A/d)$-plane.

The study of vibrated two-dimensional (mono-layer of particles along the width of the container) monodisperse granular system has been carried out in Chapter 4, with an emphasis to characterize the origin of *Leidenfrost State*. Assays have been done considering various filling depths of 2.0 mm glass beads, wherein two phases, namely, *Bouncing Bed (BB)* and *Leidenfrost State (LS)* has been observed. The onset of these states have been allegorized on a phase diagram in $(\Gamma, A/d)$-plane and an empirical expression of the critical shaking intensity for the transition from *BB* to *LS* (Γ_{crit}) has been derived. This Γ_{crit} is found to be exponentially dependent on the particle loading depth (F) as well as shaking amplitude (A/d). The mean fields, the density and temperature of these states are obtained from binary version of the snapshots and using *Particle Tracking* technique; these fields helped us to better understand and indentify the distinguishing features of these states. A study of microstructure of various regions marked in the *LS* as well as in crystalline packing of *BB* has been accomplished by calculating radial distribution function (RDF) and radial-angular distribution function (RADF). A novel unsteadiness tied to the interface and top surface of *LS* has also been reported. To check the robustness of this unsteady nature, additional experiments have been performed with 5.0 mm diameter glass beads. The inception of *Convection* has also been reported in such system by confining the beads in a longer length container. A phase diagram is prepared, that depicts the additional transition of *LS* to *Convection* (exhibiting a pair of rolls), which eventually melts to one-roll system, and then to *Gas*. The route to the gaseous state from a "2-roll" convection to "1-roll" convection is a new finding in these experiments.

Chapter 5 of this thesis is entierly new. In this chapter, the experimental results on vibrated equimolar mixture of equal sized steel-glass, brass-glass, and brass-steel particles (diameter $d = 1.0\ mm$) mixtures held in the same quasi-two-dimensional container have been dicussed in detail. A variety of unhitherto reported novel phenomena, such as phase-coexisting patterns and ratcheting/oscillating cluster have been witnessed in case of steel-glass and brass-glass mixtures, though the brass-steel mixture exhibits patterns analogous to that of monodisperse case. These patterns have been characterised and phase diagram have been obtained in (Γ, F)-plane for both upsweeping and downsweeping frequency cases. Focussing on the steel-glass mixture, experiments have also been performed in smaller length containers to examine the onset/supression of various observed patterns. A simple recipe for controlling convection by varying the bidis-

persity of the system has been proposed with experimental demonstration. We also illustrated *hysteresis* in the onset of these segregation-driven patterns while upsweeping and downsweeping experiments at atmospheric pressure; the degree of *hysteresis* decreases as one reduces the ambient pressure inside the container leading to its total suppression at very low vacuum settings. A theoretical explanation of such *hysteresis* has been proposed based on the theory of *viscous drag* experienced by the two types of particles (Burtally *et al.* 2002). The after-effects of varying the number fraction of the species in the mixture have also been studied in detail with the aid of phase diagrams in $(\Gamma, F_i/F)$-plane. Similar to the monodisperse case, the pattern formation scenario in binary mixtures has been investigated by conducting experiments with varying shaking amplitude and subsequently obtaining phase diagrams in $(\Gamma, A/d)$-plane.

Finally, conclusions arising from the findings of this investigation are remarked in Chapter 6. Suggestions are then given for possible directions towards further extension of this work.

Chapter 2

Experimental Apparatus and Techniques

2.1 Introduction

This chapter elaborates the details of the experimental setup and the experimental procedures employed in the present study. The working principle of the shaker has been explained with a description of the control electronics involved to monitor the vibration. The visualization and image acquisition of the phenomena observed have been discussed. The specifications of the high speed camera used to acquire images have been detailed. The design aspect of the container that holds the granular spherical particles has been explicated. The specifications of the particles and their size distribution is introduced. Lastly, the image processing techniques employed to carry out post-experimental quantitative analysis has been revealed, with an introduction of the PIV (particle image velocimetry) method and its related parameters exploited to obtain the coarse-grained velocity.

2.2 Experimental Setup

A sketch of the setup is shown in Fig. 2.1. The granular material is confined in a rectangular Plexiglas® container. This particle-filled container of specific height (h_0) is mounted on an electromagnetic shaker via a circular head expander and harmonically vibrated in the vertical direction. The shaker operates in a closed loop, controlled by a controller and an amplifier through a software interface. To generate a feedback signal of amplitude and frequency of the sinusoidal vibration, a piezoelectric accelerometer is mounted on the head expander. The temporal evolution of the collective motion of particles has been recorded using a high-speed camera at $1000 frames/second$. The laboratory view of the setup is displayed in Fig. 2.2. We will discuss about each part of the setup in the following subsections.

2.2.1 Electromagnetic Shaker

Electromagnetic shakers operate on the principle of magnetism. When an electric current flows in a wire, a magnetic field establishes around it. When the wire is wound in a coil the effect of the magnetic field intensifies because of the multiple windings of the coil. The change of current flow in the coil will produce a varying magnetic field.

Fig. 2.3 illustrates a coil of wire, suspended in a fixed radial magnetic field. This radial magnetic field is produced by a permanent magnet. A permeable (ferrous) inner pole piece

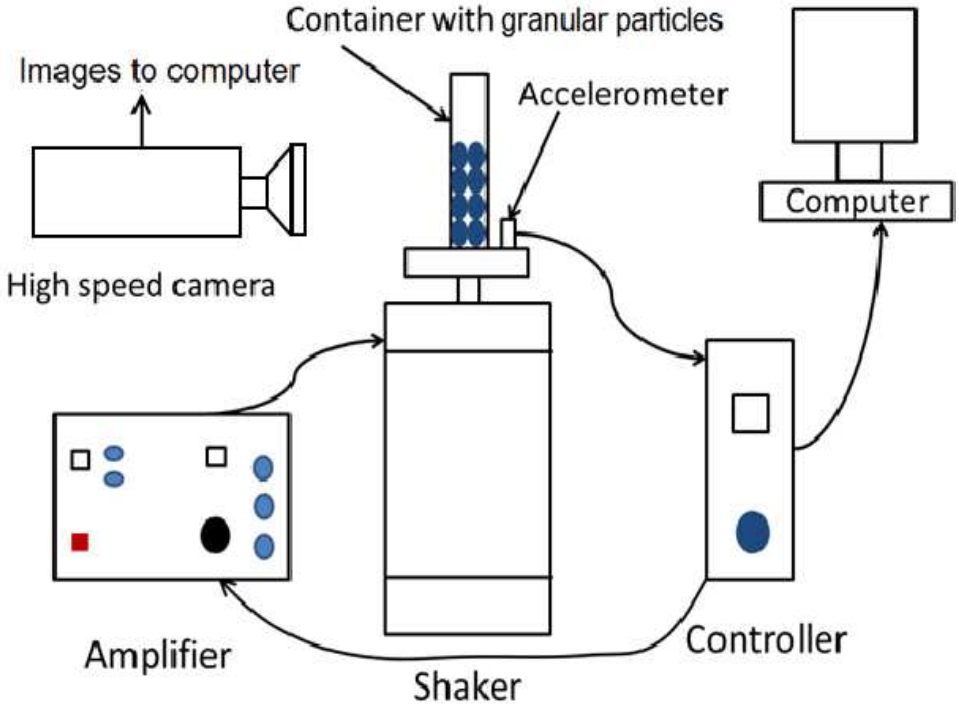

Figure 2.1: **Sketch of experimental setup and shaker control unit.** The control module utilizes feedback signal from the accelerometer mounted on the head expander. This signal is analyzed by the control module and the corrected signals are then amplified to drive the shaker. A high speed camera is employed to record the temporal evolution of the collective motion of particles.

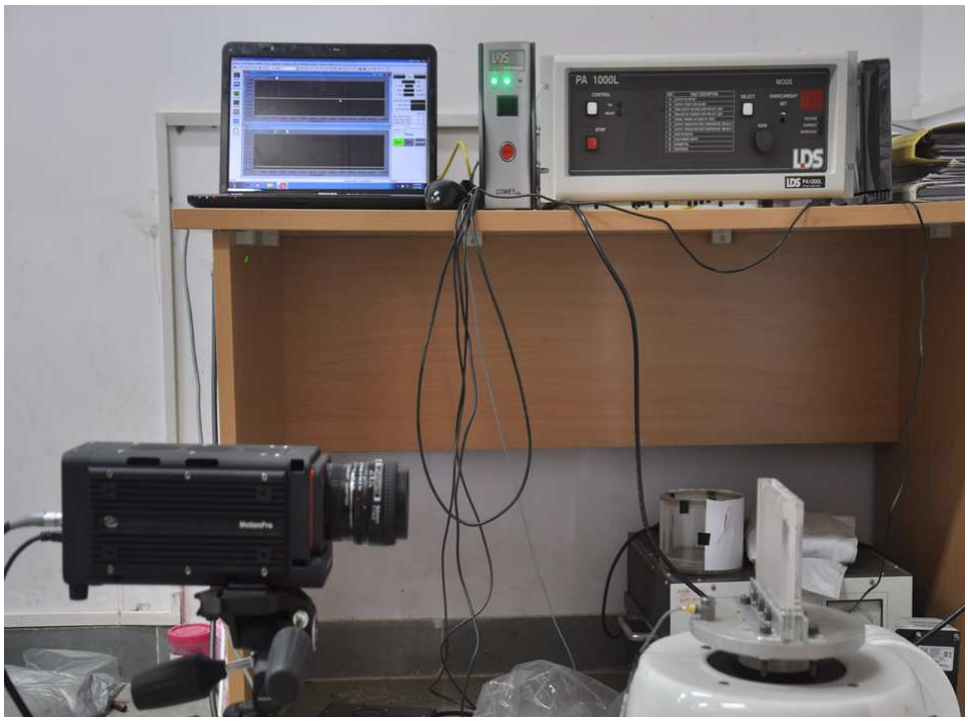

Figure 2.2: **A view of overall experimental setup.**

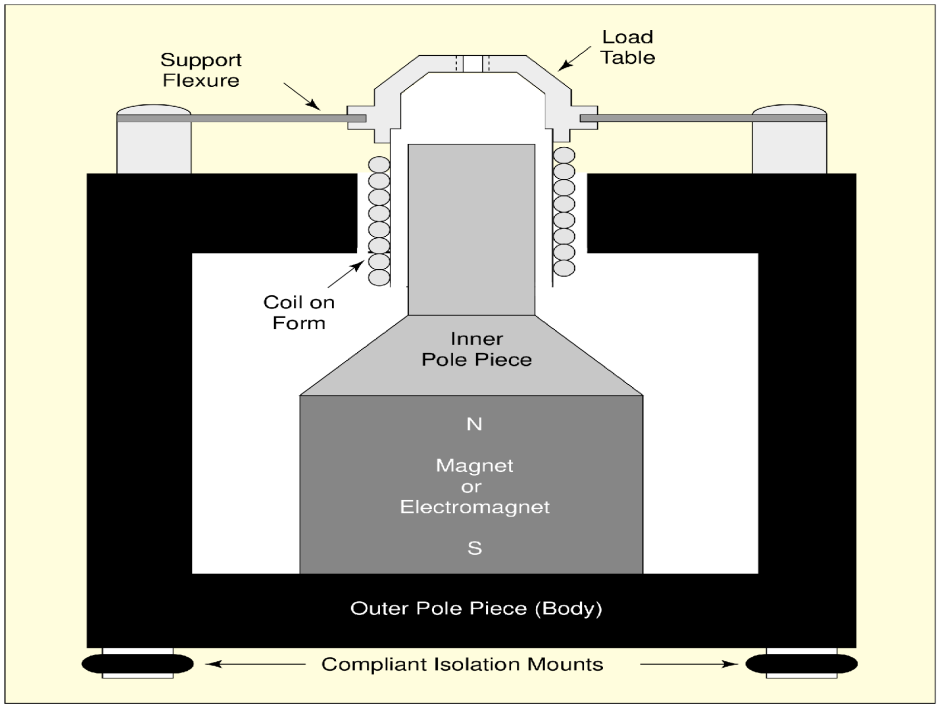

Figure 2.3: **Magnetic circuit used to create the intense magnetic field required by the shaker.** Soft iron pole pieces bend and concentrate almost all of the magnetic field into a very narrow gap. The armature coil is centered in this gap using support flexures. Figure taken from Lang & Snyder (2001).

transmits flux from one end of an axially magnetized permanent magnet or electromagnet, say, the North pole. A permeable "back structure" conducts flux from the opposite pole of the magnet to a permeable disk with a hole in its center surrounding the inner pole piece. This creates a radial flux field in the air gap between the round face of the North-polarized inner pole piece and the round hole in the South-polarized outer pole piece. The air-gap between these pole pieces is minimized to reduce the reluctance of the magnetic circuit, thus maximizing the intensity of the fixed magnetic field. If an alternating electric current is now allowed to flow in the suspended coil, then the coil is subjected to an axial force in proportion to the current, and consequently, it will develop vibratory motion. This is the principle of the electromagnetic shaker. This motion is transmitted to a table structure on which the test article may be affixed.

We have employed a shaker procured from Ling Dynamics System (Brüel & Kjær, Denmark). The performance parameters and characteristics of this shaker are:

- Sine Force (peak)-forced air cooled: $489N$
- Useful Frequency Range: $5\ Hz - 7.5\ kHz$
- Effective Mass of Moving Element: $0.426\ Kg$
- Velocity (sine peak): $2.5\ m/s$
- Maximum Acceleration (sine peak)-naturally cooled: $117g$
- Displacement (pk-pk)-continuous: $19\ mm$

- Armature Diameter: 63.5 mm

Rubber pads are placed between the trunnion base of the shaker and the floor to isolate the vibration from the ground, during the experiment.

2.2.2 Driving and Vibration Monitoring: Control Electronics & Software

During the experiment, the shaker works on a feedback-control mode. An piezoelectric accelerometer is mounted on the head expander that generates the feedback signal of the amplitude and frequency of the sinusoidal vibration. The signals from the accelerometer are sent to a control module and then compared to the pre-set parameters of the desired vibration profile. Any desired vibration profile that falls within the performance parameters of our shaker and power of the amplifier can be fed in the software interface stored in a Laptop. The control module then generates adjusted signals to the shaker. The signals from the control module are very weak and need to be amplified in order to drive the shaker. A power amplifier is employed to magnify these signals which are then put back to the shaker. The control module adjusts the acceleration of the vibration by varying the current in the suspended armature coil. Since the current in the armature coil only affects the force the shaker generates, the knowledge of the mass of the system being driven is needed for an accurate control. This is inspected during the initialization process of the shaker. During the initialization, a burst of vibration is applied to the system and the resultant accelerations are used to determine the mass of the system.

The specifications and performance characteristics of the controller, accelerometer, and power amplifier are provided in the following paragraphs.

Control-module

- Make: Ling Dynamics System (Brüel & Kjær, Denmark)
- Type: $COMET_{USB}$
- Analog input channels: Two inputs standard; differential inputs with 220 $kOhm$ impedance
- Input Harmonic distortion: $< -105\ dBfs$
- Analog output channels: One drive channel standard
- Output Harmonic distortion: $< -95\ dBfs$

Accelerometer

- Make: DeltaTron®, Brüel & Kjær, Denmark
- Type: Uniaxial Piezoelectric IEPE

Piezoelectric accelerometers use a spring-mass system to generate a force proportional to the amplitude and frequency of vibration. The force is applied to a piezoelectric element, which

produces a charge on its terminals that is proportional to the vibratory motion. Piezoelectric materials are self-generating and therefore do not require an external power source. IEPE accelerometers are special types of piezoelectric accelerometers with integral preamplifiers, which give output signals in the form of voltage modulation on the power supply line. They are hermetically sealed to protect against environmental contamination, have low susceptibility to radio frequency electromagnetic radiation, low impedance output, high signal-to-noise ratio, and wide bandwidth.

Amplifier

- Make: Ling Dynamics System (Brüel & Kjær, Denmark)
- Type: PA 1000L
- Rated Sinusoidal Power Output-matched resistive load: 1000 W
- Signal-to-noise Ratio: > 75 dB
- Total Harmonic Distortion-at rated output: Typically 0.2%
- Efficiency: 59%
- Overcurrent Trip Level: 19 A rms
- Rating: 1.4 kVA

Software

The software package includes two softwares, which allow to implement two types of operation modes for the shaker. Most of the experiments have been done with a sinusoidal wave form:

$$y = A\sin(2\pi ft), \tag{2.1}$$

where A is the amplitude of shaking and f is its frequency.

- **Value Swept Sine Software:** This software is used to set up a profile, wherein a range of frequency can be swept/ramped at a constant shaking amplitude (A) with any desirable sweep rate (linear as well as logarithmic), which in turn leads to the escalation of shaking intensity (Γ). The software allows to vary linear ramping rate from 0 to 6000 Hz/min, while logarithmic from 0 to 100 $octaves/min$. The frequency ramping rate adopted in most of the experiments is 0.01 Hz/sec. We found this sweep rate to be optimal for observing all phase transitions in detail. The frequency ramping can be performed both in the increasing direction (upsweeping) as well as in the decreasing direction (downsweeping). The maximum frequency f which can be attained (starting from a minimum frequency of 5 Hz) at a constant shaking amplitude (A) is limited by the maximum "g-level"($\equiv \Gamma$) and the peak sine force the shaker can achieve. Fig. 2.4 illustrates the maximum shaking frequency (f) which our shaker (LDS V456) can achieve at various constant shaking amplitudes for different payloads.

- **Sine Oscillator Software:** It is employed to vary the shaking amplitude (A) at a constant shaking frequency (f). In this mode, the shaker operates as an "open loop" system, wherein the accelerometer is used to measure the amplitude level of shaking. With the help of this program, the shaker can also be operated at a fixed shaking intensity (Γ) in a continuous run.

2.2.3 Visualization and Image Acquisition

The granular particles held in the vibrating container are illuminated with two white cold LED lights of $25W$, positioned at an oblique angle facing towards the container from both sides. Such type of lighting arrangement provided a uniform lighting over the region of interest. Most of the experiments reported in this thesis have been recorded at 1000 $frames/second$ and, due to the short exposure time involved ($< 1\ ms$), an intense light source is needed to capture bright images. Such type of lighting arrangement is good enough for this purpose.

We employed a high-speed camera to capture the temporal evolution of the collective motion of particles. The series of snapshots are grabbed in on-board camera memory and later on transferred to computer via USB for post-processing and data analysis.

The specifications of the high-speed camera are detailed as follows:

- Make: IDT MotionPro Y4S3
- Maximum frames per second (fps) @ Maximum Resolution: $5100 fps$ @ 1016×1016
- Plus Mode: 9820 fps @ 1016×1016
- Maximum frame rate at reduced resolution: 200000 fps @ 1016×16
- Minimum Exposure Time: 1 μs
- Sensor Type: CMOS-Polaris II
- Sensor Size: $13.9 \times 13.9\ mm$
- Sensitivity: 6000 ISO Mono, 2000 ISO Color
- Pixel Size: $13.68 \times 13.68\ \mu m$
- Pixel Depth: 10 bit mono, 30 bit color
- HDMI: 30 fps
- Memory: In-built 8 GB

2.2.4 Granular Particles

We used various types of spherical balls as granular materials, to conduct the experiments. These precision balls were imported from Italy (*R.G.P. International, Cinisello Balsamo, Italy*). The details of these balls, namely, diameter, density, grade, and sphericity tolerance are summarized in Table C.18.

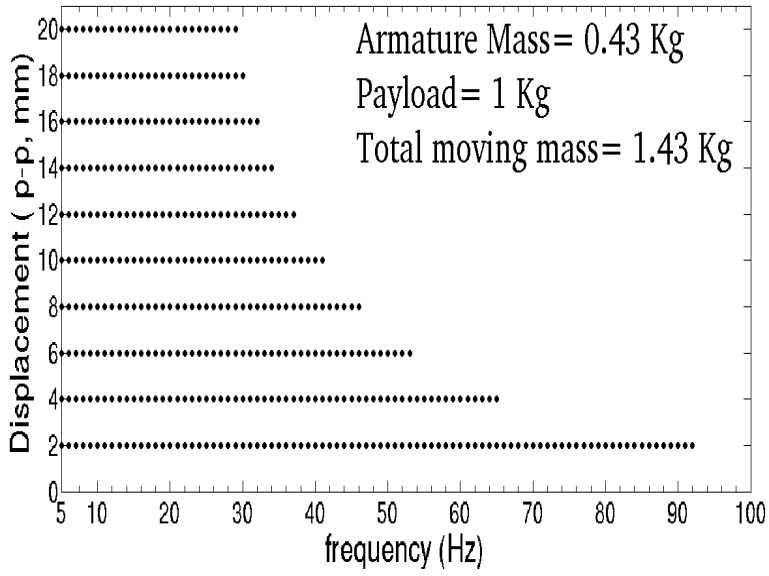

(a)

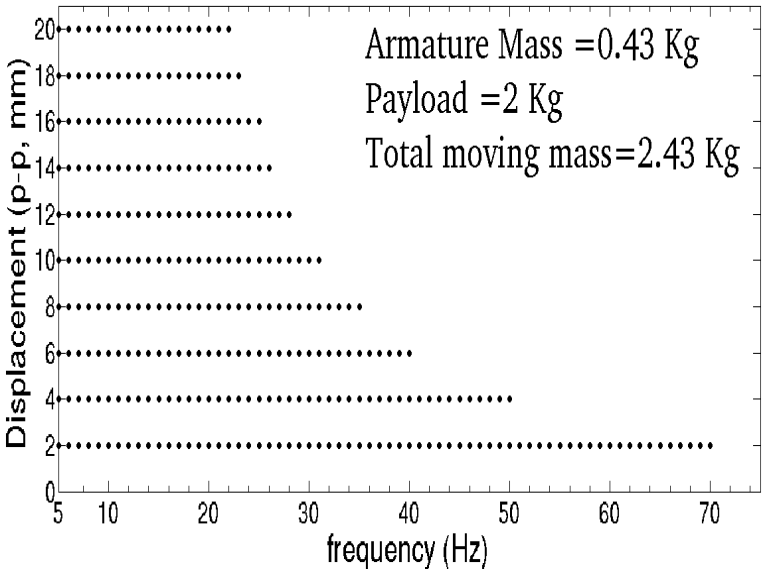

(b)

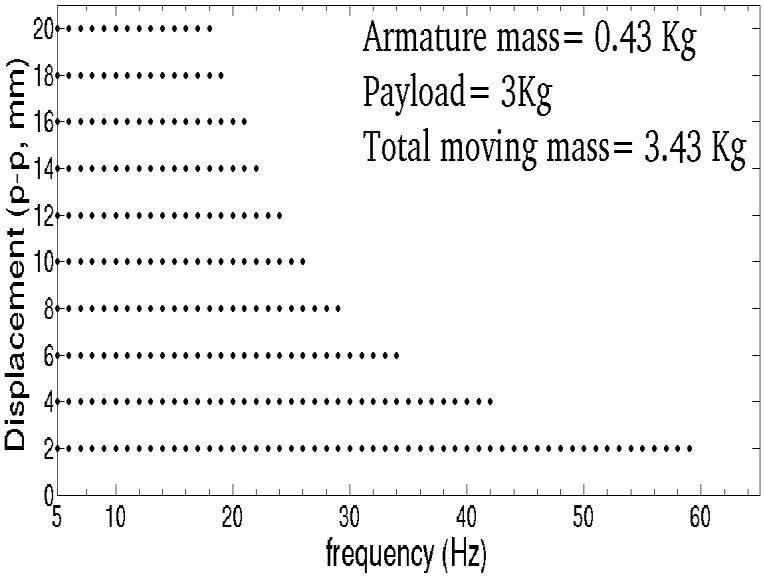

(c)

Figure 2.4: **The maximum frequency limit which can be achieved at a constant shaking amplitude A with our shaker model (LDS-V456) for various payloads: (a) 1 Kg, (b) 2 Kg, and (c) 3 Kg.** Armature is the moving element of the shaker and its mass must be included while determining the total mass which the shaker has to push on.

Material	**Diameter** (mm)	**Density** (Kg/m^3)	**Grade**	**Sphericity Tolerance** (μm)
Soda Lime Glass Balls	1.0	2500	G 500	10
Soda Lime Glass Balls	2.0	2500	G 500	10
Soda Lime Glass Balls	5.0	2500	G 200	5
Stainless Steel Balls 440C	0.5	7650	G 10	0.25
Stainless Steel Balls 440C	1.0	7650	G 10	0.25
Brass Balls	1.0	8650	G 1000	0.2

Table 2.1: **Specifications of the various particles used.**

Although these particles are of high precision and sphericity tolerance, we still looked into the level of polydispersity of these particles. To quantify the size polydispersity in the particle lot of a particular type, we obtained their particle size distibution with the help of image processing and *ImageJ* software. ImageJ is a public domain, Java-based image processing program developed at the National Institutes of Health, USA. It has extensive image analysis and enhancement capabilities. Fig. 2.5 displays a sample of raw snapshots of different types of particles, considered for the image analysis. These images are captured with a *Nikon D5200-SLR* camera (CMOS sensor having 24.1 Megapixel resolution), held almost perpendicular to the plane of particles.

To process such images a series of transformations have been applied to the original colour frame, see Fig. 2.6. Initially, the hue and saturation values of the images were adjusted to enhance their colours. After this, the image was *despeckled* to smoothen and then *outliers* were removed. These options are present under *Process* tab in *Noise* menu. Finally, the image was thresholded, i.e., any pixel below a certain threshold was assigned a value of 0 and above this threshold value, a value of 1. This yielded the binary image (refer Fig. 2.6(b)) where a pixel value of 0 (black) corresponds to the background and a value of 1 (white) to the particles. This processed image was then analyzed with the *Analyze Particles* option present in *ImageJ*. The analyzed particles are shown in Fig. 2.6(c), wherein they are labelled, as well as, have edges outlined. This analysis yielded the 2-D projected area of the particles in $pixel^2$, from which the diameter of particles were determined. The diameter is then calculated from *pixel* to mm with the help of the scale for the conversion of image-coordinate to world-coordinate. Several types of images with different lots of particles have been analyzed to obtain the histogram of their size distribution, see Fig. 2.7

In this thesis, we studied the following three types of mixture:

- **Mixture 1**: Steel Spheres (1.0 mm diameter)+ Glass Spheres (1.0 mm diameter)
- **Mixture 2**: Brass Spheres (1.0 mm diameter)+ Glass Spheres (1.0 mm diameter)
- **Mixture 3**: Brass Spheres (1.0 mm diameter)+ Steel Spheres (1.0 mm diameter)

In addition, 2.0 mm and 5.0 mm diameter glass beads are used to study the dynamics of 1-D vibrated granular system.

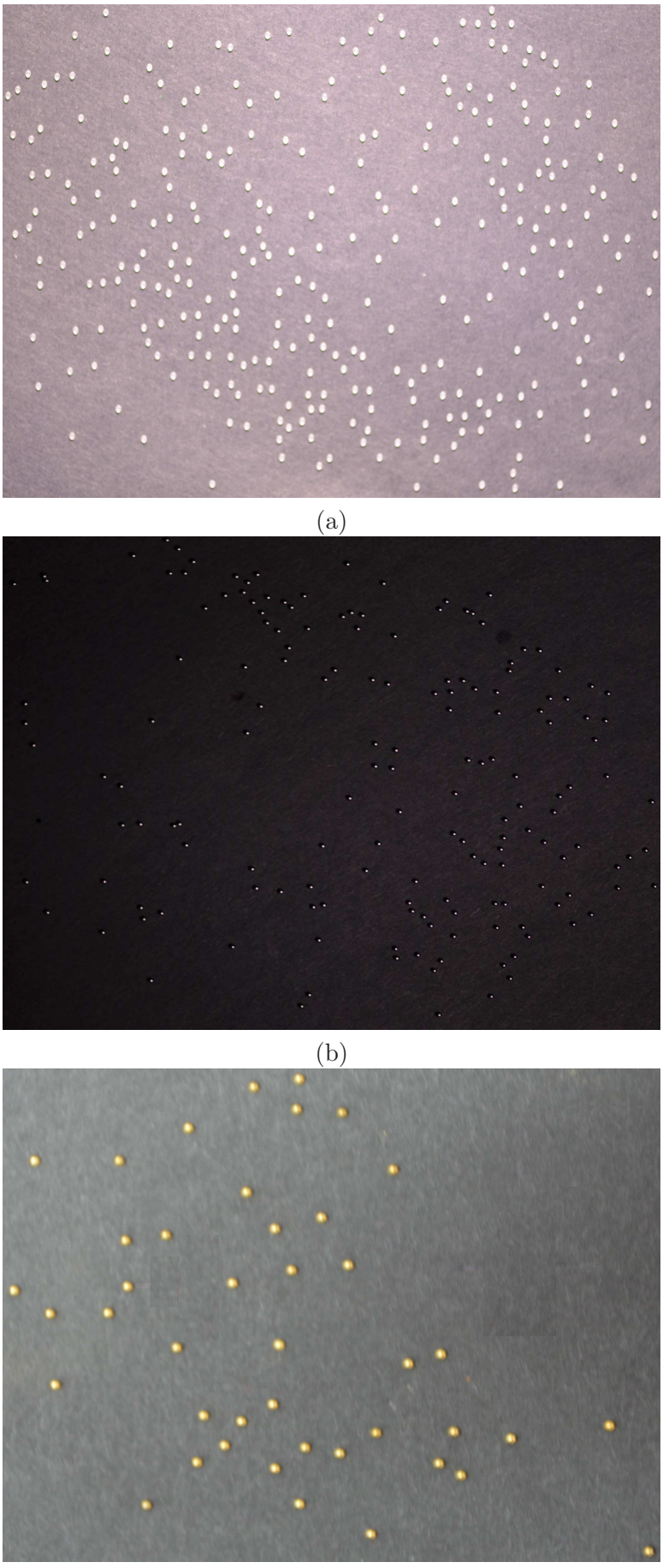

(a) (b) (c)

Figure 2.5: **The raw snapshots of bunch of spherical particles (diameter $d = 1.0\ mm$) having following materials: (a) Glass, (b) Steel, and (c) Brass.**

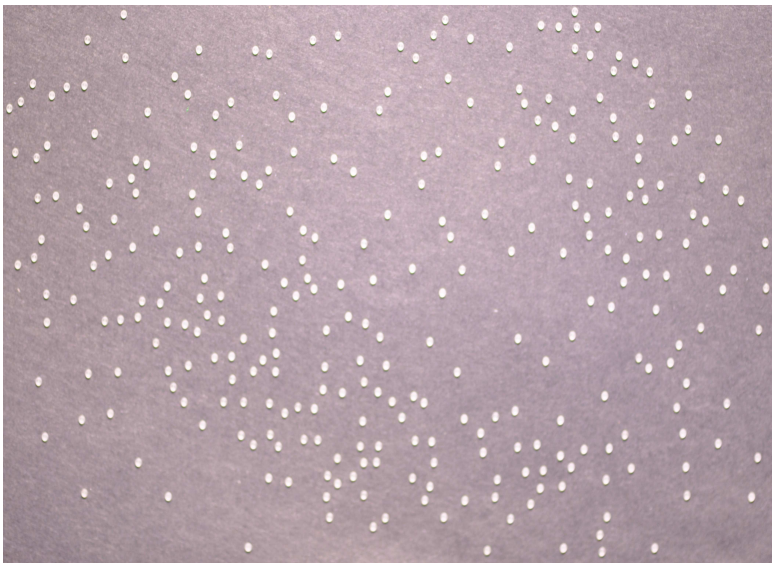

(a)

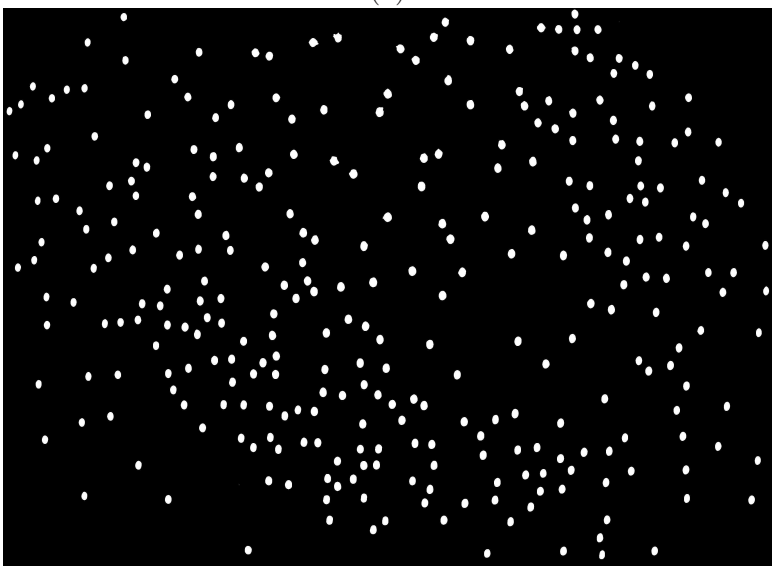

(b)

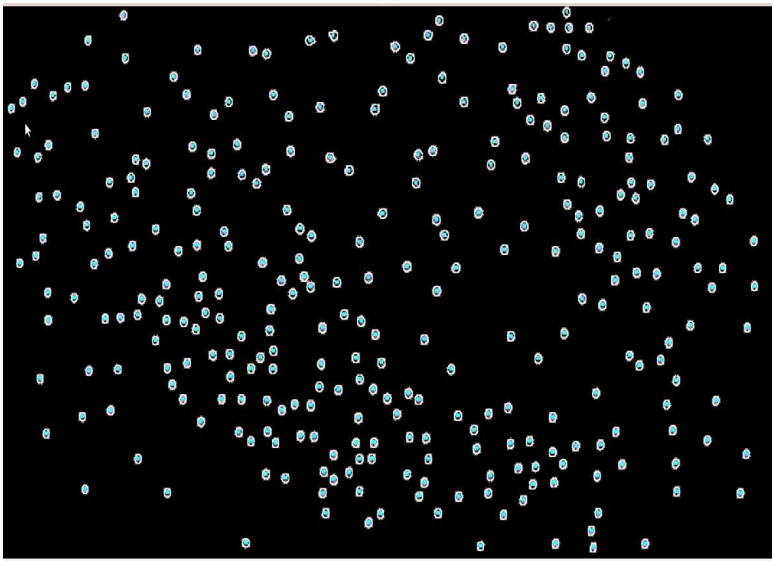

(c)

Figure 2.6: **Image processing sequence of the snapshot for analyzing the particles:** (a) the original colour frame, (b) processed frame after despeckling, removing outliers and thresholding, and (c) analyzed particles are shown labelled with their edges outlined.

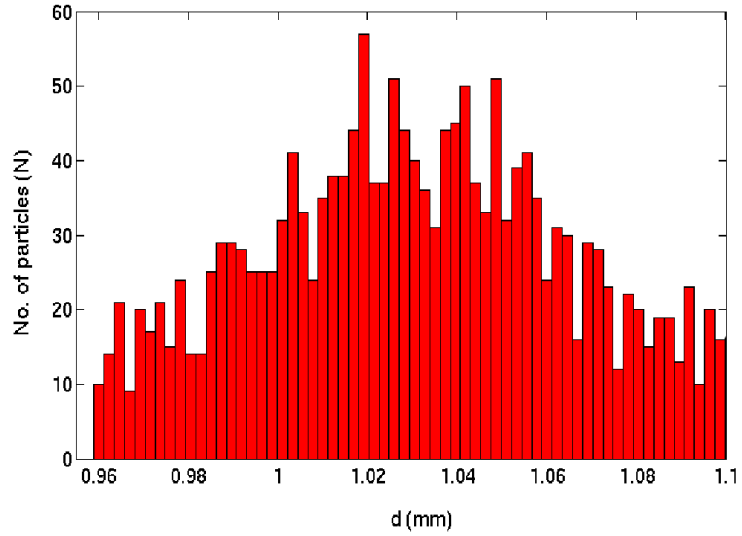

(a)

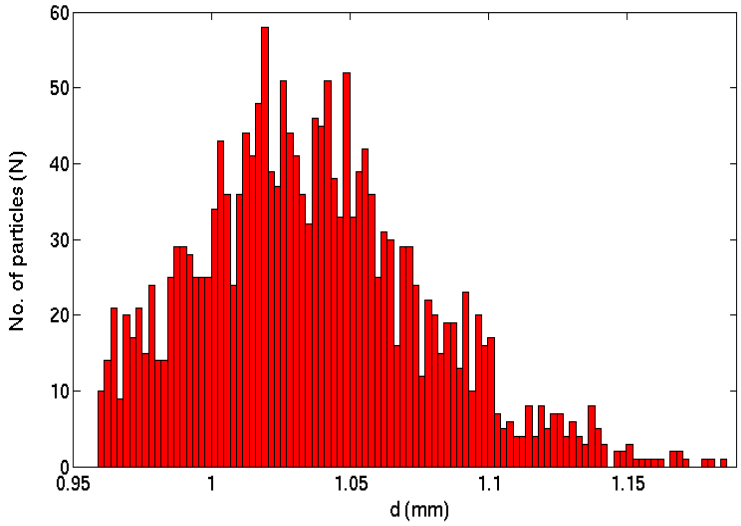

(b)

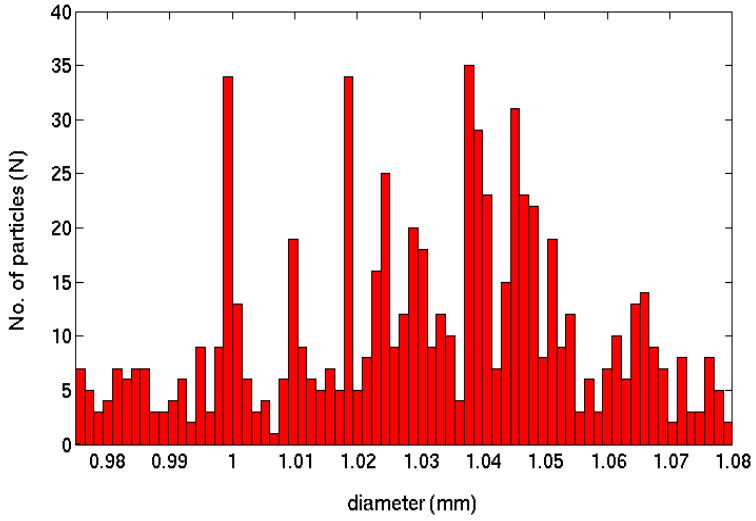

(c)

Figure 2.7: **Histogram of particle size distibution for various types of spherical particles:** (a) glass particles having mean diameter 1.038 *mm* and a standard deviation of 4.8%, (b) steel particles having mean diameter 1.036 *mm* and a standard deviation of 4.7%, and (c) brass particles having mean diameter 1.025 *mm* and a standard deviation of 5.8%.

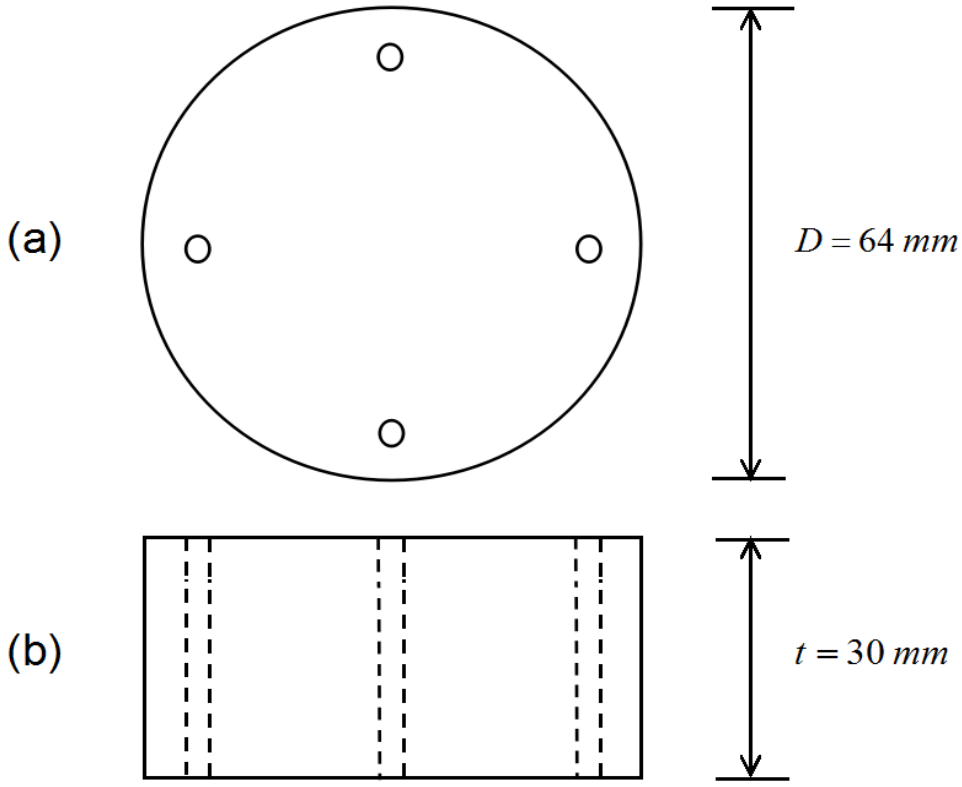

Figure 2.8: **Design aspects of head expander: (a) top view, (b) front view.** The dashed lines in the front view represent the through-hole drilled in the head expander (four holes in the top view), for fastening it on the armature of the shaker.

2.2.5 Design of Head Expander and Container

The container specimen is mounted on the shaker via a head expander. The head expander is manufactured from light-weight aluminium, providing high strength-to-weight ratio. They are employed to hold a broader mounting surface container and also to vibrate it at higher amplitudes without striking with the body of the shaker. The head expander is mounted on the shaker armature with the help of four fastening screws that passes through the hole pattern matching that of armature. The design of head expander is displayed in Fig. 2.8

The container used for holding granular material is fabricated from Plexiglas® sheet of 3 *mm* thickness. Plexiglas® is the trade name of Poly(methyl methacrylate) (PMMA), and is a transparent thermoplastic often used in sheet form as a lightweight and shatter-resistant alternative to soda-lime glass. The container is having a rectangular base as shown in Fig. 2.9. In our experiments we varied the length (L) as well as the width W of the container to study the pattern formation dynamics.

2.2.6 Design of Evacuated Container

A set of experiments has been conducted with the granules being vibrated in an evacuated container at low pressures, in order to examine the influence of interstitial air on the particle and segregation dynamics, and on the hysteresis involved in the phase transitions (see Chapter 5). The vacuum is created inside the container by employing a rotary vane vacuum pump. Rotary

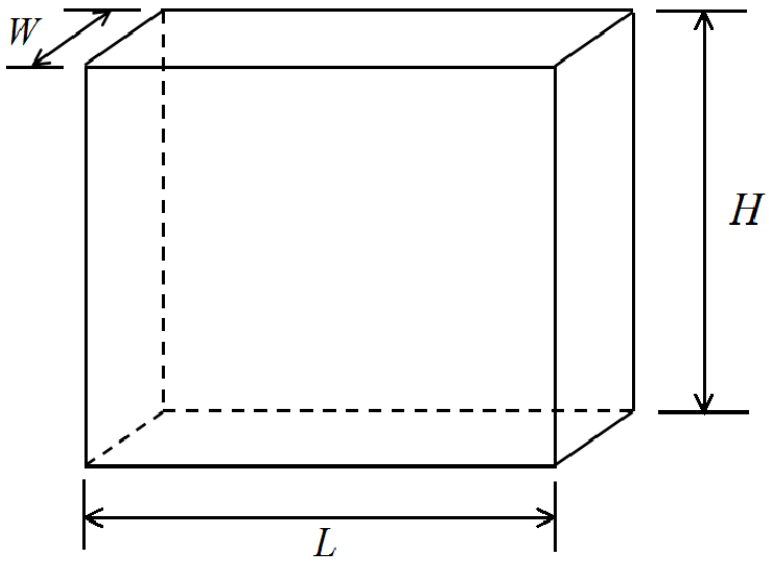

Figure 2.9: **Design of rectangular Plexiglas® container for holding granular material.**

vane vacuum pump is a common type of vacuum pump, with single-stage pumps able to reach pressures down to 0.3 *mbar*. The pump is connected to the container through a control-module which can adjust the pressure inside the container at a desired vacuum-level. The vacuum build up inside the container can be read on a digital vacuum gauge.

To vacuum seal the container from the atmosphere, we have to incorporate certain modifications in its design. A rubber O-ring is installed in a groove carved on the top surface of the container and the top lid is tightly pressed gainst it with the help of aluminium tightening clamps screwed on the container side-walls, as shown in Fig. 2.10(a). The O-ring was lubricated before installation, so as to avoid its damage by abrasion and rubbing. A fine nylon mesh is also installed at the hole made for fitting the vacuum pipeline on the top lid. This mesh filters out dust particles and micro oil droplets, that can be produced by the working fluid (oil) of the pump.

2.3 Experimental Procedure

A pre-weighed amount of a granular material that corresponds to a certain number of layers $F = h_0/d$ (h_0 is the granular bed height at rest) is poured into the rectangular Plexiglas® container. The particle-filled container is mounted on the electromagnetic shaker and vibrated harmonically along the vertical direction with a sinusoidal waveform (see Fig. 2.11):

$$y = A \sin \omega t, \tag{2.2}$$

where A is the shaking amplitude and $\omega = 2\pi f$ is the shaking angular frequency (f being the shaking frequency). The ratio of the horizontal vibration amplitude to the vertical vibration amplitude is measured and found to be less than 3%.

Most of the experiments reported in the thesis are performed by increasing the shaking frequency (f), while maintaining the shaking amplitude (A) to be constant. This consequently

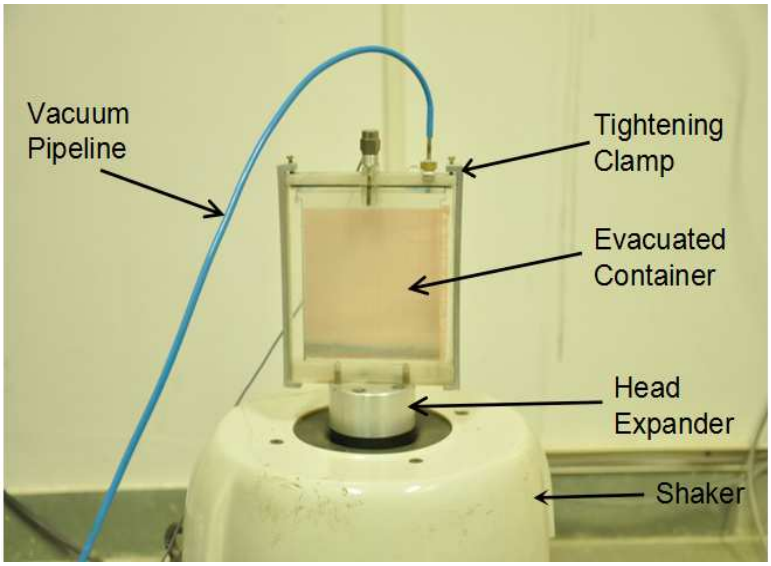

(a)

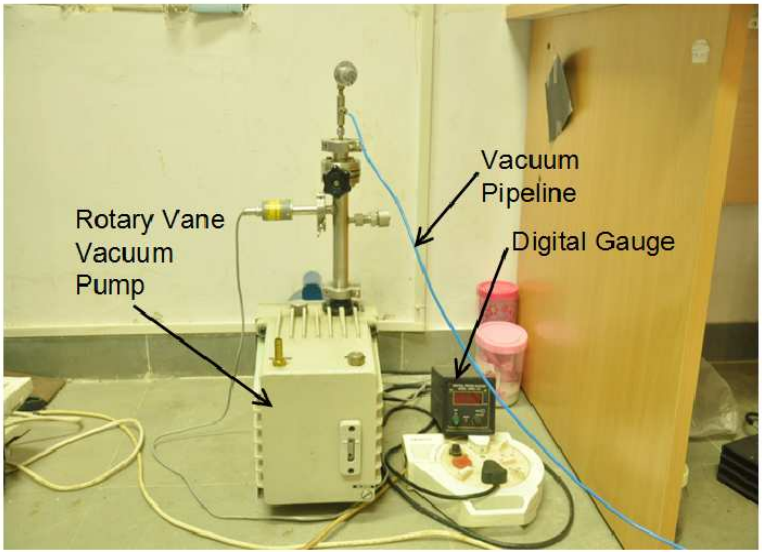

(b)

Figure 2.10: **(a) Container evacuated with air at very low pressure, (b) Rotary vane vacuum pump employed for generating vacuum inside the container.** The vacuum pump is linked to the container through a control assembly that can regulate the vacuum inside the container.

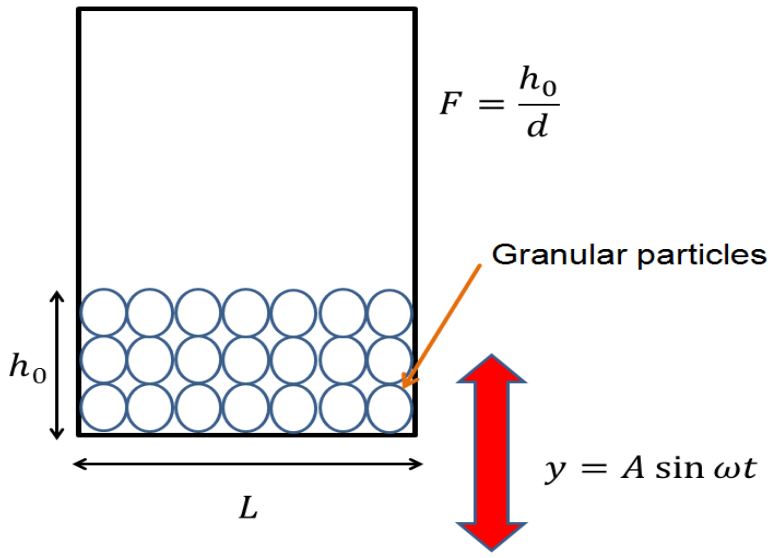

Figure 2.11: **Sketch of container filled with granular particles.** The container is shaken harmonically in vertical direction with a sinusoidal waveform, $y = A \sin \omega t$, where A and ω are the shaking amplitude and angular frequency.

results in the escalation of the shaking acceleration/intensity ($\Gamma = A\omega^2/g$) at a constant A. Such type of frequency ramping at a fixed shaking amplitude (A) is possible by operating the shaker system in a "closed-loop", and controlled by the control-module through *Value Swept Sine Software*. The frequency can be ramped in a logarithmic or a linear fashion, though we adopted linear frequency sweeping for our experiments. Almost all the experiments are conducted with a linear sweep rate of 0.01 Hz/s, unless stated otherwise. The results are found to be qualitatively similar for a ramping rate of 0.1 Hz/s, but we found differences for faster ramping rates (1.0 Hz/s or higher). To assess the stability of the observed patterns, many experiments were repeated at fixed Γ for at least 30 minutes [$> O(10^4\tau)$, where $\tau = 1/f$ is the time-period of shaking]. Aforementioned shaker operation at fixed Γ is achieved by the application of *Sine Oscillator Software*.

2.3.1 Setting the Initial Configuration of the Mixture

To inspect the hysteresis accompanied while phase transitions (Chapter 5), experiments were performed by first increasing the frequency upto the maximum limit, and then decreasing it therefrom. Upsweeping experiments were done with an initial configuration of homogeneously mixed mixture of two species of the binary mixture, and the final state of each upsweeping experiment is used as the initial state for its downsweeping evolution at the same rate of frequency ramping. To check the dependence of observed patterns on the initial state of homogeneous mixing, all experiments were also repeated with segregated initial states: (i) steel particles on top of glass particles, and (ii) glass particles on top of steel particles; the observed patterns are found to be qualitatively similar.

2.3.2 Control Parameters involved in the Experiments

The various dimensionless control parameters that govern different phenomena and are used to analyze the experiments are discussed as follows.

- **Dimensionless shaking acceleration or shaking intensity:** To quantify the effects of vibration on the dynamic behavior of particles, the dimensionless shaking intensity is usually adopted. It is the ratio of peak acceleration in a harmonic motion and the gravitational acceleration,

$$\Gamma = A\omega^2/g, \tag{2.3}$$

  where, A is the shaking amplitude, $\omega = 2\pi f$ is the shaking angular frequency (f being the shaking frequency), and g is the acceleration due to gravity. When the dimensionless acceleration exceeds unity, the free surface of a vertically vibrated bed becomes unstable and exhibits a variety of intriguing and complex phenomena, which we will discuss throughout whole of this thesis.

- **Number of particle layers (F) filling the container:** The number of layers of particles that is confined inside the container is given by,

$$F = h_0/d, \tag{2.4}$$

  where, h_0 is the bed height at rest. The number of layers filling the container is not counted, since it is cumbersome, rather we calculated the weight of the granular particles corresponding to a certain number of layers (F) in a particular dimension container and poured that much weight in the container. In binary mixture case of equal sized particles, the total number of particle layers (F) is determined as,

$$F = F_1 + F_2 = h_T/d = h_1/d + h_2/d, \tag{2.5}$$

  where, h_1, h_2 and $h_T = h_1 + h_2$, refer to the heights of species 1 and 2 and the total height at rest, respectively. In equimolar binary mixture case, $F_1 = F_2$.

- **Dimensionless shaking amplitude:** It is defined as the shaking amplitude (A) normalized with the particle diameter (d). We performed the experiments by varying this A/d withing a certain range (this range is limited by the maximum shaking amplitude A at which the shaker can vibrate), and found the paramater A/d to be crucial in studying the pattern formation. The dependence of the onset/suppression of phenomena on A/d, will be clearly evident and illustrated by the phase diagram constructed in $(\Gamma, A/d)$-plane.

- **Number fraction of species in the mixture (F_i/F):** The *number fraction* of a species in the mixture may be defined as the number of layers of that consituent species divided by the total layers of all the constituent species in the mixture, F_i/F. Since, in this thesis, we dealt only with the binary mixture case, therefore, $i = 1, 2$ and $F = F_1 + F_2$. We assessed the effect of varying number fraction of the species in the mixture $F_i/F \in (0, 1)$ and allegorized the phases observed on a phase diagram in $(\Gamma, F_i/F)$-plane.

- **Density ratio of species in the mixture:** The *density ratio* of the two species has also turned out to be a vital control paramater governing the segregation dynamics of the vertically vibrated granular mixture. For studying its role, we considered three types of binary mixtures of equal sized particles ($d = 1.0\ mm$): (i) steel and glass (density ratio, $\rho_s/\rho_g \approx 3.06$), (ii) brass and glass ($\rho_b/\rho_g \approx 3.46$), (iii) brass and steel ($\rho_b/\rho_s \approx 1.13$).

- **Aspect ratio of the container:** The geometrical dimensionless parameter, the *aspect ratio*, may be defined as,

$$\alpha = L/H \tag{2.6}$$

  where L and H are the length and vertical extent (height) of the container. We employed containers of various aspect ratios, wherein we only changed the length of the container, while the height is found to play an insignificant role (the height of the container is large enough so that even at maximum fluidization the system behaves as "open-top"). All of the 'single-phase' patterns are found to persist even in very small length container (we went down to $L = 20\ mm$), except the phase coexisting patterns whose origin is tied to the horizonatal segregation of two species. Thus, it can be inferred that the segregation dynamics in horizontal direction depends on the length of the container as we shall see in Chapter 5.

2.4 Data Analysis

In most cases, the temporal evolution of the dynamical patterns has been recorded at 1000 $frames/sec$. The images were analyzed to yield information on the onset value of Γ for different types of patterns and their characteristics (sub-harmonic or synchronous, segregation, and coexistence of different phases).

2.4.1 Particle Image Velocimetry

Particle Image Velocimetry (PIV) is an optical method of flow visualization extensively used in education and research. It is used to obtain instantaneous velocity measurements and related properties in fluids. PIV relies on examining images in sequence to determine particle movement. The fluid is seeded with tracer particles, which for sufficiently small particles, are assumed to faithfully follow the flow dynamics (the degree to which the particles faithfully follow the flow is represented by the *Stokes number*). The fluid with entrained particles is illuminated so that particles are visible. The motion of the seeding particles is used to calculate speed and direction (the velocity field) of the flow being studied.

PIV can also be used to measure the velocity field of the free surface and basal boundary in granular flows such as those in shaken containers, tumblers and avalanches. This analysis is particularly well-suited for opaque media such as sand, gravel, quartz, or other granular materials that are common in geophysics. This PIV approach is called "granular PIV". The set-up for granular PIV differs from the usual PIV setup in that the optical surface structure which is produced by illumination of the surface of the granular flow is already sufficient to detect the motion. This means one does not need to add tracer particles in the bulk material. Successful

-1	0	1
-2	0	2
-1	0	1

(a)

1	2	1
0	0	0
-1	-2	-1

(b)

Table 2.2: **Sobel Kernel**: (a) Horizontal, G_x, and (b) Vertical, G_y.

applications of the PIV technique to granular materials were reported recently for some systems, such as convection rolls in a vertically shaken granular matter (Garcimartin *et al.* 2002; Shukla *et al.* 2014), flowing granular layer in a rotating tumbler (Jain *et al.* 2002), avalanches on a rough inclined surface (Andreotti & Douady 2001), and stripe formation (Deng & Wang 2003). Lueptow *et al.* (2000) discussed the principles of the PIV applications in granular materials and implemented them in the heap formation.

The coarse-grained planar velocity field of particle motion in our experiments was determined by analyzing the images using a commercial PIV (Particle Image Velocimetry) software: "Dynamic Studio Software, Version 3.3" of Dantec Dynamics A/S, Denmark (Dantec Dynamics A/S 2012). The velocity field was calculated using an adaptive correlation technique (Dantec Dynamics A/S 2012; Scarano & Riethmuller 2000), in which the size of the interrogation window is varied adaptively from 64×64 to 16×16 pixels, with 50% overlap.

A batch of acquired image frames are imported into the database of the software. First of all, a calibration step is adopted, which will transfer velocities (displacements) from the unit of $pixel/s$ $(pixel)$ into m/s (mm); this is done by comparing the pixel distance between two points marked on the image and their corresponding real distance on the object. Before the raw image can be used for further analysis, it has to be processed by a suitable filter to remove the noise. The image may be corrupted by random variations in intensity, variations in illumination, or poor contrast that must be dealt with in the early stages of image processing. The Image Processing Library (IPL) module of "Dynamic Studio Software" features various type of filters: Low-pass, High-pass, Low-pass & Morphology (enhance image contrast), Signal processing (for non-linear calculations), Utility, Threshold, and Custom Filter (allow filtering with user defined filter kernels). After enhancing the contrast of the image, we pass the image through *Sobel filter*. This filter is found to be appropriate and reasonable for most of our images. The convolution kernel of *Soble filter* in horizontal and vertical directions is:

Having estimated the (signed) gradients in both horizontal and vertical direction, the final result is calculated as the total magnitude of the local gradients:

$$Sobel = \sqrt{G_x^2 + G_y^2} \tag{2.7}$$

If the image is still having some noise of very small pixel values, the Image Arithmetic option can be used, provided by the software. With the help of this option a constant pixel value can be substracted from the pixel values of the whole processed image; thereby suppressing the undesired features of image, which can be detected as particles. The processed images (separated by a time-interval of 1 ms, in most of our case) are now analyzed with *Adaptive Correlation Technique*. The adaptive correlation method calculates velocity vectors with an initial interro-

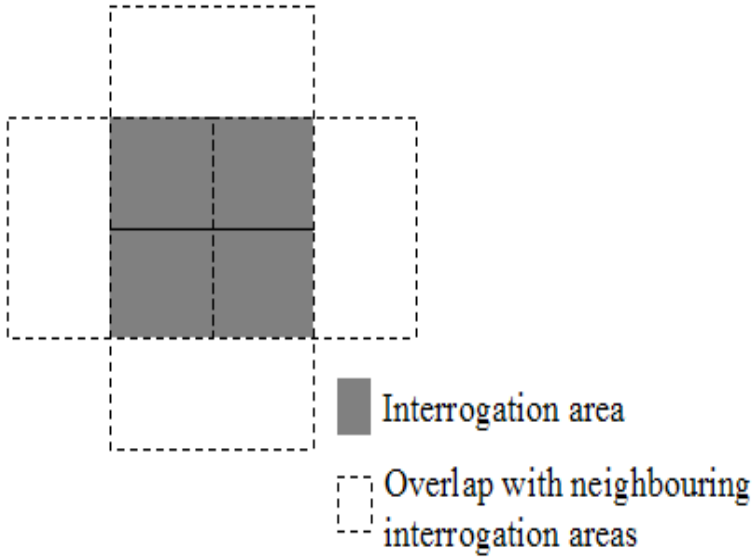

Figure 2.12: **Sketch showing the interrogation area (IA) and its overlap with neighbouring IAs.**

gation area (IA) of the size N time the size of the final IA and uses the intermediary results as information for the next IA of smaller size, until the final IA size is reached. Additionally, local validation can be added to the adaptive correlation so that viewed on all the calculations process, less 'bad' vectors are generated. To compensate for the loss of vector field resolution during the processing, overlap of IA is often used. This overlap can be set independently for the horizontal and vertical direction, offering total freedom to increase vector map resolution in any direction (refer Fig. 2.12). We found 50% overlap (in both directions) of IA to be optimal. The parameters we used for IA size in case of 1.0 mm diameter granular particles are:

- Maximum IA size: 64×64 pixels
- Grid step size: 16×16 pixels
- Minimum IA size: 16×16 pixels

Validation parameters for the adaptive correlation method are various and can also be used in combination to fine-tune the processing and, when needed, to remove spurious vectors. In the "Peak validation" section, the user can set values for the minimum and the maximum peak widths, as well as, the minimum peak height ratio (between 1st and 2nd peak), and thereby put more stringent conditions on peak identification for the subsequent determination of vectors. With "Local neighborhood validation", individual vectors are compared to the local vectors in the neighborhood vector area, whose size $(M \times M)$ is set by the user. If a spurious vector is detected, it is removed and replaced by a vector, which is calculated by local interpolation of the vectors present in the $(M \times M)$ area. Interpolation is performed using median or moving average methodology (with n iterations). Spurious vectors are identified via the value given to the "Acceptance factor". This factor effectively allows a given degree of freedom on velocity vector gradient inside the $(M \times M)$ area and if the calculated gradient is larger than set, the central vector is removed. The larger this factor is, the less the velocity vector map is spatially

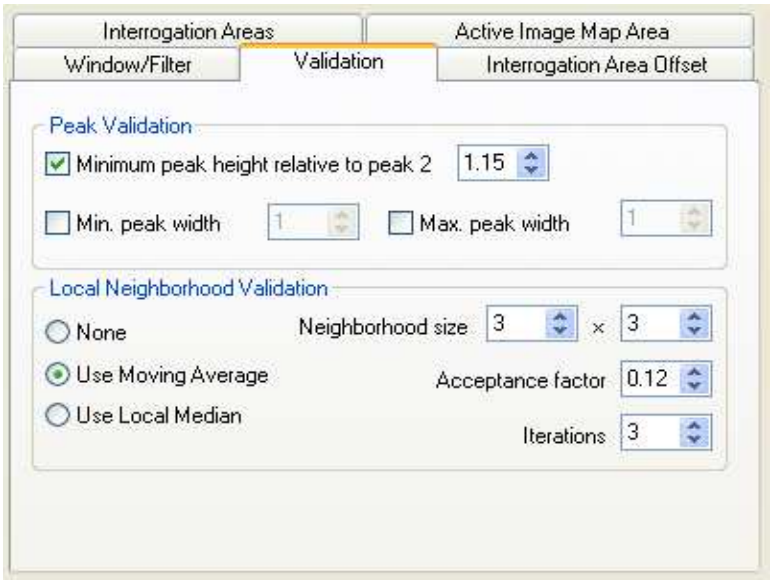

Figure 2.13: **Various validation settings employed for PIV analysis, using adaptive correlation methodology.**

corrected. The various parameters we typically employed for the validation method is displayed in Fig. 2.13.

2.4.2 Particle Detection and Tracking

To measure the velocity of the granular particles and thence the granular temperature T, the particles detection and their position information frame by frame, is required to be extracted. In this method, individual particles are tracked, so this technique is a Lagrangian approach, in contrast to PIV which is an Eulerian method that determines the velocity field of a fluid/granular flow at a grid.

Particle tracking velocimetry (PTV) has been applied for granular temperature measurements in various granular systems: chute flow (Drake 1991; Natarajan *et al.* 1995), vibro-fluidized beds (Warr *et al.* 1995; Wildman *et al.* 1999; Wildman & Huntley 2000; Feitosa & Menon 2002; Tai & Hsiau 2004; Yang 2006), sheared granular flow (Hsiau & Jang 1998; Hsiau & Shieh 2000), granular flow down an inclined plane (Azanza *et al.* 1999; Capart *et al.* 2002; Blair & Kudrolli 2003; Armanini *et al.* 2005; Perng *et al.* 2006; Armanini *et al.* 2008), and liquid fluidized beds (Capart *et al.* 2000; Spinewine *et al.* 2003). In this technique, granular flow is recorded using high speed cameras. The recorded movies are analysed frame by frame to reconstruct long-term trajectories of individual particles by matching particle positions at each successive frame of the movie. Various image analysis methods have been used to obtain the particle position on each frame, such as centroid (Drake 1991; Feitosa & Menon 2002; Azanza *et al.* 1999; Blair & Kudrolli 2003), Hough transform (Warr *et al.* 1995; Wildman *et al.* 1999), Voronoï imaging (Capart *et al.* 2002; Armanini *et al.* 2005; Perng *et al.* 2006; Armanini *et al.* 2008; Capart *et al.* 2000; Spinewine *et al.* 2003), and autocorrelation analysis method (Natarajan *et al.* 1995; Tai & Hsiau 2004; Hsiau & Jang 1998; Hsiau & Shieh 2000). Once the image analysis is completed, the particle coordinates are inputted to particle-tracking routines which calculate the velocities

of particles in all frames.

A number of particle tracking routines have been developed by various research groups and available as an open-source, in addition to commercial softwares. In our study, we employed *Particle Detector and Tracker* open-source distribution. It is an *ImageJ Plugin* for particles detection and tracking from digital videos. This plugin implements the feature point detection and tracking algorithm as described in Sbalzarini & Koumoutsakos (2005). It presents an easy-to-use, computationally efficient, two-dimensional, feature point-tracking tool for the automated detection and analysis of particle trajectories as recorded by high speed imaging. The feature point tracking problem consists of detecting images of particles in a digital image sequence and linking these detections over time to follow the tracks of individual particles. Applications of feature point tracking are numerous in several fields of science and technology, for e.g., particle imaging velocimetry, particle tracking velocimetry (Wereley *et al.* 2002) and colloids (Crocker & Grier 1996).

The method of particle detection and tracking with the use of *Particle Detector and Tracker* plugin can be splitted into two parts: Particle Detection, and Particle Linking. First of all the image sequence is imported in *ImageJ* and then the plugin is started by selecting *Particle Tracker* from the *Plugins* $->$ *Particle Detector & Tracker* menu. After starting the plugin, a dialog screen is displayed. The dialog has two parts "Particle Detection" and "Particle Linking".

Particle Detection

This part of the dialog allows to:

- Adjust parameters relevant to the particle detection (feature point detection) part of the algorithm
- Preview the detected particles in each frame according to the parameters. This options offers assistance in choosing good values for the parameters.

The parameters relevant for detection are:

- **Radius:** Approximate radius of the particles in the images in units of pixels. The value should be slightly larger than the visible particle radius.
- **Cut-off:** The score cut-off for the non-particle discrimination.
- **Percentile:** The percentile (r) that determines which bright pixels are accepted as Particles. All local maxima in the upper rth percentile of the image intensity distribution are considered candidate Particles.

Particle Linking

This part of the dialog allows one to adjust parameters relevant to the particle linking (trajectories generation) part of the algorithm. The parameters relevant for linking are:

- **Displacement:** The maximum number of pixels a particle is allowed to move between two succeeding frames.
- **Link Range:** The number of subsequent frames that is taken into account to determine the optimal correspondence matching

%% Trajectory 1

0	22.617294	73.313294	4.561034	2.671657	90.321267
1	24.122623	74.612540	5.141039	2.610912	65.146163
2	25.673120	75.342123	4.346390	2.631971	56.729148
3	23.791735	76.213571	5.248361	2.602398	71.546312
4	22.146812	77.146980	5.387131	2.591367	80.921311
5	24.142461	77.981467	4.779120	2.610781	30.147823

Table 2.3: **A sample trajectory file format.**

After setting all parameters, tracking can be started by clicking the *OK* button in the dialog window. Once tracking is finished, a trajectory file will be generated (refer Table 2.3). A trajectory will have at least two rows, each row representing a frame in this trajectory and holding the information about the particle related to this trajectory in that frame. The second and third columns contain the x and y coordinates of the particles, respectively. The x-axis points top-down and the y-axis is oriented left-right in the image plane. The fourth and fifth columns contain the intensity moments of order 0 and 2, respectively. The sixth column contains the non-particle discrimination score.

Chapter 3

Study of Vertically Vibrated Monodisperse Granular system

3.1 Introduction

In this chapter, we focus on the study of vertically vibrated monodisperse granular materials. We performed experiments on two types of monosperse system: (1) Glass particles of 1.0 mm diameter, and (2) Steel particles of 1.0 mm diameter. The particles were confined in a quasi two-dimensional Plexiglas® rectangular container whose aspect ratio is $L/W = 18.2$, where $L = 100$ mm is the length and $W = 5.5$ mm is the width of the container. The container has been clamped on the shaker, and for a constant shaking amplitude we increase the frequency f which in turn increases the shaking strength ($S = a^2\omega^2/gd = \Gamma * A/d$). The frequency can be increased at a constant shaking amplitude A/d (fixed at 3 in most experiments unless stated otheriwse) upto a maximum limit (upsweeping) depending upon the capacity of the shaker and can be decreased from this maximum limit (downsweeping). The ramping rate of frequency can be controlled in a very precise manner with the help of controller and software. Most of the experiments presented in this thesis had been performed at frequency ramping rate of 0.01 Hz/s unless stated otherwise. A comparison has been made between the phase diagrams obtained at 0.1 Hz/s and 0.01 Hz/s.

A variety of rich patterns has been exhibited by the vibrated granular bed and one type of phenomenon transits to another at a critical shaking strength. All patterns have been assimilated in a phase diagram in terms of dimensional shaking acceleration Γ versus particle loading F (see Fig. 3.14). The results are in confirmation with the experimental work of Eshuis *et al.* (2007) except the emergence of a subharmonic $f/4$ waves (Douady *et al.* 1989; Jaeger *et al.* 1996*a*; Ansari & Alam 2013) which eventually gives birth to an $f/2$-undulatory wave (UW), with increasing shaking intensity. We also performed experiments in the same box filled with $F = 25$ layers of 0.5 mm diameter steel particles and found only two states: *Bouncing Bed (BB)* and *Undulatory Waves (UW)* in contrast to 1.0 mm diameter particles where at higher shaking strengths system exhibits *Leidenfrost State (LS)*, *Gas* and *Convection*. The effect of the shaking amplitude A/d on the pattern formation dynamics has been studied with the help of phase diagrams obtained on $(\Gamma, A/d)$- plane.

3.2 Phase Diagram for Monodisperse Glass Particles

The phase diagram for glass particles ($\rho_g = 2500$ Kg/m^3) of 1.0 mm diameter is displayed in Fig. 3.1 for a linear sweep rate of 0.01 Hz/s. A variety of rich patterns are reported, which are discussed below.

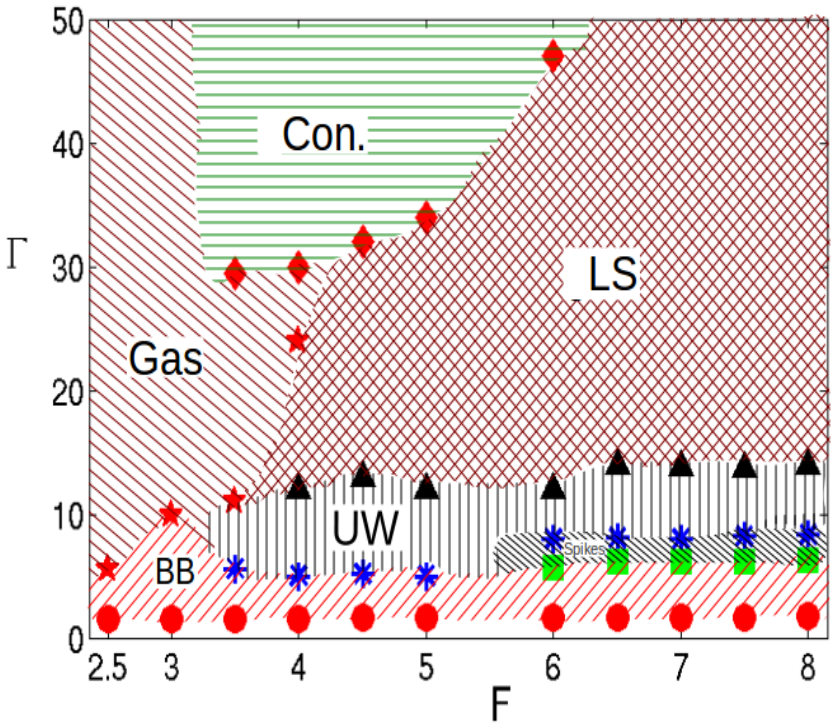

Figure 3.1: **Phase diagram in (Γ, F)-plane for 1.0 mm diameter glass particles confined in $L/d = 100$ box.** Regions of Bouncing Bed *(BB)*, *Spikes*, Undulatory Waves *UW*, granular Leidenfrost state *(LS)*, *Gas* and Convection (*Con.*) are marked; symbols represent approximate locations of transition while upsweeping at a fixed shaking amplitude $A/d = 3$ with the linear frequency-ramping of 0.01 Hz/s.

3.2.1 Bouncing Bed

For the whole range of $F = h_0/d$ (where, h_0 is the bed-height at rest and d is the particle diameter) with $\Gamma \leq 1$, the granular bed moves synchronously with the shaker motion without getting detached from the container base- this is the regime of *solid bed* (SB). As the shaking intensity is increased beyond some critical value ($\Gamma > 1$), the bed gets detached from the base and starts a collective motion resembling that of a single particle bouncing off a plate - this is the *Bouncing Bed (BB)* regime. The unshaded thin region below the bouncing bed regime in (see Fig. 3.1) represents the *SB* region. The three successive snapshots of the bouncing-bed regime at $t = 0$, $\tau/2$ and τ, where $\tau = 1/f$ is the period of shaking, are displayed in Fig. 3.2(a), (b) and (c),respectively. The corresponding coarse-grained velocity vector map for each image is also displayed below its raw image. It is observed that the directions of velocity vectors are primarily vertical, and the velocity vectors undergo a change in orientation (from upward to downward and vice versa) after every half time-period ($t = \tau/2$). This overall pattern repeats after every cycle ($t = \tau$), see Fig. 3.2(a-c). Therefore the bouncing bed is synchronized with the frequency of external shaking, and hence is also called an f-wave.

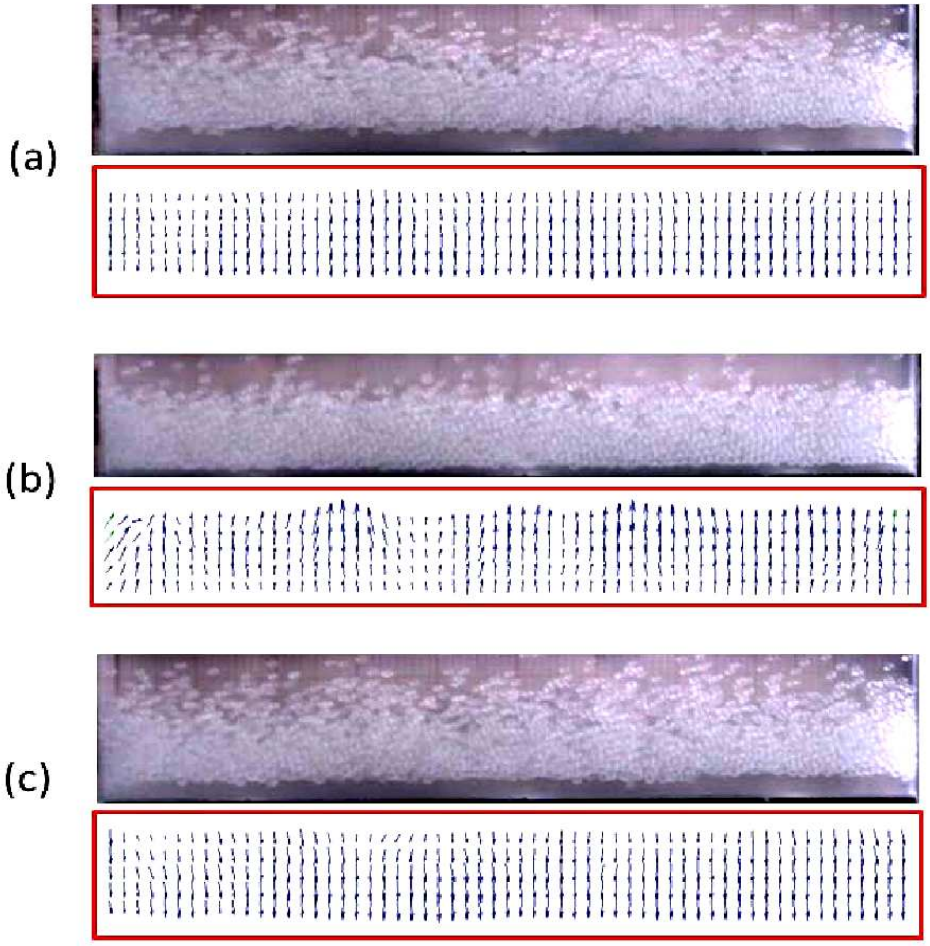

Figure 3.2: **Snapshots of the *BB* and its coarse- grained velocity field at three successive time instants of the cycle: (a) $t = 0\tau$, (b) $t = \tau/2$ and (c) $t = \tau$,** where $\tau = 1/f$ is the time period of shaking and $y = a\sin(2\pi ft)$. Parameter values are $F = 7$ and $\Gamma = 4.35$ ($A/d = 3.0$ and $f = 19\ Hz$).

3.2.2 Subharmonic Spikes

When the layer depth is large ($F > 6$), we found a new pattern, see Fig. 3.3, which is comprised of an array of peaked structures. These peaked structures seem to be quasi-2D analogue of oscillons (Umbanhowar *et al.* 1996) and are called "Spikes". They are characterized by a typical wavelength λ and a maximum peak height a (see Fig. 3.3). The maxima position (peak) exchanges with the minima (valley) in every two shaking periods (compare Fig. 3.3(a), Fig. 3.3(b) and Fig. 3.3(c)). In other words, these structures regain their shape after every four shaking periods, and hence they are also called $f/4 - waves$. The following features of these structures have been observed:

- During the free flight (ignoring boundary contacts) of the granular string (Fig. 3.4 at $t = \tau$), the amplitude of the peaks grows until the base of the container hits the bed (see Fig. 3.4(c)).
- The granular string is carried in the upward direction by the base, relaxing the peak amplitude.
- The maxima position (peak) exchanges with the minima (valley) in every two shaking periods (see Fig. 3.3 and Fig. 3.4).

Fig. 3.5 displays the velocity field obtained from each snapshot of Fig. 3.4 by PIV analysis. It is noteworthy that when the 'peak' of *Spikes* grows, the motion of the whole bed can be divided into two regions of opposite phases. The particles consituting the peak part keep surging in the upward direction until the 'peak' attains its maximum heght, while concurrently, the lower 'flat' part of the bed coherently moves in the downward direction. These features are clearly evident from PIV fields at $t = 0\tau$ and $t = 2\tau$, as shown in Fig. 3.5. A reversal of such type of scenario is also seen, when the 'peak' starts relaxing. During this case, the particles forming the peak structure streams down, while the lower 'flat' part of the bed collectively moves upward. Such type of opposite phase motion gives rise to the contraction of bed, leading to the birth of a compact granular string, as depicted in the snapshot of Fig. 3.4 at $t = \tau$.

These $f/4$ sub-harmonic spikes were not reported in recent experiments of Eshuis et al. (Eshuis *et al.* 2007) with a quasi-two dimensional box (same as in our experiments), but was found previously by Sano et al (Sano *et al.* 1999) in a three-dimensional experimental setup. A similar array of peaked structures was reported in the experiments of Clément *et al.* (1996) as well as in recent simulations of Carrillo *et al.* (2008); however, the frequency of the pattern was $f/2$ in both works and hence they correspond to a lower-order subharmonic wave and are fundamentally different from ours.

In our experiments the spikes ($f/4$ subharmonic- wave) emerged from the bouncing bed regime by gradually increasing the shaking strength for deep beds ($F \geq 6$) and for moderate values of Γ- the related phase- diagram in the (Γ, F)-plane is shown in Fig. 3.6. We found spikes only for larger values of shaking amplitudes ($A/d \geq 3$), whereas this pattern was not observed for smaller values of $A/d \leq 2$. It is seen in Fig. 3.6 that the Γ-value for the onset of spikes remains almost constant ($\Gamma \approx 7$) with increasing number of layers F. With further increase of Γ, there is a transition from spikes to undulatory waves that represent a lower-order ($f/2 - wave$) subharmonic wave as we discuss below.

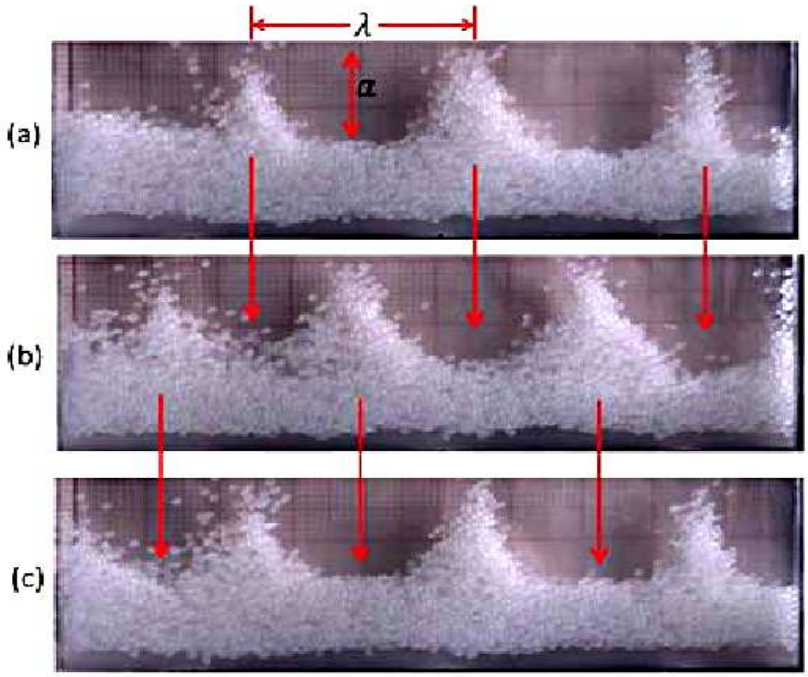

Figure 3.3: **Snapshots of sub-harmonic *Spikes* observed in $F = 9$ layers of 1.0 mm diameter particles at three successive time instants of the shaking cycle: (a) $t = 0\tau$, (b) $t = 2\tau$, and (c) $t = 4\tau$,** where $\tau = 1/f$ is the time period of shaking. Parameter values are $\Gamma = 8.35$ ($A/d = 3$ and $f = 26.31$ Hz). The 'peaks' exchange with the 'valleys' after two shaking cycles and the whole pattern repeats itself after four shaking cycles. Hence, these waves are also named as $f/4$-waves.

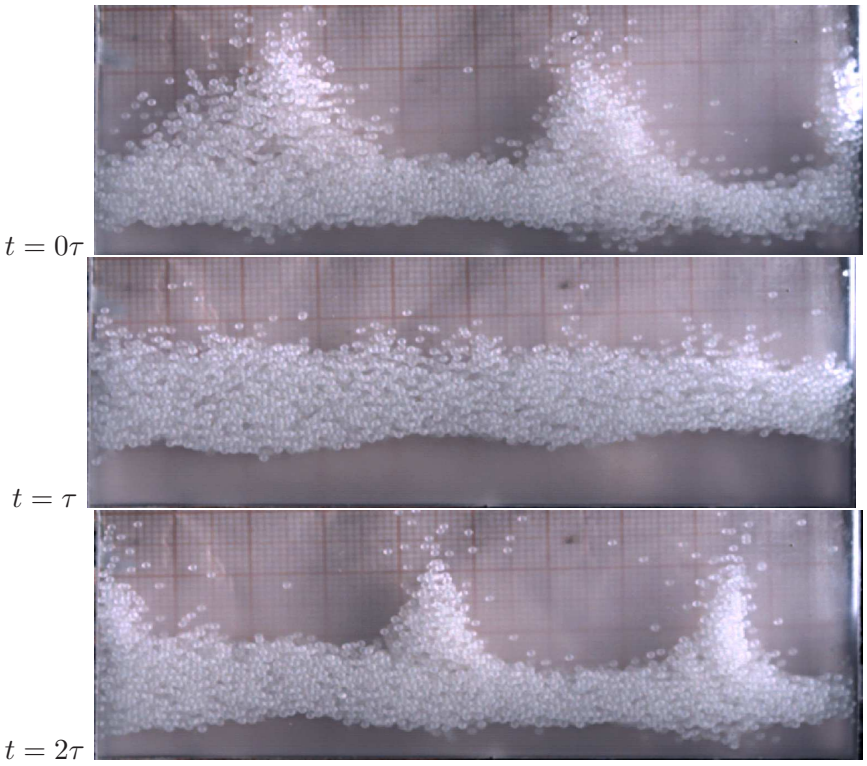

Figure 3.4: **Snapshots of $f/4$-wave (*Spikes*) showing exchange of maxima (peak) with minima (valley) (and vice versa) in two shaking periods for $F = 8$ layers of 1.0 mm diameter glass particles.** Parameter values are $\Gamma = 8.3$ ($A/d = 3.0$ mm and $f = 26.23$ Hz). It should be noted that after one shaking period the bed becomes completely flat.

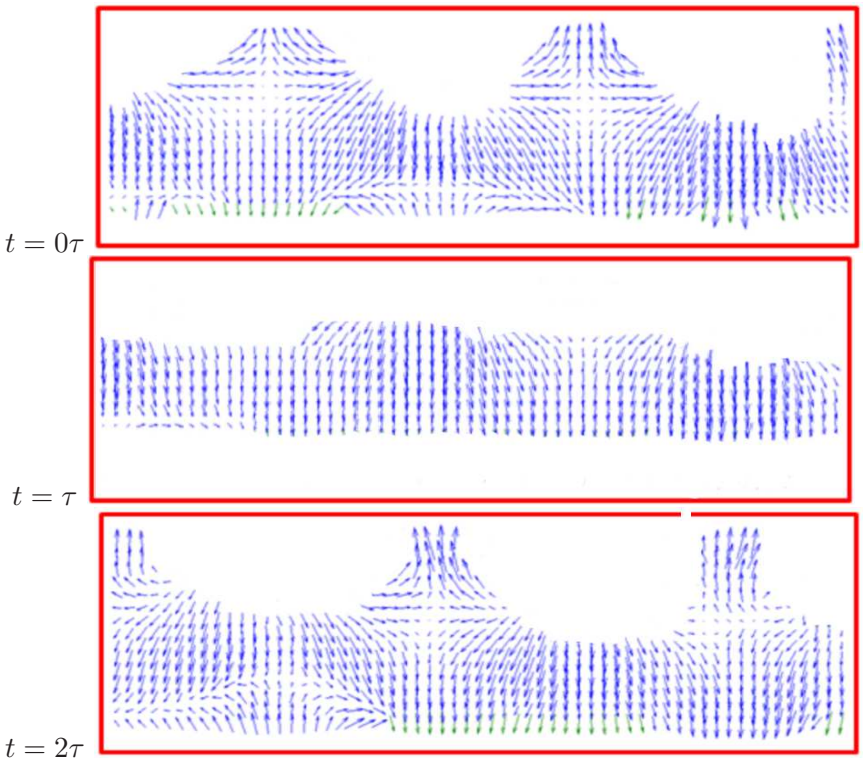

Figure 3.5: **Corresponding velocity field of Fig. 3.4.**

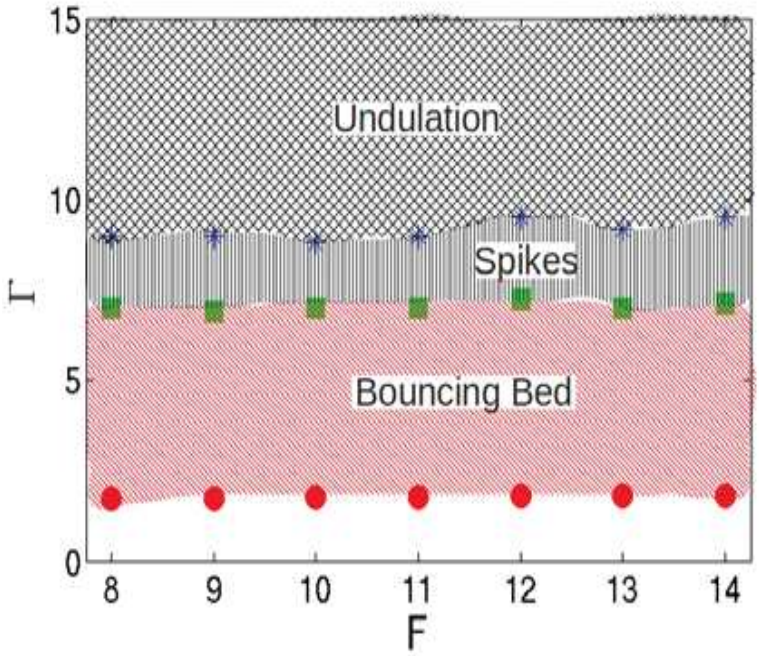

Figure 3.6: **Phase-diagram for large F and moderate values of Γ, displaying transitions from *BB* to *spikes* to *UW* at $A/d = 3$.** The critical shaking intensity Γ_c for the transition from *BB* to *Spikes* is almost constant with the increasing filling depth F while Γ_c for *Spikes* to *UW* shows variation.

3.2.3 Undulatory Waves

The undulatory waves are standing wave patterns exhibited by the granular bed similar to a vibrating string. Three successive snapshots of an undulatory wave are displayed in Fig. 3.7- they look similar to standing wave patterns exhibited by a vibrating string. The wavelength (λ) of the undulatory wave is defined such that $L = n\lambda/2$, where $n = 1, 2, ...$ is the mode-number and L is the length of the box; in other words, the mode number n corresponds to an integer of half wavelength of the undulatory-wave that can be accommodated in a box of length L. It is clear from Fig. 3.7 that the time-period of oscillation of these standing waves is twice the time period of shaking ($\tau = 1/f$) and this is why the undulatory waves are called $f/2 - waves$ (Eshuis *et al.* 2007; Melo *et al.* 1994; Sano 2005). When the bed of particles collides with the vibrating base of the container, it is subjected to horizontal dilatancy (Sano 2005), which causes the dilation of the string of particles in contact with the base. If this dilation crosses a certain threshold level, it will give rise to buckling of the string and the particles start following an arch shape.

Let s denote the position along the contour of the undulatory wave, and $\theta(s)$ be the angle which the bed makes with the horizontal at any position s as shown in Fig. 3.8; the equation for $\theta(s)$ is given by Sano (2005)

$$\frac{d^2\theta}{ds^2} = -\alpha^2 \sin\theta, \tag{3.1}$$

where $\alpha = \sqrt{R/EI}$, with R being the reaction force from the side walls on the bed, E the effective Young's modulus of the bed, I its moment of inertia. In small angle approximation (Eshuis *et al.* 2007) $\sin\theta \approx \theta$, the above Eqn. 3.1 transforms to harmonic oscillator equation:

$$\frac{d^2\theta}{ds^2} = -\alpha^2\theta. \tag{3.2}$$

Solving the above differential equation within proper boundary conditions ($\theta(0) = 0$ and $\theta(L) = 0$), we get

$$\theta(s) = C_2 \sin\left(\frac{n\pi s}{L}\right), \tag{3.3}$$

where C_2 is a constant of integration. Now, in small angle approximation $s \approx x$, i.e. the distance along the contour is approximately equal to horizontal distance. Thus, the vertical position of any point on the center of mass of undulatory wave is given by

$$y = C_2\left(\frac{L}{n\pi}\right)\left[1 - \cos\left(\frac{n\pi x}{L}\right)\right], \qquad n = 1, 2, 3... \tag{3.4}$$

3.2.4 Leidenfrost State

A liquid drop placed on a hot plate can float over its own vapor layer if the temperature of the plate exceeds a minimum value (Leidenfrost temperature)-this is the celebrated Leidenfrost effect (Leidenfrost 1756; Quere 2013). Expectedly, the Leidenfrost temperature is higher than the boiling point of the liquid, for example, $T_L \approx 200°C$ for water. When the temperature of the hot plate is less than the Leidenfrost temperature, the drop strews over the surface and rapidly

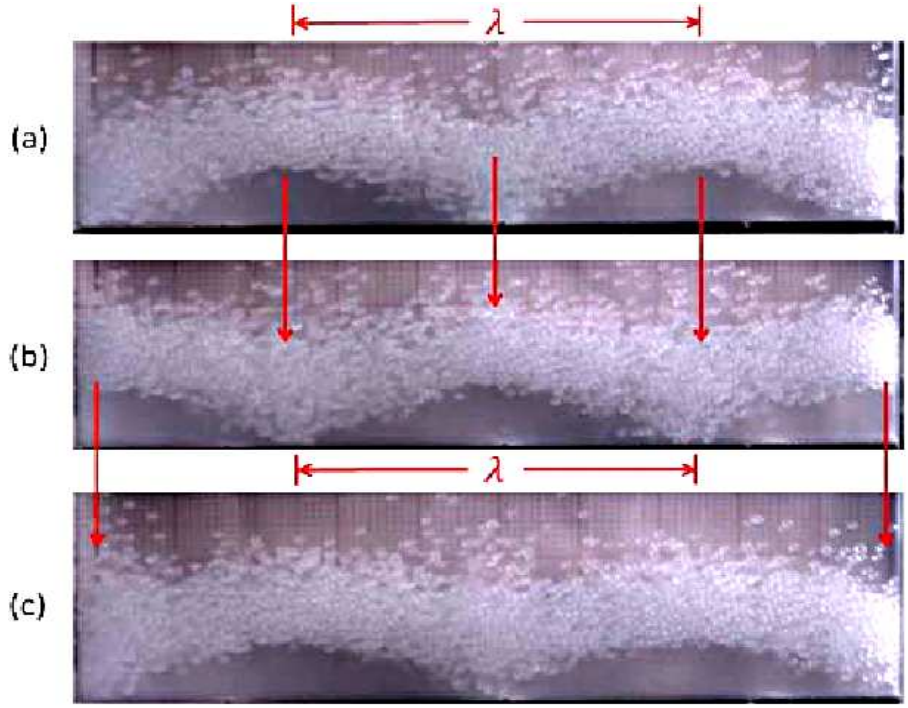

Figure 3.7: **Snapshots of UW ($n = 4$ mode) for $F = 7$ layers of $d = 1.0\ mm$ glass particles at three successive time instants of the shaking cycle: (a) $t = 0\tau$, (b) $t = \tau$ and (c) $t = 2\tau$.** Parameter values are $\Gamma = 12.35$ ($A/d = 3$ and $f = 32\ Hz$). The 'peaks' (maxima) exhange with the 'valleys' (minima) after each oscillation cycle and the whole pattern repeats itself after two oscillation cycles. Hence, these waves are also called $f/2$-waves.

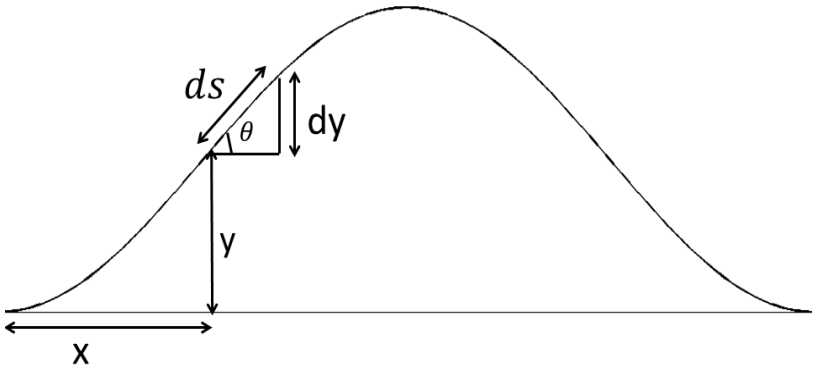

Figure 3.8: **Sketch showing an arc of "Undulatory Wave" (UW).** This contour corresponds to $n = 2$ mode.

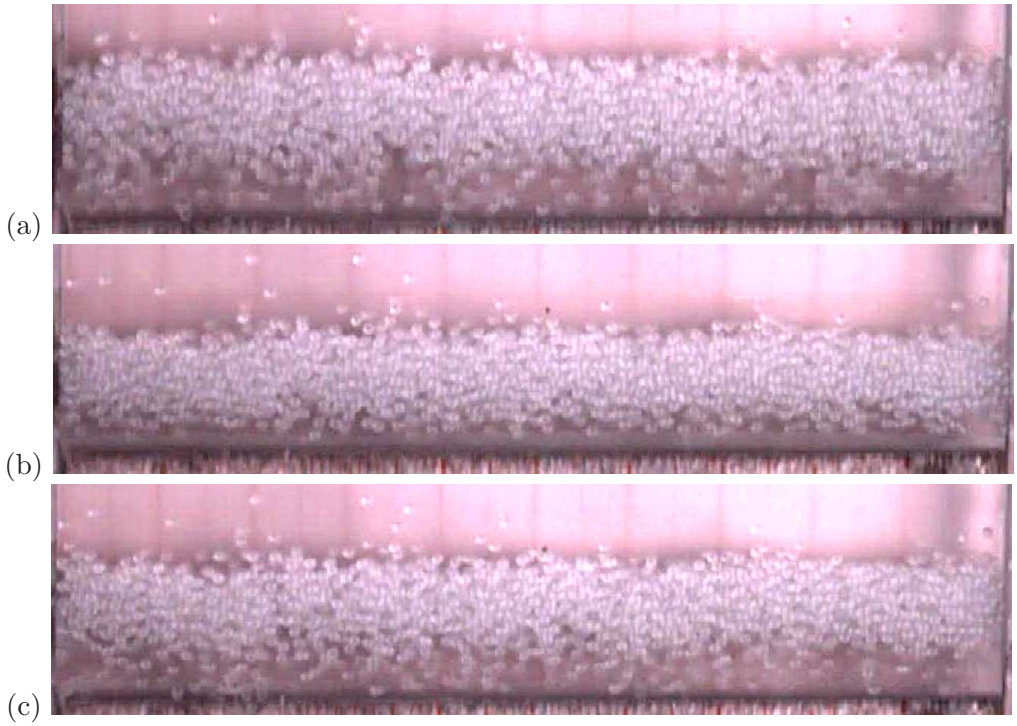

Figure 3.9: **Snapshots of granular Leidenfrost State (*LS*) observed in $F = 6$ layers of 1.0 *mm* diameter glass particles at: (a) $t = 0\tau$, (b) $t = 0.5\tau$, and (c) $t = \tau$.** Parameter values are $\Gamma = 40$ ($A/d = 3$ and $f = 57.59\ Hz$).

conducts heat through it, resulting in complete vaporization within a short time. However, when the plate temperature is above the Leidenfrost temperature, the bottom layer of the drop which is in contact with the plate vaporizes immediately and the gas pressure of this vapor layer acts as a cushion that helps the drop to stay in a floating state. Due to its poor conductance the vapor layer slows down the rate of heat transfer from the hot plate to the drop and hence the drop survives for a long time. Akin to the original Leidenfrost state, a dense, compact layer of particles can be supported by a dilute gaseous region of fast moving particles underneath it in vertically shaken granular materials. This was dubbed *granular Leidenfrost state (LS)* by (Eshuis *et al.* 2005) who established this connection first with the original Leidenfrost state in experiments on vertically vibrated bed of a mono-layer of glass beads in a quasi-two-dimensional cell. More specifically, they found that a dense region of particles with crystalline-type structure floats over a granular gas at moderate values of shaking intensity. Previous molecular dynamics (MD) simulations had also predicted the possibility of such extreme density inversion (Lan & Rosato 1995*b*) or floating-cluster (Meerson *et al.* 2003) in a similar setup.

Fig. 3.9 depicts the snapshots of the granular *Leidenfrost State* at three successive time instants of the shaking cycle $t = 0\tau$, $t = 0.5\tau$ and $t = \tau$, wherein a dense compact layer of particles is floating over a dilute gaseous region of fast moving particles underneath it. The PIV anlysis of its hydrodynamic velocity field, Fig. 3.10, indicates correlated motion of the bed suggesting a *liquid-like* state of the granular *Leidenfrost state*.

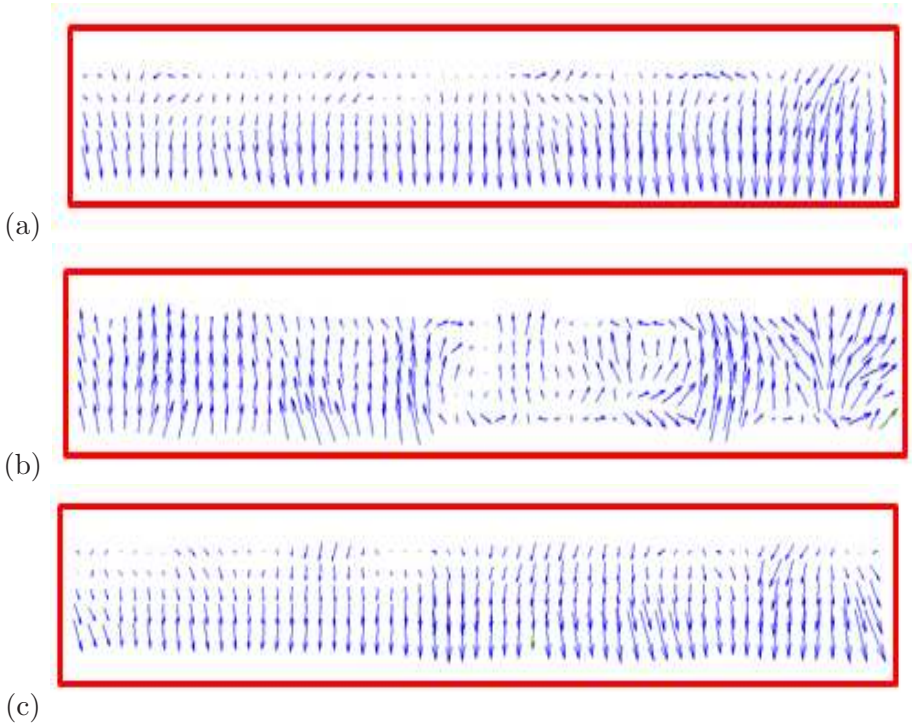

Figure 3.10: **Instantaneous coarse-grained velocity fields for the snapshots of *LS* shown in Fig. 3.9 at: (a) $t = 0\tau$, (b) $t = 0.5\tau$ and (c) $t = \tau$.**

3.2.5 Convection

When the shaking strength is increased from the Leidenfrost regime, a convection pattern with counter-rotating rolls emerges, as shown in the raw snapshot of particles in figure (see Fig. 3.11); the value of the shaking strength is S = 150. The pictures such as in Fig. 3.11 were subsequently analysed with the aid of PIV (particle image velocimetry) software (Ansari & Alam 2013). The corresponding velocity-vector map is displayed in see Fig. 3.12 , which shows six counter-rotating rolls. It should be noted that Fig. 3.12 represents an instantaneous velocity map implying that we have not made any temporal averaging but only spatial averaging with a variable spatial box of 16 pixels × 16 pixels to 64 pixels × 64 pixels. Approximately 10 pixels corresponds to one particle diameter $d = 1.0\ mm$.

These convection rolls are similar to Rayleigh-Bénard convection rolls in a classical fluid heated from below, where the onset of instability in fluid motion is controlled by the Rayleigh number which is the ratio of buoyancy force to the dissipative force (Chandrasekhar 1961; Bodenschatz *et al.* 2000; Ahlers *et al.* 2009). Granular convection has been extensively studied experimentally (Clément & Rajchenbach 1991; Knight *et al.* 1993; Ehrichs *et al.* 1995; Aoki *et al.* 1996; Knight *et al.* 1996; Hsiau & Chen 2000; Wildman *et al.* 2001), numerically (Gallas *et al.* 1992; Taguchi 1992; Luding *et al.* 1994*a*; Aoki & Akiyama 1994; Ramírez *et al.* 2000; Sunthar & Kumaran 2001; Talbot & Viot 2002; Cordero *et al.* 2003), and theoretically (Hayakawa *et al.* 1995; He *et al.* 2002; Ohtsuki & Ohsawa 2003; Khain & Meerson 2003; Miao *et al.* 2004). These studies dealt with mild fluidization for which convection is nearly boundary-driven (such boundary-driven convection occurs at lower values of $\Gamma < 5$ in a small-aspect-ratio box), and induced by friction at two side walls (Gallas *et al.* 1992; Luding *et al.* 1994*a*) but the convection

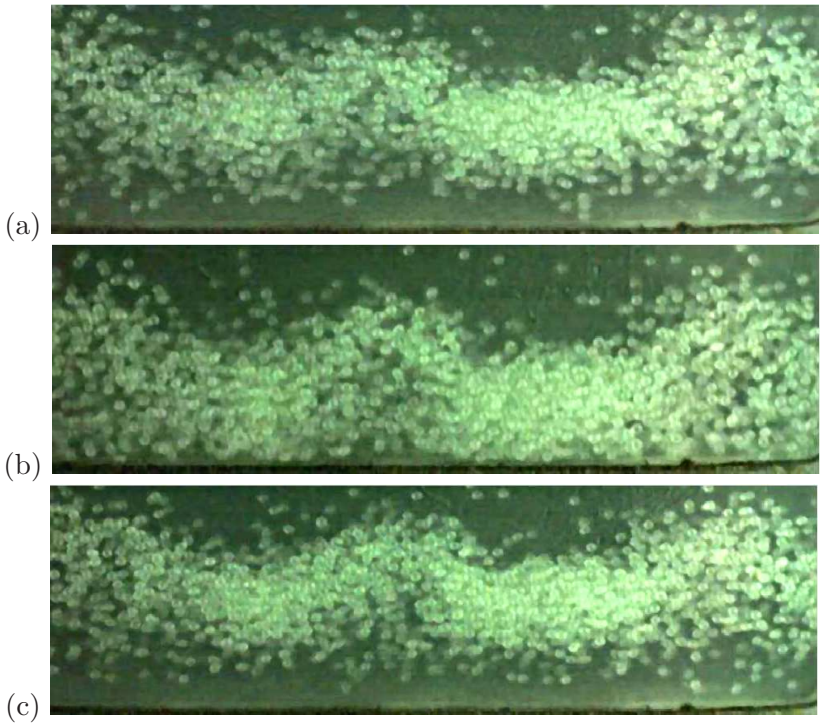

Figure 3.11: **Snapshots of granular convection (*Con.*) observed in $F = 6$ layers of 1.0 *mm* diameter glass particles at: (a) $t = 0\tau$, (b) $t = 0.5\tau$, and (c) $t = \tau$.** Parameter values are $\Gamma = 50$ ($A/d = 3$ and $f = 64.35\ Hz$) and hence the shaking strength is $S = \Gamma * (A/d) = 150$.

we observed is buoyancy-driven and occurs at strong fluidization ($\Gamma > 25$) showing large density differences, similar to Eshuis *et al.* (2007, 2010). Such type of convection was first reported by Ramírez *et al.* (2000) in molecular dynamics simulations of inelastic hard disks in a box with top and bottom thermal walls that were maintained at different granular temperatures. The resulting flow patterns with convective cells show a striking resemblance to those in classical Rayleigh-Bénard convection (Chandrasekhar 1961). The experimental work of Wildman *et al.* (2001) on harmonically shaken particles in a cylinder (with open top) showed strong evidence of buoyancy-induced convection, although the walls might have played some role in these experiments.

We observed multiple convection rolls spanning whole length of the container resembling those of Eshuis *et al.* (2007). Multiple convection rolls were predicted earlier in two-dimensional particle dynamics simulations by Bizon *et al.* (1998); Sunthar & Kumaran (2001). Unlike in a classical fluid, where convection is governed by the competing effects of buoyancy versus viscous and thermal diffusion only, the granular convection also depends crucially on inelastic dissipation. One noteworthy difference with Eshuis *et al.* (2007) is that we found the transition to convection regime from both Leidenfrost state and gaseous state (discussed in section 3.7). In contrast, Eshuis *et al.* (2007) found this transition occuring from the Leidenfrost state as well as from the bouncing bed state.

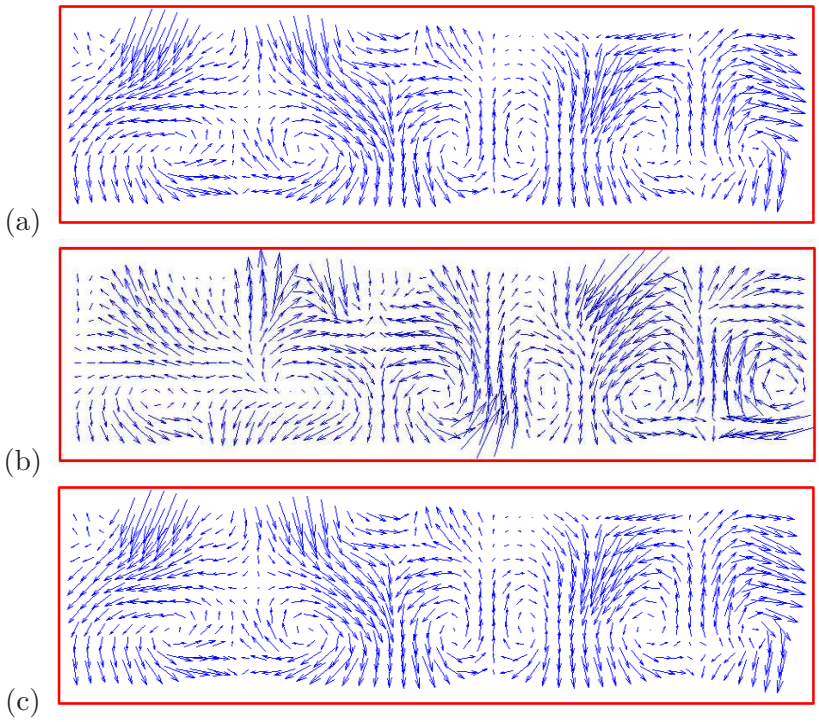

Figure 3.12: **Instantaneous coarse-grained velocity fields for the snapshots of convection shown in Fig. 3.11 at: (a) $t = 0\tau$, (b) $t = 0.5\tau$ and (c) $t = \tau$.** The velocity field shows six counter-rotating rolls.

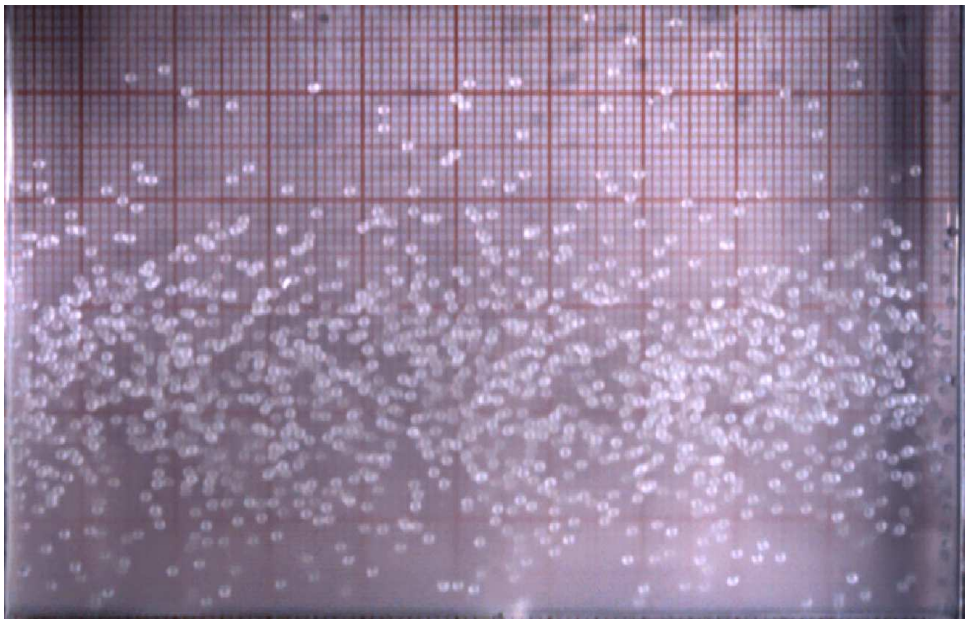

Figure 3.13: **Snapshots of Granular gas observed in $F = 3$ layers of $d = 1.0\ mm$ glass particles at shaking acceleration $\Gamma = 40$ ($A = 3.0\ mm, f = 57.56\ Hz$).** This gaseous regime has been directly originated from bouncing bed.

3.2.6 Granular Gas

A collection of solid particles can be fluidized to a gaseous state by the application of sufficiently strong forcing with $\Gamma \gg 1$. In our experiments this granular gas has been realised by injecting the vibration energy into the system above a critical value (see Fig. 3.13). This state has been observed in other experiments and is well explained by hydrodynamic models (Goldhirsch 2003; Eggers 1999). In a granular gas the particles interact via instantaneous collisions (compared with the mean free time) in a way that is reminiscent of the classical picture of a molecular gas. This is the reason this fluidized phase of particles is known as a "granular gas" Goldhirsch & Zanetti (1993). In spite of the similarity of a granular gas to that of a classical molecular gas, there are important differences between the two kinds of "gases". In a granular gas particle collisions are typically inelastic and this property plays a major role on the behavior of collections of particles.

3.3 Effect of Variation of Ramping Rate

We have performed experiments by linearly sweeping the frequency at various rates (ramping rate), which can be precisely controlled and maintained with the help of software and controller of our shaker system. Comparing phase diagrams at "0.01 Hz/s" and "0.1 Hz/s" (see Fig. 3.14), we find that two phase diagrams look qualitatively similar except the change in quantitative values for the onset of various patterns. In addition, at a higher ramping rate the *Spikes* pattern has been supressed, and this is expected too, since at higher rate the patterns do not get enough relaxation time to form the *Spikes* patterns (since it is a moderate Γ value phenomena). We also did experiments at other ramping rates such as 0.001, 0.05 and 1 Hz/s, but witnessed only variation of Γ_{crit} in the phase diagram, while qualitatively phase diagrams were found to be similar.

3.4 Effect of Container Length on Number of Convection Rolls

We changed the aspect ratio of the container (by decreasing the length of container while keeping its depth to be constant) and tried to study the effect on the emergence of number of convection rolls. These sets of experiments have been performed on glass particles confined in a container of length $L_x/d = 80$ and depth $D/d = 5.5$, with an open top (Shukla *et al.* 2014). The raw snapshots for the particles undergoing covective motion is shown Fig. 3.15 and their corresponding PIV in Fig. 3.17. A similar convective pattern at a higher shaking strength $S = 150$ is shown in Fig. 3.18.

It is evident from the velocity fields that the number of convection rolls has been decreased to four (see Fig. 3.17) while the experiments shown in Fig. 3.12 exhibits six counter-rotating rolls. This reduction of number of rolls is expected as the size of the rolls are same (since the shaking strength in both case is same) but the length of the container over which these rolls span has been reduced and hence a lesser number of rolls fits in that length span.

In addition to calculating the PIV velocity field, the coarse-grained density map has been obtained from the digitized version of the particle snapshots by calculating an 'effective' density field in terms of the average light intensity over a box of 10 pixels $\times$ 10 pixels (see Fig. 3.16). This

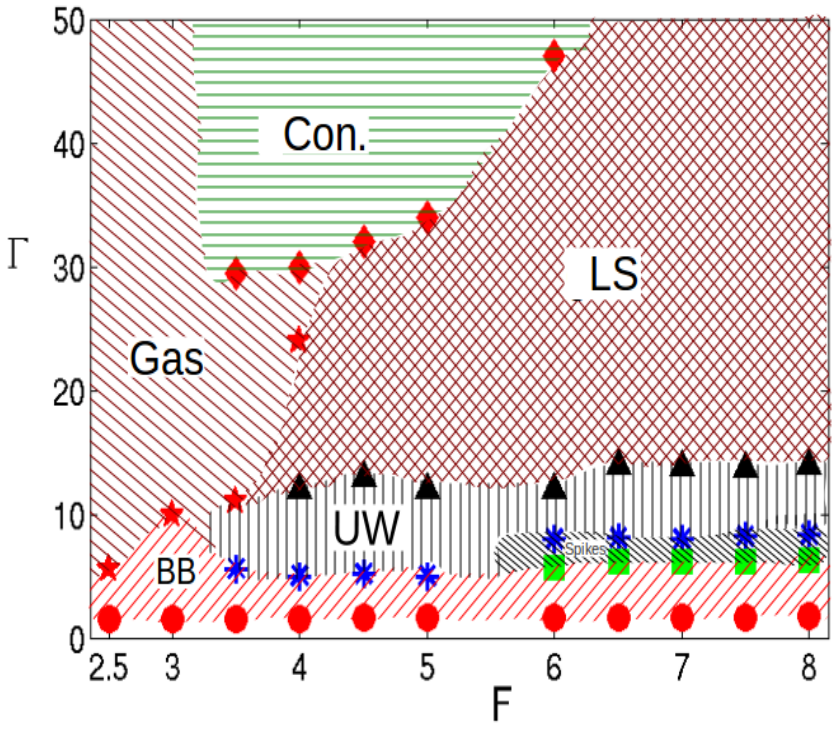

(a)

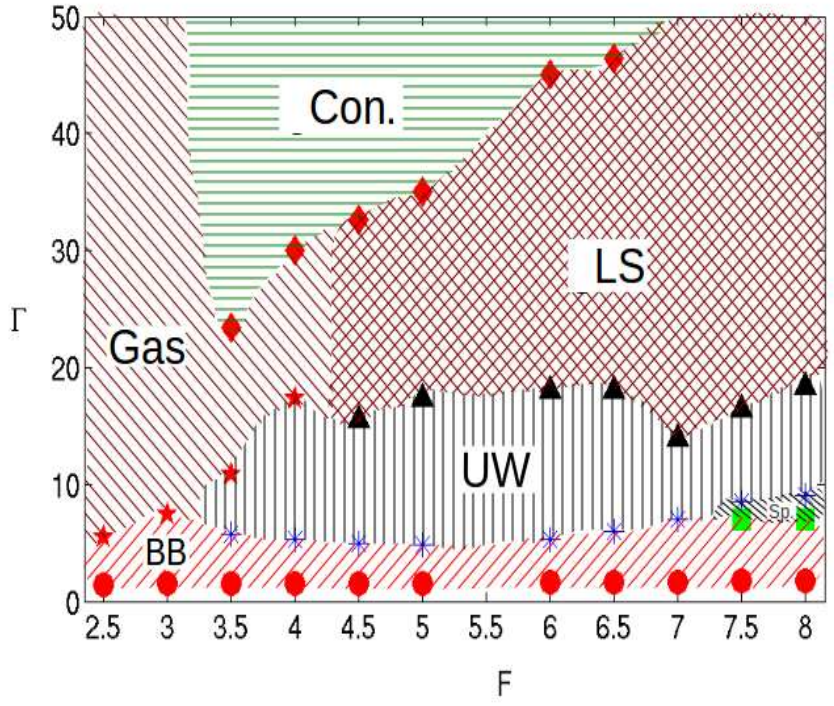

(b)

Figure 3.14: **Phase diagram of monodisperse glass particles of diameter $d = 1.0\ mm$ at constant shaking amplitude $A/d = 3$ for two linear frequency ramping rates: (a) 0.01 Hz/s, (b) 0.1 Hz/s.** The two phase diagrams are qualitatively similar except the suppression of *Spikes* and comparatively larger area occupied by *UW* at higher ramping rate.

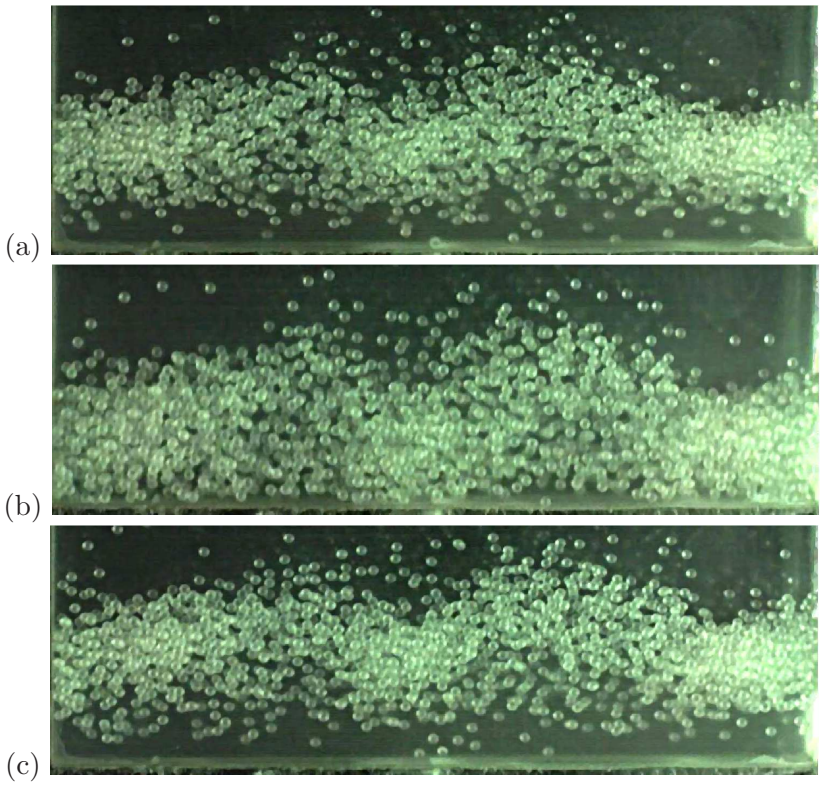

Figure 3.15: **Snapshots of particles undergoing convective motion in $F = 6$ layers of 1.0 mm diameter particles confined in $L/d = 80$ box at: (a) $t = 0\tau$, (b) $t = 0.5\tau$, and (c) $t = \tau$.**. Other parameter values are $\Gamma = 40$ ($A/d = 3$, $f = 57.56\ Hz$).

is displayed in Fig. 3.16 and Fig. 3.18(b) which represent the instantaneous spatially averaged density field at $S = 120$ and 150, respectively. In each case, a Gaussian filter with a width of 2σ (σ is the standard deviation) was used to smoothen the density field. It is seen in (Fig. 3.16) that there is a band of dense particle clusters around a vertical height of $y/d \approx 6.5$, punctuated by dilute regions. On comparing Fig. 3.16 with its raw image in Fig. 3.15, we find that the particles shoot up through these relatively dilute regions. Once the Leidenfrost state becomes unstable at a critical shaking strength ($S = S_c(F)$), the particles shoot up through the dense bed, creating relatively dilute channels at different horizontal locations, and rain down on two sides of each channel, thus creating two dense clusters at a lower elevation as well as two counter-rotating rolls. A comparison of Fig. 3.16 and Fig. 3.18(b) indicates that increasing the shaking strength results in a more modulated density field, with the row of dense clusters being located at a relatively higher elevation ($y/d \approx 9$ in Fig. 3.18(b)), as expected.

3.5 Phase Diagram for Monodisperse Steel Particles

We performed experiments with monodisperse steel particles ($\rho_s = 7650\ Kg/m^3$) of 1.0 mm diameter and assimilated all the phenomena on a phase diagram shown in Fig. 3.19. As expected, all the phenomena which appeared in phase diagram of glass particles (Fig. 3.1) are exhibited by steel particles too. There is a striking resemblance between the phase diagram of these two materials although the spike patterns have been shifted towards lower number of particle layers F in case of steel particles. The various patterns exhibited in the phase diagrams are discussed

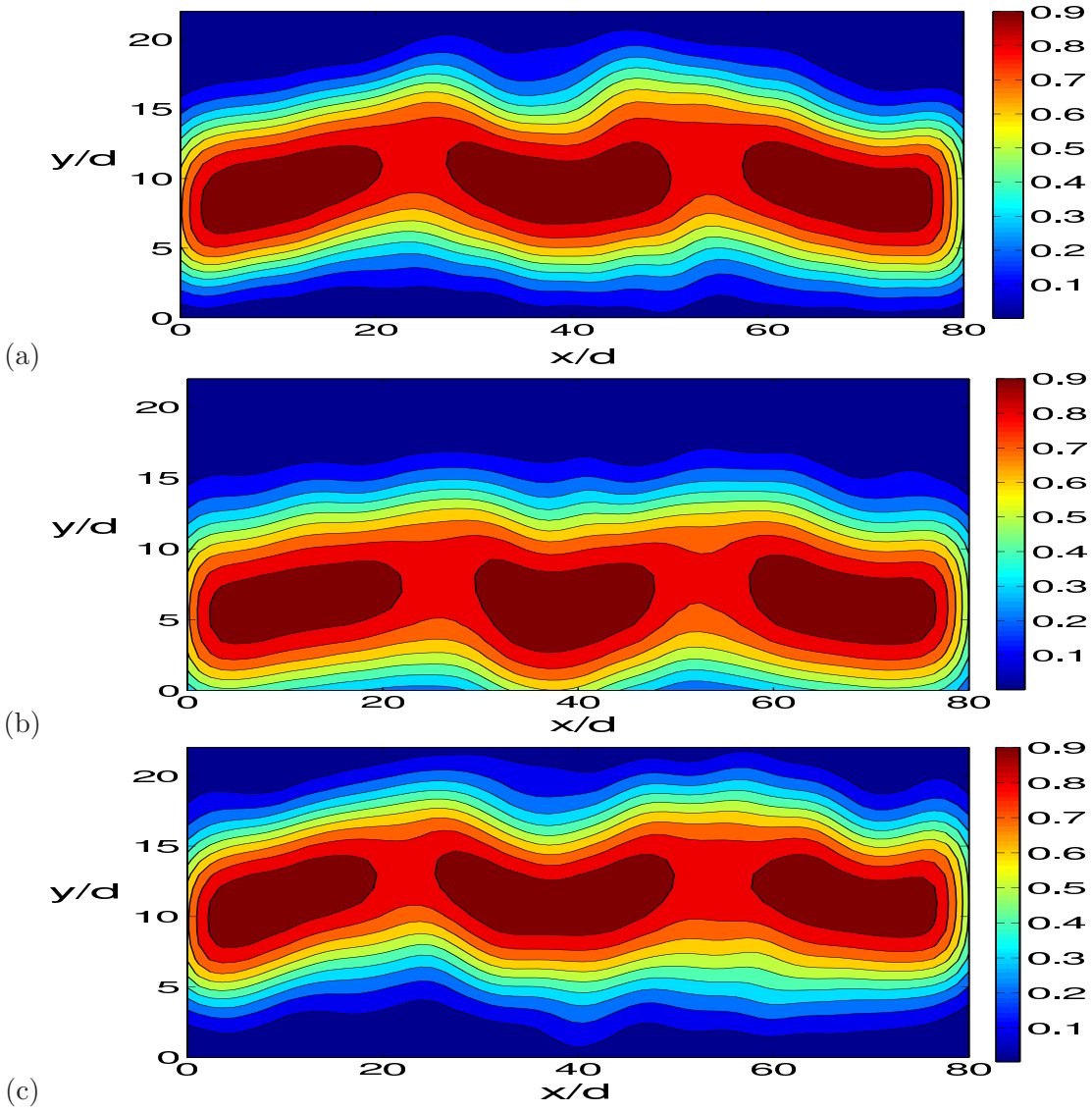

Figure 3.16: **Instantaneous (spatially) coarse-grained maps of density for snapshots shown in see Fig. 3.15.**

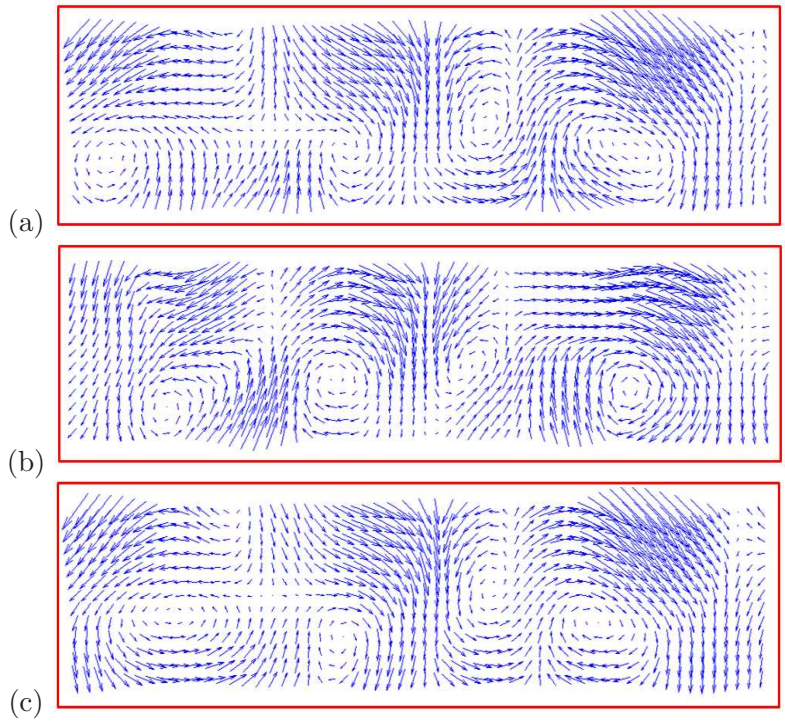

Figure 3.17: **Instantaneous (spatially) coarse-grained maps of velocity vectors for snapshots shown in Fig. 3.15.**

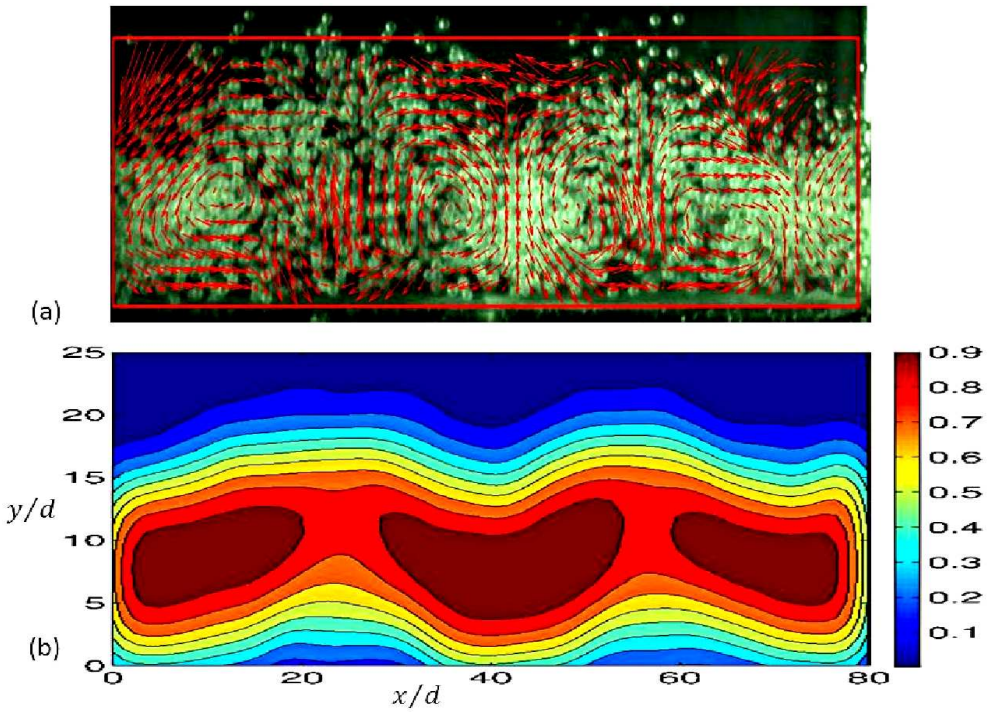

Figure 3.18: ***Convection* in $F = 6$ layers of $1.0\ mm$ diameter glass particles: (a) Superimposed velocity fields on the snapshots of particles undergoing convective motion, (b) Instantaneous (spatially) coarse-grained maps of density.** The particles are confined in a box of $L/d = 80$ and parameter values are $\Gamma = 50$, $A/d = 3$ ($f = 64.35\ Hz$).

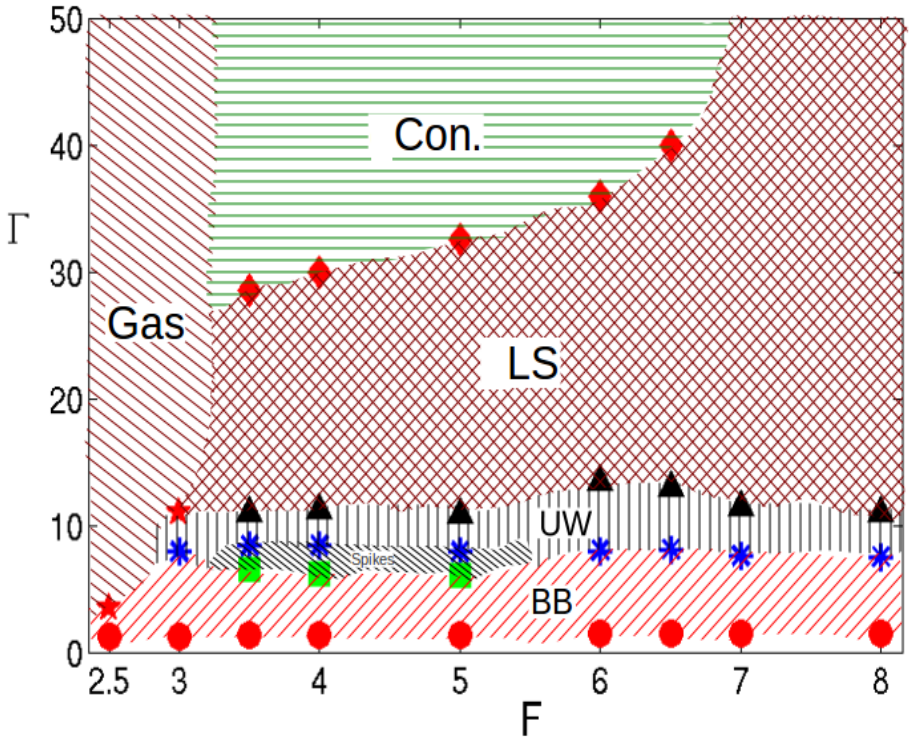

Figure 3.19: **Phase diagram in (Γ, F)-plane for 1.0 mm diameter steel particles confined in $L/d = 100$ box.** Regions of Bouncing Bed *(BB)*, *Spikes*, Undulatory Waves *UW*, granular Leidenfrost state *(LS)*, *Gas* and Convection (*Con.*) are marked; symbols represent approximate locations of transition while upsweeping at a fixed shaking amplitude $A/d = 3$ with the linear frequency-ramping of 0.01 Hz/s.

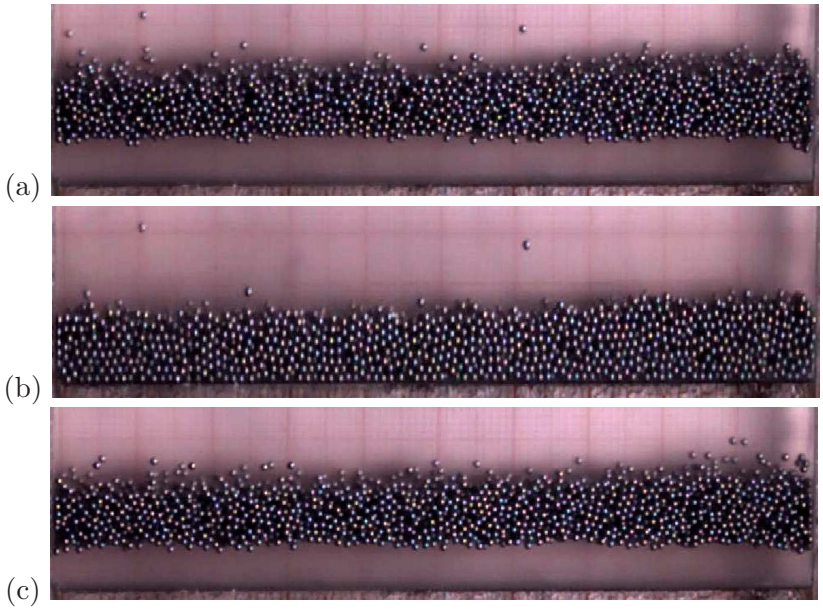

Figure 3.20: **Snapshots of *BB* observed in $F = 6$ layers of steel particles (diameter $d = 1.0\ mm$) at : (a) $t = 0\tau$, (b) $t = 0.5\tau$, and (c) $t = \tau$.** Parameter values are $\Gamma = 3.4$, $A/d = 3$ ($f = 16.8\ Hz$).

in the following paragraphs.

Let us focus on the transition at $F = 6$ layers of particles as one increases the shaking intensity Γ. At very low Γ ($\Gamma > 1$), the bed starts bouncing off the vibrating base and this is the *Bouncing Bed (BB)* state as shown in Fig. 3.20. Further increasing the Γ sets up "Undulatory Waves" (UW) in the system. These UW have been displayed in Fig. 3.21 for two Γ-levels 7 and 8, wherein $n = 3$ mode shows up at $\Gamma = 7$ whilst increasing the shaking intensity Γ to 8 transforms the UW string to $n = 4$ mode. Thus, we witnessed that as the Γ-level increases higher mode number waves form in the system. If one increases the Γ even more, the system admits granular *Leidenfrost State (LS)*, wherein a densely packed bed of particles hovers over highly fluidized dilute gaseous region, as shown in Fig. 3.22. Increasing this Γ beyong certain critical value Γ_c eventually makes the bed unstable and the particles eject from the dense bed at certain horizontal locations following circular motion giving birth to granular convection. This *Convection* has been displayed in Fig. 3.23 and Fig. 3.24 for two Γ- levels 50 and 55.

There can be one more pattern, *Spikes*, sandwiched between BB and UW regime but this subharmonic wave does not sustain at filling depth $F = 6$, nevertheless, for $F = 5$ layers *Spikes* have been displayed in Fig. 3.25. One can observe that the peaks of this *Spikes* are not very high, in contrast to *Spikes* formed in glass particles shown in Fig. 3.3 due to the reason that Fig. 3.25 corresponds to a shallow layer ($F = 5$) and the steel particles are heavier than glass particles.

3.6 Pattern Formation in Beds of Smaller Sized Particles

We performed experiments with monodisperse steel particles of 0.5 mm diameter. The layer filling depth is $F = 25$ and the particles are confined in a similar box of dimension $L/d = 200$

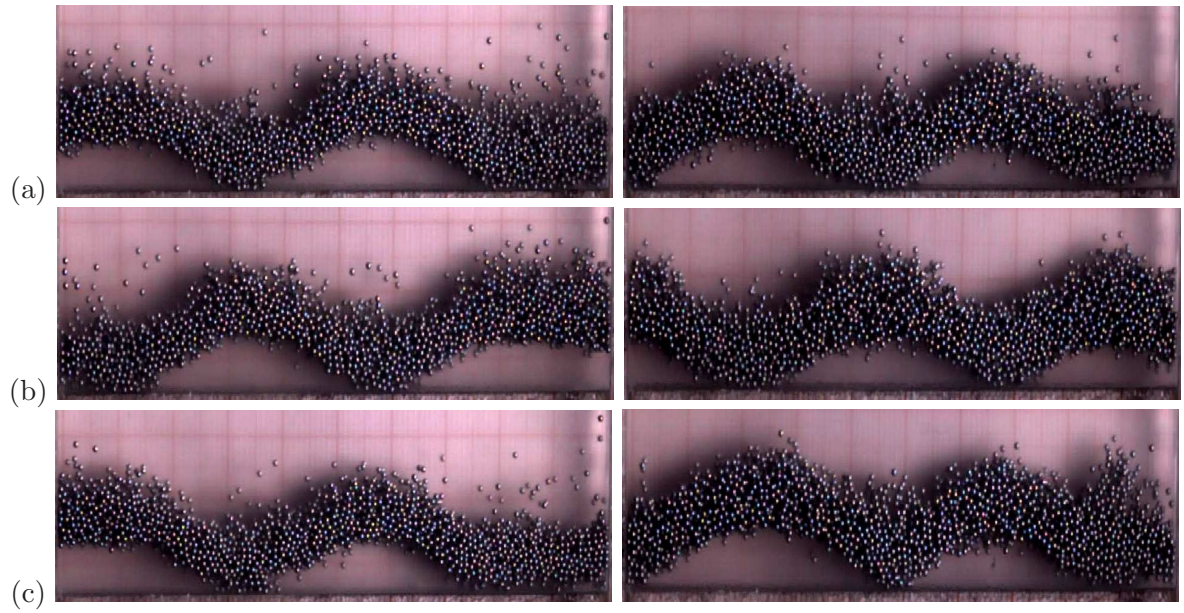

Figure 3.21: **Snapshots of UW observed in $F = 6$ layers of steel particles (diameter $d = 1.0\ mm$) at $A/d = 3$: (a) $t = 0\tau$, (b) $t = \tau$, and (c) $t = 2\tau$.** Left and right panel shows the UW at $\Gamma = 7$ ($n = 3$ mode) and $\Gamma = 8$ ($n = 4$ mode), respectively.

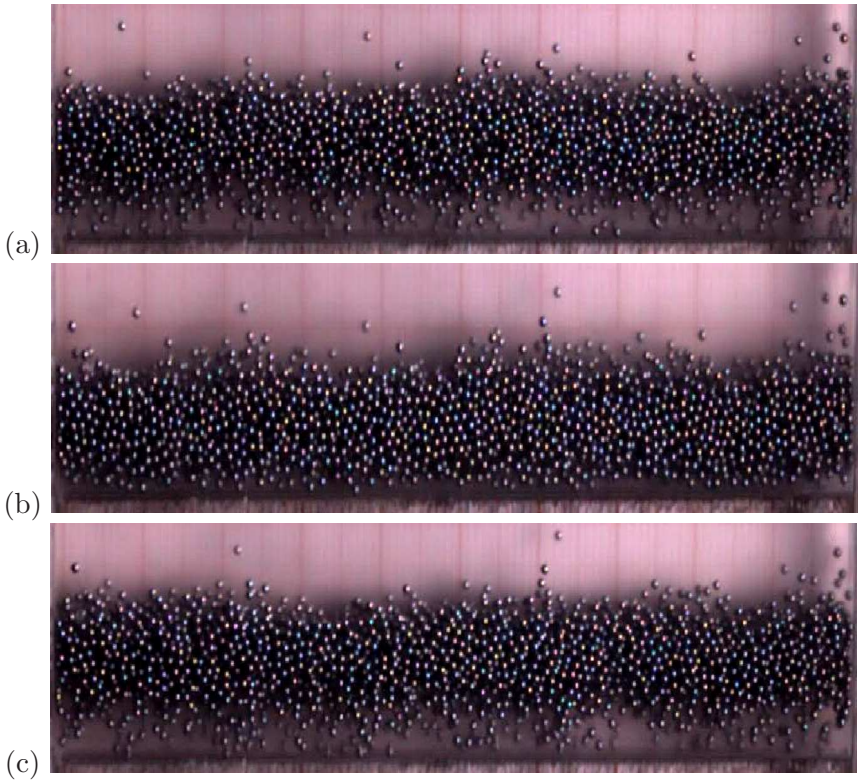

Figure 3.22: **Snapshots of granular Leidenfrost State (LS) observed in $F = 6$ layers of steel particles (diameter $d = 1.0\ mm$) at: (a) $t = 0\tau$, (b) $t = 0.5\tau$, and (c) $t = \tau$.** Parameter values are $\Gamma = 25$, $A/d = 3$ ($f = 45.5\ Hz$)

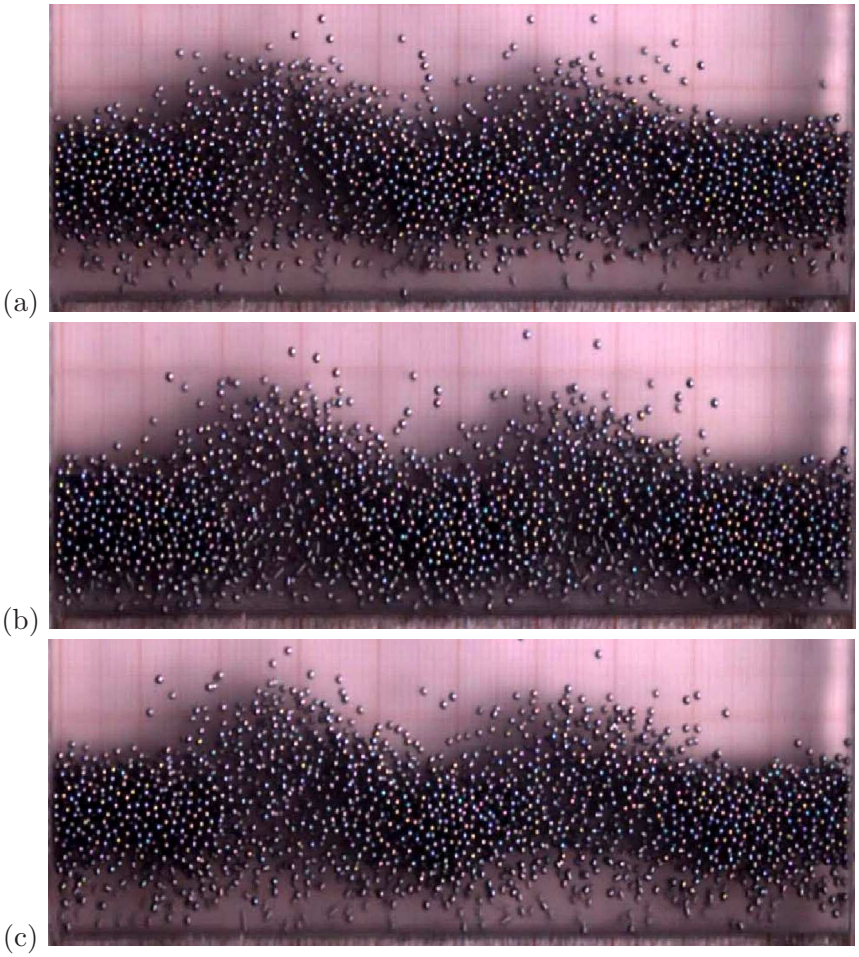

Figure 3.23: **Snapshots of $F = 6$ layers of 1.0 mm diameter steel particles undergoing convective motion at: (a) $t = 0\tau$, (b) $t = 0.5\tau$, and (c) $t = \tau$.** Parameter values are $\Gamma = 50$, $A/d = 3$ ($f = 64.35\ Hz$).

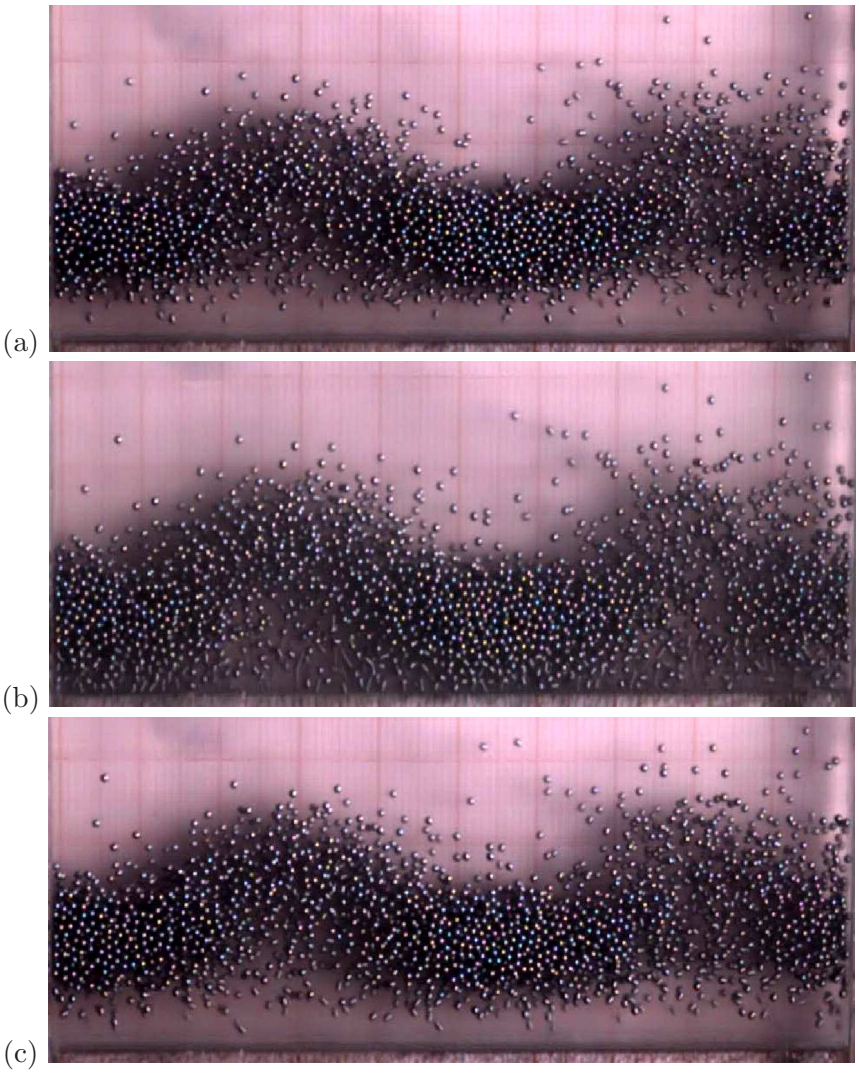

Figure 3.24: **Snapshots of $F = 6$ layers of 1.0 mm diameter steel particles undergoing convective motion at: (a) $t = 0\tau$, (b) $t = 0.5\tau$, and (c) $t = \tau$.** Parameter values are $\Gamma = 55$, $A/d = 3$ ($f = 67.5\ Hz$).

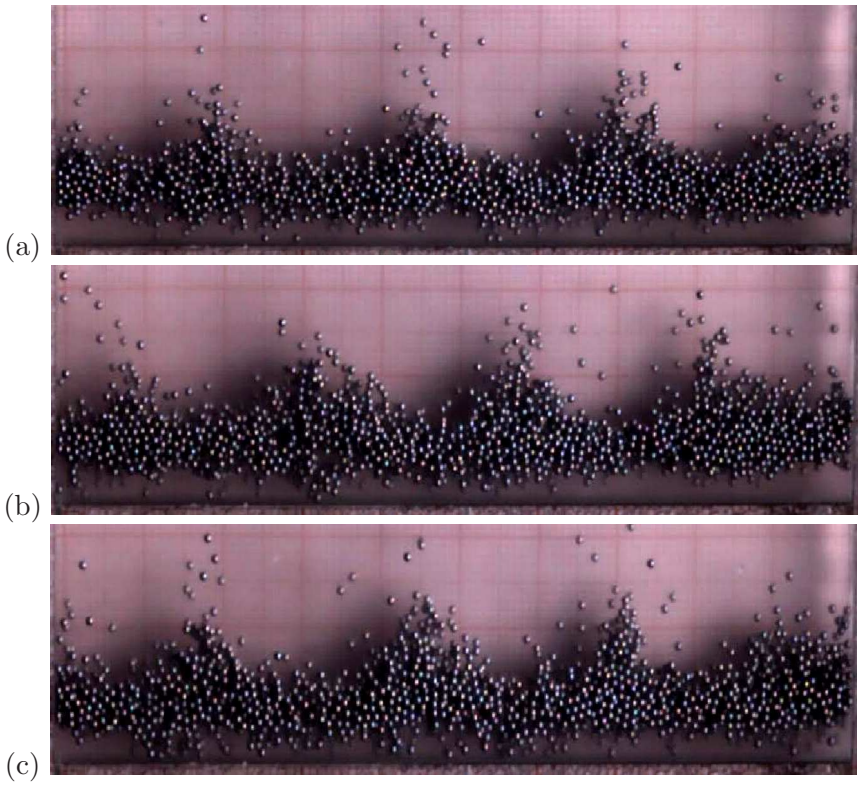

Figure 3.25: **Snapshots of *Spikes* observed in $F = 5$ layers of steel particles (diameter $d = 1.0\ mm$) at: (a) $t = 0\tau$, (b) $t = 2\tau$, and (c) $t = 4\tau$.** Parameter values are $\Gamma = 7.1$, $A/d = 3$ ($f = 24.35\ Hz$)

and $W/d = 11$. The number of layers has been chosen so that the system exhibits only two states: "Bouncing Bed" *(BB)* and "Undulatory Waves" *UW*. Fig. 3.26(a) shows the *BB* state and increasing the shaking intensity Γ at constant shaking amplitude $A/d = 3$ will transit the system to *UW* of $n = 1$ mode (see Fig. 3.26(b) and Fig. 3.26(c)). This $n = 1$ mode sustains till $\Gamma = 8$ beyond which $n = 2$ mode sets up in the system as shown in Fig. 3.26(d).

Further increasing the Γ-level will generate waves of mode number 3, 4 and even higher as shown in Fig. 3.27. Thus, we found that higher-mode number *UW* builds up in the system with increasing shaking intensity Γ, implying that higher frequency vibration will aid the granular string to buckle much easily. It is noticeable that mode number 5 and 8 are the most stable mode since they persists for a larger range of Γ.

A closer inspection of these waves reveals that beyond mode number $n = 5$, the buckling of granular string does not occur across the full height, rather only the bottom layers (which are in continuous cotact with vibrating base) buckle while the top layers remain flat. Such type of tendency is expected, since the length of the bed is not much greater than its height. and it can not sustain such higher modes with the bed being buckled across the whole height. constraining the lower surface of the bed being buckled and upper surface remaining flat. The highest mode which has been observed at the maximum shaking intensity which our shaker can achieve ($\Gamma = 55$) is the $n = 9$ mode, see Fig. 3.28(n).

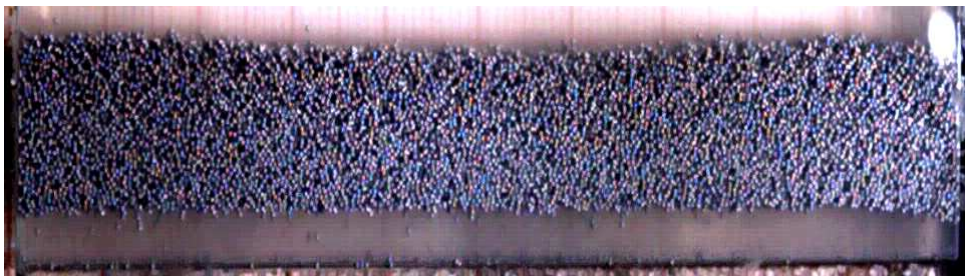

(a)

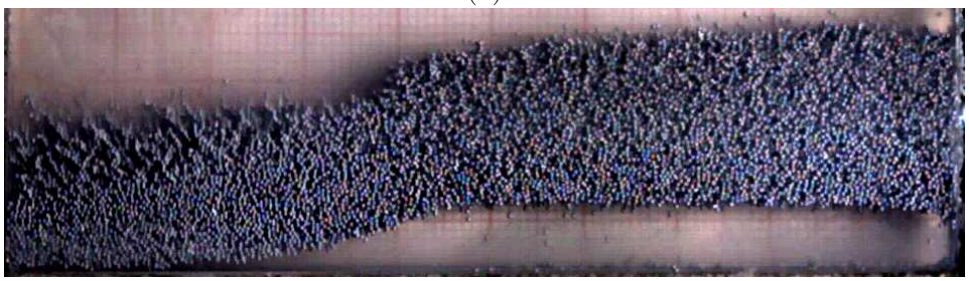

(b)

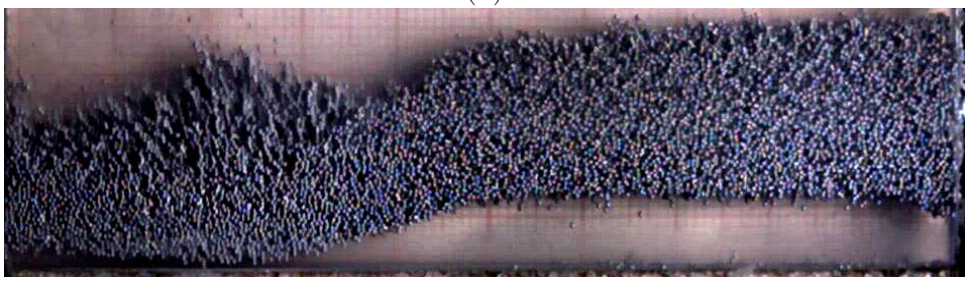

(c)

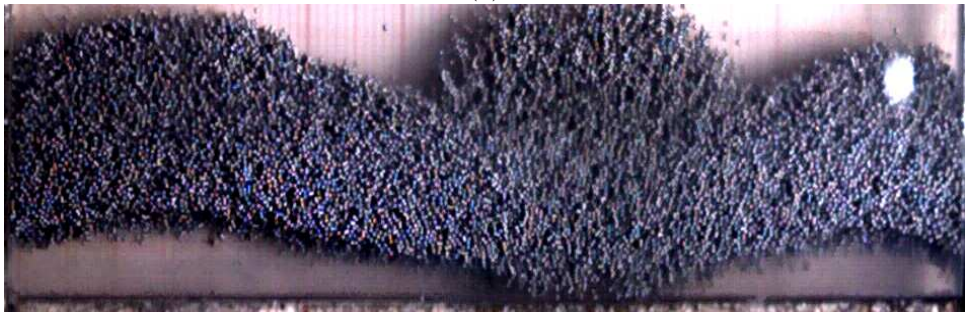

(d)

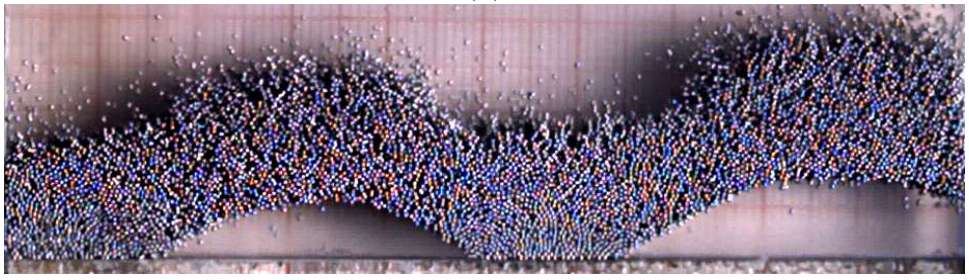

(e)

Figure 3.26: **Transition from "Bouncing Bed" (BB) to various modes of "Undulatory Waves" (UW) in $F = 25$ layers of 0.5 mm diameter monodisperse steel particles:** (a) BB at $\Gamma = 3$ ($f = 15.76\ Hz$), (b) UW ($n = 1$ mode) at $\Gamma = 6$ ($f = 22.3\ Hz$), (c) UW ($n = 1$ mode) at $\Gamma = 7$ ($f = 24.07\ Hz$), (d) UW ($n = 2$ mode) at $\Gamma = 8$ ($f = 25.74\ Hz$), and (e) UW ($n = 3$ mode) at $\Gamma = 8.7$ ($f = 26.84\ Hz$). Other parameter values are $A/d = 3$ and ramping rate 0.01 Hz/s.

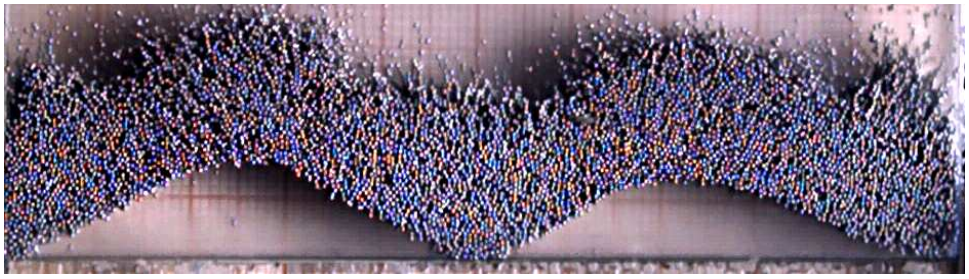

(f)

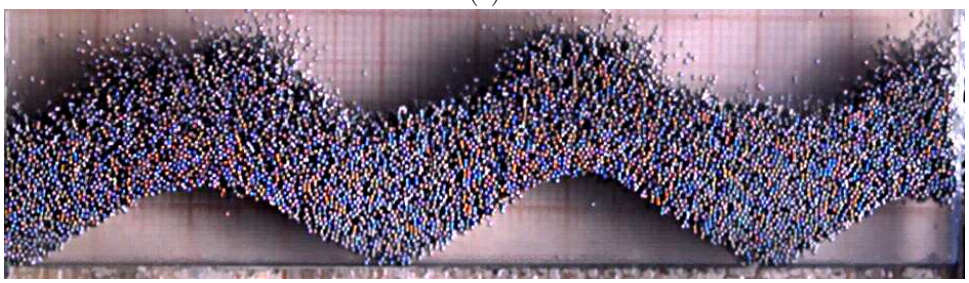

(g)

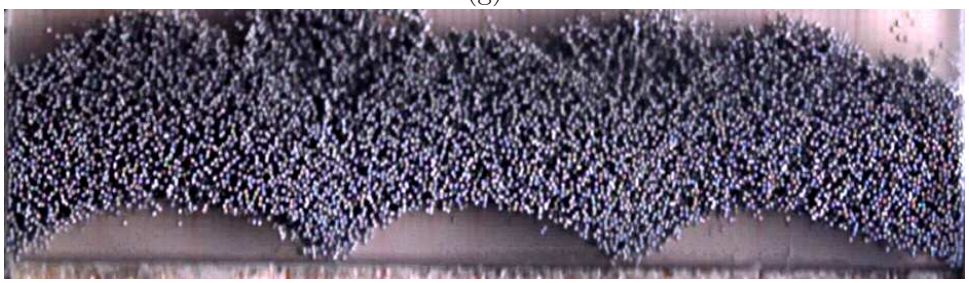

(h)

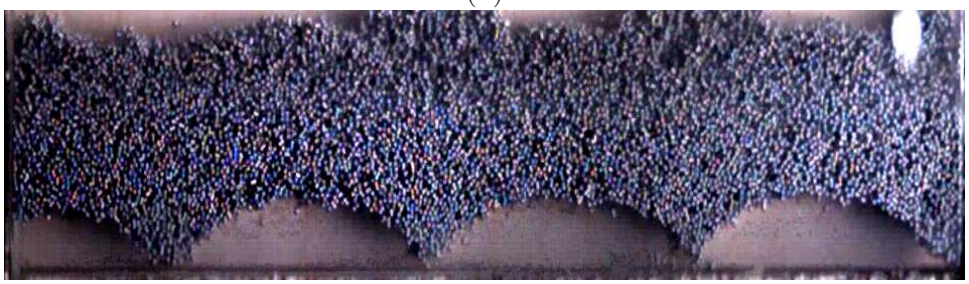

(i)

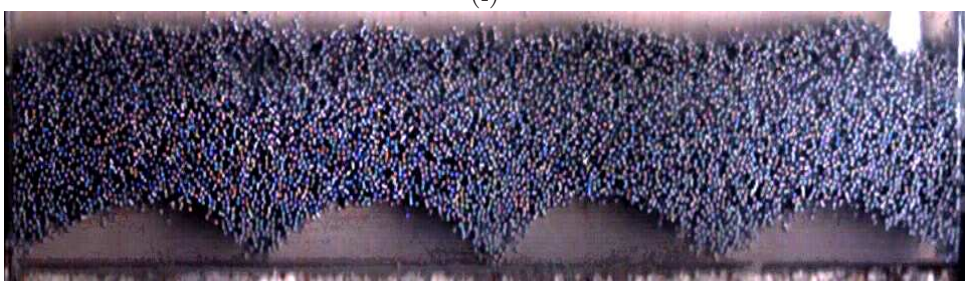

(j)

Figure 3.27: **Transition from "Bouncing Bed" (BB) to various modes of "Undulatory Waves" (UW) in $F = 25$ layers of 0.5 mm diameter monodisperse steel particles:** (f) UW ($n = 4$ mode) at $\Gamma = 9$ ($f = 27.3\ Hz$), (g) UW ($n = 5$ mode) at $\Gamma = 10$ ($f = 28.78\ Hz$), (h) UW ($n = 6$ mode) at $\Gamma = 28$ ($f = 48.15\ Hz$), (i) UW ($n = 7$ mode) at $\Gamma = 33$ ($f = 52.3\ Hz$), and (j) UW ($n = 8$ mode) at $\Gamma = 37.6$ ($f = 55.8\ Hz$). Other parameter values are $A/d = 3$ and ramping rate 0.01 Hz/s.

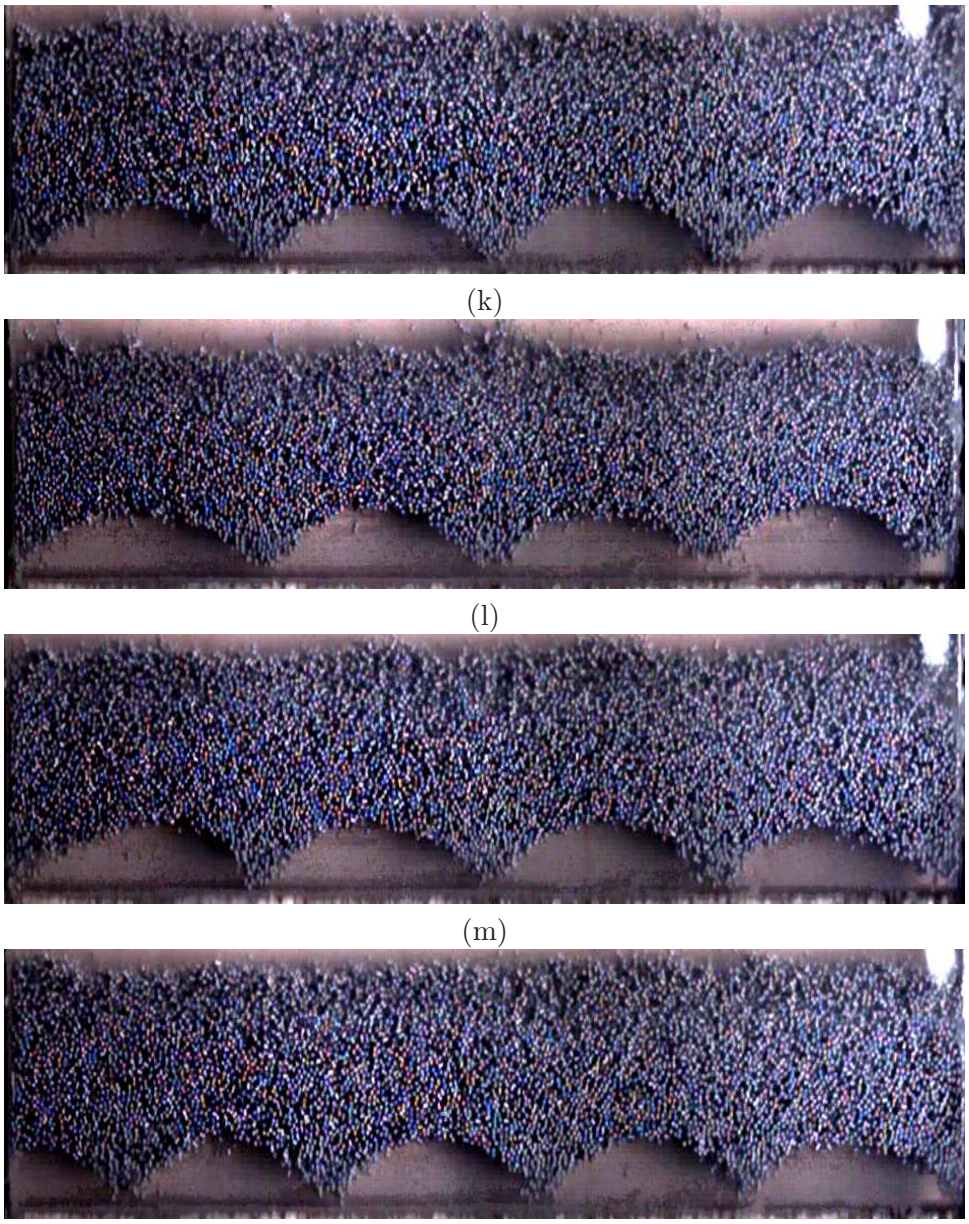

(k) (l) (m) (n)

Figure 3.28: **Transition from "Bouncing Bed" (BB) to various modes of "Undulatory Waves" (UW) in $F = 25$ layers of 0.5 mm diameter monodisperse steel particles:** (k) UW ($n = 8$ mode) at $\Gamma = 42$ ($f = 59\ Hz$), (l) UW ($n = 8$ mode) at $\Gamma = 46$ ($f = 61.7\ Hz$), (m) UW ($n = 8$ mode) at $\Gamma = 50$ ($f = 64.35\ Hz$), and (n) UW ($n = 9$ mode) at $\Gamma = 55$ ($f = 67.5\ Hz$). Other parameter values are $A/d = 3$ and ramping rate 0.01 Hz/s.

3.7 Effect of Amplitude Variation: Phase Diagram on $(\Gamma, A/d)$-plane

Till now, we studied the pattern formation dynamics by considering the various phenomena while varying the particle loading F at fixed values of A/d. But one can also be curious to know that at a fixed F what is the effect of dimensionless shaking amplitude A/d while increasing the shaking strength S. For such type of study, we had focussed on two layer-depths $F = 3$ and 6, and obtained the phase diagram on $(\Gamma, A/d)$-plane for both steel and glass particles (diameter $d = 1.0\ mm$) confined in a box of length $L/d = 80$, as shown in Fig. 3.29 and Fig. 3.39. These phase diagrams will be discussed in detail in the following paragraphs.

3.7.1 Monodisperse Steel Particles

We will first discuss various transitions occuring in $F = 3$ layers and later move on to $F = 6$ layers of steel particles. Fig. 3.30 and Fig. 3.31 show various states observed in $F = 3$ layers while increasing the shaking amplitude A/d at constant shaking intensity $\Gamma = 10$. Starting from *LS* at $A/d = 0.5$, further increasing the shaking amplitude vaporizes the system to a granular *Gas*. Nevertheless, as one increases the shaking amplitude the extent of this gas occupies more and more vertical span of the container and this is expected since at higher amplitudes the particles bounce off the plate upto a greater height. It is evident from Fig. 3.29(a) that the *LS* regime is narrowed down to a thin stripe whilst a large area is occupied by gaseous phase suggesting that the system has a higher propensity to boil into a gas and this gas becomes more chaotic at higher amplitudes.

Stepping towards a higher shaking intensity $\Gamma = 30$, the various states reported are depicted in Fig. 3.32 and Fig. 3.33, wherein at $A/d = 0.5$ a gas is observed and at higher but intermediate values of $A/d = 1.5$ and 3 the particles undergo convective motion. Further increasing the shaking amplitude checks this convective motion and the chaotic agitation of particles again lead to granular gas. In a similar manner, at even higher $\Gamma = 50$, the system shows a granular gas except at $A/d = 1.5$ wherein convective motion sets up, as shown in Fig. 3.34 and Fig. 3.35.

As one increases the filling depth to $F = 6$ layers, the gaseous phase has been suppressed completely (see Fig. 3.29(b)). This is because to fluidize this deep granular bed it requires a very high shaking intensity which is beyond the capacity of our shaker. Fig. 3.36 displays the various states observed at $\Gamma \approx 7.5$ while incresing A/d. "Bouncing Bed" *BB* has been reported at lower shaking amplitudes $A/d = 0.5$ and 1.5, although at the same $\Gamma - level$ and at higher amplitudes subharmonic $f/4$-*Spikes* sets up in the system, see Fig. 3.36. This suggests that higher shaking amplitude aids the formation and sustenance of *Spikes*. It should be noted that when Γ is increased gradually, these *Spikes* eventually give birth to "Undulatory Waves" *UW*.

At even higher $\Gamma = 20$, *BB* is reported for very small amplitudes below 0.5, which fluidizes to *Leidenfrost State (LS)* at higher shaking amplitudes, as shown in Fig. 3.37, which displays *LS* at various shaking amplitudes. Focussing on the transition at $\Gamma = 50$ with increasing A/d (see Fig. 3.29(b)), one witnesses that *BB* still persists for very low amplitudes, whereas further increasing A/d yields *LS* (upto $A/d \approx 1.4$). As once traverses higher amplitudes, convection rolls are clearly observed as shown in Fig. 3.38. A close observation of these rolls suggests that

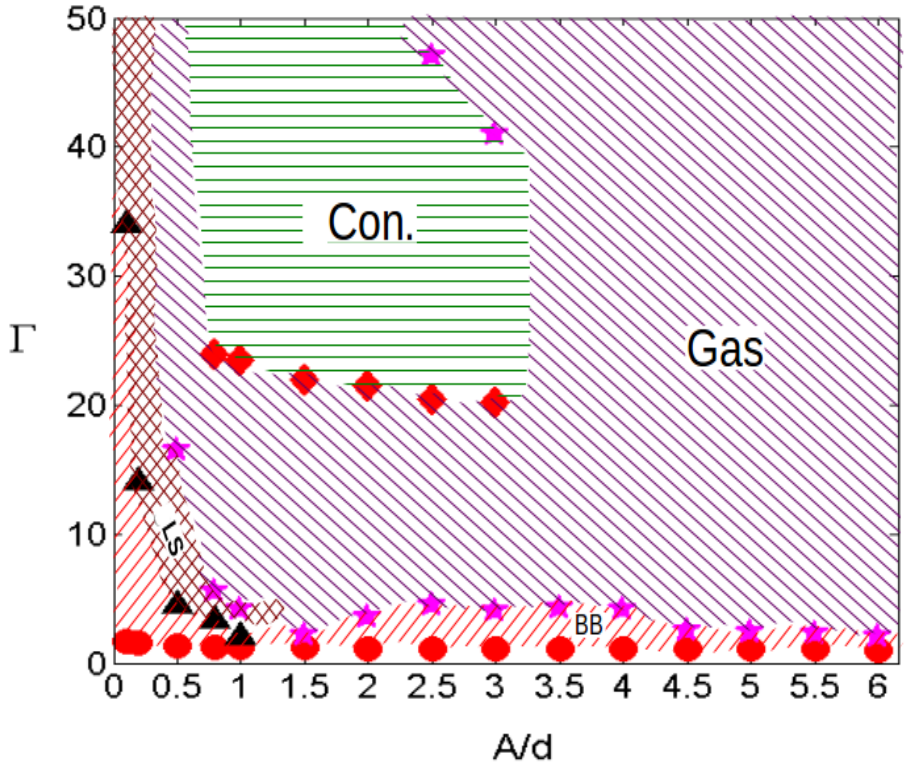

(a)

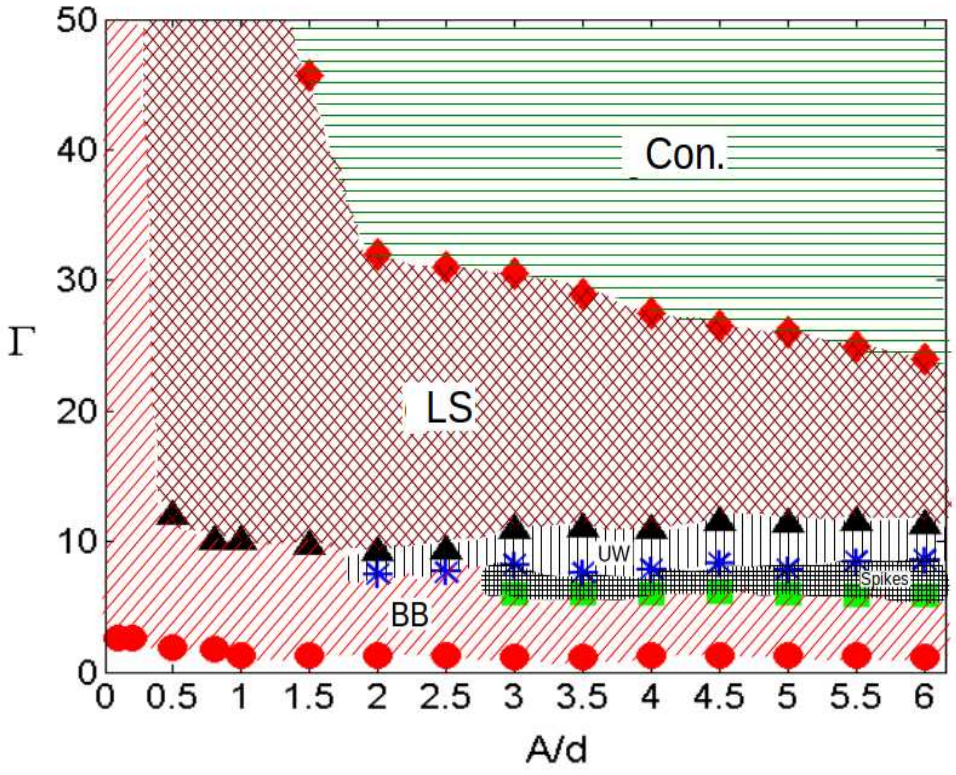

(b)

Figure 3.29: **Phase diagram for steel particles (diameter $d = 1.0\ mm$) confined in $L/d = 80$ box on $(\Gamma, A/d)$-plane for two filling depths: (a) $F = 3$, and (b) $F = 6$.** The shaking intensity Γ has been increased at a constant shaking amplitude A/d via ramping frequency at a linear rate of 0.01 Hz/s.

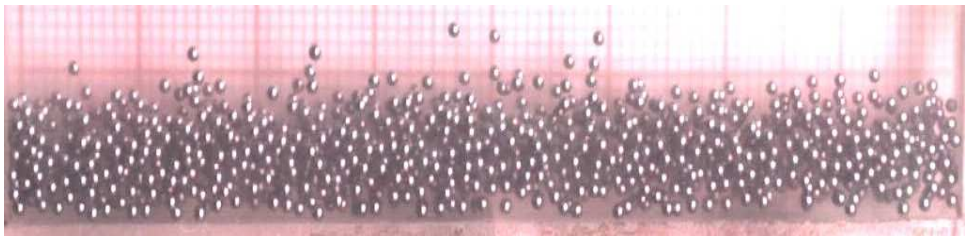

(a)

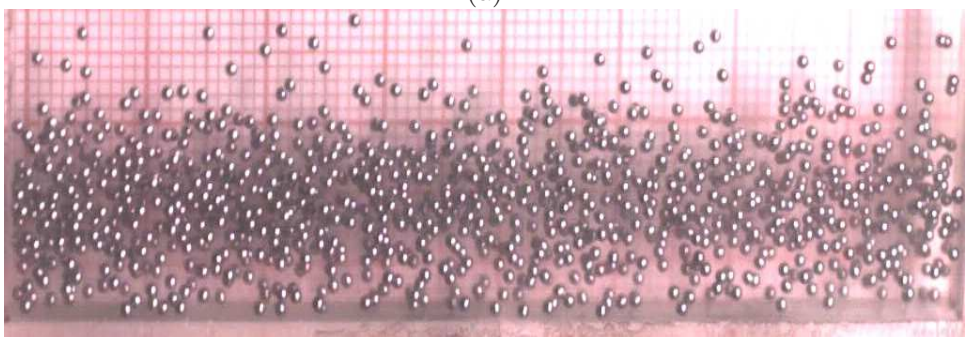

(b)

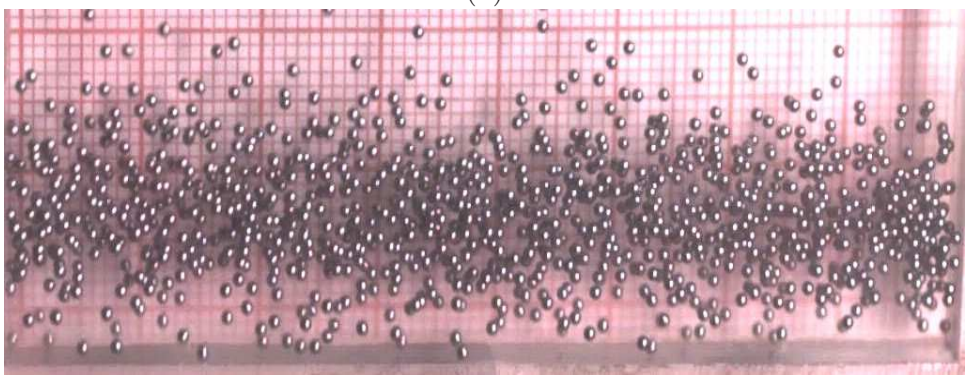

(c)

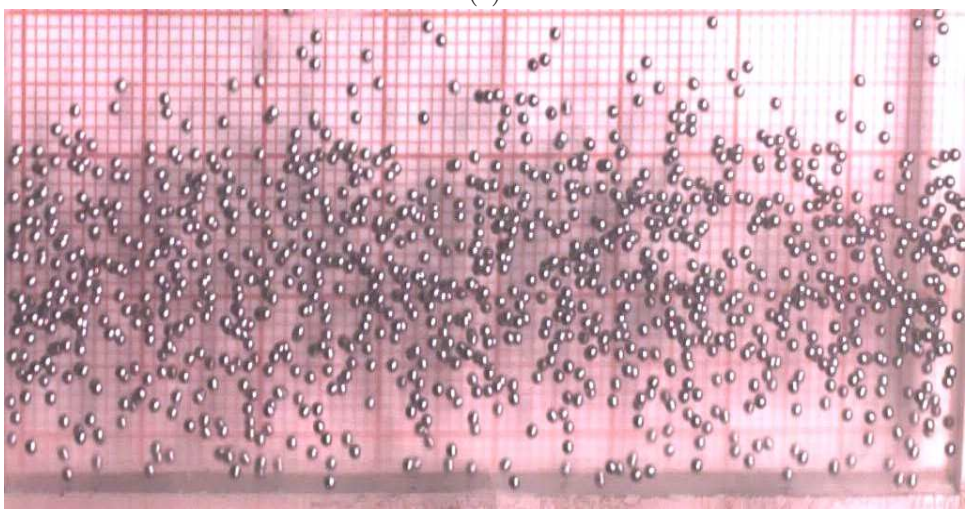

(d)

Figure 3.30: **Transition at constant shaking intensity $\Gamma = 10$ in $F = 3$ layers of monodisperse steel particles with increasing shaking amplitude A/d:** (a) *LS* at $A/d = 0.5$ ($f = 70.5\ Hz$), (b) *Gas* at $A/d = 1.5$ ($f = 40.7\ Hz$), (c) *Gas* at $A/d = 3$ ($f = 28.78\ Hz$), and (d) *Gas* at $A/d = 4.5$ ($f = 23.5\ Hz$).

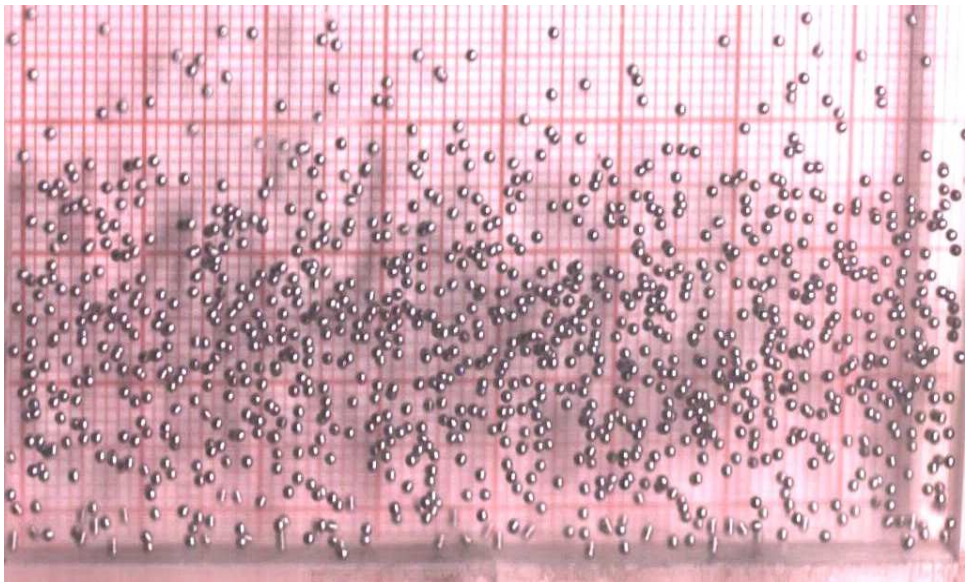

(e)

Figure 3.31: *Continued Fig. 3.30* **Transition at constant shaking intensity $\Gamma = 10$ in $F = 3$ layers of monodisperse steel particles with increasing shaking amplitude A/d:** (e) *Gas* at $A/d = 6$ ($f = 20.35\ Hz$).

particles shoot up through the dense bed, creating relatively rarer channels at two different horizontal locations, and rain down on two sides of each channel, thus creating three dense clusters at a lower elevation as well as four counter-rotating rolls. As is evident from Fig. 3.38 that these channels become more and more diluted and the vertical heights of the channels as well as the dense clusters increase as one increases the shaking apmlitude further.

3.7.2 Monodisperse Glass Particles

Now, we will focus our attention on the phase diagrams for granular bed of 1.0 *mmm* diameter glass particles in $(\Gamma, A/d)$-plane, as depicted in Fig. 3.39. Fig. 3.39(a) and Fig. 3.39(b) show the various phases and transitions for filling depths $F = 3$ and $F = 6$, respectively. Let us first discuss various phases and their transitions in $F = 3$ layers when the shaking amplitude A/d is increased at a constant shaking intensity. Fig. 3.40 and Fig. 3.41 show various phases encountered with increasing A/d, wherein for lower shaking amplitudes (upto $A/d = 2$) one observes the *Leidenfrost State (LS)* (see Fig. 3.40(a),(b)) and further increasing A/d beyond 2 melts the bed into a granular *Gas* (see Fig. 3.40(c),(d) and Fig. 3.41(e)).

At a higher Γ-level ($\Gamma = 30$) one witnesses the onset of convection rolls having dense clusters and dilute channels at alternate horizontal positions as depicted in Figs. 3.42(b) and (c). Further increasing A/d beyond 3 vaporizes these rolls into gas (see Fig. 3.42(d)). Considering this type of transition at constant shaking intensity at even higher $\Gamma = 50$, we observe the same trend, wherein at lower ampltude *LS* is found (see Fig. 3.43(a)) and at intermediate values of A/d ($0.5 < A/d < 3$) convection sets up in the system (see Fig. 3.43(b)) and beyond this A/d ($3 \leq A/d$) granular gas emerges (see Fig. 3.43(c),(d)). It should be noted that at the shaking amplitude $A/d = 3$, the system shows convection at $\Gamma = 30$ (Fig. 3.42(c)) and boils into a gas

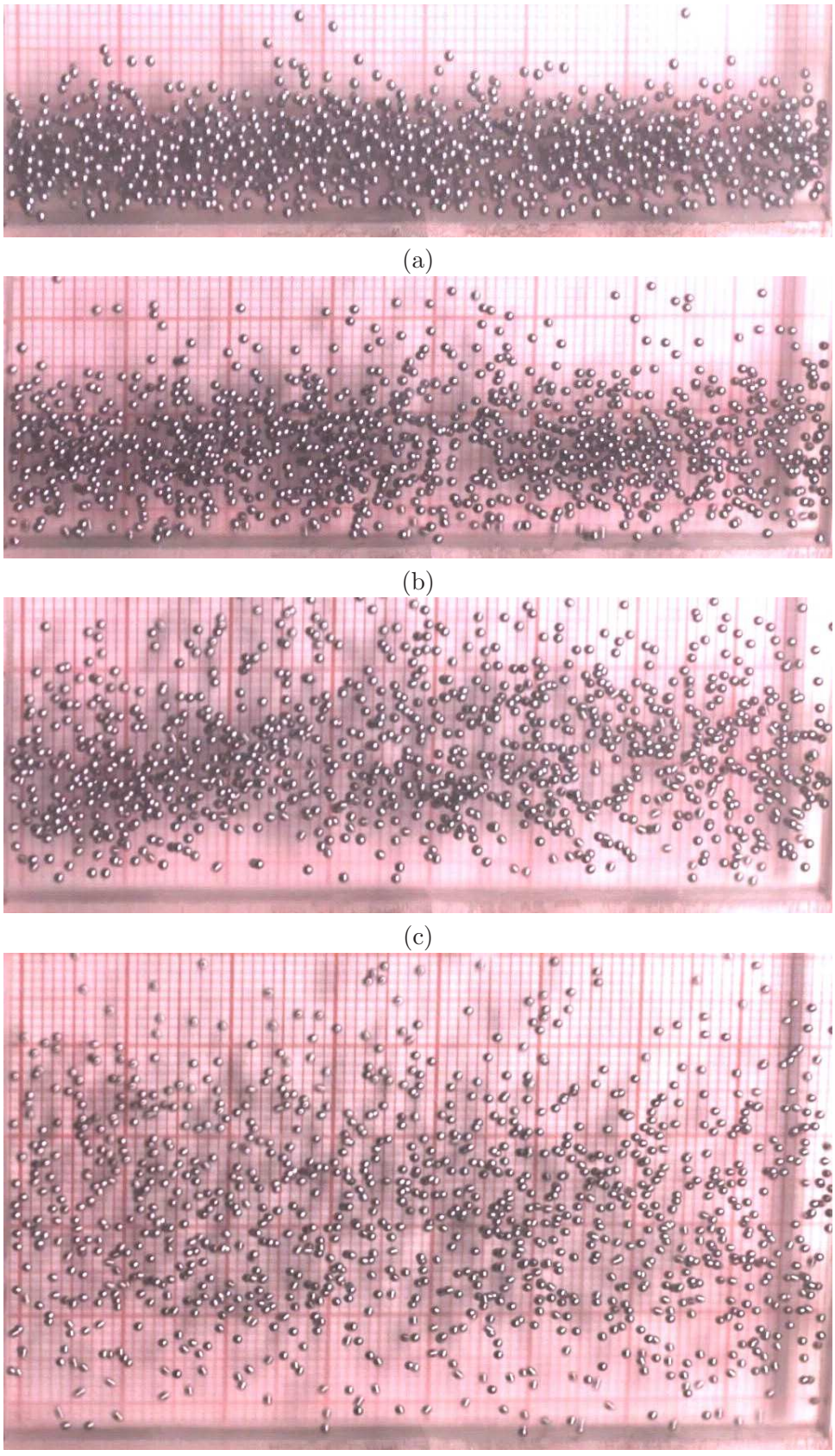

(a) (b) (c) (d)

Figure 3.32: **Transition at constant shaking intensity $\Gamma = 30$ in $F = 3$ layers of monodisperse steel particles with increasing shaking amplitude A/d:** (a) *Gas* at $A/d = 0.5$ ($f = 122\ Hz$), (b) *Convection* at $A/d = 1.5$ ($f = 70.5\ Hz$), (c) *Convection* at $A/d = 3$ ($f = 49.84\ Hz$), and (d) *Gas* at $A/d = 4.5$ ($f = 40.7\ Hz$).

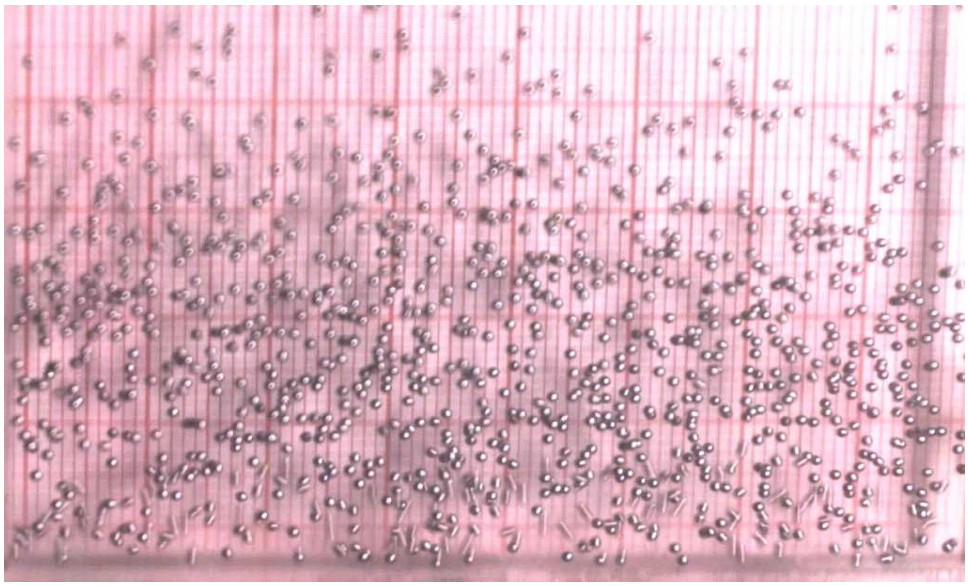

(e)

Figure 3.33: *Continued Fig. 3.32* **Transition at constant shaking intensity $\Gamma = 30$ in $F = 3$ layers of monodisperse steel particles with increasing shaking amplitude A/d:** (e) *Gas* at $A/d = 6$ ($f = 35.24\ Hz$).

at $\Gamma = 50$ (Fig. 3.43(c)).

Comparing Fig. 3.39(a) and Fig. 3.29(a), it is evident that in case of steel particles the gaseous phase occupied a larger area of the phase diagram and the gas persists even at lower shaking amplitudes due to the fact that at the same level of S, steel particles will have more kinetic energy (due to heavier mass) than glass particles and hence can be fluidized easily. Due to this fact, the *LS* regime in Fig. 3.29(a) is narrowed down to a thin stripe.

The transition from *Gas* $\rightarrow$ *Convection* (Fig. 3.29(a) and Fig. 3.39(a)) is interesting and a novel one which was not reported by Eshuis *et al.* (2007). The convection regime in both the phase diagrams has almost a similar span covering a range of $A/d \in (0.8, 3)$. Both the phase diagrams Fig. 3.29(a) and Fig. 3.39(a) have not shown any signs of subharmonic waves (*UW* and *Spikes*). This conforms that there exists a minimum filling depth of granular particles below which these waves cannot appear in the system.

As we increase the filling depth F to 6, the *Undulatory Waves (UW)* appears for a range $A/d \in (0.2, 6)$ upto a moderate value of $\Gamma = 12$, see Fig. 3.39(b). In contrast, for $F = 6$ layers of steel particles (Fig. 3.29(b)) these *UW* are being delayed and spans over a range $A/d \in (2, 6)$. This indicates that the "granular" string of glass particles is more elastic to form standing waves (*UW*) as compared to a string of steel particles. Note that the spike pattern has been suppressed a little bit in case of glass particles. These subharmonic waves have emerged from the synchronized bouncing bed state (*BB*), reminiscent to the type of transition (*BB*$\rightarrow$ *Spikes*$\rightarrow$ *UW*) realized in the phase diagrams discussed earlier. The critical shaking strength S_c for the transition to *LS* appears to be a constant (albeit having small variations) with the dimensionless shaking amplitude A/d and this result is in accord with S_c on (Γ, F)-plane (see Fig. 3.1 and Fig. 3.19). Nevertheless, the critical shaking strength S_c responsible for the transition *LS*$\rightarrow$*Con* decreases with increasing A/d, following a hyperbolic trend in case of glass particles whereas

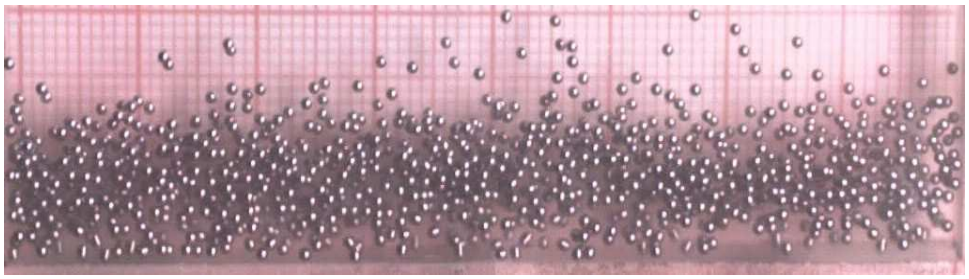

(a)

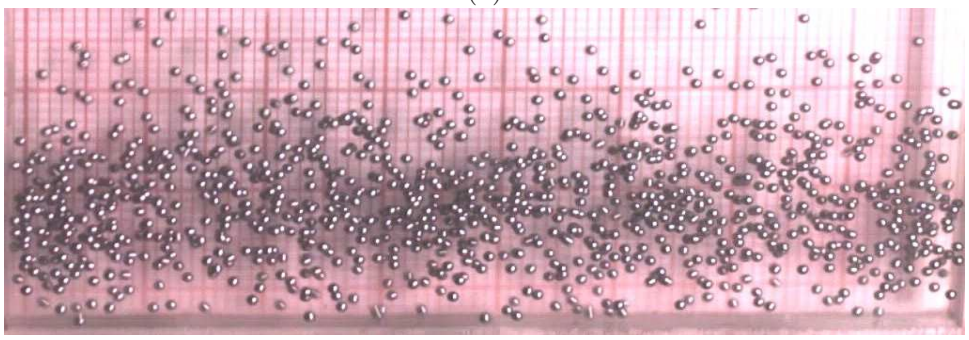

(b)

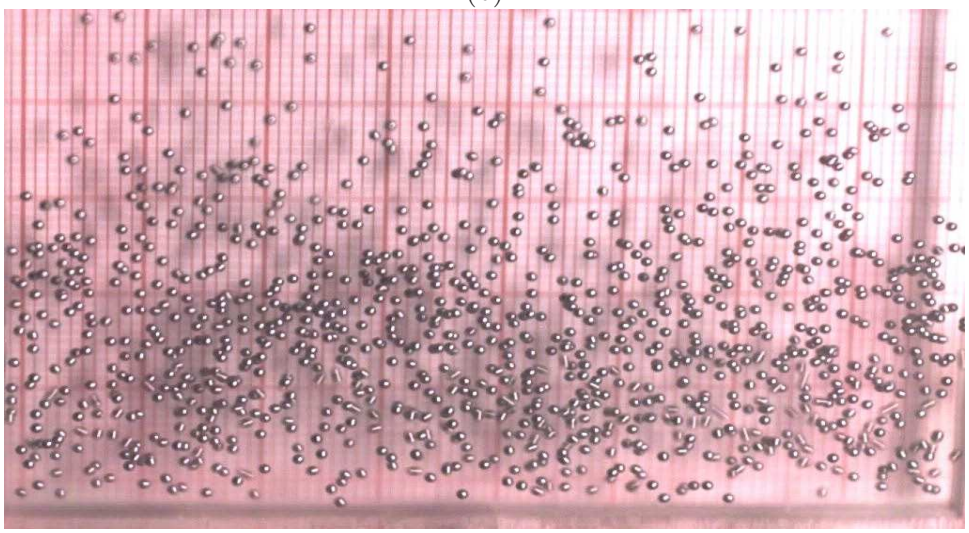

(c)

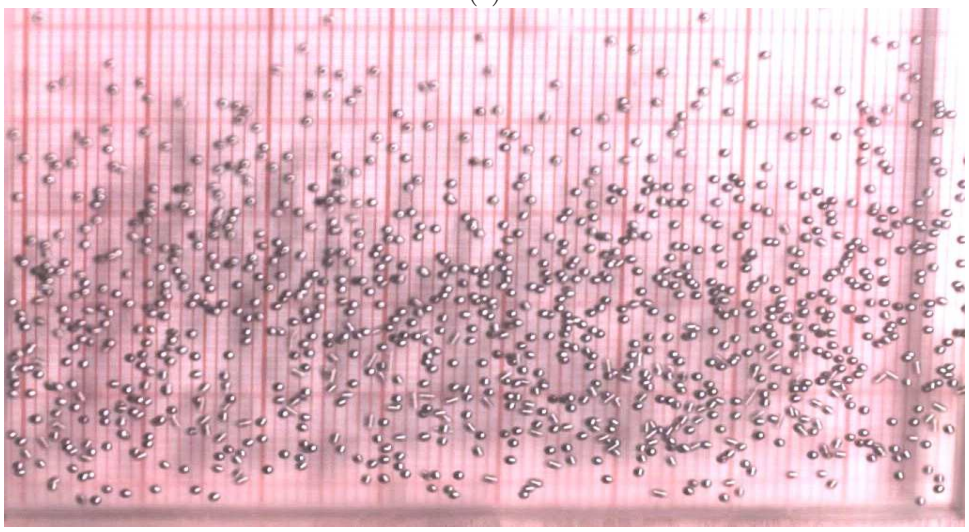

(d)

Figure 3.34: **Transition at constant shaking intensity $\Gamma = 50$ in $F = 3$ layers of monodisperse steel particles with increasing shaking amplitude A/d:** (a) *Gas* at $A/d = 0.5$ ($f = 157.6\ Hz$), (b) *Convection* at $A/d = 1.5$ ($f = 91\ Hz$), (c) *Gas* at $A/d = 3$ ($f = 64.35\ Hz$), and (d) *Gas* at $A/d = 4.5$ ($f = 52.5\ Hz$).

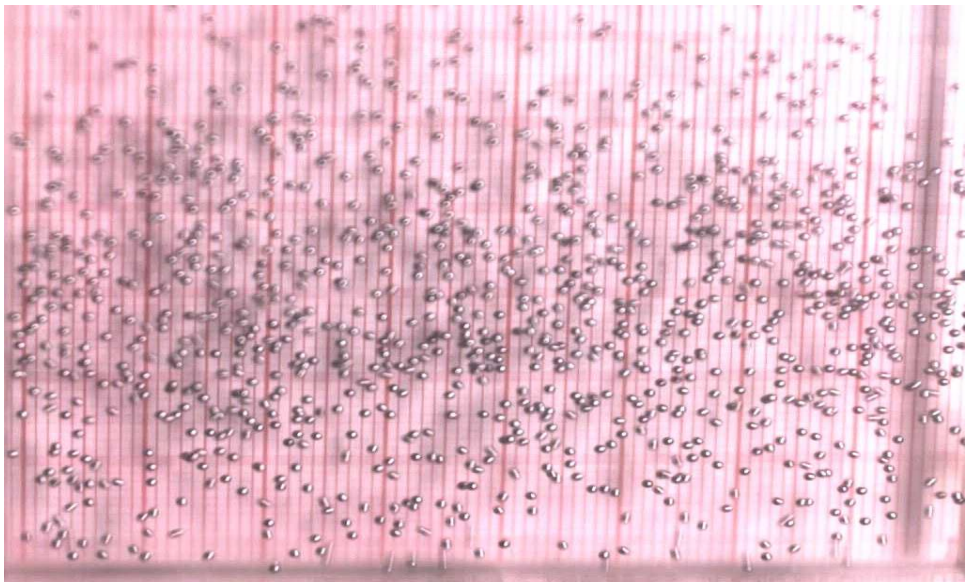

(e)

Figure 3.35: *Continued Fig. 3.34* **Transition at constant shaking intensity $\Gamma = 50$ in $F = 3$ layers of monodisperse steel particles with increasing shaking amplitude A/d:** (e) *Gas* at $A/d = 6$ ($f = 45.5\ Hz$).

almost linear for steel particles, see Fig. 3.29(b) and Fig. 3.39(b).

Fig. 3.44 shows various waves that appear in the system as one increases the shaking amplitude A/d maintaining Γ to be a constant at 7.8. Figs. 3.44(a),(b),(c) show UW of mode $n = 7, 1$ and 2, respectively. Note that as A/d increases, the height of peaks of these waves also increases proportionally. Futher increasing A/d builds up another subharmonic waves,*Spikes*, in the bed (see Fig. 3.44(d),(e)). Fig. 3.45 shows the *Leidenfrost States (LS)* observed at a constant shaking intensity $\Gamma = 20$ with increasing A/d. At a very high shaking intensity $\Gamma = 50$, the system shows LS at moderate amplitudes (see Fig. 3.46(a),(b)) while at higher amplitudes the particles start undergoing convective motion, as displayed in Fig. 3.46(c),(d)) and Fig. 3.47(e)). These convection rolls are qualitatively similar to those observed in monodisperse steel particles (see Fig. 3.38).

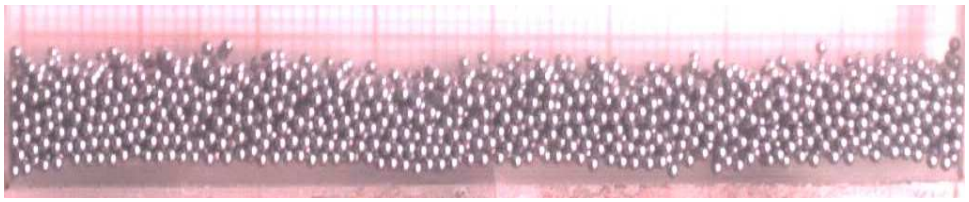

(a)

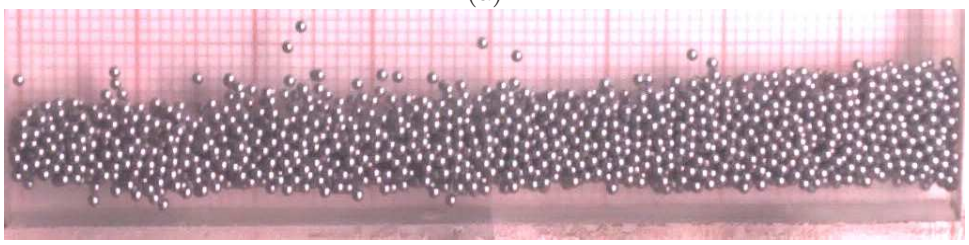

(b)

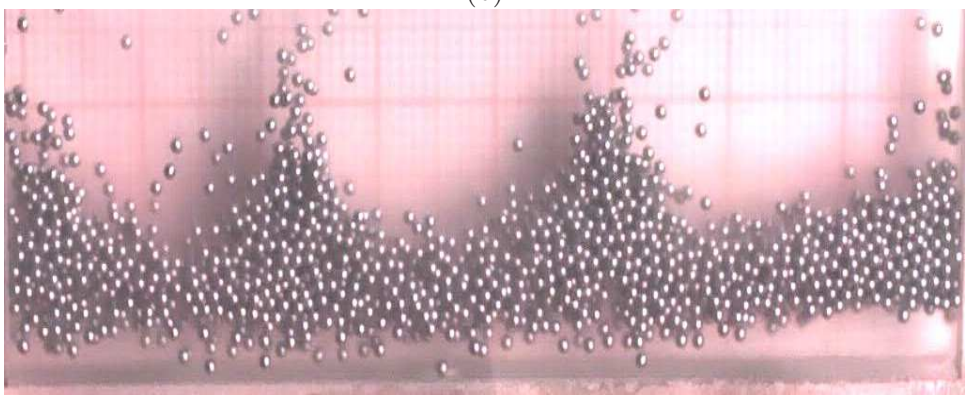

(c)

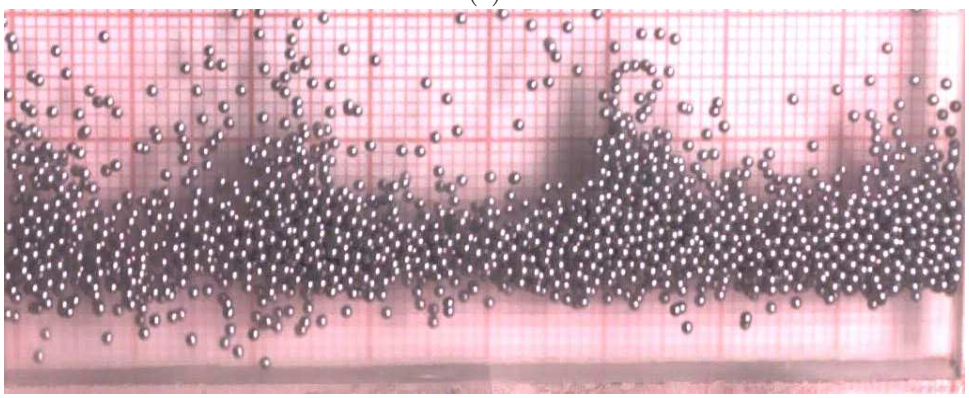

(d)

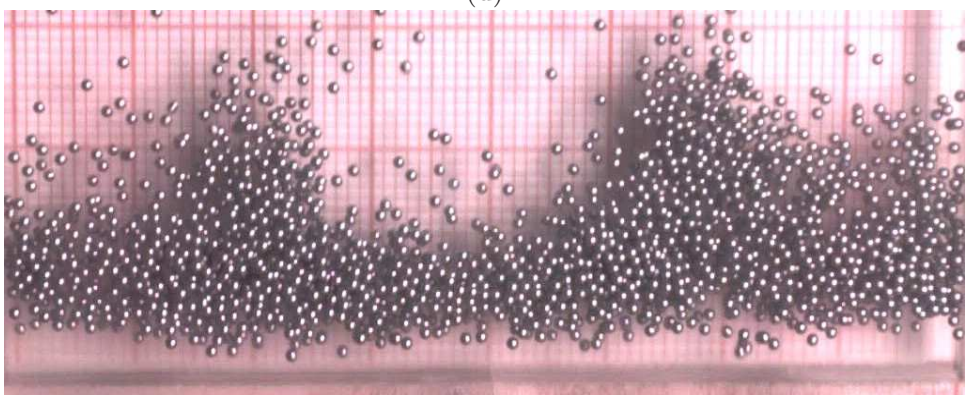

(e)

Figure 3.36: **Transition at constant shaking intensity $\Gamma \approx 7.5$ in $F = 6$ layers of monodisperse steel particles with increasing shaking amplitude A/d:** (a) *BB* at $A/d = 0.5$ ($f = 61\ Hz$), (b) *BB* at $A/d = 1.5$ ($f = 35.24\ Hz$), (c) *Spikes* at $A/d = 3$ ($f = 24.9\ Hz$), (d) *Spikes* at $A/d = 4.5$ ($f = 20.35\ Hz$), and (e) *Spikes* at $A/d = 6$ ($f = 17.6\ Hz$).

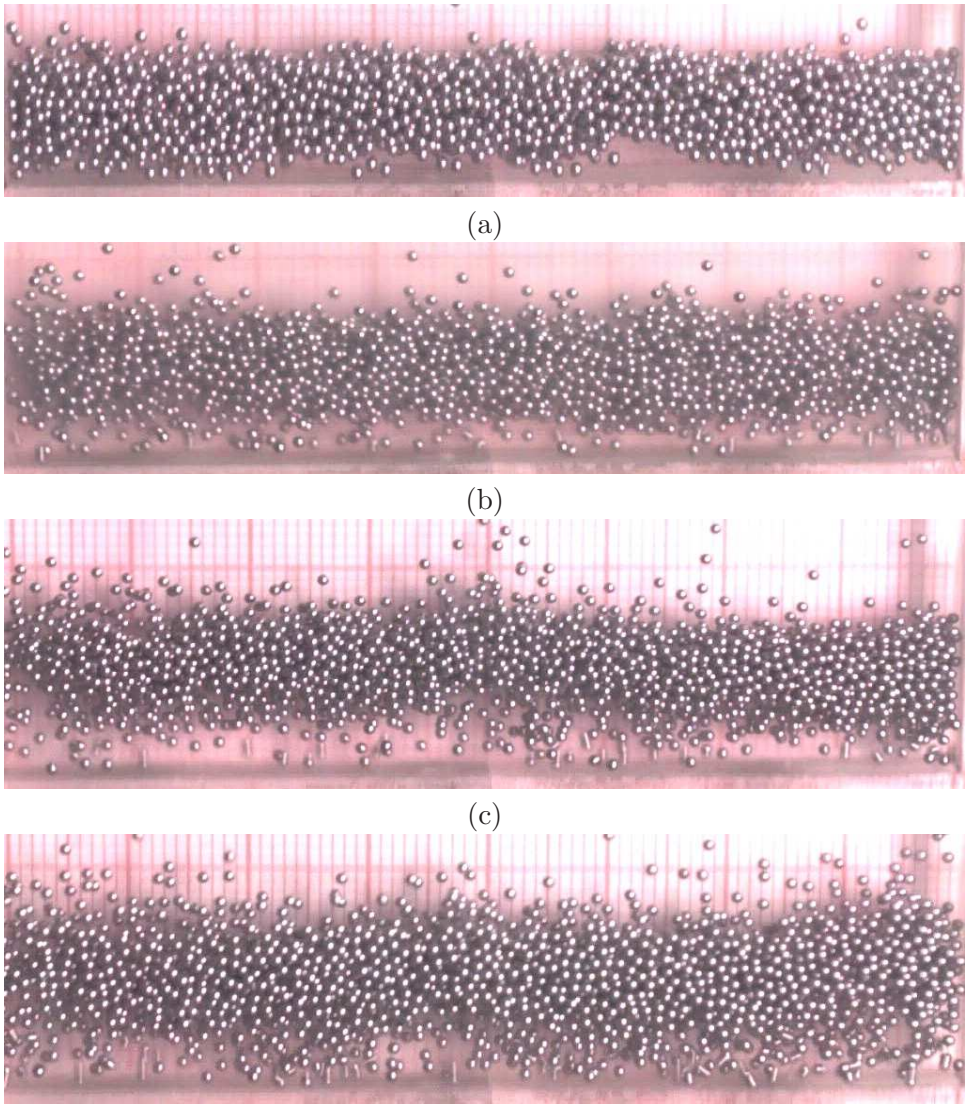

(a)

(b)

(c)

(d)

Figure 3.37: ***Leidenfrost State (LS)*** **observed at constant shaking intensity $\Gamma = 20$ in $F = 6$ layers of monodisperse steel particles with increasing shaking amplitude A/d:** (a) $A/d = 1.5$ ($f = 57.5\ Hz$), (b) $A/d = 3$ ($f = 40.7\ Hz$), (c) $A/d = 4.5$ ($f = 33.2\ Hz$), and (d) $A/d = 6$ ($f = 28.8\ Hz$).

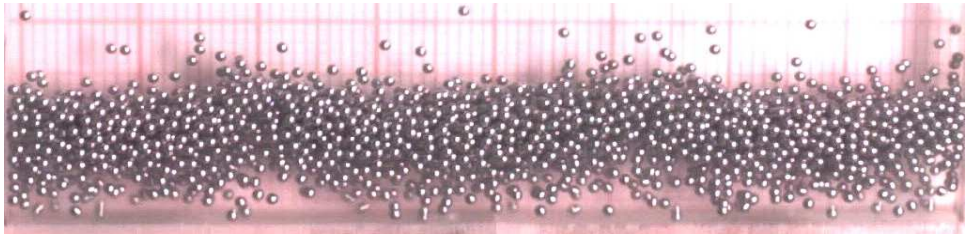

(a)

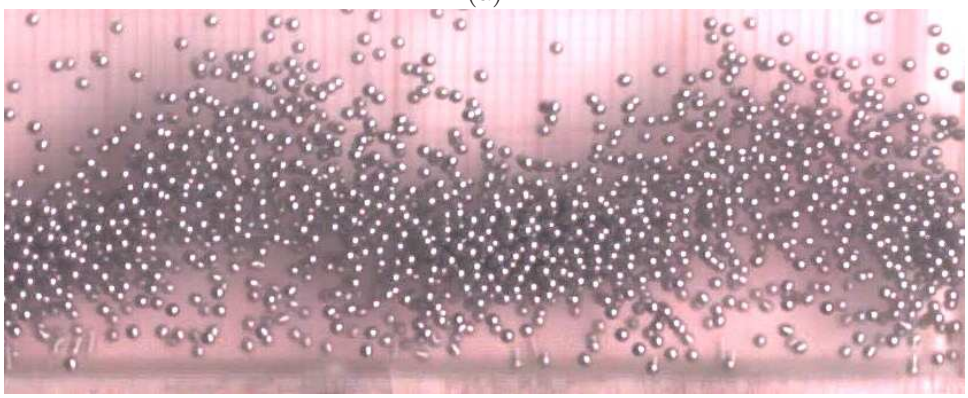

(b)

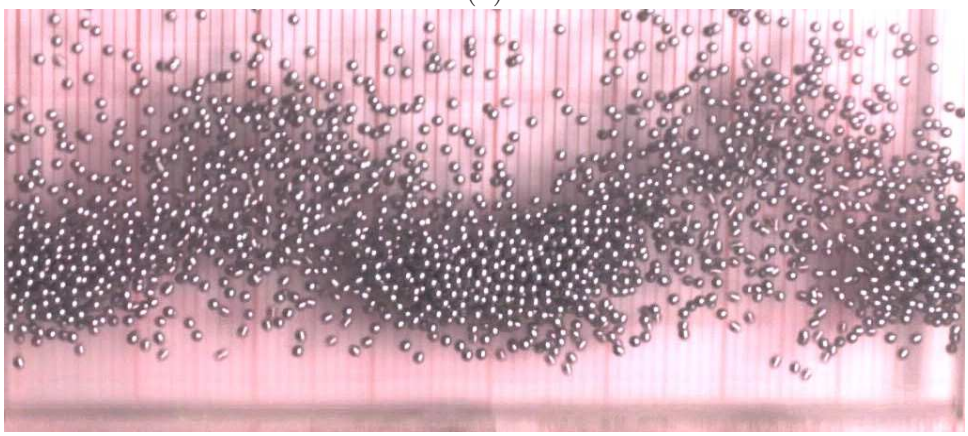

(c)

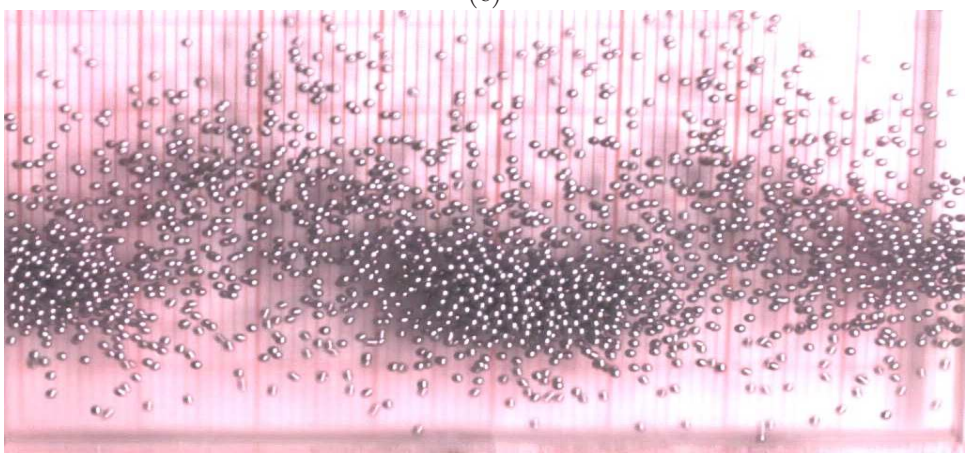

(d)

Figure 3.38: ***Convection*** **observed at constant shaking intensity $\Gamma = 50$ in $F = 6$ layers of monodisperse steel particles with increasing shaking amplitude A/d:** (a) $A/d = 1.5$ ($f = 91\ Hz$), (b) $A/d = 3$ ($f = 64.35\ Hz$), (c) $A/d = 4.5$ ($f = 52.5\ Hz$), and (d) $A/d = 6$ ($f = 45.5\ Hz$).

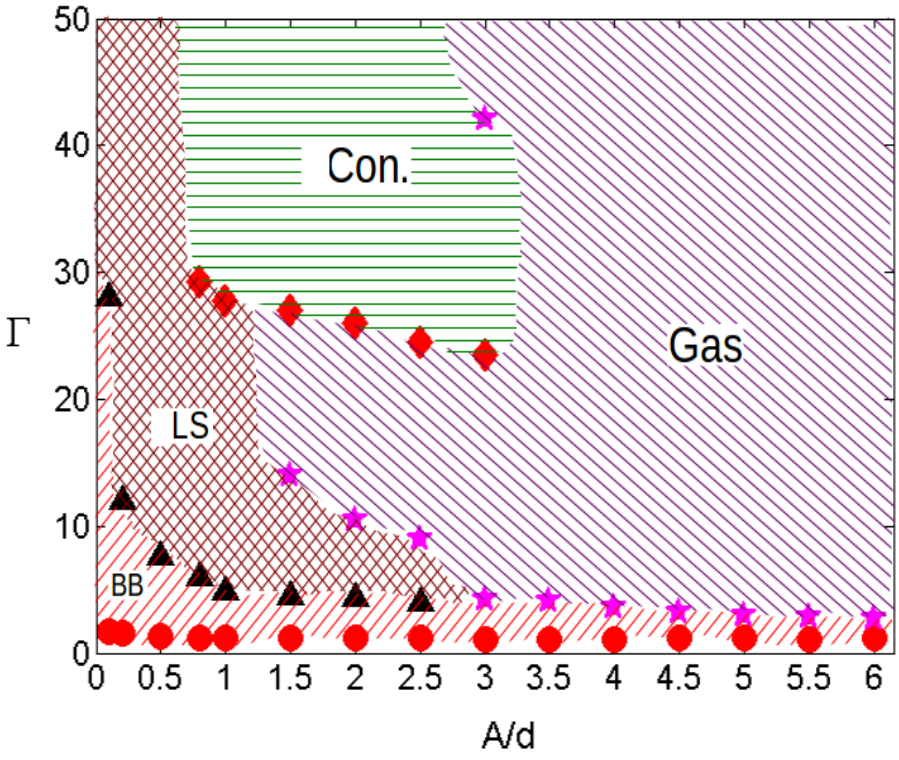

(a)

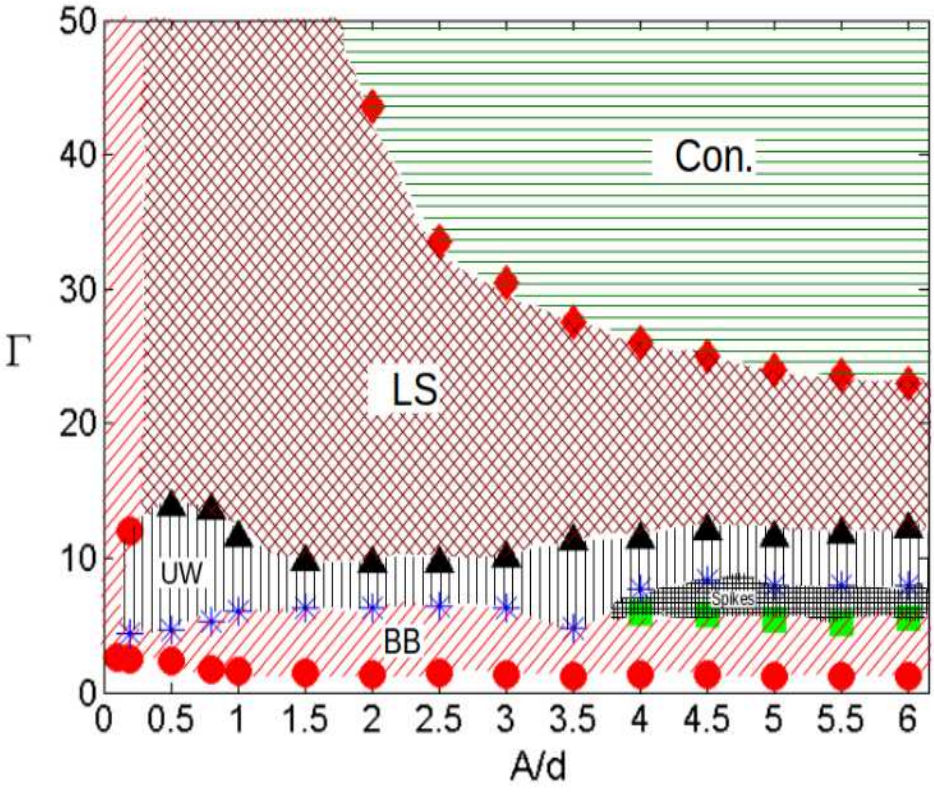

(b)

Figure 3.39: **Phase diagram for glass particles (diameter $d = 1.0\ mm$) confined in $L/d = 80$ box on $(\Gamma, A/d)$-plane for two filling depths: (a) $F = 3$, and (b) $F = 6$.** The shaking intensity Γ has been increased at a constant shaking amplitude A/d via ramping frequency at a linear rate of 0.01 Hz/s.

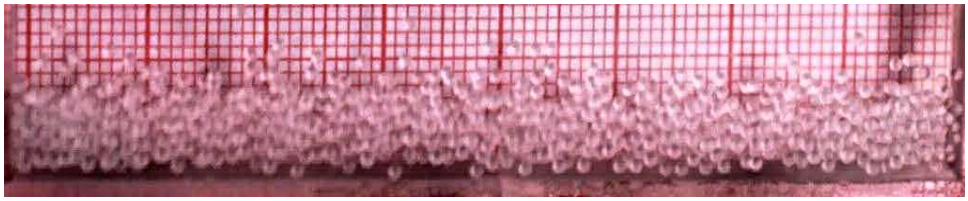

(a)

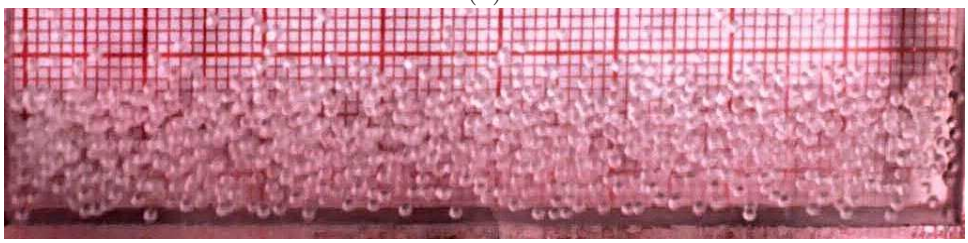

(b)

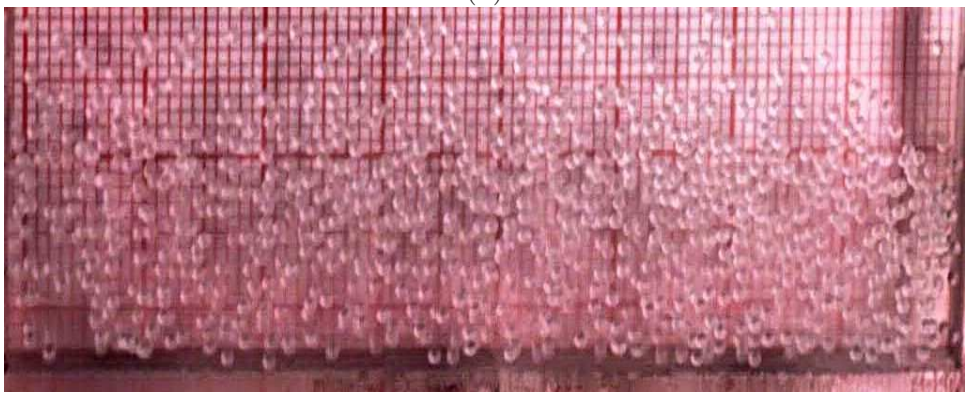

(c)

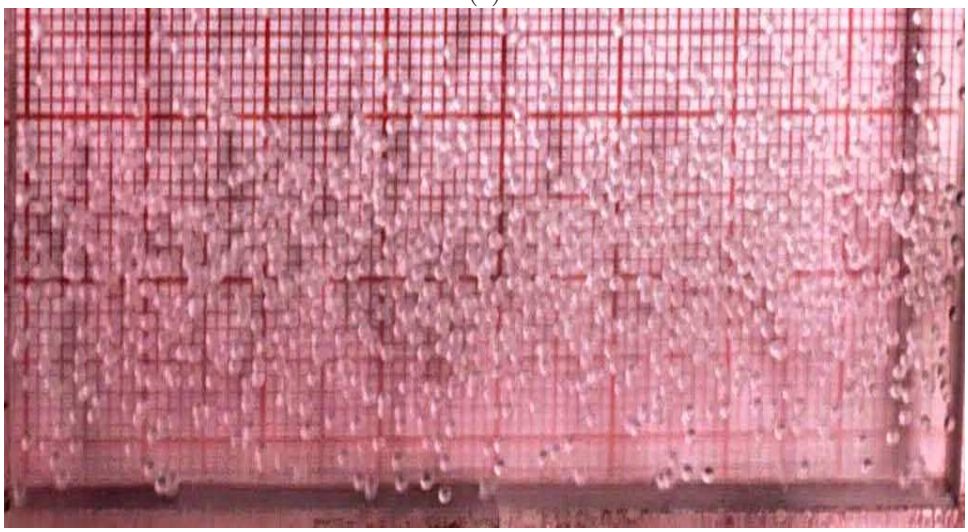

(d)

Figure 3.40: **Transition at constant shaking intensity $\Gamma = 10$ in $F = 3$ layers of monodisperse glass particles with increasing shaking amplitude A/d:** (a) *LS* at $A/d = 0.5$ ($f = 70.5\ Hz$), (b) *LS* at $A/d = 1.5$ ($f = 40.7\ Hz$), (c) *Gas* at $A/d = 3$ ($f = 28.8\ Hz$), and (d) *Gas* at $A/d = 4.5$ ($f = 23.5\ Hz$).

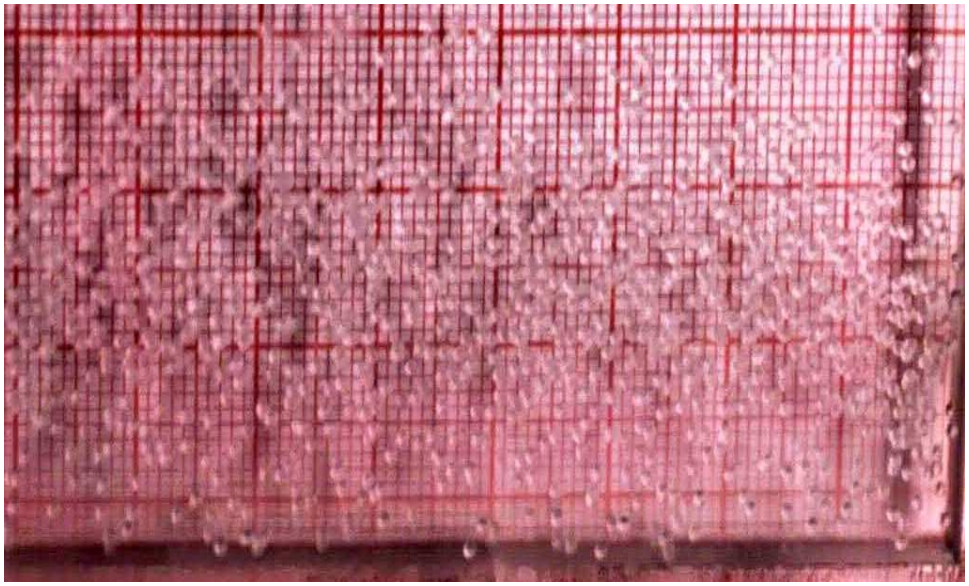

(e)

Figure 3.41: *Continued Fig. 3.40* **Transition at constant shaking intensity $\Gamma = 10$ in $F = 3$ layers of monodisperse glass particles with increasing shaking amplitude A/d:** (e) *Gas* at $A/d = 6$ ($f = 20.35\ Hz$).

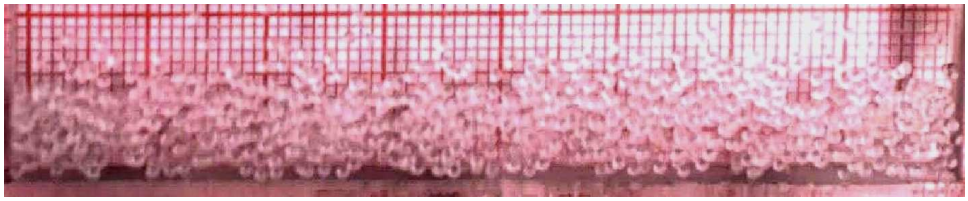

(a)

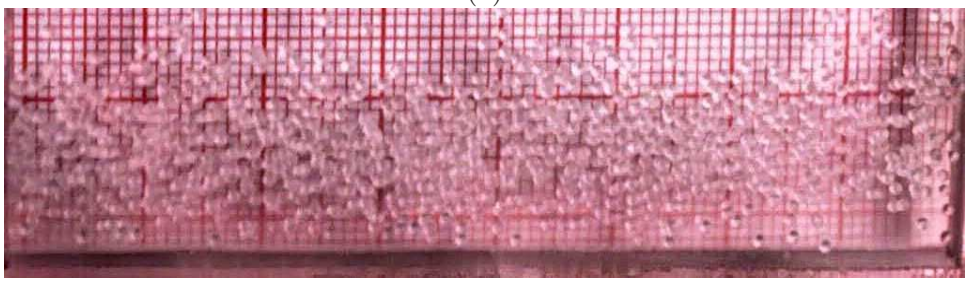

(b)

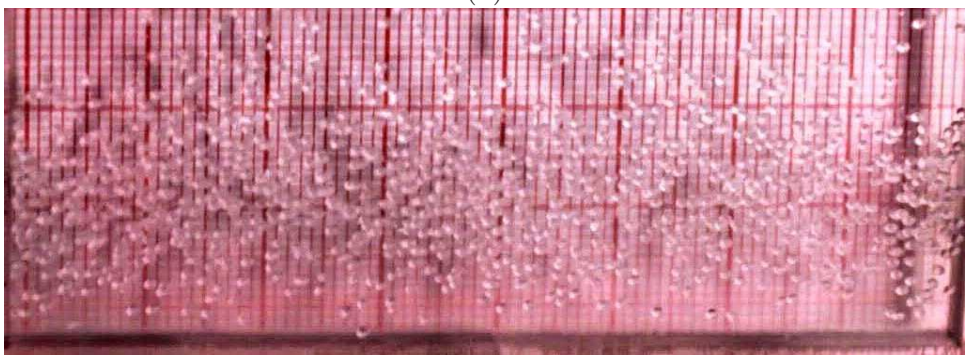

(c)

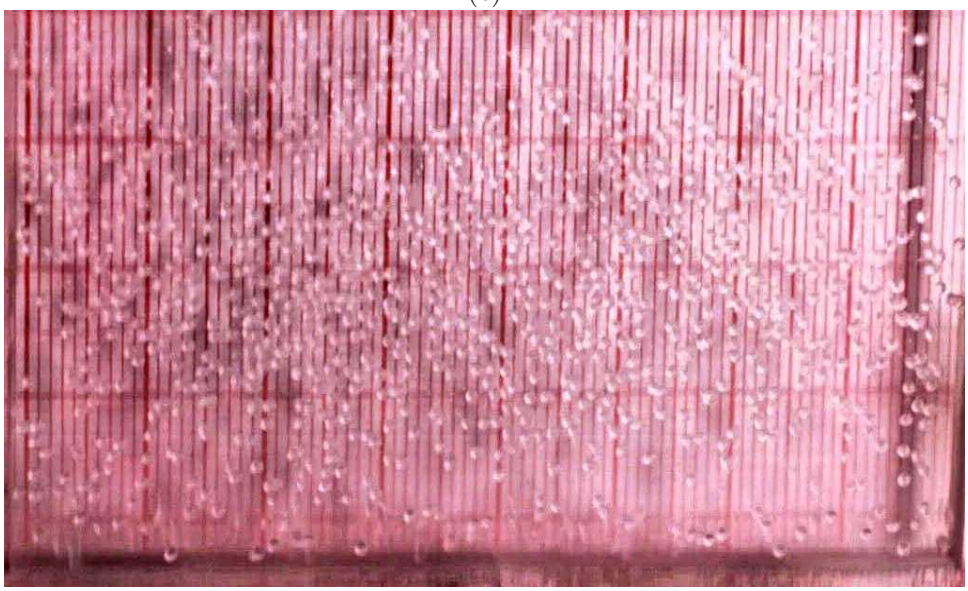

(d)

Figure 3.42: **Transition at constant shaking intensity $\Gamma = 30$ in $F = 3$ layers of monodisperse glass particles with increasing shaking amplitude A/d:** (a) *LS* at $A/d = 0.5$ ($f = 122.1\ Hz$), (b) *Convection* at $A/d = 1.5$ ($f = 70.5\ Hz$), (c) *Convection* at $A/d = 3$ ($f = 49.84\ Hz$), and (d) *Gas* at $A/d = 4.5$ ($f = 40.7\ Hz$).

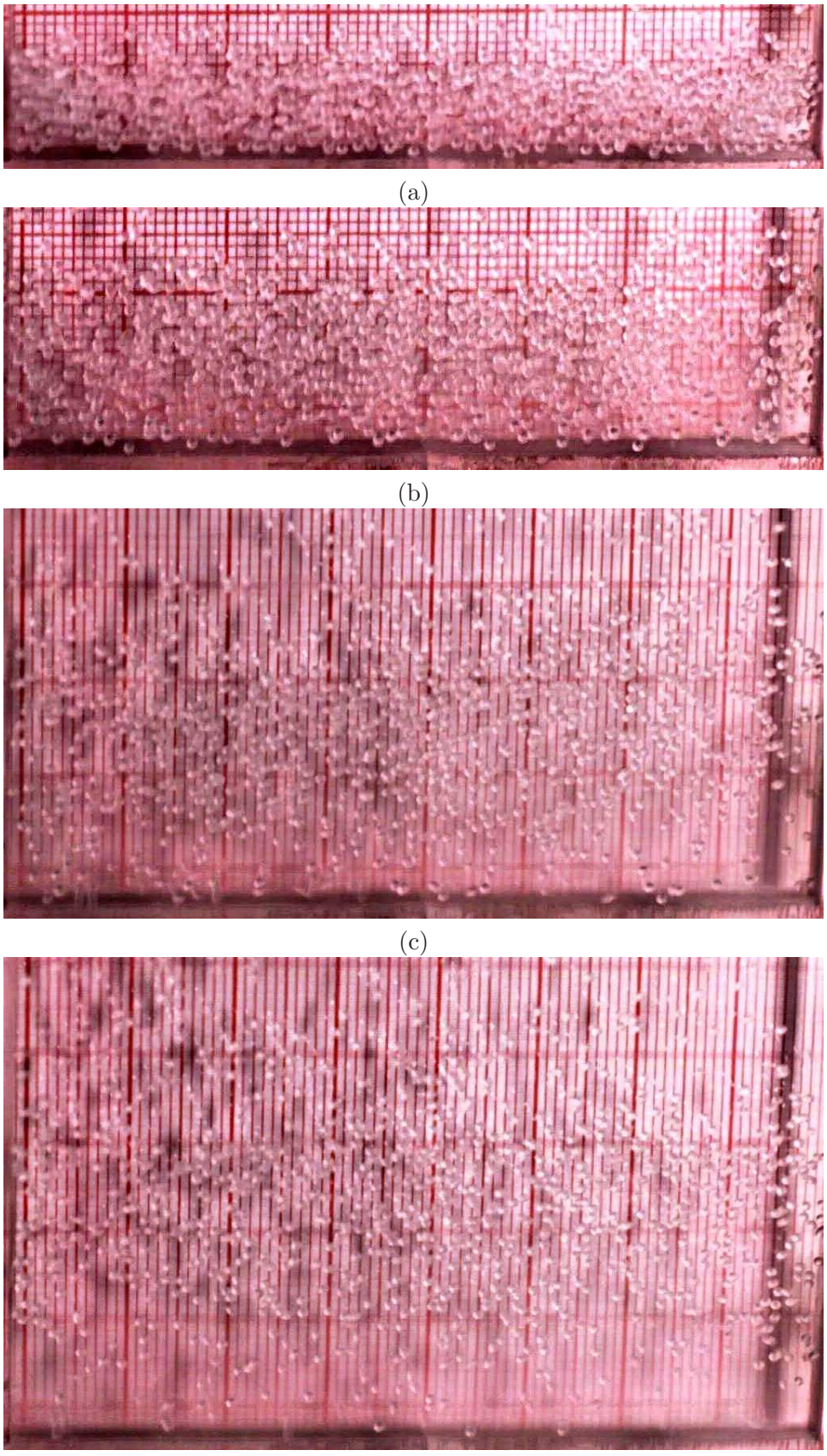

(a) (b) (c) (d)

Figure 3.43: **Transition at constant shaking intensity $\Gamma = 50$ in $F = 3$ layers of monodisperse glass particles with increasing shaking amplitude A/d:** (a) *LS* at $A/d = 0.5$ ($f = 157.6\ Hz$), (b) *Convection* at $A/d = 1.5$ ($f = 91\ Hz$), (c) *Gas* at $A/d = 3$ ($f = 64.35\ Hz$), and (d) *Gas* at $A/d = 4.5$ ($f = 52.5\ Hz$).

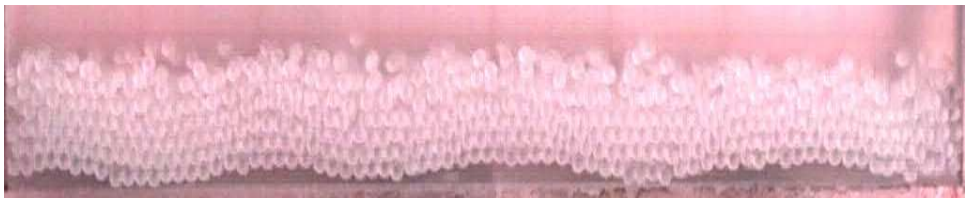

(a)

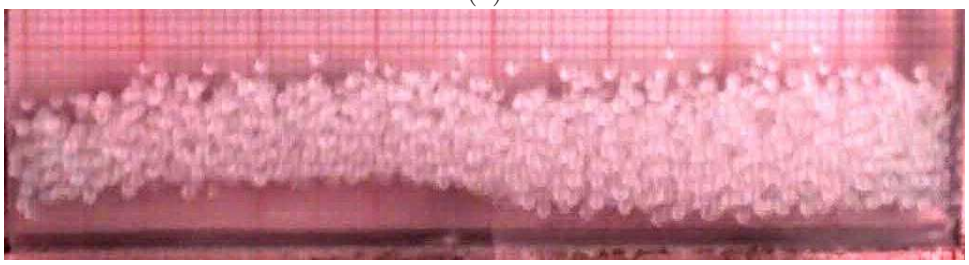

(b)

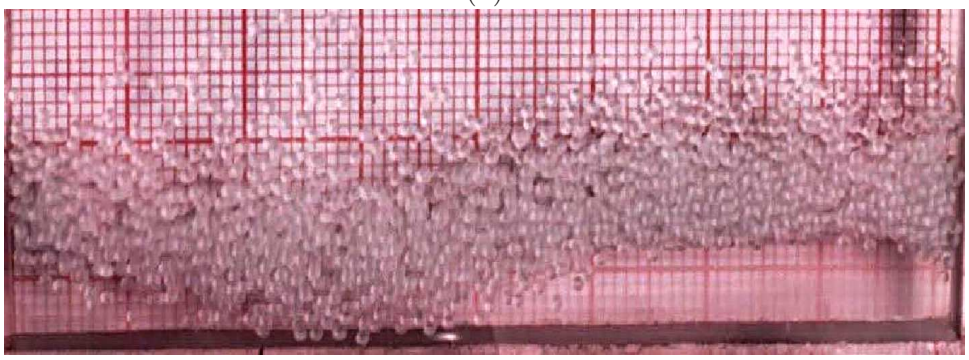

(c)

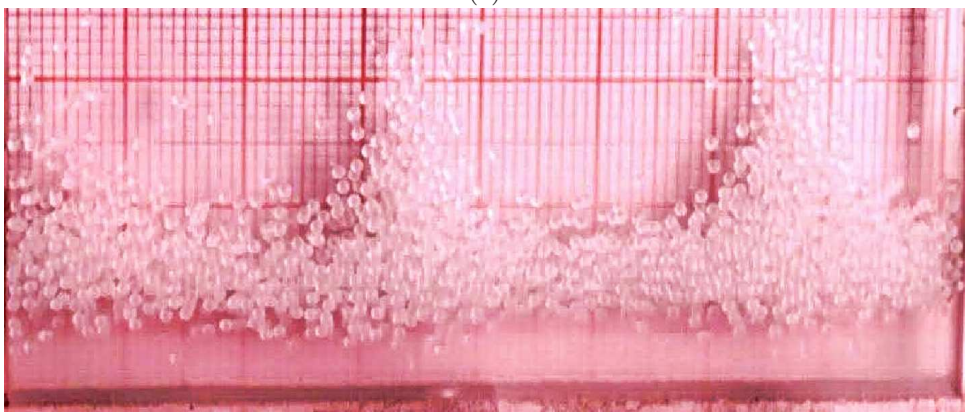

(d)

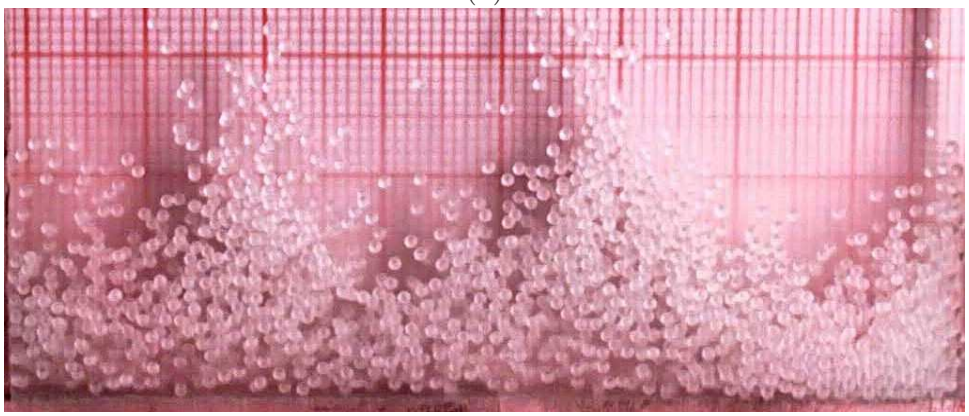

(e)

Figure 3.44: **Transition at constant shaking intensity $\Gamma \approx 7.8$ in $F = 6$ layers of monodisperse glass particles with increasing shaking amplitude A/d:** (a) *UW* ($n = 7$ mode) at $A/d = 0.5$ ($f = 62.26\ Hz$), (b) *UW* ($n = 1$ mode) at $A/d = 1.5$ ($f = 35.9\ Hz$), (c) *UW* ($n = 2$ mode) at $A/d = 3$ ($f = 25.4\ Hz$), (d) *Spikes* at $A/d = 4.5$ ($f = 20.75\ Hz$), and (e) *Spikes* at $A/d = 6$ ($f = 17.97\ Hz$).

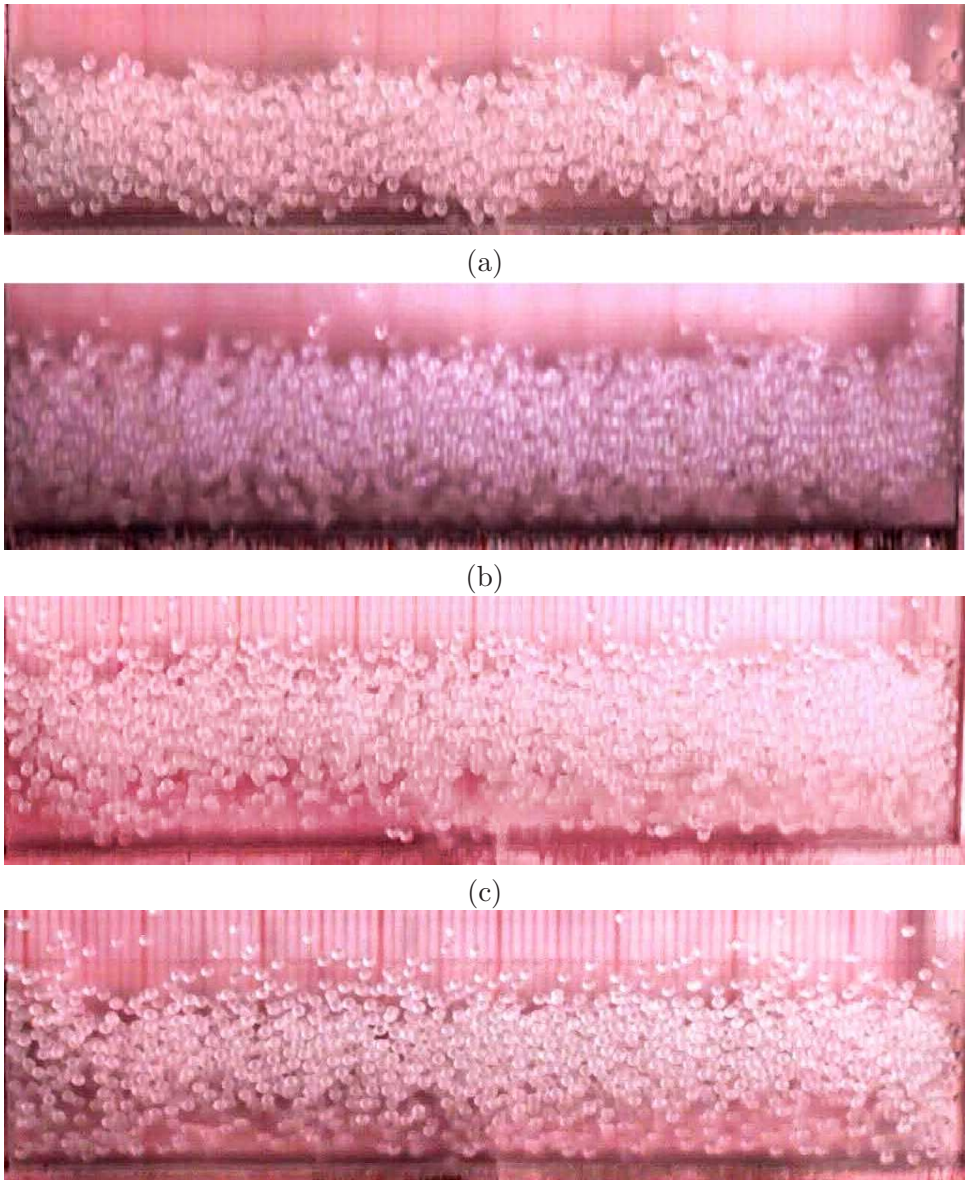

(a)

(b)

(c)

(d)

Figure 3.45: ***Leidenfrost State (LS)* observed at constant shaking intensity $\Gamma = 20$ in $F = 6$ layers of monodisperse glass particles with increasing shaking amplitude A/d:** (a) $A/d = 1.5$ ($f = 57.56\ Hz$), (b) $A/d = 3$ ($f = 40.7\ Hz$), (c) $A/d = 4.5$ ($f = 33.2\ Hz$), and (d) $A/d = 6$ ($f = 28.78\ Hz$).

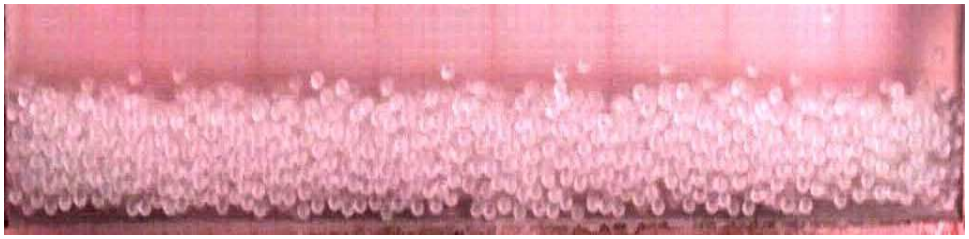

(a)

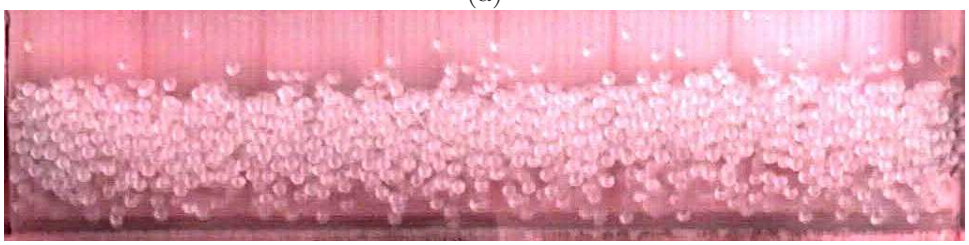

(b)

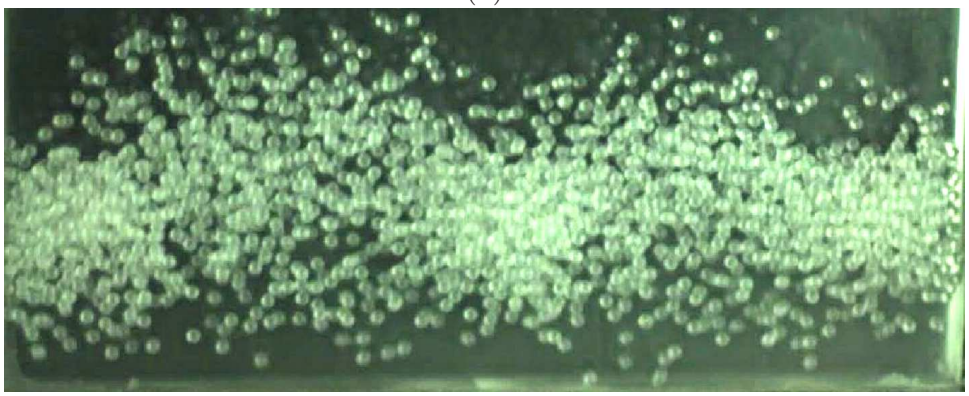

(c)

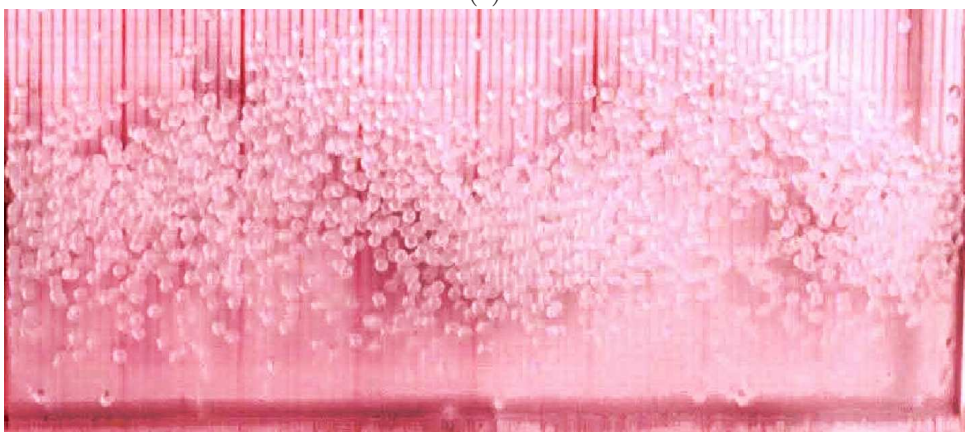

(d)

Figure 3.46: **Transition at constant shaking intensity $\Gamma = 50$ in $F = 6$ layers of monodisperse glass particles with increasing shaking amplitude A/d:** (a) *LS* at $A/d = 0.5$ ($f = 157.6\ Hz$), (b) *LS* at $A/d = 1.5$ ($f = 91\ Hz$), (c) *Convection* at $A/d = 3$ ($f = 64.35\ Hz$), and (d) *Convection* at $A/d = 4.5$ ($f = 52.5\ Hz$).

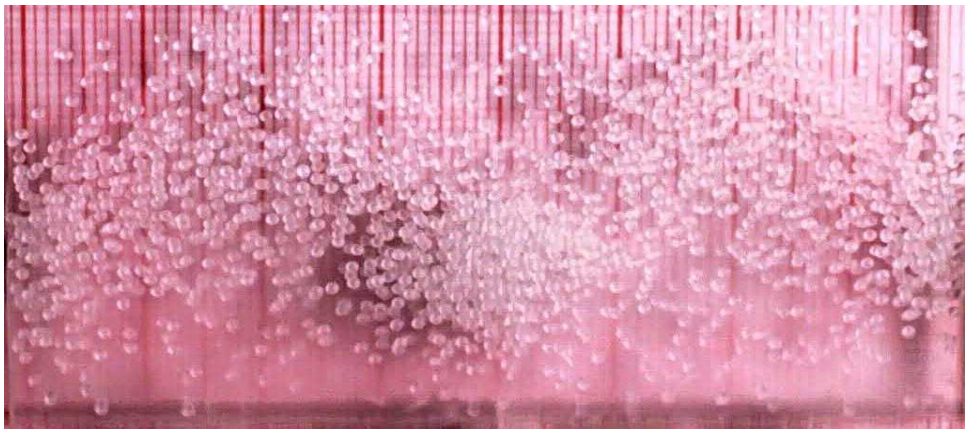

(e)

Figure 3.47: *Continued Fig. 3.46* **Transition at constant shaking intensity $\Gamma = 50$ in $F = 6$ layers of monodisperse glass particles with increasing shaking amplitude A/d:** (e) *Convection* at $A/d = 6$ ($f = 45.5\ Hz$).

Chapter 4

Study of Vertically Vibrated Two-Dimensional Mono-layer Granular System

4.1 Introduction

[1] In this chapter, the experimental results of a two-dimensional granular system are discussed in detail. With two-dimensionality we mean that the width of the container is slightly greater than the diameter of particles such that the container can accommodate only one layer of particles along the width. Due to the two-dimensional nature of the system it is easier to calculate the density, velocity and temperature fields from image-analyses as well as the microstructure of the related phenomena. One phenomenon of major interest is the *Leidenfrost State* in which a dense compact layer of particles is supported by highly fluidized dilute particles. We uncover an unhitherto reported unsteady nature of this state, where the interface separating the dense clustered region from the gaseous region oscillates sinusoidally closely following the vibrating base. In addition to this interface, the top surface of the clustered region is also found to be oscillating harmonically with the frequency of the vibrating plate.

The granular material consists of spherical glass particles of diameters 2 mm and 5 mm. Most of the experiments were performed on monodisperse 2 mm diameter particles confined in a Plexiglas® box of dimension $L = 40$ mm and $W = 2.2$ mm, where L and W are the length and width of the box, respectively. To establish the generality and robustness of our findings, additional experiments have been performed with 5 mm diameter particles held in a box of dimension $L = 100$ mm and $W = 5.5$ mm. The experimental procedure is the same as discussed in the previous chapters, i.e., increasing the shaking intensity (Γ) while maintaining the shaking amplitude (A) to be constant. Two states have been witnessed in the experiments, namely, *Bouncing Bed* that emerges from *Soild Bed* and the *Leidenfrost State*. The critical shaking acceleration Γ_{crit} for the transition $BB \rightarrow LS$ depends strongly on the shaking amplitude A/d and the particle loading F. These transitions have been assimilated on the phase diagram in $(\Gamma, A/d)$-plane and has been discussed in detail in later sections. In the above mentioned experiments, the convection rolls do not emerge, but if one increases the length of box L to 80 mm, particles are reported to start convective motion. This bolsters the fact that a minimum length of the box is required to accommodate at least one convection roll. The transition in such box is as follows: the SB transits to BB which in turn shows LS at a critical shaking intensity. Further increasing the shaking intensity Γ sets up a pair of convection rolls in the system, which

[1] Portions of this chapter have been contributed for the publication: Pattern transition, microstructure, and dynamics in a two-dimensional vibrofluidized granular bed, *Phys. Rev. E*, 93,052901, 2016.

transits to single roll at even higher Γ and this single roll eventually fluidize to granular gas.

4.2 Phase Diagram and Discussions

A liquid drop placed on a hot plate can float over its own vapor layer if the temperature of the plate exceeds a minimum value (Leidenfrost temperature)– this is the celebrated Leidenfrost effect (Leidenfrost 1756; Quere 2013). Expectedly, the Leidenfrost temperature is higher than the boiling point of the liquid, for example, $T_L \approx 200^oC$ for water. When the temperature of the hot plate is less than the Leidenfrost temperature, the drop strews over the surface and rapidly conducts heat through it, resulting in complete vaporization within a short time. However, when the plate temperature is above the Leidenfrost temperature, the bottom layer of the drop which is in contact with the plate vaporizes immediately and the gas pressure of this vapor layer acts as a cushion that helps the drop to stay in a floating state. Due to its poor conductance the vapor layer slows down the rate of heat transfer from the hot plate to the drop and hence the drop survives for a longer time.

Akin to the original Leidenfrost state, a dense, compact layer of particles can be supported by a dilute gaseous region of fast moving particles underneath it in vertically shaken granular materials. This was dubbed *granular Leidenfrost state (LS)* by Eshuis *et al.* (2005) who established this connection first with the original Leidenfrost state in experiments on vertically vibrated bed of a monolayer of glass beads in a quasi-two-dimensional cell. More specifically, they found that a dense region of particles with crystalline-type structure floats over a granular gas at moderate values of shaking intensity. Previous molecular dynamics (MD) simulations had also predicted the possibility of such extreme *density inversion* (Lan & Rosato 1995*b*) or *floating-cluster* (Meerson *et al.* 2003) in a similar setup. Experiments and simulations have noted that the *LS* is a *stationary* state that bifurcates from a time-periodic bouncing bed state (Eshuis *et al.* 2007) with increasing shaking intensity. The stationarity assumption was invoked by Eshuis *et al.* (2010) to carry out the stability analysis of the *LS*. The latter theoretical analysis explained the onset of convection as a pitchfork (stationary) bifurcation from the *LS*. In this chapter, we revisit these experiments and establish that the granular Leidenfrost state is in fact an oscillatory state. Our experimental results *partially* corroborate with recent results from continuum and MD simulations (Bougie *et al.* 2012) in a similar setup. The transition from synchronized oscillatory motion to a probable "steady" state with increasing shaking intensity is more subtle and seems to depends on the shaking amplitude.

Our experimental setup is similar to that of Eshuis *et al.* (2005). It consists of a quasi-two-dimensional rectangular Plexiglas® container with length (L), width (W) and height (H) of 40, 2.2 and 100 mm, respectively. The width of the cell has been chosen such that it fits a monolayer of spherical glass beads of diameter 2 mm and hence forming a two-dimensional system. To establish the generality of our results we performed additional experiments with spherical glass beads of diameter 5 mm in a container with length (L), width (W) and height (H) of 100, 5.5 and 100 mm, respectively. The length of these cells (L/d) has been chosen such that the shaken system admits three types of patterns: (i) solid bed, (ii) bouncing bed, and (iii) Leidenfrost state. Here our primary focus is on the transition from the bouncing bed to the Leidenfrost state and to analyze the dynamics of the latter state.

The container is partially filled with spherical glass beads (density 2500 Kg/m^3) of specified layer depth $F = h_0/d$ (where, h_0 is the bed height at rest) and is vibrated along the vertical direction via an electromagnetic shaker using a sine-wave of the form:

$$y = A\sin(\omega t) = A\sin(2\pi f t), \tag{4.1}$$

where A is the shaking amplitude and f is the frequency of shaking. Most of the results are presented for $d = 2.0\ mm$ diameter glass beads having a filling height of $F = 25$ layers. The dimensionless shaking acceleration/intensity

$$\Gamma = \frac{A\omega^2}{g} = \frac{4\pi^2 A f^2}{g}, \tag{4.2}$$

is used as a control parameter and finally a phase diagram is obtained on $(\Gamma, A/d)$-plane showing various phenomena.

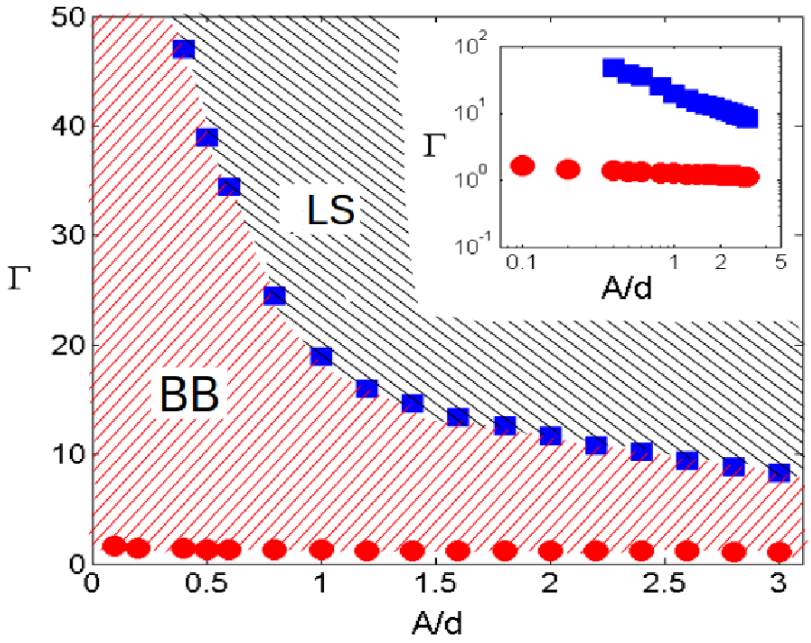

Figure 4.1: **Phase diagram in $(\Gamma, A/d)$-plane for $F = 25$ layers of 2.0 mm diameter glass beads confined in $L/d = 20$ cell.** Regions of Bouncing Bed *(BB)* and granular Leidenfrost state *(LS)* are marked; symbols represent approximate locations of transition while upsweeping at a specified shaking amplitude A/d with the linear frequency-ramping of 0.01 Hz/s. Inset shows the same in logarithmic scale.

The phase diagram in $(\Gamma, A/d)$-plane for $F = 25$ layers of 2.0 mm diameter glass beads is displayed in Fig. 4.1. The experiments have been carried out at a specified shaking amplitude A/d by increasing frequency f linearly at a rate of 0.01 Hz/sec (thence increasing Γ). There are three regimes in Fig. 4.1: the Solid Bed (SB), Bouncing Bed (BB) and Leidenfrost state (LS). For the whole range of A/d with $\Gamma \leq 1$, the granular bed moves synchronously with the shaker

motion without getting detached from the container base- this is the regime of *Solid Bed (SB)*. As the shaking intensity is increased beyond some critical value ($\Gamma > 1$), the bed gets detached from the base and starts a collective motion resembling that of a single particle bouncing off a plate- this is the *Bouncing Bed (BB)* regime. Three successive snapshots of the *BB* at $t = 0$, $\tau/2$, and τ, where $\tau = 1/f$ is the period of shaking, are displayed in Fig. 4.2 for parameter values of $\Gamma = 5$ and $A/d = 2.4$. The inset in Fig. 4.1 indicates that the transition from the solid bed to the bouncing bed regimes occurs at a shaking intensity Γ_{SB}^{BB} that remains relatively independent of the shaking amplitude A/d.

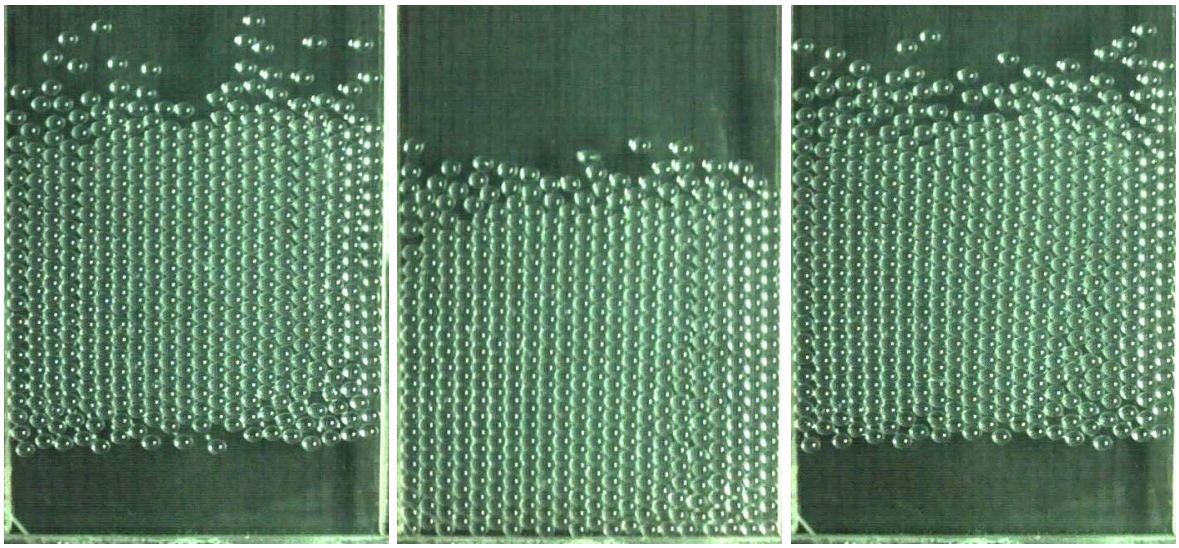

Figure 4.2: **Snapshots of *BB* for $F = 25$ layers of 2.0 mm diameter glass beads, at three successive time instants of the oscillation cycle at $A/d = 2.4$: $t = 0\tau$ (left), $t = \tau/2$ (middle), and $t = \tau$ (right).** Other parameter values are $\Gamma = 5$ ($f = 16.08\ Hz$).

If one increases the shaking intensity (Γ) from the *BB*-regime beyond some critical value, the bouncing bed transits to a *density inverted Leidenfrost state (LS)*: a state where hexagonally packed colder particles float over a dilute region of fast moving hotter particles. Such type of direct transition from *BB*→*LS* should be contrasted with the transition discussed in previous chapters for quasi-2D vibrated bed, where, *Spikes* and *Undulatory Waves (UW)* were the intermediate states. The absence of *UW* in such type of system is due to the inability of the granular string to buckle, as the bed height (H) is much greater than its length (L). One should expect the recurrence of these subharmonic waves when $L > H$. The temporal evolution of the *LS* over an oscillation cycle for $\Gamma = 11$, $\Gamma = 30$, and $\Gamma = 50$ is shown in top, middle and bottom row of Fig. 4.3, respectively. It is noteworthy, that as the shaking intensity is increased the span of the floating cluster shrinks, accompanying with an overall expansion of dilute gaseous region adjacent to the vibrating base.

The blue squares in Fig. 4.1 (see also its inset) indicates that the transition from the bouncing bed *BB* to the granular Leidenfrost state *LS* depends strongly on the shaking amplitude. This result is expected since at higher shaking amplitudes the *LS* can be achieved at lower Γ. The inset and curve fitting confirms that the corresponding critical shaking acceleration Γ_{BB}^{LS} at

which this transition occurs follows a power law:

$$\Gamma_{BB}^{LS} \equiv \Gamma_c \approx 20.74\left(\frac{A}{d}\right)^{-\frac{7}{8}}. \tag{4.3}$$

Rewriting this in terms of shaking strength,

$$S = \Gamma \times (A/d) \tag{4.4}$$

we find,

$$S_c = 20.74\left(\frac{A}{d}\right)^{\frac{1}{8}} \tag{4.5}$$

which too depends on A/d, albeit weakly.

We performed experiments by varying the filling depth F of 2 mm beads and also the diameter of beads (see Fig. 4.4a), and interestingly found that the critical shaking acceleration Γ_{BB}^{LS} depends on the number of layers too and follows the power law:

$$\Gamma_{BB}^{LS} \equiv \Gamma_c = \alpha F^{\beta}\left(\frac{A}{d}\right)^{-\frac{7}{8}} \tag{4.6}$$

This proportionality dependence on the number of layers F is expected since increasing F will increase the weight of the bed which will in turn require higher shaking intensity (Γ) to get fuidized and to spawn *LS*. From the above Eqn. 4.6, we can form two types of scaled Γ:

$$\widehat{\Gamma} = \frac{\Gamma_c}{\alpha F^{\beta}} \tag{4.7}$$

$$\widetilde{\Gamma} = \Gamma_c / \left(\frac{A}{d}\right)^{-\frac{7}{8}} \tag{4.8}$$

This dimesionless $\widehat{\Gamma}$ is independent of F and $\widetilde{\Gamma}$ is independent of shaking amplitude A/d.

Combining Eqn. 4.6 and Eqn. 4.7, we get

$$\widehat{\Gamma} = \left(\frac{A}{d}\right)^{-\frac{7}{8}} \tag{4.9}$$

We plotted the variation of $\widehat{\Gamma}$ with A/d (see Fig. 4.4b) and the various experimental data collapsed very well on a single curve. The same variation has been shown on a logarithmic scale in the inset of Fig. 4.4(b), which also exhibits a good collapse of data. From Eqn. 4.6 and Eqn. 4.8, we can write $\widetilde{\Gamma}$ as

$$\widetilde{\Gamma} = \alpha F^{\beta} \tag{4.10}$$

Taking logarithm on both sides of Eqn. 4.10, we get

$$\ln \widetilde{\Gamma} = \ln \alpha + \beta \ln F \tag{4.11}$$

To obtain the constants, α and β we plotted $\ln \widetilde{\Gamma}$ versus $\ln F$ (see Fig. 4.4*b*). The slope and intercept of the best fit curve (red line) confirms that $\alpha = 0.414$ and $\beta = 1.217$ Therefore, the

critical shaking acceleration Γ_{BB}^{LS} follows the following power law

$$\Gamma_{BB}^{LS} \equiv \Gamma_c = 0.414\, F^{1.217} \left(\frac{A}{d}\right)^{-\frac{7}{8}} \tag{4.12}$$

4.3 Mean Fields: Density and temperature

To assess the unfolding of structure of bed packing while it is vertically vibrated at various shaking intensities, we looked over the density profiles of the bed. The density profiles have been calculated from the digitized (binary) version of the experimental snapshots by determing an "effective" normalized pixel density (i.e., counting pixels that constitute the beads) over a box of height 5 pixels and width equal to image width in pixels. The averaged density profile for the *BB* state observed at $\Gamma = 5$ is indicated in Fig 4.5(a) by the red curve; note that the averaging has been done over hundreds of oscillation cycles. The density shows an increase from the base of the container to a height corresponding to 'maximum' density, beyond which it nearly remains constant for a certain thickness indicating that this is a region wherein particles are packed hexagonally. The 'maximum' density attained is very close to the packing density pertaining to hexagonally packed crystal lattice. This observation is a clear signature of the crystalline structure of particles within the bouncing bed. Such type of crystalline structure in *BB* has been previously observed by Clément & Rajchenbach (1991); Fiscina & Cáceres (2005) and theoretically modelled by Hayakawa & Hong (1997). Beyond a certain height the density shows a rapid fall indicating the existence of a dilute gas-like layer of fast moving particles on the top of bed. It is noteworthy that, the density profile of *BB* at a higher shaking intensity $\Gamma = 10$ (just below the transition point to *LS*), has initiated manifesting a weak "density inversion". Furthermore, the 'maximum' density which the bed has achieved is smaller than the 'maximum' density attained in case of *BB* at $\Gamma = 5$; this is anticipated since the bed at higher Γ will be loosely packed due to relatively higher fluidization. Nevertheless, the density profile of *BB* at $\Gamma = 10$ follows almost the same trend of density decay as that of *BB* at $\Gamma = 5$ beyond this maximal density height. It is also noticeable that, the density profile at higher Γ spans upto a larger height due to higher bounce-off of the top gaseous layers, and this trend is successfully captured in various other density profiles of Fig 4.5(a).

If we further increase the shaking intensity Γ, we observe from the density profile in Fig. 4.5(a) that at $\Gamma = 11$ (magenta curve) there is an extreme *density inversion*, showing that the system transited to Leidenfrost state (*LS*). Note that the maximum density within the *floating* cluster is lower than in the *crystalline* bouncing bed, implying a liquid-like structure within the *floating* cluster in the *LS*. Further increasing the shaking acceleration leads to an overall expansion of the granular bed in which the size and density of the floating cluster gradually reduces but the dilute gaseous region grows in size. These features are clearly evident from the density profiles in Fig. 4.5(a). Comparing the black and blue curves, we find that the density reduction above the floating cluster becomes more gradual with increasing Γ, implying that there exists a 'saltating' layer of fast-moving particles above the dense-cluster. We have thus identified three regions in granular Leidenfrost state: (i) the hexagonally packed compact *floating cluster*, (ii) the dilute

gaseous *collisional layer* adjacent to the base of vibrating container and acting as a cushion for the floating cluster and, hence, supporting it, and (iii) the *ballistic layer* consisting of fluidized particles on the top of clustered region. This *ballistic* layer is even observed in case of *BB*, wherein bunch of particles move in a chaotic fashion over the crystalline packed bed.

In granular physics, it is often customary to invoke the classical definition of "granular temperature" T, as an extension of its thermodynamic equivalent. It is a useful concept which provides an important characterization of fluidized granular matter, and is defined as the mean-square of the velocity fluctuations around the mean flow velocity:

$$T = \frac{1}{2} m \langle (v - u)^2 \rangle, \tag{4.13}$$

where v is the particle velocity and u is the mean flow velocity (which vanishes in the vibrated bed case) and the angular bracket denotes a suitable averaging over many snapshots of the system.

The temperature T and temperature ratio (T_x/T_y) profile for the corresponding states of Fig. 4.5(a) has been shown in Fig. 4.5(b) and Fig. 4.5(c), respectively. The temperature has been obtained by determining each individual particle's position frame by frame. Once the individual particle position is extracted for a batch of snapshots using the Particle Tracking Velocimetry method as discussed in Chapter 2, the velocity can be determined and thence granular temperature by deploying Eqn. 4.13. The profile is generated by binning the particles in a box of height of 2 particle diameters and width as that of snapshot; the temperature of particles whose centre of mass lies inside a considered bin is averaged and this averaging is further run on a batch of 400 snapshots or even more, to obtain granular temperature at a specified height of the flow field. Furthermore, the temperature has been normalized with the constant temperature T_0 at the base to yield the scaled temperature $\widetilde{T} = T/T_0$. In case of *BB* at $\Gamma = 5$, the temperature remains almost constant upto height of the "crystalline" packed bed. At the top of this hexagonally packed crystalline structure of the *BB*, the temperature increases due to the higher kinetic energy possessed by the fluidized particles constituting the *ballistic layer*. On the contrary, in case of *LS*, the temperature monotonously decreases from the vibrating base to the floating cluster. This confirms the fact that in granular Leidenfrost state cold cluster of particles float over fast moving hotter gaseous particles. Nevertheless, moving above this cold *floating cluster*, the temperature shows a tendency to increase because of comparatively more agitated *ballistic* particles at the top of the cluster. The temperature profile of *BB* just below the point of transition to *LS* (at $\Gamma = 10$), clearly shows a weak sign of such monotonic decrease of temperature from the vibrating base, betokening the onset of *LS*. Thus, on comparing the temperature profiles for *BB* at $\Gamma = 5$ and $\Gamma = 10$, it can be well concluded that the system already started showing the weak density inversion which fully develops in the temperature profile of *LS* at shaking intensity $\Gamma = 11$ and higher ones. It should be noted that the temperature is lower near the base for *BB* in contrast to the *LS* for which it is maximum at the base. This behavior of temperature variation is a distinguishing criterion between *BB* and *LS*; the comparatively higher temperature near the base in case of *LS* sets up due to the hotter dilute gaseous region which is absent in *Bouncing Bed* state.

From the temperature ratio (T_x/T_y) profile of the *LS* at $\Gamma = 11$ (refer Fig. 4.5(c)), it is

evident that the temperature in vertical direction is much larger than that in the horizontal direction near the base and this is expected too since the system is vertically driven and thence vertical velocity should be much higher than the horizontal one. It is also noteworthy, that away from the base the particles show the tendency to possess more horizontal velocity as compared to particles near the base, this is due to the fact that the *ballistic layer* is rarely populated region, and hence particles can gain momentum in horizontal direction much easily. The temperature ratio profiles for *LS* at even higher shaking intensities presents a much clear picture of relative magnitudes of horizontal and vertical granular temperatures, wherein the vertical temperature is found to be much greater that horizontal one near the base while moving away from the base an exactly antipodal scenario is witnessed. Nevertheless, such drastic variation of the temperature ratio with the height is not evident in case of *BB*. The temperature ratio for *BB* at $\Gamma = 5$ is almost constant at a very small value ($T_x/T_y \approx 0.15$), due to the fact that the bed is compact and vertically driven; in contrast, temperature ratio profile for *BB* at $\Gamma = 10$ tries to approach the same trend as that of *LS* at $\Gamma = 11$, forerunning the onset of *LS*.

Fig. 4.6 shows the instantaneous coarse grained velocity fields of these states, obtained from the analysis of the snapshots using PIV (particle image velocimetry) software. The velocity vectors change their direction after every half time-period ($\tau/2$) of the shaking cycle indicating that these states (*BB* as well as *LS*) are synchronized with the vibrating base. Nevertheless, the velocity vectors in case of *BB* show strong correlation which indicates that the whole bed moves coherently like a single body. This correlation of velocity vectors decreases as one increases the shaking strength S, which is evident from Fig. 4.6. In particular, for *LS* at stronger shakings, the gaseous "collisional" region shows uncorrelated velocity fields as anticipated.

Let us traverse the phase diagram (see Fig. 4.1) at constant shaking intensity $\Gamma = 50$ while increasing the shaking amplitude (A/d). The density, temperature and temperature ratio profiles have been compared in Fig. 4.7. At small A/d the bouncing bed is observed and density profile for this *BB* shows that the particles are arranged in a crystalline structure as discussed earlier. However, in a very thin regime of about 3 particle diameters just adjacent to the the vibrating base, the density is found to be curtailed in comparison to the maximal density of the crystalline packed bed, due to the loosely packed bed near the base. Increasing the shaking amplitude (A/d) beyond a critical value causes the *density inversion* (see Fig. 4.7(a)), marking the onset of *LS* in the system. This density attains its maximum value at a certain height away from the base once it crosses the *collisional layer* and encounters the *floating cluster*, remains constant at this maximal value upto the thickness corresponding to the hexagonally packed *floating cluster*, and then further droops rapidly across the rarefied *ballistic layer*. The thickness pertaining to the unvarying maximal density regime contracts as one increases the shaking amplitude A/d, indicating that the crystalline *floating cluster* region fluidizes and shrinks at higher amplitudes.

The temperature for *BB* states shows an increasing trend from the base to the top due to the decrease in compactness of the arrangement of particles as one moves away from the base, and further due to the encounter with *ballistic* layer (refer Fig. 4.7(b)). On the contrary, in case of *LS*, the temperature shows a decaying behavior away from the base within the collisional regime attaining a minimum value and then increasing, albeit mildly, due the presence of free *ballistic* layer at the top of the *floating* cluster. The segment of almost constant temperature in

the temperature profile of *LS*, corresponds to the 'cold' *floating cluster*. Further, comparing the temperature profiles of *BB* at $A/d = 0.1$ and 0.2, one realizes that the larger shaking amplitude imparts a relatively higher temperature, owing to the fact that larger amplitude shaking makes the packing of the bed sparse and loose, rendering increased mobility of particles and thence higher temperature. The temperature ratio profiles (refer Fig. 4.7(c)) show a close agreement in their tenor when compared with those presented in Fig. 4.5(c).

Let us now consider the transition *BB*→*LS* when the shaking intensity Γ is kept constant at 30, this corresponds to increasing amplitude (A/d) and decreasing frequency (f) in our experiments (see Fig. 4.1). Fig. 4.8 shows a comparison of density and temperature profiles for the various states: (a) *BB* at $A/d = 0.5$, (b) *LS* at $A/d = 1.2$, and $A/d = 2.2$. It is interesting to note that although the blue curve in Fig. 4.8(a) represents the density profile of *BB* state, yet there is a weak discernible density inversion. Such type of behavior is anticipated since the data point corresponding to this curve lies just before the onset of *LS* state (refer Fig. 4.1), and hence it should display the mixed characteristic of *BB* approaching towards *LS*. Nevertheless, the red and blue curves of Fig. 4.8(a) exhibits the fully developed "density inversion" characterizing *Leidenfrost State*. Withal, the maximum density attained in case of hexagonally packed *BB* is highest and the maximum density achieved in the region of *floating cluster* of *LS* decreases as one escalates the shaking amplitude at constant shaking intensity owing to the fact that bed shaken by larger amplitude engenders loosely packed crystalline structure.

Now turning our contemplation towards the corresponding temperature profiles in Fig. 4.8(b), it can be inferred that these temperature profiles corroborate the tenor of previously discussed one; in case of *LS*, the temperature declines off monotonously as one traverses away from the vibrating base, attains a minima at the commence of *floating cluster* region, remains almost constant throughout this clustered layer, and then steps-up on encountering the *ballistic layer*. Comparing the temperature profiles of *LS* at $A/d = 1.2$ and 2.2, we observe that both the curves follow each other in their trend, except that the temperature in case of $A/d = 2.2$ surpasses that of *LS* at $A/d = 1.2$ in the *ballistic* regime due to larger amplitude vibration. The temperature profile for *BB* state exhibits approximately constant magnitude within the crystalline packed bed and increases rapidly while confronting the top *ballistic layer*. It is noteworthy that the normalized temperature for *BB* realized at $A/d = 0.5$ and $\Gamma = 30$ is higher than the normalized temperature for *BB* observed at $A/d = 0.1, 0.2$ and $\Gamma = 50$ (refer Fig. 4.7(b)); this suggests that the dynamics of fluidized bed depends in a much subtle manner on both the vibration parameters, viz, frequency and amplitude of vibration.

We will now discuss some set of experimental results with $F = 12$ layers of 5 mm diameter glass beads confined in a Plexiglas® box of dimension $L = 100$ mm and $W = 5.5$ mm. The snapshots for the transition *BB*→*LS* at constant $A/d = 1$ while increasing shaking intensity Γ (refer Fig. 4.4(a)) is displayed in Fig. 4.9. The averaged density profiles for various states of this transtion has been compared in Fig. 4.10. As cofirmed in previous paragraphs, we find the maximum local density within the floating cluster of *LS* to be much lower than that in the crystalline *BB*-state. It is seen that the height of the bed (y_{crys}) as well as the extent of the dilute gaseous region (y_{coll}) increase with Γ, owing to the fact that higher shaking intensity generates more vigorous fluidization, and aids the expansion of bed in vertical direction. However, the

dense region of the bed (floating cluster) remains compact on its top layer since the density reduces sharply above the *floating cluster* region (see the red and blue curve). It is remarkable that the "density inversion" is again undisputably witnessed in case of *LS*, warranting the previous established criterion for its onset.

4.4 Microstructure

An important quantity employed for studying the structural characteristics of a particulate system is the so-called pair correlation function (also called radial distribution function) $g(r)$, which describes how on average the particles in a fluid are radially packed around each other. Mathematically, the radial distribution function is given by (Allen & Tildesley 1989)

$$g(\mathbf{r}) = \frac{1}{N\rho(r)} \sum_{i=1}^{N} \sum_{j \neq i}^{N} \langle \delta(\mathbf{r} + \mathbf{r}_j - \mathbf{r}_i) \rangle, \tag{4.14}$$

where, $\rho(r)g(r)$ is the conditional probability of finding a particle at a distance r away from the reference particle, and

$$\int_{r=0}^{\infty} \rho(r) g(r) 2\pi r dr = N - 1 \tag{4.15}$$

We calculated pair correlation function $g(r)$ for the various regions of the granular Leidenfrost state to study the microstructure of arrangement of particles. The $g(r)$ has been calculated considering two types of geometries: (a) stripe of thicknes $1.5d$ at the centre of respective regions, and (b) square geometry of side equal to the height to which the various regions span. The $g(r)$ for various regions of *LS* observed in $F = 25$ layers of 2.0 *mm* diameter glass beads at $A/d = 2.4$ and $\Gamma = 30$, has been shown in Fig. 4.11, considering these two types of geometries The $g(r)$ for dense *floating cluster* shows signature of crystalline structure with peaks at regular intervals. The first peak evolves at the contact point, i.e., at $r \approx 1.002d$, with the other subsequent peaks occuring at regular spacings signifying the highly ordered hexagonally packed crystalline structure of this clustered region. The *collisional* and *ballistic* regions of the *LS* are gaseous in nature whose signature is clearly evident from their $g(r)$ in Fig. 4.11. The $g(r)$ shows a peak at a distance equal to particle diameter and then decays rapidly with distance until it asymptotes to unity, showing that particles are uncorrelated at large distances. It should be noted that for an ideal gas of hard spheres, $g(r)$ is independent of position and is equal to unity everywhere, except at $r = d$ where it has a peak ($g(r = d) > 1$) and $r < d$ where $g(r < d) = 0$.

However, the peak for *ballistic* region is higher than that of *collisional* one, suggesting that *ballistic* region is comparatively denser than *collisional* one. This is the reason why the granular temperature within *collisional layer* is much greater than that of the *ballistic layer* (see previous temperature profiles of *LS* for reference). It is noticeable that the radial expanse of $g(r)$ for *ballistic* and *collisional* realm has shrinked, when same has been calculated considering square section because the vertical extent of *collisional* and *ballistic* region is smaller in comparison to their horizontal extent, in case if *LS* at $A/d = 2.4$ and $\Gamma = 30$; it should be recalled that the side of square considered is equal to the vertical extent of a particular region. Furthermore, the radial expanse of $g(r)$ for *cluster* region remains unaltered implying that the vertical extent of

cluster region is of the order of its horizontal extent; this vertical extent decreases for higher shakings.

Fig. 4.12 displays the pair correlation function $g(r)$ for the three regions of *Leidenfrost States* observed at a constant shaking intensity $\Gamma = 50$ for three shaking amplitudes $A/d = 0.5, 1$ and 2.4. As the shaking amplitude increases, the *collisional layer* and *ballistic layer* of *LS* expands and become less denser due to higher fluidization, consequently there is a decrease in contact value of $g(r)$, albeit this drop is small (compare respective red and black curves of Fig. 4.12(a),(b) and (c)). In a like manner, the packing of *floating cluster* also gets more and more loose with increasing shaking amplitude, causing a minor drop in the contact value of $g(r)$ (compare blue curves of Fig. 4.12(a),(b) and (c)). It is noteworthy that at very low shaking amplitudes such as $A/d = 0.5$, *ballistic* region will be nearly absent because the particles of upper layer would not have that large thrust so as to escape the bed, and hence $g(r)$ pertaining to *ballistic* layer is not shown in Fig. 4.12(a).

We also attempted to look into the orientational correlation of the various structures coupled with their radial correlation by calculating radial-angular pair correlation function (also called radial-angular distribution function) $g(r, \theta)$ and mapping it onto polar plot. The $g(r, \theta)$ is defined as (Bogdan 2006)

$$g(r,\theta) = \frac{1}{N\rho(r,\theta)} \sum_{i=1}^{N} \sum_{j \neq i}^{N} \langle \delta(r - r_{ij}) \delta(\theta - \theta_{ij}) \rangle, \tag{4.16}$$

which gives correlations for the pair of particles i and j, the distance between whose centers of mass is r_{ij} and the angle between the plane containing particles i, j and horizonatal plane is θ_{ij}, $\rho(r, \theta)g(r, \theta)$ is the conditional probability of finding a particle at a distance r from a reference particle and in a plane containing reference particle, which makes an angle θ with respect to the horizontal plane.The contour plot of the $g(r, \theta)$ in the (r, θ) plane is likely to reveal the "contact network" of particles in the granular bed, indicating the most probable spatial configuration of the particles around a reference particle.

For calculating $g(r, \theta)$, in addition to binning the particles in radial direction we also binned them in angular sense. The number of bins considered in radial and angular directions are 100 and 20, respectively. The $g(r, \theta)$ for the various regions of the *LS* namely: *collisional layer*, *floating cluster* and *ballistic layer* have been presented in Fig. 4.13. The reference particle considered in these polar plot presentations is located at the centre of the circle. The $g(r, \theta)$ for the floating cluster is highly anisotropic in nature and hence shows directional dependence with increased probability of "head-on" collisions (i.e. $\theta = \pi/2, 3\pi/2$). This fact is also evident from the visual inspection of the snapshots; also the probability of finding a particle at a large radial distance along the preferred directions is very small, and such type of behavior is evident in Fig. 4.11(b) also, wherein peak of $g(r)$ decays rapdidly at large radial separation. On the contrary, the *collisional* and *ballistic* layer shows angular isotropy and that is expected since these regions are in gaseous phase and hence on an average the particles are equally probable to be found at any angular orientation. A closer look at Fig. 4.13(a) reveals that the six fold symmetry of the contact network still survives in the LS, but the hexagonal lattice structure seem to have been significantly modified, with more collisions likely to occur at $\theta = 2\pi/3$ and $4\pi/3$

in addition to head on collisions. This indicates that the packing of particles in the *LS* is much looser than the "ideal" hexagonal packing. The latter observation can be further rationalized if we analyze the radial component of the $g(r,\theta)$ of Fig. 4.13 which is displayed in Fig. 4.11(b). Note that $g(r) \equiv \langle g(r,\theta)\rangle_\theta$, and hence it provides information on the radial configuration of particles around a test particle over a circular region of diameter equal to the height of the floating cluster. The $g(r)$ in the floating-cluster region [the blue curve Fig. 4.11(b)] resembles more a liquid-like structure, with its second peak being located at $r/d \approx 1.9$. Therefore the floating cluster region is in a liquid state, which hovers over a gas-like collisional layer underneath, and this makes the connection with the original Leidenfrost state more appropriate.

To study, how the non-isotropy of the hexagonally packed crystalline structure of *Bouncing Bed* evolves with increasing shaking amplitude we have shown $g(r,\theta)$ at contant shaking intensity ($\Gamma = 5$) while escalating A/d (see Fig. 4.14). The six-fold symmetry of the contact network, resembling the hexagonally packed crystalline structure of the bouncing bed, is clearly evident in Fig. 4.14(a). With increasing shaking amplitude (A/d), the lattice points of hexagonal packing dislodges from their positions, thereby, breaking the "exact" directional symmetry. This is because, as A/d increases the particles get more loosely packed making them more mobile to move around each other and hence destroying the angular anisotropy of their positions. Alike, one can witness the gradual development of isotropy in the *floating cluster* layer of the *LS* at constant shaking amplitude $A/d = 2.4$ while increasing the energy injection via Γ (refer Fig. 4.15).

4.5 Granular Leidenfrost state: Evidence of oscillations

The inset in Fig. 4.16 shows a sketch of the granular Leidenfrost state *(LS)*. There are two characteristic lengths: the heights of the interface (y_{coll}) and the top surface (y_{crys}) from the base of the container. Analyzing the images from camera, we measured these heights at various time instants of shaking cycle in order to check whether the *LS* is steady/unsteady. Any unsteadiness is likely to be implicated in the temporal variations of y_{coll} and y_{crys} as we demonstrate below.

We first consider the case of *LS* observed in $F = 25$ layers of 2 mm diameter glass beads at $\Gamma = 30$ ($A/d = 1.6, f = 48.26\ Hz$). The variation of y_{coll}/d and y_{crys}/d with the shaking cycle is shown in Fig. 4.16. The external vibration frequency corresponding to this case is

$$\omega_d = 303.26\ rad/s \Rightarrow \tau_d = 20.7\ ms$$

The time interval between two consecutive maxima/minima in the oscillation of y_{coll} or y_{crys} is 21 ms i.e.

$$\tau_{coll} \approx \tau_{crys} \approx 20.7\ ms \approx \tau_d$$

This simple argument suggests that the time period of external vibration closely approximates the oscillation time period of interface and top surface of *LS*. We further found that the variation

in y_{coll} and y_{crys} are best fitted by sinusoids (blue curve in Fig. 4.16) of the following form

$$y_{coll}/d = 2.4175 + 2.5\sin(0.305t + 1.159) \tag{4.17}$$

$$y_{crys}/d = 24.46 + 1.2\sin(0.307t + 1.231) \tag{4.18}$$

where t is the time in ms. From the above equations, the angular frequencies ω_{coll} and ω_{crys} are 305 rad/s and 307 rad/s respectively, which closely match the driving frequency (ω_d). Thus, the interface and top surface of the LS vibrates harmonically being synchronized with the external vibration.

To check the robustness of this experimental finding, we analyzed the images of LS observed in 5 mm diameter beads confined in a box of length, $L/d = 20$ and width, $W/d = 1.1$ which is again a monolayer 2D system. The first case we consider is LS at $\Gamma = 30$ ($A/d = 0.6, f = 49.84\ Hz$). The variation of y_{coll}/d and y_{crys}/d with the shaking cycle is shown in Fig. 4.17(a). The external vibration frequency corresponding to this case is

$$\omega_d = 313\ rad/s \Rightarrow \tau_d = 20.06\ ms$$

The time interval between two consecutive maxima/minima in the oscillation of y_{coll} or y_{crys} is 20 ms i.e.

$$\tau_{coll} \approx \tau_{crys} \approx 20\ ms \approx \tau_d$$

Thus, the time period of external vibration closely approximates the oscillation time period of interface and top surface of LS. The experimental data are best fitted by sinusoids (blue curve in Fig. 4.17(a)) of the following form

$$y_{coll}/d = 2.2 + 1.84\sin(0.315t + 0.62) \tag{4.19}$$

$$y_{crys}/d = 15.7 + 0.66\sin(0.31t + 0.864) \tag{4.20}$$

From the above equations, the angular frequencies ω_{coll} and ω_{crys} are 314.7 rad/s and 310 rad/s respectively, which closely match the driving frequency (ω_d). Thus, the interface and top surface of the LS vibrates harmonically being synchronized with the external vibration.

Let us consider one more data point on the phase diagram (Fig. 4.4a) at the same shaking amplitude $A/d = 0.6$ but at a higher value of $\Gamma = 43.4$. The variation of y_{coll}/d and y_{crys}/d has been shown in Fig. 4.17(b). The external vibration frequency corresponding to this case is $\omega_d = 376\ rad/s \Rightarrow \tau_d = 16.6\ ms$ The time interval between two consecutive maxima/minima in the oscillation of y_{coll} or y_{crys} is 16.5 ms i.e. $\tau_{coll} \approx \tau_{crys} \approx 16.5 \approx \tau_d$. The data points obtained are best fitted by following sinusoids

$$y_{coll}/d = 2.7 + 2.53\sin(0.37t + 0.322) \tag{4.21}$$

$$y_{crys}/d = 16.8 + 0.616\sin(0.377t + 0.118) \tag{4.22}$$

From above equations the frequencies of interface and top surface oscillation are $\omega_{coll} = 370\ rad/s$ and $\omega_{crys} = 377\ rad/s$ which again agree with the external vibration frequency $\omega_d = 376\ rad/s$.

Lastly, we consider one more data point at a relatively smaller shaking amplitude $A =$

1.0 mm ($A/d = 0.2$) at $\Gamma = 50$ and $f = 111.46\ Hz$. This particular experiment we have captured at 2000 fps just to increase the number of images recorded in an oscillation cycle and hence to achieve more data points. The variation of y_{coll}/d and y_{crys}/d has been shown in Fig. 4.18. The data points are fitted by the following sinusoids

$$y_{coll}/d = 1.44 + 1.5\sin(0.72t - 0.18) \tag{4.23}$$

$$y_{crys}/d = 13.15 + 0.19\sin(0.713t + 0.038) \tag{4.24}$$

From the above Eqs. the interface and top surface oscillation frequency ω_{coll} and ω_{crys} are 720 rad/s and 713.5 rad/s which is in close agreement with driving frequency $\omega_d = 700\ rad/s$.

To check the robustness of the oscillating nature of LS, we have carried out additional experiments with $F = 6$ layers of glass beads having diameter $d = 1.0\ mm$ in the same Hele-Shaw cell. Note that five particles can now fit along the width of the container and hence this is no longer a monolayer system. These experiments are done at a shaking amplitude of $A/d = 3$ and the granular Leidenfrost state has been observed for a range of $\Gamma \in (25, 45)$ as in the experiments of Eshuis *et al.* (2007). A series of snapshots at $\Gamma = 30$ is displayed in Fig. 4.19. For this case, the external vibration frequency is $\omega_d = 313\ rad/s$ and hence $\tau_d = 20.07 \times 10^{-3}\ s$.

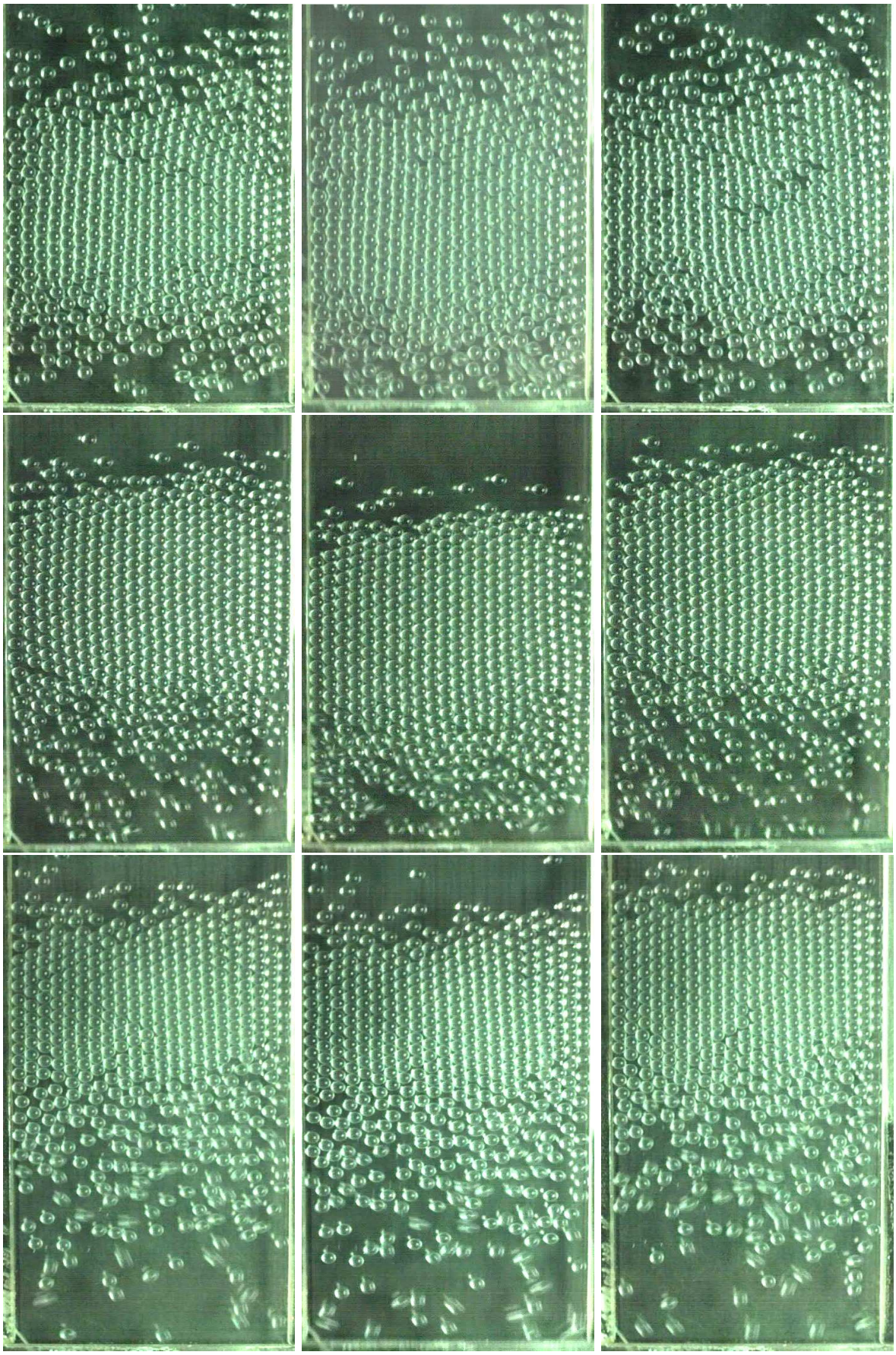

Figure 4.3: **Snapshots of the granular Leidenfrost state for $F = 25$ layers of 2.0 mm diameter glass beads, at three successive time instants of the oscillation cycle at $A/d = 2.4$: $t = 0\tau$ (left), $t = \tau/2$ (middle) and $t = \tau$ (right).** Top row: $\Gamma = 11$ ($f = 23.86\ Hz$); Middle row: $\Gamma = 30$ ($f = 39.4\ Hz$); Bottom row: $\Gamma = 50$ ($f = 50.87\ Hz$).

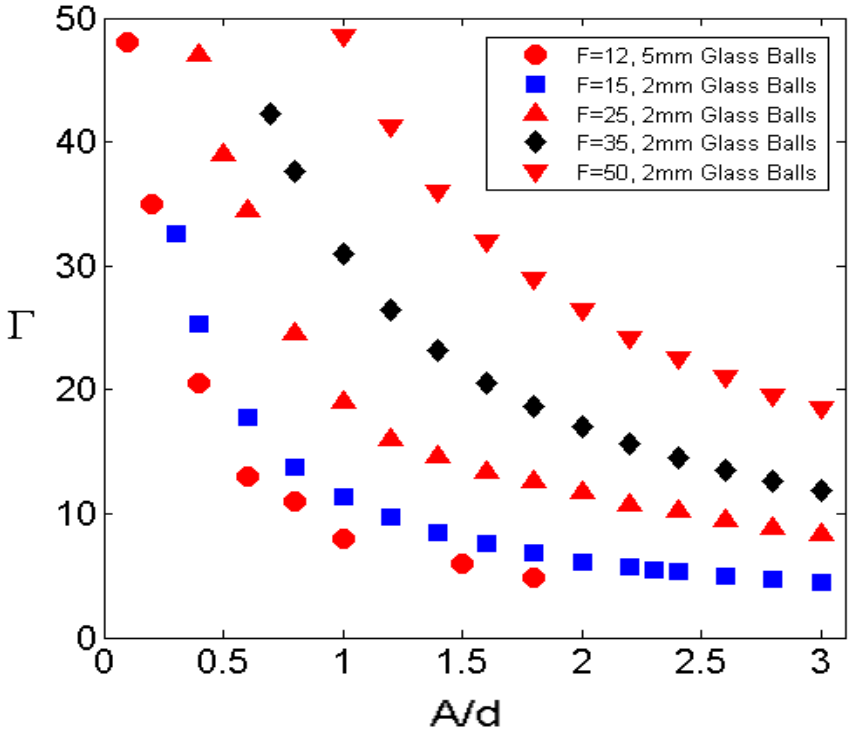

(a)

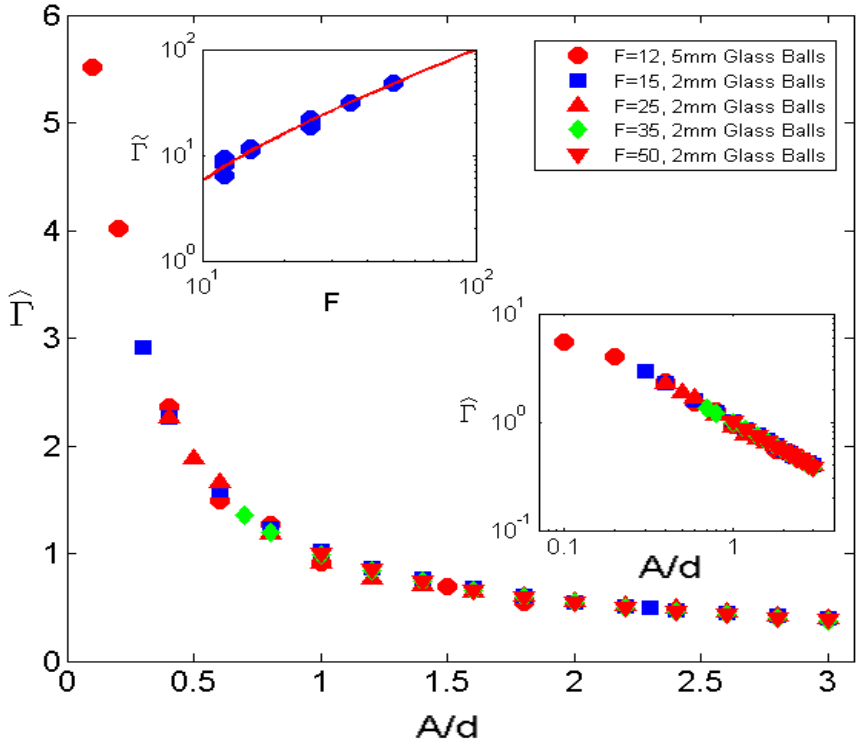

(b)

Figure 4.4: **(a) Plot showing the variation of critical Γ_{BB}^{LS} with increasing A/d for various set of experiments. This critical Γ_{BB}^{LS} follows the power law given by Eqn. 4.12; (b) Plot showing variation of $\widehat{\Gamma}$ with A/d.** Top inset: Variation of $\widetilde{\Gamma}$ with F. Red line is the best fit curve. Bottom inset: main plot on the logarithmic scale.

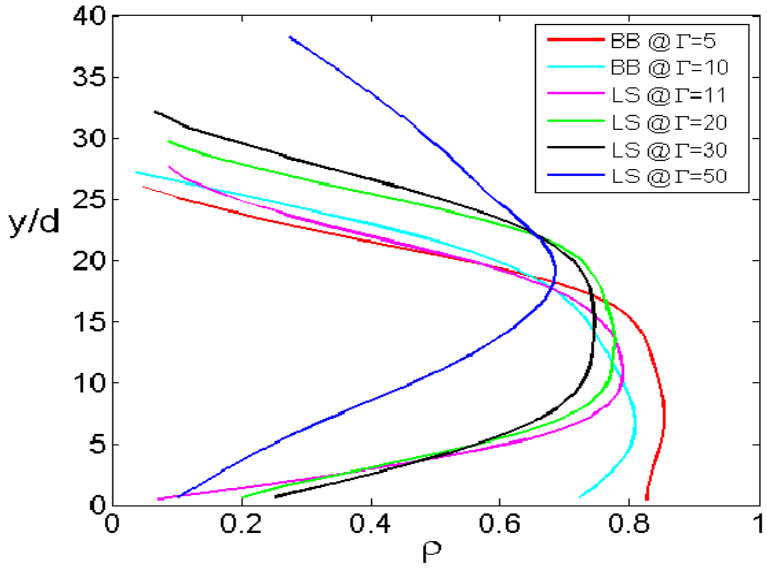

(a)

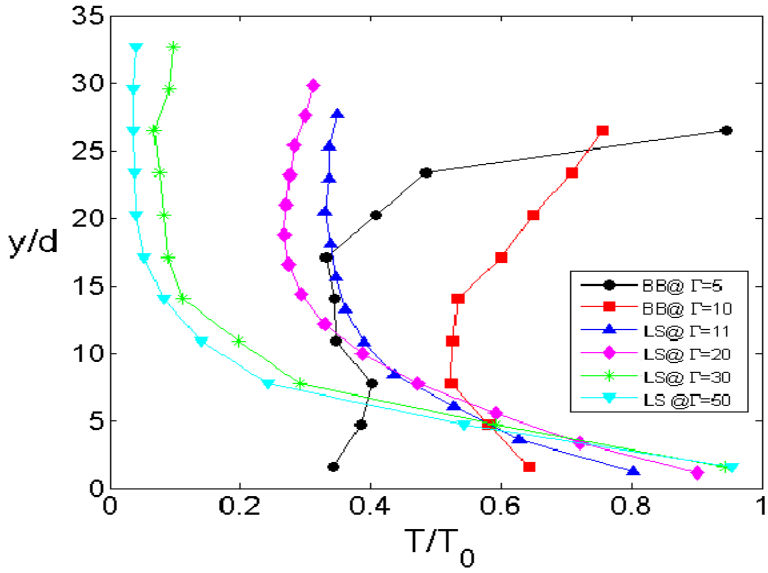

(b)

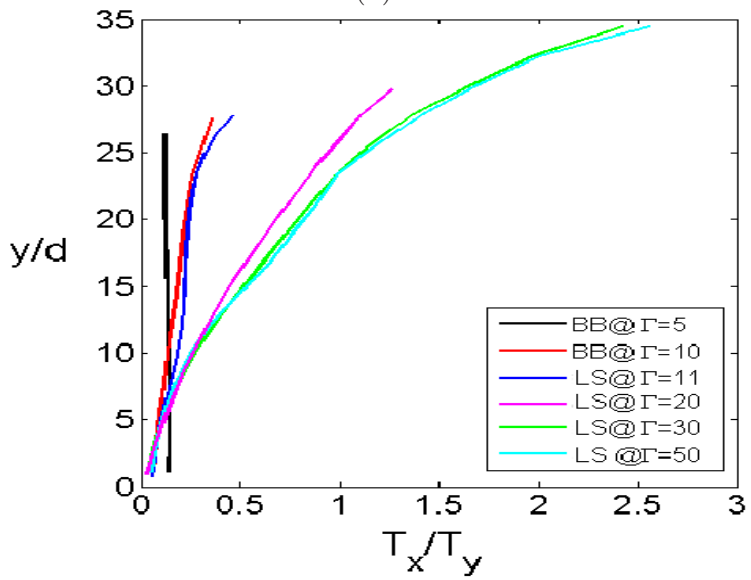

(c)

Figure 4.5: **(a) Averaged density profiles for the various states in $F = 25$ layers of 2.0 mm diameter glass beads at constant $A/d = 2.4$ with increasing shaking intensity Γ; (b) temperature profiles; and (c) temperature ratio profiles.**

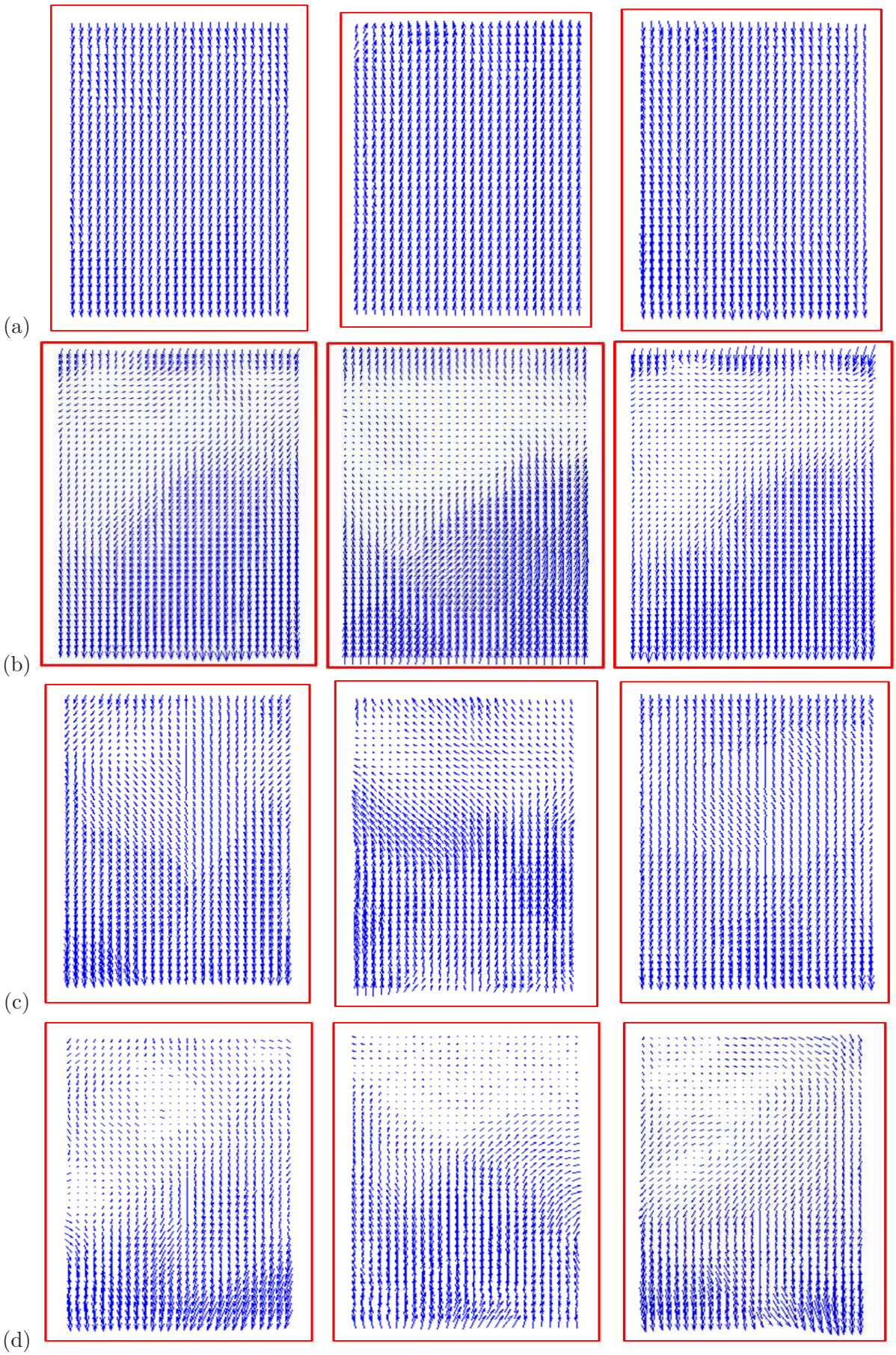

Figure 4.6: **Coarse-grained velocity fields for the various states in $F = 25$ layers of 2.0 mm diameter glass beads at $A/d = 2.4$: (a) *BB* at $\Gamma = 5$; (b) *LS* at $\Gamma = 11$; (c) *LS* at $\Gamma = 30$; and (d) *LS* at $\Gamma = 50$,** at three successive time instants of the oscillation cycle: $t = 0\tau$ (left), $t = \tau/2$ (middle) and $t = \tau$ (right).

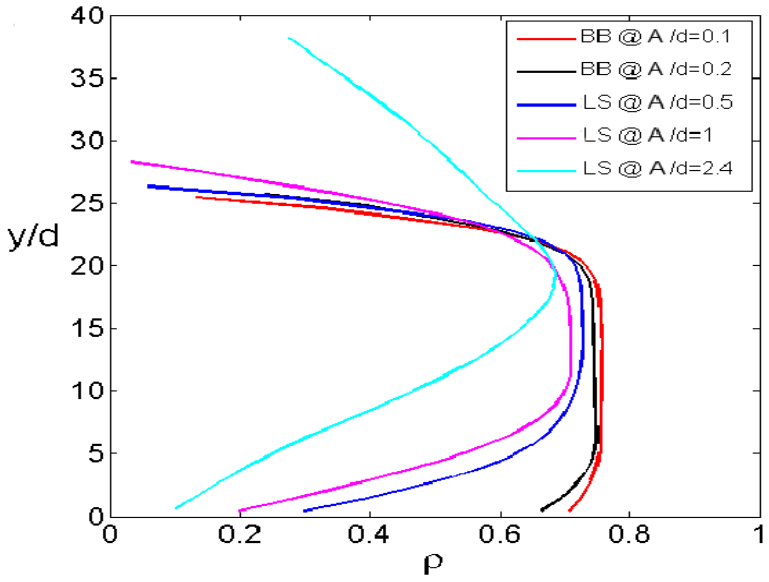

(a)

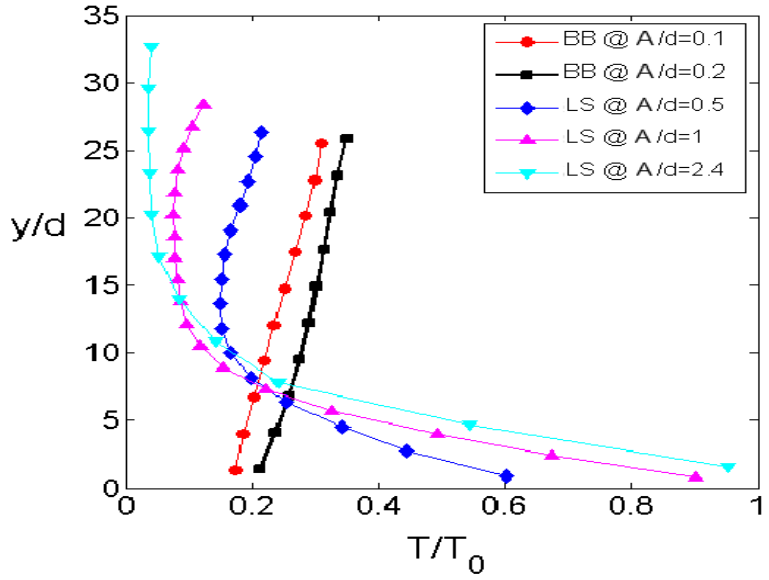

(b)

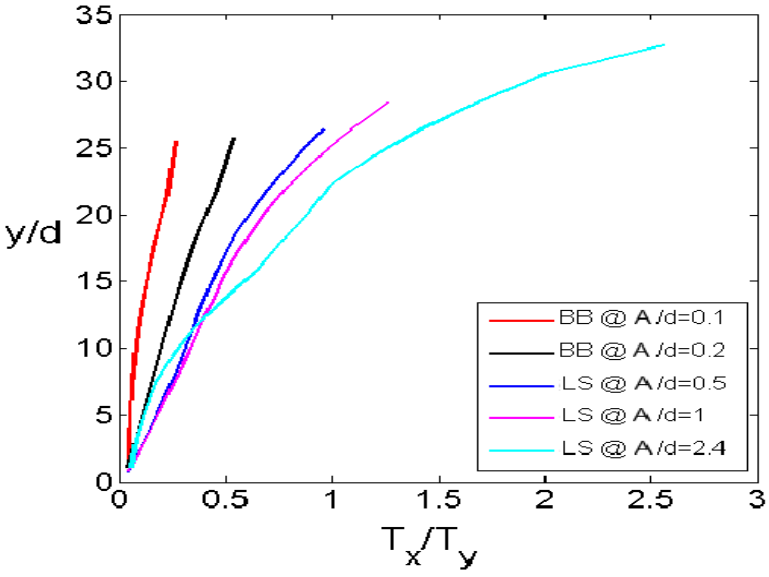

(c)

Figure 4.7: **(a) Averaged density profiles for the various states in the transition at constant shaking intensity $\Gamma = 50$ while increasing shaking amplitude for $F = 25$ layers of 2.0 mm diameter glass beads; (b) their temperature profiles; and (c) their temperature ratio profiles.**

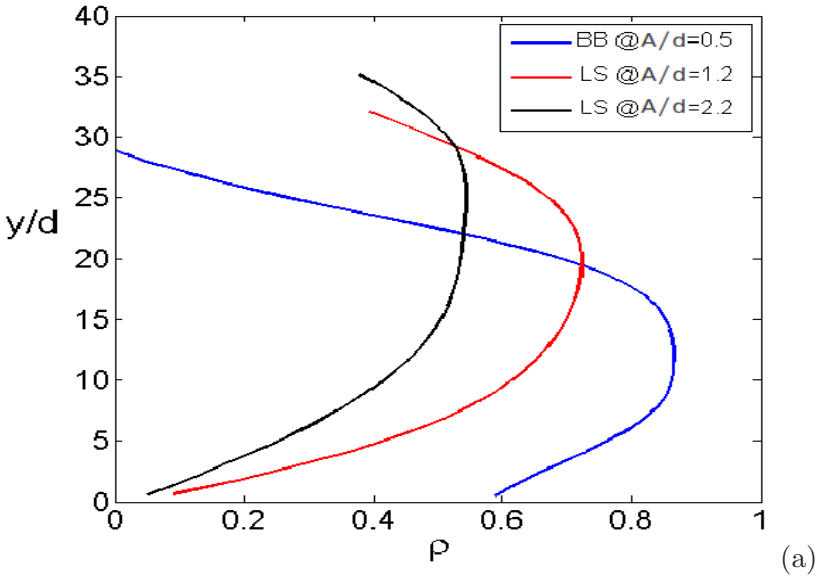

(a)

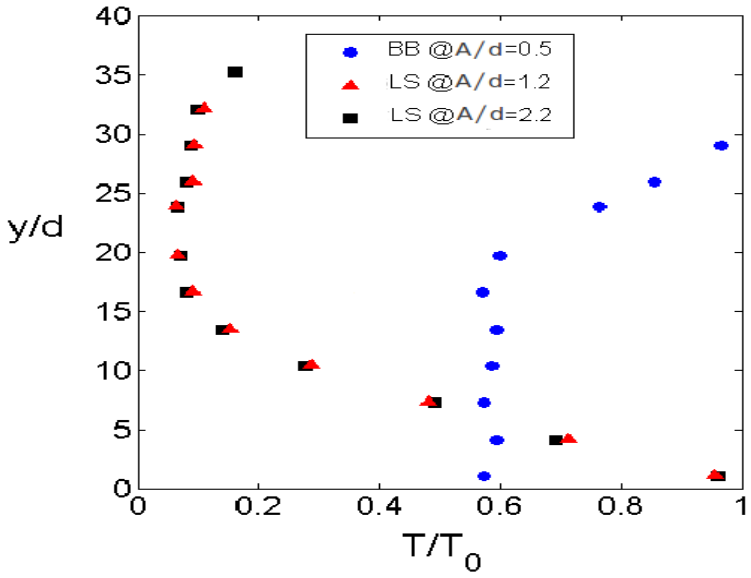

(b)

Figure 4.8: **(a) Density profiles showing the transition at constant shaking intensity $\Gamma = 30$ while increasing A/d for $F = 25$ layers 2 mm glass beads: BB at $A/d = 0.5$, LS at $A/d = 1.2$, and $A/d = 2.2$, (b) the corresponding temperature profiles.**

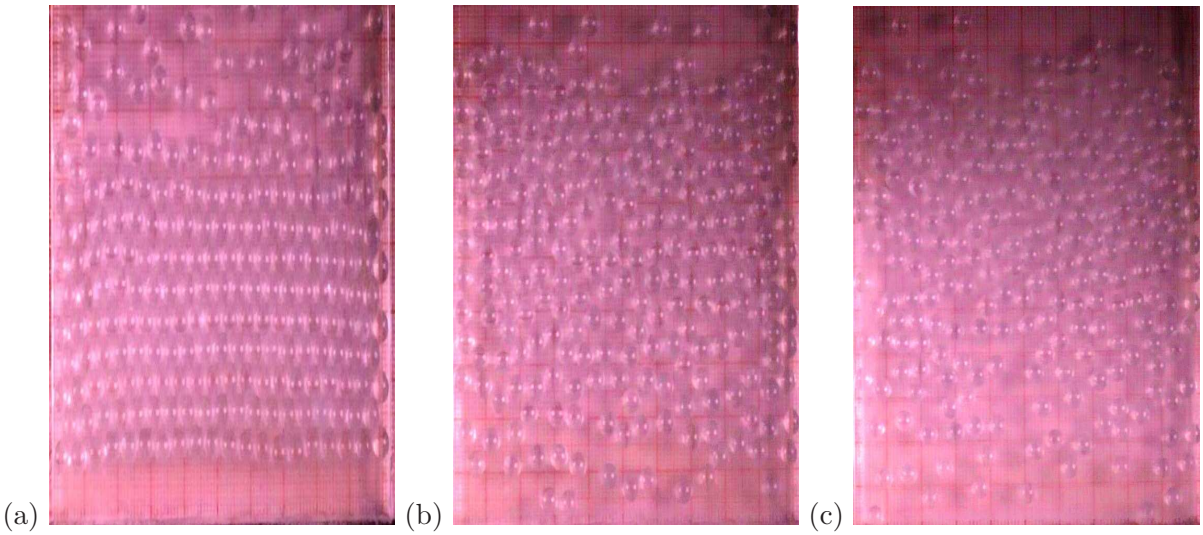

Figure 4.9: **Transition from *BB* to *LS* for $F = 12$ layers of 5 *mm* diameter glass beads at a fixed shaking amplitude $A/d = 1$:** (a) ***BB*** **at** $\Gamma = 3$ ($f = 12.2$ *Hz*); (b) ***LS*** **at** $\Gamma = 22$ ($f = 33.06$ *Hz*), **and** (c) ***LS*** **at** $\Gamma = 48$ ($f = 48.84$ *Hz*).

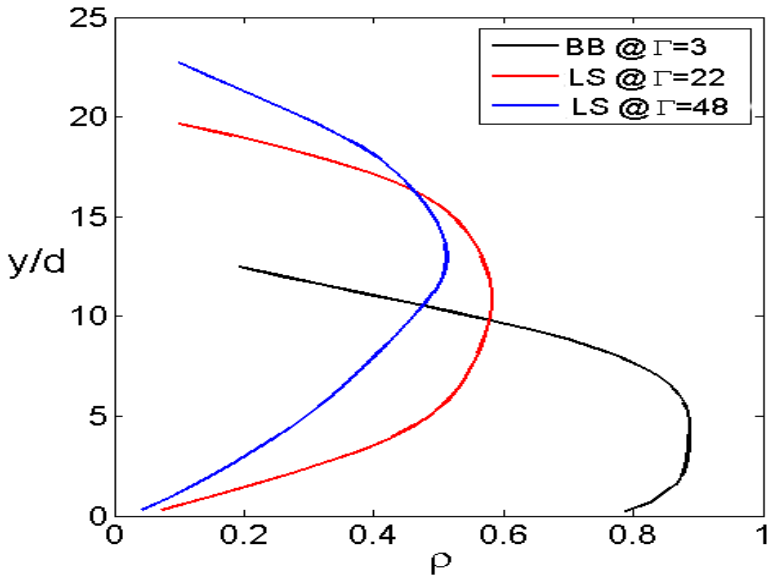

Figure 4.10: **Averaged density profiles for $F = 12$ layers of 5.0 *mm* diameter glass beads:** (a) ***BB*** **at** $\Gamma = 3$, (b) ***LS*** **at** $\Gamma = 22$, **and** (c) ***LS*** **at** $\Gamma = 48$. The shaking amplitude is kept constant at $A/d = 1$

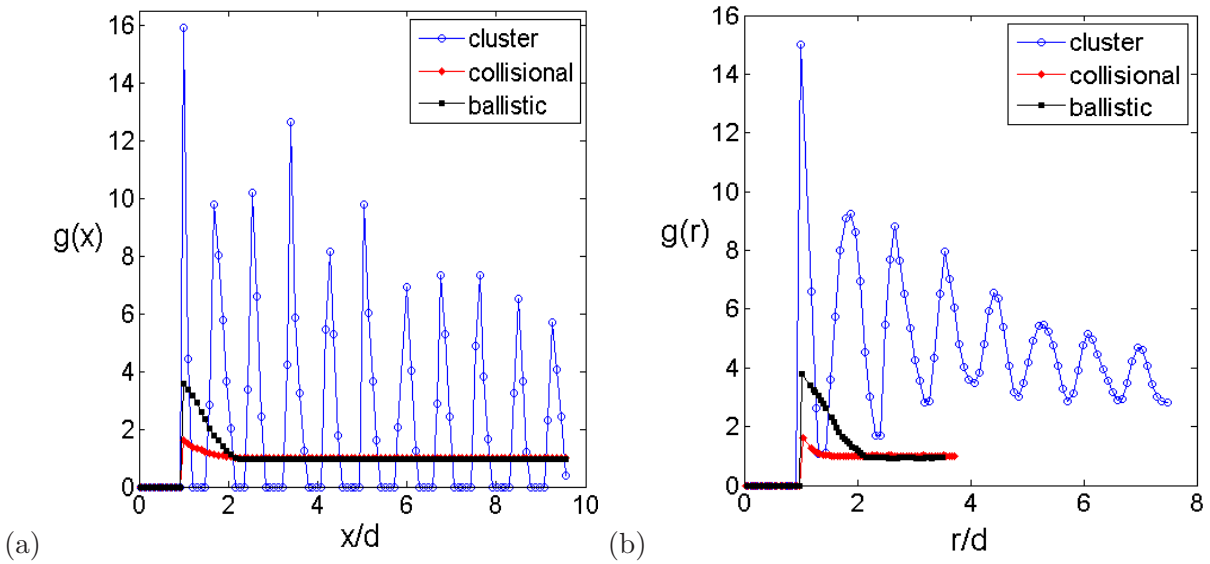

(a) (b)

Figure 4.11: **Pair correlation function $g(r)$ for the various regions of LS observed for $F = 25$ layers of 2.0 mm diameter glass beads at $A/d = 2.4$ and $\Gamma = 30$.** This function has been evaluated in two geometries: (a) stripe of thickness $1.5d$ (where d is the diameter of beads) and (b) square of side equal to the height of extent of various regions

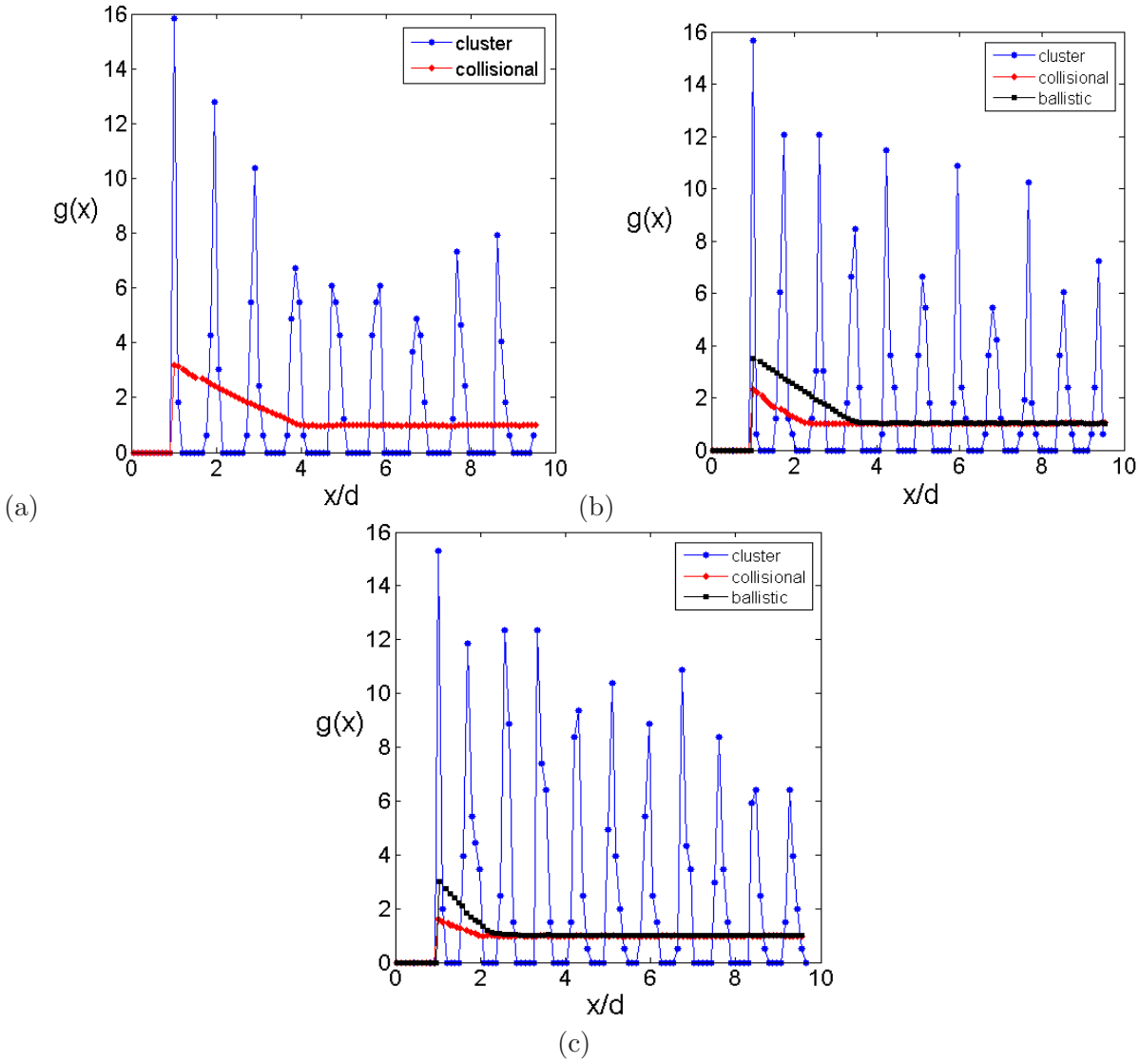

Figure 4.12: **Pair correlation function $g(x)$ for the various *Leidenfrost States* observed at constant shaking intensity $\Gamma = 50$ in $F = 25$ layers of 2.0 mm diameter glass beads: (a) $A/d = 0.5$, (b) $A/d = 1$, and (c) $A/d = 2.4$.** Stripe of thickness $1.5d$ (where d is the diameter of beads) is considered for calculating $g(x)$.

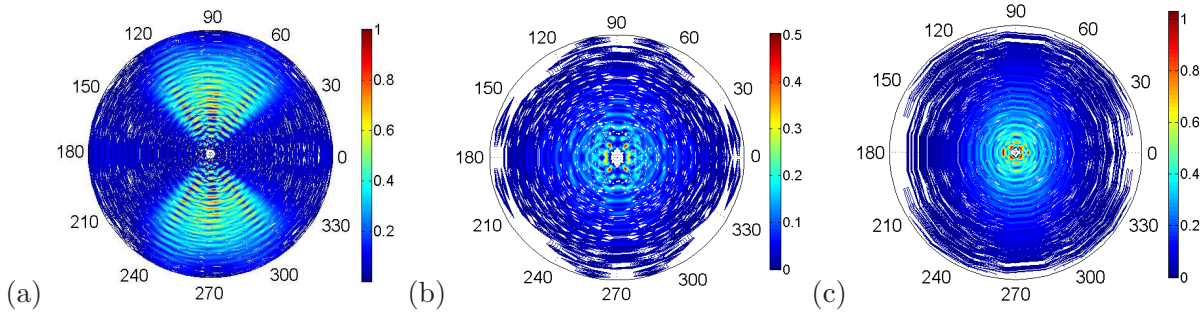

Figure 4.13: **The radial-angular correlation function $g(r, \theta)$ for the various regions of *LS*: (a) clustered layer; (b) collisional layer and (c) ballistic layer.** Other parameters are same as Fig. 4.11.

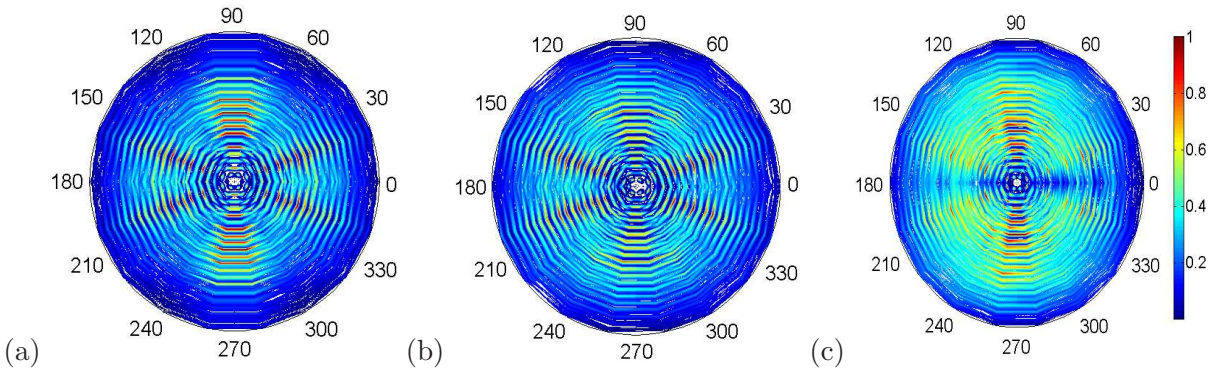

Figure 4.14: **The radial-angular correlation function $g(r, \theta)$ for the BB at constant $\Gamma = 5$ with increasing shaking amplitudes: (a) $A/d = 0.5$; (b) $A/d = 1$, and (c) $A/d = 2.4$.**

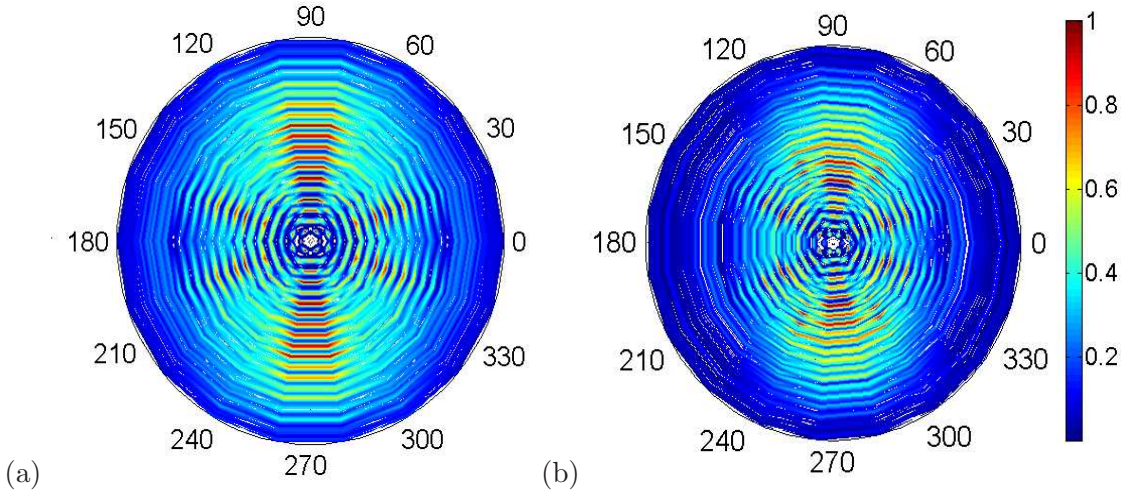

Figure 4.15: **The radial-angular correlation function $g(r, \theta)$ for the floating cluster region of LS at constant shaking amplitude $A/d = 2.4$ with increasing shaking accleration: (a) $\Gamma = 11$; (b) $\Gamma = 50$.**

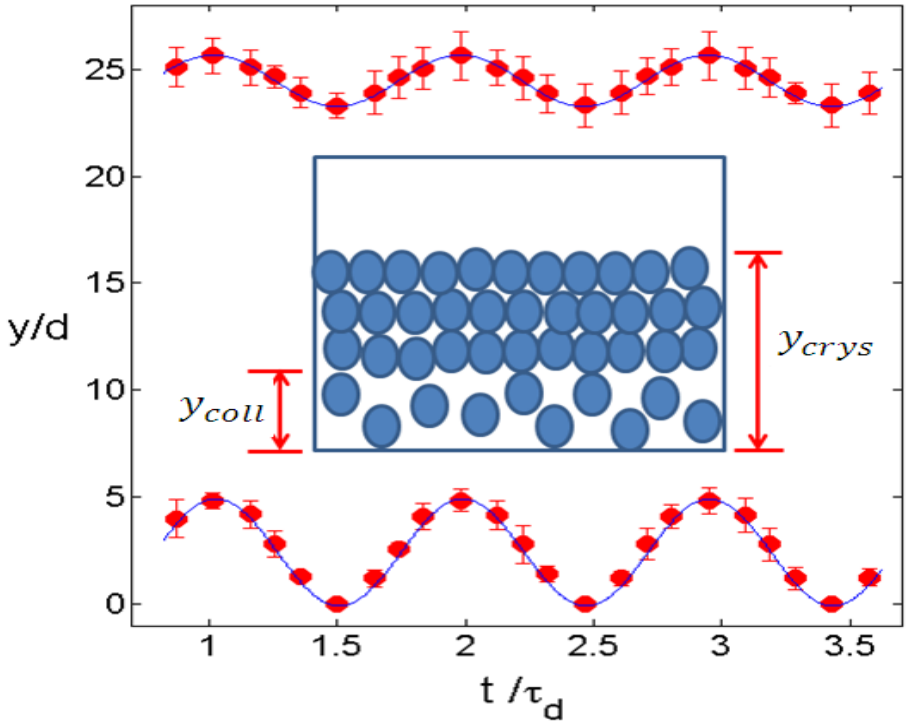

Figure 4.16: **Temporal variation of the interface y_{coll} and the top surface y_{crys} of the bed at $\Gamma = 30$ and $A/d = 1.6$ for $F = 25$ layers of 2.0 mm diameter glass beads.** Red symbols are experimental data and the best fitted curve is shown in blue. Inset is an sketch of LS showing the location of the interface separating the dense and dilute regions: y_{coll} is the height of this interface and y_{crys} is top surface height.

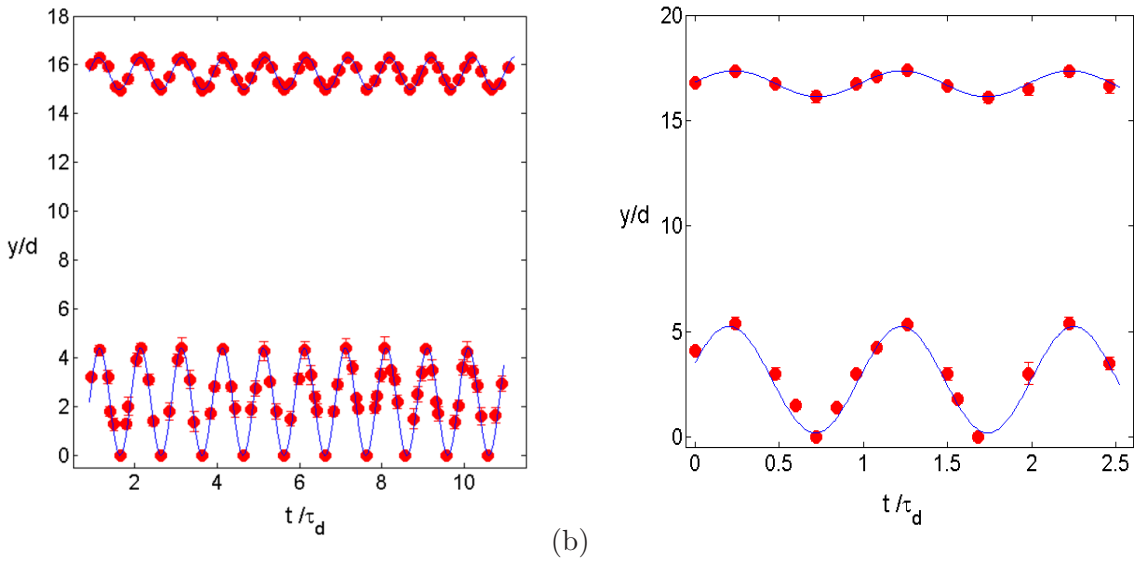

(a) (b)

Figure 4.17: **Temporal variation of the interface y_{coll} and the top surface y_{crys} for the bed of $F = 12$ layers of 5.0 mm diameter glass beads at: (a) $\Gamma = 30$, (b) $\Gamma = 43.4$.** Other parameter value is $A/d = 0.6$. Red symbols are experimental data and the best fitted curve is shown in blue.

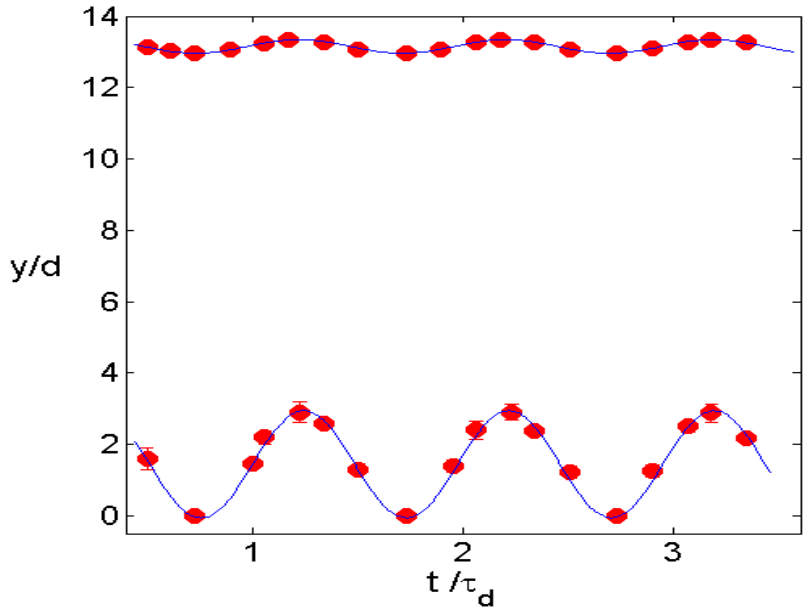

Figure 4.18: **Temporal variation of the interface y_{coll} and the top surface y_{crys} of LS at $\Gamma = 50$ and $A/d = 0.2$ with various time instants of oscillation cycle.** Other parameters as in Fig. 4.17. Red symbols are experimental data and the best fitted curve is shown in blue.

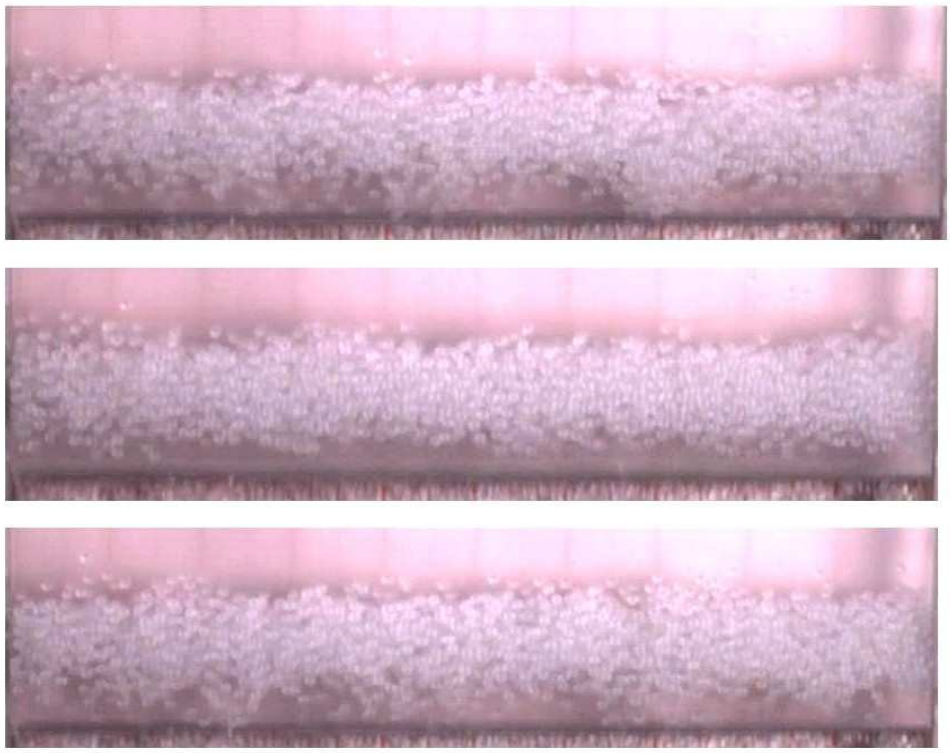

Figure 4.19: **Snapshots of granular Leidenfrost State LS observed in $F = 6$ layers of 1.0 mm diameter glass beads for $A/d = 3$ at $\Gamma = 30$.** Note that now 5 layers can fit along the width of the same box, hence the system is no longer a monolayer.

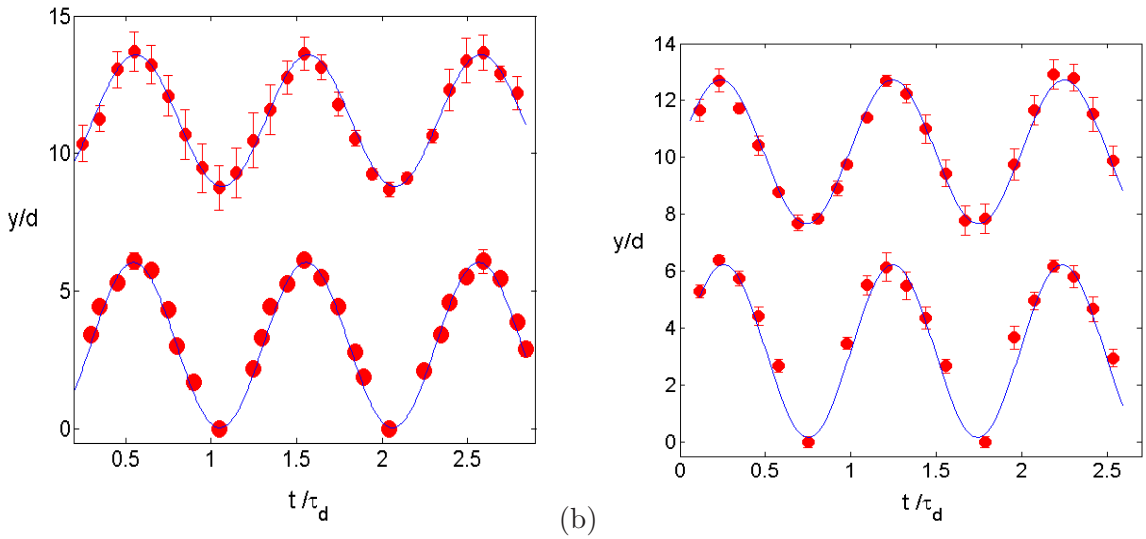

Figure 4.20: **Temporal variations of y_{coll} and y_{crys} for the *LS* observed in $F = 6$ layers of 1.0 mm diameter glass beads at $A/d = 3$: (a) $\Gamma = 30$ and (b) $\Gamma = 40$.** Red symbols are experimental data and the best fitted curve is shown in blue.

For the quasi-2D case as in Fig. 4.19, the temporal variations of y_{coll} and y_{crys} are shown in Fig. 4.20(a). The best fit is obtained by the sinusoids of the form

$$y_{coll}/d = 3.05 + 3\sin(0.31t + 4.46) \tag{4.25}$$

$$y_{crys}/d = 11.2 + 2.39\sin(0.31t + 4.38) \tag{4.26}$$

The time interval between two consecutive maxima/minima in the oscillation of y_{coll} or y_{crys} is 20 ms (see Fig. 15), i.e. $\tau_{coll} \approx \tau_{crys} \approx 20\ ms$ which matches with τ_d. Thus, the interface and the top surface of Leidenfrost state vibrate harmonically and are synchronized with external vibration frequency for this case too.

Analyzing the snapshots for even higher values of $\Gamma = 40$ ($A/d = 3$), we found (see Fig. 4.20(b)):

$$y_{coll}/d = 3.2 + 3.03\sin(0.365t - 0.0523) \tag{4.27}$$

$$y_{crys}/d = 10.2 + 2.52\sin(0.36t + 0.0872) \tag{4.28}$$

where t is the time in ms. For this case, the driving frequency is $\omega_d = 362\ rad/s$ and time period $\tau_d = 17.3\ ms$. The latter agrees with the experimental finding:

$$\tau_{coll} \approx \tau_{crys} \approx 17\ ms \approx \tau_d$$

Collectively, the above analysis indicates that both the interface between the collisional-layer and the floating-cluster and the top surface of the floating-cluster oscillates harmonically and are synchronized with the frequency of the external vibration. Therefore, the granular Leidenfrost state is a $period - 1\ wave$ (i.e. an $f - wave$) as is the case for the bouncing-bed.

The characteristic lengths y_{crys} and y_{coll} also helped us to identify the onset of *BB* and *LS*. A

natural dimensionless parameter which can be formulated out of these two characteristic lengths is the amplitude ratio (A_R) defined as

$$A_R = \frac{\langle y_{crys} \rangle}{\langle y_{coll} \rangle} \tag{4.29}$$

where $\langle y_{crys} \rangle$ and $\langle y_{coll} \rangle$ are the amplitude of top surface and interface calculated as

$$\langle y_{crys} \rangle = \frac{\langle y_{crys}^{max} \rangle - \langle y_{crys}^{min} \rangle}{2} \tag{4.30}$$

$$\langle y_{coll} \rangle = \frac{\langle y_{coll}^{max} \rangle - \langle y_{coll}^{min} \rangle}{2} \tag{4.31}$$

where averaging of height is done from the snapshots over thirty oscillation cycles.

The variation of A_R with increasing shaking intensity Γ is shown for $F = 25$ layers of 2.0 mm diameter glass beads for two shaking amplitudes $A/d = 1.6$ and 3 (see Fig. 4.21). The first peak in the curve marks the approximate location of transition from *BB* to *LS*. It is evident from Fig. 4.21 that as we increase Γ in the *Bouncing Bed* regime the magnitude of top surface oscillation keeps on increasing relative to interface oscillation, till the onset of *LS*. Further increasing Γ beyond the *BB* regime, reduces A_R sharply suggesting the dominant interface oscillations $\langle y_{coll} \rangle$ of the *LS*. The second transition point lying in the *LS* regime indicates that the magnitude of interface oscillation saturates at a maximum limit while the upper layer of the floating cluster getting more and more fluidized. The inset shows the evolution of the thickness h_{crys} of the compact floating cluster while increasing shaking intensity. The thickness h_{crys} decreases linearly with Γ due to continuous fluidization of the upper as well as lower layer of the compact cluster, which is clearly evident from the experimental snapshots.

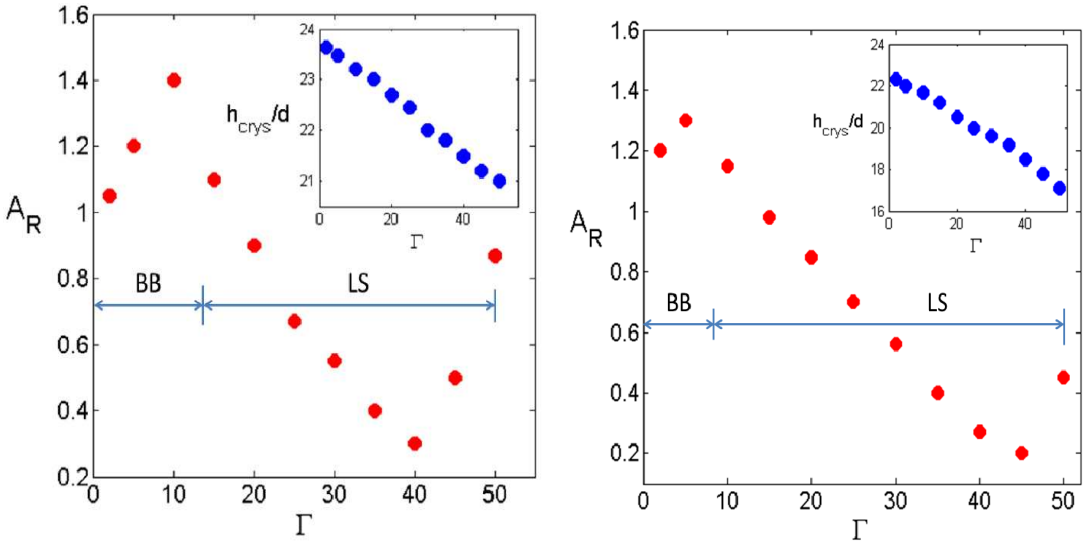

Figure 4.21: **Amplitude ratio vs shaking intensity for $F = 25$ layers of 2.0 mm diameter glass beads at two shaking amplitudes: (a) $A/d = 1.6$ and (b) $A/d = 3$.** Inset shows the evolution of thickness of the compact floating cluster h_{crys} with the shaking intensity.

We denote the thicknesses of *collisional* and *ballistic* layers by h_{coll} and h_{bls}, respectively and their variation with increasing shaking intensity has been shown in Fig. 4.22 for $F = 25$, 35 and 50 layers of 2.0 mm diameter glass beads at shaking amplitude $A/d = 1.6$. The h_{coll} is found to monotonously increase with increasing Γ because there is an overall expansion of *collisional* layer due to higher energy injection into the system. Nevertheless, beyond a certain Γ this h_{coll} saturates to a maximum value. Similarly, when one injects more energy into the system progressively, the *ballistic* layer also expands due to the continuous fluidization of compact cluster leading to increase in h_{bls}, and consequently decrease in h_{crys} with increase in shaking strength, as displayed in the inset of Fig. 4.22.

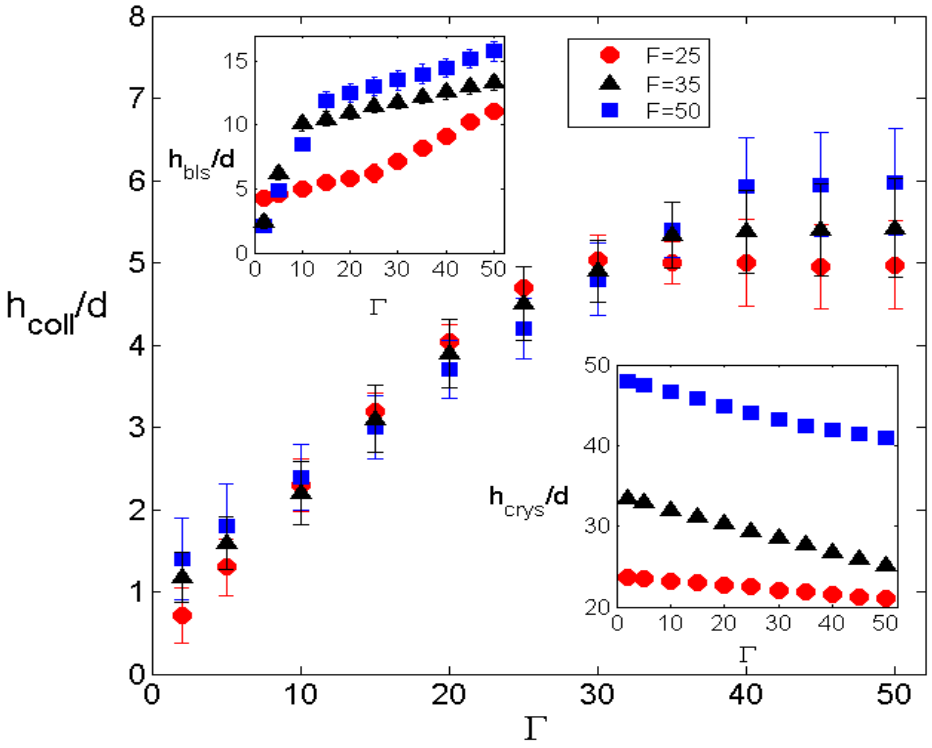

Figure 4.22: **Variation of collisional layer height h_{coll} with shaking intensity Γ for $F = 25$, 35 and 50 layers of 2.0 mm diameter glass beads at shaking amplitude $A/d = 1.6$.** Inset shows the evolution of thickness h_{crys} and h_{bls} with the shaking intensity.

4.6 Effect of Larger L/d: Route to Convection

In this section we will present and discuss the results of phase transition and related patterns observed in glass beads in a box of larger length, wherein the system admits *Convection* rolls and *Gas* in addition to *BB* and *LS*. The primary motivation of using a larger-box is to investigate if there is any inception of convective motion in the bed, wherein the origin of convective motion may be tied to the instability of the Leidenfrost state. Similar transition has been reported previously (Eshuis *et al.* 2007; Ansari & Alam 2012, 2013), however, in a "quasi-2D" box (with a depth of few particle diameters, $W/d \approx 5$) as well as in a 3-D box, but not in purely two dimensional monolayer system. The glass beads (diameter $d = 2.0$ mm) are filled in box of

length $L = 80$ and $W = 2.2$ upto a depth of $F = 12$ layers. It should be noted that the system is still monolayer as only one layer of beads can be fitted along the width. The various states observed and their transit into one another has been assimilated on a phase diagram constructed in $(\Gamma, A/d)$-plane (refer Fig. 4.23). The experimental procedure is similar as adopted in previous assays, wherein the shaking intensity is increased via frequency ramping at a rate of 0.01 Hz/s while maintaining shaking amplitude (A/d) to be constant. At shaking intensity $\Gamma \gtrsim 1$ the bed starts bouncing off the vibrating base giving birth to *BB* which eventually mutates to the density inverted *LS*. The critical shaking intensity corresponding to the onset of *LS* (Γ^{LS}_{BB}) follows the same trend of declining with increasing shaking amplitude A/d (as reported in previous experiments, refer Fig. 4.1), conforming with the power-law as given by Eqn. 4.12. Further escalating shaking intensity Γ gradually, one witnesses transition of *LS* to *Convection*. It is remarkable that such transition was absent in the phase diagram corresponding to the granular system vibrated in $L/d = 20$ box (compare Fig. 4.1 and Fig. 4.23). The PIV analysis of this *Convection* reveals a pair of convection rolls, though to our surprise these pair of rolls melt into a single roll at even higher shaking intensity and for higher shaking amplitudes, as marked in the phase diagram (see Fig. 4.23). Intensifying the vibration further vaporizes the whole system to *Gas*. We will discuss the charateristic and related density, temperature and velocity fields of these phases in the following paragraphs.

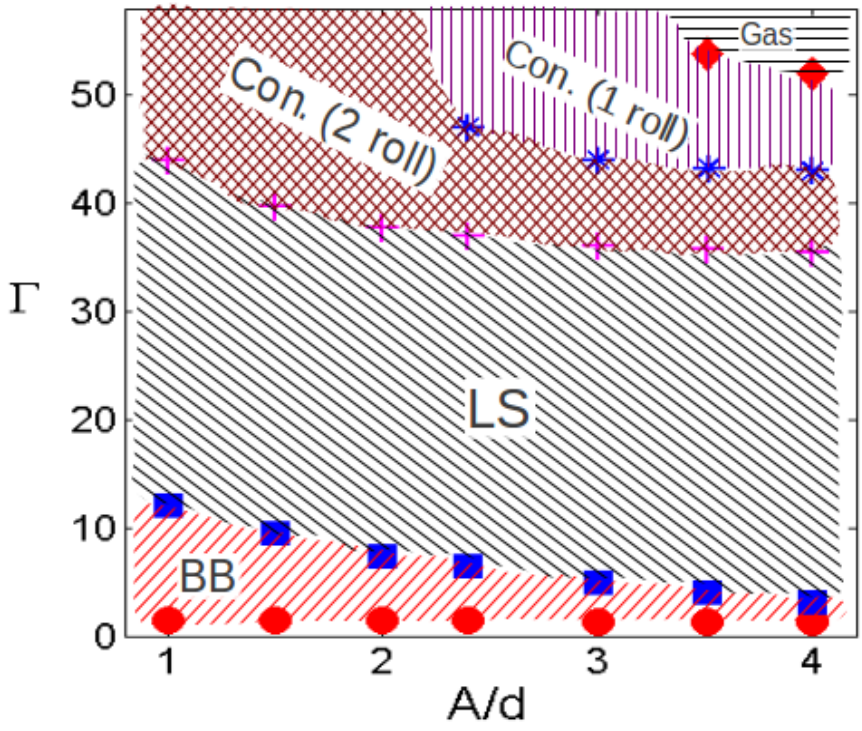

Figure 4.23: **Phase diagram in $(\Gamma, A/d)$-plane for $F = 12$ layers of 2.0 mm diameter glass beads confined in $L/d = 40$ cell.** Regions of bouncing bed *(BB)*, granular Leidenfrost state *(LS)*, *Convection* (2 roll), *Convection* (1 roll) and *Gas* are marked; symbols represent approximate locations of transition while upsweeping at a specified shaking amplitude A/d with the linear frequency-ramping of 0.01Hz/s.

Let us commence the discussion with the identification of various states encountered at

dimensionless shaking amplitude $A/d = 1$, while the shaking intensity is increased gradually from 0 to 55, as displayed in Fig. 4.24. The left panel of Fig. 4.24 presents the LS at $\Gamma = 40$ at various time instants of the shaking cycle: $t = 0\tau, 0.5\tau$ and τ, therein we observe a densely packed layer of beads is supported over a dilute gaseous region of beads. If one escalates the shaking intensity to $\Gamma = 50$, the bed is seen to furcate horizontally into two dense clustered region leaving a dilute channel in between. The beads shoot up spouting from the bed through this dilute channel and stream downwards along the two sidewalls of the container generating a pair of counter-rotating convective rolls, as shown in the right panel of Fig. 4.24. The critical shaking intensity for the onset of this "2-roll" convection, Γ_{LS}^{Con} (denoted by the plus symbols in Fig. 4.23), decreases with increasing shaking amplitude,

$$\Gamma_{LS}^{Con} = 42.7(A/d)^{-0.157} \tag{4.32}$$

and therefore the related shaking strength,

$$S_{LS}^{Con} \equiv \Gamma_{LS}^{Con}(A/d) = 42.7(A/d)^{0.843}, \tag{4.33}$$

increases strongly with increasing shaking amplitude. Stepping towards a higher shaking amplitude ($A/d = 2.4$) scenario, one should expect higher fluidification of bed and this is even reflected in the transition displayed in Fig. 4.25, wherein LS gets transited into a pair of convection rolls, which eventually boils down to a single roll, while one increases shaking intensity gradually. To our knowledge, such "1-roll" convective pattern is novel and has not been reported in previous experiments on vibrofluidized beds at strong shaking. The bottom row of Fig. 4.25 displays such sort of single roll system at $\Gamma = 55$. This single roll spans across the full length of the box and the mechanism for the genesis of this roll is as follows: the beads gushes in the upward direction along a side wall of the box and convected towards the other side where they pour down along the wall forming a relatively dense region of beads. We confirmed that this dense region of beads can develop on either side of the box and thence can spawn rolls in both clockwise and counter-clockwise sense.

In a similar manner, Fig. 4.26 and Fig. 4.27 represent a series of transition at very high shaking amplitude $A = 8\ mm$ ($A/d = 4$). At such a high shaking amplitude and within the same maximum achievable shaking intensity ($\Gamma = 55$), we also observed the evaporation of the single roll into *Gas*, as depicted in Fig. 4.23. The top row of Fig. 4.26 depicts the *Bouncing Bed* state at $\Gamma = 2$, whereas, the middle row displays the LS state at $\Gamma = 30$ for various time instants of the shaking cycle. At a higher shaking intensity $\Gamma = 40$, the system shows a pair of convection rolls (refer bottom row of Fig. 4.26), which degenerates to a single roll at even higher $\Gamma = 45$ (see top row of Fig. 4.27. Further increasing shaking intensity to $\Gamma = 50$, we still observed one roll, albeit, the dense cluster reduces to comparatively sparse aggregate of beads (refer middle row of Fig. 4.27). Furthermore, as we surmised, intensifying the vibration more vigoroulsy leads to extreme agitation of beads, which in turn kills the convective motion and vaporizes the sytem to granular *Gas*, as shown in bottom row of Fig. 4.27. The route to the gaseous state from a "2-roll" convection to "1-roll" convection is a new finding of our experiments. The PIV velocity fields of the various states discussed above have been displayed in Fig. 4.28. Fig. 4.28(a) shows the

velocity fields of *LS* at various time instants of the shaking cycle. The velocity vectors reverse their direction after every half time period of the shaking cycle and get aligned in the same direction after a complete cycle; this velocity dynamics is in conformation with the previous studies of flow field in a *LS* and bolsters the fact that *LS* is a synchronized state with the vibrating base. It is also evident that the magnitude of coarse-grained velocity is higher near the base, i.e., within the *collisional layer*.

At a higher shaking intensity $\Gamma = 40$, the velocity field exhibits a pair of convection rolls (see Fig. 4.28(b)); the roll formation dynamics is as follows: particles torrent downward along both the side-walls of the container, both these current of particles incurvate and merge with each other near the centre of the container, then gushes upwards as a whole, bifurcates again at a particular height in opposite direction towards each wall of the container, thereby, consummating the circulation of rolls. Further, increasing the shaking intensity to $\Gamma = 45$, the double roll system trasmutes into a single roll, as shown in Fig. 4.28(c), whose circulation is in clockwise sense. We have confirmed by repeating experiments, that this single roll can even born having counter-clockwise circulation. This single roll persists even at vigoruos shakings of $\Gamma = 50$, as displayed in Fig. 4.28(d).

Till now, we looked at the qualitative aspects of the various observed states, but for a thorough understanding of the underlying physics one must extract quantitative information about density and granular temperature. Fig. 4.29 displays the averaged density and temperature variation across the bed height, for the different phases realized at shaking amplitude $A/d = 4$. For *BB* at $\Gamma = 2$ the density shows an increasing trend from the base, attains a maximum value at certain height and starts declining sharply afterwards. The maxima in the value corresponds to the maximal density which the hexagonally packed bed of spherical beads can achieve. The temperature profile of the same state shows an inverse behavior, wherein, temperature falls off from the base upto height corresponding to maximum density, and thereafter increases rapidly. Such tendency is expected since the densely packed bed region will have relatively less agitation, and thence it will be comparatively colder. As the height increases, the beads become more mobile and agitated leading to rise in temperature. The top surface of the bed is *ballistic* in nature, wherein the beads are in gas-like state and this upraise the temperature even higher. At increased shaking intensity $\Gamma = 5$ the system exhibits *LS* and the corresponding density profile manifests an apparent *density inversion*. At higher shaking intensity ($\Gamma = 30$), the density profile of the *LS* shows a drop in the maximum density attained, due to the continuous fluidization of the *floating cluster*. The encounter with the *ballistic layer* in these *LSs* marks a sharp decrease in the density with height. The temperature profiles of these *Leidenfrost States* show a continuous monotonous decay in temperature above from the vibrating base till the achievement of the high density *floating cluster*; having traversed across this *floating cluster* region temperature shows the tendency to increase again, due to encounter with *ballistic layer*. The convective states also show such sort of *density inversion*, owing to the fact that near the base of the vibrating box, the particles are in gaseous state and at some height there exist dense clusters, nontheless the density profiles of *Convection* do not attain such high 'maximum' density (as compared to *LS*) due to the fact that in *LS* a hexagonally packed bed that spans across whole length of box is supported over a dilute region while in *Convection* particles form an aggregate only near the

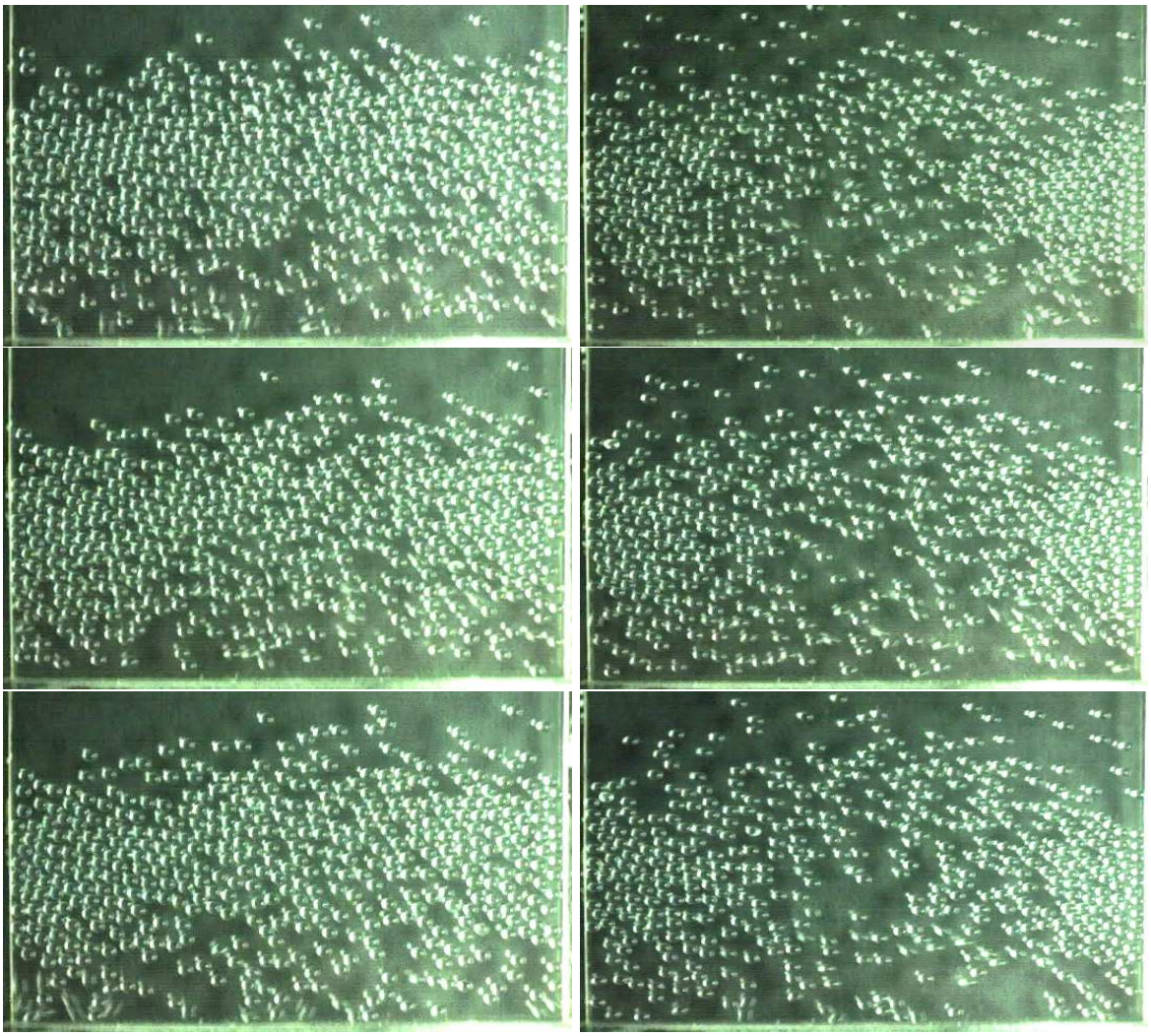

Figure 4.24: **Snapshots for $F = 12$ layers of 2.0 mm diameter glass beads confined in $L/d = 40$ cell, for three successive time instants of the oscillation cycle at $A/d = 1$: $t = 0\tau$ (top row); $t = \tau/2$ (middle row); $t = \tau$ (bottom row).** Left panel: *LS* at $\Gamma = 40$ ($f = 70.5\ Hz$); Right panel: *Convection* showing a pair of rolls at $\Gamma = 50$ ($f = 78.8\ Hz$);

side-walls of the vibrating box. Comparing the density profiles of *Convection* at $\Gamma = 40$ and 50, one finds that drop in the 'maximum' density is rapid, and there exists a tenuous *density inversion* at increased Γ. The granular temperature profiles again show a reverse trend with respect to that of density profiles, as established previously. Further increasing the shaking intensity at $\Gamma = 55$ exhibits *gaseous state*, whose density profile has almost flattened out. It is discernible from the snapshots of *Gas* (refer Fig. 4.27), that there is mild agglomeration of beads in the vicinity of the middle of the bed along the vertical direction; this has imparted a bump in the density profile exhibiting a maxima, and consequently a dip in the temperature profile. We conjecture that, at very high shaking intensities (which is beyond the capacity of our shaker), this density profile should become almost flat, showing a uniform density field vertically across the fluidized gas. It should be noted that, all these density and temperature profiles keep broadening along the vertical height, as one escalates the shaking intensity (Γ), owing to the fact that the expansion of granualar bed amplifies proportionally with Γ.

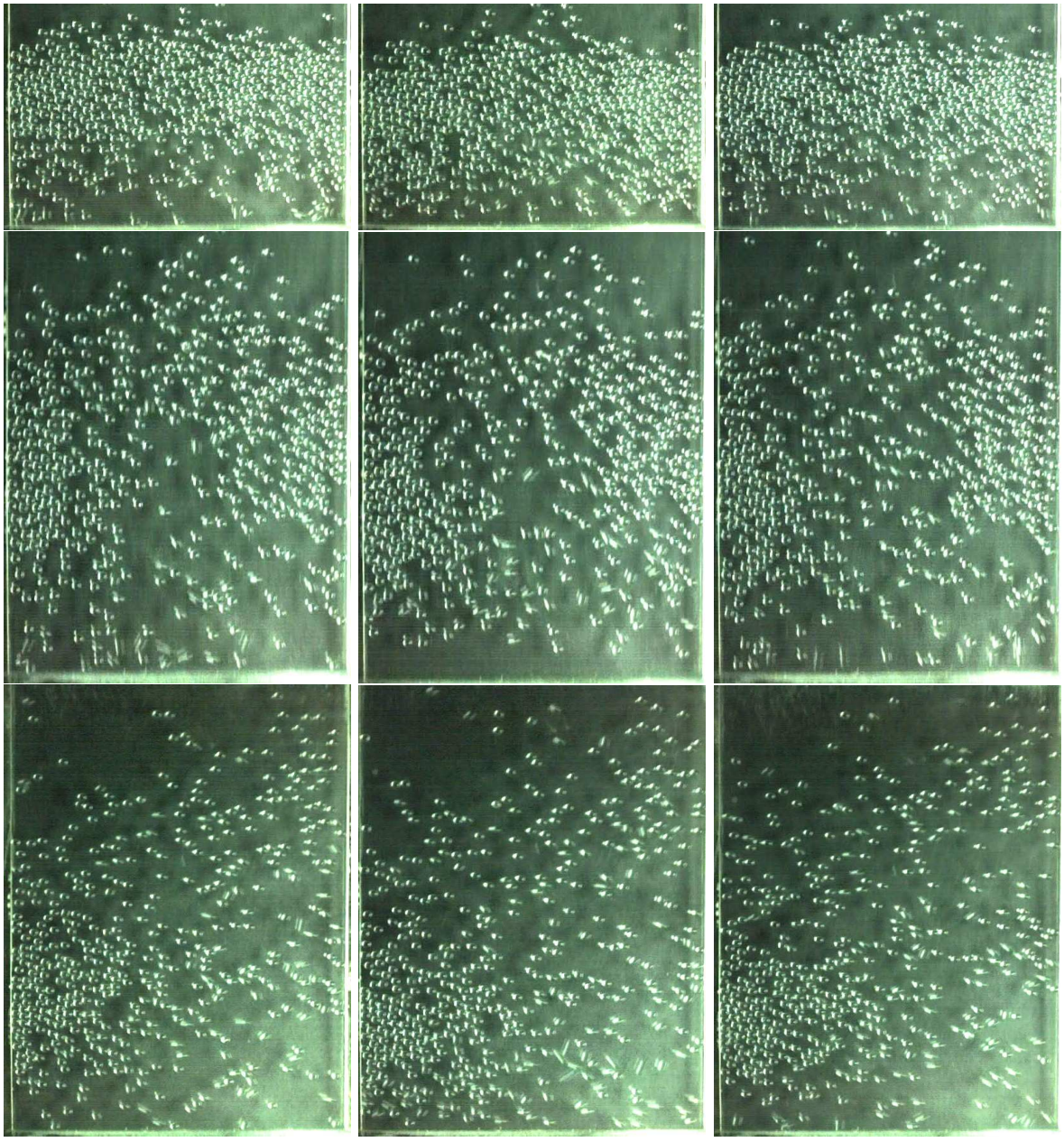

Figure 4.25: **Snapshots for $F = 12$ layers of 2.0 mm diameter glass beads confined in $L/d = 40$ cell, at three successive time instants of the oscillation cycle at $A/d = 2.4$: $t = 0\tau$ (left), $t = \tau/2$ (middle) and $t = \tau$ (right).** Top row: *LS* at $\Gamma = 30$ ($f = 39.4\ Hz$); Middle row: *Convection* showing a pair of rolls at $\Gamma = 45$ ($f = 48.3\ Hz$); Bottom row: *Convection* showing single roll at $\Gamma = 55$ ($f = 53.35\ Hz$).

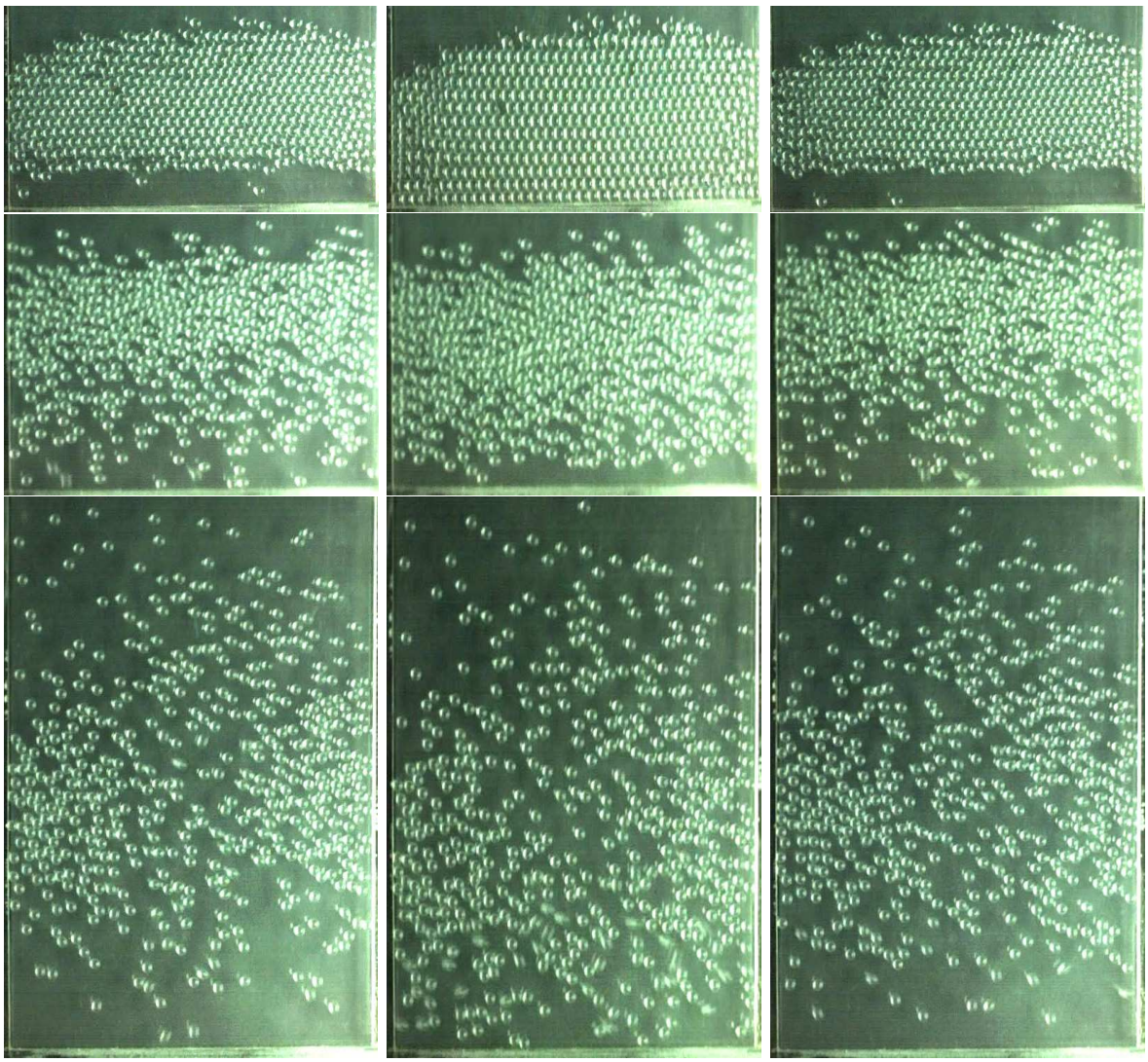

Figure 4.26: **Snapshots for $F = 12$ layers of 2.0 mm diameter glass beads confined in $L/d = 40$ cell, at three successive time instants of the oscillation cycle at $A/d = 4$: $t = 0\tau$ (left), $t = \tau/2$ (middle) and $t = \tau$ (right).** Top row: *BB* at $\Gamma = 2$ ($f = 7.8\ Hz$); Middle row: *LS* at $\Gamma = 30$ ($f = 30.5\ Hz$); Bottom row: *Convection* showing a pair of rolls at $\Gamma = 40$ ($f = 35.24\ Hz$).

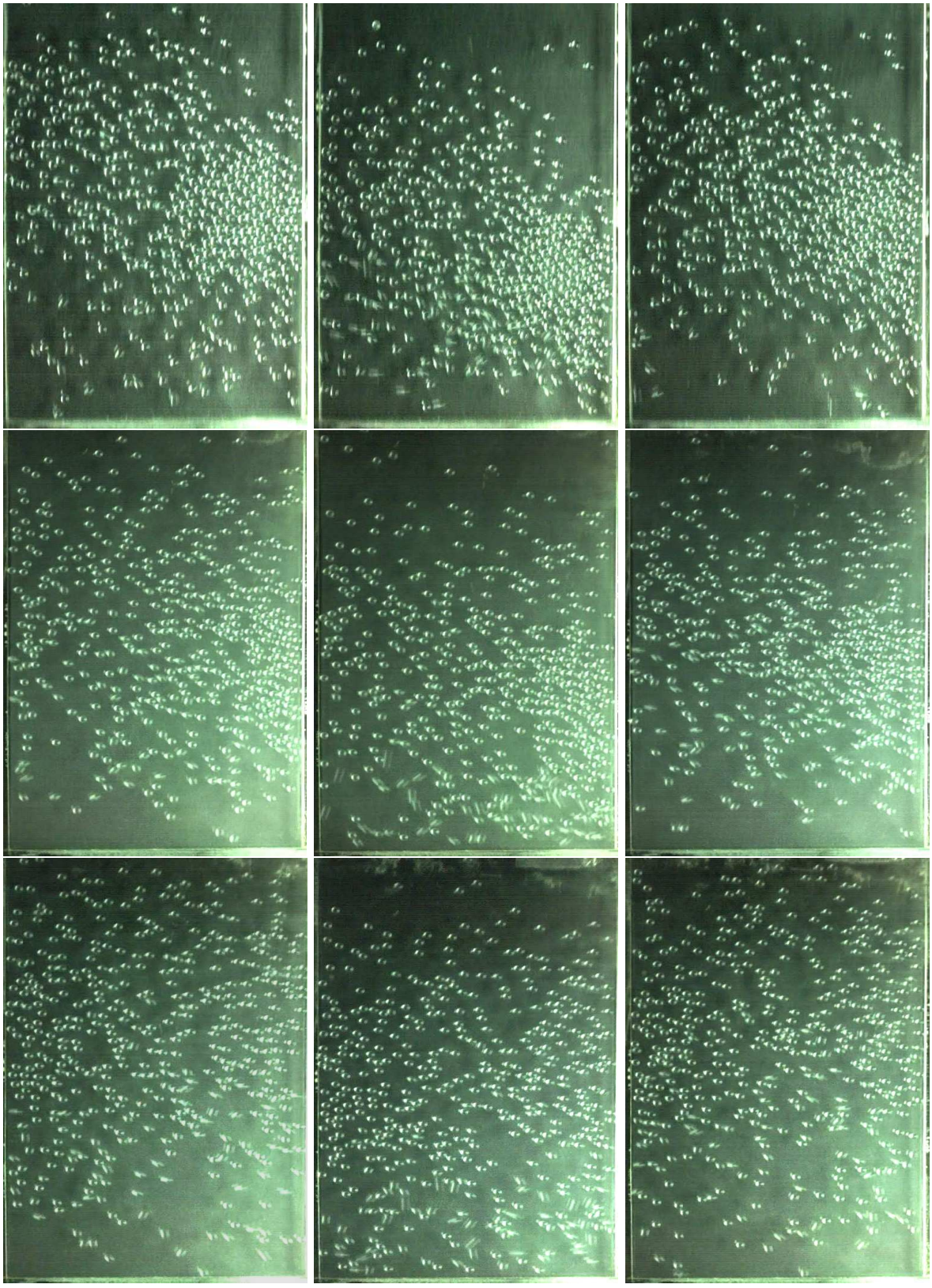

Figure 4.27: *Continued Fig. 4.26* **Snapshots for $F = 12$ layers of 2.0 mm diameter glass beads confined in $L/d = 40$ cell, at three successive time instants of the oscillation cycle at $A/d = 4$: $t = 0\tau$ (left), $t = \tau/2$ (middle) and $t = \tau$ (right).** Top row: *Convection* showing a single roll at $\Gamma = 45$ ($f = 37.4\ Hz$); Middle row: *Convection* showing a single roll at $\Gamma = 50$ ($f = 39.4\ Hz$); Bottom row: *Gas* at $\Gamma = 55$ ($f = 41.3\ Hz$).

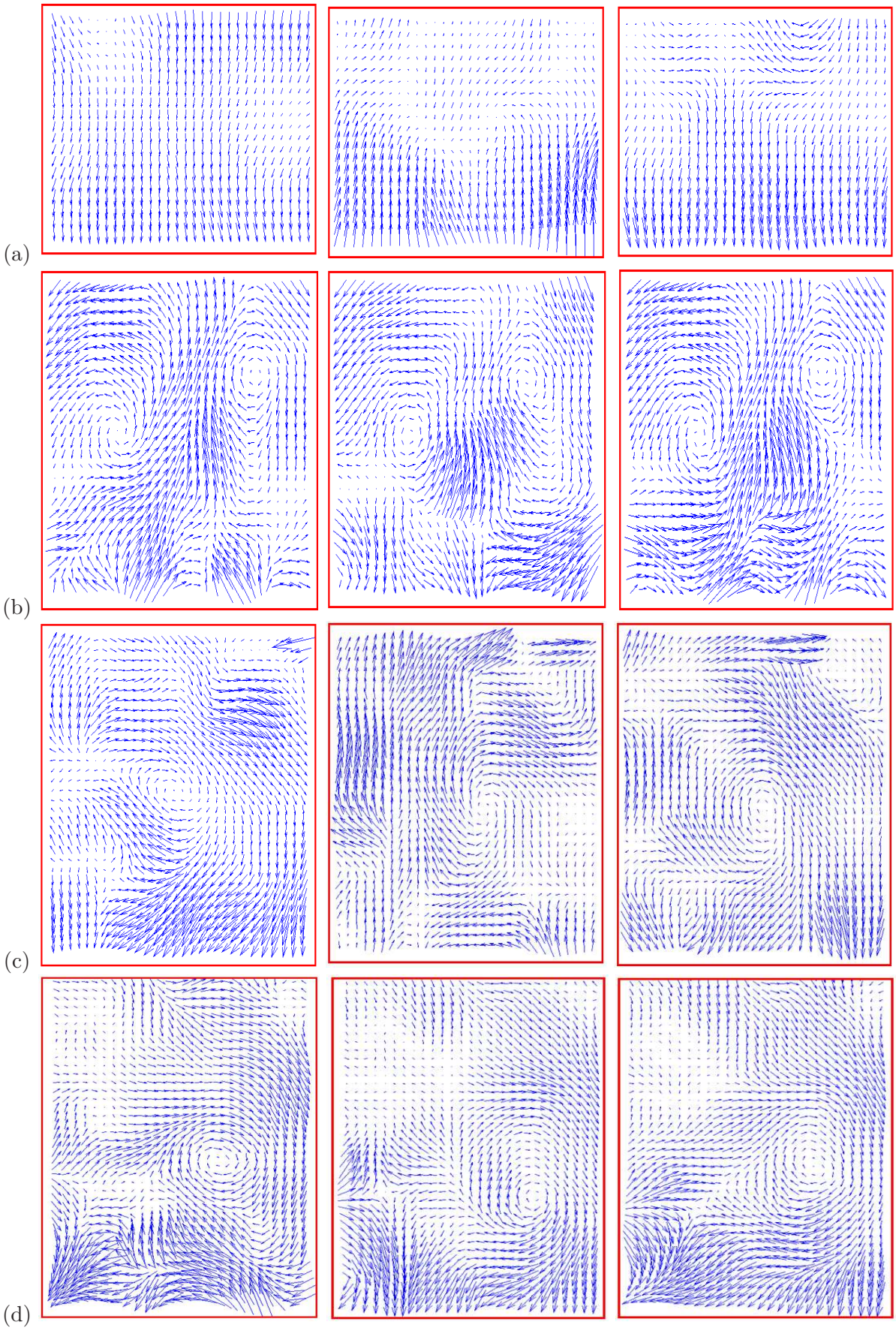

Figure 4.28: **Coarse-grained velocity fields for the various states in $F = 12$ layers of 2.0 mm diameter glass beads confined in $L/d = 40$ cell at $A/d = 4$: (a) *LS* at $\Gamma = 30$; (b) *Convection* showing a pair of rolls at $\Gamma = 40$; (c) *Convection* showing single roll at $\Gamma = 45$; and (d) *Convection* showing single roll at $\Gamma = 50$.** The left, middle and right panel corresponds to $t = 0\tau$, $t = \tau/2$, and $t = \tau$, respectively.

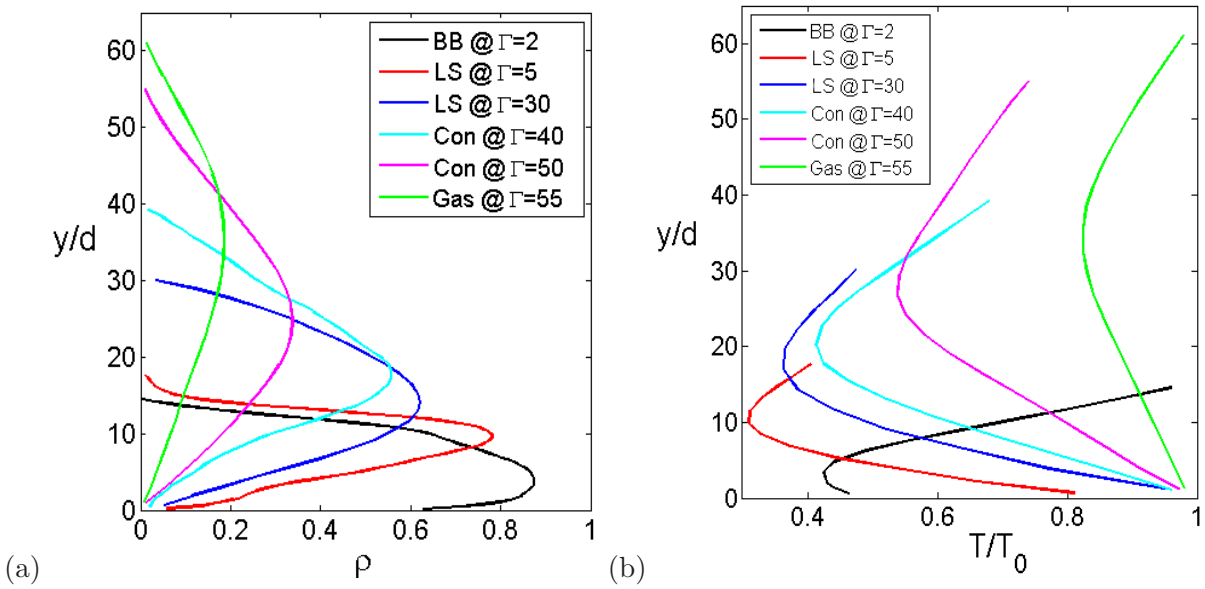

Figure 4.29: **(a) Averaged density profiles, and (b) Temperature profiles for various states observed in $F = 12$ layers of** $2.0\ mm$ **diameter glass beads confined in $L/d = 40$ cell.** The shaking intensity Γ has been increased gradually at constant shaking amplitude $A/d = 4$.

Chapter 5

Study of Vertically Vibrated Bidisperse Granular System

5.1 Introduction

In this chapter, entirely novel experimental results on binary granular mixtures are discussed in detail. The following three types of mixtures have been considered for this study: (1) mixture of glass and steel particles (density ratio, $\rho_s/\rho_g \approx 3.06$ and both having daimater 1.0 mm), (2) mixture of brass and glass particles ($\rho_b/\rho_g \approx 3.46$ and both having daimater 1.0 mm) and, (3) mixture of brass and steel particles ($\rho_b/\rho_s \approx 1.13$ and both having daimater 1.0 mm). Most of the experiments have been conducted by holding the mixture in a harmonically shaken quasi two-dimensional Plexiglas® rectangular container whose aspect ratio is $L/W = 18.2$, where L and W is the length and width of the container, respectively. The experimental procedure adopted is the same as discussed in previous chapters, i.e., increasing the shaking frequency f linearly upto a maximum limit, while maintaining the shaking amplitude A to be a constant (which in turn increases S) and thereby decreasing f linearly from this peak to a certain value of S. In general a linear ramping rate of 0.01 Hz/s has been employed, unless stated otherwise. A multitude of unhitherto reported phase coexisting patterns have been observed and analyzed, whose progenitor seems to be the segregation of the two species of mixture in the horizontal direction.

In the initial stage of this chapter, pattern formation dynamics in equimolar (50 : 50) mixture have been discussed and later on the effect of varying the species proportion in the mixture F_h/F (where, F_h is the filling depth of heavier particles and $F = F_h + F_l$) and the shaking amplitude A have been studied. These control parameters F_l/F_h and A have played a crucial role in developing our understanding of the segregation-driven patterns and finding ways to control them. Unlike in molecular fluids, segregation or demixing occurs spontaneously in driven granular mixtures of different density and/or size particles which can be a nuisance/boon in processing industries dealing with granular materials. Therefore, we have also taken into account the study of the impact of the density ratio ρ_l/ρ_h (where, ρ_l and ρ_h has been defined in the same way as above) on these patterns and found that ρ_l/ρ_h governs the segregation which in turn controls the patterns.

We have also studied the effect of the ambient pressure P_{amb} on the vibrated mixture and found *hysteresis* in the system: this hysteresis seems to be tied to the air-drag on the particles because it vanished in case of very low pressure (vaccuum) inside the container.

Additional experiments have been performed varying the aspect ratio L/W (by varying the length L of the container) of the container and it is found that due to very less segregation in a smaller container, the segregation-driven patterns no longer persisted. This study confirms that segregation gives birth to phase-coexistence of subharmonic and synchronous states. The effect

of shaking amplitude A on the nature of various patterns have also been studied and compared.

5.2 Dynamical Patterns in Steel-Glass Particles Mixture

The equimolar mixture of equal sized steel and glass particles (both having diameter $d = 1.0\,mm$) is held in the container of length $L/d = 100$ and width $W/d = 5.5$. The container is filled upto a specified filling depth $F = F_s + F_g$, where F_s and F_g are the number of layers of steel and glass particles in the mixture, respectively. The complete phase diagram of all patterns is shown in Fig. 5.1 for 'upsweeping' and 'downsweeping' experiments. Upsweeping experiments were done with an initial configuration of randomly mixed mixture of steel and glass particles, and the final state of each upsweeping experiment is used as the initial state for its *downsweeping* evolution at the same rate of frequency ramping. To check the dependence of observed patterns on the initial state of random mixing, all experiments were also repeated with segregated initial states: (i) steel particles on top of glass particles and (ii) glass particles on top of steel particles; the observed patterns are found to be qualitatively similar. The shaking intensity for the onset (Γ_{onset}) of any pattern is accompanied by a small amount of *hysteresis*, as is evident by comparing Fig. 5.1(a) and Fig. 5.1(b). We will discuss this hysteresis in a more detailed way in later paragraphs. For $\Gamma \sim 1$, the kinetic energy of the particles is not able to overcome their dead-weight and hence the granular bed moves synchronously with the container without getting detached from the base plate- this is called *solid bed* (SB). With increasing $\Gamma > 1$, the bed detaches from the base and starts bouncing like a single body, akin to a particle bouncing off a plate with zero restitution coefficient- this is the regime of *bouncing bed* (BB) as depicted in Fig. 5.2 as three successive snapshots at $t = 0, \tau/2$ and τ, where $\tau = 1/f$ is the period of shaking. The corresponding coarse-grained velocity vector maps, displayed on the bottom of each raw image of Fig. 5.2, confirm that the velocity vectors undergo a change in orientation (from upward to downward and vice versa) after every half shaking time- period ($\tau/2$), implying a 'bouncing' solid-body motion of the bed at any time instant. This overall pattern repeats after every cycle, see Fig. 5.2(a-c), and therefore the BB is synchronized with the external shaking frequency and hence called a *synchronous/harmonic* or an f-wave.

The snapshots in Fig. 5.2 indicate that the center of mass of heavier steel particles is located above that of the lighter glass particles. Such vertical segregation of particles resembles the well-known Brazil-nut segregation (Williams 1976*a*; Harwood 1977; Rosato *et al.* 1987; Alam *et al.* 2006; Shinbrot & Muzzio 1998) wherein the larger and/or heavier particles rise to the top, leaving the smaller and/or lighter particles at the bottom of the shaken bed.

In particular, the SB gives birth to a "partial" BB state (in which a granular gas coexists with a BB state on two sides of the container) for $F < 3.75$ and a complete BB for $F \geq 3.75$ (such as those displayed in Fig. 5.2. The partial BB state is a phase-coexisting state where a glass-rich bouncing bed coexists with a steel rich granular gas. This state is a clear signature of the 'horizontal segregation' of lighter and heavier species in the vibrating container (see Fig. 5.4 for more details). The onset value (Γ_{onset}) for BB patterns slightly increases with increasing F, and they are stable over a range of shaking intensity, $1 \leq \Gamma \leq 7$, beyond which new patterned states (see Fig. 5.1) are born that are discussed below.

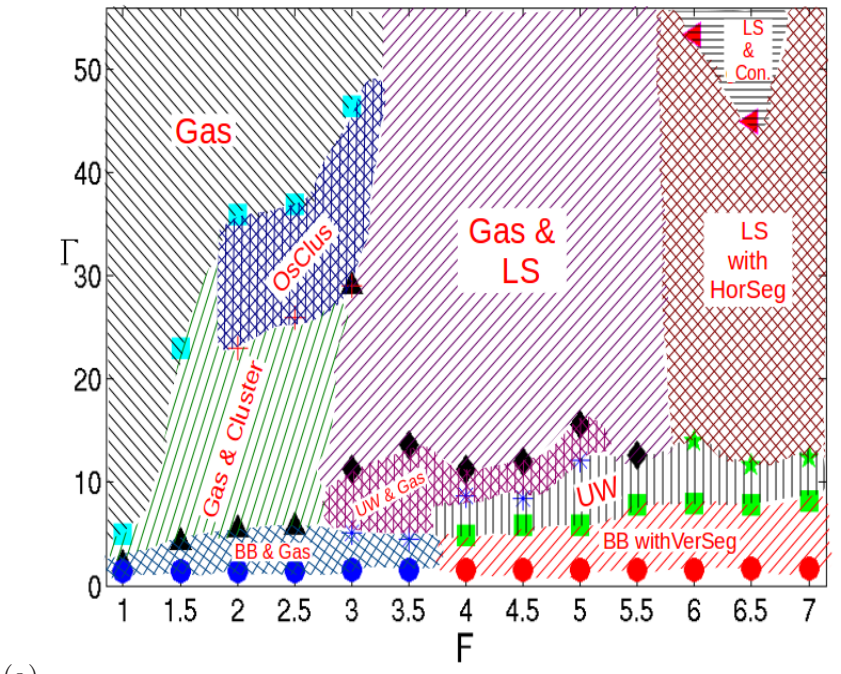

(a)

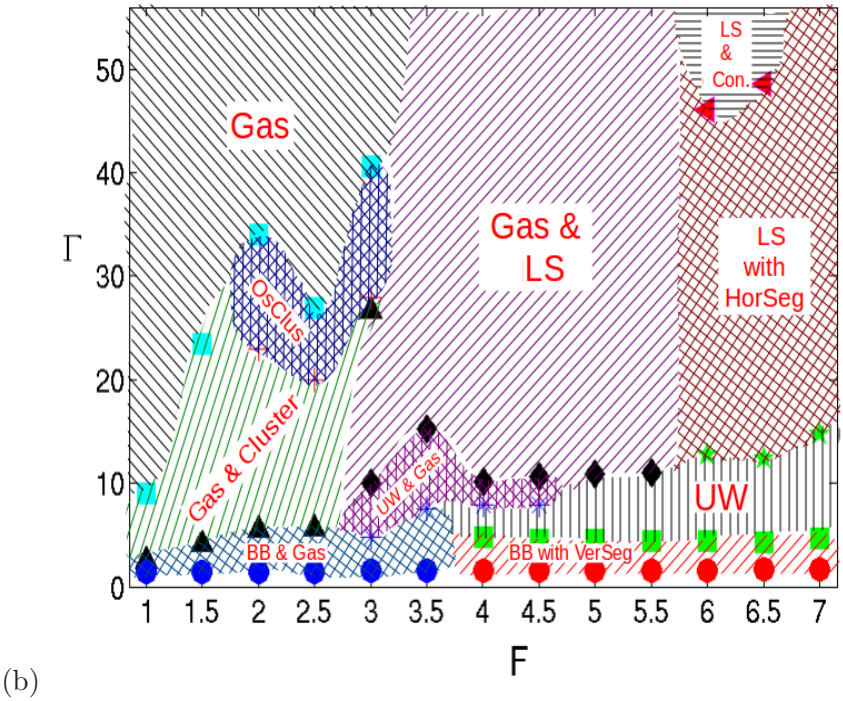

(b)

Figure 5.1: **Phase diagram of dynamical patterns in** (Γ, F)**-plane during (a) upsweeping and, (b) downsweeeping epxeriments.** The *SB* (solid bed) regime lies below the *BB* (bouncing bed) regime (denoted by circles at $\Gamma \sim 1$). Other regions are marked as: UW (undulatory wave), LS (granular Leidenfrost state), Con. (granular Convection) OsCluster (oscillating cluster), VerSeg (vertical segregation) and HorSeg (Horizontal Segregation). Parameter values are $A/d = 3$, $F_g = F_s$ and $ramping\ rate = 0.01\ Hz/sec$.

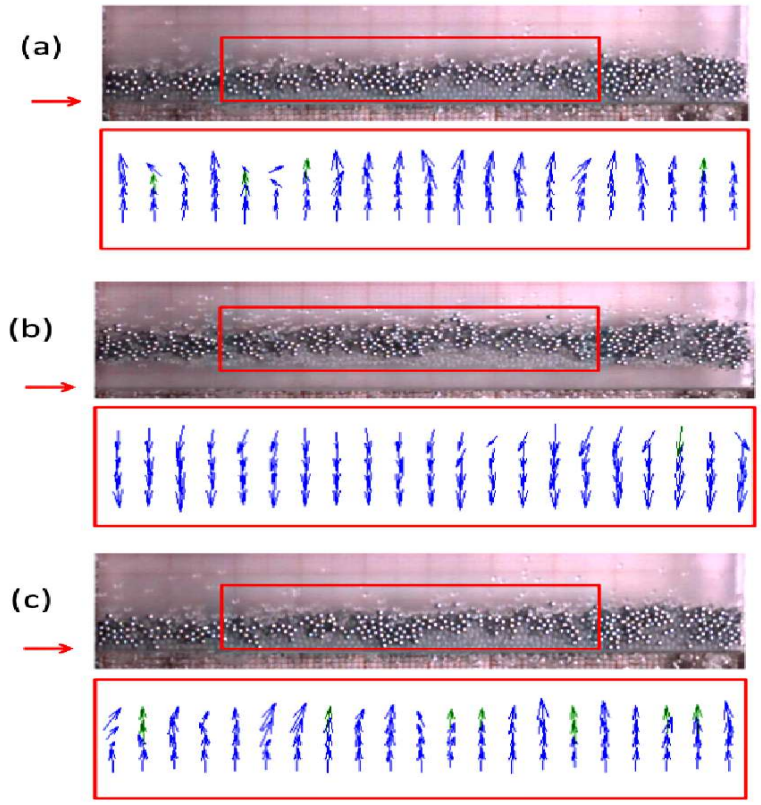

Figure 5.2: **Snapshots of the bouncing bed exhibiting "Brazil nut segregation", at three successive time instants of the oscillation cycle: (a)** $t = 0$**, (b)** $t = \tau/2$**, and (c)** $t = \tau$**, where** $\tau = 1/f$. The dark/black and light/grey particles are steel and glass beads, respectively; the left arrow on each snapshot indicates the position of the base of the container. The coarse-grained velocity field from PIV within the red box of each raw image is shown on its bottom panel. Parameter values are $F = F_g + F_s = 6$ and $\Gamma = 4.1$ ($A/d = 3$ and $f = 18.4\ Hz$).

5.2.1 Phase Coexisting Patterns and Horizontal Segregation

For the sake of clarity and to study in depth the phase coexisting patterns we have performed additional experimental runs at intermediate data points of phase diagram (shown in Fig. 5.1) for $\Gamma \in (0, 20)$ and $F \in (2.5, 8)$ and displayed the resulting phase diagram in Fig. 5.3; for both upsweeping and downsweeeping experiments.

We will begin discussing novel phase-coexisting patterns with a transition as displayed in Fig. 5.3(a), where it is shown that how a partial bouncing bed, *BB+Gas*, transforms into a complete bouncing bed *BB* state with increasing filling depth $F = F_g + F_s$ (see Fig. 5.5). Fig. 5.6 depicts the gradual evolution of the density profiles along the length of the container for these "partial" *BB* states which eventually transform into "complete" *BB* state, while one increases the filling depth F gradually (refer Fig. 5.5). These coarse-grained density fields have been realized by calculating an 'effective' density in terms of the average light intensity over a stripe of thickness $2d$ (where d is the particle diameter) as shown by the red box in Fig. 5.6. The density profiles in Fig. 5.6 have successfully captured the two different regions of the pattern, viz, 'solid' and 'gaseous' regions structuring the "partial" *BB* state; the signature of 'solid' region being the unit normalized density, while the sporadic fluctuations in normalized density characterizes the 'gaseous' region, wherein particles are expectedly in random chaotic motion that leads the normalized density to droop much below unity.

The other interesting transition showing how these two-phase patterns gradually boil down to a single phase is shown in Fig. 5.7, where a series of images with increasing total filling depth ($F = F_g + F_s$) at $\Gamma \approx 9$ are shown. A stationary cluster of glass-rich particles is seen on the left of the container in Fig. 5.7(a) that coexists with a gas-like state of heavier steel particles on the right of the container at $F_g = F_s = 1.25$. We confirmed that this type of stationary cluster can also born on the right side of the container. In either case once formed the cluster retains its position for a long time, in contrast to the 'oscillating' cluster state which we will discuss in detail in later section.

It has been established in experiment (Feitosa & Menon 2002), simulation (Alam & Luding 2002) and theory (Garzó & Dufty 1999) that the collisional dissipation is responsible for the *unequal* partition of granular energy between heavier and lighter particles. The steel particles being heavier possess higher kinetic energy and hence are in a more mobile gas-like state; in contrast, the lighter glass particles possess lower kinetic energy and they are relatively less mobile leading to a cluster of glass rich particles.

Fig. 5.8 displays three snapshots of "$Gas-Cluster$" state at different times of the oscillation cycle: (a) $t = 0$, (b) $\tau/2$ and τ. A gas-like state on the right side of the container coexists with a cluster (a loose aggregate of particles) on its left-both are period-1 patterns, i.e., the composite pattern stays synchronous with the vibrating container. This is an example of phase-coexistence between two states (a granular gas and a liquid-like cluster) that have different spatial order but same temporal symmetry. The right panel of Fig. 5.8 shows that the birth of this cluster is equally probable on right side of the container and the gas on left of the container.

When the total layer depth is increased to $F = 3$ (see Fig. 5.7(b)), we find another coexisting phase of (i) a granular gas on the right of the container and (ii) an undulatory wave ($n = 2$ mode) on its left. These undulatory waves are *subharmonic* standing waves whose time-period

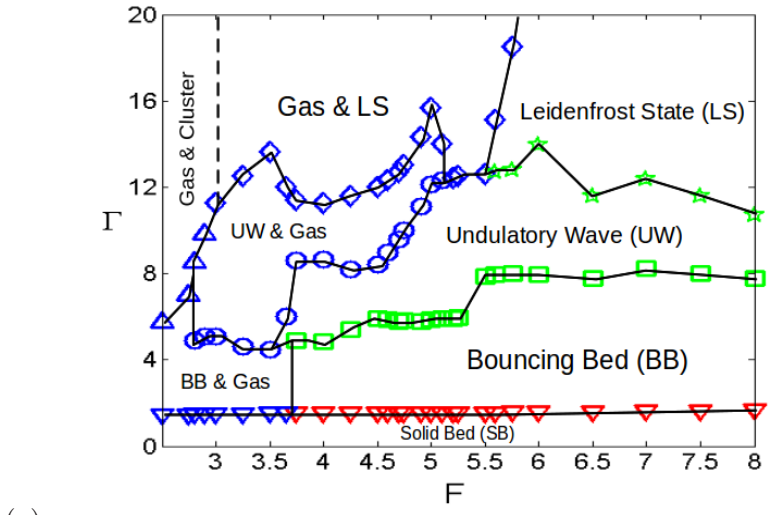

(a)

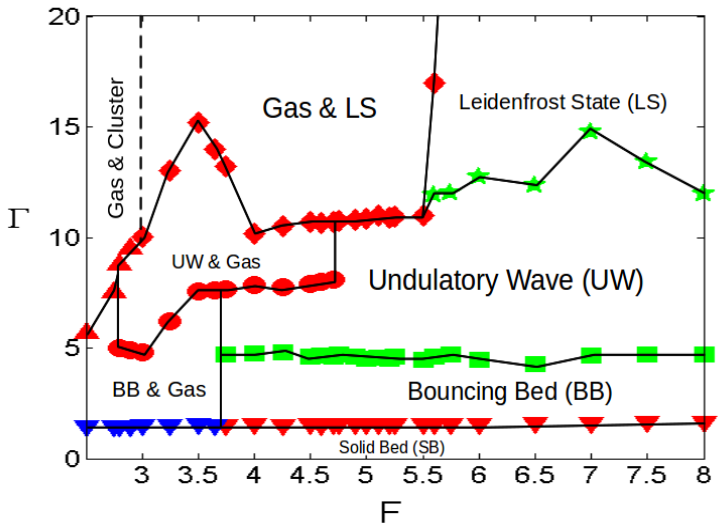

(b)

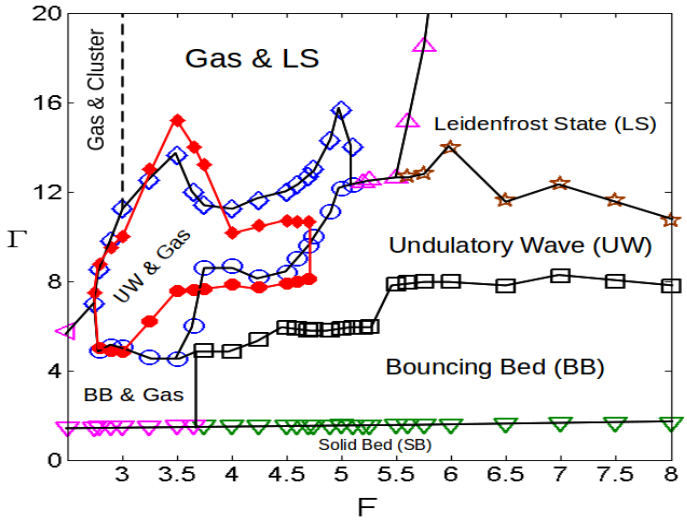

(c)

Figure 5.3: **Phase diagram of dynamical patterns in (Γ, F)-plane upto $\Gamma = 20$ during (a) upsweeping, (b) downsweeeping and (c) upsweeping and downsweeping experiments superimposed for UW+Gas regime.** The 'upsweeping' and 'downsweeping' experiments are accompanied by a small amount of hysteresis. Parameter values are $A/d = 3$, $F_g = F_s$ and *ramping rate* $= 0.01$ Hz/sec.

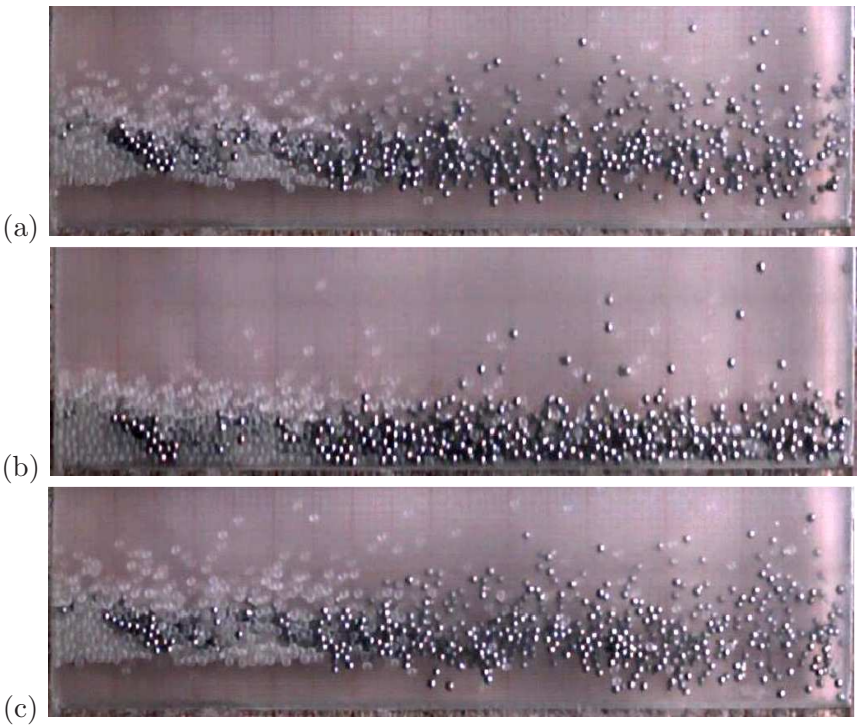

Figure 5.4: **Snapshots of the bouncing bed coexisting with a granular gas (*BB+Gas*) at three successive time instants of the oscillation cycle: (a)** $t = 0$**, (b)** $(t = \tau/2)$ **and (c)** $t = \tau$**, where** $\tau = 1/f$. The dark/black and light/grey particles are steel and glass beads, respectively. The glass-rich '*BB*' is coexisting with a steel-rich granular gas. Parameter values are $F = F_g + F_s = 3$ and $\Gamma = 3.5$ $(A/d = 3$ and $f = 17.02\ Hz)$.

of oscillation is twice the time-period of shaking ($\tau = 1/f$) and hence called '$f/2$' or 'period-2' waves. These waves are similar in nature to those undulatory wave discussed in Chapter 3.

Note in Fig. 5.7(b) that most of the steel particles are in the gaseous state while the glass particles are undergoing a sub-harmonic undulatory motion, representing a state of horizontal segregation as in the gas-cluster state of Fig. 5.7(a). For the same parameter values, the undulation wave can exist on right side of the container as shown in Fig. 5.10. However, the span of undulatory wave inside the container is more in left panel than in the right panel. This implies that in both these experimental runs the degree of segregation is different giving rise to larger or smaller steel and glass-rich regions. In either case, the subharmonic nature of undulation wave is confirmed from these three snapshots in Fig. 5.10 since the peaks and valleys exchange after one time period of shaking (τ) and the wave repeats itself after 2τ. This is an example of rare phase- coexistence between two states that have different spatial order as well as different temporal symmetry. Similar to the gas-cluster state in Fig. 5.7(a) and Fig. 5.8, we have horizontal segregation in Fig. 5.10 too, with most steel-particles are in gaseous state and most glass-particles in an undulatory liquid-like state. If one increases the layer filling depth to $F = 4$, it is found that mode-3 undulatory wave coexists with a granular gas (see Fig. 5.11), whose characteristic features are the same as in the pattern shown in Fig. 5.10.

The mode number (n) of an undulatory wave is defined as the number of half-wavelengths $\lambda/2$ that can be accommodated in a container of sength L such that $L = n\lambda/2$. Therefore, Fig. 5.10 and Fig. 5.11 correspond to *mode-2* and *mode-3* undulatory waves. The phase-coexisting states

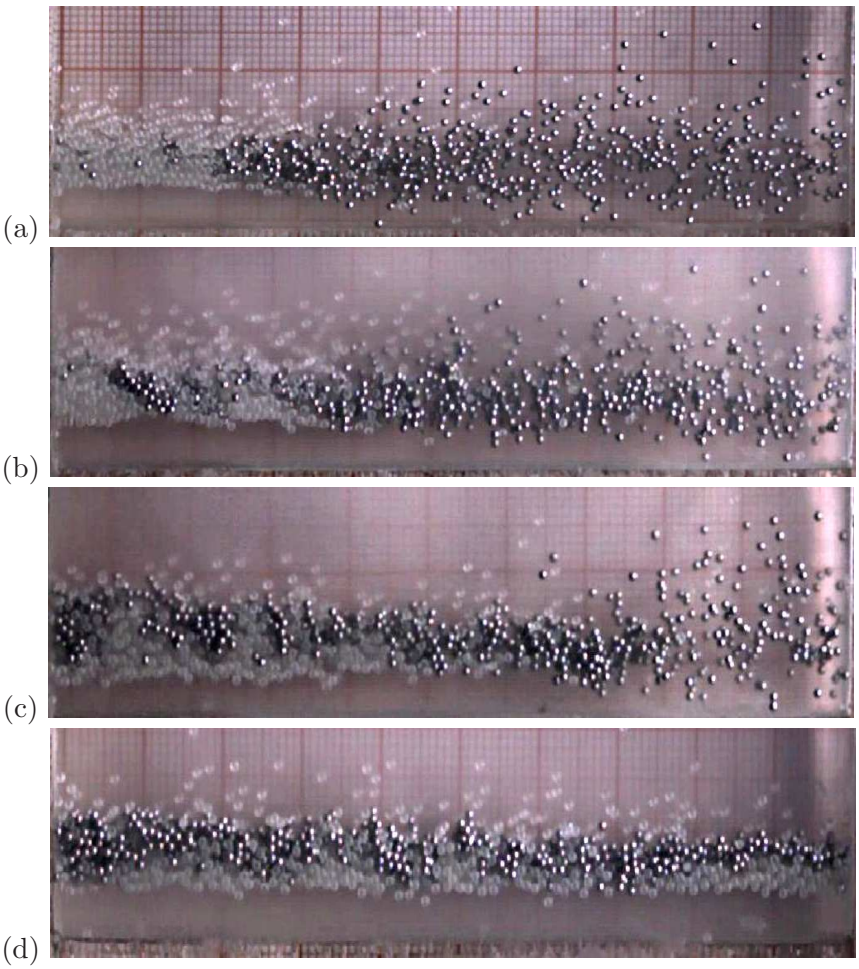

Figure 5.5: **Gradual change from 'partial' *BB* to complete *BB* state with increasing filling depth (F) at $\Gamma \approx 3.5$ with $A/d = 3$, $F_g = F_s$:** (a) *BB+Gas* at $F = F_g + F_s = 2.5$; (b) *BB+Gas* at $F = 3$; (c) *BB+Gas* at $F = 3.65$; (d) complete *BB* at $F = 4$.

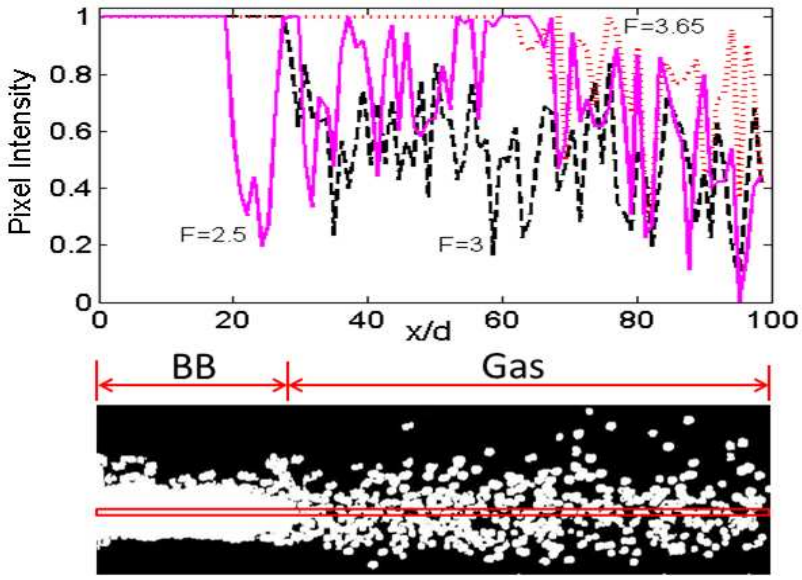

Figure 5.6: **The normalized density of the patterns calculated considering a stripe of thickness $2d$ (where d is the particle diameter) along the length of the container.** This coarse-grained density has been obtained from the digitized version of the particle snapshots (shown at the bottom of the plot) by calculating an 'effective' density field in terms of the average light intensity over the stripe shown by the red box.

such as in Fig. 5.10 and Fig. 5.11 survive experimental time-scales of $O(10^4\tau)$ which has been confirmed by repeating these experiments at fixed Γ for long enough time. An interseting theoretical question about Fig. 5.10 is: how does a "partial" undulatory wave survive with one end being in continual touch with a granular gas? The mode number and the wavelength of a complete undulation wave spanning the whole length of the container has been previously predicted (Sano 2005) using elastic theory of bending with appropriate boundary conditions at two ends. What boundary condition should one use for "partial" undulatory waves? If the effective elasticity of a collection of particles is assumed to be a function of its mobility (or, the granular temperature), then one can construct a theory to explain "partial" undulation waves.

If the filling depth is increased further to $F = 5$ at constant $\Gamma \approx 9$ (see Fig. 5.12) the granular gas vanishes in the system and "complete" undulatory waves set up spanning whole length of the container. So, it is evident that phase coexistence ceased for $F > 4.6$ at this Γ level and only one type of phase exists in the system.

Figure 5.1 indicates that the 'UW+Gas' state can be accessed with increasing Γ either from 'BB+Gas' state or from complete BB-state. For monodiperse systems, the genesis of complete undulatory waves as a bifurcation from the bouncing bed (with increasing Γ, see Fig. 3.14) has been explained by drawing an anlogy with the buckling phenomenon of an elastic bar (Sano 2005). More specifically there is horizontal dilation of a compact layer of granular materials (BB state) upon its impact on the base plate that creates an effective horizontal tension along this layer (made of a collection of particles with its two ends being pinned at two end walls). The dilation (and hence effective tension) increases with increasing Γ which eventually gives birth to a buckled state of the granular layer beyond some critical Γ-leading to undulatory waves such as Fig. 5.7(d). Such an analogy is difficult to reconcile with the present finding of UW that

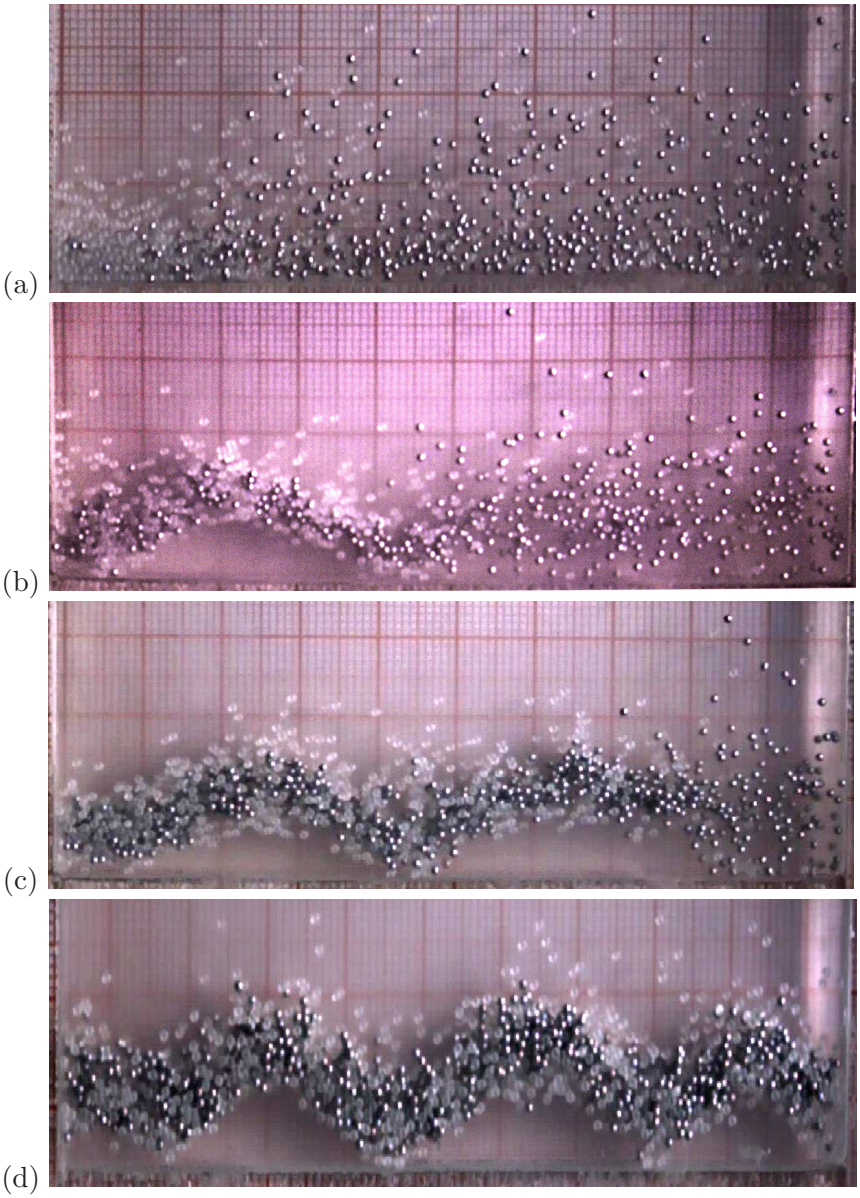

Figure 5.7: **Transition among different states with increasing filling depth (F) at $\Gamma \approx 9$ with $A/d = 3$, $F_g = F_s$:** (a) Gas-Cluster state at $F = F_g + F_s = 2.5$ and $\Gamma = 9$ ($f = 27.3\ Hz$); (b) Gas-Undulation ($n = 2$ mode) state at $F = 3$ and $\Gamma = 9$ ($f = 27.15\ Hz$); (c) Gas-Undulation ($n = 3$ mode) state at $F = 4$ and $\Gamma = 9.1$ ($f = 27.45\ Hz$); (d) Undulation ($n = 6$ mode) state at $F = 5$ and $\Gamma = 8.93$ ($f = 27.2\ Hz$).

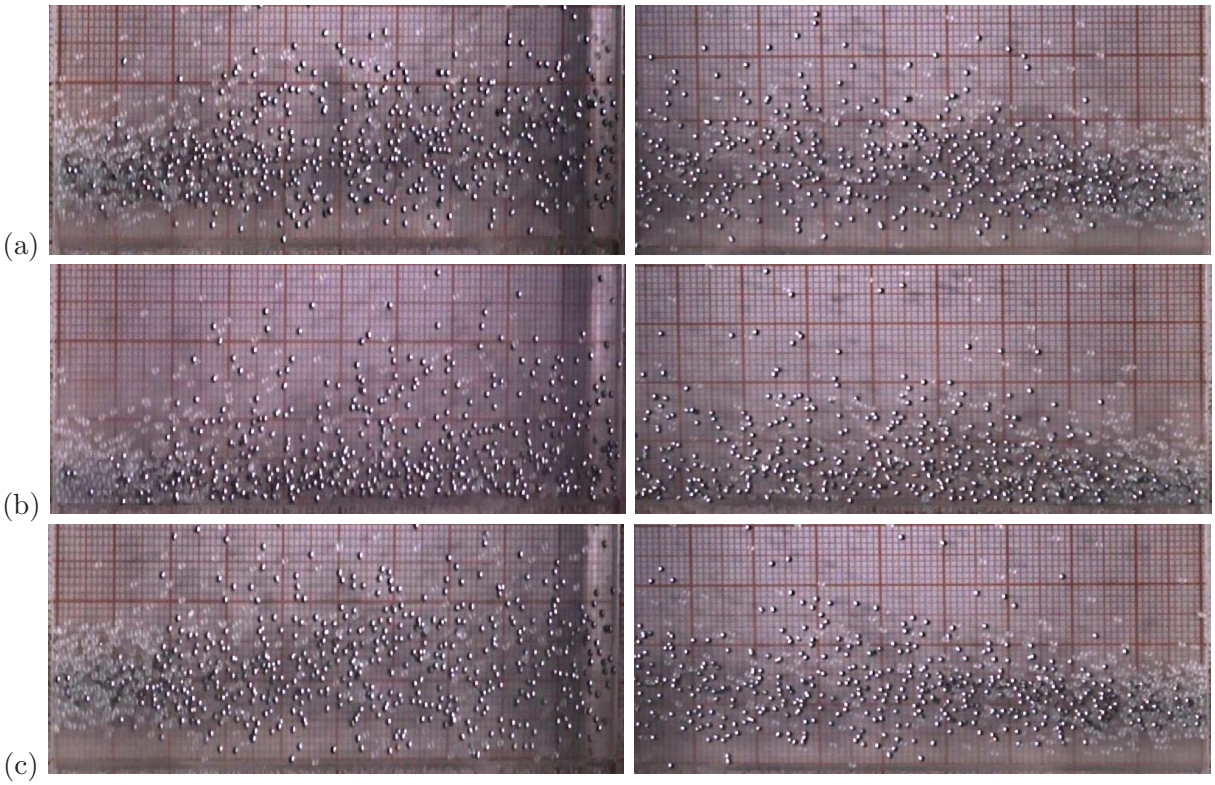

Figure 5.8: **Phase-coexisting pattern: time sequence snapshots of stationary gas-cluster state: (a) $t = 0\tau$, (b) $t = 0.5\tau$ and (c) $t = \tau$, where, $\tau = 1/f$ is the period of shaking.** Right panel: the glass-rich cluster on the right of the container coexists with a steel-rich granular gas on its left at $\Gamma = 9.4$ ($f = 27.9\ Hz$) Left panel: the glass-rich cluster on the left of the container coexists with a steel-rich granular gas on its right at $\Gamma = 9$ ($f = 27.3$) in another experimental run. Other parameter values are $F = F_g + F_s = 2.5$ and $A/d = 3$.

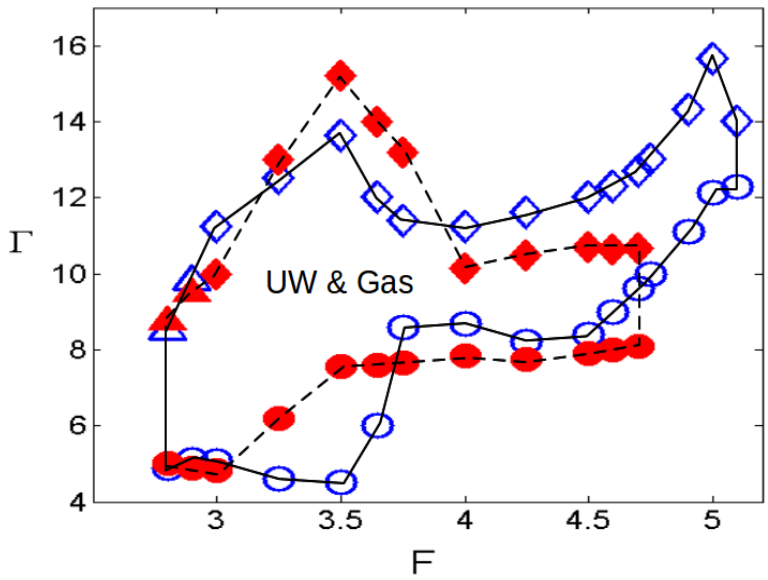

Figure 5.9: **The zoomed view of UW+Gas regime corresponding to Fig. 5.3 showing the hysteresis in upsweeping and downsweeping experiments.** The open blue and closed red symbols denotes the Γ_{onset} for upsweeping and downsweeping experiments, respectively.

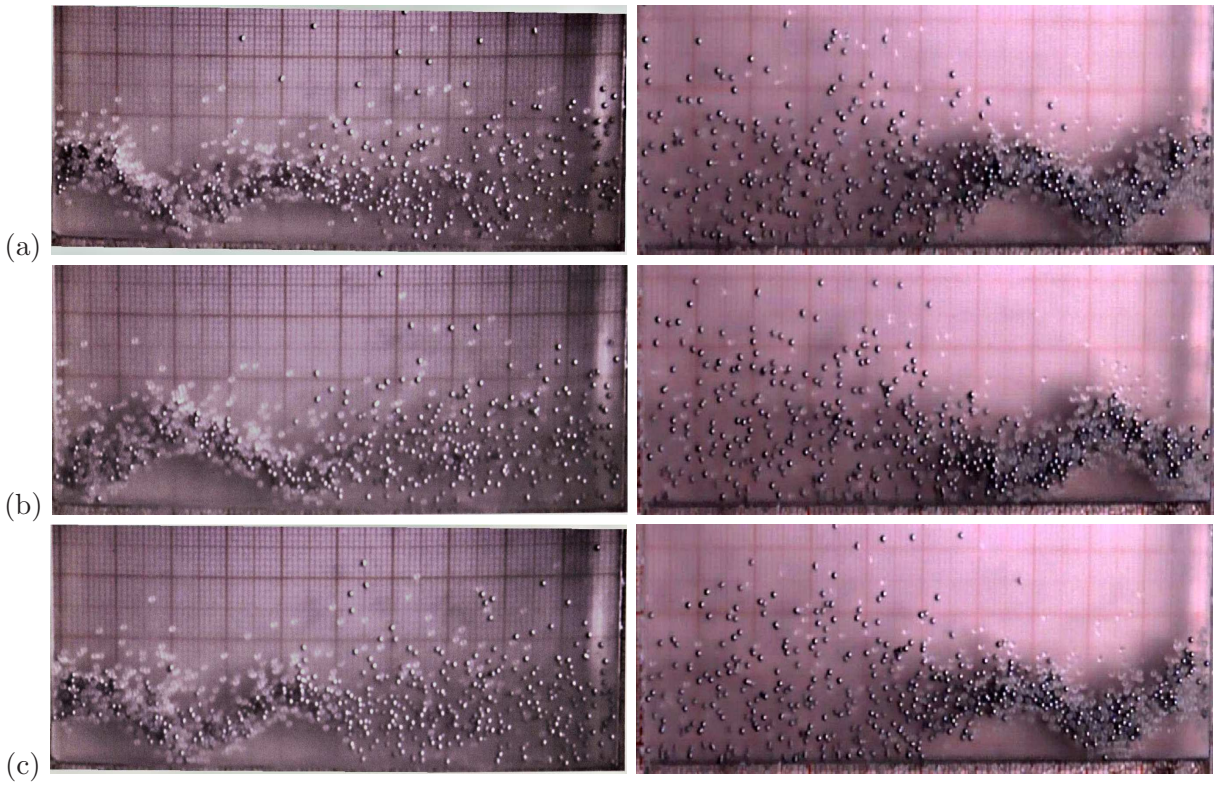

Figure 5.10: **Phase-coexisting pattern: time sequence snapshots of Fig. 5.7(b) consisting of a period-2 subharmonic wave 'mode-2' and a granular gas: (a)** $t = 0\tau$**, (b)** $t = \tau$ **and (c)** $t = 2\tau$**, where,** $\tau = 1/f$ **is the period of shaking.** Note that peaks and valleys of the undulatory wave exchange their positions exactly over one shaking period (τ), and this undulatory wave repeat itself over 2τ; hence this is a *period-2 wave*. The gaseous regime moves synchronously (i.e., *period-1*) with the bottom plate. Right panel: undulatory wave on the left side of the container coexisting with granular gas. Left panel: undulatory wave on the right side of the container coexisting with granular gas found in repeated experimental run. This shows that birth of undulatory wave is equally probable on both sides. Parameter values are $F = F_g + F_s = 3$ and $\Gamma = 9$ ($A/d = 3$ and $f = 27.3\ Hz$.)

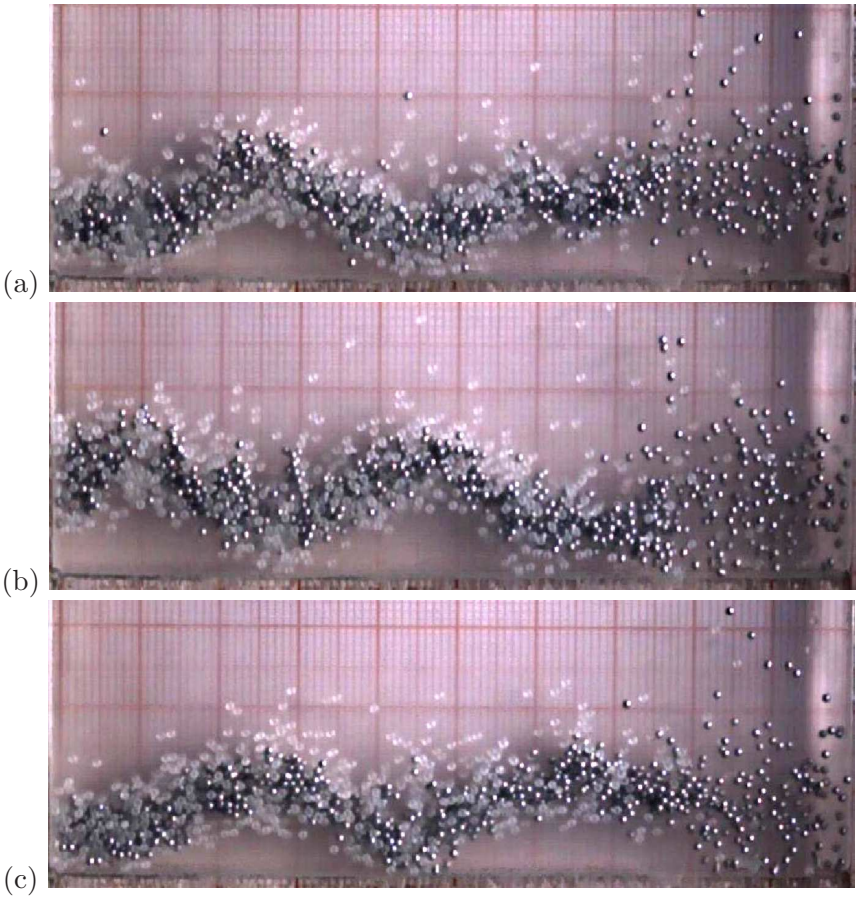

Figure 5.11: **Coexistence of a "mode-3" undulatory wave with a granular gas similar to Fig. 5.10**. (a) $t = 0\tau$, (b) $t = \tau$ and (c) $t = 2\tau$, where $\tau = 1/f$ is the period of external shaking. Parameter values are $F_g + F_s = 4$ and $\Gamma = 9.2$ ($A/d = 3$ and $f = 27.6\ Hz$.)

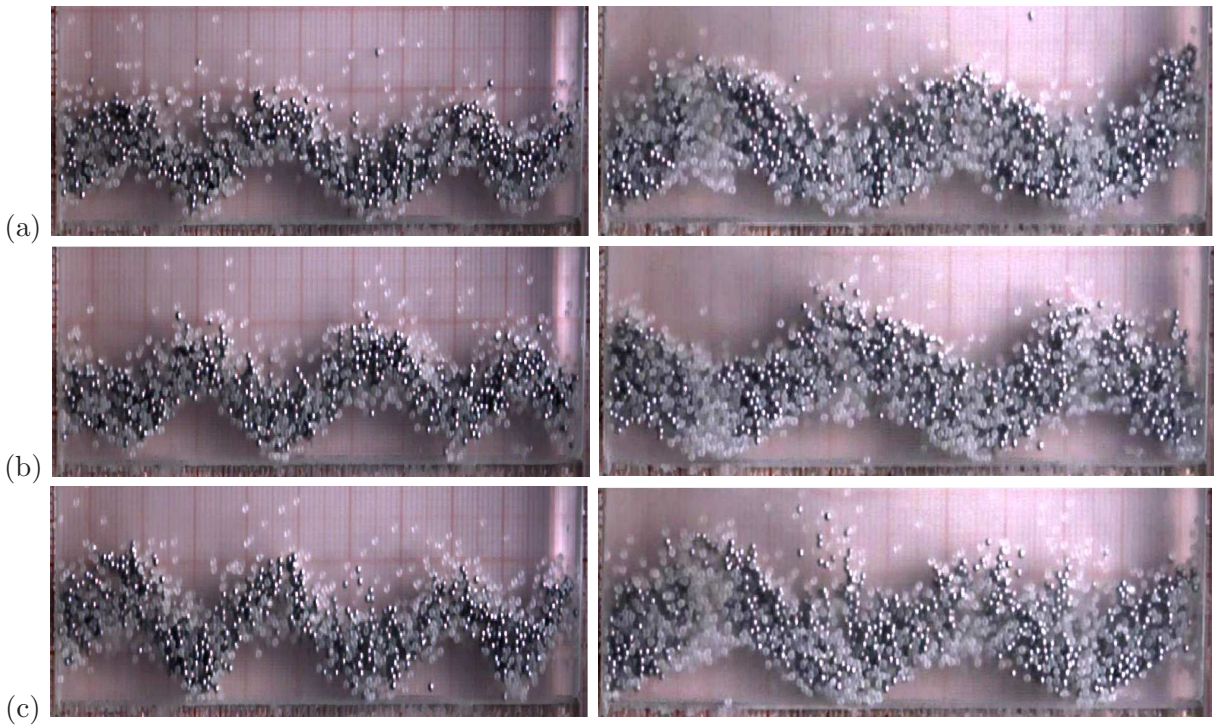

Figure 5.12: **Time sequence snapshots of complete undulatory wave UW**: (a) $t = 0\tau$, (b) $t = \tau$ and (c) $t = 2\tau$. Note that peak and valleys of undulatory wave exchange their positions exactly over one shaking period (τ), and the complete pattern repeats itself over 2τ; hence this is a "period-2" undulatory wave. Left panel: "mode-6" for $F_g = F_s = 2.5$ and $\Gamma = 8.93$ ($A/d = 3$ and $f = 27.2\ Hz$). Right panel: "mode-5" for $F_g = F_s = 3.5$ and $\Gamma = 8.9$ ($A/d = 3$ and $f = 27.16\ Hz$)

coexists with a granular gas since the compact granular layer is free to dilate near one end where it is in constant touch with a granular gas.

We postulate the following modified scenario for the genesis of 'partial' *UW* in binary mixtures. Since the steel-rich granular gas carries a higher granular energy, it imparts a larger momentum on collisions with the glass-rich cluster. Possibly the collisional pressure within the steel-rich gaseous region plays the role of a dynamic barrier, thereby rendering the gaseous region as a 'soft' porous wall. One end of the compact granular layer is constrained by a hard wall and the other end by a soft porous wall. and therefore the arguments based on elastic theory (Sano 2005) still holds. This soft-wall will eventually be broken due to diffusion and mixing of particles, and hence such partial *UW* cannot continue forever. In experiments, we found that a partial UW forms at one end of the container, dissolves and reborns at the other end.

From Fig. 5.3(a) and Fig. 5.3(b) it is evident that the regimes of all patterns are reproduced, but there is some hysteresis with respect to the regime of undulatory waves coexisting with granular gas. The zoomed view of "Uw+Gas" phase-space is shown Fig. 5.9. It is also noteworthy that for $F > 4.7$ the *UW+Gas* totally gets suppressed during downsweeping (see Fig. 5.9).

Till now the phase-coexisting patterns that show up at moderate shaking intensities Γ have been discussed, but there are some patterns that sustain at strong shakings too. At higher intensities ($\Gamma > 15$, Fig. 5.1) , the system goes through different states with increasing filling depth (F). At $\Gamma = 50$, there is a gaseous state for filling depths of $F \leq 3$ (as shown in Fig. 5.13)

and this gives birth to a mixed state, Fig. 5.14 at $F = 4$, of a granular gas and a cluster on the right and left of the container, respectively. It has been verified that the cluster is in a *granular Leidenfrost state* (Lan & Rosato 1995*b*; Eshuis *et al.* 2005) that corresponds to a density-inverted state wherein a dense cloud of particles is supported by a relatively dilute gaseous region of fast moving particles below it. Therefore, Fig. 5.14 represents a 'partial' LS that coexists with a graular gas. A complete LS spanning the whole length of the container appears for $F > 5.5$, see Fig. 5.15 at $\Gamma = 50.1$, with discernible horizontal segregation of the particles. The PIV anlysis of its hydrodynamic velocity field, Fig. 5.15, indicates correlated motion of the bed suggesting a *liquid-like* state of the granular Leidenfrost state.

If one increases the filling depth to $F = 6.5$ at the same Γ-level convective motion sets up on one side of the container and the other side of the container is in Leidenfrost state (see Fig. 5.16). It is interesting to note that this 'partial' convection, *LS+Con*, has originated from the complete *LS* state that spans over whole container. It has already been discussed that there is significant horizontal segregation in this *LS* state, so the steel-rich region which has higher granular energy transits to convective motion whereas the glass-rich region still remains in the *liquid-like* Leidenfrost state. This type of convective motion which we found in our experiments is "buoyancy-driven" granular convection (Eshuis *et al.* 2007; Hayakawa *et al.* 1995; Ramírez *et al.* 2000) since it originates from a "density inverted" state (*LS*), and hence this is fundamentally different from "base-plate-modulation-driven" (Gallas *et al.* 1992) and "side-wall-friction-driven" (Ehrichs *et al.* 1995) convection that occurs in small aspect ratio boxes at much lower values of Γ.

We also studied the effect of shaking amplitude on these dynamical patterns. For this purpose, the experiments were carried out at higher shaking amplitude $A = 6$ and it has been found that the phase-diagram of patterns (Fig. 5.17) looks similar to that for $A = 3$ as displayed in Fig. 5.1, with two differences: (i) the region of "UW+Gas" extends to larger values of $\Gamma \sim 20$ (compare Fig. 5.17(c) and Fig. 5.9), and (ii) there is a new pattern spikes ($f/4$ or period-4 wave or *subharmonic wave*) for a narrow range of $\Gamma \sim (6, 7)$ in deep beds $F \geq 5$.

The *UW+Gas* has been realized in shallow beds $2.6 \leq F \leq 4.6$ (Fig. 5.17(c)) and has similar structural features as discussed earlier (see left-panel of Fig. 5.18). Nevertheless, we also found that the peaks of the *Undulatory Wave* are higher in case of higher shaking amplitude and this is an expected result since at higher A the bed is driven to a greater height and relaxes to a greater depth (see Fig. 5.18).

Increasing the layer filling depth to $F = 6.6$ at the constant $\Gamma = 8.5$ produces complete *UW* of "mode n=4" as shown in right-panel Fig. 5.18. These *UW* are again confirmed as $f/2$ or period-2 wave similar to their analog shown in Fig. 5.12.

At a filling depth of $F = 6.6$ if one gradually decreases or increases the shaking strength S, the Spikes and Leidenfrost-state coexisting with a granular gas, called *LS+Gas*, respectively, emerge in the system, Fig. 5.19 and Fig. 5.20 This spikes pattern are similar in nature to the one discussed in monodiperse vibrated bed in chapter, i.e., they are subharmonic waves of period four (Fig. 5.19). For upsweeping experiments these spikes are found to be sandwiched between the *BB*-regime and *UW*-regime akin to the spikes found in the monodiperse case (compare Fig. 3.14 and Fig. 5.17(a)). In case of downsweeping experiments these spikes are found to be

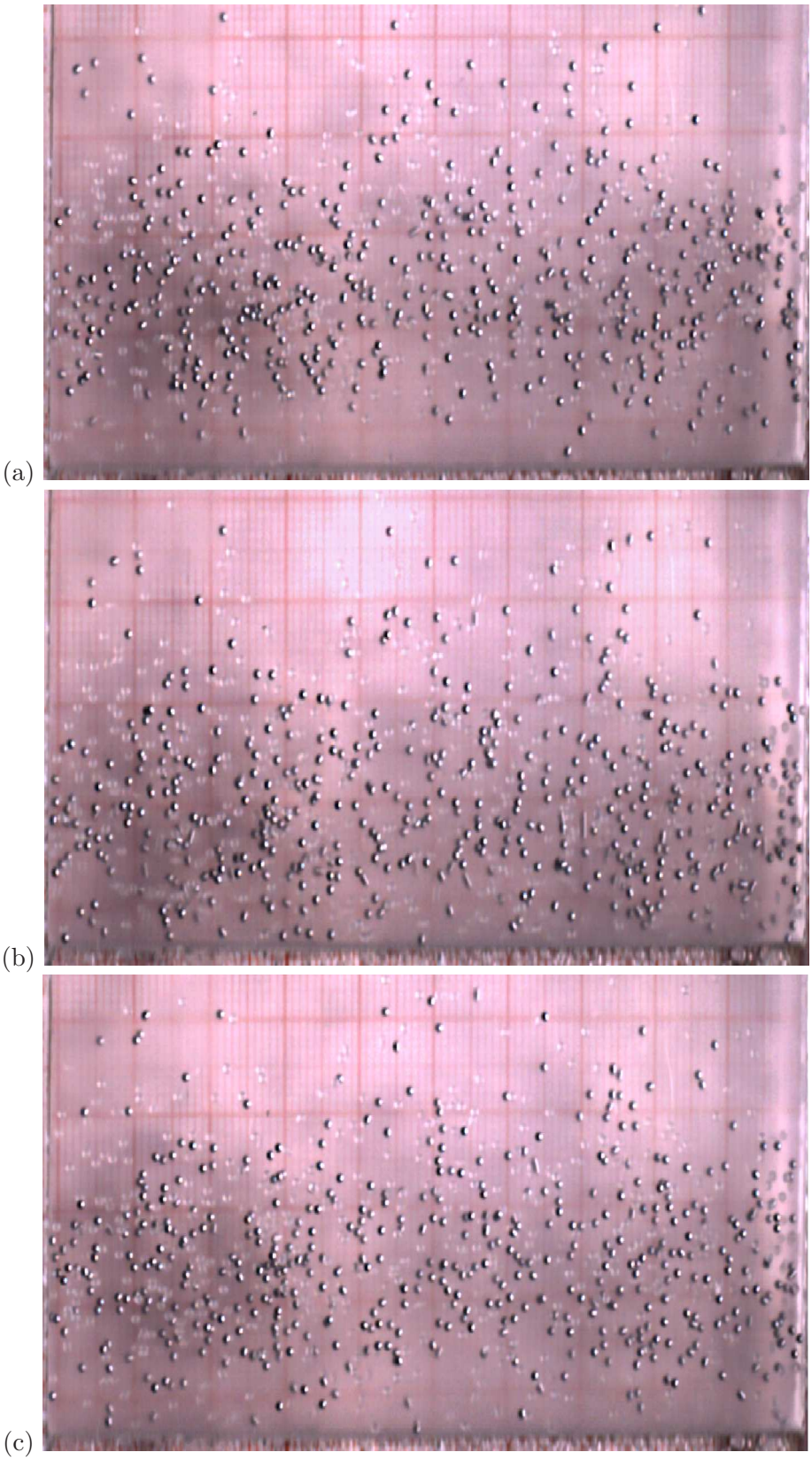

Figure 5.13: **Time sequence snapshots of granular gas: (a)** $t = 0\tau$**, (b)** $t = 0.5\tau$ **and (c)** $t = \tau$**.** Note that the particles are in chaotic motion that is totally uncorrelated and gas covers the whole span of the container. Parameter values are $F_g = F_s = 1$ and $\Gamma = 50$ ($A/d = 3$ and $f = 64.38\ Hz$).

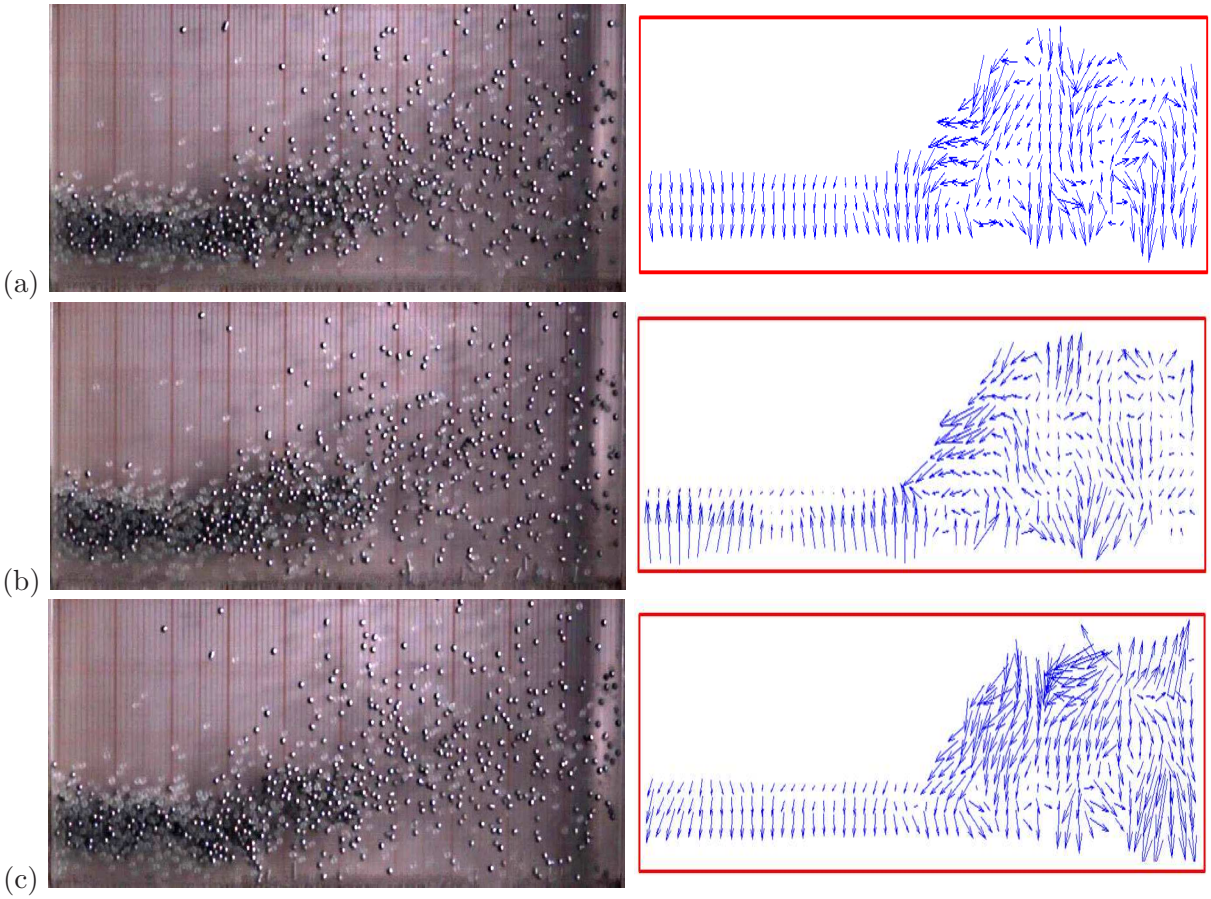

Figure 5.14: **Coexistence of granular Leidenfrost state and a granular gas *LS+Gas*** Left-panel: Time sequence snapshots of *LS+Gas* at (a) $t = 0\tau$, (b) $t = 0.5\tau$ and (c) $t = \tau$. Right-panel: Their corresponding PIV maps. Note that the velocity maps show considerable correlations of hydrodynamic velocity for LS region and uncorrelations for gaseous region. Parameter values are $F_g = F_s = 2$ and $\Gamma = 50.22$ ($A/d = 3$ and $f = 64.5\ Hz$)

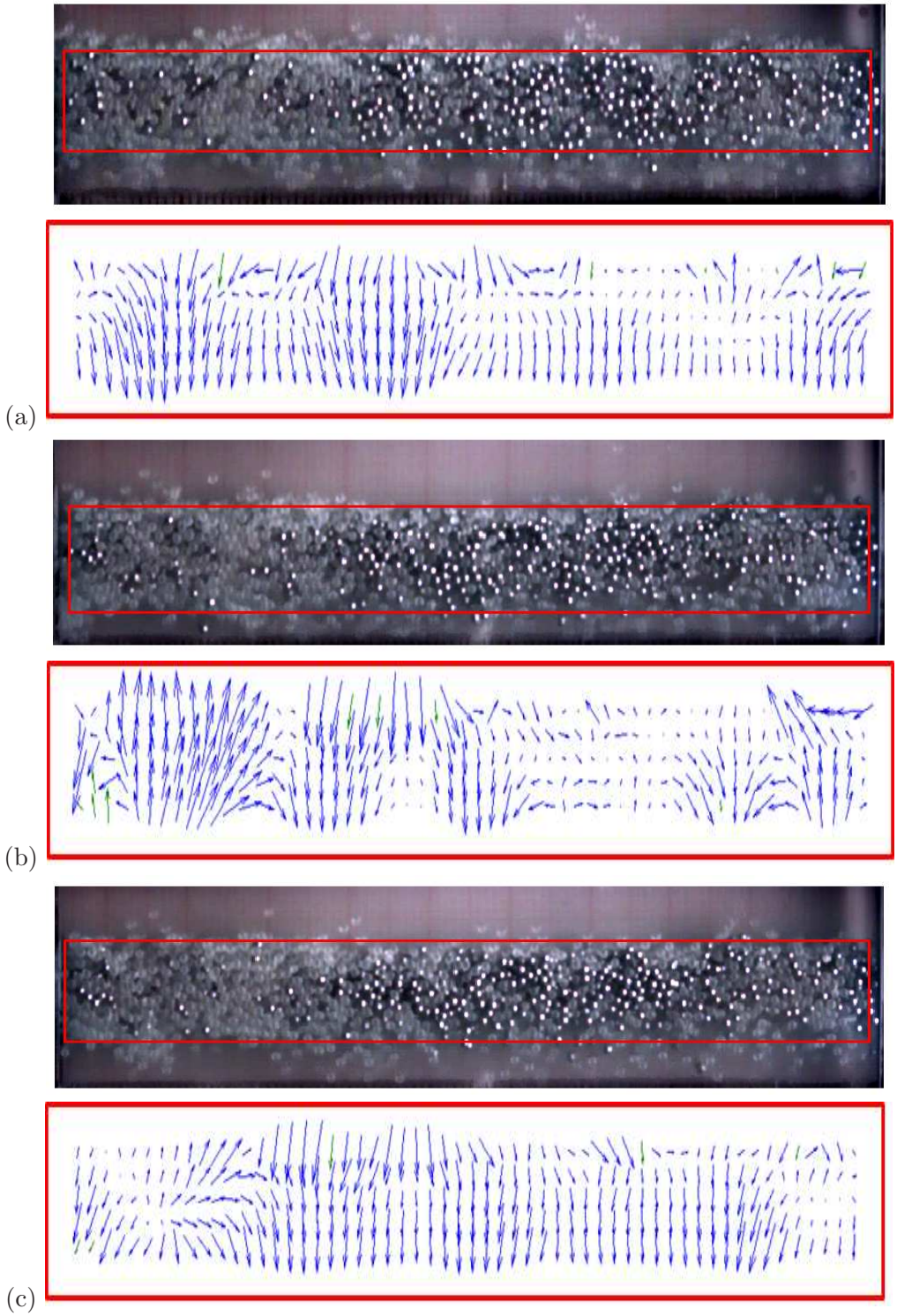

Figure 5.15: **Complete Leidenfrost state *LS*** Time sequence snapshots of LS and their corresponding PIV maps at (a) $t = 0\tau$, (b) $t = 0.5\tau$ and (c) $t = \tau$. Note that the velocity maps show considerable correlations of hydrodynamic velocity and the pattern shows a discernible horizontal segregation. Parameter values are $F_g = F_s = 3$ and $\Gamma = 50.1$ ($A/d = 3$ and $f = 64.4\ Hz$).

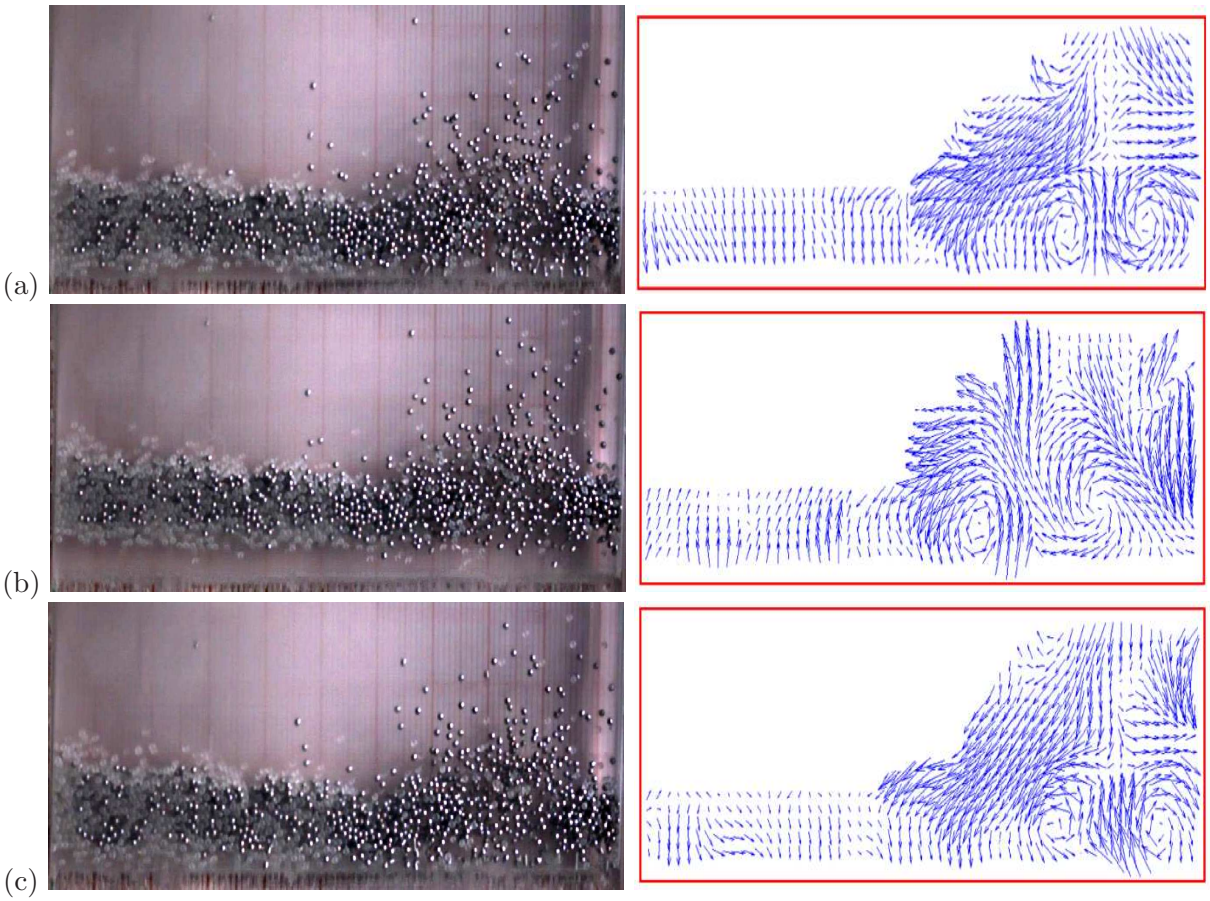

Figure 5.16: **Coexistence of Leidenfrost state and granular convection *LS+Con***. Left-panel: Time sequence snapshots of *LS+Con* at (a) $t = 0\tau$, (b) $t = 0.5\tau$ and (c) $t = \tau$. Right-panel: Their corresponding PIV maps showing two counter rotating rolls on the right of the container. Parameter values are $F_g = F_s = 3.25$ and $\Gamma = 50$ ($A/d = 3$ and $f = 64.38\ Hz$)

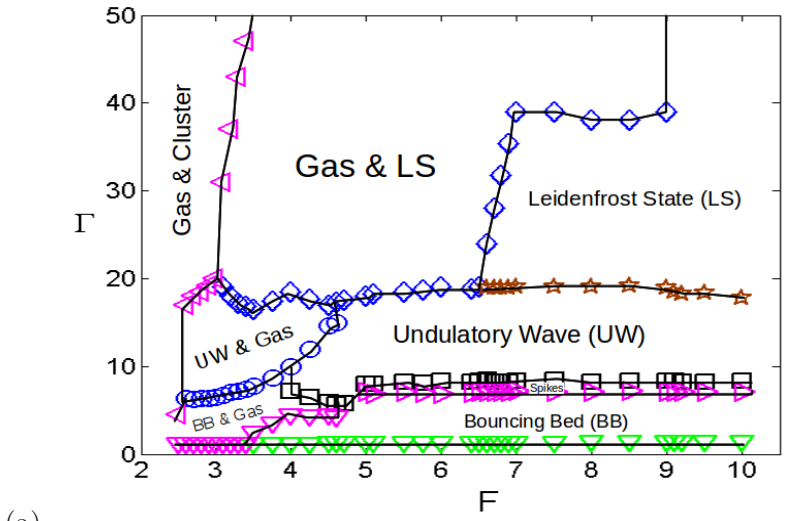

(a)

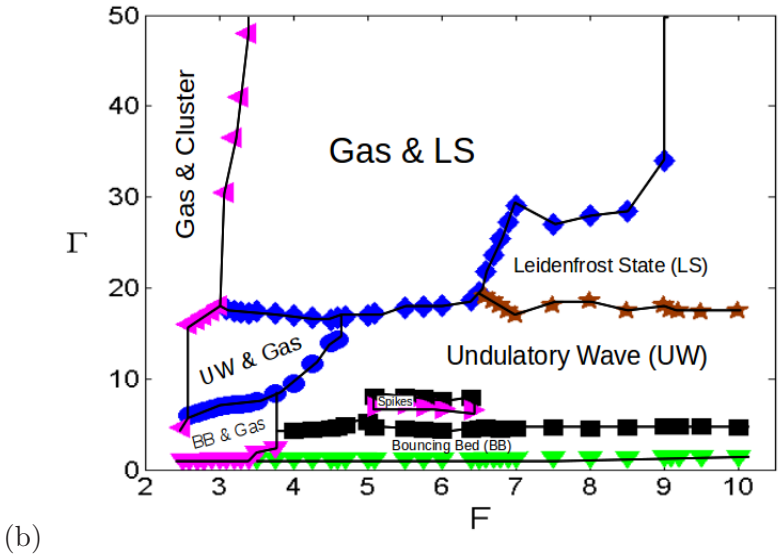

(b)

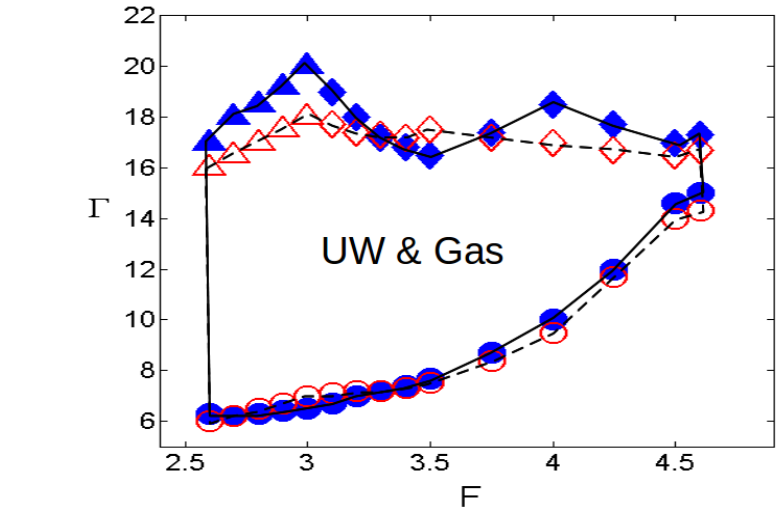

(c)

Figure 5.17: **Phase diagram of dynamical patterns in (Γ, F)-plane during (a) up-sweeping experiments, (b) downsweeeping experiments and (c) the zoomed view of *UW+Gas* regime in the phase diagram.** The *SB* (solid bed) regime lies below the *BB* (bouncing bed) and *BB+Gas* regime (denoted by down triangles at $\Gamma \sim 1$). Parameter values are $A/d = 6$, $F_g = F_s$ and *ramping rate* $= 0.01\ Hz/sec$.

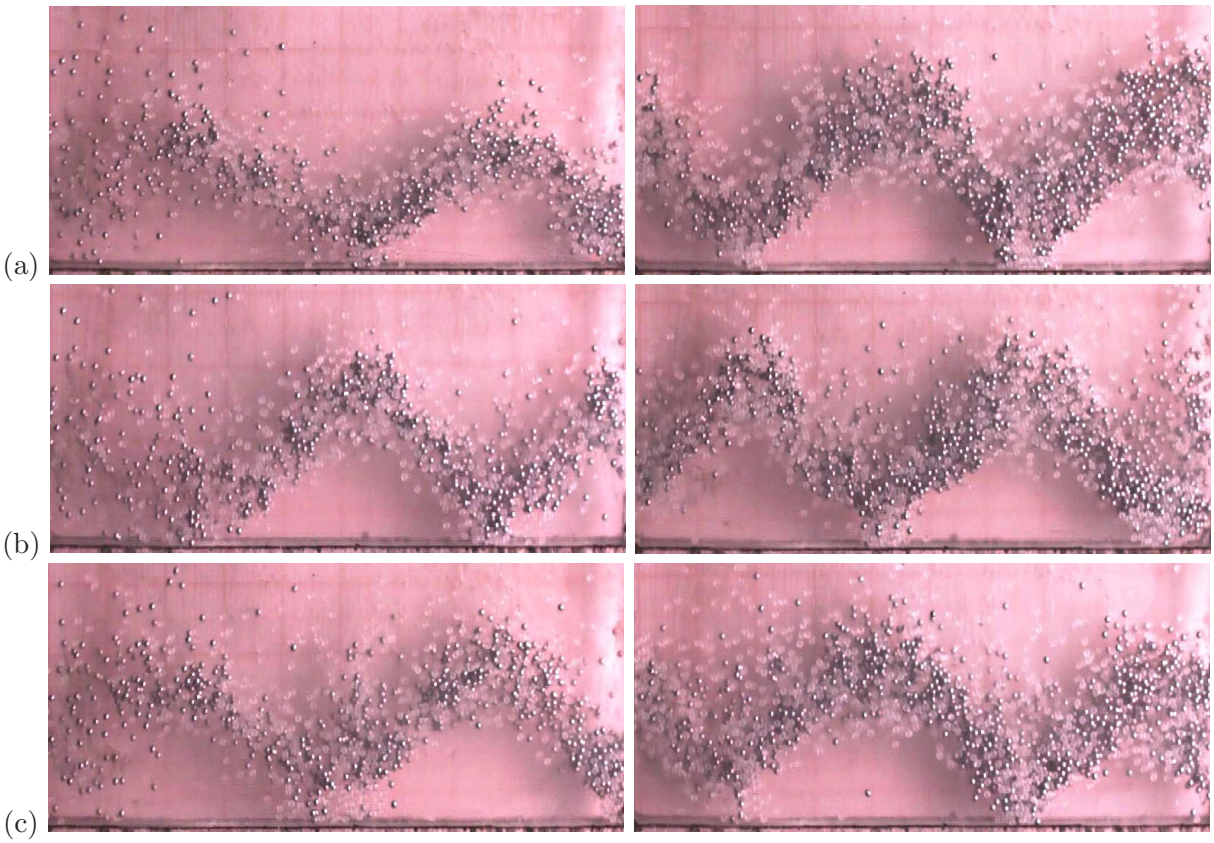

Figure 5.18: **Left-panel: Time sequence snapshots of undulatory wave coexisting with a granular gas *UW+Gas* with $F = F_g + F_s = 3.75$. Right-panel: Time sequence snapshots for complete undulatory wave *UW* with $F = F_g + F_s = 6.6$.** (a) $t = 0\tau$, (b) $t = \tau$ and (c) $t = 2\tau$. Note that peak and valleys of undulatory wave exchange their positions exactly over one shaking period (τ), and the complete pattern repeats itself over 2τ; hence this is a "period-2" wave. Other parameter values are $\Gamma = 8.5$ ($A/d = 6$, $f = 18.77\ Hz$) for both panels.

sandwiched between two *UW* regimes, i.e., *UW* relaxes to spikes pattern at a certain Γ_{onset}, which eventually transits to *UW* again and finally these *UW* relaxes to *BB* (see Fig. 5.17(b)). Such type of transition indicates that during downsweeping experiments the *Spikes* pattern is unstable and this can be a probable reason why they did not appear in the experiments at low $A/d = 3$ (Fig. 5.1) because this pattern is not much stable in binary granular mixtures in comparison to its monodisperse analog. The pattern in Fig. 5.19 is in a horizontally segregated state with most of the steel particles on the right and the glass particles on the left of the container. However, the heights and depths of both the glass-rich and steel-rich peaks and valleys are almost the same.

The *LS+Gas* pattern in Fig. 5.20 is similar to its analog for $A/d = 3$ (Fig. 5.14), wherein the steel-rich region in gaseous state whereas the glass-rich region in *liquid-like* Leidenfrost state. At the same shaking strength if the filling depth is decreased to $F = 3.1$ the same Leidenfrost cluster which was compact takes form of a loose aggregate of glass-rich particles, see Fig. 5.21

5.2.2 Effect of Container Length on Phase Coexisting Patterns

To study the effect of the length of the container on these patterned states, additional experiments have been performed in smaller length containers. Two containers of length $L = 50$ and 20 mm have been chosen and the layer filling depths are $F = 3$ and 6. We found that the vibration induced segregation in the horizontal direction is suppressed in $L/d = 20$ container. This is because although the vertical vibration tries to demix the species in horizontal direction, the length constraint of the container forces the species to mix again. Therefore, in smaller container of length 20 mm, none of the phase coexisting patterns are found, and the binary mixture shows the same basic patterns of the equivalent monodisperse system. Fig. 5.22 shows the complete undulatory wave *UW* in the container of length 50 and 20 mm having a filling depth of $F = F_g + F_s = 6$ at $\Gamma = 7.8$. It should be noted that the larger container is able to accommodate higher mode number $n = 2$ but the smaller one at the same shaking intensity shows up $n = 1$ mode. This depicts the dependence of the mode number of the *UW* on the length of the container.

Further increasing the shaking intensity gradually to $\Gamma = 20$, the granular bed confined in $L = 50$ mm container exhibits a complete Leidenfrost state *LS* (see Fig. 5.23). If Γ is still increased to 30 then due to horizontal segregation of particles there is a coexistence of Leidenfrost state with a granular gas *LS+Gas* as shown in the left panel of Fig. 5.24. This must be contrasted with the right panel of Fig. 5.24, wherein the granular bed held in $L = 20$ mm container shows a complete Leidenfrost state due to the suppression of horizontal segregation. This comparison indicates that there is a competition between mixing and demixing of the particles subjected to vertical vibration, and when the length of the container decreases below a minimum value, the segregation in horizontal direction disappears. At a lower filling depth of $F = 3$ in $L = 50$ mm container, there is a coexistence of stationary cluster with a granular gas at a shaking intensity $\Gamma = 20$ which eventually melts into complete granular gas at higher shaking strength $\Gamma = 30$ as depicted in Fig. 5.25.

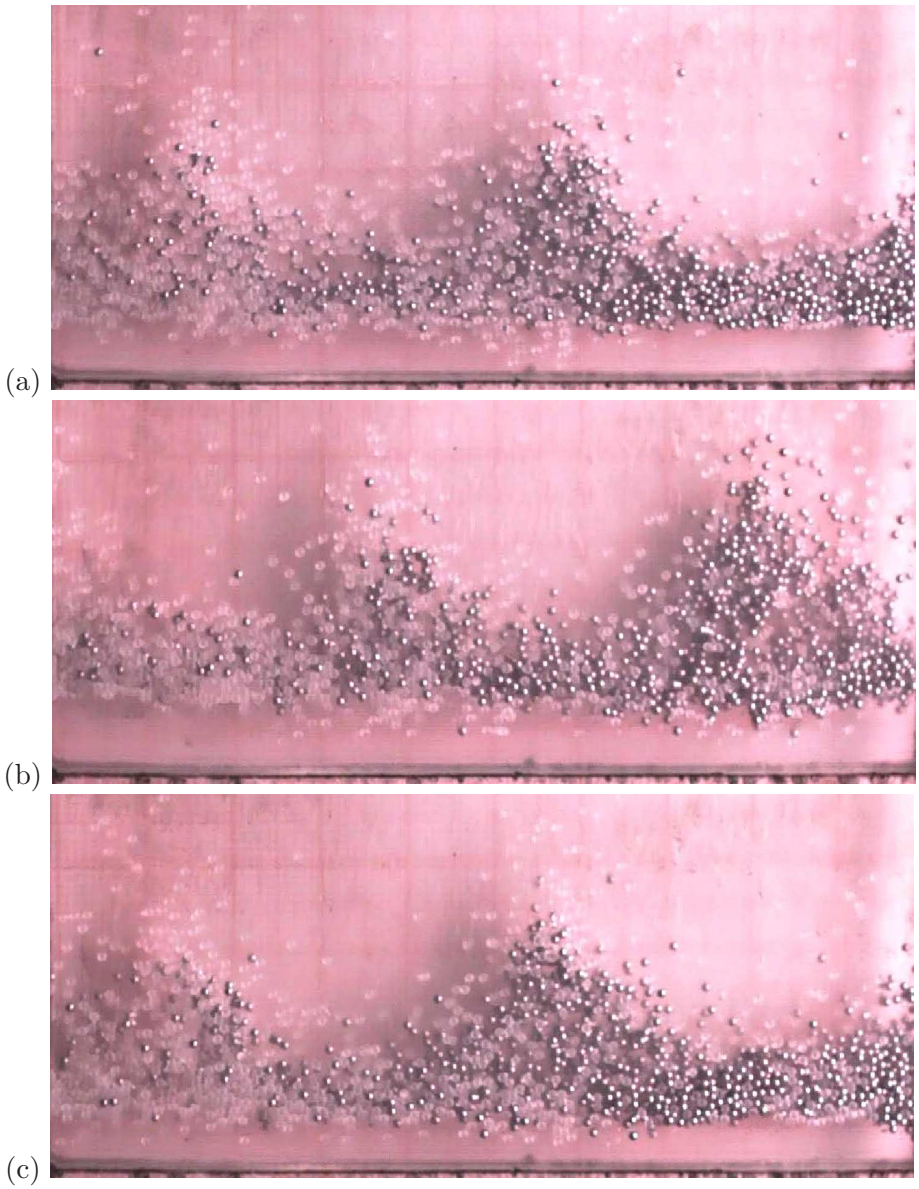

Figure 5.19: **Time sequence snapshots of spikes pattern at (a)** $t = 0\tau$**; (b)** $t = 2\tau$**; (c)** $t = 4\tau$. Parameter values are $F = F_g + F_s = 6.6$, $\Gamma = 7.55$ ($A/d = 6$, $f = 17.7\ Hz$). Note that the peaks (maxima) is getting exchanged by valleys (minima) over two shaking time-periods (τ) and this spikes pattern repeats itself over four shaking time-periods and hence they are called '$f/4$' wave or period-4 wave.

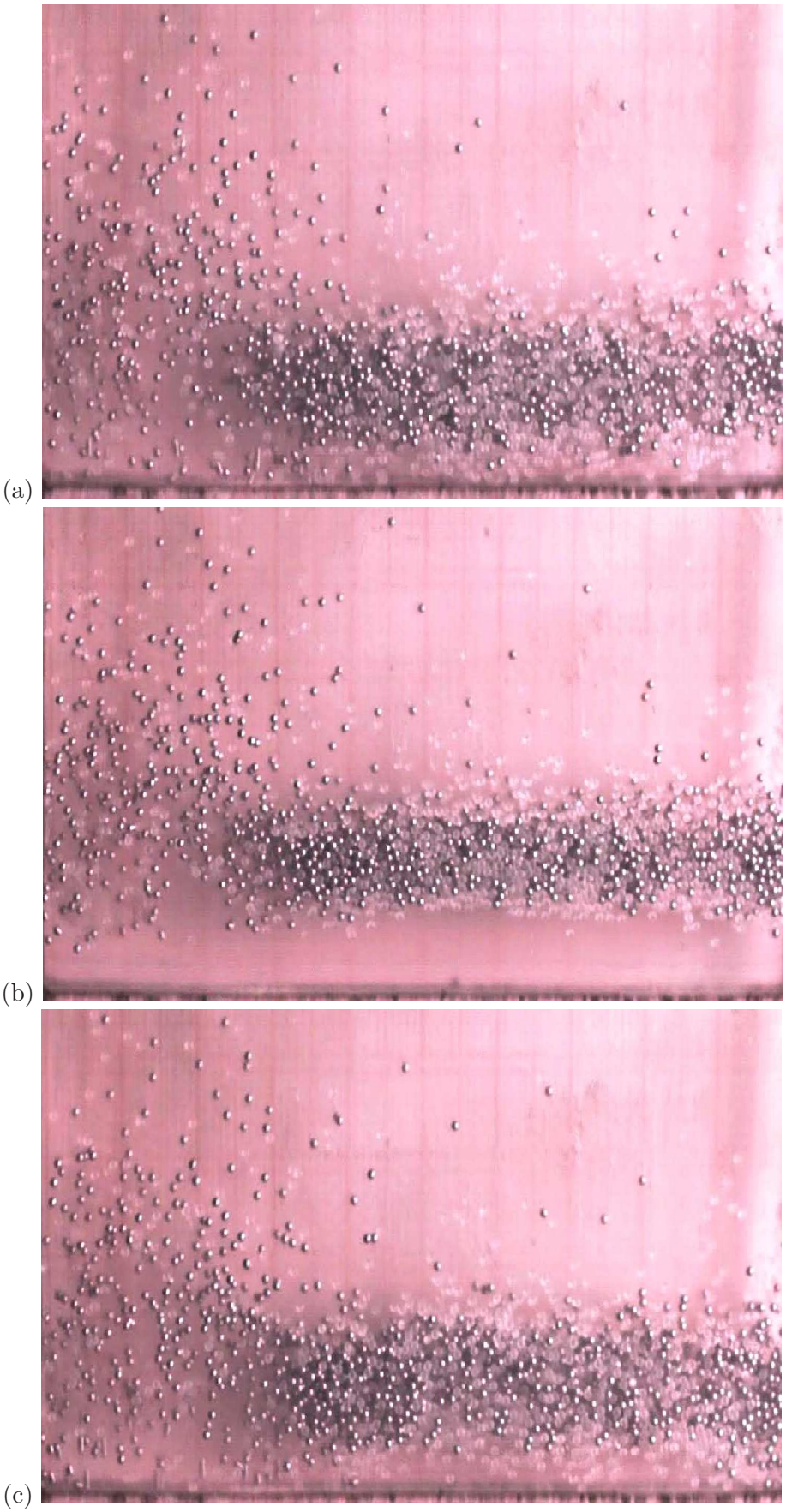

Figure 5.20: **Time sequence snapshots of Leidenfrost state coexisting with a granular gas at (a)** $t = 0\tau$**; (b)** $t = 0.5\tau$**; (c)** $t = \tau$. Parameter values are $F = F_g + F_s = 6.6$, $\Gamma = 50$ $(A/d = 6,\ f = 45.5\ Hz)$.

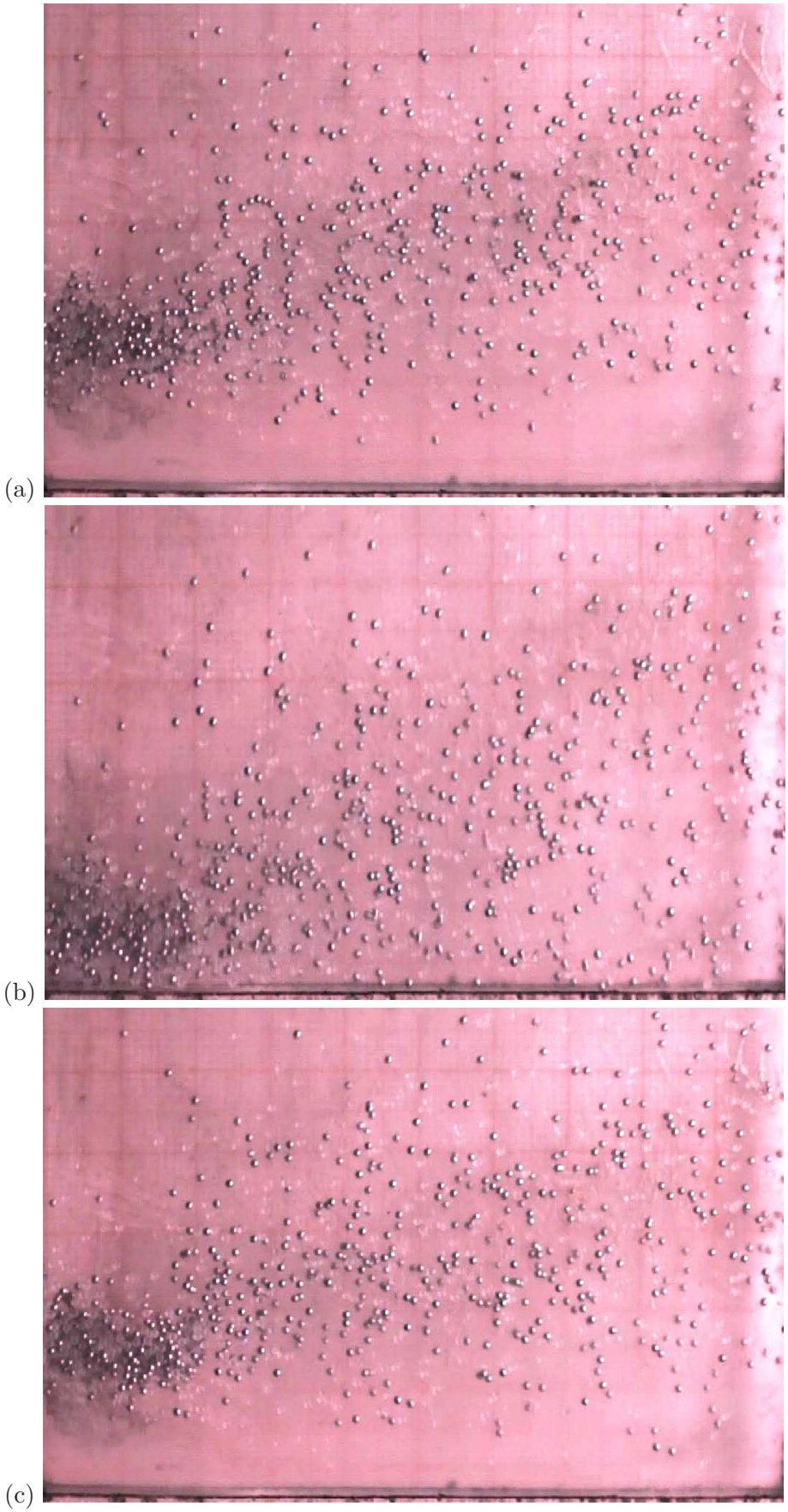

Figure 5.21: **Time sequence snapshots of cluster (stationary) coexisting with a granular gas at (a)** $t = 0\tau$**; (b)** $t = 0.5\tau$**; (c)** $t = \tau$. Parameter values are $F = F_g + F_s = 3.1$, $\Gamma = 50$ ($A/d = 6$, $f = 45.5\ Hz$).

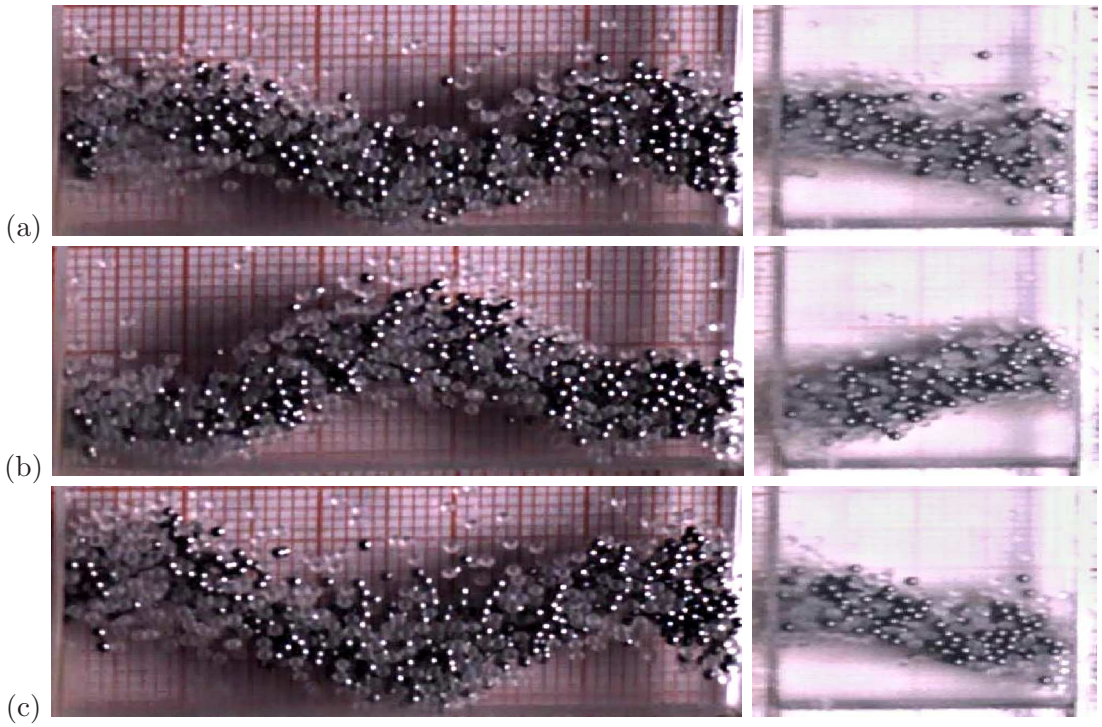

Figure 5.22: **Time sequence snapshots of complete undulatory wave UW**: (a) $t = 0\tau$, (b) $t = \tau$ and (c) $t = 2\tau$. Note that peak and valleys of undulatory wave exchange their positions exactly over one shaking period (τ), and the complete pattern repeats itself over 2τ; hence this is a "period-2" undulatory wave. Left-panel: "mode-2" wave in $L/d = 50$ box; Right-panel: "mode-1" wave in $L/d = 20$ box. Parameter values are $F_g = F_s = 3$ and $\Gamma = 7.8$ ($A/d = 3$ and $f = 25.4\ Hz$). At the same shaking intensity smaller box is not able to accommodate mode-2 wave and this shows that mode number depends on the length of the box.

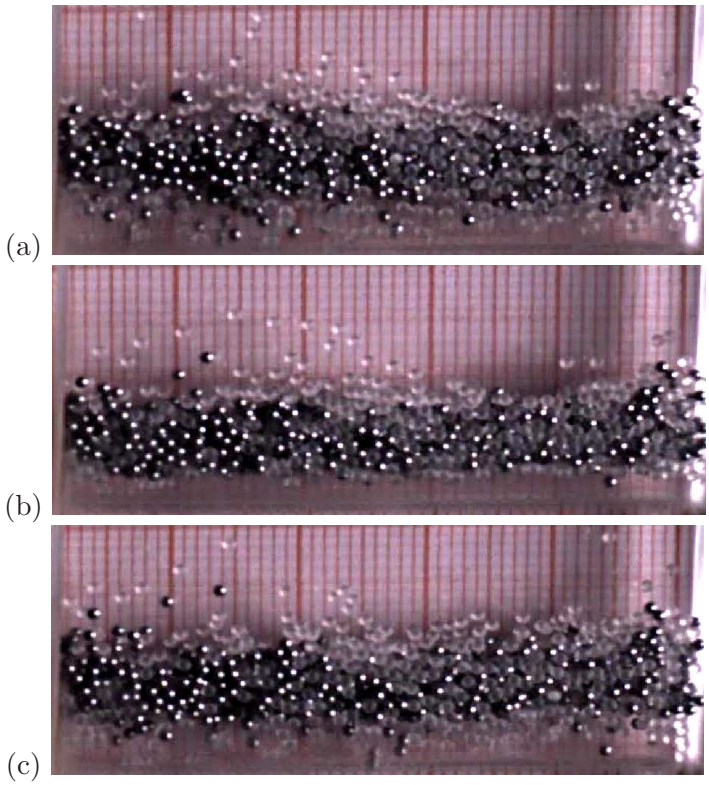

Figure 5.23: **Time sequence snapshots of complete Leidenfrost state in $L/d = 50$ box at $\Gamma = 20$:** (a) $t = 0\tau$, (b) $t = 0.5\tau$ and (c) $t = \tau$. Parameter values are $F_g = F_s = 3$, $\Gamma = 20$ ($A/d = 3$ and $f = 40.7\ Hz$).

5.2.3 Oscillating/Ratcheting Cluster

It has been discussed that the stationary cluster of glass-rich particles can coexist with a steel-rich granular gas for $1 \leq F \leq 3$ at lower shakings $5 < \Gamma < 28$ (see Fig. 5.7(a)). This cluster can born on either side of the container but once formed it retains its position over tens of thousands of shaking cycles. In contrast, at higher shaking intensities $28 < \Gamma < 46$ and for filling depths $2 \leq F \leq 3$ this cluster is found to drift from one side of the container to the other side as shown in Fig. 5.26. A detailed analysis (via Movie) reveals a more complicated, *stick-slip-type* oscillatory motion: a cluster of glass-rich particles forms at one end of the container, grows over a period of time till it achieves a critical size, then starts moving to the other end, the size of the cluster decreases upon collision with the end-wall but it regrows again to its original size by accumulating particles, and finally starts moving backward to its original end.

The following notations are used to study the oscillatory motion of this cluster:

t_f=time taken by the cluster to drift from one end to the other,

t_{wait}= wait time of the cluster at either end,

τ_{clus}=time-period of the cluster drift=$2t_f$,

V_{clus}=Characteristic velocity of the cluster=L/t_f,

where L is the length of the container.

This oscillatory motion continues for a long time as confirmed in Fig. 5.27, which shows the variation of the normalized velocity of this cluster with the number of overturns it makes from one end to the other end of the container. These experiments were run for thousands of shaking cycles

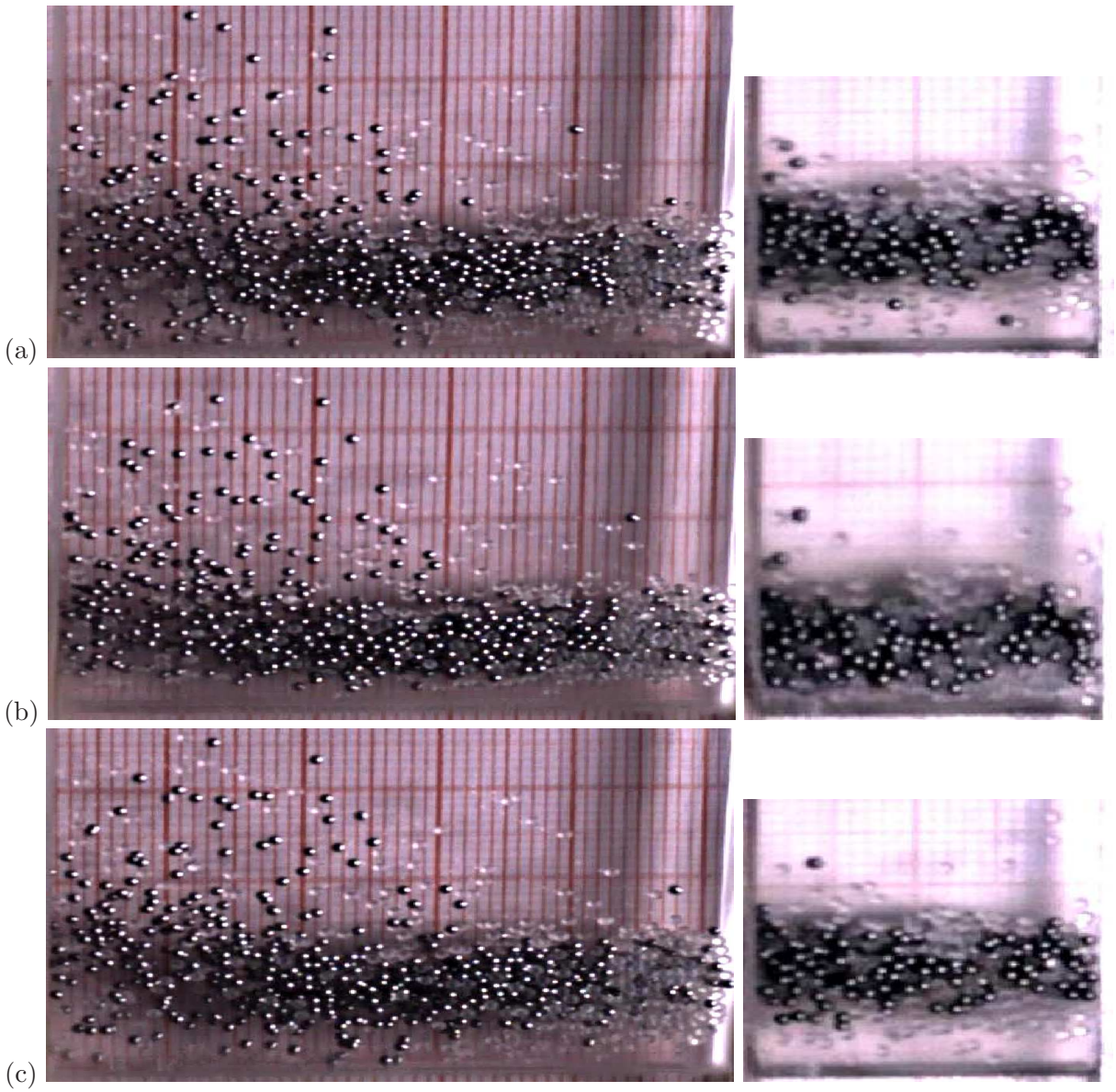

Figure 5.24: **Left panel: Time sequence snapshots of partial Leidensfrost state coexisting with a granular gas in $L/d = 50$ box. Right-panel: Time sequence snapshots of Leidenfrost state spanning whole $L/d = 20$ box.** (a) $t = 0\tau$, (b) $t = 0.5\tau$ and (c) $t = \tau$. Parameter values are $F_g = F_s = 3$ and $\Gamma = 30$ ($A/d = 3$ and $f = 49.84\ Hz$). At the same shaking intensity larger box enforces horizontal segregation of the species displaying *LS+Gas* while in smaller box particles can not segregate and hence complete *LS* shows up.

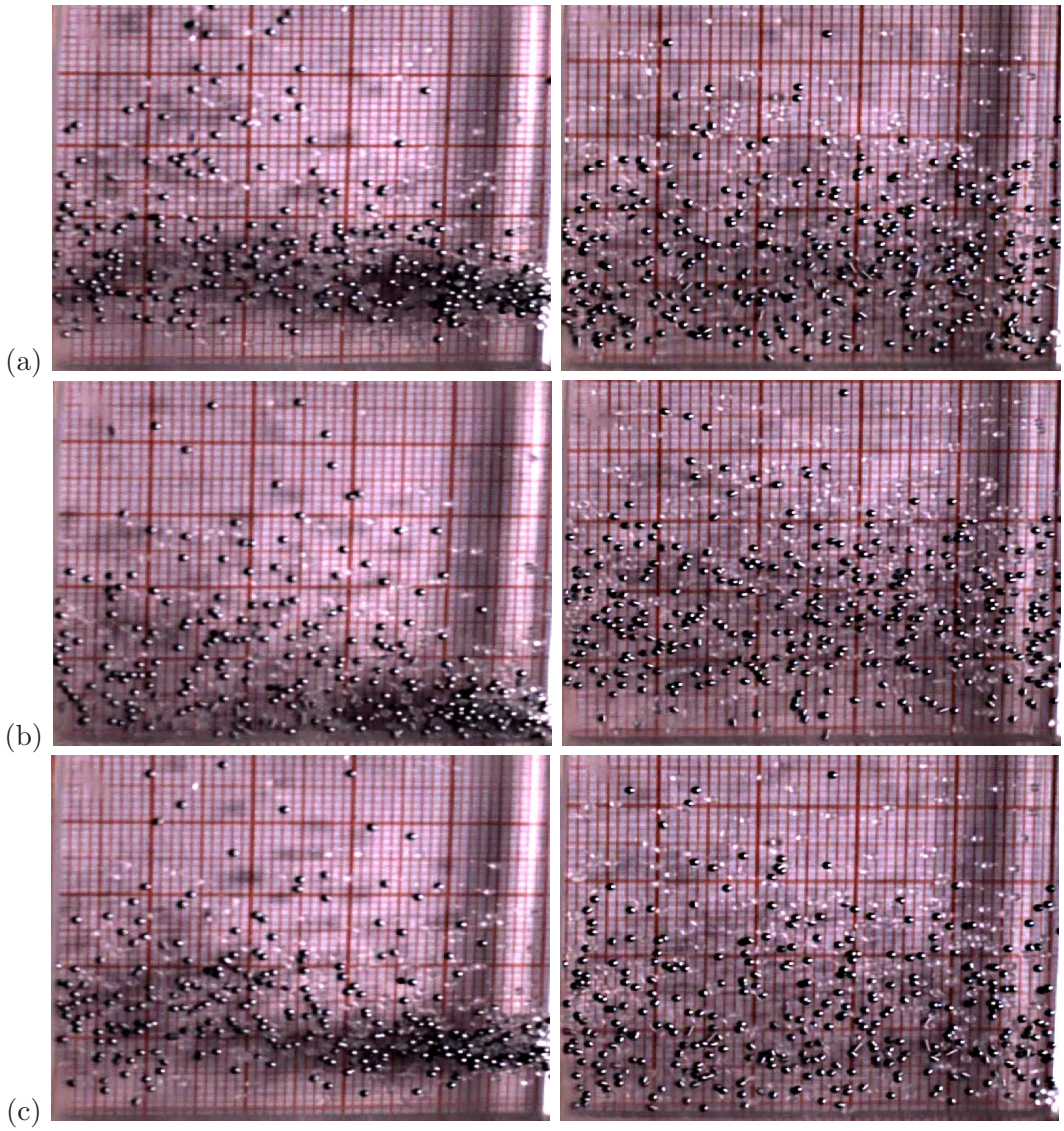

Figure 5.25: **Left panel: Time sequence snapshots of cluster coexisting with a granular gas at $\Gamma = 20$ ($A/d = 3$ and $f = 40.7\ Hz$). Right-panel: Time sequence snapshots of granular gas spanning whole length of the box at $\Gamma = 30$ ($A/d = 3$ and $f = 49.84\ Hz$).** (a) $t = 0\tau$, (b) $t = 0.5\tau$ and (c) $t = \tau$. Parameter values are $F_g = F_s = 1.5$ and $L/d = 50$. Note that as one increases the Γ-level *Gas+Cluster* melts into complete *Gas*.

at fixed values of Γ to ascertain the life-time of oscillating cluster. The characteristic velocity of this cluster is about 1% of the maximum plate velocity (see right inset of Fig. 5.27(a)), with a time-period of $\tau_{clus} \sim O(10^3\tau)$. It should also be noted that the waiting time of the cluster at either end, t_{wait}, is significant (see left inset of Fig. 5.27(a)) and comparable to τ_{clus}. The characteristic velocity of the cluster keeps on fluctuating about a mean value of 0.01 and this tendency does not subsides even after a large number of overturns, implying that the cluster oscillation is sporadic and spontaneous. Furthermore, it is evident that the characteristic parameters involved in the dynamics of this oscillating cluster do not depend on the shaking intensity Γ, provided that shaking amplitude A/d is held constant.

Fig. 5.26 shows the snapshots of the drifting cluster while upsweeping experiments and the plots shown in Fig. 5.27 have been prepared for the experiments carried out at constant shaking strength $S = 78, 84$ and 90 at $A/d = 3$. For experiments at a higher shaking strengths $S = 160$ ($A/d = 4$), the plots for normalized time-period, velocity and waiting time with respect to number of overtruns N_T are shown in Fig. 5.28. Comparing Fig. 5.27 and Fig. 5.28, one can infer that the time-period of the oscillating cluster is almost independent of the shaking strength; in both cases $\tau_{clus} \sim O(10^3\tau)$, though the normalized waiting time in case of larger S is comparatively higher. However, the normalized velocity in lower shaking strength experiments shows more fluctuations and have a smaller magnitude.

The same characteristic features of the oscillating cluster has been obtained for equimolar mixture of brass and glass particles (both having diameter 1.0 mm) at $S = 160$ ($A/d = 4$) as shown in Fig. 5.29. In these experiments, the waiting time of the cluster t_{wait} is found to be significantly small (almost zero), i.e., the cluster drifts from one end to the other end of the container and without any delay drifts back to its original position. The time-period found is again in accord with that of equimolar steel-glass mixture, i.e., it is about $10^3\tau$. Moreover, the range of velocity fluctuations also seems to be almost similar to that of steel-glass mixture at the same shaking strength S. This implies that the cluster dynamics of brass-glass and steel-glass mixtures at the same S is almost similar, and this is an expected result since the density ratio of these mixtures are not very different ($\rho_s/\rho_g \approx 3.06$ and $\rho_b/\rho_g \approx 3.46$). Focussing on the plot of cluster position vs time for brass-glass mixture, it is evident that the cluster on touching one end of the container immediately reverses its motion without any delay, i.e., $t_{wait} \approx 0$.

Similar ratchet type collective motion of particles has been found in a vertically vibrated setup with a 'saw-tooth' bottom plate (Farkas *et al.* 1999) as well as in 'compartmentalized' granular gas (Meer *et al.* 2004) which are in stark contrast to our finding of spontaneous ratcheting motion in an unpartitioned box with an unbiased flat bottom plate. The normal restitution coefficient (and hence inelastic disspation) seems to be a key player for the onset of cluster and its mobility. This ratcheting cluster eventually melts with further increasing Γ to give birth to a complete gaseous state.

What drives the ratchet-type oscillating cluster?

Conjecture: "Competition between differential dissipation rate ($e_n^s \neq e_n^g$, e_n^s and e_n^g are the normal restitution coefficient of steel and glass particles, respectively) and shaking intensity Γ".

The following three arguments have been proposed regarding the driving mechanism of this

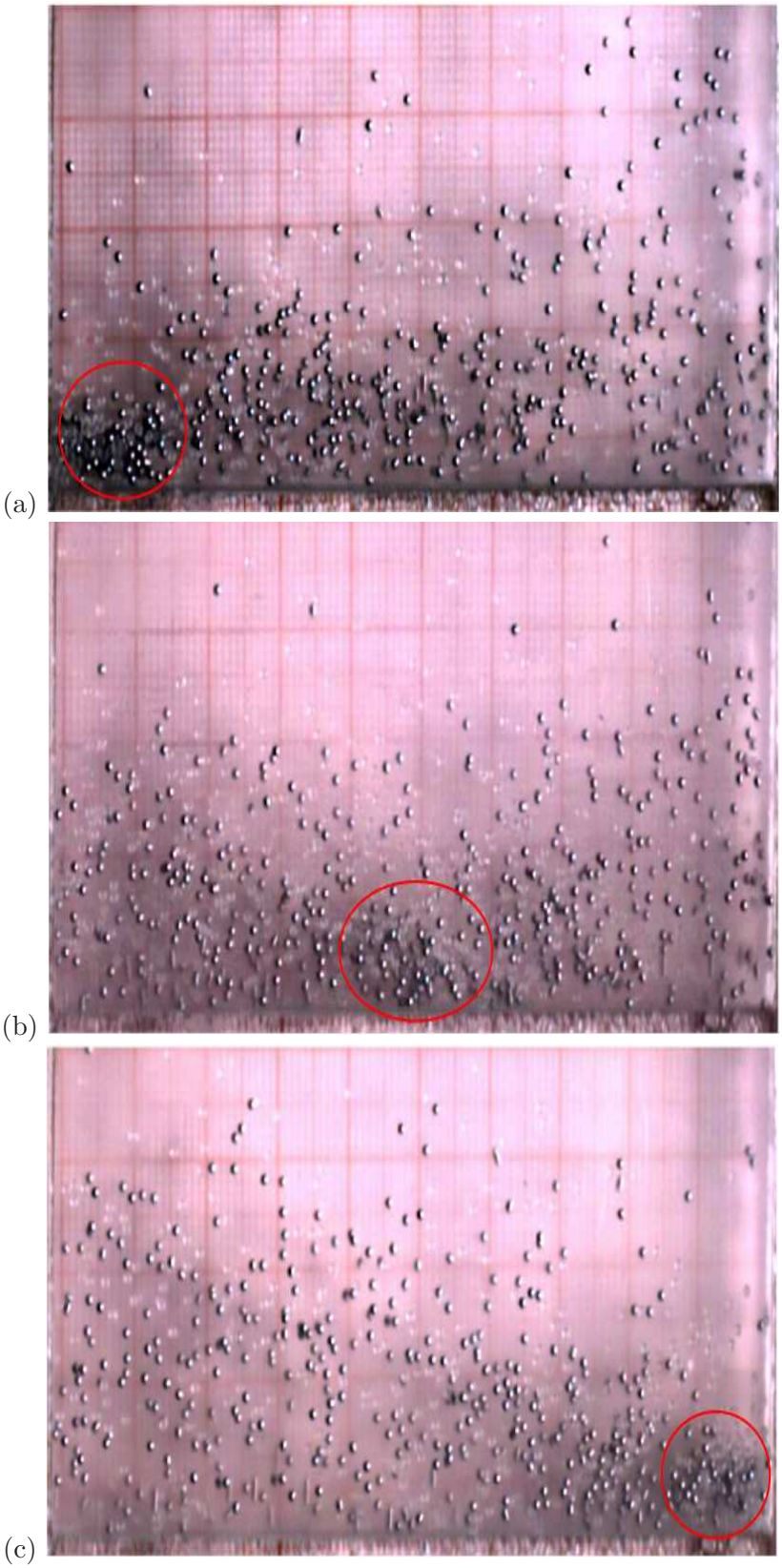

Figure 5.26: **Drift of the oscillating/ratcheting gas-cluster in equimolar mixture of steel-glass particles of** 1.0 mm **diameter from (a) the left of the container to (b) the middle and subsequently to (c) the right of the container during upsweeping experiments at a ramping rate of** 0.01 Hz/sec**.** Parameter values are $F_g = F_s = 1$ and $A/d = 3$, with (a) $\Gamma = 30.78$ ($f = 50.5\ Hz$), (b) $\Gamma = 30.9$ ($f = 50.6\ Hz$) and (c) $\Gamma = 31.09$ ($f = 50.75\ Hz$). These experiments were also repeated at fixed values of Γ for tens of thousands of shaking cycles, confirming the ratchet-type oscillation of the cluster, with its speed being 1% of the maximum base plate velocity, with a time period of about $10^3\tau$ (see Fig. 5.27).

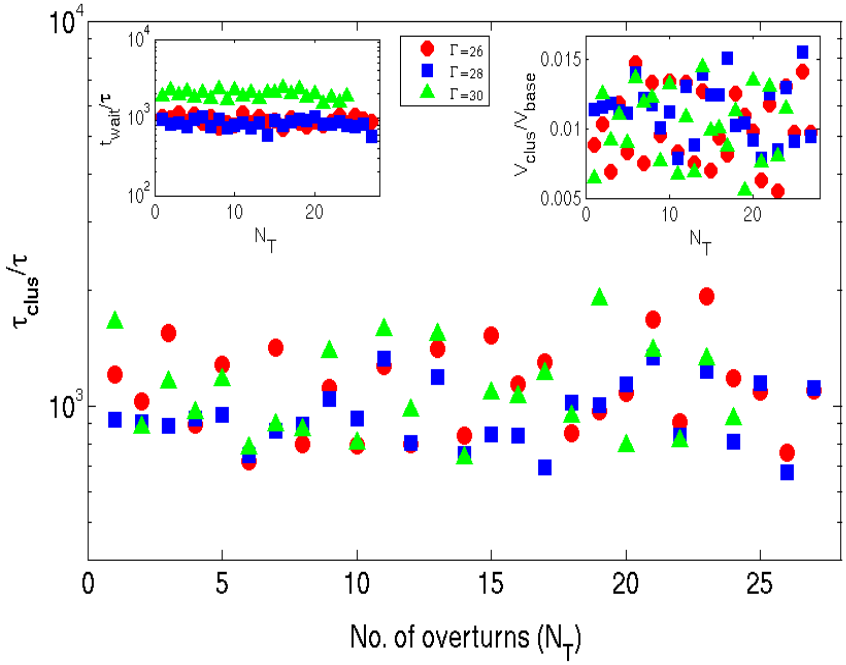

(a)

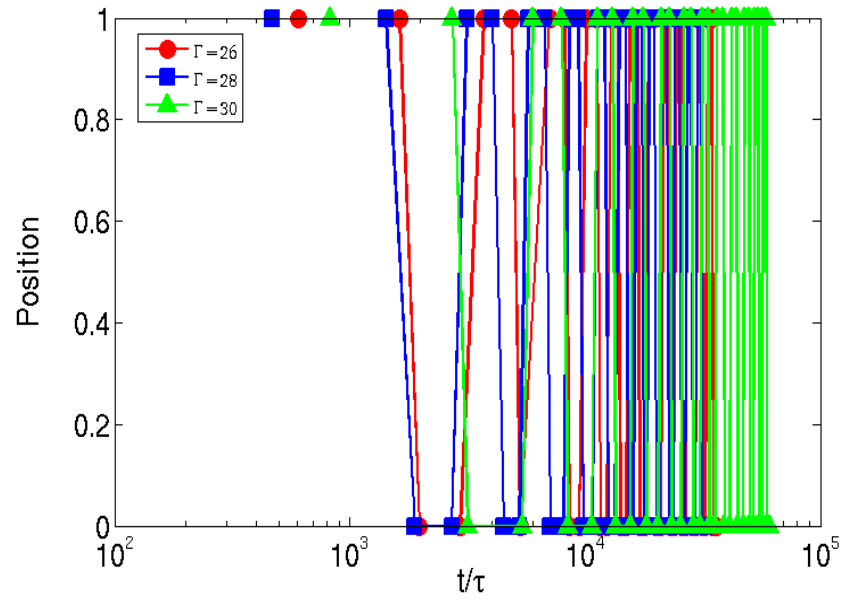

(b)

Figure 5.27: **Top: Time-period of oscillating/ratcheting cluster (main panel), its velocity (right inset) and waiting time (left inset). Bottom: Temporal evolution of the left and right position of the cluster.** Characteristic oscillation time period is about $10^3\tau$, where τ is the shaking period. Here $V_{base} = 2\pi Af$ is the maximum speed of the base plate. Parameter values are same as in Fig. 5.26 with $\Gamma = 26, 28$ and 30.

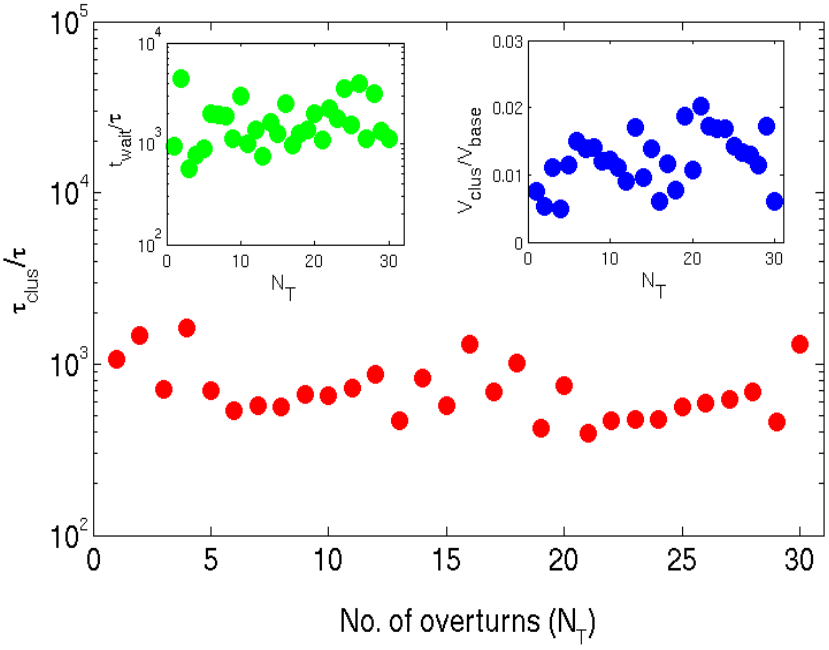

Figure 5.28: **Time-period of oscillating/ratcheting cluster (main panel), its velocity (right inset) and waiting time (left inset) for equimolar mixture of steel-glass particles of** 1.0 *mm* **diameter.** Characteristic oscillation time period is about $10^3\tau$, where τ is the shaking period. Here $V_{base} = 2\pi Af$ is the maximum speed of the base plate. Parameter values are $F = F_g + F_s = 3$, $F_g = F_s$, $\Gamma = 40$ ($A/d = 4, f = 49.84\ Hz$).

ratcheting/oscillating cluster:

- Argument-1 (Effect of dissipation): The experiments suggest that the horizontal segregation of two species is a prequisite for any phase-coxisting pattern. Experiments with monodisperse systems (equal size particles of same material) do not show horizontal non-uniformity in the present setup. Simulations by Nicolas Rivas *et al.* (Private Communication 2013) confirm that different density particles with same restitution coefficient (i.e $e_n^s = e_n^g$) do not show horizontal segregation. Therefore, the differential dissipation rate (due to $e_n^s \neq e_n^g$) may drive horizontal segregation-this is presumably due to different levels of fluidizations of two species (here, the x-component temperature of two species must be different, i.e., $T_x^{steel} \neq T_x^{glass}$).

- Argument-2 (Effect of F and Γ): Beyond the regime of solid bed $\Gamma > 1$, if the filling depth is small ($F \sim 1$),there is no cluster - only a gaseous state can exist. If F is too large, a cluster spans the full length of the container (which also depends on Γ). Therefore, along with differential dissipation, a competition between shaking intensity (Γ) and fill-level (F) would decide the formation of 'Cluster+Gas' regime. The larger the fill-level, the higher the Γ-level for the onset of *Gas+Custer* state- this is confirmed in phase-diagram (Fig. 5.1) since the boundary between *Gas* and *Gas+Cluster* regimes is inclined forward.

- Argument-3 (Competition between dissipation and shaking intensity): Assume that we are in the *Gas+Cluster* regime [i.e. a finite differential dissipation ($e_n^s \neq e_n^g$) is assumed as expected for glass and steel particles, i.e. we have a cluster of finite size, lesser that

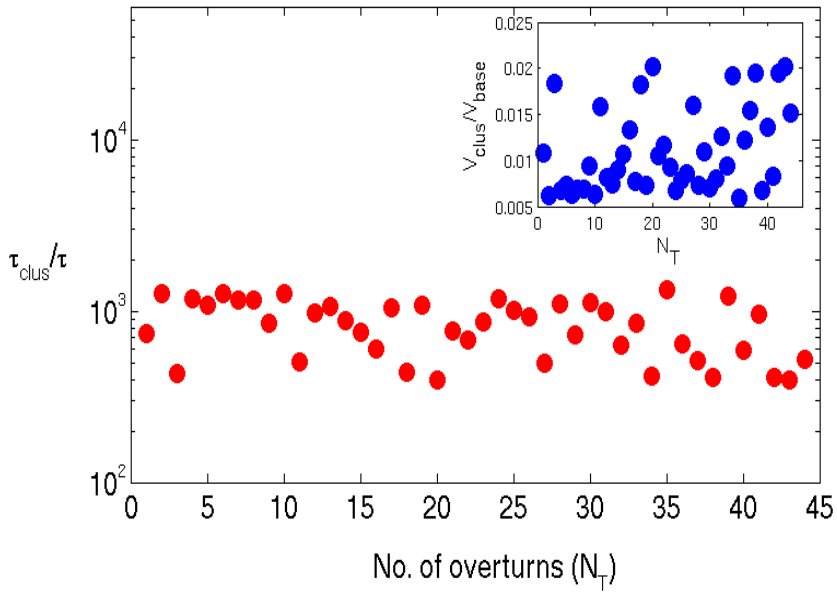

(a)

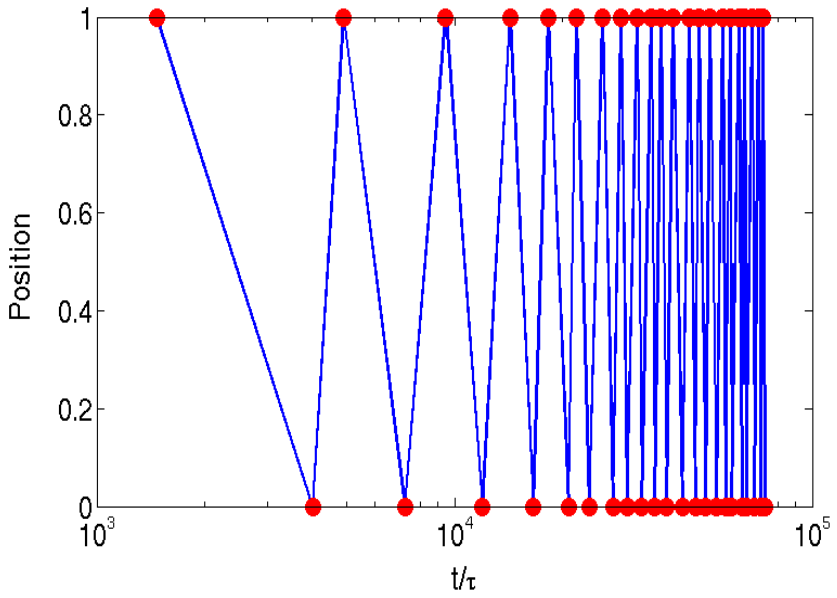

(b)

Figure 5.29: **Top: Time-period of oscillating/ratcheting cluster (main panel), its velocity (inset) for equimolar mixture of brass-glass particles of** 1.0 mm **diameter. Bottom: Temporal evolution of the left and right position of the cluster.** Characteristic oscillation time period is about $10^3\tau$, where τ is the shaking period. Here $V_{base} = 2\pi Af$ is the maximum speed of the base plate. Parameter values are $F = F_b + F_g = 3$, $F_b = F_g$, $\Gamma = 40$ $(A/d = 4, f = 49.84\ Hz)$.

L] at some fixed value of F. Increasing Γ will eventually melt the cluster, leading to the Gas-regime, see (Fig. 5.1).

At any value of Γ, the cluster is of finite size, say, D_{clus} which is assumed to be an "effective" rough frictional sphere. Upon collision with the bottom plate and end-wall (end-walls play an active role by providing the initial direction as well as an enhanced thrust), this rough cluster can acquire a small horizontal velocity (V_{clus}) which is expected due to translation-rotation coupling (Gayen & Alam 2008). Of course, V_{clus} is small and D_{clus} is large for small Γ, hence the cluster either stays static or moves intermittently, neither leading to any net horizontal transport and therefore there cannot be any ratchet at small Γ. With increasing Γ, D_{clus} decreases and V_{clus} increases, the cluster is likely to be increasingly active, showing small but intermittent horizontal movement. Only at some intermediate critical value of Γ_{crit}, D_{clus} would be of optimal size and V_{clus} would be large enough to trigger a horizontal movement of the cluster, leading to the birth of a ratchet-type oscillating cluster. [This completes the tentative justification for the initial conjecture on the birth of ratcheting cluster from a competition between two effects: (i) differential dissipation rate and (ii) shaking intensity.]

With all other parameters being fixed in the *Gas+Cluster* regime, (i) very small differential disspation ($e_n^s \approx e_n^g$) would lead to a small-size cluster with intermittent motion; (ii) very large differential disspation would lead to larger but static cluster, and finally (iii) by fine tuning a right combination of e_n^s and e_n^g could result in a ratchet-type motion.

5.2.4 Convection Control

In this section, we demostrate that the buoyancy-driven granular convection can be enhanced or diminished by adding a very small amount of heavier particles into a collection of lighter particles (or vice versa) at the same energy input. Controlling dynamical states in driven granular matter using such a simple recipe is likely to have a far reaching consequences from application viewpoint. Whether this finding can be tailored to suit potential applications in pharmaceutical and chemical processing industries remains an intriguing challenge for future work.

It has been discussed in Chapter 3 that at a shaking intensity of $\Gamma = 50$ and a shaking amplitude of $A/d = 3$, in $F = 6$ layers of monodisperse glass particles, there exist six counter-rotating rolls which spans the whole container (see Fig. 3.11 and Fig. 3.12). With the addition of 1% steel particles ($F_s/F = 0.01$), the number of convection rolls remain the same, see Fig. 5.30. Surprisingly, however, the number of rolls decreases to four at $F_s/F = 0.02$ (Fig. 5.31), and to two at $F_s/F = 0.05$ (Fig. 5.32). In the latter case, we no longer have 'complete' convection spanning the whole length of the container, rather a "partial" convection state, characterized by a pair of counter-rotating rolls, develops on one side of the container and a Leidenfrost state on the other side. Therefore, one can conclude that a small amount of steel particles in a mixture of steel-glass particles is sufficient to initiate this partial-convection state. Further, increasing the number fraction of steel particles in the mixture as shown in Fig. 5.33 and Fig. 5.34 does not effect the convection pattern and the number of rolls remains the same as two. But if one

increases the number fraction of steel particles to 0.5, i.e., considering an equimolar mixture, the convection gets totally suppressed and 'complete' Leidenfrost state sets up spanning whole container length, as discussed earlier and depicted in Fig. 5.15.

A closer inspection of these images in Fig. 5.31-Fig. 5.34 reveals that the convective rolls in binary mixtures are populated by steel particles and the Leidenfrost state by glass particles. The non-uniform fluidization due to non-equipartition of granular energy between steel and glass particles is responsible for partial convection. Interestingly, the resulting convective rolls appear irregularly (see Fig. 5.32) and are hence unsteady. The origin of this unsteadiness might be related to particles segregating, giving rise to convective motion, and the resulting particle mixing, due to the convective motion.

The effect of relative number fraction (F_s/F) on different patterns is summarized as a phase-diagram in (Γ, F_s/F)-plane in Fig. 5.35. The onset value of Γ for convection decreases sharply with increasing heavier steel particles (F_s/F) up-to $F_s/F \leq 0.05$ and increases thereafter: therefore, the heavier particles play a dual role of enhancing and supressing the convection intensity. The delayed convection beyond a critical value of F_s/F (≥ 0.05) is presumably due to non-uniform fluidization of two-species ($E_s > E_g$). In general, bidispersity delays convection and can eventually suppress it with increasing number fraction of one species $F_s/(F_g + F_s) \in (0, 0.5)$.

From Fig. 5.35, it can be inferred that for lower Γ and $0.04 \leq F_s/F \leq 0.375$, Leidenfrost state coexists with a granular gas but outside this region a complete Leidenfrost state spanning the whole container length has been seen. Thus, the partial *LS* state occurs for the intermediate values of relative number fraction and it is expected since the partial state is difficult to achieve with the mixture approaching monodipersity or equimolarity. The full phase diagram for $F_s/(F_g + F_s) \in (0, 1)$ and $\Gamma \in (0, 55)$ will be discussed in later section where a more detailed study of the effect of relative number fraction on other dyanamical patterns will be carried out.

5.2.5 Phase Diagram in ($\Gamma, F_i/F$)-plane: Effect of Species Number Fraction

Until now, the equimolar mixture of steel and glass particles ($F_s = F_g$) has been considered for the study of pattern formation. In this section, we will study on the influence of the variation of number fraction of species F_i/F ($i = 1, 2$) in the mixture vibrated at a constant shaking amplitude $A/d = 3$ on the pattern formation dynamics. For this purpose, two layer depths $F = F_g + F_s = 3$ and 6 have been considered and various phenomena observed are reported on a phase diagram in ($\Gamma, F_s/F$)-plane.

We will first focus on the phase diagram for filling depth $F = 3$, which is shown in Fig. 5.36(a). As one increases the shaking intensity Γ, the first pattern observed is the 'partial' *BB* state (*BB+Gas*) for $0.1 \leq F_s \leq 0.55$ and 'complete' *BB* for $0 \leq F_s \leq 0.05$ and $0.6 \leq F_s \leq 1$; both patterns are born from the 'Solid Bed' *SB*. Nevertheless, further increasing the shaking intensity will make the 'complete' *BB* state to eventually transit into 'partial' *BB* state. We have established in previous sections that the formation of all phase coexisting patterns is tied to the horizontal segregation of the two species in the mixture. Thus, it can be inferred that at lower shakings, a small amount of steel particles is enough to induce horizontal segregation

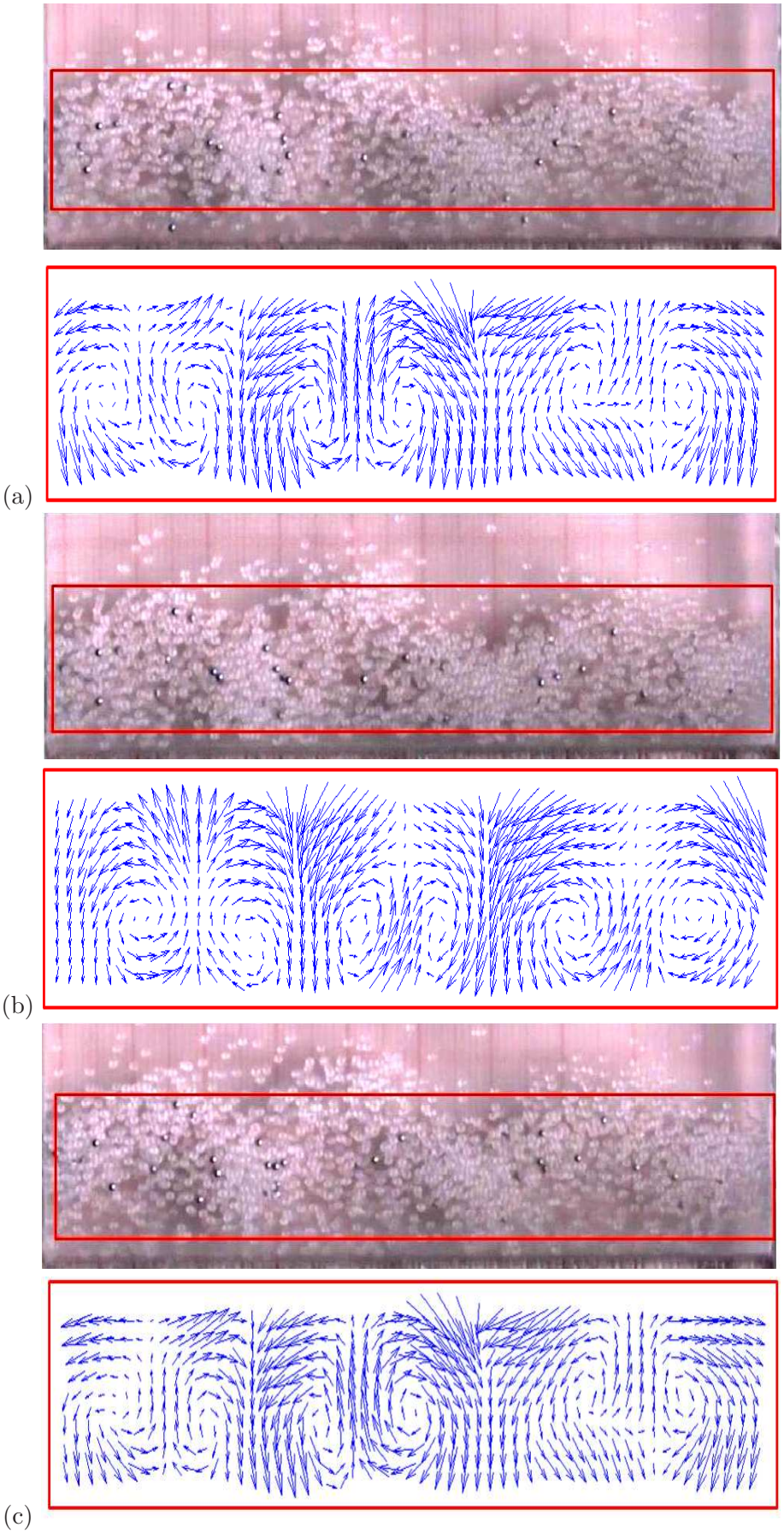

Figure 5.30: **'Complete' convection *Con*, spanning the whole length of the container.** Left-panel: Time sequence snapshots of *LS+Con* in mixture of steel-glass particles having 1% steel particles at (a) $t = 0\tau$, (b) $t = 0.5\tau$ and (c) $t = \tau$. Right-panel: Their corresponding PIV maps showing six counter-rotating rolls. Parameter values are $F = F_g + F_s = 6$, $F_s/F = 0.01$ and $\Gamma = 50$ ($A/d = 3$ and $f = 64.35\ Hz$).

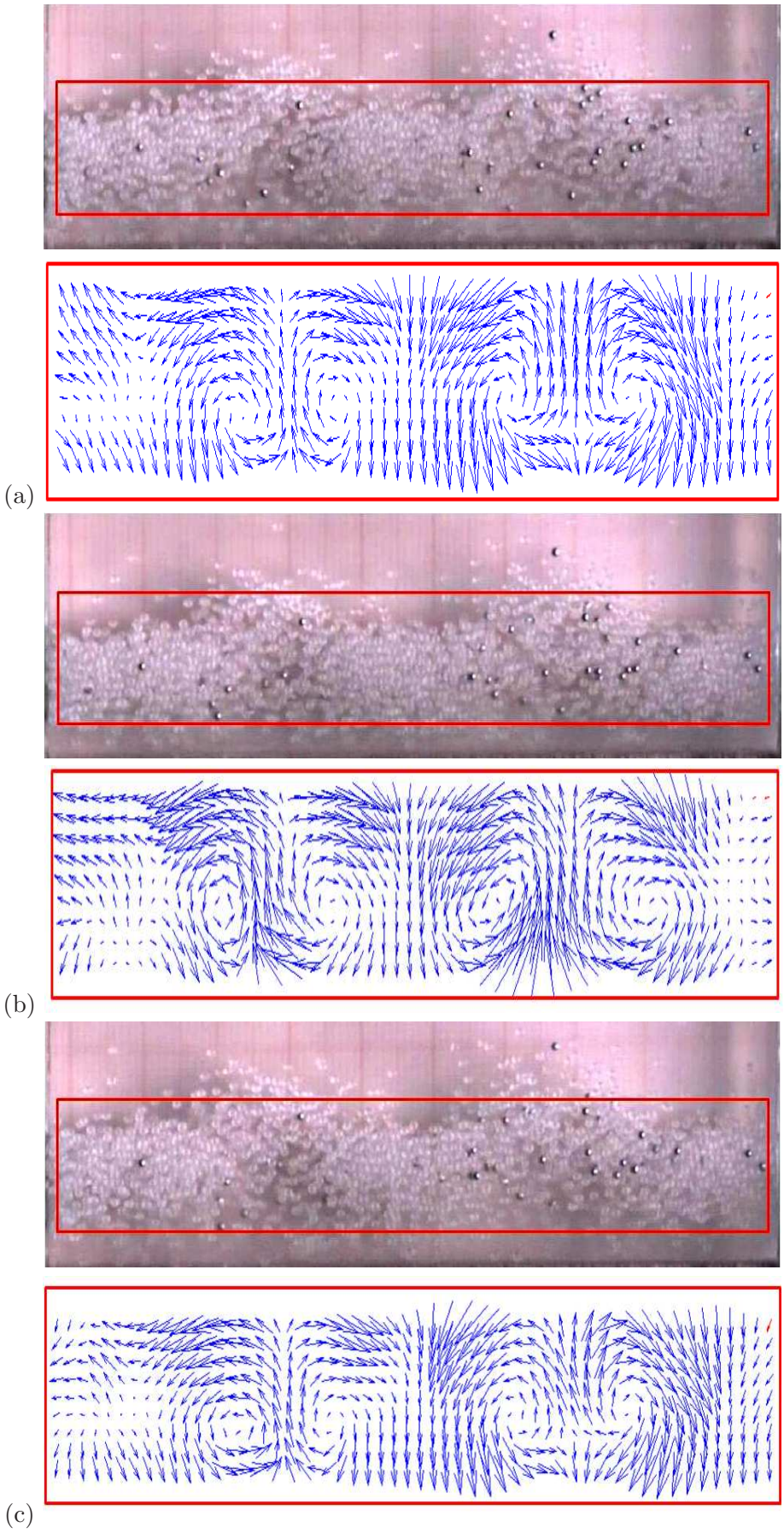

Figure 5.31: **'Complete' convection *Con*, spanning the whole length of the container.** Left-panel: Time sequence snapshots of *LS+Con* in mixture of steel-glass particles having 2% steel particles at (a) $t = 0\tau$, (b) $t = 0.5\tau$ and (c) $t = \tau$. Right-panel: Their corresponding PIV maps showing four counter-rotating rolls spanning the whole length of the container. $F_s/F = 0.02$ and other parameters are same as in Fig. 5.30

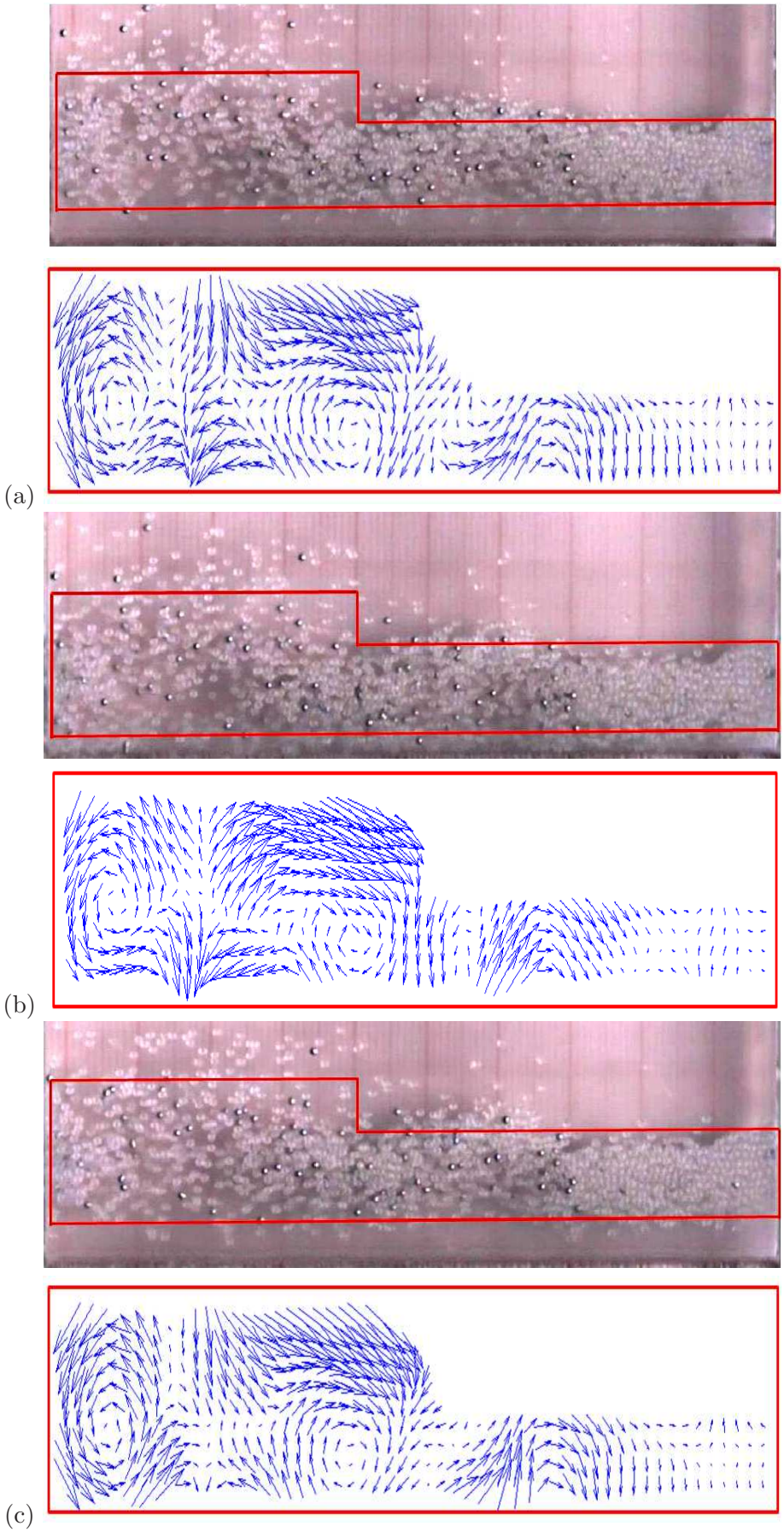

Figure 5.32: **'Partial' convection *LS+Con*.** Left-panel: Time sequence snapshots of *LS+Con* in mixture of steel-glass particles having 5% steel particles at (a) $t = 0\tau$, (b) $t = 0.5\tau$ and (c) $t = \tau$. Right-panel: Their corresponding PIV maps showing two counter-rotating rolls on the left of the container. $F_s/F = 0.05$ and other parameters are same as in Fig. 5.30

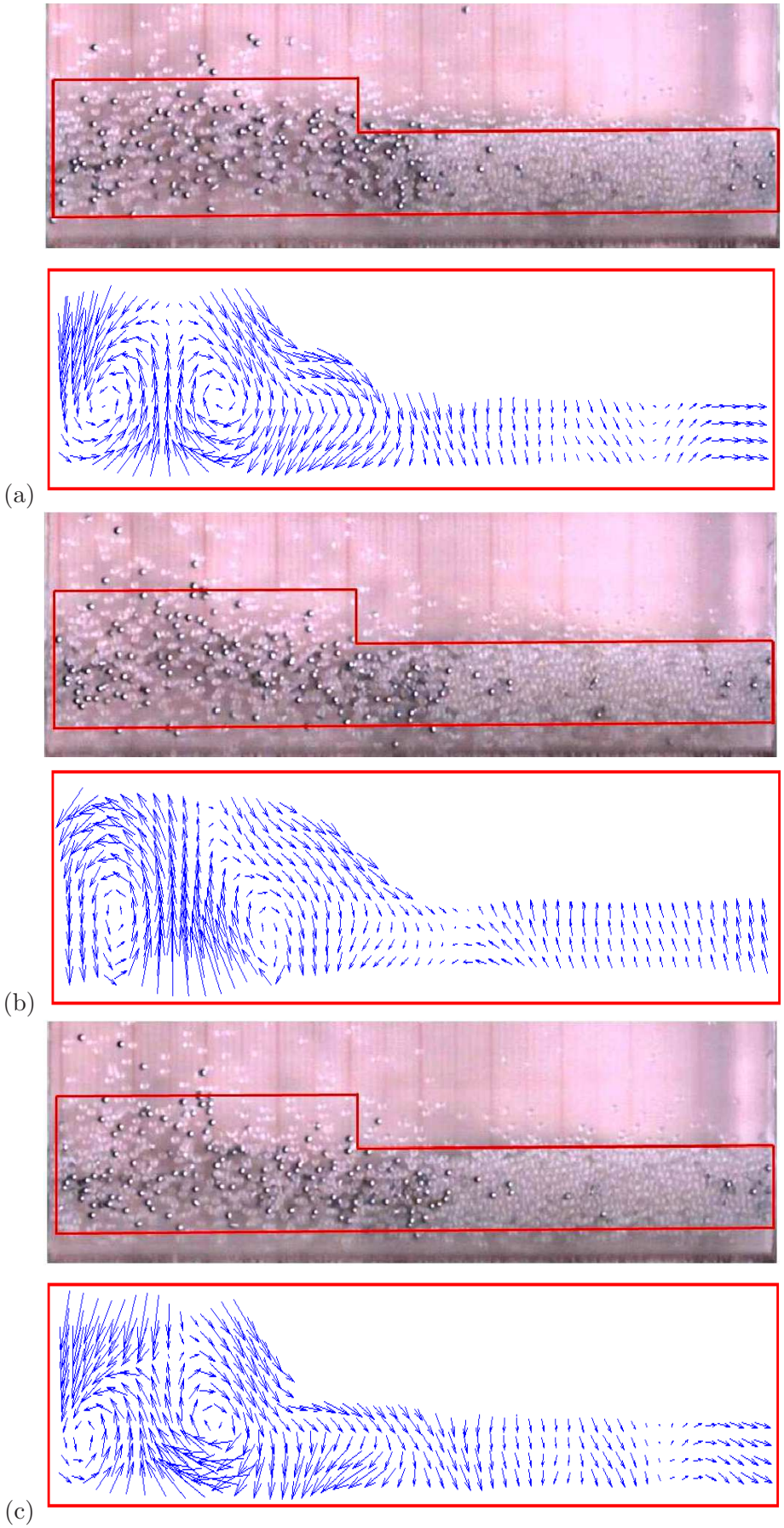

Figure 5.33: **'Partial' convection *LS+Con*.** Left-panel: Time sequence snapshots of *LS+Con* in mixture of steel-glass particles having 10% steel particles at (a) $t = 0\tau$, (b) $t = 0.5\tau$ and (c) $t = \tau$. Right-panel: Their corresponding PIV maps showing two counter-rotating rolls on the left of the container. $F_s/F = 0.1$ and other parameters are same as in Fig. 5.30

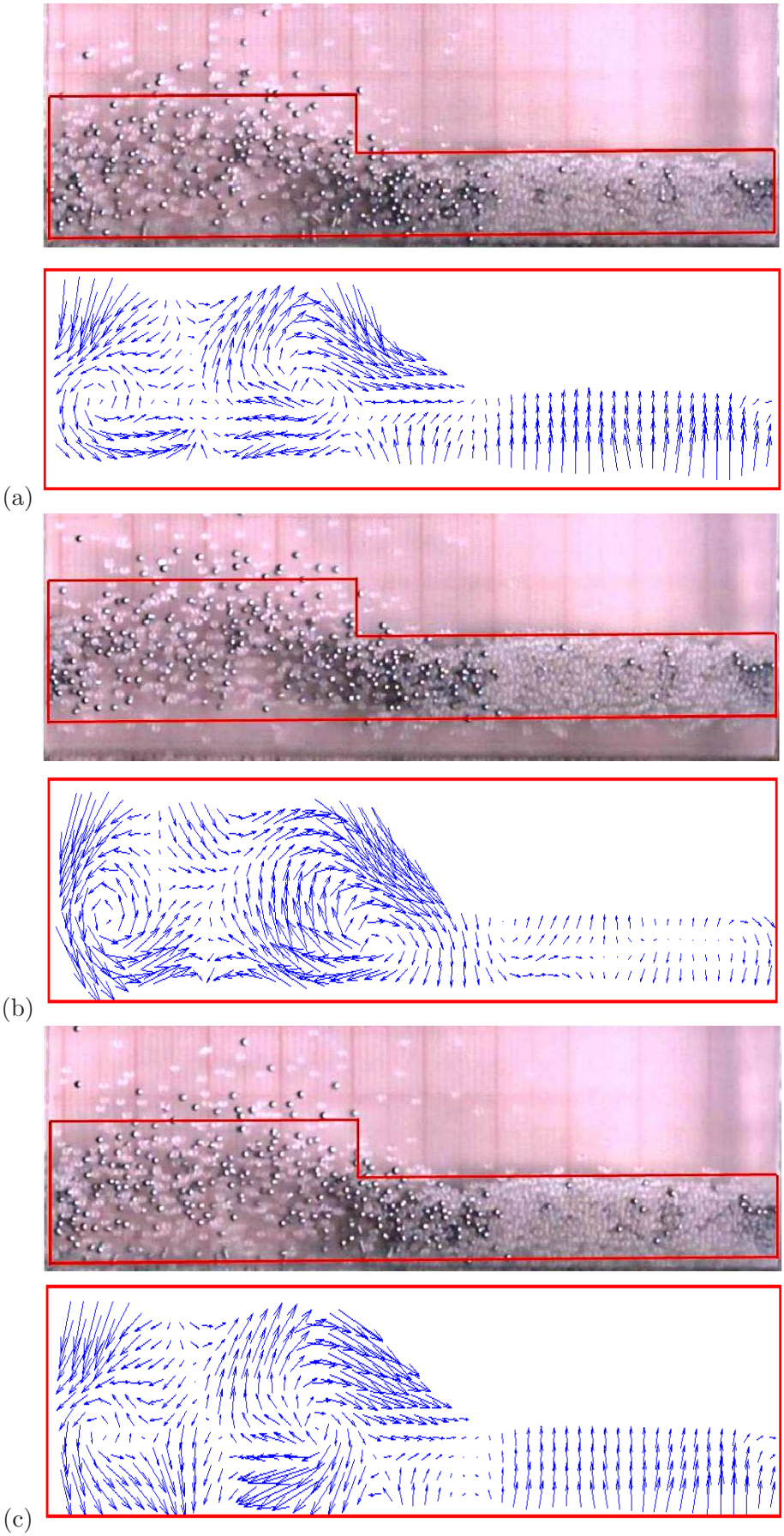

Figure 5.34: **'Partial' convection *LS+Con*.** Left-panel: Time sequence snapshots of *LS+Con* in mixture of steel-glass particles having 20% steel particles at (a) $t = 0\tau$, (b) $t = 0.5\tau$ and (c) $t = \tau$. Right-panel: Their corresponding PIV maps showing two counter-rotating rolls on the left of the container. $F_s/F = 0.2$ and other parameters are same as in Fig. 5.30

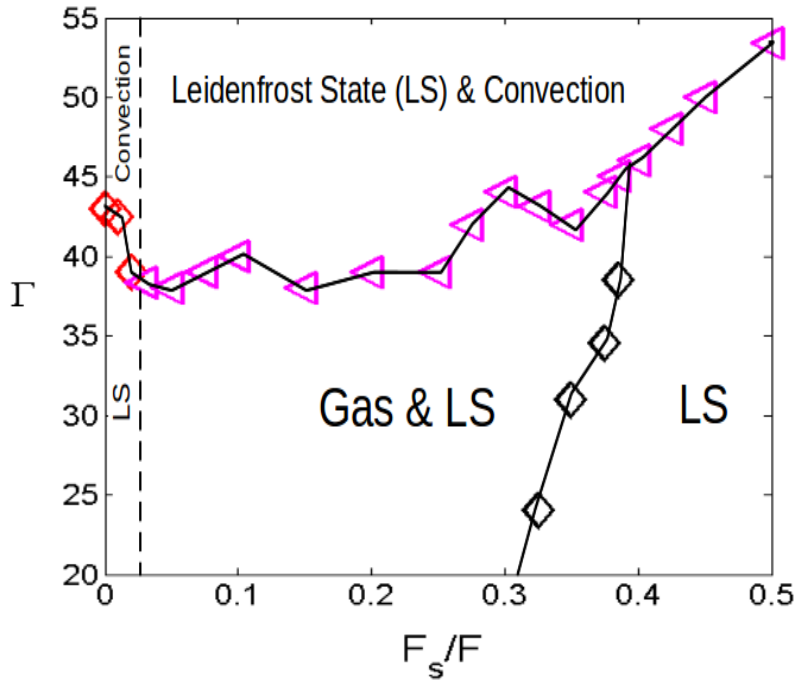

Figure 5.35: **Phase diagram of patterns in $(\Gamma, F_s/(F_g + F_s))$-plane showing the 'giant' effect of relative number of heavier particles (steel) on different patterns.** Parameter values are $F = F_g + F_s = 6$ and $A/d = 3$.

in the mixture in contrast to the glass particles. If one increases Γ even more, the next phase-coexisting pattern emerged is the "*UW+Gas*". Figure 5.37, shows these *UW+Gas* states at a shaking intensity $\Gamma = 9$ for two number fractions $F_s/F = 0.2$ and 0.8. It is observed that an *UW* of $n = 1$ mode coexists with a granular gas for $F_s/F = 0.2$ (see left panel) whilst at the same $\Gamma = 9$, an *UW* of $n = 2$ mode is found coexisting with gas for $F_s/F = 0.8$ (see right panel). It can be again seen that the granular gas is mostly populated with steel particles.

Now, traversing to a higher shaking intensity $\Gamma = 30$, we observe three states: (i) *Gas+LS*, (ii) *Oscillating Cluster* for the mixture approaching equimolarity, and (iii) a 'stationary' cluster. These states are shown in Fig. 5.38, where panel (c) depicts an oscillating cluster; left and right bottom panel show the oscillating cluster on right and left side of the container. It should be noted that 'complete' granular gas spanning the whole of the container exists for monodiperse cases, at all shakings beyond $\Gamma = 10$. In fact, at very high shakings of Γ around 50, a gas perists for lower F_s/F ($F_s/F \leq 0.1$), intermediate F_s/F ($0.4 \leq F_s/F \leq 0.6$) and higher F_s/F ($F_s/F \geq 0.9$). Fig. 5.39 displays the gaseous states for various number fraction of steel particles in the mixture. It is evident that the height upto which this gaseous regime spans depends on the number fraction of the species in the mixture irrespective of the same Γ-level. The phase diagram (see Fig. 5.36(a)) also depicts that there are three regions of *Oscillating Cluster*: located at (i) lower, (ii) intermediate, and (iii) higher values of F_s/F. This indeed implies that there is a requirement of properly tuned mixture proportions to drift the cluster from one end of the container to the other.

Turning towards the phase diagram for increased filling depth of $F = 6$ layers (see Fig. 5.36(b)),

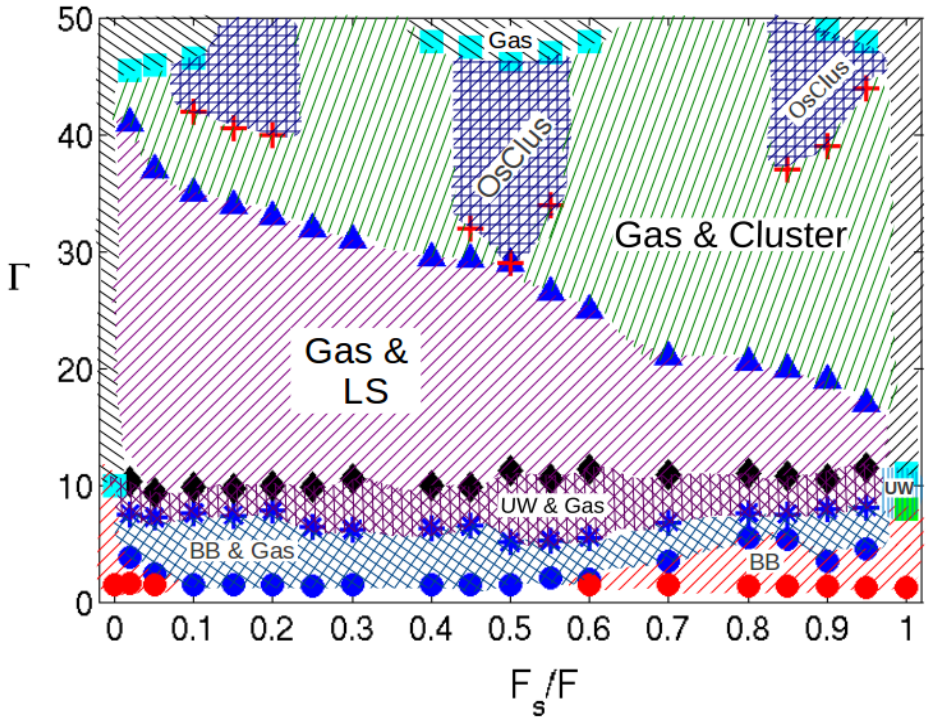

(a)

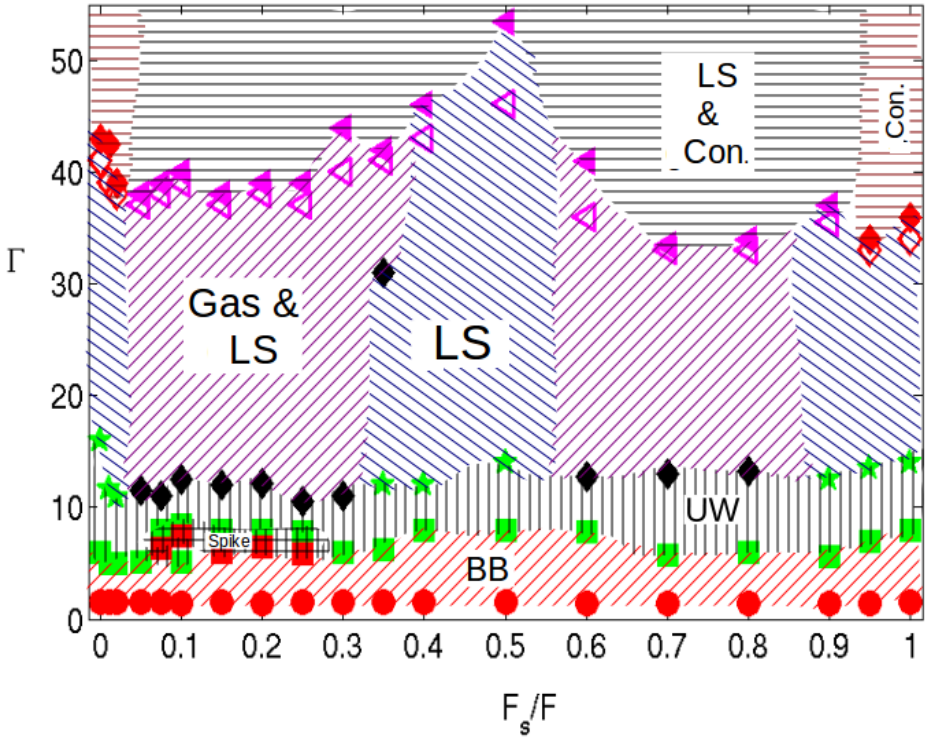

(b)

Figure 5.36: **Phase diagram in $(\Gamma, F_s/F)$-plane for mixture of steel and glass particles (both having diameter $d = 1.0\ mm$) for total filling depth: (a) $F = F_g + F_s = 3$, and (b) $F = F_g + F_s = 6$** . Other parameters are $A/d = 3$ and $ramping\ rate = 0.01\ Hz/sec$.

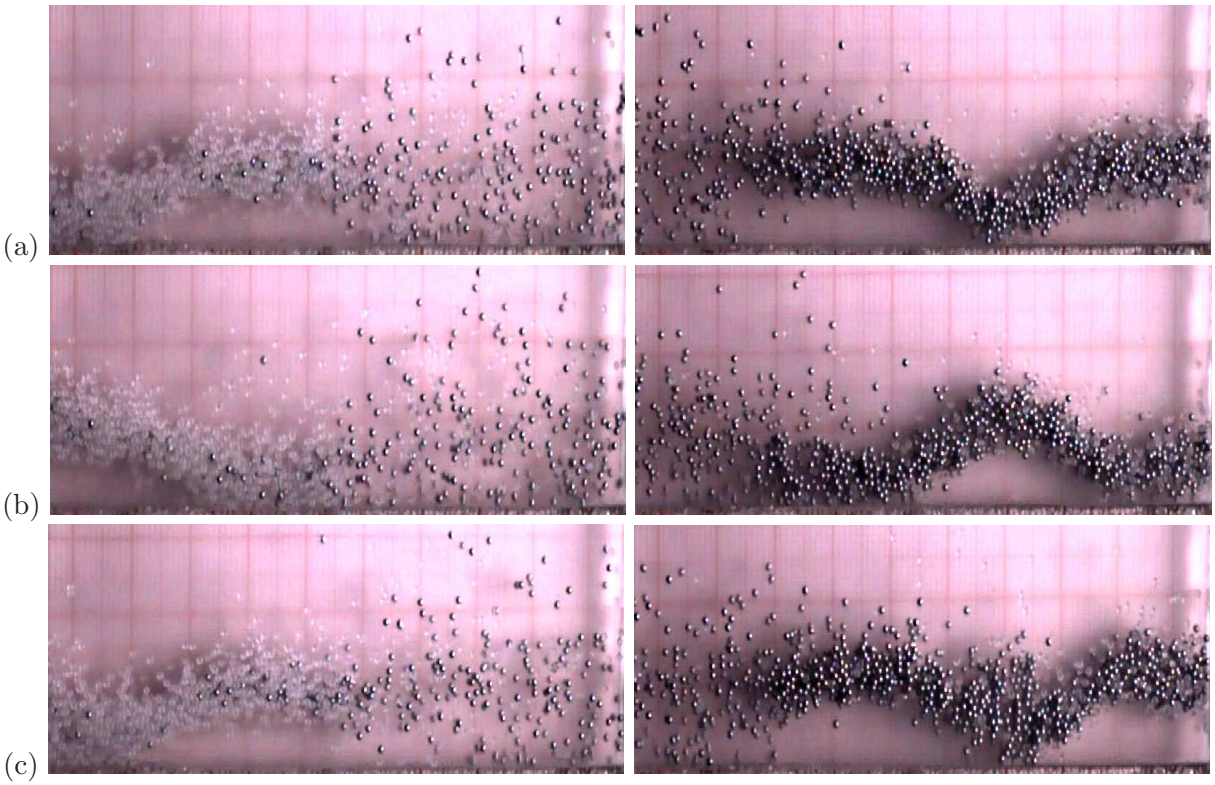

Figure 5.37: **Time sequence snapshots of *UW+Gas* consisting of a subharmonic wave *UW* and a granular gas: (a) $t = 0\tau$, (b) $t = \tau$ and (c) $t = 2\tau$, where, $\tau = 1/f$ is the period of shaking.** Note that peaks and valleys of the undulatory wave exchange their positions exactly over one shaking period (τ), and this undulatory wave repeat itself over 2τ; hence this is a *period-2 wave*. Left panel: '$n = 1$' mode for number fraction $F_s/F = 0.2$. Right panel: '$n = 2$' mode for number fraction $F_s/F = 0.8$. Both panels should be compared with its analog Fig. 5.10, where, '$n = 2$' mode UW coexists with a granular gas. Other parameter values are $F = F_g + F_s = 3$, and $\Gamma = 9$ ($A/d = 3$ and $f = 27.3\ Hz$).

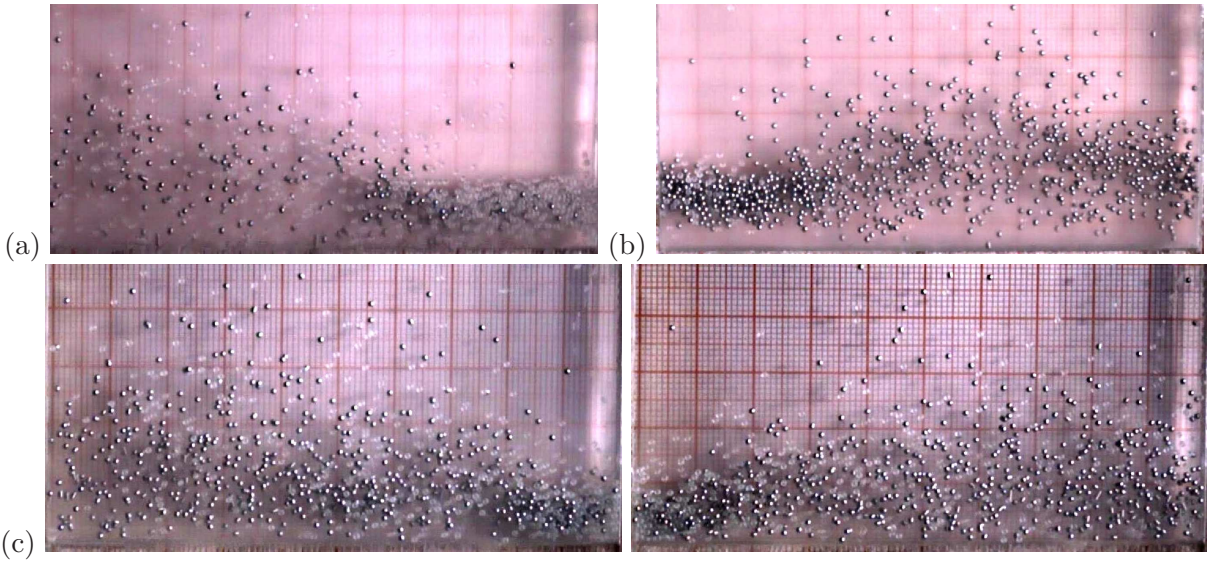

Figure 5.38: **Snapshots of: (a) *Gas+LS* for $F_s/F = 0.2$, (b) *Gas+cluster* for $F_s/F = 0.8$, and (c) *Gas+cluster* for $F_s/F = 0.5$. Note that panel (c) depicts an oscillating cluster with cluster on right and left side of the container in left and right images at $\Gamma = 29$ and 32, respectively.** Other parameters are $F = F_s + F_g = 3$, $\Gamma = 30$ ($A/d = 3$ and $f = 49.84\ Hz$).

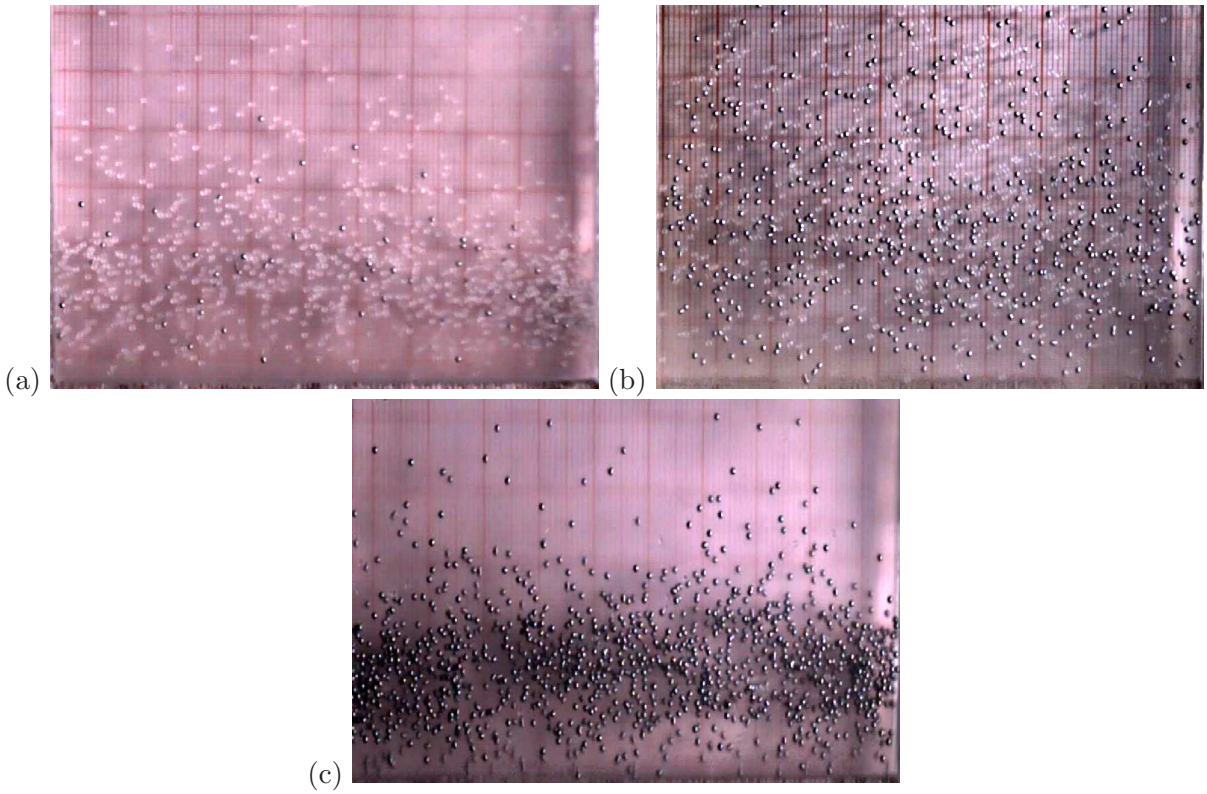

Figure 5.39: **Snapshots of granular gas for: (a) $F_s/F = 0.05$, (b) $F_s/F = 0.5$, and (c) $F_s/F = 0.95$**. Other parameter values are $F = F_g + F_s = 3$, $\Gamma = 50$ ($A/d = 3$ and $f = 64.35\ Hz$).

we observe that 'partial' *BB* state no longer persists, instead, a 'complete' *BB* state survies at lower shaking intensity. Increasing Γ gradually transits this *BB* into *Spikes* for a certain range of F_s/F ($0.09 \leq F_s/F \leq 0.25$) and to *UW* outside this F_s/F range. The *Spikes* are found sandwiched between the *BB* and *UW* regimes in a similar way as observed in phase diagrams for monodiperse cases. It is noticeable that we did not observe any *Spikes*-pattern for all filling depths F in an equimolar mixture of steel and glass particles (see Fig. 5.1).

Fig. 5.40 displays the *Spikes* and *UW* for different number fractions at constant shaking intensity $\Gamma \approx 8$. These *Spikes* patterns also seem to be strongly dependent upon the proportion of steel and glass particles in the mixture. On the other hand, *Undulatory Waves (UW)* appear in the system for any mixture proportion. Further increasing the shaking intensity (Γ) enforces these *UW* to become unstable, giving birth to either a 'partial' *Leidenfrost State* (*LS+Gas*) or a 'complete' *LS* as depicted in phase diagram (see Fig. 5.36(b)). When one traverses at a constant Γ along the number fraction axis in Fig. 5.36(b), it is found that the *LS* and *LS+Gas* states mutually transit into one another depending upon the number fraction of the steel particles in the mixture. In any case, the monodipersity always sanctions the build up of 'complete' *LS*, whereas introducing bidispersity (except near the equimolar limit) causes the two species to segregate out and hence results in *LS+Gas* in the system. Various states originated at constant $\Gamma = 30$ while increasing the number fraction of steel particles are shown in Fig. 5.41: for $F_s/F = 0.2$ and 0.8 the 'partial' *LS* subsists, while for $F_s/F = 0.5$, a 'complete' *LS* spans the full container length. Injecting more energy via increasing Γ to 50 induces convective motion in the gaseous regime of $LS + Gas$ (observed at $\Gamma = 30$), leading to a 'partial' *Convection* state. This is shown in Fig. 5.42. Note in Fig. 5.36(b), however, that a complete *LS* persists even at $\Gamma = 50$.

5.2.6 Phase Diagram in $(\Gamma, A/d)$-plane: Effect of Shaking Amplitude

In this section, we will probe the consequence of the shaking amplitude (A/d) on the dynamical patterns in vibrated binary granular mixtures. To accomplish this objective we converge our attention to an equimolar mixture of steel and glass particles having filling depths of $F = 3$ and 6. The phase diagrams for these two cases on $(\Gamma, A/d)$-plane are exhibited in Fig. 5.43. We first direct our focus to phase diagram of $F = 3$ layers as shown in Fig. 5.43(a). We observe that the phase diagram is dominated by various 'partial' states (coexisting with a gas) while 'complete' states are observed only at lower shaking amplitudes. Figure 5.44 displays *UW+Gas* states at two shaking amplitudes $A/d = 1.5$ and 4.5; both of them consists of $n = 1$ mode undulatory wave. Further increasing the shaking intensity to $\Gamma = 20$ at these amplitudes, one lands up in the LS+Gas and *Gas+Cluster* regimes as depicted in Fig. 5.43(a) and the related images are displayed in Fig. 5.45. It is noteworthy that at higher shaking amplitudes the *Leidenfrost* region of "*LS+Gas*" becomes unstable and takes the form of a loose dense cluster which is dubbed "*Gas+Cluster*" state. If one increases Γ to 45, the *Leidenfrost* region of the "*LS+Gas*" observed at $A/d = 1.5$ and $\Gamma = 20$ (see left panel of Fig. 5.45) melts to a cluster, yielding "*Gas+Cluster*" state (see Fig. 5.46(a)); this cluster is stationary in nature. On the contrary, the 'stationary' cluster observed at $A/d = 4.5$ and $\Gamma = 20$ starts drifting and thereby oscillating

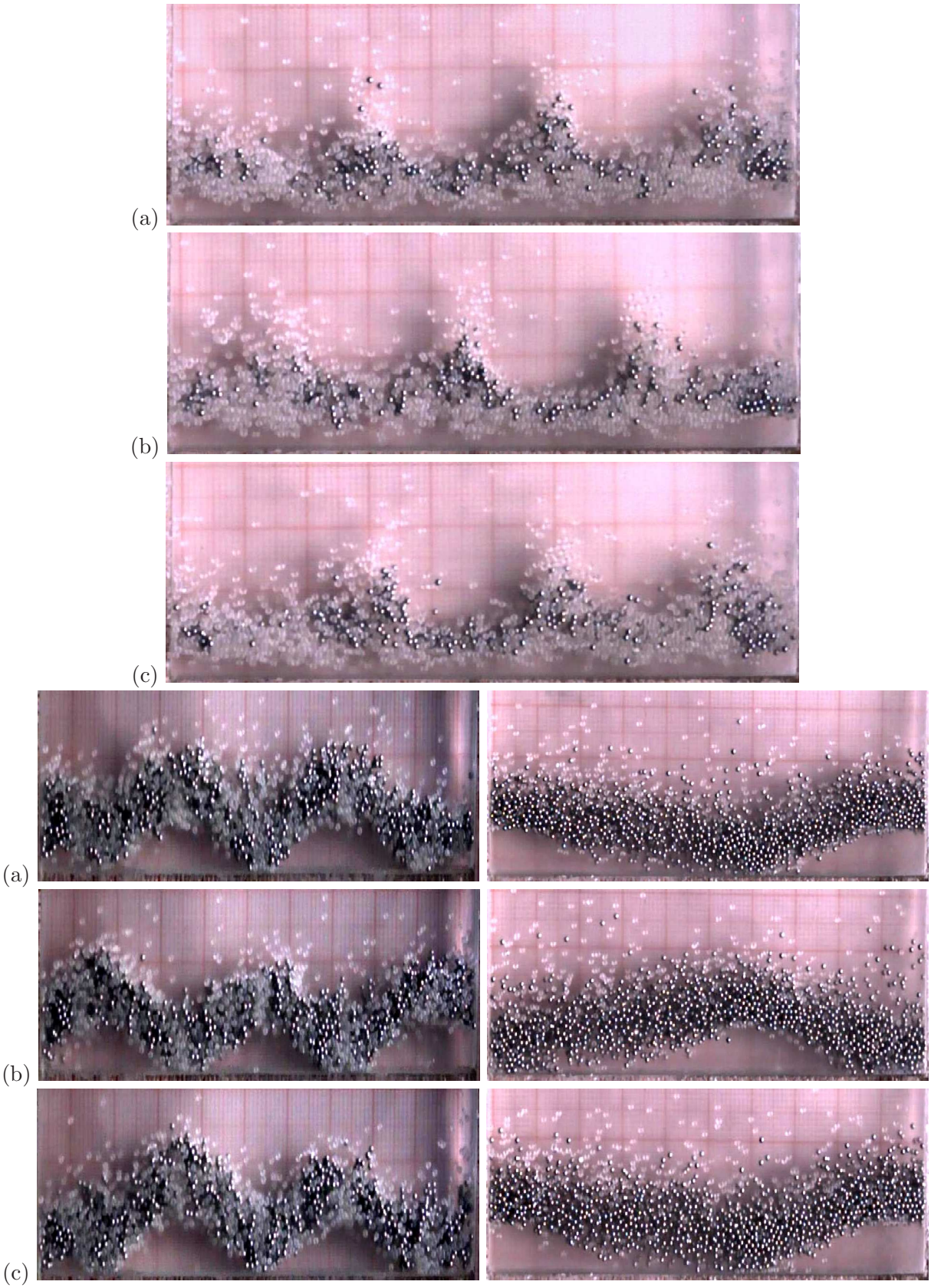

Figure 5.40: **Top panel: Time sequence snapshots of spikes pattern for $F_s/F = 0.2$ at (a) $t = 0\tau$, (b) $t = 2\tau$, and (c) $t = 4\tau$. Bottom-left panel: Time sequence snapshots of undulatory waves UW ($n = 4$ mode) for $F_s/F = 0.5$. Bottom-right panel: Time sequence snapshots of UW ($n = 2$ mode) for $F_s/F = 0.8$. Time sequence for bottom panel: (a) $t = 0\tau$, (b) $t = \tau$, and (c) $t = 2\tau$.** Other parameter values are $F = F_g + F_s = 6$, $\Gamma \approx 8$ ($A/d = 3$).

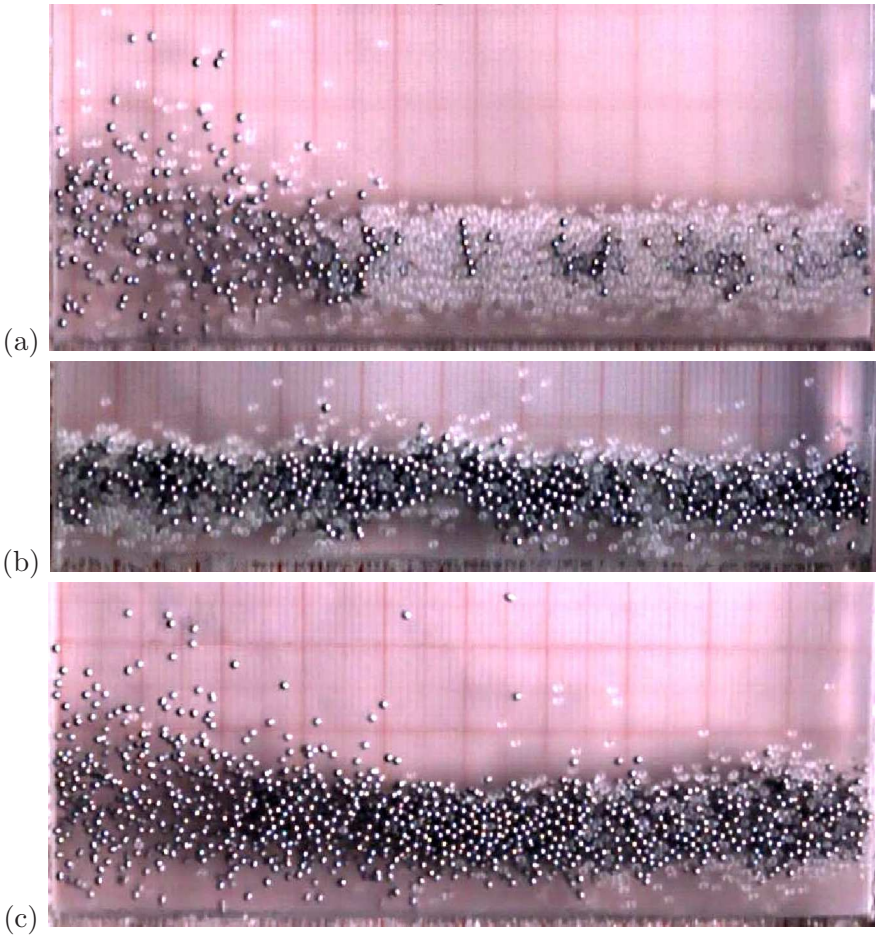

Figure 5.41: **Transition at constant shaking intensity $\Gamma = 30$ ($A/d = 3$ and $f = 49.84$ Hz in $F = F_g + F_s = 6$ layers of mixture of steel and glass particles**: (a) *LS+Gas* for $F_s/F = 0.2$, (b) 'complete' *LS* for $F_s/F = 0.5$, and (c) *LS+Gas* for $F_s/F = 0.8$. Note that the transition between *LS+Gas* and *LS* strongly depends on the number fraction of the species as depicted in Fig. 5.36(b).

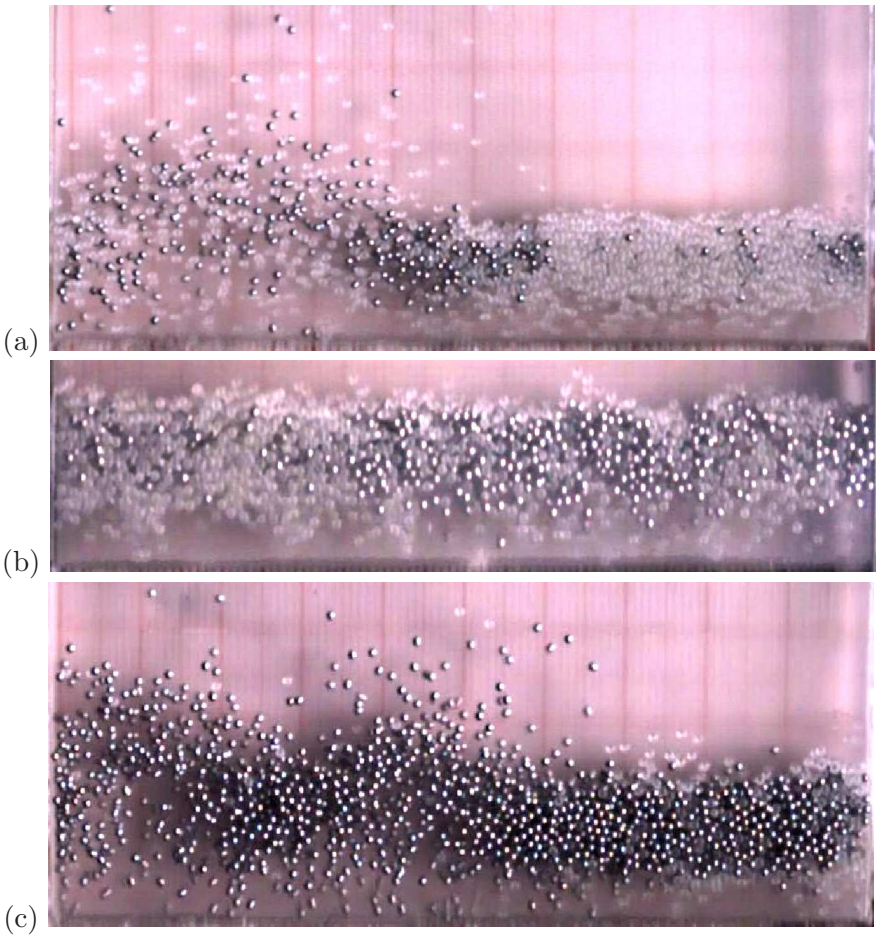

Figure 5.42: **Transition at constant shaking intensity $\Gamma = 50$ ($A/d = 3$, $f = 64.38$ Hz) in $F = F_g + F_s = 6$ layers of mixture of steel and glass particles**: (a) *LS+Con* for $F_s/F = 0.2$, (b) 'complete' *LS* for $F_s/F = 0.5$, and (c) *LS+Con* for $F_s/F = 0.8$. Note that the transition between *LS+Con* and *LS* strongly depends on the number fraction of the species as depicted in Fig. 5.36(b). This result should be compared with its analog in Fig. 5.41.

at $\Gamma = 45$, as shown in Fig. 5.46(b).

On increasing the filling depth to $F = 6$, the 'partial' *BB* and *UW* states no longer persists and the 'complete' BB and *UW* evolves in the system. The related phase diagram is shown in Fig. 5.43(b). Figure 5.47 displays *BB* and *Spikes* at $A/d = 1.5$ and 4.5 at a shaking intensity $\Gamma \approx 7.8$. A close observation of these states shows a discernible horizontal segregation of lighter and heavier particles. Further increasing Γ to 11 at the same shaking amplitudes transform the *BB* and *Spikes* into *UW* as shown in Fig. 5.48. The undulatory wave at $A/d = 1.5$ seems to be well mixed whilst the one at $A/d = 4.5$ still exhibits horizontal segregation, demonstrating that a higher shaking amplitude can induce segregation. Similarly, we notice in Fig. 5.49 that at higher Γ ($\Gamma = 30$) the *UW* at $A/d = 1.5$ transits to a 'complete' *LS*, on the other hand, *UW* at $A/d = 4.5$ displays segregated *LS+Gas* state. The snapshots in the left panel of Fig. 5.49 clearly indicates that even this 'complete' *LS* apparently shows some amount of horizontal segregation of steel particles (the left end of the container is more populated with steel particles). When one increases Γ to 50, these steel particles shoot up with a higher kinetic energy and outturns a comparatively dilute gaseous regime (see Fig. 5.50). Note that, the *LS+Gas* state observed in the right panel of Fig. 5.49 transits to a 'partial' convective state at this higher Γ.

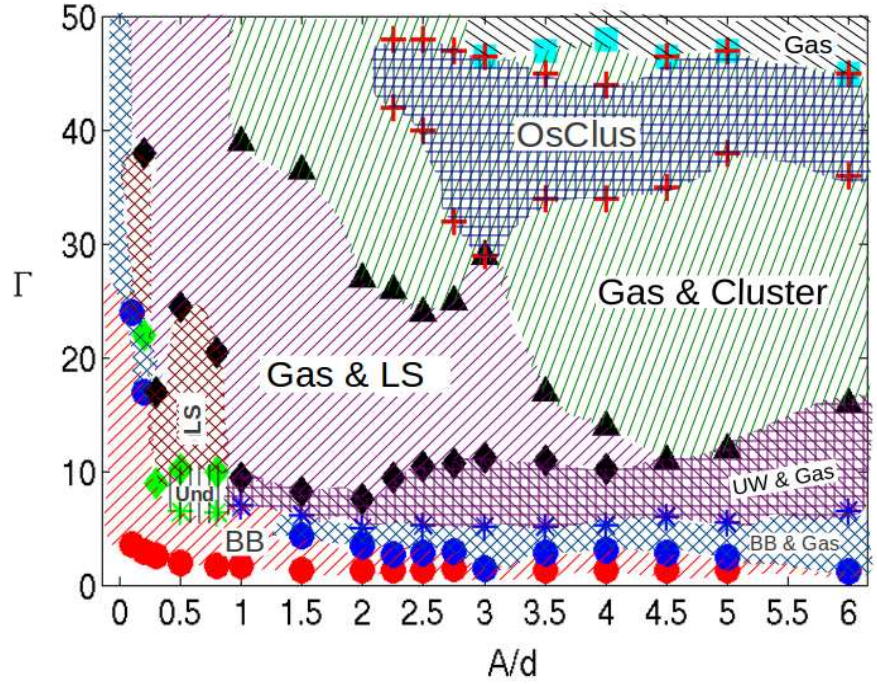

(a)

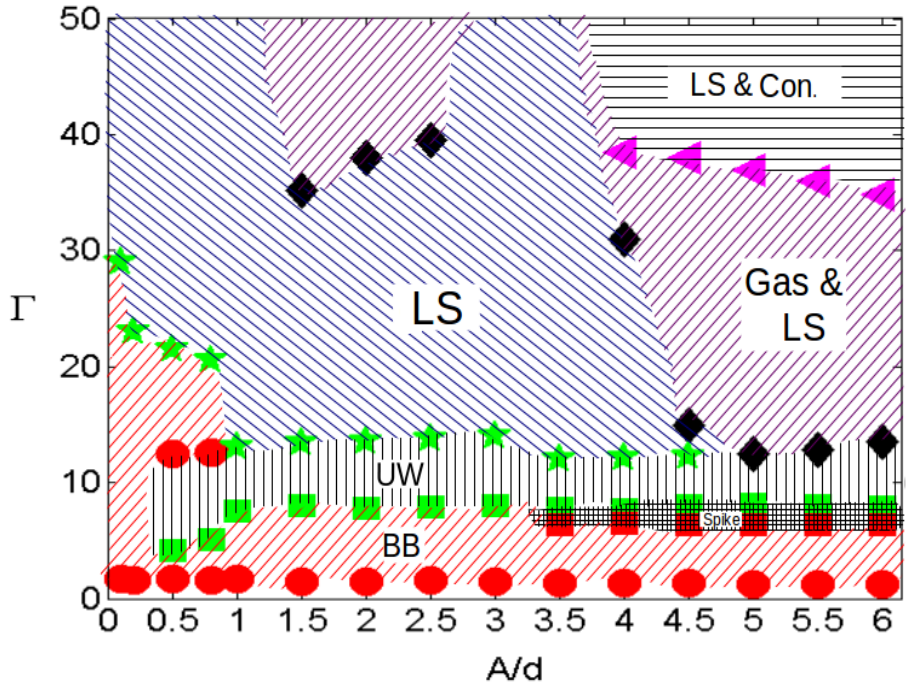

(b)

Figure 5.43: **Phase diagram in $(\Gamma, A/d)$-plane for equimolar mixture of steel and glass particles (both having diameter $d = 1.0\ mm$) for total filling depth: (a) $F = F_g + F_s = 3$, and (b) $F = F_g + F_s = 6$.** *Ramping rate* is 0.01 Hz/sec.

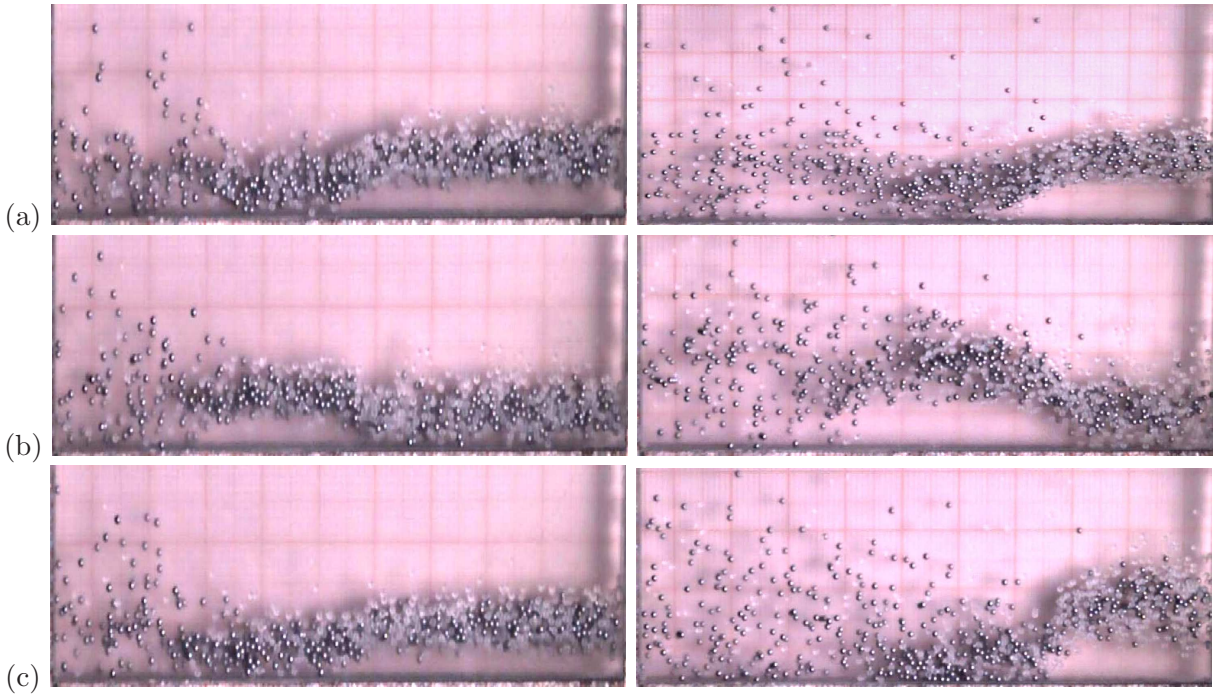

Figure 5.44: ***UW+Gas* at constant shaking intensity $\Gamma \approx 6.5$ for $F = F_g + F_s = 3$ layers of equimolar mixture of steel and glass particles ($F_s = F_g$)**: (a) $t = 0\tau$, (b) $t = \tau$, and (c) $t = 2\tau$. Left panel: $A/d = 1.5$ ($f = 32.8\ Hz$), Right panel: $A/d = 4.5$ ($f = 19\ Hz$).

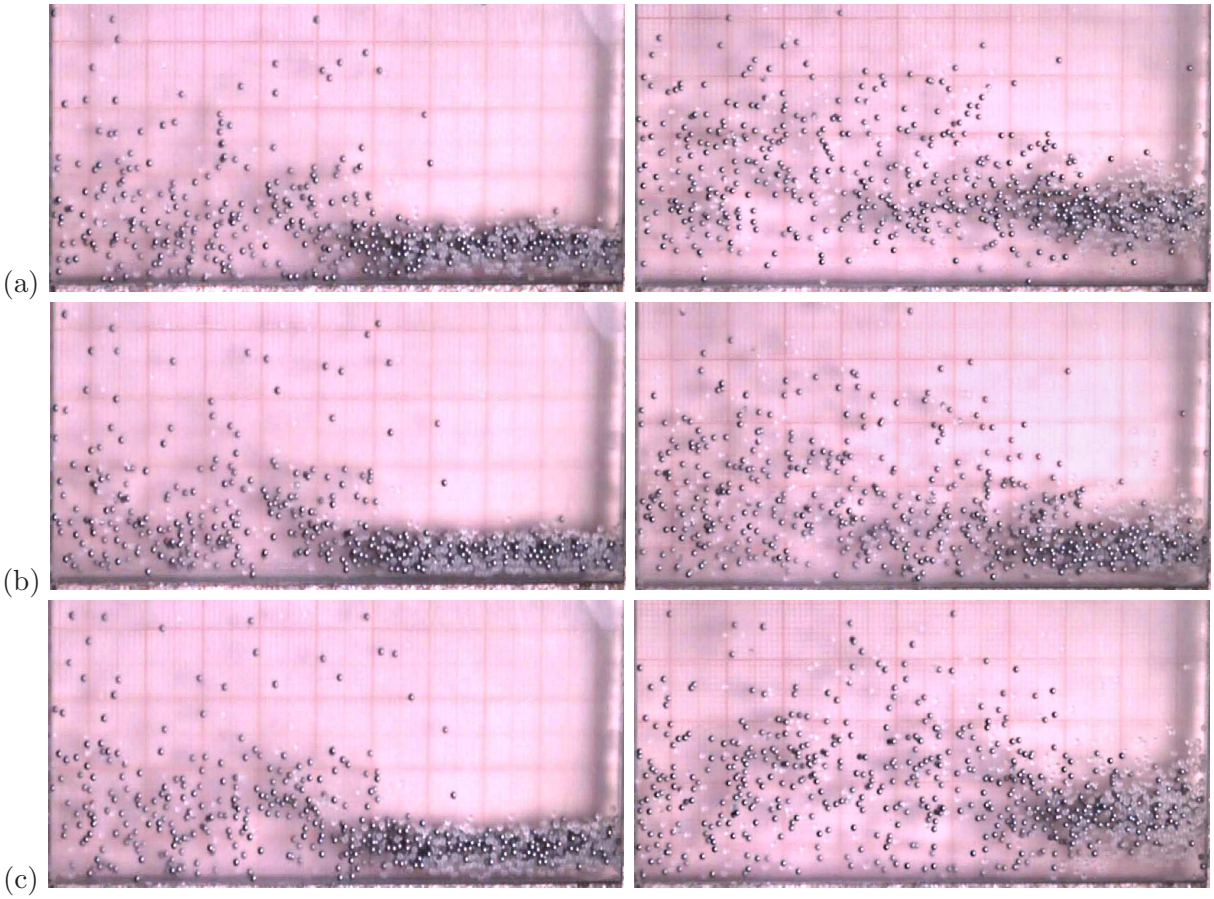

Figure 5.45: **Transition at constant shaking intensity $\Gamma = 20$ for $F = F_g + F_s = 3$ layers of equimolar mixture of steel and glass particles:** (a) $t = 0\tau$, (b) $t = 0.5\tau$, and (c) $t = \tau$. Left panel: *LS+Gas* at shaking amplitude $A/d = 1.5$ ($f = 57.56\ Hz$), Right panel: cluster (stationary) coexisting with a granular gas at shaking amplitude $A/d = 4.5$ ($f = 33.2\ Hz$).

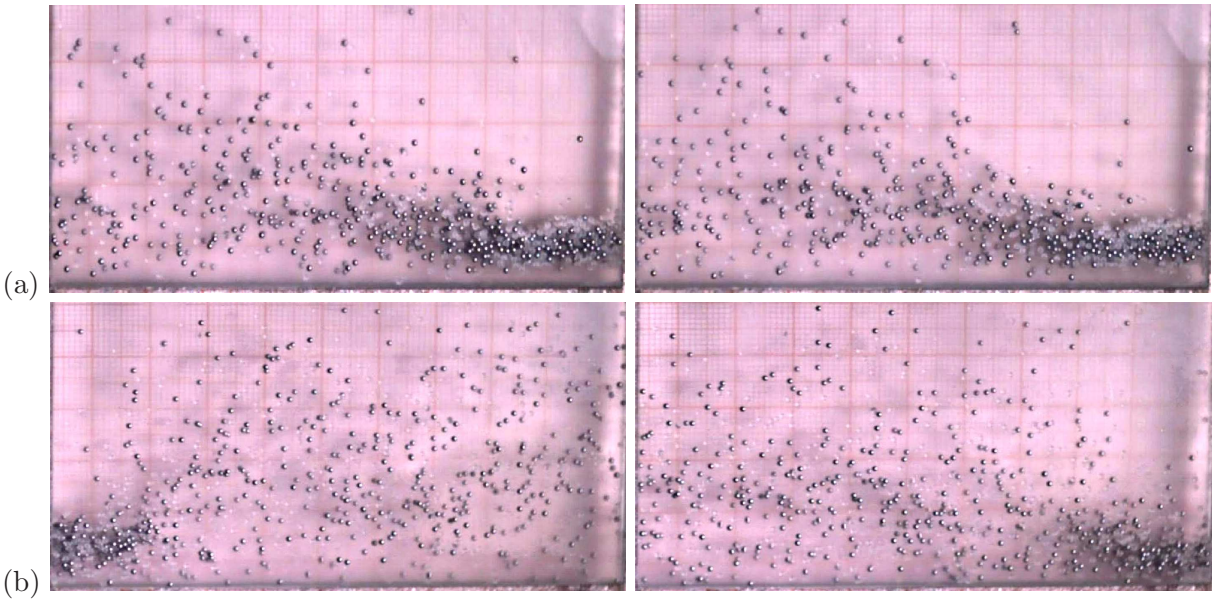

Figure 5.46: **Transition at constant shaking intensity $\Gamma = 45$ for $F = F_g + F_s = 3$ layers of equimolar mixture of steel and glass particles:** (a) Stationary cluster coexisting with a granular gas at time sequence $t = 0\tau$ and $t = \tau$ for shaking amplitude $A/d = 1.5$ ($f = 86.3\ Hz$) (b) Oscillating cluster coexisting with a granular gas showing cluster at the left and right side of the container, respectively, for shaking amplitude $A/d = 4.5$ ($f = 49.84\ Hz$).

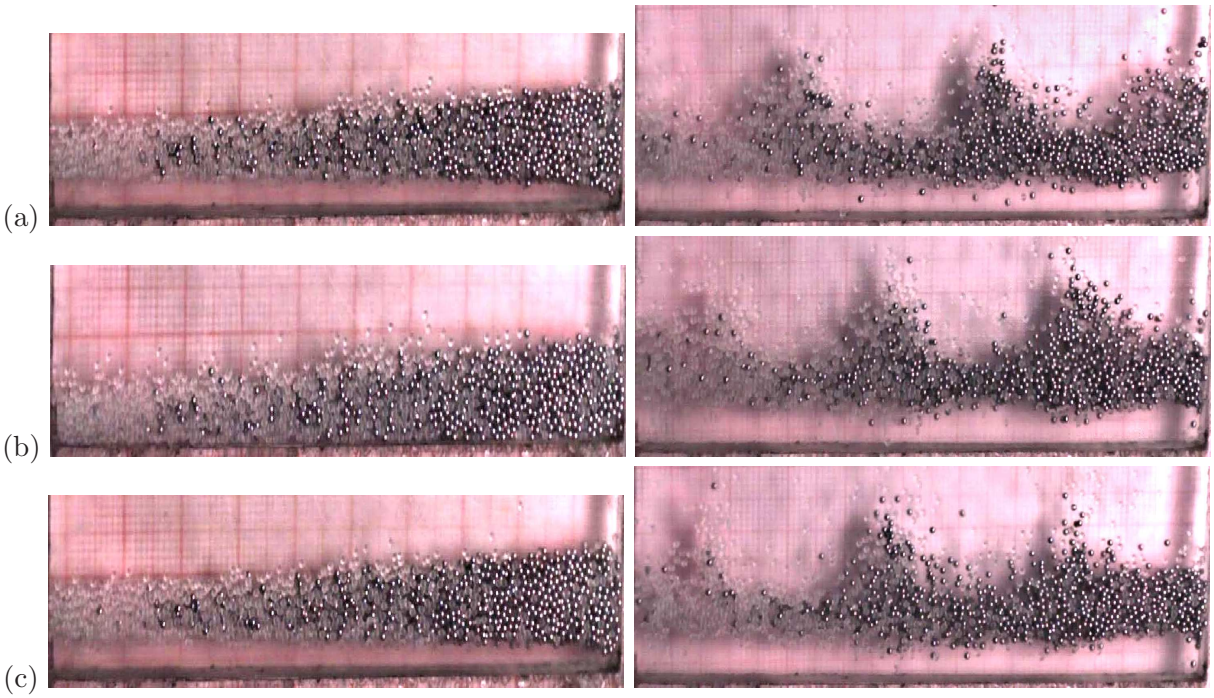

Figure 5.47: **Transition at constant shaking intensity $\Gamma \approx 7.8$ for $F = F_g + F_s = 6$ layers of equimolar mixture of steel and glass particles.** Left panel: 'Complete' *BB* at (a) $t = 0\tau$, (b) $t = 0.5\tau$, and (c) $t = \tau$ for shaking amplitude $A/d = 1.5$ ($f = 35.94\ Hz$). Right panel: Spikes pattern at (a) $t = 0\tau$, (b) $t = 2\tau$, and (c) $t = 4\tau$ for shaking amplitude $A/d = 4.5$ ($f = 20.75\ Hz$).

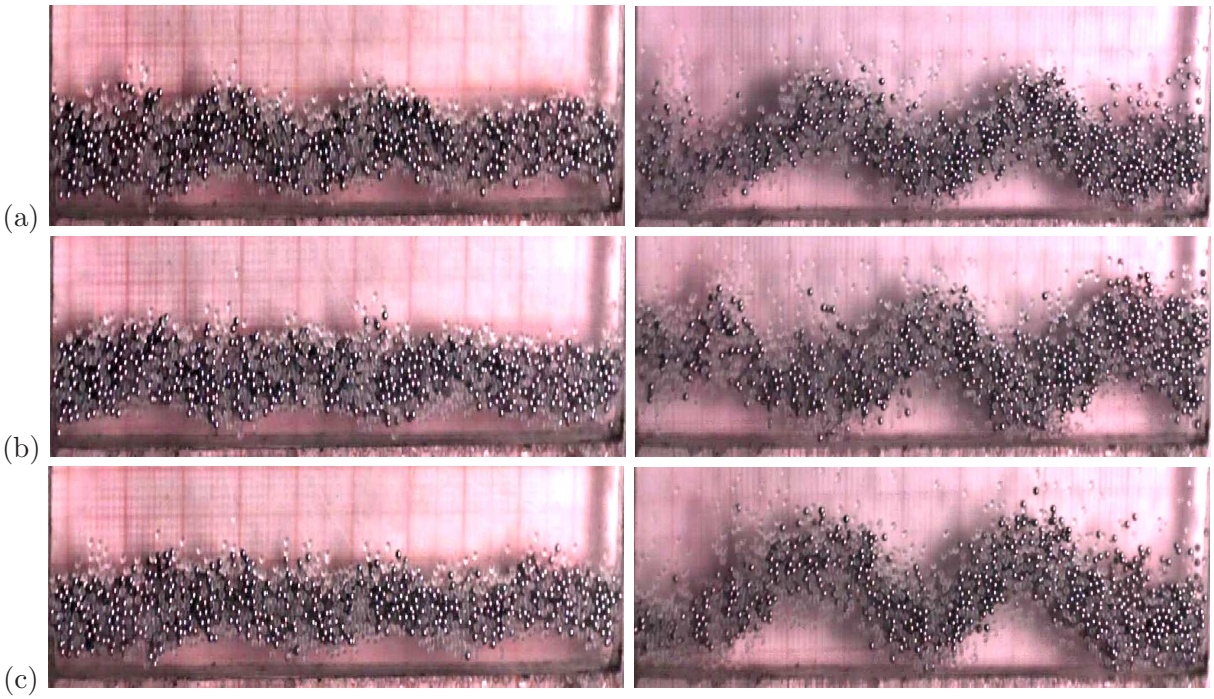

Figure 5.48: **Transition at constant shaking intensity $\Gamma = 11$ for $F = F_g + F_s = 6$ layers of equimolar mixture of steel and glass particles:** (a) $t = 0\tau$, (b) $t = \tau$, and (c) $t = 2\tau$. Left panel: UW at shaking amplitude $A/d = 1.5$ ($f = 15.76\ Hz$), Right panel: UW at shaking amplitude $A/d = 4.5$ ($f = 24.6\ Hz$).

5.3 Effect of ambient pressure on patterns: Hysteresis

Most studies on granular matter are concerned with relatively large particles ($> 1\ mm$), where the effects of interstitial air can be safely ignored. However, for smaller particles, the effects of ambient air cannot be neglected: it has been demonstrated in several experiments that air can have a pronounced influence on the system's behavior. The role of air in vibrated bed phenomena has been noted as a deterant in the dynamic response of the granular bed to agitation. One well-known example is Faraday heaping, which has become the common name for the general observation that fine particles on a vibrating or resonating plate tend to gather in piles, lines, or heaps (Faraday 1831). It is clear that the presence of air is responsible for these phenomena, since under vacuum conditions no heaping of any kind is observed as already found by Faraday. Pak *et al.* (1995) showed how convection and heaping are greatly reduced in vacuum; Faraday tilting has been related to the flow of air through the bed (Thomas & Squires 1998) and has been studied also with water as the interstitial fluid (Leaper *et al.* 2005).

Another demonstration of the influence of air was given by Möbius *et al.* (2001, 2004); Mobius *et al.* (2005). Mobius *et al.* (2005) found that the air pressure has a profound effect on the rising time of a large intruder, submerged in a bed of smaller particles, to the extent that the intruders might even sink: the reverse Brazil nut effect. A remarkable and important property of granular materials is that particles of different kinds often have a tendency to segregate. A well-known example of this segregation is the so-called "Brazil nut effect" (BNE) (Williams 1976*a*; Harwood 1977; Rosato *et al.* 1987; Alam *et al.* 2006; Shinbrot & Muzzio 1998) in which larger and/or heavier particles are seen to rise to the top when a mixture of particles is shaken

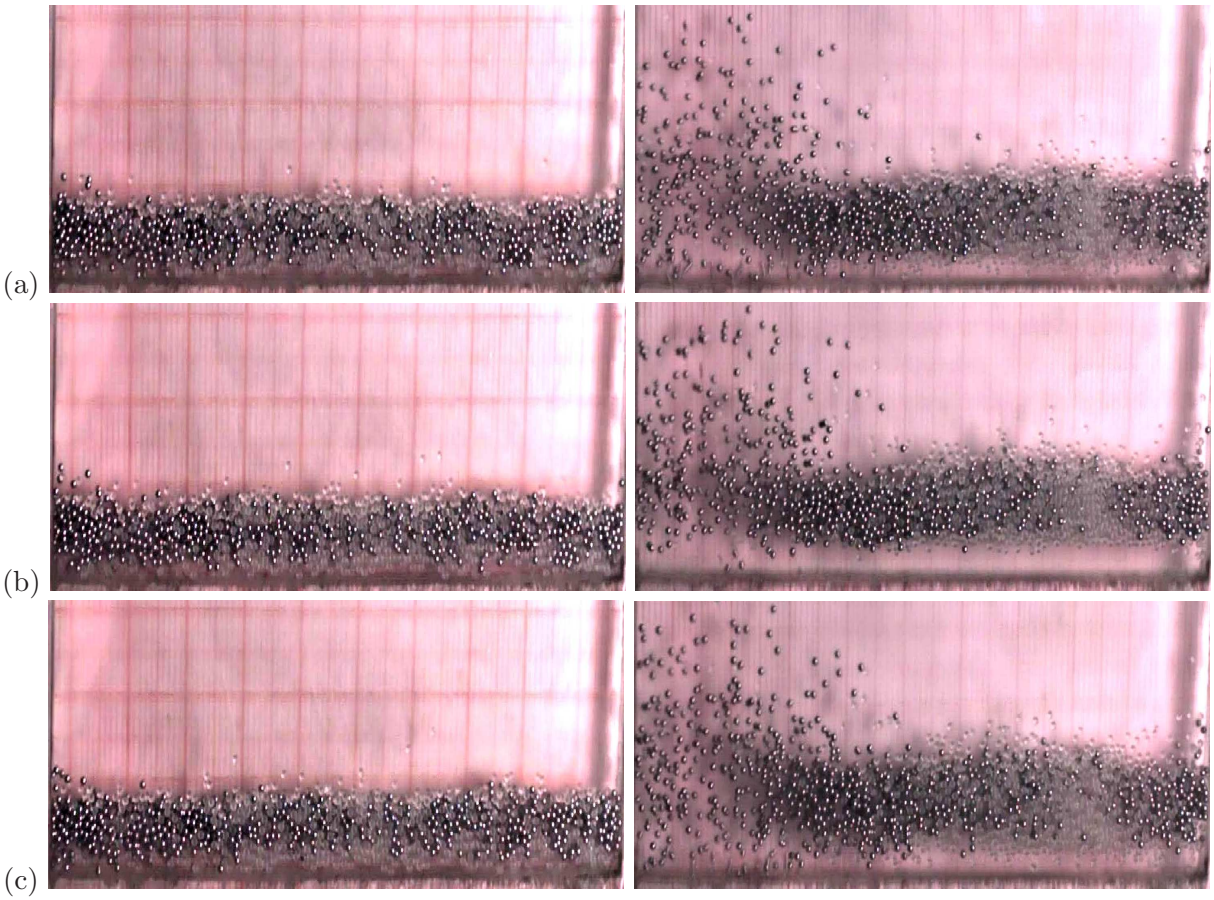

Figure 5.49: **Transition at constant shaking intensity $\Gamma = 30$ for $F = F_g + F_s = 6$ layers of equimolar mixture of steel and glass particles:** (a) $t = 0\tau$, (b) $t = 0.5\tau$, and (c) $t = \tau$. Left panel: 'Complete' *LS* at shaking amplitude $A/d = 1.5$ ($f = 70.5\ Hz$), Right panel: *LS+Gas* at shaking amplitude $A/d = 4.5$ ($f = 40.7\ Hz$).

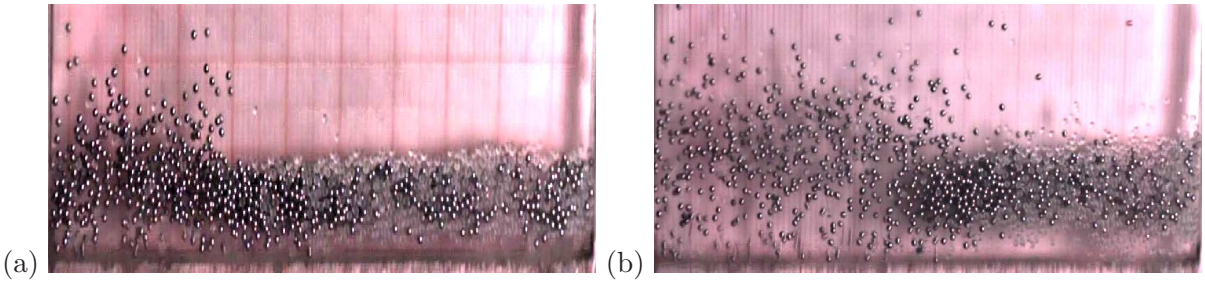

Figure 5.50: **Transition at constant shaking intensity $\Gamma = 50$ for $F = F_g + F_s = 6$ layers of equimolar mixture of steel and glass particles:** (a) *LS+Gas* at shaking amplitude $A/d = 1.5$ ($f = 91\ Hz$), (b) *LS+Con* at shaking amplitude $A/d = 4.5$ ($f = 52.54\ Hz$).

in a container. Segregation is well affected by the presence of air (Naylor *et al.* 2003; Mobius *et al.* 2005; Gutiérrez *et al.* 2004) and the density related effects such as reverse buoyancy disappear in vacuum (Yan *et al.* 2003). The fluid-grain interaction, well understood, could be used to adequately rescale a particular configuration in order to avoid or enhance some effect [convection, segregation, vertical transport] (Reyes *et al.* 2005; King *et al.* 2007).

One of the remarkable demonstrations of the effect of air on granular segregation was reported by Burtally *et al.* (2002, 2003) who found experimentally that a mixture of fine bronze and glass particles of equal size (55 μm radius) segregates under vertical vibrations; the light particles are found to sink to the bottom, but only when air is forced through the granular bed. The effect appears to be very robust, and was also found in numerical simulations with few particles (3000) and a simplified description of the gas phase is given by Biswas *et al.* (2003). Zeilstra *et al.* (2006, 2008) investigated the effects of air forcing, friction and restitution coefficient, and the box size on the segregation behavior. They found that in addition to the interstitial air, friction also has a large influence on the formation of the sandwich structure of segregation. Burtally *et al.* (2002) reported the observation of the spontaneous separation of vertically vibrated mixtures of bronze and glass spheres of similar diameters. They investigated the interplay between granular separation and the influence of air on the motion. They found that if the air is slowly evacuated from the box containing mixtures, the segregation is eventually lost. In the low-frequency regime, the downward convection of the bronze at the front and the back faces of the box becomes increasingly evident as the pressure falls. At 10 to 15 $mbar$ with 20 Hz and at 20 to 25 $mbar$ with 40 Hz, rapid global convection thwarts any tendency to separate. At somewhat lower pressures, the surface Faraday tilting disappers. In the high-frequency regime, the bronze-rich region becomes increasingly diluted with glass and expands as the pressure is lowered. At 60 $mbar$ with 80 Hz, and at 90 $mbar$ with 140 Hz, the bronze-rich region has expanded to occupy the whole volume which now contains well-mixed grains carried on rapid convection currents. Thus, they showed that there is a strong tendency for glass and bronze particles to separate under vibration in the presence of air and the fact that segregation is avoided only if the air-pressure is substantially reduced suggested that air effects are important.

By treating the granular bed as a porous medium, the local variation in air-pressure, P', can be modeled by Darcy-Brinkman equation

$$\phi \frac{\partial P'}{\partial t} = P_0 \boldsymbol{\nabla} \cdot \left(\phi \frac{\kappa}{\mu} \boldsymbol{\nabla} P' \right) - P_0 \boldsymbol{\nabla} \cdot \boldsymbol{u} \tag{5.1}$$

where ϕ is the local porosity, κ is the permeability of the granular bed to air, μ is air viscosity, $\mathbf{u}$ is granular velocity, $\boldsymbol{\nabla}$ is the gradient operator, and P_0 is ambient air pressure (McNamara *et al.* 2000). At high ambient pressures and low vibrational frequencies, the time derivative in Eqn. 5.1 can be neglected. In this limit, the resultant force on the grains acts as viscous damping in the reference frame of container and is independent of P_0. An order of magnitude analysis of Eqn. 5.1 suggests that viscous damping will dominate for pressures greater than $10^{-6}\omega L^2/a^2$ $mbar$, where a is the radius of the grains and L is the length of the bed. Burtally *et al.* (2002) observed visible segregation only for pressures exceeding this value, hence segregation occurs in the damping-dominated regime.

Here, we will consider this theory of damping-dominated segregation to explain the hysteretic

transition which we observed in our experiments. We focussed on $F = 6$ layers of equimolar mixtures of steel and glass particles particles (both having diameter $d = 1.0\ mm$) confined in a container whose ambient air pressure can be controlled and maintained below the atmospheric pressure. The details of this pressure controlled container and the related equipments is discussed in Chapter 2. The experiments were done at a constant shaking amplitude $A/d = 3$ while upsweeping frequency upto a maximum value and then downsweeping it. Thus, the final state of the granular bed in upsweeping experiments is taken to be the initial state for the downsweeping experiments.

The maximum vertical extent h_{max}/d of various patterns are recorded for these upsweeping and downsweeping experiments and a bifurcation diagram has been prepared for various vaccuum levels inside the container as shown in Fig. 5.51. The sudden and sharp increase in the maximum height of the patterns h_{max}/d in Fig. 5.51(a) is a signature of the onset of the 'partial' convection *LS+Con* from *LS*, which can be identified in the phase diagrams shown in Fig. 5.1 at atmospheric pressure. It can be inferred that the transition *LS*→ *LS+Con* is hysteretic in nature at atmospheric pressure P_{atm} and interestingly this hysteresis keeps on decreasing as one evacuates the container and decreases the pressure inside the container more and more as depicted in Figs. 5.51(a-f). Note that the route followed by h_{max}/d with respect to Γ during downsweeping is different from the route while upsweeping, i.e., the onset value of *LS+Con* during upsweeping Γ_{crit} is different from onset value during downsweeping Γ^*_{crit}.

The above hysteresis can be explained based on the above viscous damping theory for segregation. We have established in the previous section that the horizontal segregation of steel and glass particles is the progenitor of *LS+Con* state in which the *LS* state is mostly dominated by glass particles and most of the steel particles were undergoing convective motion. Thus, the final state of the upsweeping experiments is the horizontally segregated *LS+Con* state (whose h_{max}/d is higher than that of other patterns as is evident in Fig. 5.51) and to mix the particles from this segregated state will require that the particles should be mobile enough in the horizontal direction. From Eqn. 5.1, we can work out the value of the vaccuum gauge pressure above which the dynamics will be viscous damping dominated and this value turns out to be 14.6 $mbar$ in our case for $L = 100\ mm$, $a = 0.5\ mm$ and for an average value of $\Gamma = 40(\omega = 361.66\ rad/s)$. Thus, the particles above this threshold value of pressure will be subjected to a viscous drag force and this drag force will increase with increasing pressure. The steel and glass particles will experience the same amount of viscous damping force when moving at the same velocity due to their equal size. Thus, above $P_0 \approx 14.6\ mbar$, particles will not be mobile enough to mix this already segregated state easily (it should be noted that a mixed state is required to give birth to complete *LS*) and as a result $\Gamma_{crit} > \Gamma^*_{crit}$ for the *LS+Con* resulting in a hysteresis. The degree of hysteresis will keep on increasing with increasing pressure inside the container due to increased drag and is maximum at atmospheric pressure P_{atm}. To check the robustness of this theoretical explanation of hysteresis we have plotted the same bifurcation diagrams for monodisperse glass particles as in Fig. 5.52 and expectedly found no hysteresis. Of course, since this is a monodisperse system there is no question of segregation (i.e. horizontal non-uniformity of the distribution of particles) and hence the onset values of 'complete' convection $\Gamma_{crit} \approx \Gamma^*_{crit}$ as depicted in Fig. 5.52.

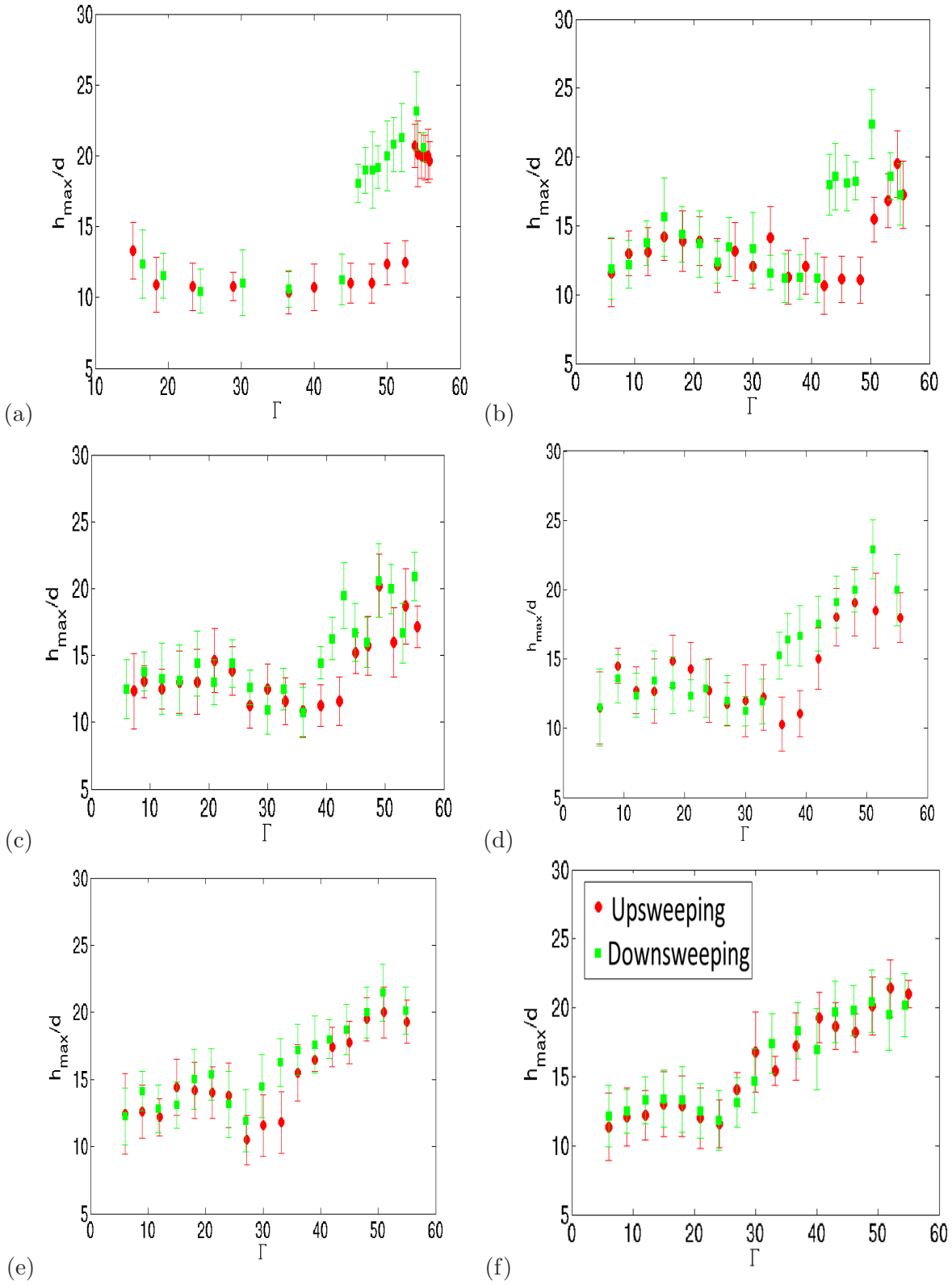

Figure 5.51: **Bifurcation diagram for the upsweeping and downsweeping experiments at (a) P_{atm}, (b) 780 $mbar$, (c) 700 $mbar$, (d)500 $mbar$, (e) 100 $mbar$, and (f) 30 $mbar$ showing hysteretic transition $LS \rightarrow LS+Con$ in equimolar mixture of steel and glass particles (both having diameter 1.0 mm). This hysteresis decreases as one decreases the ambient pressure inside the container.** Parameter values are $F_g + F_s = 6$ and $A/d = 3$.

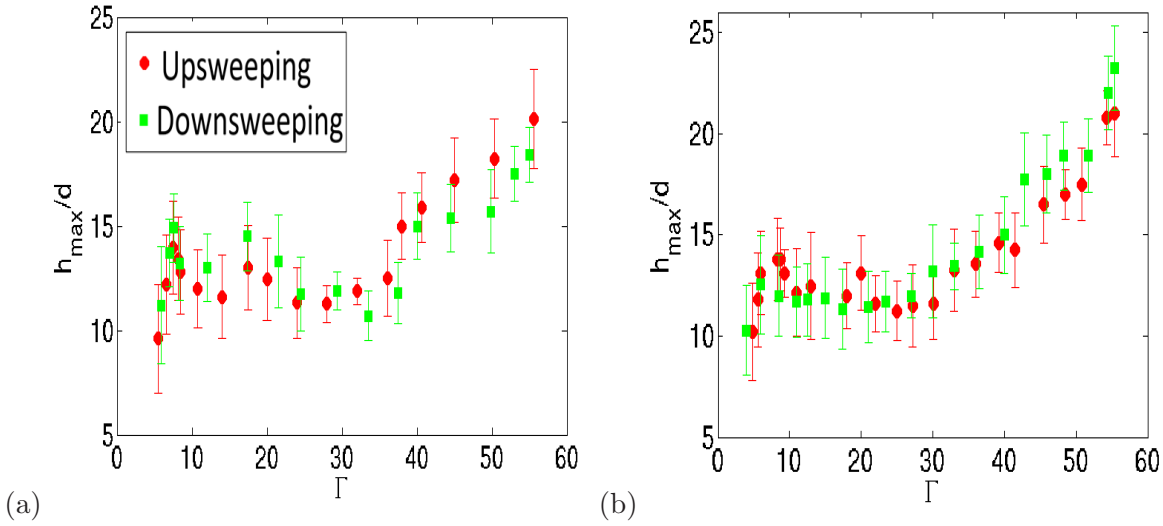

Figure 5.52: **Bifurcation diagram for the upsweeping and downsweeping experiments at (a) 30 *mbar*, and (b) P_{atm} for monosdisperse system of glass particles (1.0 *mm* diameter). Hysteresis is not observed for the transition *LS*→*Con* as expected.** Parameter values are $F = 6$ and $A/d = 3$.

5.4 Dynamical Patterns in Brass-Glass Particles Mixture

In this section we will discuss the pattern formation scenario in a mixture of brass and glass particles ($\rho_b/\rho_g \approx 3.46$ and both having diamater $d = 1.0\ mm$). This mixture is anologous to the steel-glass mixture in the sense that lighter particles are same (glass) while the density of heavier particles have been mildly increased to $\rho_b \approx 8650\ Kg/m^3$ in comparison to steel $\rho_s \approx 7650\ Kg/m^3$. Thus, due to the increased density difference between the two species (in comparison to steel-glass mixture) the segregation phenomenon is expected to be exhibited in a much pronounced way. The mixture is confined in the same standard Plexiglas® box of length $L/d = 100$ and width $W/d = 5.5$. The box is filled with a specified number of layers $F = F_b + F_g$, where F_b and F_g are the filling depths of brass and glass particles in the mixture, respectively. The various patterns observed are qualitatively and structurally similar to that realized in steel-glass mixture, but there are crucial differences in the phase diagrams. We will study the influences of species number fraction F_b/F and shaking amplitude A/d on the onset and suppression of various patterns by considering two filling depths $F = 3$ and 6, and thereby summarizing all the phenomena on $(\Gamma, F_b/F)$ and $(\Gamma, A/d)$-plane.

5.4.1 Phase Diagram in $(\Gamma, F_i/F)$-plane: Effect of Species Number Fraction

In this subsection, the phase diagrams depicting the influence of species number fraction on the onset of various patterns is discussed in a detailed manner. Since the system is bidisperse due to the density difference between two species, the phase-coexisting patterns are expected to appear. The related phase diagrams on $(\Gamma, F_b/F)$-plane are displayed in Fig. 5.53 for $F = 3$ and $F = 6$ layer depths. We will study the effect of varying number fraction of the two species in the mixture by traversing across various number fractions at a constant shaking intensity (Γ)

line on the phase diagram.

Focussing on Fig. 5.53(a), we observe that at lower shakings the bed transits from *Solid Bed (SB)* to 'complete' *Bouncing Bed (BB)* as the system approaches towards monodispersity ($F_b < 0.05$ and $F_b > 0.9$) but the bidispersity ($0.1 \leq F_b \leq 0.8$) leads to 'partial' *BB*. Further increasing Γ gradually leads the genesis of *LS+Gas* and *UW+Gas* from the *BB+Gas* state, while the *BB* state yields gaseous phase and *LS* at lower and higher values of F_b/F, respectively. Fig. 5.54 displays the various states encountered while increasing the proportion of brass particles in the mixture at constant $\Gamma \approx 7$. If one escalates Γ even more, the Leidenfrost region of *LS+Gas* state eventually melts into a loose cluster (stationary) at $\Gamma \approx 16$, whereas the gaseous regime at the two extremities of F_b/F (~ 0 and ~ 1) range still persists. This is evident from Fig. 5.55 and Fig. 5.56, where *Gas* and *Gas+Cluster* states are shown at constant $\Gamma = 20$ for different number fractions. Fig. 5.55(c) shows the clustered region in the middle of the container, while Fig. 5.55(d) shows the cluster on the left end. At very high shakings, convection evolves from the *Gas+Cluster* and *Gas* phase for $0.6 \leq F_b/F \leq 1$, but the gaseous regime at lower $F_b/F(< 0.1)$ does not transforms to *Convection*. We have displayed various transitions with increasing F_b/F at constant shaking intensity $\Gamma = 50$ in Fig. 5.57. It is noteworthy that in *Gas+Cluster* states at $\Gamma = 20$ and 50 (see Fig. 5.55(d) and Fig. 5.57(c)) the cluster can appear on the left and right ends of the container, this implies that stationary cluster can also occasionally shift from one end to another but these clusters are inherently different from *Oscillating Cluster* (wherein the cluster continuously drifts horizontally from one end of the container to another). Furthermore, the snapshots in Fig. 5.55(d) and Fig. 5.57(c) reveal that the size of the cluster has decreased at higher shaking intensity ($\Gamma = 50$) due to the expulsion of brass particles from the clustered chunk of mixture with increasing Γ.

Let us shift our attention to the phase diagram for $F = 6$ layer depth as displayed in Fig. 5.53(b). Since the filling depth has been increased, the 'partial' BB and the 'partial' UW are absent in the phase diagram, instead 'complete' states are observed at lower shaking strengths. The *Spikes* pattern is seen to be more stable than in the mixture of steel-glass, but they still occupy a very small range of Γ. The *Spikes*-patterns for different number fractions at constant $\Gamma \approx 7$ are shown in Fig. 5.58. It is remarkable that although various *Spikes*-patterns in Fig. 5.58(a-d) correspond to the same shaking amplitude $A/d = 3$, the heights upto which the peak rises differ, suggesting that the evolution of the peak strongly depends on the mixture proportion.

Increasing the shaking intensity (Γ) to $\Gamma = 8$ transforms *Spikes* into *UW* as shown in Fig. 5.59 where different modes are displayed. Further escalating the shaking intensity transits the bed to *LS* and *LS+Gas*, though the 'partial' *LS* state rapidly transforms to a 'complete' *LS* state. Fig. 5.60 displays various states at constant $\Gamma \approx 13$ and it is noteworthy that the gaseous phase of the *LS+Gas* state occupies a small volume (although it is discernible) since the snapshot correpsonds to a lower Γ.

At even higher shaking intensity ($\Gamma = 30$) the *LS* and *LS+Gas* states mutually transform into one another for different ranges of F_b/F as depicted in Fig. 5.61. At very high shakings ($\Gamma = 50$), the particles in the bed start undergoing the convective motion either 'partial' or spanning the whole of the container (see Fig. 5.63). The system undergoes 'complete' *Convection* in the

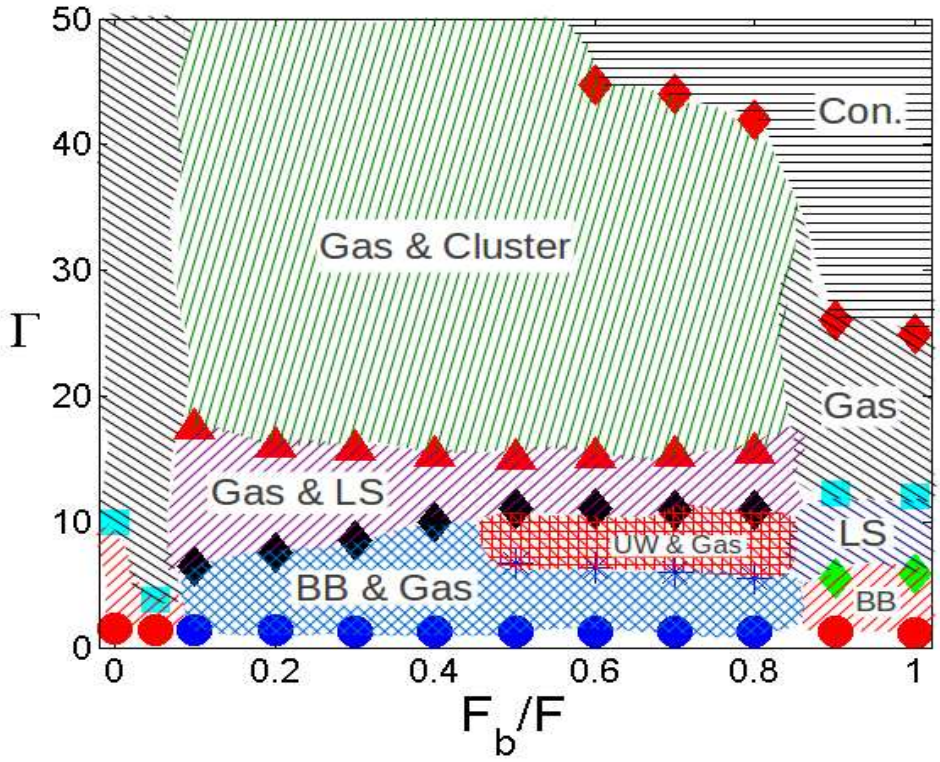

(a)

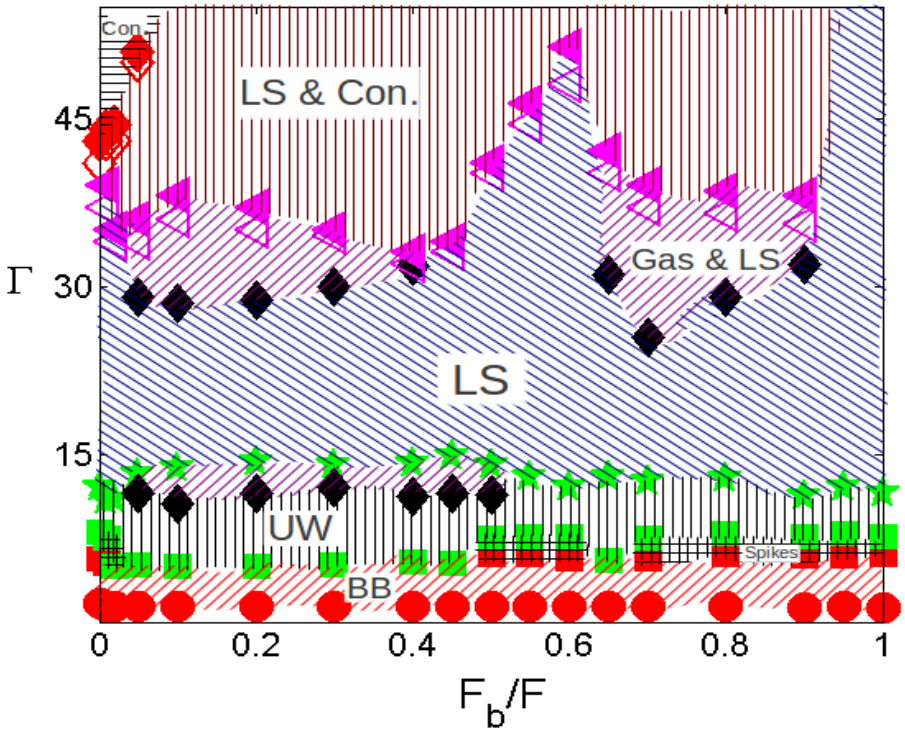

(b)

Figure 5.53: **Phase diagram in $(\Gamma, F_b/F)$-plane for mixture of brass and glass particles (both having diameter $d = 1.0\ mm$) for total filling depth: (a) $F = F_b + F_g = 3$, and (b) $F = F_b + F_g = 6$.** *Ramping rate* is 0.01 Hz/sec.

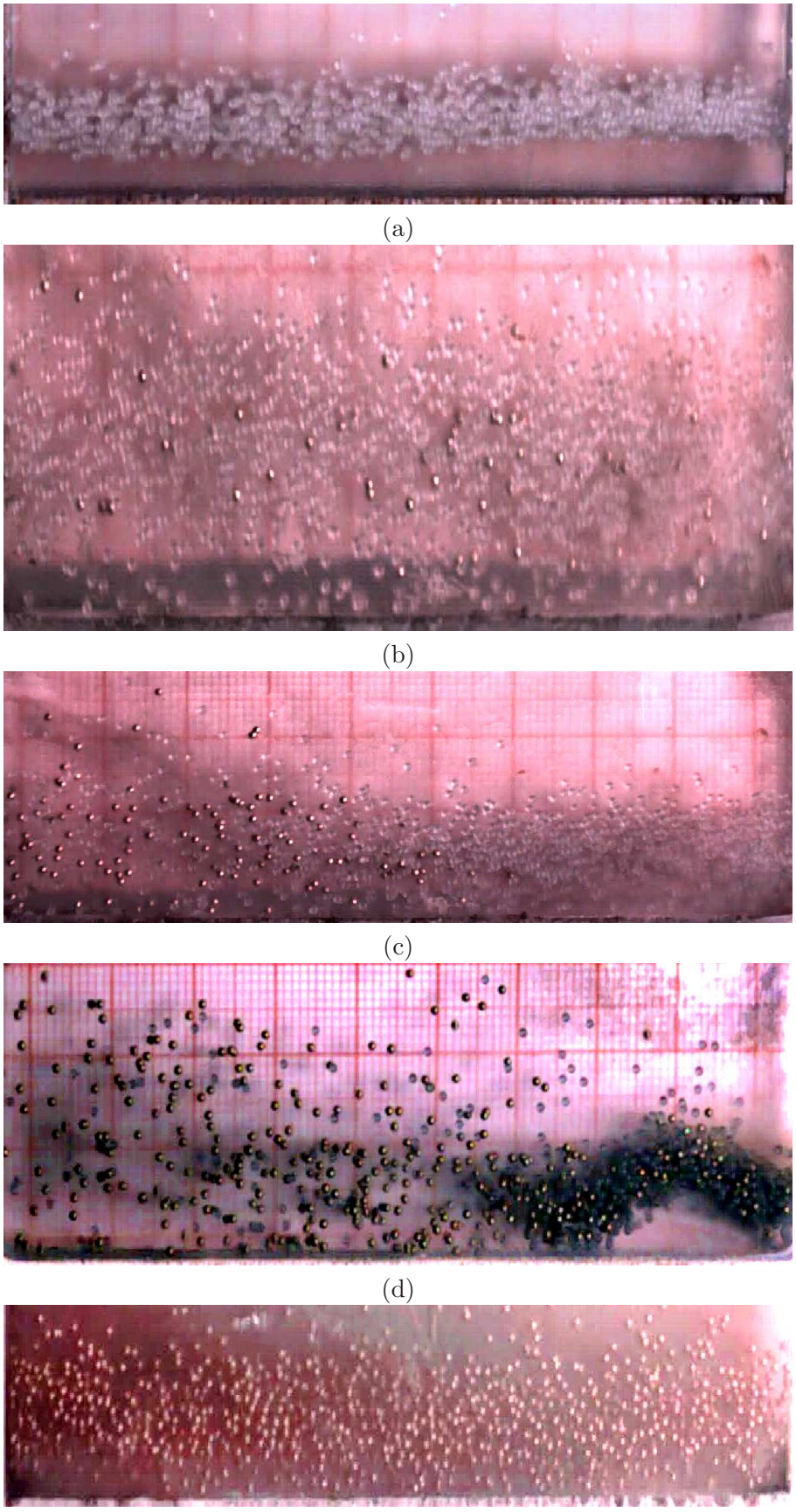

(a)

(b)

(c)

(d)

(e)

Figure 5.54: **Transition at constant shaking intensity $\Gamma \approx 7$ in $F = F_b + F_g = 3$ layers of mixture of brass and glass particles:** (a) *BB* at $F_b/F = 0$, (b) *Gas* at $F_b/F = 0.05$, (c) *Gas+LS* at $F_b/F = 0.1$, (d) *UW+Gas* at $F_b/F = 0.5$, and (e) *LS* at $F_b/F = 1$. Other parameters values are $A/d = 3$ and $f \approx 24\ Hz$.

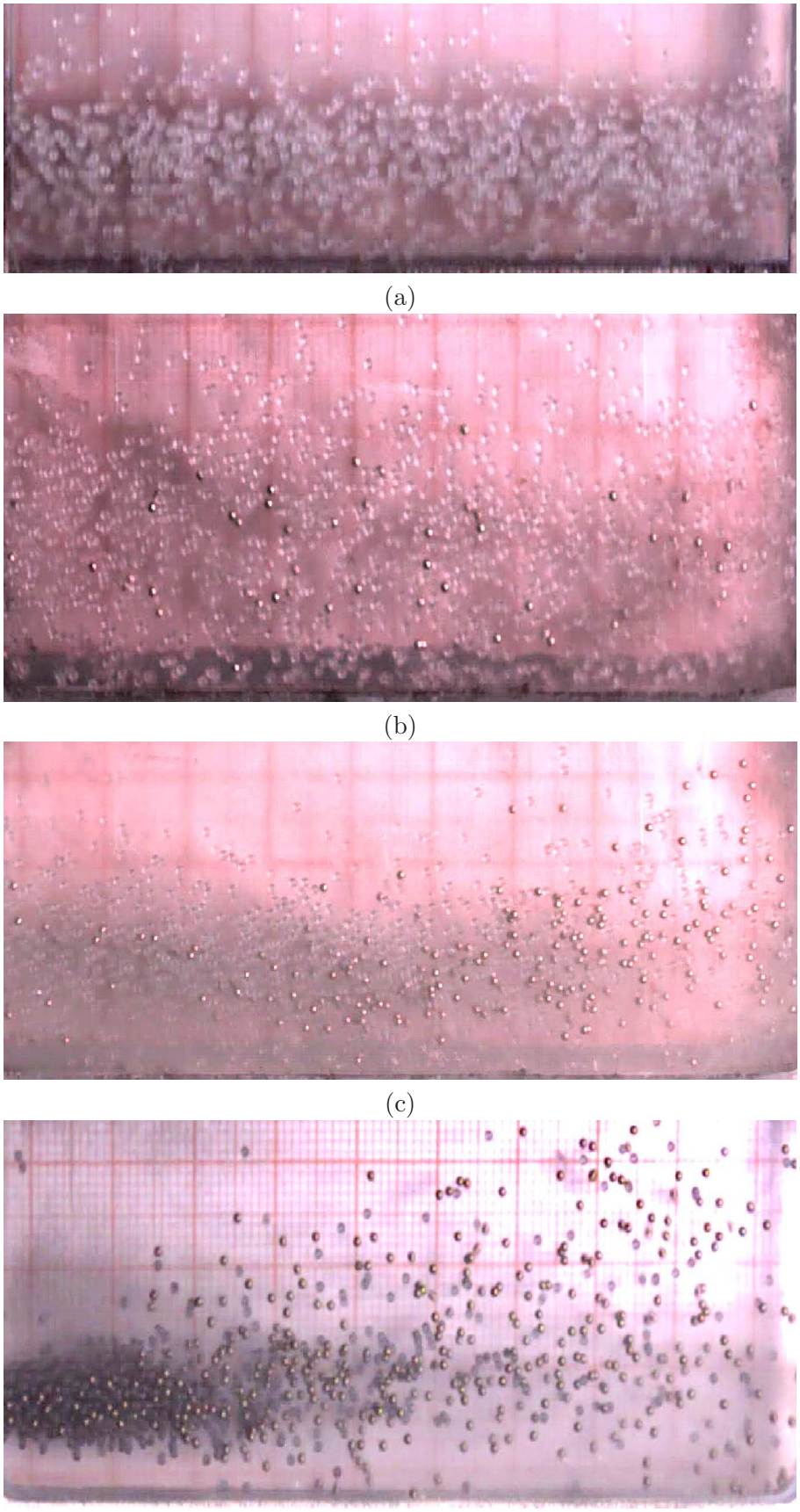

(a) (b) (c) (d)

Figure 5.55: **Transition at constant shaking intensity $\Gamma = 20$ in $F = F_b + F_g = 3$ layers of mixture of brass and glass particles:** (a) *Gas* at $F_b/F = 0$, (b) *Gas* at $F_b/F = 0.05$, (c) *Gas+Cluster* at $F_b/F = 0.2$, (d) *Gas+Cluster* at $F_b/F = 0.5$. Other parameters values are $A/d = 3$ and $f = 40.7\ Hz$.

(e)

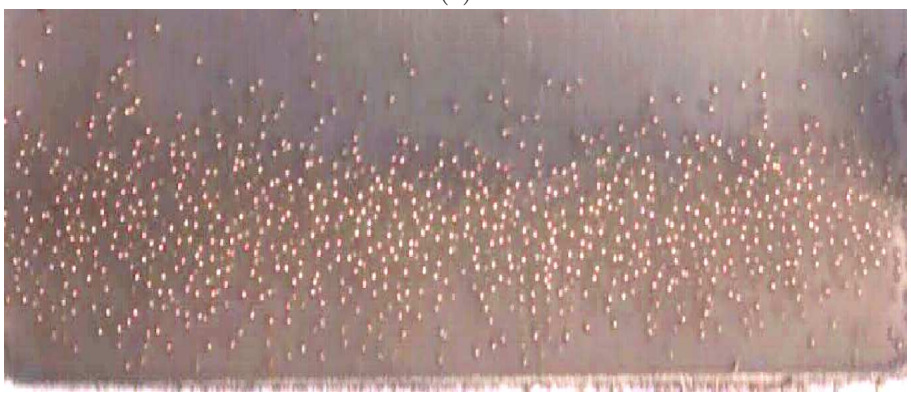

(f)

Figure 5.56: *Continued Fig. 5.55* **Transition at constant shaking intensity $\Gamma = 20$ in $F = F_b + F_g = 3$ layers of mixture of brass and glass particles:** (e) *Gas* at $F_b/F = 0.9$ and (f) *Gas* at $F_b/F = 1$. Other parameters values are $A/d = 3$ and $f = 40.7\ Hz$.

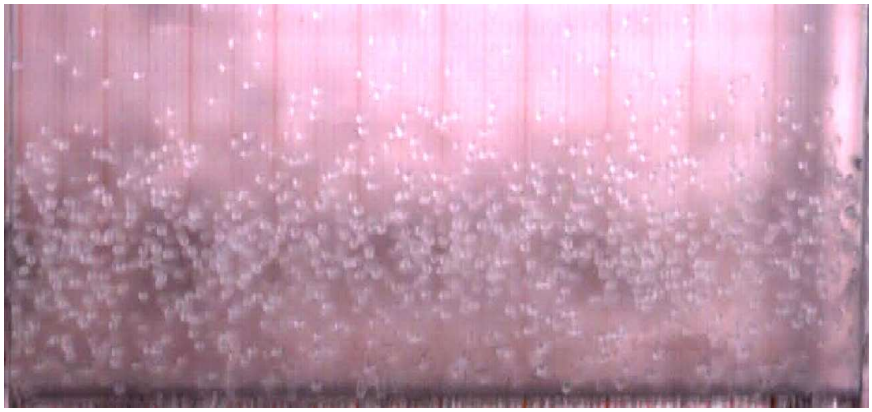

(a)

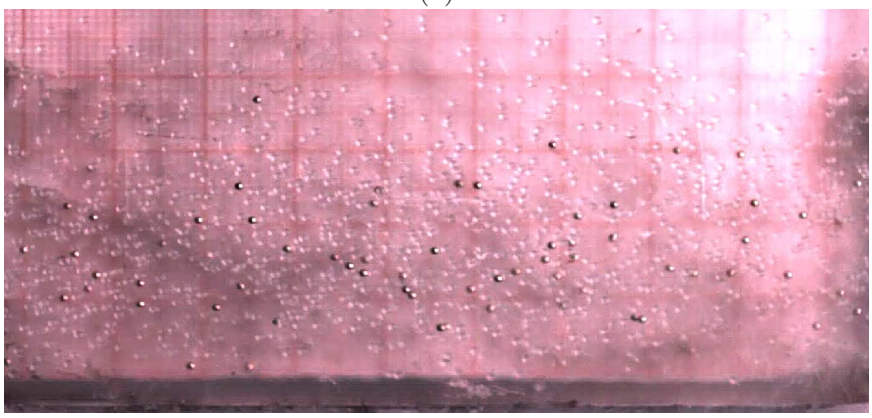

(b)

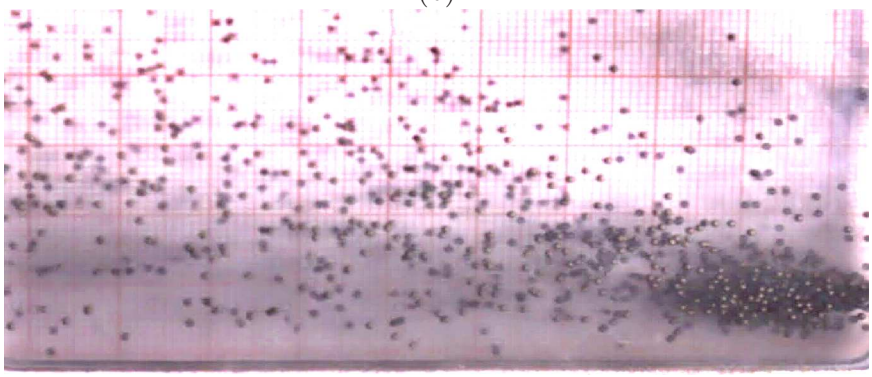

(c)

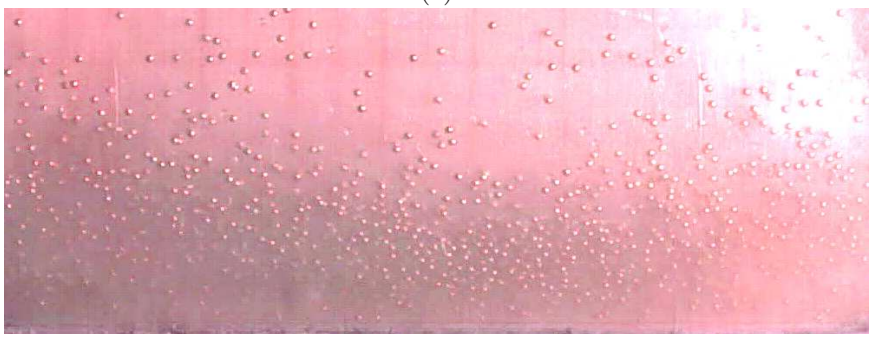

(d)

Figure 5.57: **Transition at constant shaking intensity $\Gamma = 50$ in $F = F_b + F_g = 3$ layers of mixture of brass and glass particles:** (a) *Gas* at $F_b/F = 0$, (b) *Gas* at $F_b/F = 0.05$, (c) *Gas+Cluster* at $F_b/F = 0.5$. (d) *Convection* at $F_b/F = 0.9$. Other parameters values are $A/d = 3$ and $f = 64.35\ Hz$.

monodiperse glass case ($F_b/F = 0$) and this persists when a small bidispersity is introduced in the system (with the addition of heavier brass particles), but increasing this bidispersity transforms the system to a 'partial' convective state, *LS+Con*, as shown in Fig. 5.62. We did not observe *Convection* in this mixture having very high proportion of brass particles ($F_b/F > 0.5$), instead *LS* is realized (refer Fig. 5.62(e)). Figure 5.63 shows the PIV maps for the 'complete' and 'partial' convective states of Fig. 5.62, wherein six counter rotating convection rolls are identified for $F_b/F = 0.01$ and a pair of counter rotating rolls coexisting with *LS* in cases of $F_b/F = 0.2$ and 0.5. This once again bolsters our demonstration of 'Convection Control' by addition of heavier particles in the mixture as discussed in subsection 5.2.4.

5.4.2 Phase Diagram in $(\Gamma, A/d)$-plane: Effect of Shaking Amplitude

We will now discuss the phase diagrams depicting the effect of shaking amplitude A/d on various phenomena in $F = 3$ and 6 layer depths of an equimolar mixture of brass and glass particles. These phase diagrams are displayed in Fig. 5.64. Focussing on the phase diagram for $F = 3$ filling depth (see Fig. 5.64(a)), it is evident that for very low shaking intensity ($\Gamma \sim 2$) the bed shows 'complete' *BB* at smaller A/d but at larger A/d this *BB* sustains for a very small range of Γ which eventually transits to *BB+Gas*. Note that for $A/d \in (0.9, 3)$ ranging from $(0.9, 3)$ the bed directly transforms from *SB* to *BB+Gas*. As one increases the Γ-level a little more, this *BB+Gas* state switches to *UW+Gas* state for $2 \leq A/d \leq 5$, while for even higher shaking amplitude A/d the 'partial' *BB* transits to a *Gas+Cluster* state. It can be easily perceived that a higher shaking amplitude is likely to loosen the compact aggregate of particles forming the *BB* portion of the *BB+Gas* state and thereby melts it into a loose blob, giving birth to a *Gas+Cluster* state.

The various states realized at constant $\Gamma \approx 8$ with increasing A/d are displayed in Fig. 5.65. Figure 5.65(d) shows $n = 2$ mode of *UW* coexisting with gas, while Fig. 5.65(e) depicts $n = 1$ mode coexisting with a gas. Further increasing the shaking intensity (Γ) to 25 leads to new states of *LS*, *LS+Gas*, *Gas+Cluster*, and 'complete' *Gas* depending upon the mixture proportion as displayed in Fig. 5.66.

Returning to the phase-diagram in Fig. 5.64(a), we see that at higher shakings ($\Gamma > 30$) and amplitudes ($3.25 \leq A/d \leq 6$), the 'stationary' cluster starts oscillating, giving birth to *Oscillating Cluster (OsClus)* state. Figure 5.67 shows such *OsClus* at $A/d = 3.25$ and 4.5, which has been realized while ramping the frequency linearly at a rate of 0.01 Hz/s. Note that *OsClus* is not achieved below $A/d = 3.25$ (see Fig. 5.64(a)) and this is the reason why it was not shown in Fig. 5.53(a) (since the phase diagram of Fig. 5.53(a) is obtained at constant $A/d = 3$). Comparing the phase diagram of brass-glass mixture (Fig. 5.64(a)) with that of steel-glass (refer Fig. 5.43(a)), one finds a remarkable difference that in the case of steel-glass mixtures the *OsClus* state eventually melts into a 'complete' *Gas* at higher shakings, thereby shrinking the *OsClus* regime along Γ- axis, though comparatively it spans over a larger range of shaking amplitude A/d. A similar transition from "*OsClus*" to a gas may occur also for the brass-glass mixture if we could apply even higher Γ-levels (> 50).

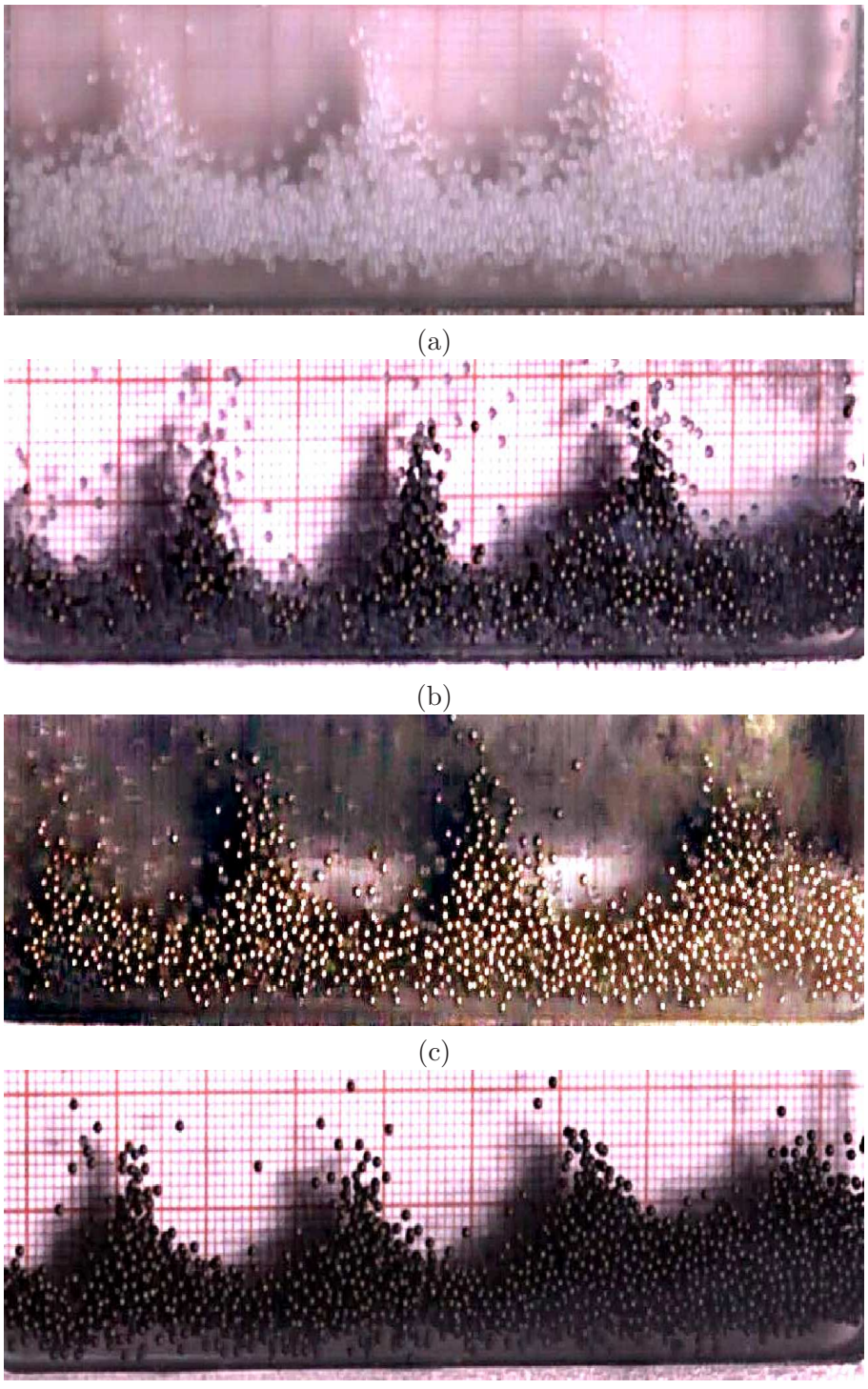

(a) (b) (c) (d)

Figure 5.58: ***Spikes*** **pattern at constant shaking intensity $\Gamma \approx 7$ in $F = F_b + F_g = 6$ layers of mixture of brass and glass particles for various species number fraction:** (a) $F_b/F = 0$, (b) $F_b/F = 0.5$, (c) $F_b/F = 0.8$, (d) $F_b/F = 1$. Other parameters values are $A/d = 3$ and $f \approx 24\ Hz$.

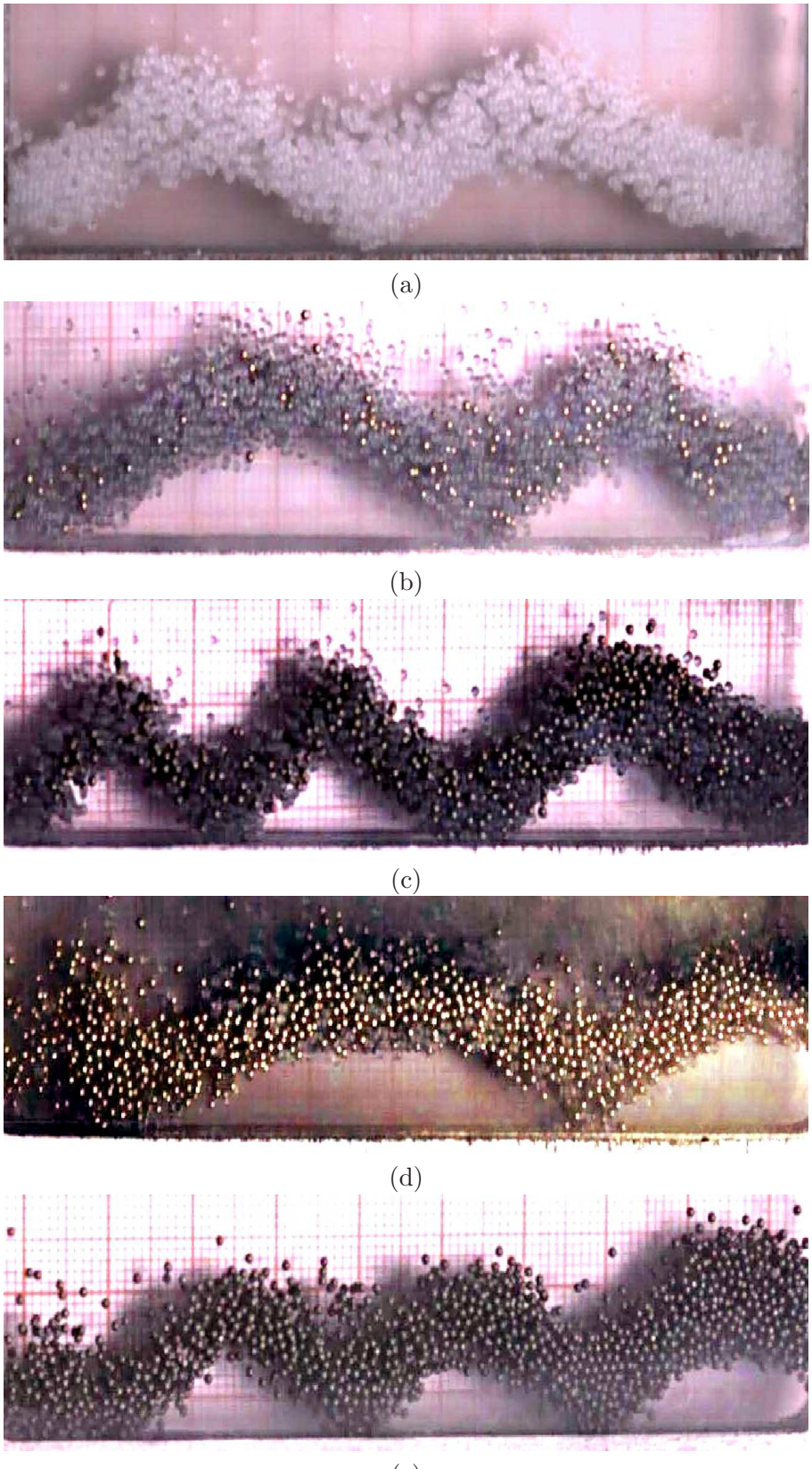

(a)

(b)

(c)

(d)

(e)

Figure 5.59: ***Undulatory Waves*** **at constant shaking intensity $\Gamma \approx 8$ in $F = F_b + F_g = 6$ layers of mixture of brass and glass particles for various species number fraction:** (a) $n = 4$ mode at $F_b/F = 0$, (b) $n = 4$ mode at $F_b/F = 0.2$, (c) $n = 6$ mode at $F_b/F = 0.5$, (d) $n = 3$ mode at $F_b/F = 0.8$, and (e) $n = 5$ mode at $F_b/F = 1$. Other parameters values are $A/d = 3$ and $f \approx 25.7\ Hz$.

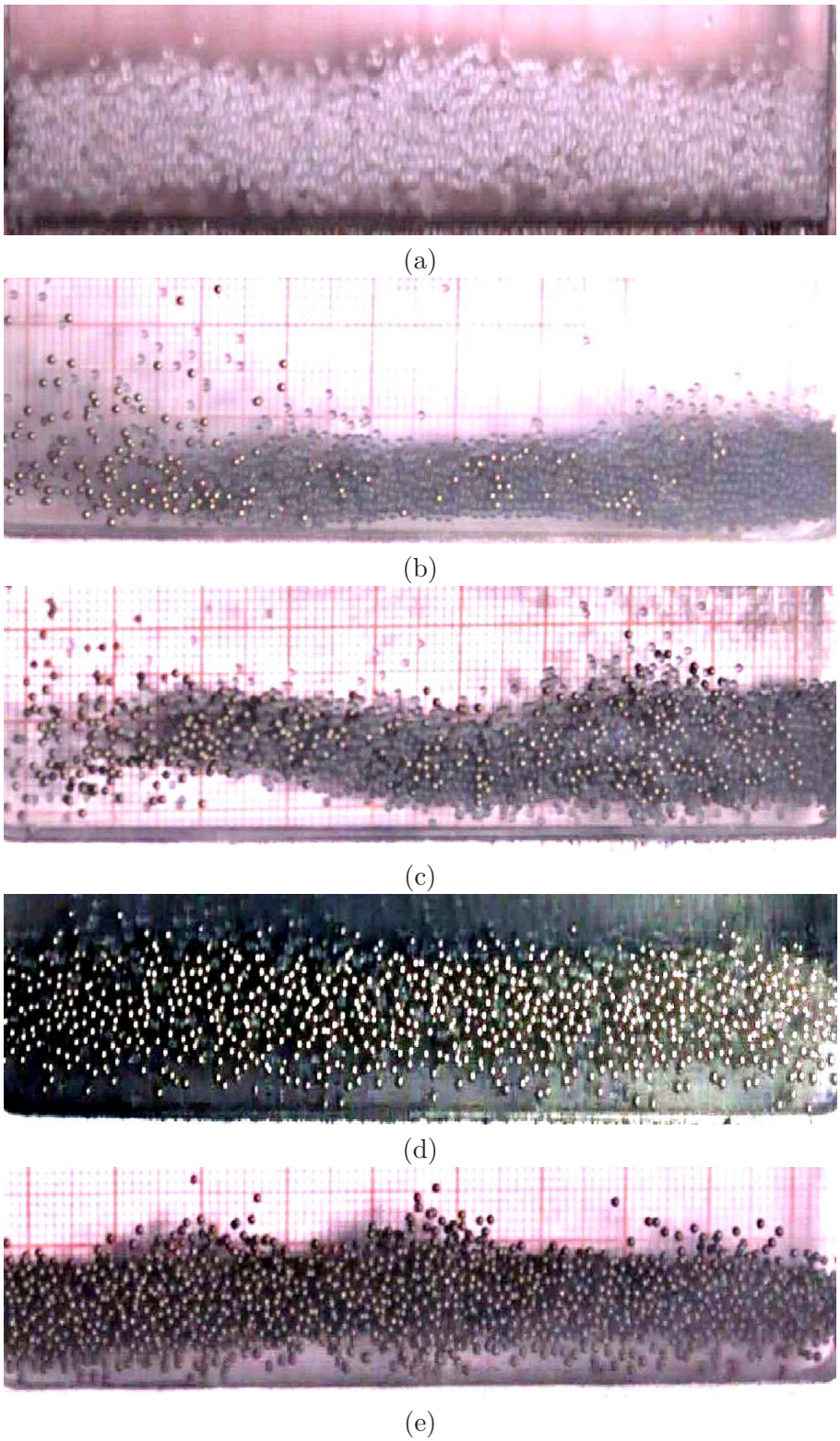

(a)

(b)

(c)

(d)

(e)

Figure 5.60: **Transition at constant shaking intensity $\Gamma \approx 13$ in $F = F_b + F_g = 6$ layers of mixture of brass and glass particles:** (a) *LS* at $F_b/F = 0$, (b) *Gas+LS* at $F_b/F = 0.2$, (c) *Gas+LS* at $F_b/F = 0.5$, (d) *LS* at $F_b/F = 0.8$, and (e) *LS* at $F_b/F = 1$. Other parameters values are $A/d = 3$ and $f \approx 32.8\ Hz$.

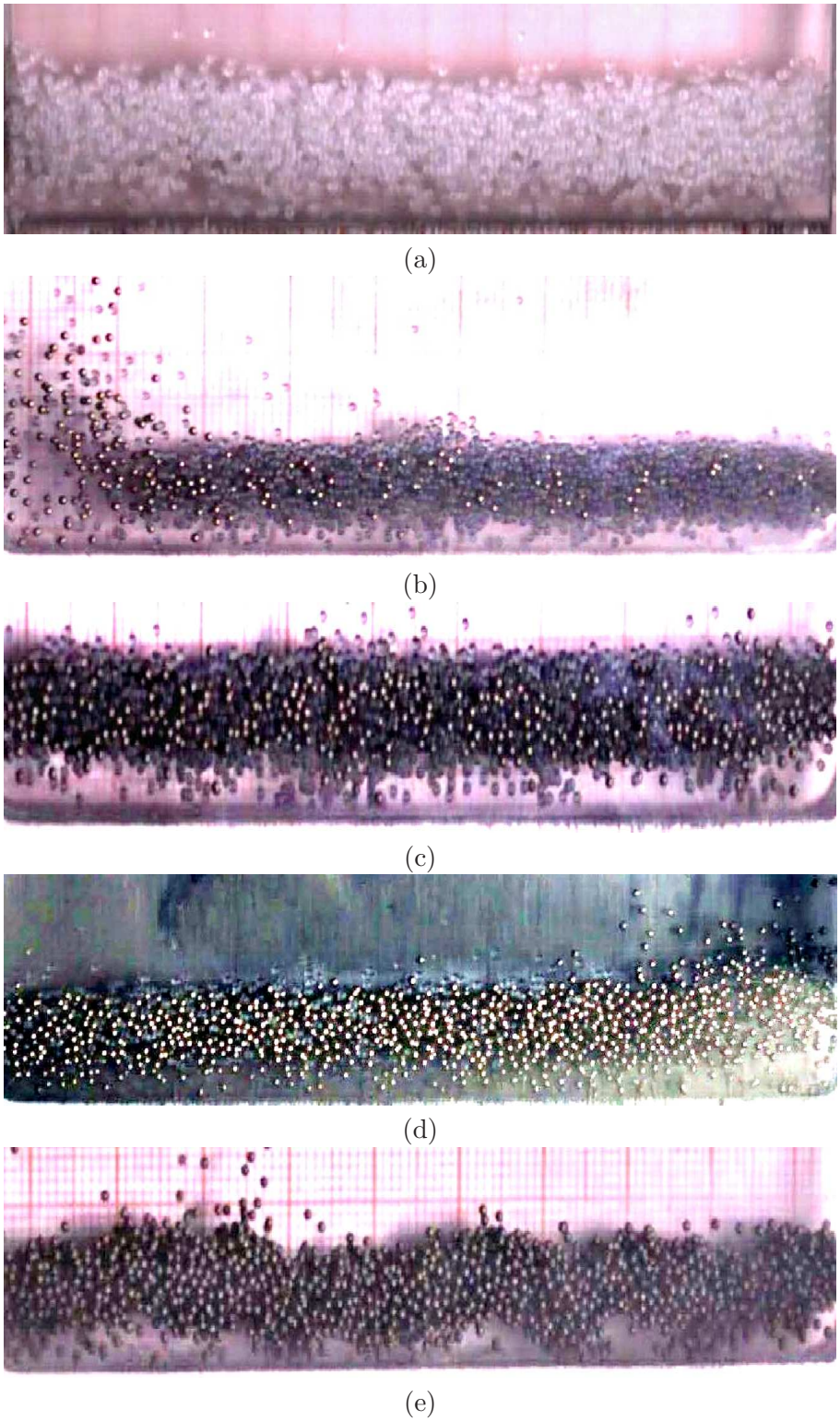

Figure 5.61: **Transition at constant shaking intensity $\Gamma = 30$ in $F = F_b + F_g = 6$ layers of mixture of brass and glass particles:** (a) *LS* at $F_b/F = 0$, (b) *Gas+LS* at $F_b/F = 0.2$, (c) *LS* at $F_b/F = 0.5$, (d) *Gas+LS* at $F_b/F = 0.8$, and (e) *LS* at $F_b/F = 1$. Other parameters values are $A/d = 3$ and $f = 49.84\ Hz$.

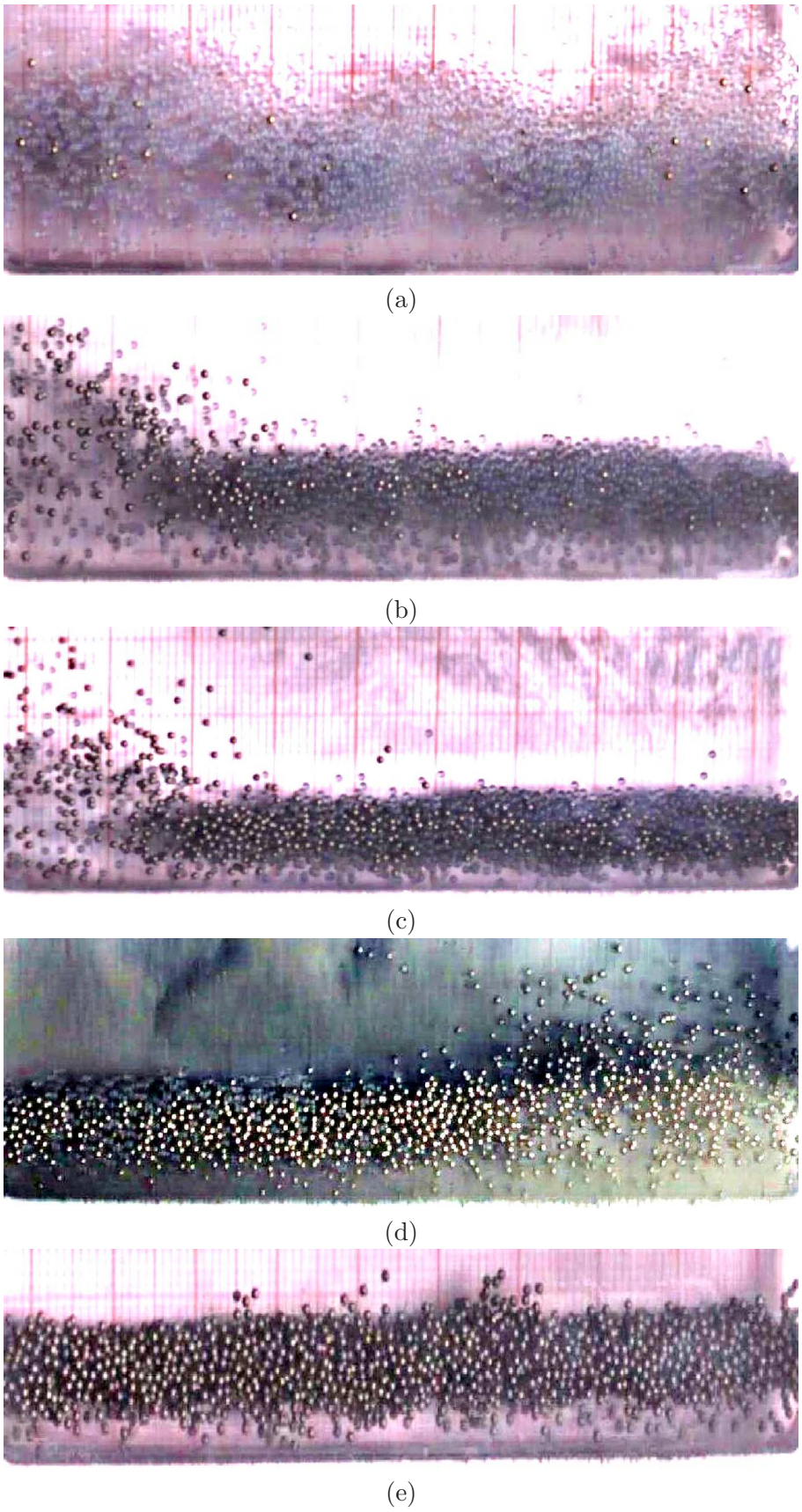

(a) (b) (c) (d) (e)

Figure 5.62: **Transition at constant shaking intensity $\Gamma = 50$ in $F = F_b + F_g = 6$ layers of mixture of brass and glass particles:** (a) *Convection* at $F_b/F = 0.01$, (b) *LS+Con.* at $F_b/F = 0.2$, (c) *LS+Con.* at $F_b/F = 0.5$, (d) *LS+Con.* at $F_b/F = 0.8$, and (e) *LS* at $F_b/F = 1$. Other parameters values are $A/d = 3$ and $f = 64.35\ Hz$.

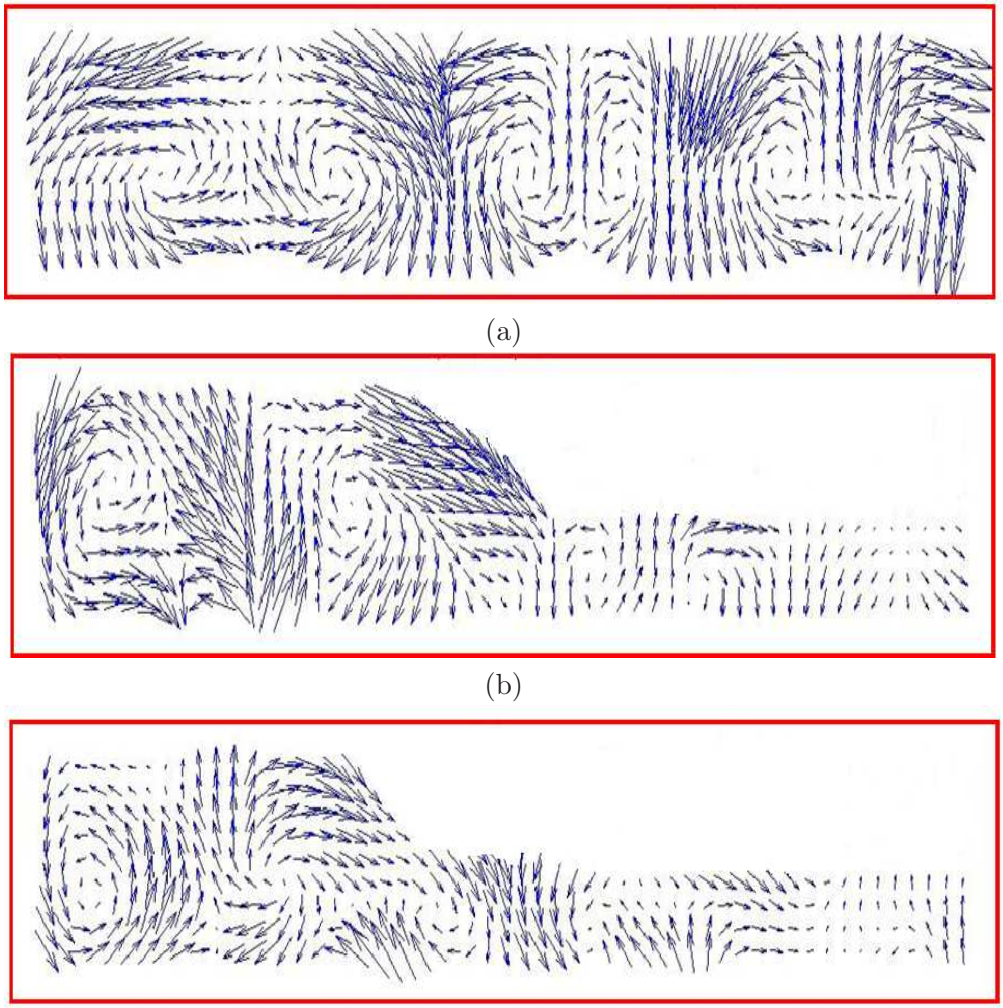

(a)

(b)

(c)

Figure 5.63: **Velocity vectors obtained from PIV of Fig. 5.62(a), Fig. 5.62(b), and Fig. 5.62(c).**

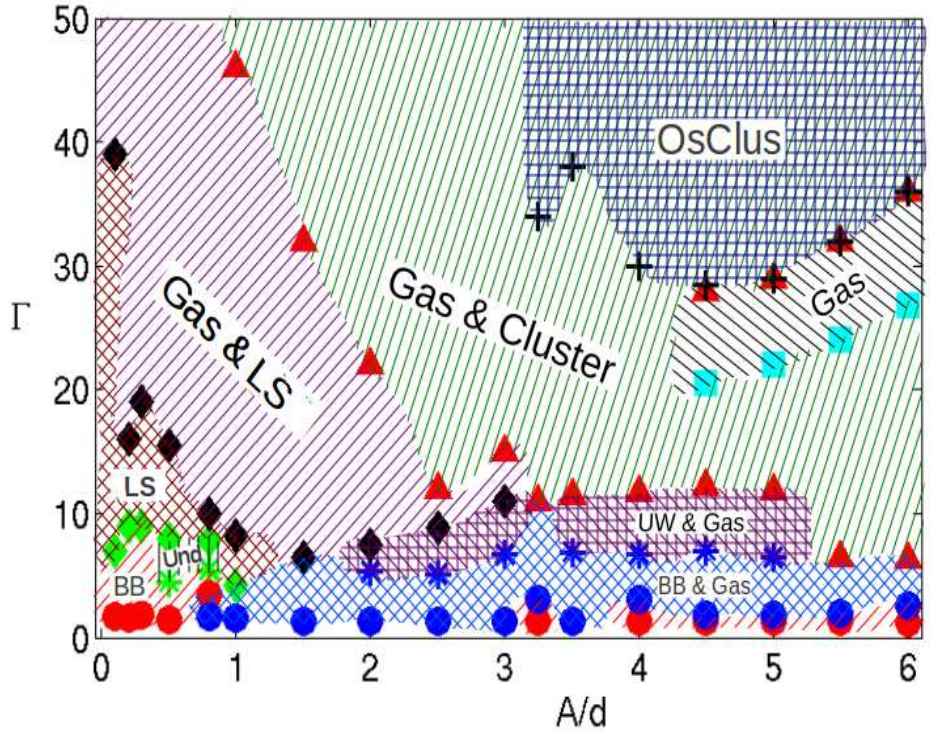

(a)

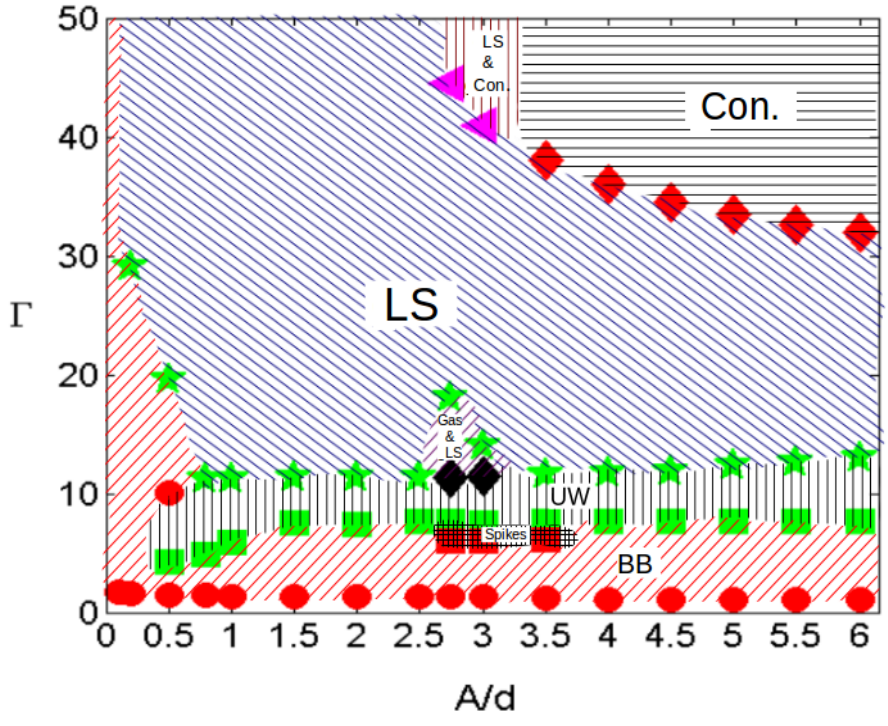

(b)

Figure 5.64: **Phase diagram in $(\Gamma, A/d)$-plane for equimolar mixture of brass and glass particles (both having diameter $d = 1.0\ mm$) for total filling depth: (a) $F = F_b + F_g = 3$, and (b) $F = F_b + F_g = 6$.** *Ramping rate* is 0.01 Hz/sec.

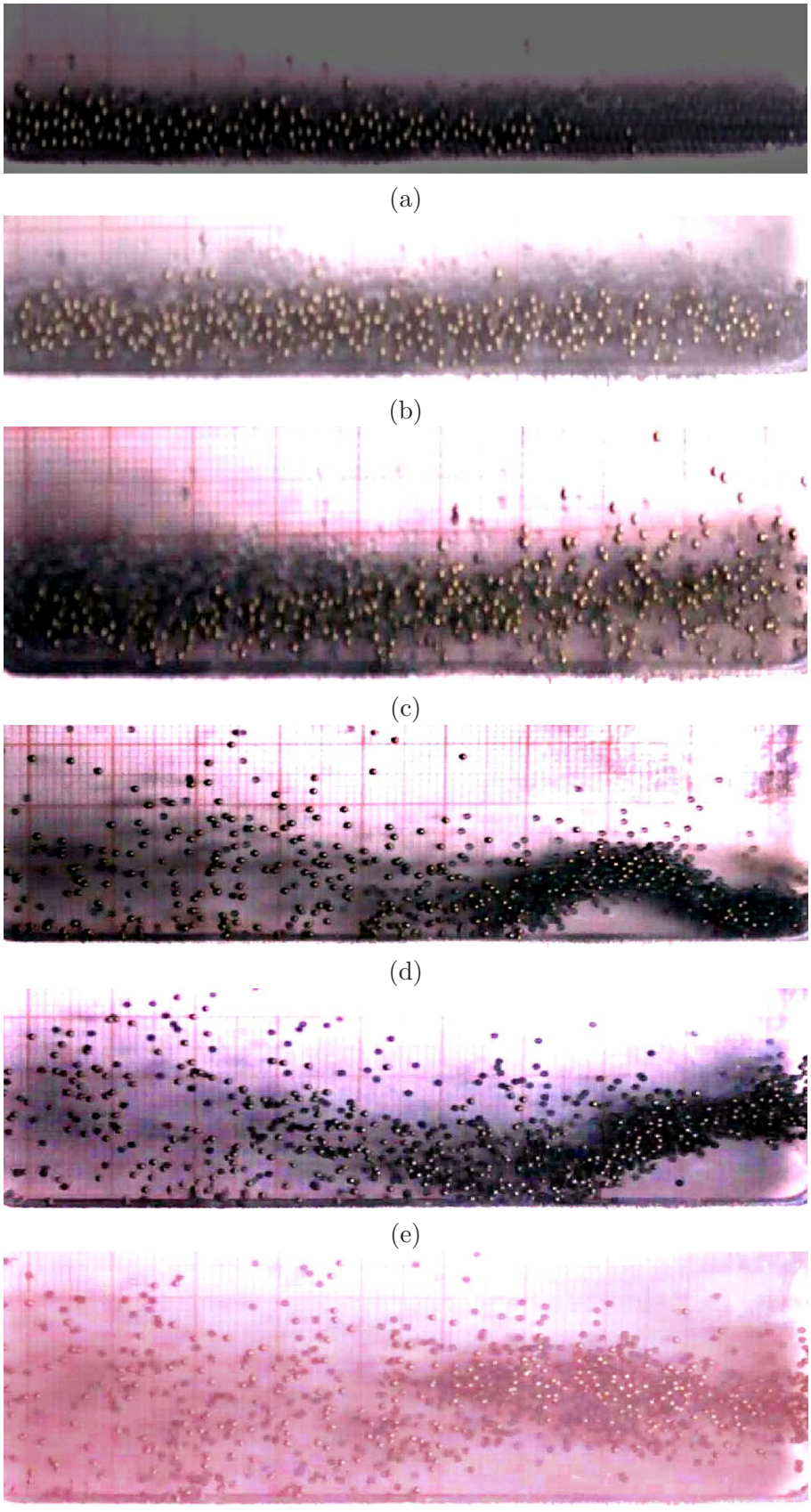

(a)

(b)

(c)

(d)

(e)

(f)

Figure 5.65: **Transition at constant shaking intensity $\Gamma \approx 8$ in $F = F_b + F_g = 3$ layers of equimolar mixture of brass and glass particles:** (a) *BB* at $A/d = 0.3$ ($f = 81.4\ Hz$), (b) *LS* at $A/d = 1$ ($f = 44.58\ Hz$), (c) *Gas+LS* at $A/d = 1.5$ ($f = 36.4\ Hz$), (d) *UW+Gas* at $A/d = 3$ ($f = 25.7\ Hz$), (e) *UW+Gas* at $A/d = 4.5$ ($f = 21\ Hz$), and (f) *Gas+Cluster* at $A/d = 6$ ($f = 18.2\ Hz$).

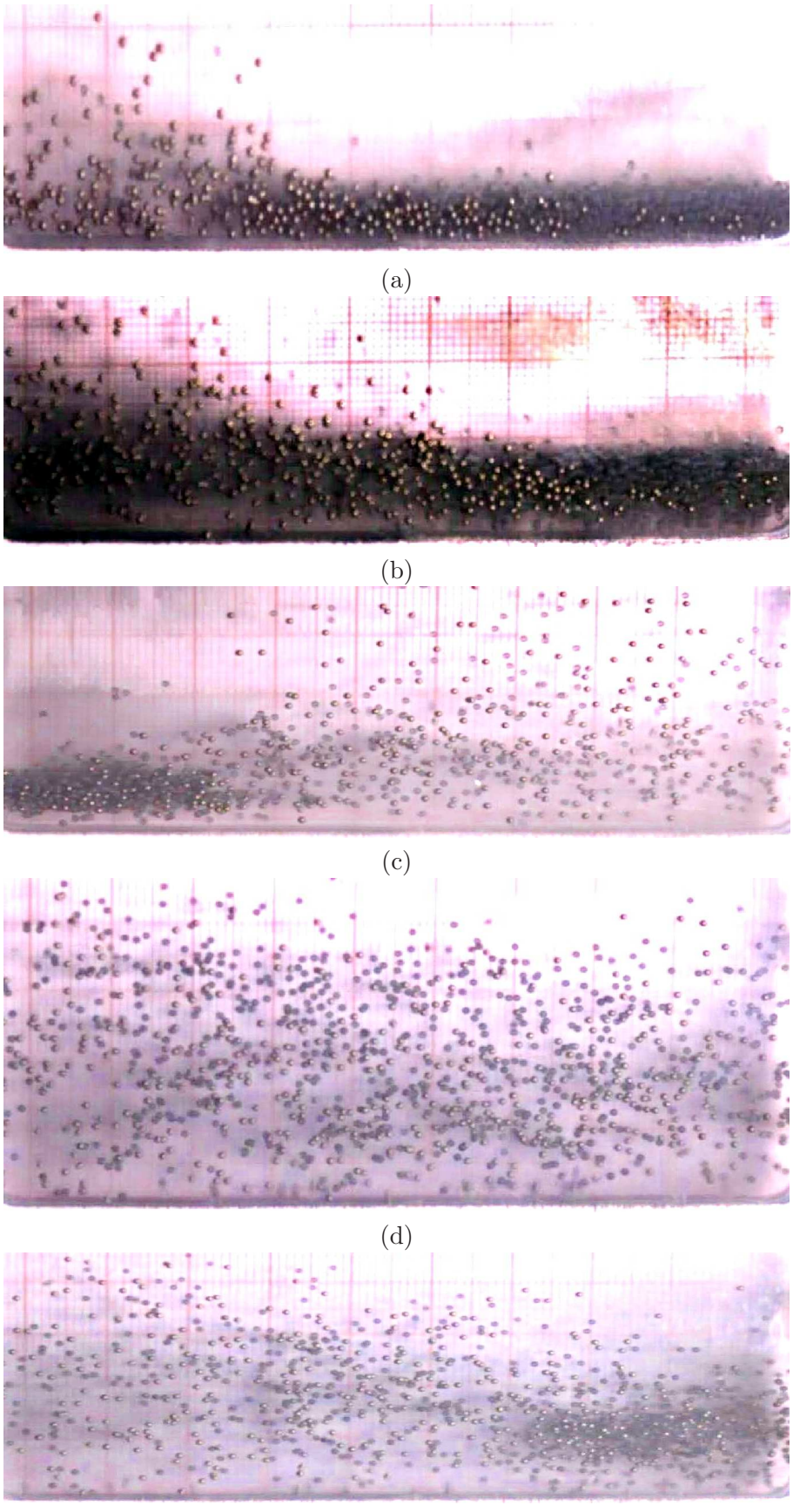

(a)

(b)

(c)

(d)

(e)

Figure 5.66: **Transition at constant shaking intensity $\Gamma = 25$ in $F = F_b + F_g = 3$ layers of equimolar mixture of brass and glass particles:** (a) *Gas+LS* at $A/d = 0.5$ ($f = 111.5\ Hz$), (b) *Gas+LS* at $A/d = 1.5$ ($f = 64.35\ Hz$), (c) *Gas+Cluster* at $A/d = 3$ ($f = 45.5\ Hz$), (d) *Gas* at $A/d = 4.5$ ($f = 37.15\ Hz$), and (e) *Gas+Cluster* at $A/d = 6$ ($f = 32.17\ Hz$).

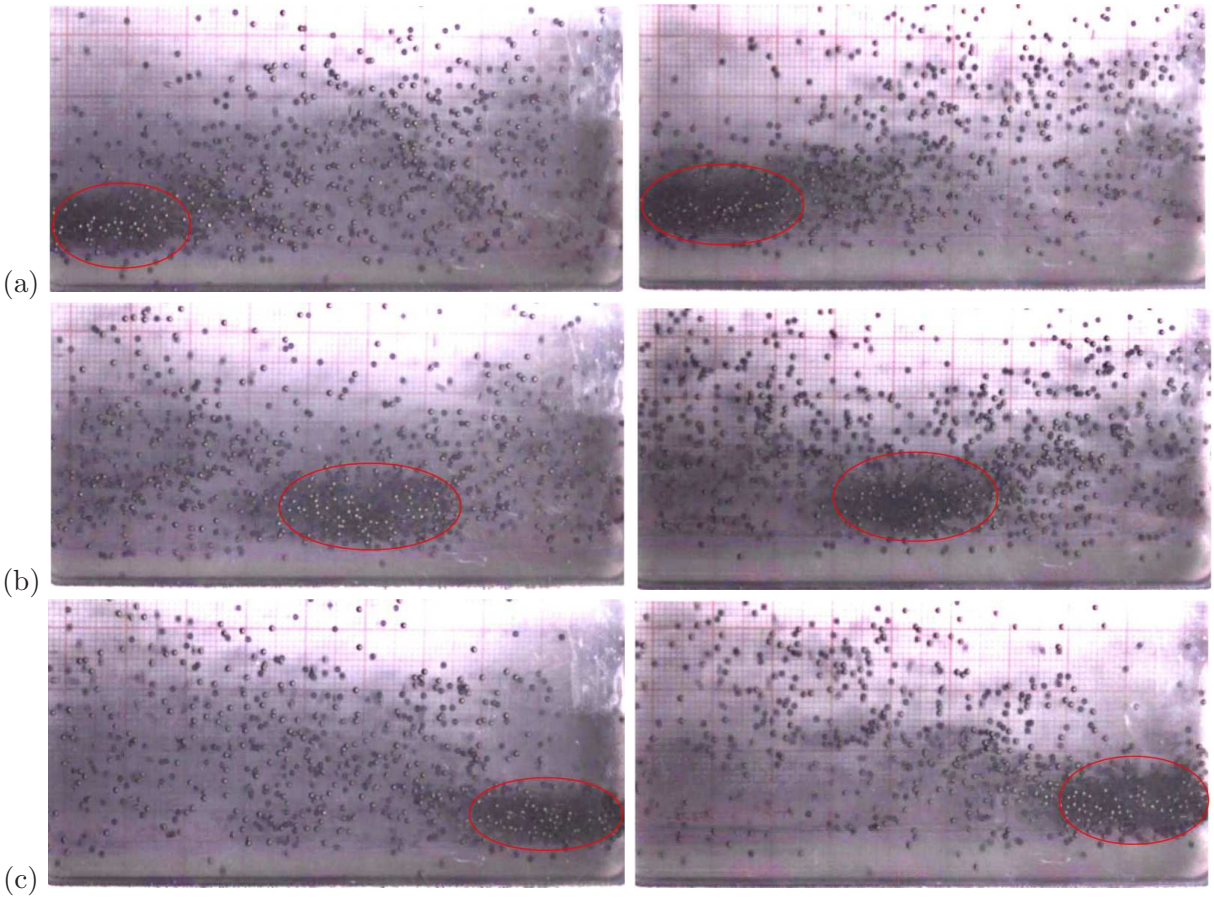

Figure 5.67: **Snapshots of *Oscillating Cluster* in $F = F_b + F_g = 3$ layers of equimolar mixture of brass and glass particles:** (a) cluster on the left side of the container, (b) cluster in the mid of the container, and (c) cluster on the right side of the container. Left panel: $A/d = 3.25$ ($\Gamma = 43.36 - 44.46$, $f = 57.58 - 58.31\ Hz$). Right panel: $A/d = 4.5$ ($\Gamma = 36.5 - 37.82$, $f = 44.9 - 45.7\ Hz$). Frequency ramping rate is 0.01 Hz/s

Now, we turn our focus to the higher filling depth case ($F = 6$) of the same equimolar mixture of brass and glass particles, for which we will attempt to discuss the effect of varying shaking ampltude A/d on the onset and suppression of various types of pattern, the related phase diagram is diplayed in Fig. 5.64(b)). In consistency with the previously discussed results, as the filling depth is increased, the 'partial' states have almost vanished, but these states in the steel-glass mixture have occupied a larger area of the phase diagram than in the brass-glass mixture (compare Fig. 5.43(b) and Fig. 5.64(b)).

The various states observed at constant $\Gamma \approx 7$ with increasing A/d are shown in Fig. 5.68. The *Spikes* pattern has been realized for a very small range of $2.75 \leq A/d \leq 3.5$, sandwiched between *BB* and *UW* regimes, and the *UW* states are found to be consistenly stable for a large range of A/d. These *UW* states are displayed in Fig. 5.69 at various shaking ampltudes A/d for constant $\Gamma \approx 9$, therein it can be figured out clearly that the peak height increases proportionally with A/d. Further increasing the Γ gradually makes the bed to transit to *LS*, save for a small interval of $A/d \in (2.75, 3)$ which shows *LS+Gas* that too switches immediately to 'complete' *LS*. The transition at such increased $\Gamma \approx 15$ is shown in Fig. 5.70. At even higher $\Gamma = 35$, the *LS* still persists, nevertheless for high shaking amplitude (A/d exceeding 4) this *LS* transforms into a *Convection* State (see Fig. 5.71(c)). It is noteworthy that the particles in Fig. 5.71(c) do not shoot higher from the bed like a fountain, suggesting that this is not a fully developed convective motion but it is just an onset of *Convection*. Fig. 5.71(d) displays four counter-rotating rolls on the PIV map pertaining to Fig. 5.71(c). At very high shaking $\Gamma = 50$, the system still remains in *LS* for small shaking amplitude, however further increasing A/d transits this *LS* to "*LS+Con*" and later on to *Convection*. Such type of transition has been displayed in Fig. 5.72. It is noticeable that the number of convection rolls at $A/d = 4.5$ for two shaking intensities $\Gamma = 35$ (Fig. 5.71(d)) and 50 Fig. 5.72(d) remains the same.

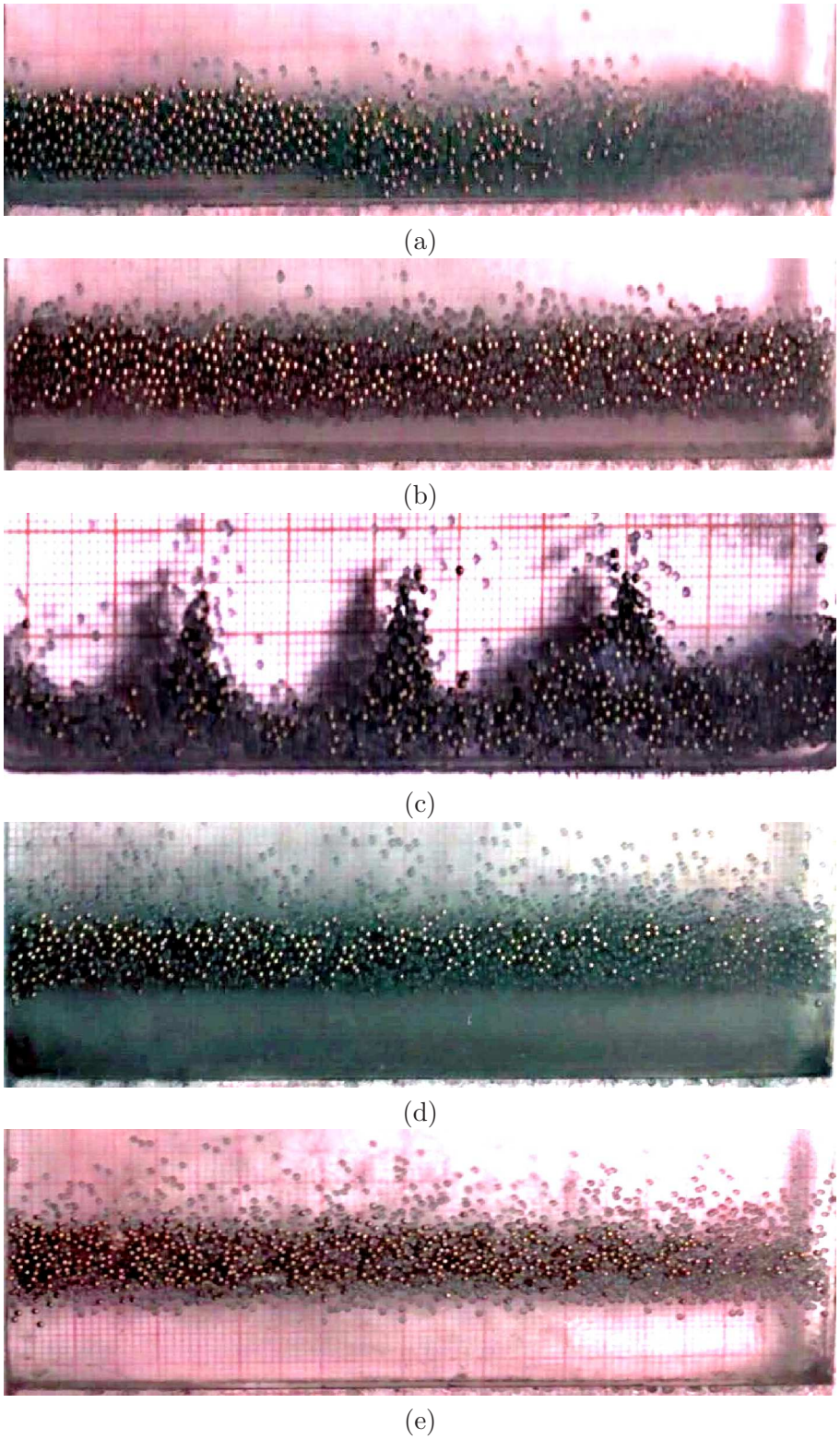

(a)

(b)

(c)

(d)

(e)

Figure 5.68: **Transition at constant shaking intensity $\Gamma \approx 7$ in $F = F_b + F_g = 6$ layers of equimolar mixture of brass and glass particles:** (a) *UW* ($n = 2$ mode) at $A/d = 0.8$ ($f = 46.6\ Hz$), (b) *BB* at $A/d = 1.5$ ($f = 34\ Hz$), (c) *Spikes* at $A/d = 3$ ($f = 24\ Hz$), (d) *BB* at $A/d = 4.5$ ($f = 19.66\ Hz$), and (e) *BB* at $A/d = 6$ ($f = 17\ Hz$).

5.5 Dynamical Patterns in Steel-Brass Particles Mixture

In this section, we will study the pattern formation dynamics in a mixture of equal sized steel and brass particles (both having diameter $d = 1.0\ mm$) with a density ratio $\rho_b/\rho_s \approx 1.13$. The mixture is confined in the same customary quasi two-dimensional Plexiglas® rectangular box of length $L/d = 100$ and width $W/d = 5.5$, the box being filled upto a specified layer depth $F = F_b + F_s$, where F_b and F_s are the number of layers of brass and steel particles. The box is held on the shaker and vibrated with sinusoidal waveform $y = A\sin(\omega t)$ at a constant shaking amplitude A and the intensity of vibration is escalated via ramping frequency (f) at a linear rate of 0.01 Hz/s. A crucial difference between this type of experiment with previously discussed ones (steel-glass and brass-glass mixtures) lies in the type of mixture used; here the density of brass and steel particles in the mixture is close to each other, making the system almost resembling to that of monodiperse case. The segregation of two species was not observed, and consequently none of the phase-coexisting patterns have been reported. It should be noted that the objective behind employing this type of mixture with a small density contrast is to check the validity of our hypothesis that the origin of all phase-coexisting patterns is indeed the horizontal segregation of two species (due to their density difference) and the *non-equipartition* of granular energy between heavier and lighter particles. In particular, the phase diagram of dynamical patterns realized in brass-steel mixture is found to be similar to that obtained for the case of monodiperse granular system discussed in Chapter 3.

Figure 5.73 displays the phase diagram of the patterns observed in equimolar brass-steel mixture for various filling depths at a constant shaking amplitude $A/d = 3$. This phase diagram should be compared with that of monodiperse system of glass and steel particles discussed in Chapter 3 (refer Fig. 3.1 and Fig. 3.19). We will discuss this phase diagram by focussing on various transitions in $F = 3$ and 6 layer depths while increasing the shaking intensity. In addition, we will also consider the effect on pattern formation when the filling depth is increased at a constant shaking intensity.

For very small filling depths $F \in (2, 2.5)$ the system transits from *BB* to *Gas* immediately. Figure 5.74 displays the various phases observed in $F = 3$ layers when Γ is increased gradually as the bed transits from *BB* to *LS* and then to *Gas*. Further increasing Γ induces a convective motion in the system as exhibited in Fig. 5.74(d) and Fig. 5.74(e). The PIV analysis of these convective states reveals two and four counter-rotating rolls for Convection at $\Gamma = 30$ and 50, respectively. Increasing the filling depth by two fold ($F = 6$) will suppress *Gas* state and the subharmonic waves appear in the system which at higher Γ switches to *LS* and later on to *Convection* as displayed in Fig. 5.76 and Fig. 5.77.

Now, we will traverse the phase diagram in Fig. 5.73 along the horizontal direction, i.e., increasing the filling depth and observing the evolution of patterns at a constant shaking strength. Figure 5.78 displays various transitions occuring at constant $\Gamma = 8.5$, wherein for $F = 2$ layers the *Gas* is realized which transits to *LS* for a deeper bed ($F = 3.5$) and later on to various modes of *UW* at even higher filling depths. At a moderate shaking $\Gamma = 20$, one encounters two phases, *Gas* for $2 \leq F \leq 3.5$ and *LS* for $3.5 \leq F \leq 8$; these phases are displayed in Fig. 5.79. At very high shaking $\Gamma = 50$, for small filling depth we observed *Gas*, which transforms to *Convection* (Fig. 5.80(b) and Fig. 5.80(c) at $F = 3.5$ and 6 respectively) as the layer depth (F)

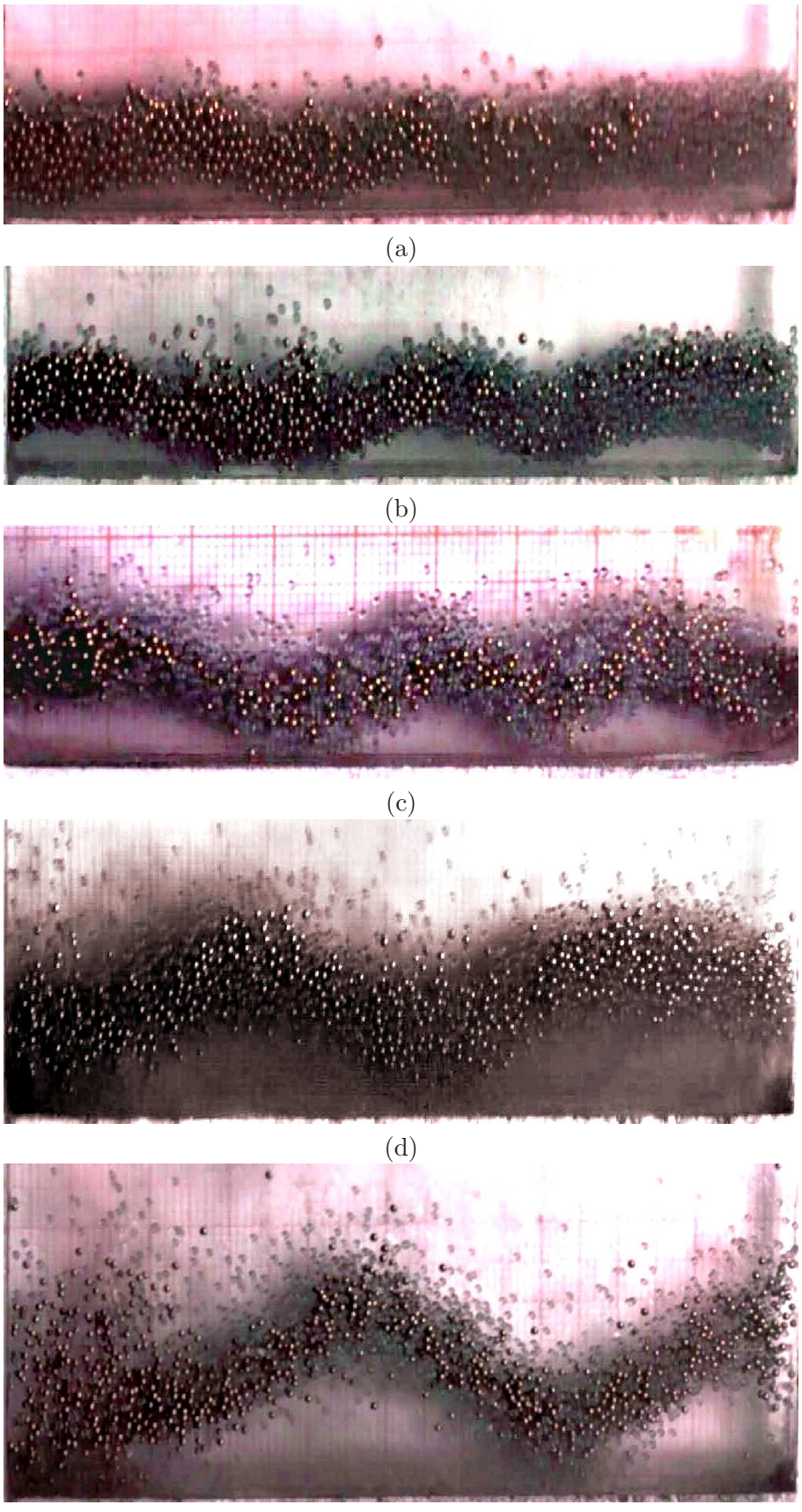

(a)

(b)

(c)

(d)

(e)

Figure 5.69: **Snapshots of *Undulatory Waves* at constant shaking intensity $\Gamma \approx 9$ for $F = F_b + F_g = 6$ layers of equimolar mixture of brass and glass particles:** (a) UW ($n = 6$ mode) at $A/d = 0.8$ ($f = 52.8\ Hz$), (b) UW ($n = 5$ mode) at $A/d = 1.5$ ($f = 38.6\ Hz$), (c) UW ($n = 5$ mode) at $A/d = 3$ ($f = 27.3\ Hz$), (d) UW ($n = 3$ mode) at $A/d = 4.5$ ($f = 22.3\ Hz$), and (e) UW ($n = 3$ mode) at $A/d = 6$ ($f = 19.3\ Hz$).

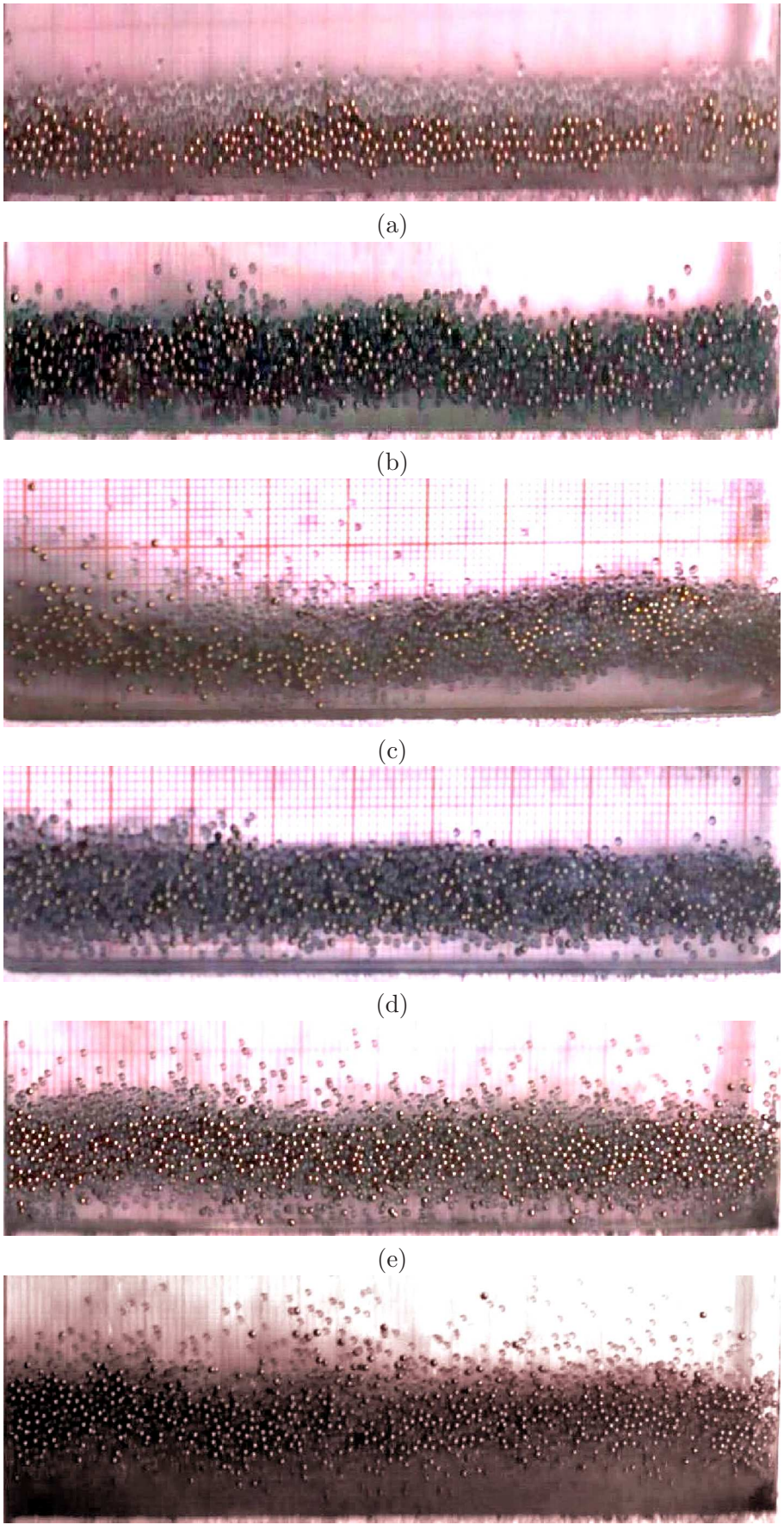

(a) (b) (c) (d) (e) (f)

Figure 5.70: **Transition at constant shaking intensity $\Gamma \approx 15$ for $F = F_b + F_g = 6$ layers of equimolar mixture of brass and glass particles:** (a) *BB* at $A/d = 0.5$ ($f = 86.34\ Hz$), (b) *LS* at $A/d = 1.5$ ($f = 49.84\ Hz$), (c) *LS+Gas* at $A/d = 2.75$ ($f = 36.8\ Hz$), (d) *LS* at $A/d = 3$ ($f = 35.24\ Hz$), (e) *LS* at $A/d = 4.5$ ($f = 28.8\ Hz$), and (f) *LS* at $A/d = 6$ ($f = 24.9\ Hz$).

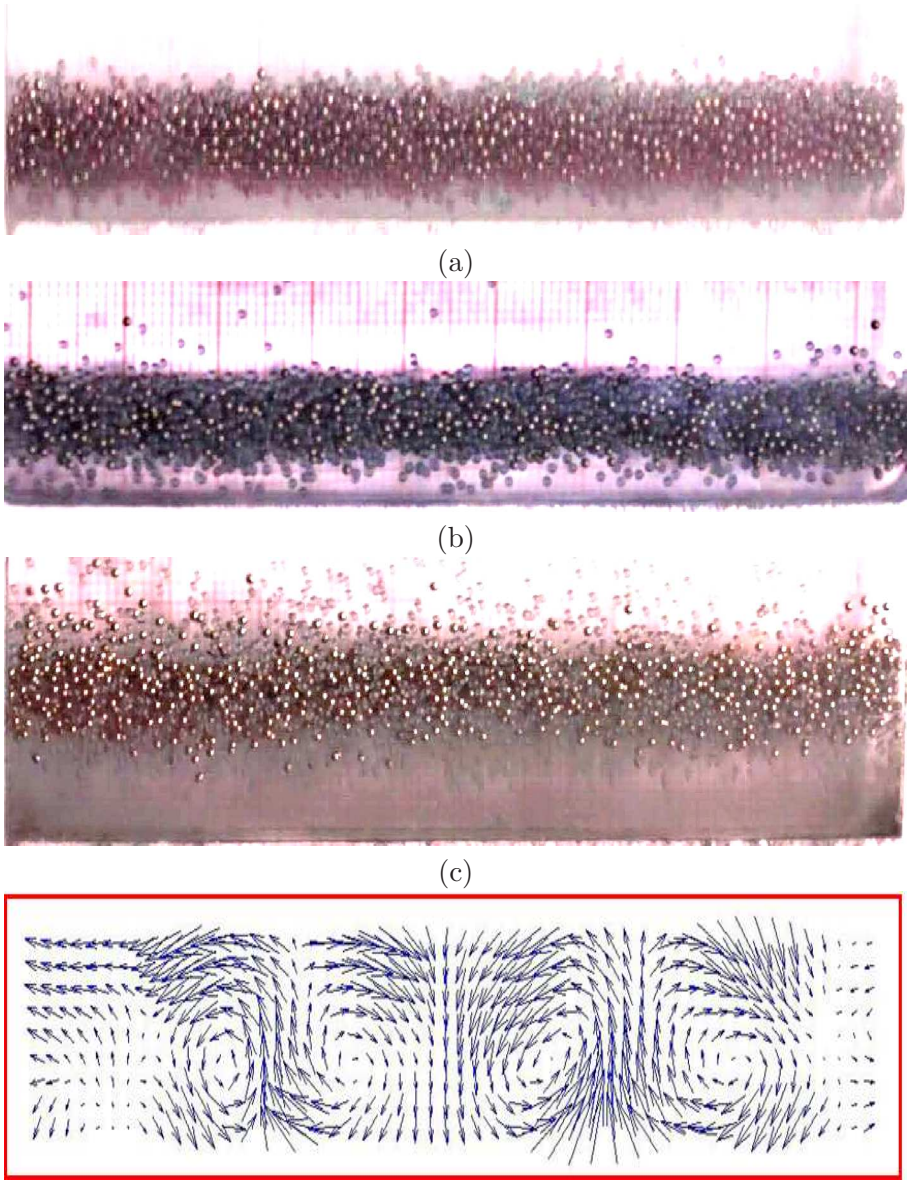

Figure 5.71: **Transition at constant shaking intensity $\Gamma = 35$ for $F = F_b + F_g = 6$ layers of equimolar mixture of brass and glass particles:** (a) *LS* at $A/d = 1.5$ ($f = 76.14\ Hz$), (b) *LS* at $A/d = 3$ ($f = 53.84\ Hz$), (c) *Convection* at $A/d = 4.5$ ($f = 43.9\ Hz$). (d) corresponding PIV of panel-(c).

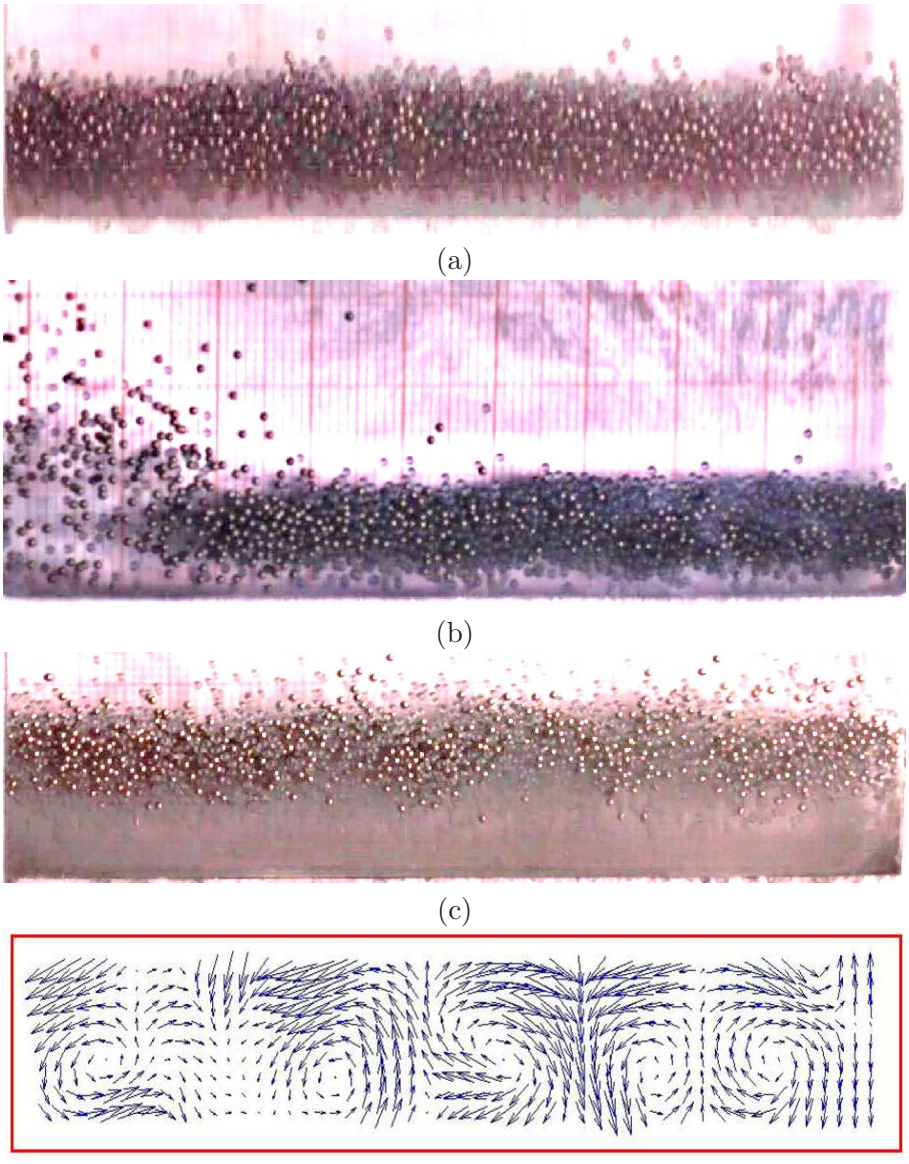

(a)

(b)

(c)

(d)

Figure 5.72: **Transition at constant shaking intensity $\Gamma = 50$ for $F = F_b + F_g = 6$ layers of equimolar mixture of brass and glass particles:** (a) *LS* at $A/d = 1.5$ ($f = 91\ Hz$), (b) *LS+Con.* at $A/d = 3$ ($f = 64.35\ Hz$), (c) *Convection* at $A/d = 4.5$ ($f = 52.5\ Hz$), and (d) corresponding PIV of panel-(c).

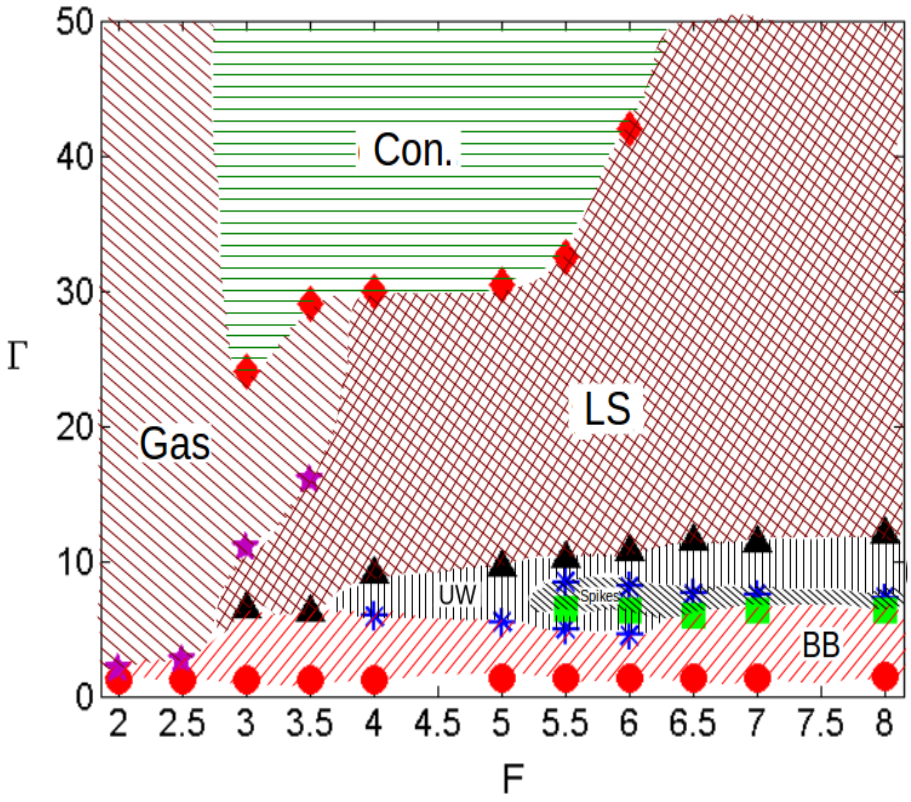

Figure 5.73: **Phase diagram of dynamical patterns in (Γ, F)-plane for equimolar mixture of steel and brass particles (both having diameter** 1.0 mm**).** Other parameter values are shaking amplitude $A/d = 3$ and $ramping\ rate = 0.01\ Hz/s$.

increases. In even deeper beds ($F \geq 6.5$) the system further admits LS expectedly, due to the inability to fluidize particles at this large F. The latter type of transition at $\Gamma = 50$ are shown in Fig. 5.80(d) and Fig. 5.80(e).

5.5.1 Phase Diagram in $(\Gamma, F_i/F)$-plane: Effect of Species Number Fraction

Here we investigate the outcome of varying the number fraction of two species in the steel-brass mixture (F_b/F) on the pattern formation dynamics as well as on the phase diagram. Akin to the previous cases, we consider two filling depths $F = 3, 6$ and obtained phase diagrams on $(\Gamma, F_b/F)$-plane at a constant shaking intensity $A/d = 3$ as presented in Fig. 5.81. The shaking intensity (Γ) pertaining to the onset of various patterns shows almost no dependence on F_b/F in these phase diagrams, except for the onset of convective state in $F = 6$ layers wherein the Γ_{onset} increases with the addition of heavier (brass) particles.

Let us now focus on the phase diagram for a filling depth $F = 3$, as shown in Fig. 5.81(a), and traverse across various mixture proportions at constant shaking intensities. One type of transition at constant $\Gamma = 9$ is presented in Fig. 5.82, wherein towards the limit of monodiperse steel particles we observed UW (Fig. 5.82(a) for $F_b/F = 0$), and thereafter LS with increasing

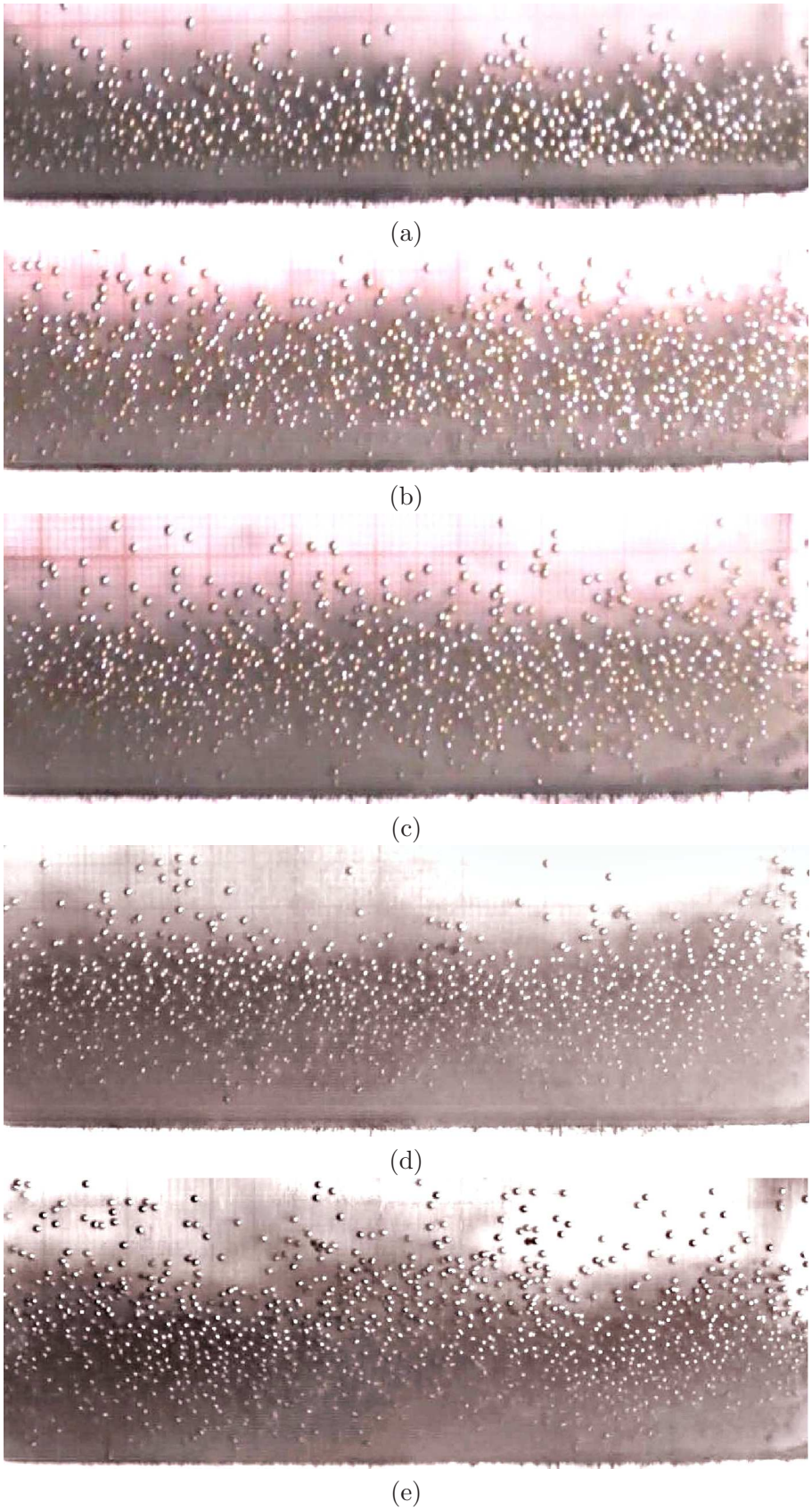

(a) (b) (c) (d) (e)

Figure 5.74: **Various transitions occuring in $F = F_s + F_b = 3$ layers of equimolar mixture of steel and brass particles with increasing shaking intensity Γ at $A/d = 3$:** (a) *BB* at $\Gamma = 2.5(f = 14.4\ Hz)$, (b) *LS* at $\Gamma = 7(f = 24.07\ Hz)$, (c) *Gas* at $\Gamma = 15(f = 35.24\ Hz)$, (d) *Convection* at $\Gamma = 30(f = 49.84\ Hz)$, and (e) *Convection* at $\Gamma = 50(f = 64.35\ Hz)$

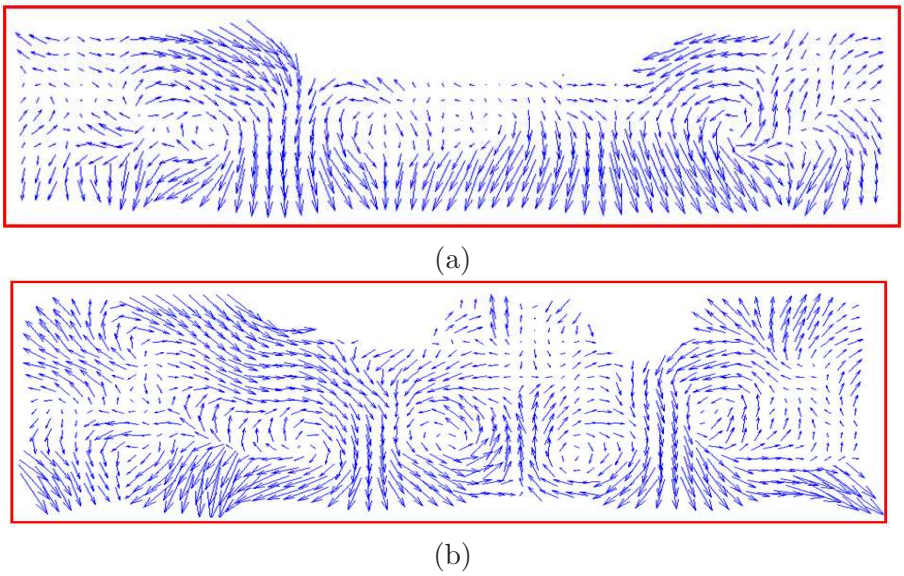

(a)

(b)

Figure 5.75: **Corresponding PIV of 'complete' convection shown in Fig. 5.74:** (a) PIV of panel-(d), (b) PIV of panel-(e).

F_b/F as shown in Fig. 5.81(b),(c),(d) and (e). At a higher shaking intensity of $\Gamma = 20$, the *Gas* has been realized for the whole range of mixture proportion as displayed in Fig. 5.83. At even higher shakings, as the mixture approaches monodipersity in steel particles, the Gas phase emerges, while the bidispersity and monodipersity in brass particles ($F_b/F > 0.05$) favors the genesis of *Convection* in the system. Such sort of evolution is shown in Fig. 5.84, which displays different phases at $\Gamma = 50$ while F_b/F is increased.

We will now address various phase transitions taking place in $F = 6$ layers of the steel-brass mixture, which has been compiled on the phase diagram displayed in Fig. 5.81(b). Various states are displayed in Fig. 5.85 for constant $\Gamma = 7$ where the bed bounces in the case of $F_b/F = 0$ and builds up *Spikes* structure for higher F_b/F. We observed an interesting trend in the phase diagram: Fig. 5.81(b): for $0.4 \leq F \leq 0.6$, the *UW* evolves at a relatively lower shaking intensity ($\Gamma \sim 7$) and rapidly transforms into *Spikes* which remain dynamic for a small range of Γ and once again transforms to *UW* at $\Gamma \sim 8$. Consequently, the *Spikes* pattern has been found to be sandwiched between (i) *BB* and UW regimes as well as (ii) between two *UW* regimes, as depicted in Fig. 5.81(b). Figure 5.86 displays the different modes of *UW* at constant $\Gamma = 8$, but the equimolar mixture ($F_b/F = 0.5$) at $\Gamma = 8$ still exhibits *Spikes*. These *UW* patterns subsequently relax to *Leidenfrost State (LS)*; the regime of *LS* is continuous over the whole range of F_b/F as seen in Fig. 5.81(b). The *LS* at different mixture proportion (F_b/F) are presented in Fig. 5.87. Further escalating Γ gradually leads to the transition of *LS* to *Convection*. However, for mixture appraching the monodipersity limit in brass particles ($F_b/F > 0.8$), *LS* stays on till $\Gamma = 50$. The images of three distinct phases with increasing F_b/F at $\Gamma = 50$ are displayed in Fig. 5.88.

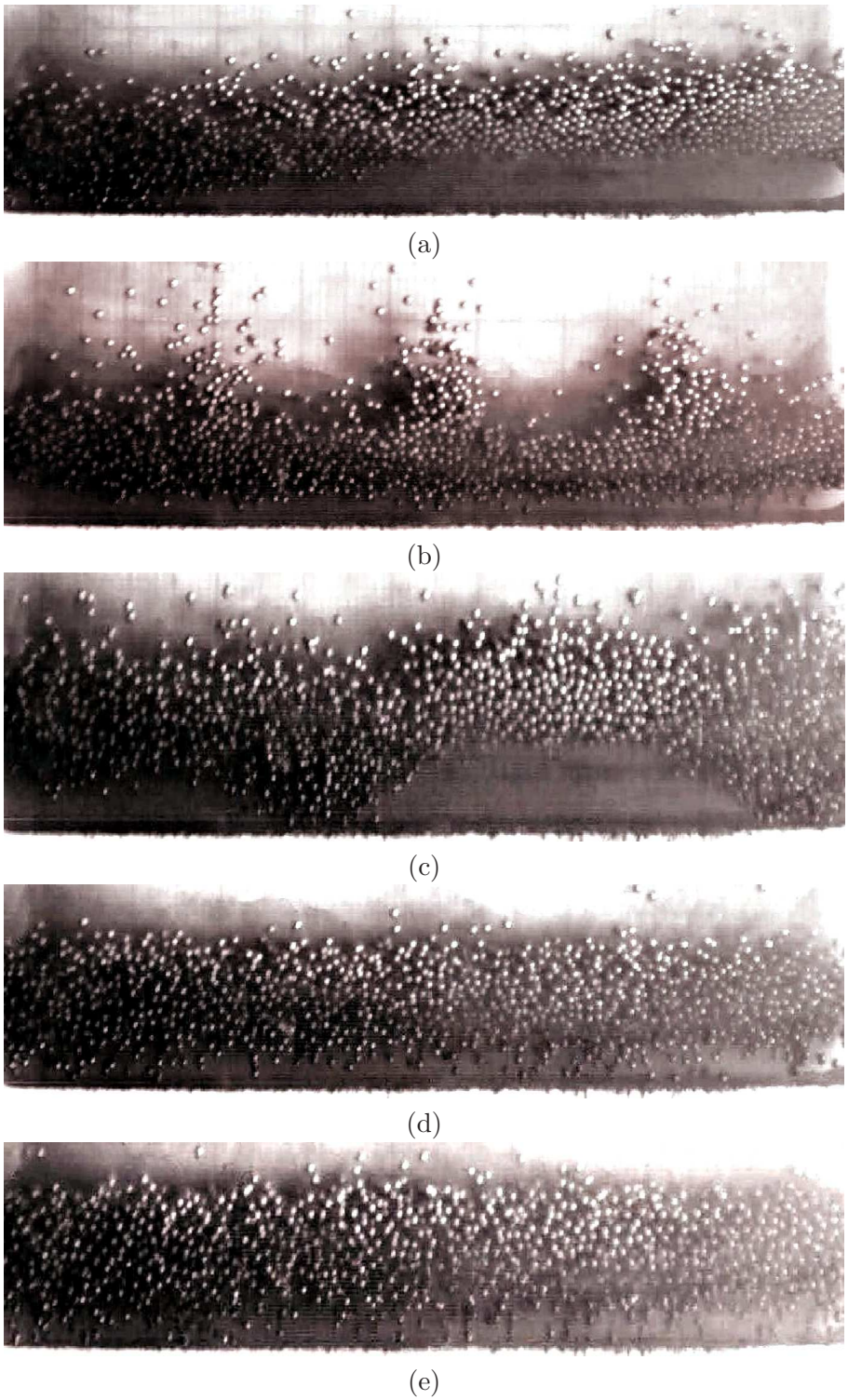

Figure 5.76: **Various transitions occuring in $F = F_s + F_b = 6$ layers of equimolar mixture of steel and brass particles with increasing shaking intensity Γ at $A/d = 3$:** (a) *UW* ($n = 1$ mode) at $\Gamma = 6(f = 22.3\ Hz)$, (b) *Spikes* at $\Gamma = 8(f = 25.74\ Hz)$, (c) *UW* ($n = 3$ mode) at $\Gamma = 9.1(f = 27.45\ Hz)$, (d) *LS* at $\Gamma = 15(f = 35.24\ Hz)$, (e) *LS* at $\Gamma = 30(f = 49.84\ Hz)$.

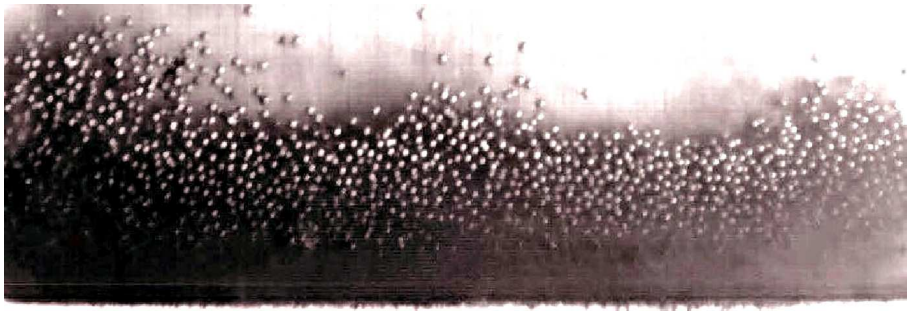

(f)

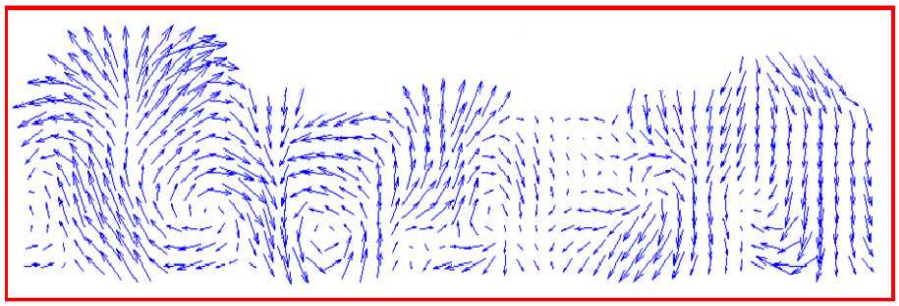

(g)

Figure 5.77: *Continued Fig. 5.76* **Various transitions occuring in $F = F_s + F_b = 6$ layers of equimolar mixture of steel and brass particles with increasing shaking intensity Γ at $A/d = 3$:** (f) *Convection* at $\Gamma = 50 (f = 64.35\ Hz)$, and (g) corresponding PIV of (f).

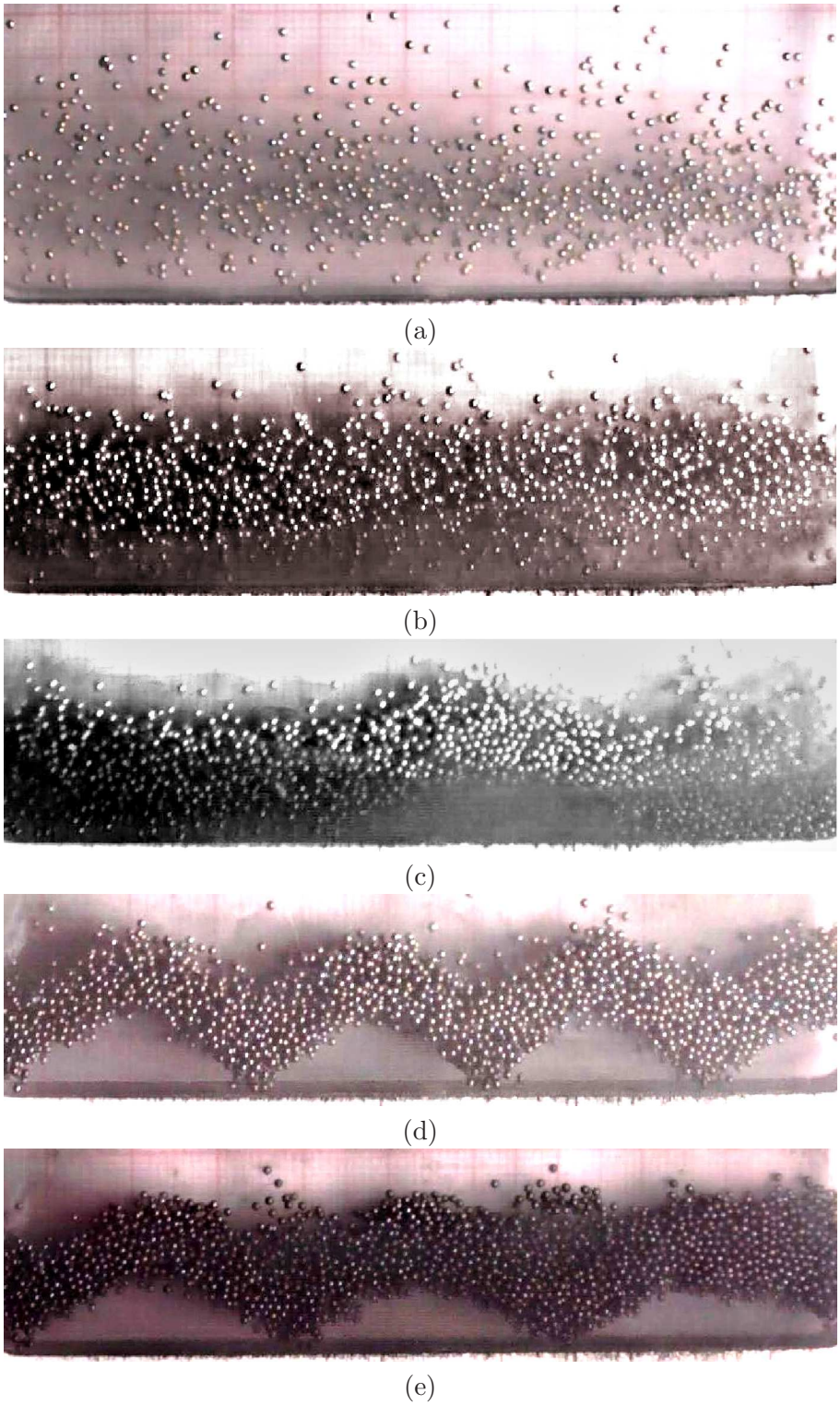

Figure 5.78: **Transitions occuring at constant shaking intensity $\Gamma = 8.5$ with increasing filling depth $F = F_s + F_b$:** (a) *Gas* at $F = 2$, (b) *LS* at $F = 3.5$, (c) *UW* ($n = 2$ mode) at $F = 5.5$, (d) *UW* ($n = 7$ mode) at $F = 6.5$, and (e) *UW* ($n = 6$ mode) at $F = 8$.

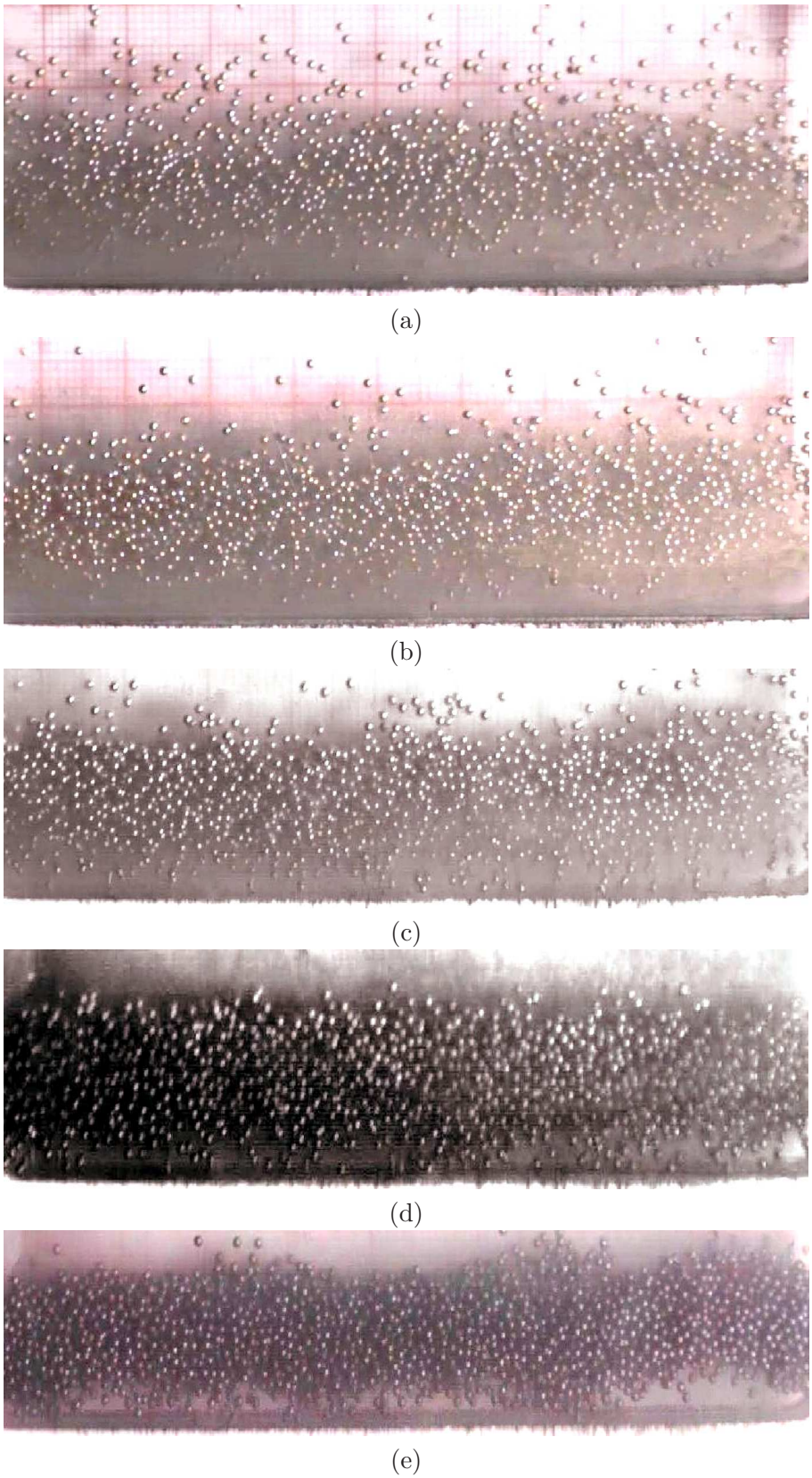

(a)

(b)

(c)

(d)

(e)

Figure 5.79: **Transition at constant shaking intensity $\Gamma = 20$ with increasing filling depth $F = F_s + F_b$:** (a) *Gas* at $F = 3$, (b) *Gas* at $F = 3.5$, (c) *LS* at $F = 4$, (d) *LS* at $F = 6$, and (e) *LS* at $F = 8$.

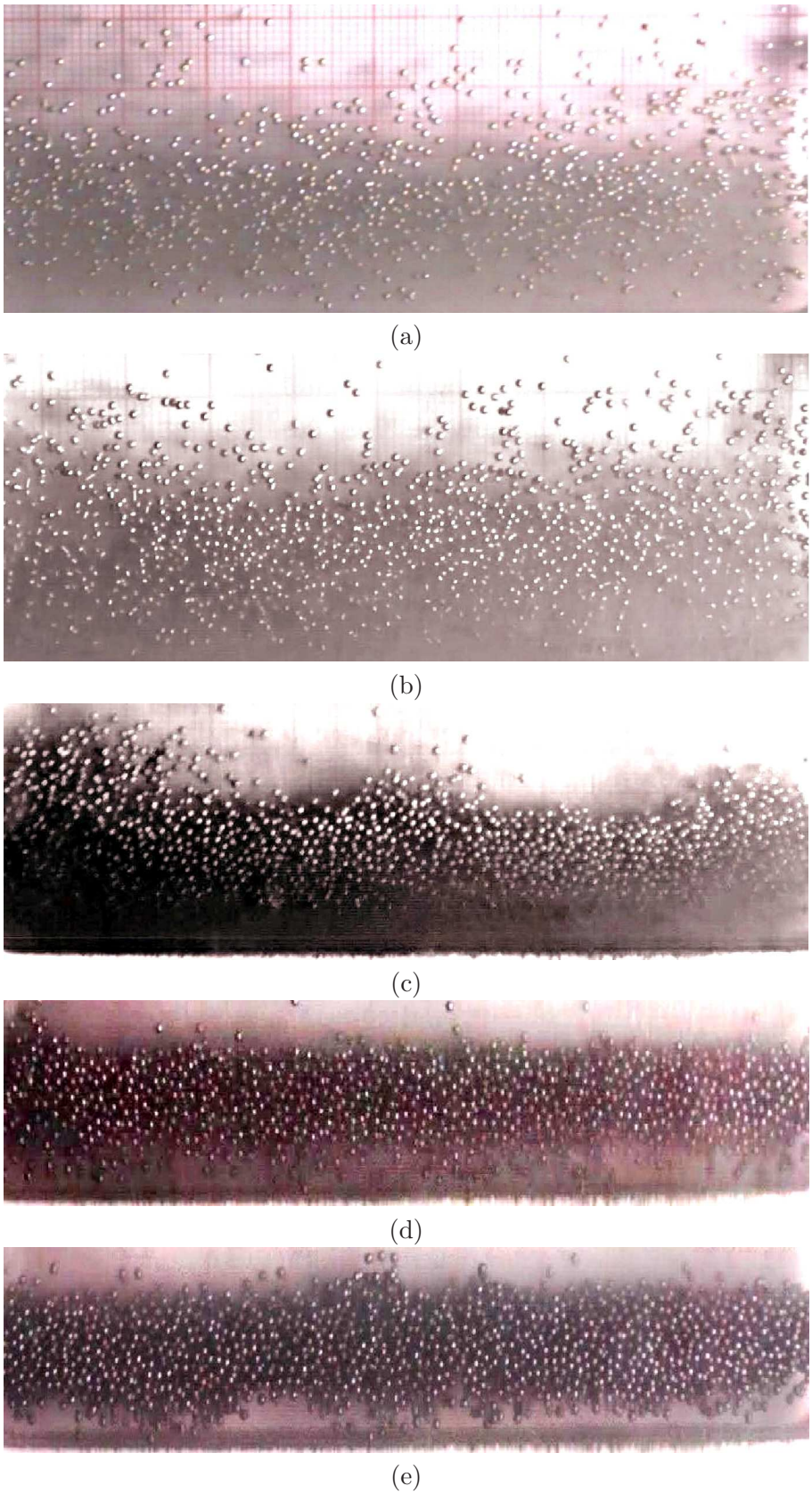

Figure 5.80: **Transition at constant shaking intensity $\Gamma = 50$ with increasing filling depth $F = F_s + F_b$:** (a) *Gas* at $F = 2.5$, (b) *Convection* at $F = 3.5$, (c) *Convection* at $F = 6$, (d) *LS* at $F = 6.5$, and (e) *LS* at $F = 8$.

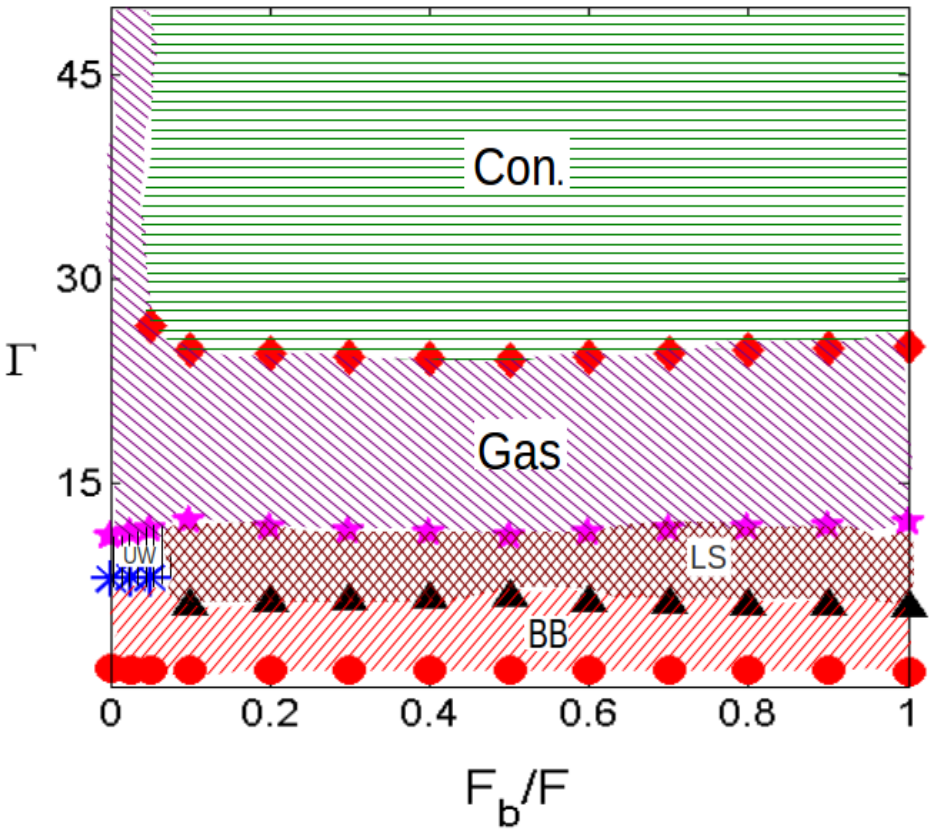

(a)

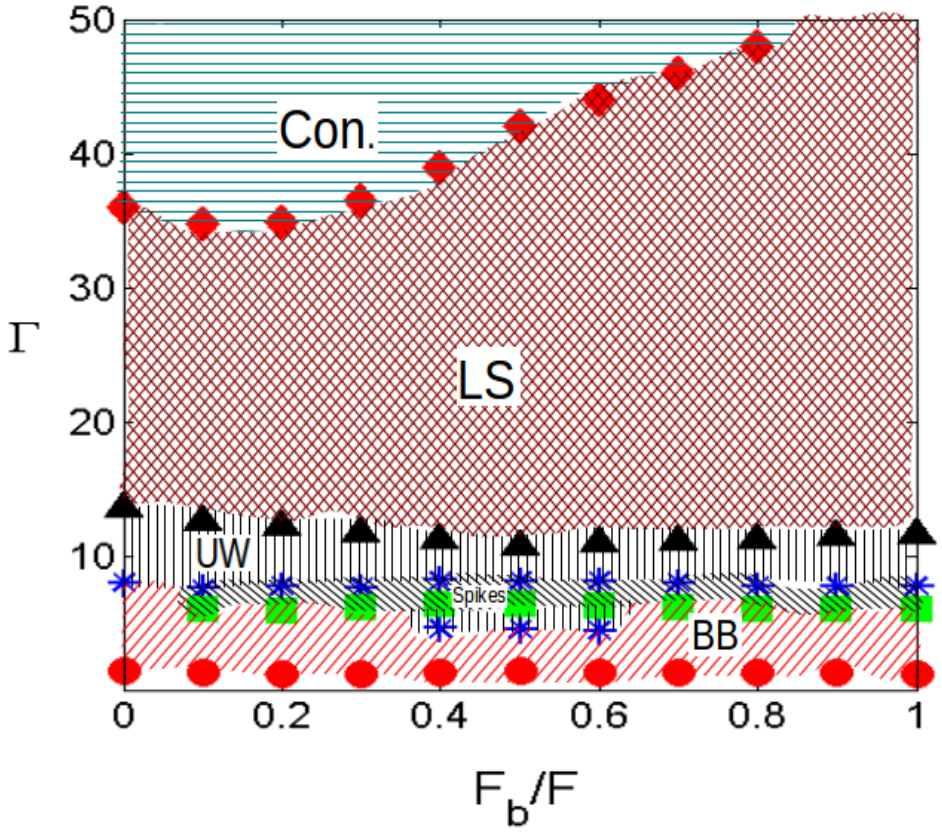

(b)

Figure 5.81: **Phase diagram of dynamical patterns in $(\Gamma, F_b/F)$-plane for mixture of steel and brass particles (both having diameter** 1.0 mm**) for total filling depth $F = F_s + F_b$:** (a) $F = 3$, and (b) $F = 6$. Other parameter values are shaking amplitude $A/d = 3$ and *ramping rate* $= 0.01\ Hz/s$.

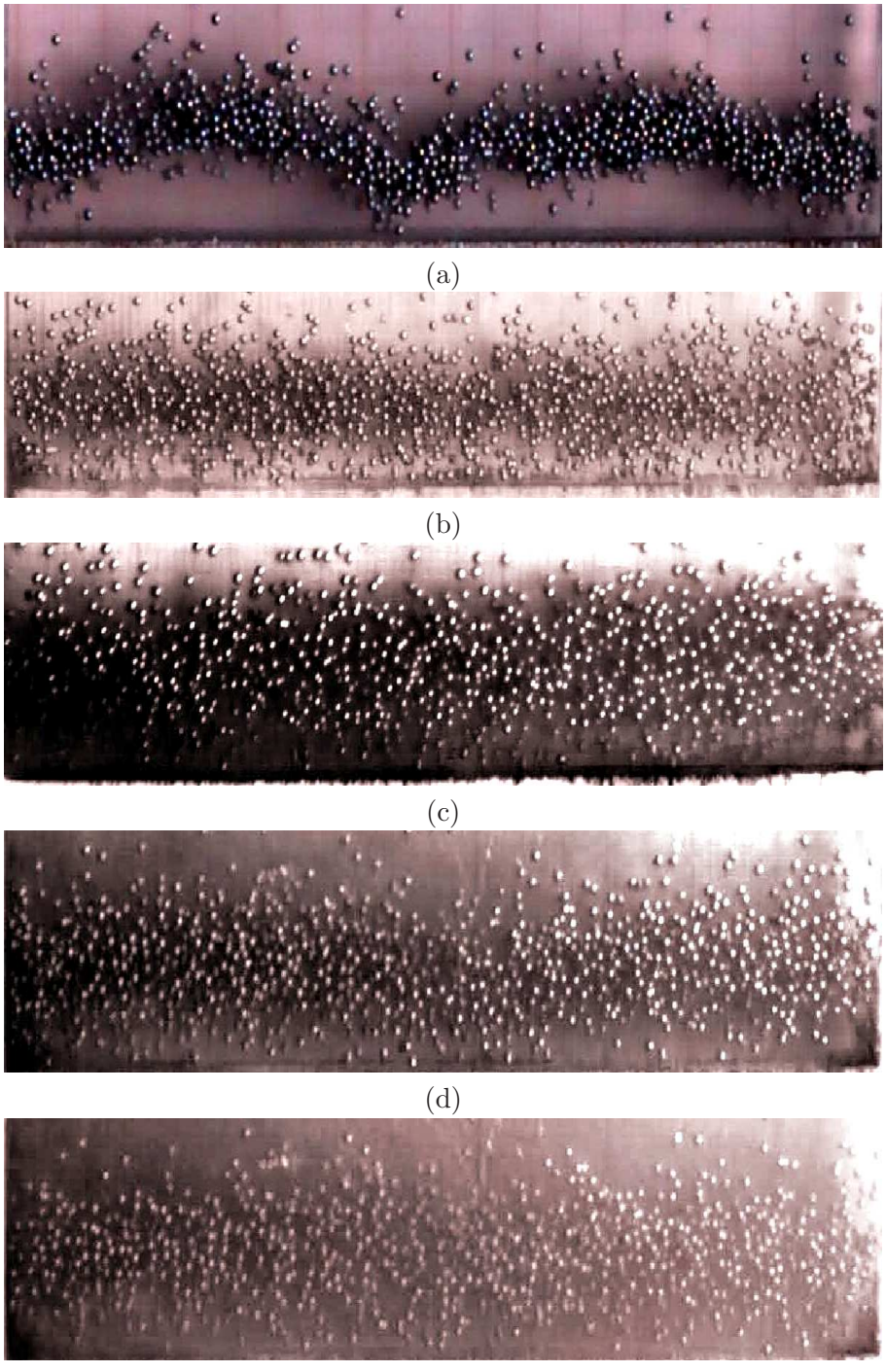

(a)

(b)

(c)

(d)

(e)

Figure 5.82: **Transition at constant shaking intensity $\Gamma = 9$ in $F = F_s + F_b = 3$ layers of mixture of brass and steel particles (both having diamter of 1.0 mm) with increasing F_b/F:** (a) *UW* ($n = 4$ mode) at $F_b/F = 0$, (b) *LS* at $F_b/F = 0.1$, (c) *LS* at $F_b/F = 0.5$, (d) *LS* at $F_b/F = 0.8$, and (e) *LS* at $F_b/F = 1$.

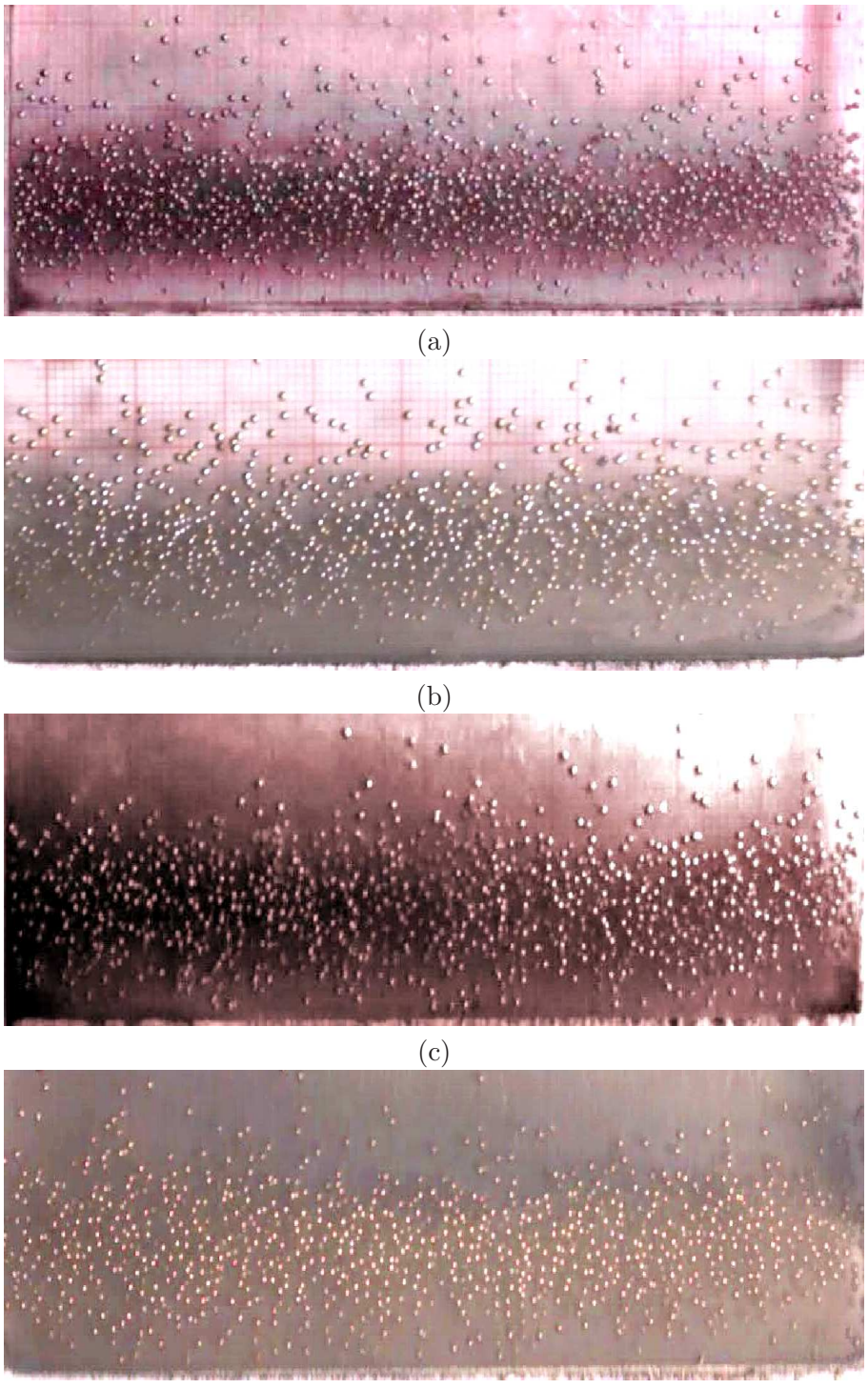

(a)

(b)

(c)

(d)

Figure 5.83: **Granular gas observed at constant shaking intensity $\Gamma = 20$ in $\boldsymbol{F = F_s + F_b = 3}$ layers of mixture of brass and steel particles (both having diamter of 1.0 $\boldsymbol{mm}$) with increasing $\boldsymbol{F_b/F}$:** (a) *Gas* at $F_b/F = 0.2$, (b) *Gas* at $F_b/F = 0.5$, (c) *Gas* at $F_b/F = 0.8$, and (d) *Gas* at $F_b/F = 1$.

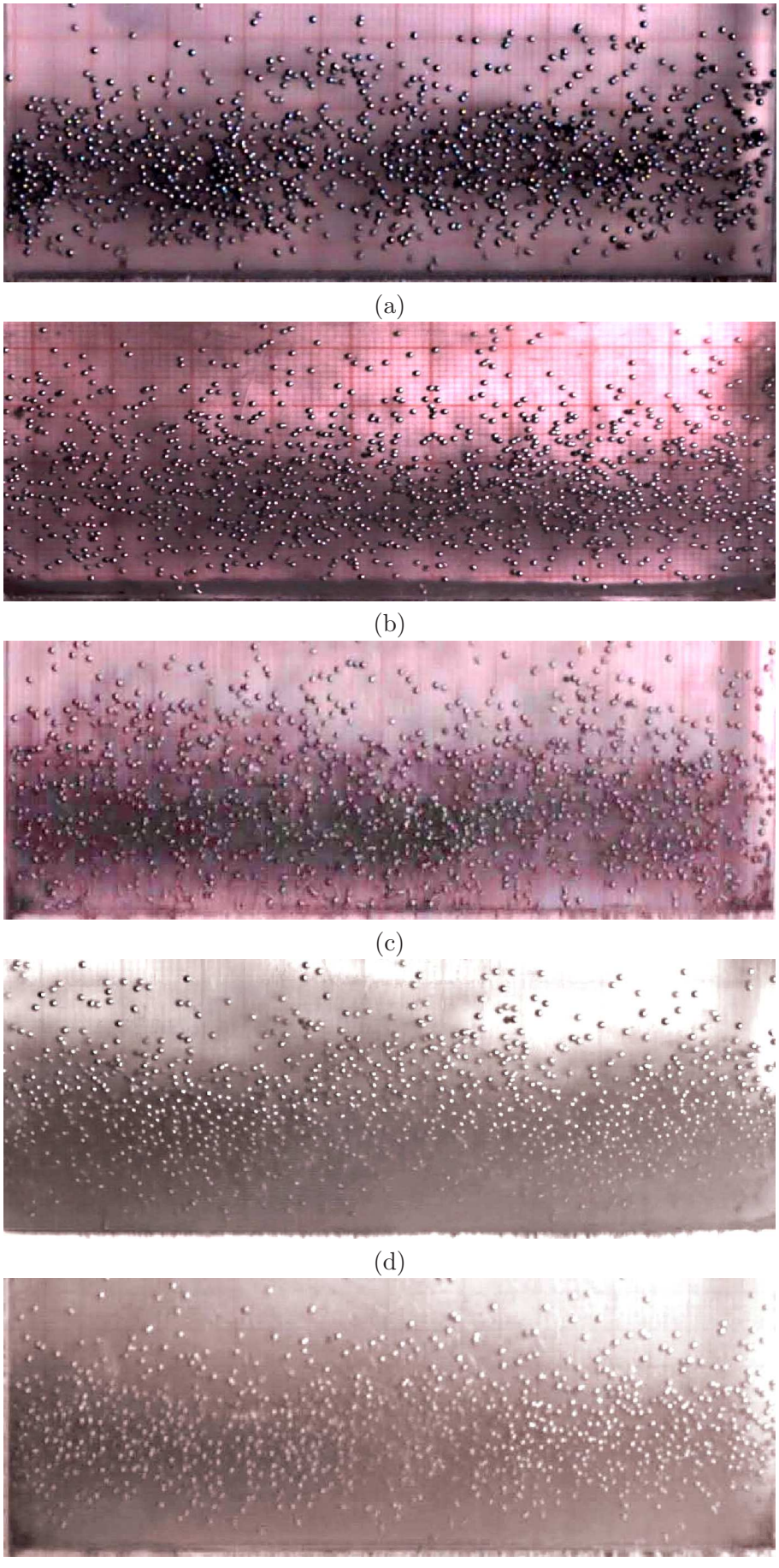

(a) (b) (c) (d) (e)

Figure 5.84: **Transition at constant shaking intensity $\Gamma = 50$ in $F = F_s + F_b = 3$ layers of mixture of brass and steel particles (both having diamter of 1.0 mm) with increasing F_b/F:** (a) *Gas* at $F_b/F = 0$, (b) *Gas* at $F_b/F = 0.025$, (c) *Convection* at $F_b/F = 0.1$, (d) *Convection* at $F_b/F = 0.5$, and (e) *Convection* at $F_b/F = 0.8$.

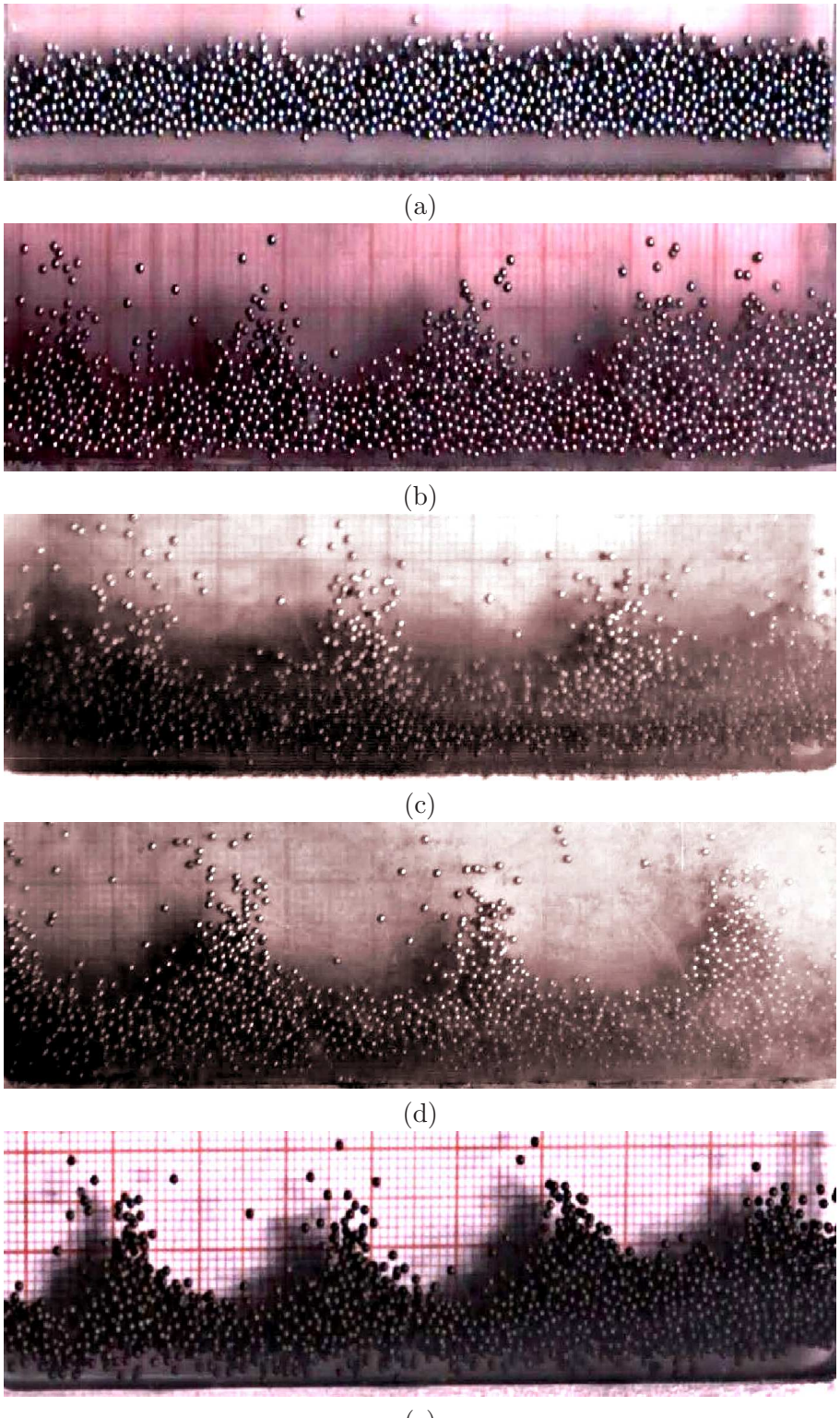

(a)

(b)

(c)

(d)

(e)

Figure 5.85: **Transition between various patterns at constant shaking intensity $\Gamma = 7$ in $F = F_s + F_b = 6$ layers of mixture of brass and steel particles (both having diamter of 1.0 mm) with increasing F_b/F:** (a) *BB* at $F_b/F = 0$, (b) *Spikes* at $F_b/F = 0.1$, (c) *Spikes* at $F_b/F = 0.5$, (d) *Spikes* at $F_b/F = 0.8$, and (e) *Spikes* at $F_b/F = 1$.

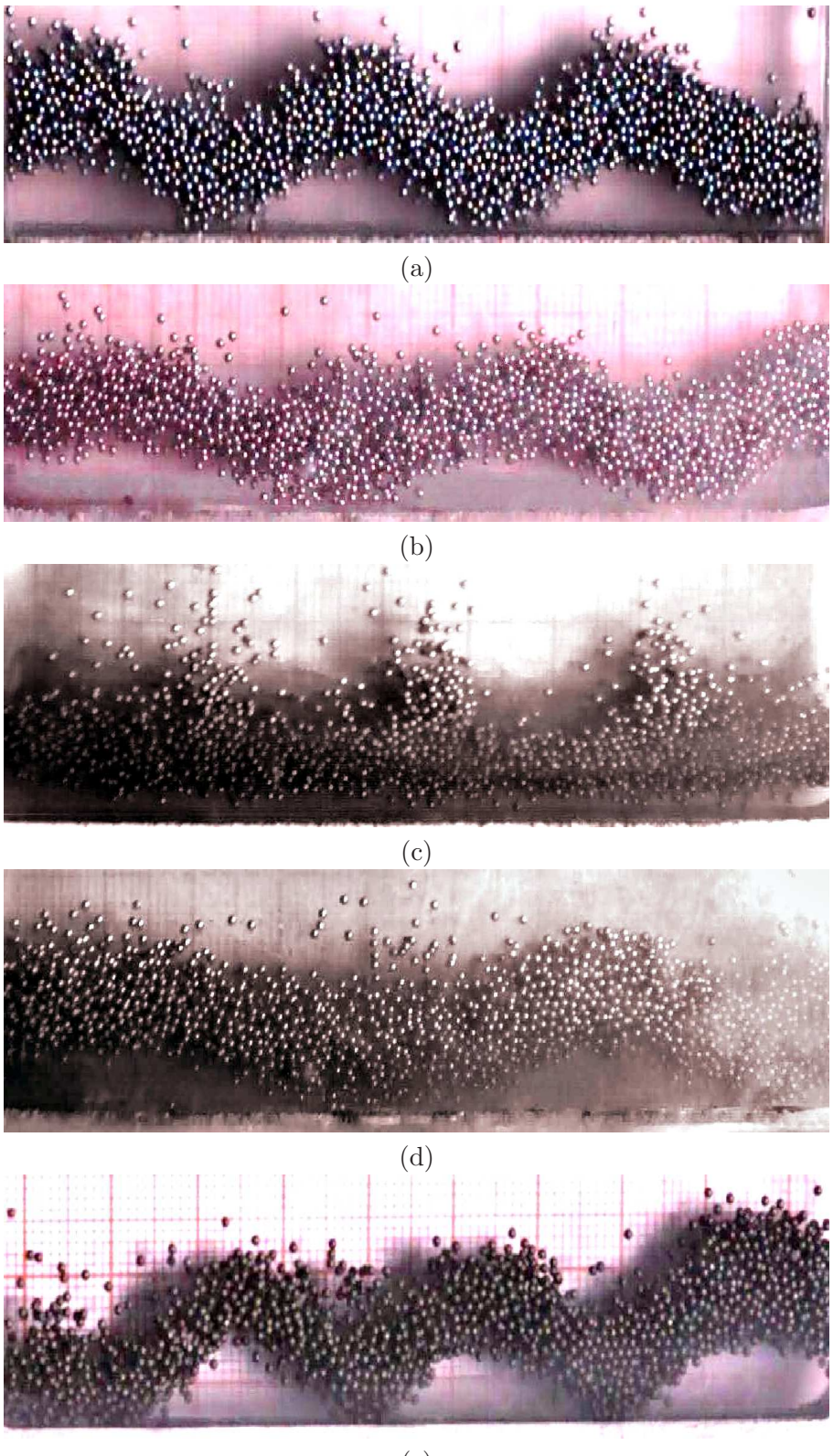

(a)

(b)

(c)

(d)

(e)

Figure 5.86: **Transition between various patterns at constant shaking intensity $\Gamma = 8$ in $F = F_s + F_b = 6$ layers of mixture of brass and steel particles (both having diamter of 1.0 mm) with increasing F_b/F:** (a) *UW* ($n = 5$ mode) at $F_b/F = 0$, (b) *UW* ($n = 4$ mode) at $F_b/F = 0.1$, (c) *Spikes* at $F_b/F = 0.5$, (d) *UW* ($n = 3$ mode) at $F_b/F = 0.8$, and (e) *UW* ($n = 5$ mode) at $F_b/F = 1$.

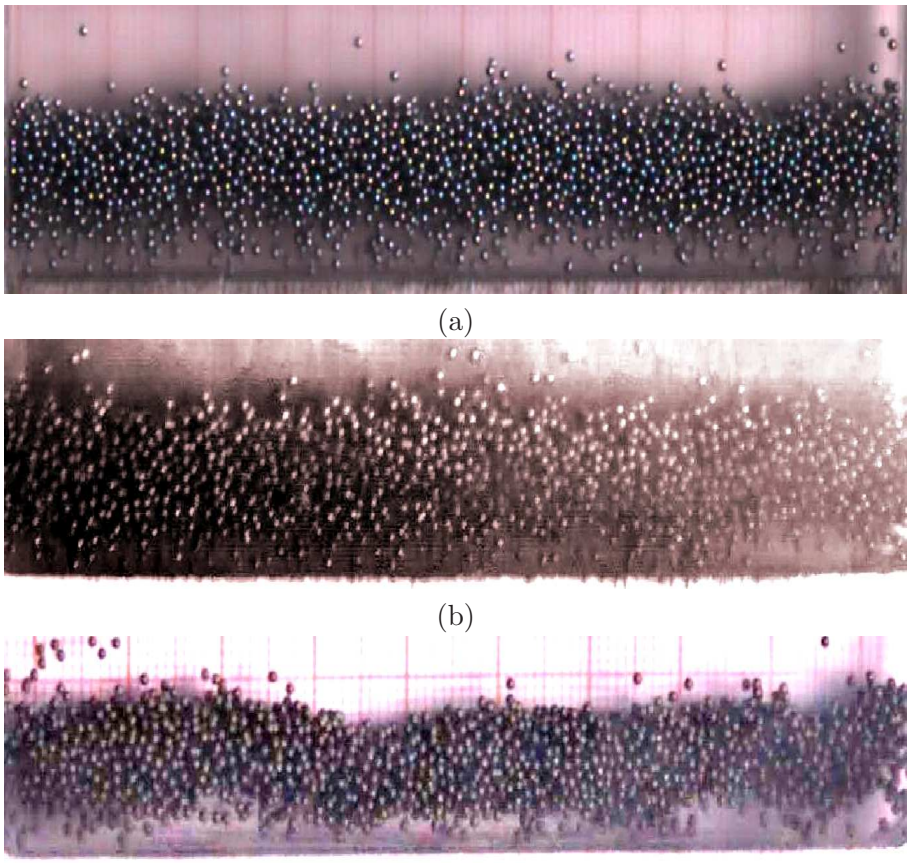

(a) (b) (c)

Figure 5.87: **Leidenfrost states *LS* observed at constant shaking intensity $\Gamma = 25$ in $F = F_s + F_b = 6$ layers of mixture of brass and steel particles (both having diamter of 1.0 *mm*) with increasing F_b/F:** (a) *LS* at $F_b/F = 0$, (b) *LS* at $F_b/F = 0.5$, and (c) *LS* at $F_b/F = 1$.

5.5.2 Phase Diagram in $(\Gamma, A/d)$-plane: Effect of Shaking Amplitude

Now, we turn our focus towards the impact of increasing shaking amplitude A/d on the various patterns originating in vibrated equimolar mixture of steel and brass particles. As before, we considered two filling depths of the equimolar mixture $F = 3, 6$ and obtained phase diagrams on $(\Gamma, A/d)$-plane which are displayed in Fig. 5.89. Let us discuss the phase diagram in Fig. 5.89(a) and the related patterns observed in $F = 3$ layers, wherein we notice that at higher shaking amplitudes ($A/d > 3.5$), the mixture system vaporises instantly into a *Gas* from *BB*. The gaseous phase is realized even at lower shaking amplitudes ($A/d < 3.5$) though the onset value is comparatively higher than that for larger A/d case; in any case, the Γ_{onset} for $BB \rightarrow Gas$ is expectedly found to decrease with increasing A/d. This decrease is sharp for $A/d < 3.5$, but while almost flattens off for $A/d > 3.5$. Once again we witness the transition *Gas*→*Convection* in Fig. 5.89(a) which corroborates our previous finding of such sort of transition. We also observed *UW* but for lower shaking amplitudes ($0.5 \leq A/d \leq 1.5$) and these *UW* eventually transit to *LS*.

A series of transitions at constant shaking intensity $\Gamma = 7$ with increasing A/d has been

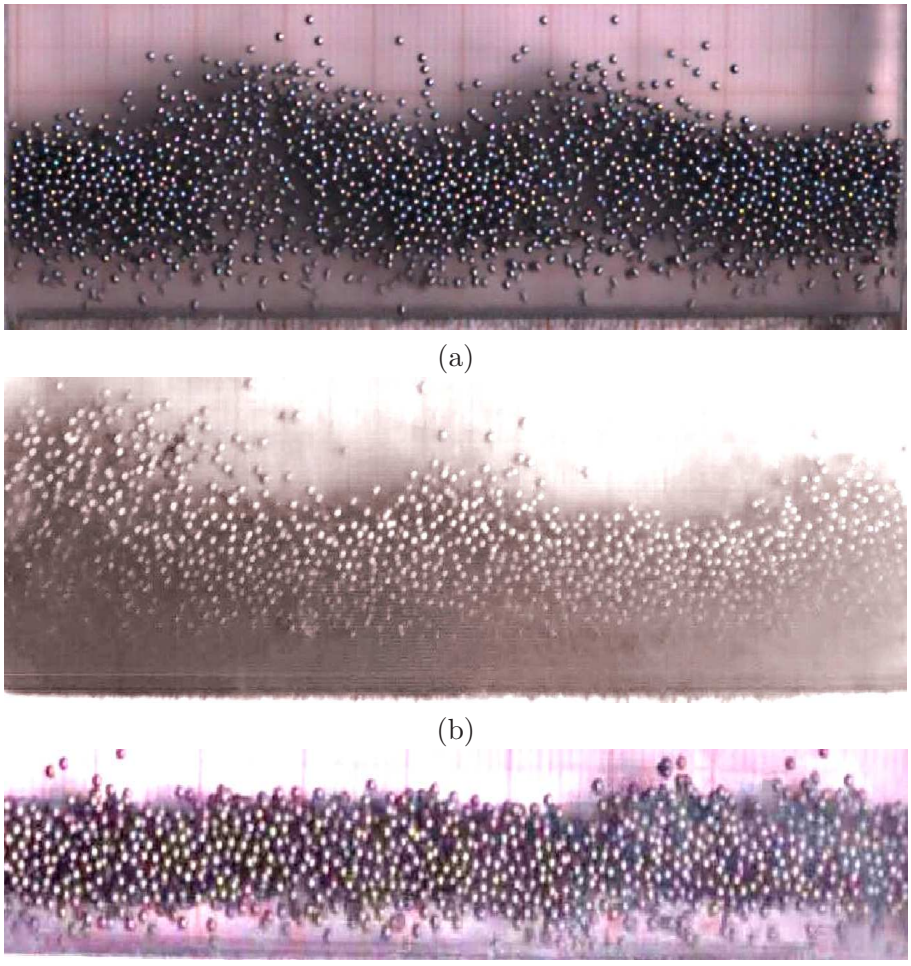

(a)

(b)

(c)

Figure 5.88: **Transition at constant shaking intensity** $\Gamma = 50$ **in** $\boldsymbol{F = F_s + F_b = 6}$ **layers of mixture of brass and steel particles (both having diamter of 1.0** $\boldsymbol{mm}$**) with increasing** $\boldsymbol{F_b/F}$**:** (a) *Convection* at $F_b/F = 0$, (b) *Convection* at $F_b/F = 0.5$, and (c) *LS* at $F_b/F = 1$.

displayed in Fig. 5.90. Fig. 5.90(a) exhibits a $n = 4$ *UW*, wherein the buckling of the string is very small. Moving to a higher shaking intensity ($\Gamma = 25$), one still observes *BB* at very low amplitude vibration as depicted in Fig. 5.91(a), whereas increasing A/d further at this constant Γ leads to the realization of *LS* at $A/d = 1$, *Gas* at $A/d = 2$, *Con.* at $A/d = 3$ and once again gaseous phase at very high amplitudes ($A/d = 4.5, 6$). At very high shaking intensity ($\Gamma = 50$), the various states observed while increasing A/d are displayed in Fig. 5.93.

We now discuss the phase diagram for $F = 6$ layers of equimolar mixture of steel and brass particles which is shown in Fig. 5.89(b). The mixture bed commences bouncing off the base plate for $\Gamma \gtrsim 1$ and with increased shaking intensity eventually transits to *Spikes* and subsequently to *UW*. Here again the *Spikes* regime is found to be sandwiched between two *UW* regimes at the initial stage of its development (with escalating A/d) as well as between *BB* and *UW* regimes for $A/d > 3.5$. These *UW* patterns gradually relax to *LS* at even higher shaking intensity, wherein *LS* persists for a wide range of Γ. Further increasing Γ transforms the *LS* to *Convection* beyond a minimal value of $A/d \approx 2$. It is evident from Fig. 5.89(b) that the onset value of Γ for the inception of *Convection* falls linearly with increasing A/d and this is expected since at higher amplitudes the system can undergo fluidization readily leading to the convective motion of particles.

The various states evolved at constant $\Gamma = 7$ while increasing shaking amplitude A/d are displayed in Fig. 5.94. It is interesting to note that the structure of *Spikes* pattern shown in Fig. 5.94(d) displays the characteristic as if the half of the granular string is in the buckled state (*UW*) while the remaining half constitutes peaks and valleys pertaining to *Spikes*. This indeed indicates that this *Spikes* pattern has been born from *UW*. It is confirmed in Fig. 5.94(e-f) that at higher shaking amplitudes, the full-fledged *Spikes* patterns evolves in the system. At higher intensity of $\Gamma = 25$, one observes a *BB* at $A/d = 0.2$ and *LS* for various higher shaking amplitudes as shown in Fig. 5.95. Likewise, the various phases realized at $\Gamma = 50$ with increasing A/d are displayed in Fig. 5.96. It is noteworthy that at very low shaking amplitudes, the bed shows a *BB* state even upto $\Gamma = 50$ (compare Fig. 5.94(a), Fig. 5.95(a) and Fig. 5.96(a)).

To conclude this chapter, we witnessed that the vertically shaken granular mixtures of equal sized, distinct density (large density ratio) particles have unfolded a diverse variety of patterns as detailed in Chapter 5. The most intriguing case is that of horizontal-segregation-driven 'phase-coexisting' patterns. These novel patterns display the coexistence of (i) sub-harmonic and synchronous states having different spatial and temporal orders and (ii) that of gas- and liquid-like states (both having the same temporal order but different spatial order), along with horizontal segregation, and (ii) a "partial" convection state that coexists with a Leidenfrost state (LS). For instance, an *UW* (undulatory wave) coexisting with a granular *Gas* is an example of a phase-coexisting pattern that has different spatial order (UW is in a liquid state and 'Gas' is spatially disordered) as well as different temporal symmetry (UW is a period-2 or f/2-wave, but the 'Gas' temporally disordered). On the other hand, both the *Cluster+Gas* and the *LS+Gas* have different spatial order but both being f-waves (i.e. synchronous with the excitation frequency) and hence have the same temporal symmetry. In summary, we have discovered an array of phase-coexisting patterns: (1) a granular gas coexisting with (1a) a subharmonic ($f/2$) undulatory wave (*UW*), (1b) a synchronous solid-like bouncing bed (*BB*), (1c) a static or an

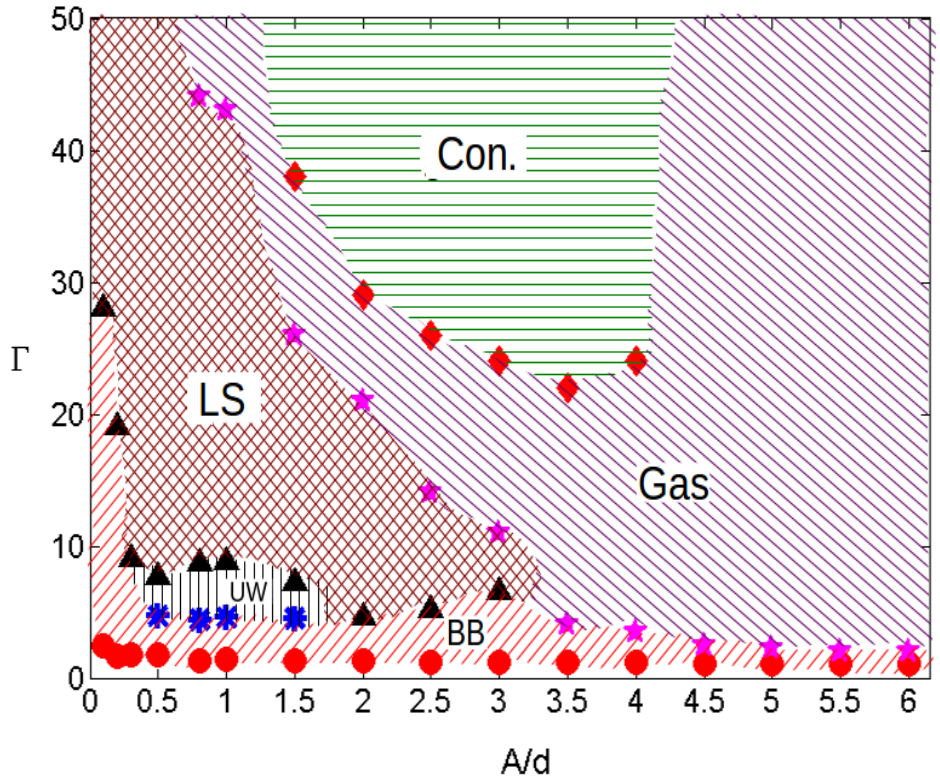

(a)

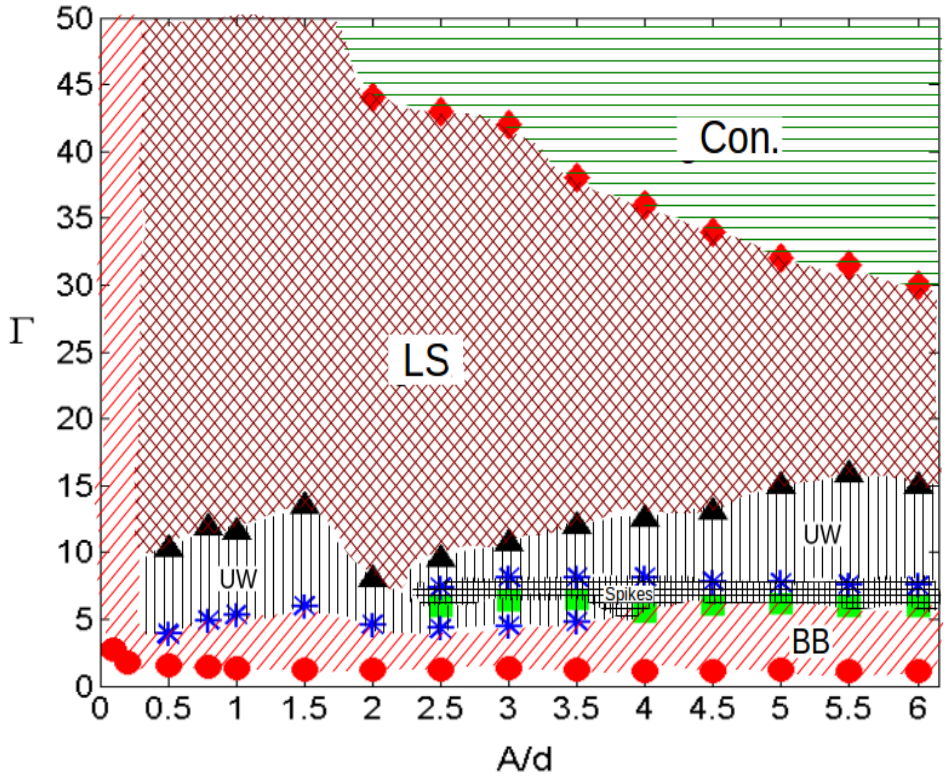

(b)

Figure 5.89: **Phase diagram of dynamical patterns in $(\Gamma, A/d)$-plane for equimolar mixture of steel and brass particles (both having diameter** 1.0 mm**) for total filling depth $F = F_s + F_b$:** (a) $F = 3$, and (b) $F = 6$. *Ramping rate* $= 0.01\ Hz/s$.

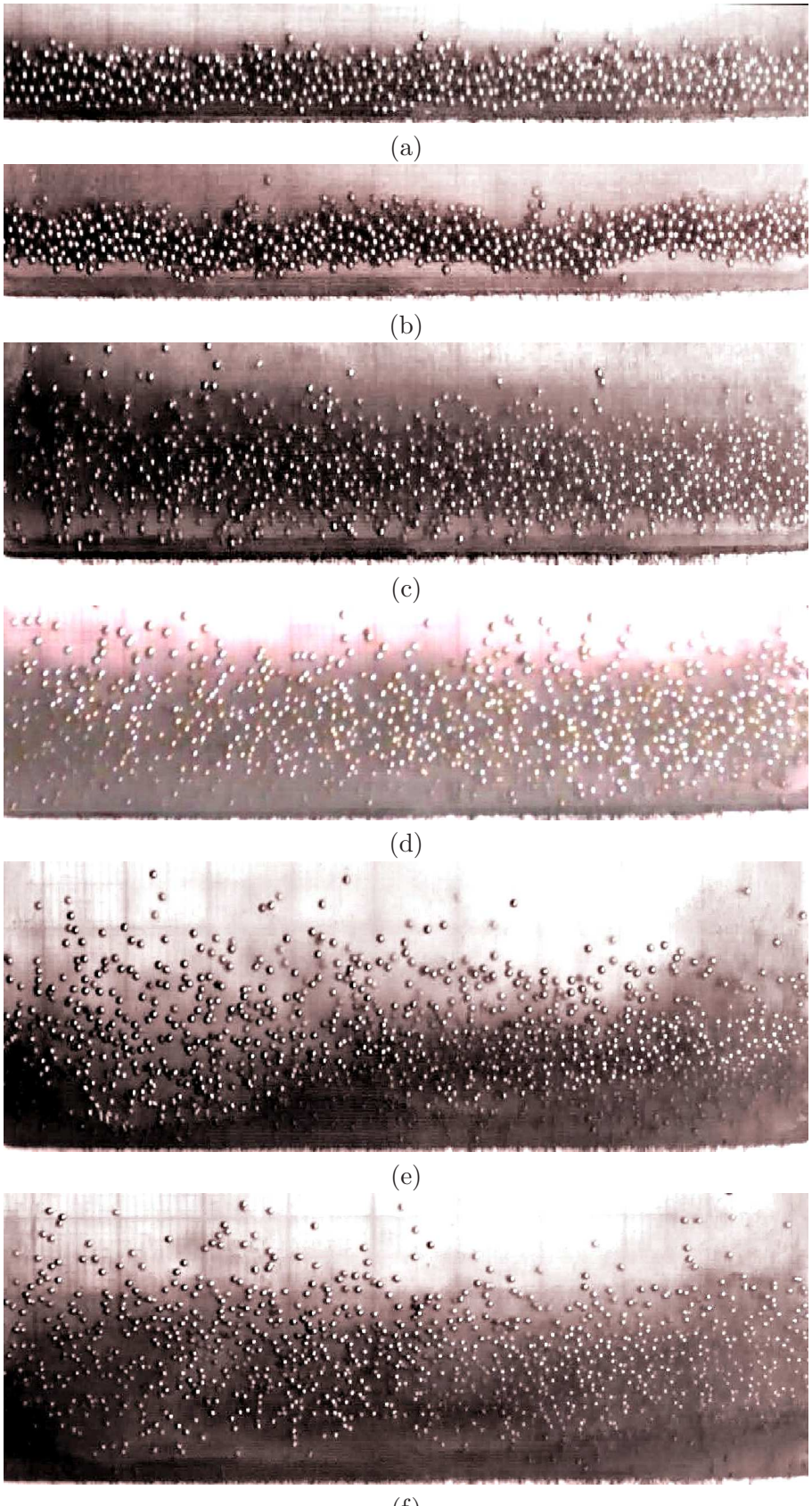

Figure 5.90: **Transition between various patterns at constant shaking intensity $\Gamma = 7$ in $F = F_s + F_b = 3$ layers of equimolar mixture of brass and steel particles (both having diameter 1.0 mm) with increasing A/d:** (a) *BB* at $A/d = 0.3$, (b) *UW* ($n = 4$ mode) at $A/d = 1$, (c) *LS* at $A/d = 2$, (d) *LS* at $A/d = 3$, (e) *Gas* at $A/d = 4.5$, and (f) *Gas* at $A/d = 6$.

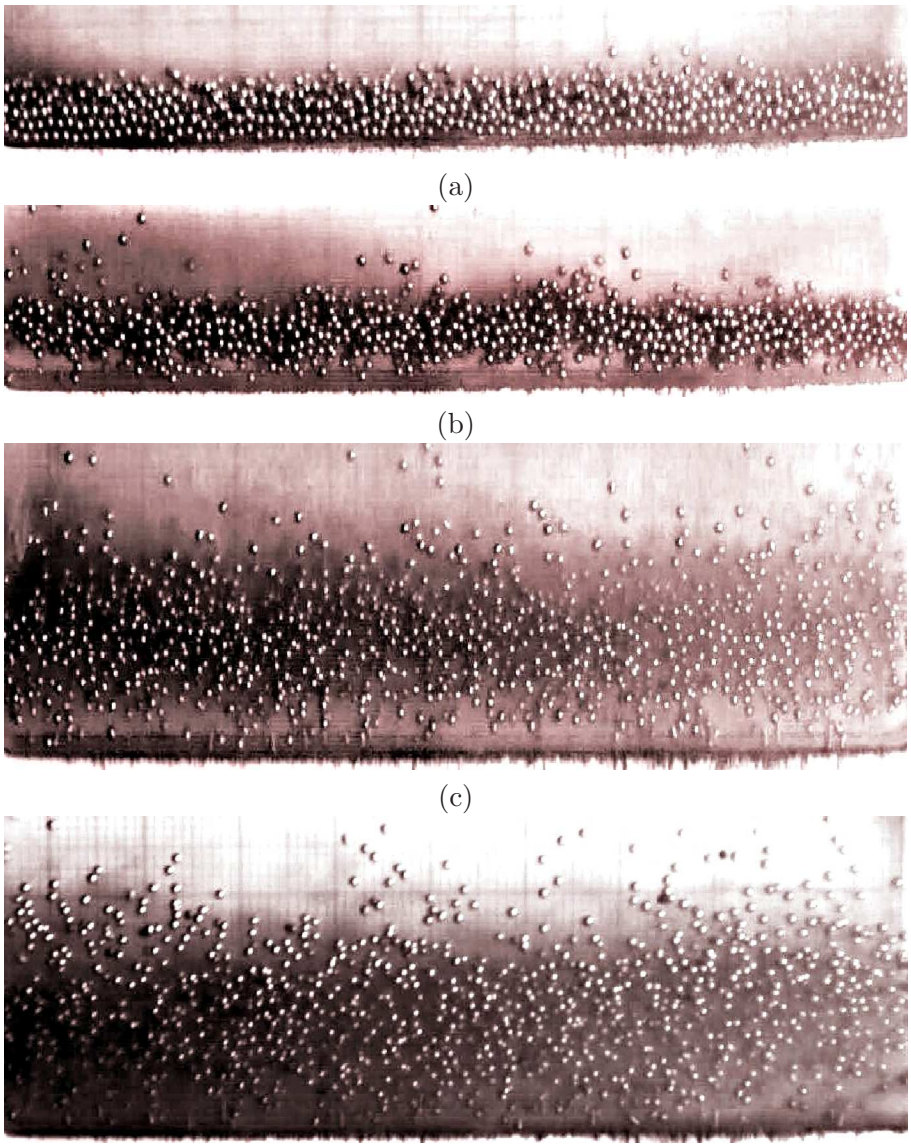

(a) (b) (c) (d)

Figure 5.91: **Transition between various patterns at constant shaking intensity $\Gamma = 25$ in $F = F_s + F_b = 3$ layers of equimolar mixture of brass and steel particles (both having diameter 1.0 mm) with increasing A/d:** (a) *BB* at $A/d = 0.1$, (b) *LS* at $A/d = 1$, (c) *Gas* at $A/d = 2$, and (d) *Convection* at $A/d = 3$.

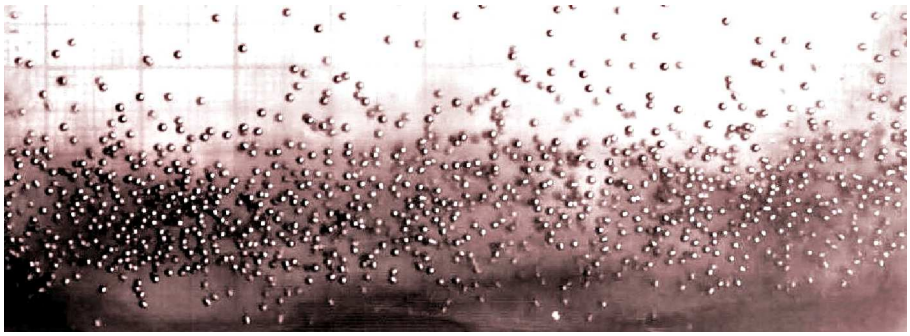

(e)

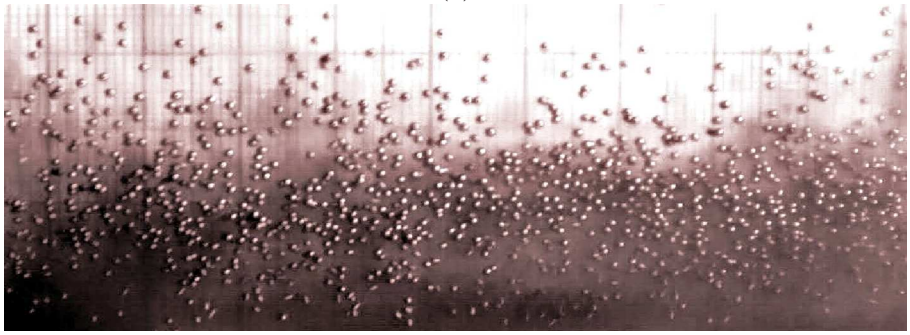

(f)

Figure 5.92: *Continued Fig. 5.91* **Transition between various patterns at constant shaking intensity** $\Gamma = 25$ **in** $\boldsymbol{F = F_s + F_b = 3}$ **layers of equimolar mixture of brass and steel particles (both having diameter 1.0** $\boldsymbol{mm}$**) with increasing** $\boldsymbol{A/d}$**:** (e) *Gas* at $A/d = 4.5$, and (f) *Gas* at $A/d = 6$.

oscillating/ratcheting synchronous cluster and, (1d) a synchronous granular Leidenfrost state (LS), and (2) a synchronous LS coexisting with unsteady convection. In all these new states, the gaseous region is always found to be dominated with heavier particles, while the lighter particles-rich region exists in a *solid-like* or *liquid-like* state. Therefore, the origin of these phase-coexisting patterns is tied to the horizontal segregation of heavier and lighter particles, which, in turn, is tied to the "non-equipartition" of granular energy. To establish the validity of our claim, we performed experiments with two types of mixtures: (i) two different high density-ratio mixtures [steel-glass mixture ($\rho_s/\rho_g \approx 3.06$) and brass-glass mixture ($\rho_b/\rho_g \approx 3.46$)] and (ii) a mixture with a small density-ratio [brass-steel ($\rho_b/\rho_s \approx 1.13$)]. We found that the mixtures with high-density disparity resulted in phase-separation while the mixture with slight density disparity behaved akin to the monodisperse system manifesting single phase patterns.

The variation of species number fraction in the mixture was found to influence the segregation dynamics dramatically, which in turn affected the onset/suppression of various types of patterns. In particular, the bidispersity of a mixture leads to patterns exhibiting phase separation, while, as the mixture approaches the limits of monodispersity ($F_i/F \to 0$ or 1), the binary mixture consisted of patterns with a single phase (gas or liquid or solid). Such characteristic features of patterns were ascertained from the examination of phase diagrams constructed on $(\Gamma, F_i/F)$-plane in Chapter 5.

We also discovered a simple recipe to control the buoyancy-driven convective motion in the shaken granular bed. We demonstrated this recipe in Chapter 5, wherein we showed that the

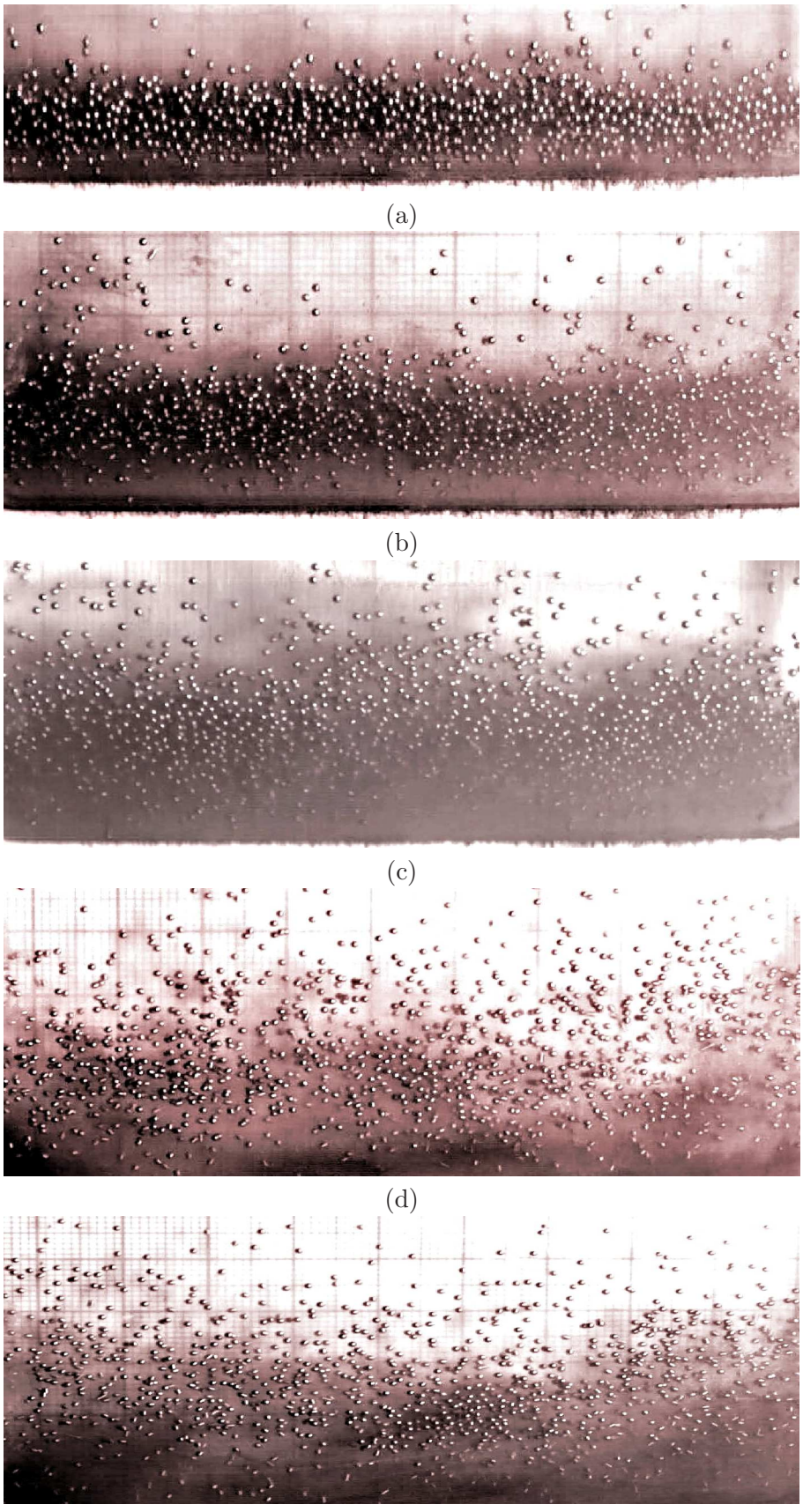

(a) (b) (c) (d) (e)

Figure 5.93: **Transition between various patterns at constant shaking intensity $\Gamma = 50$ in $F = F_s + F_b = 3$ layers of equimolar mixture of brass and steel particles (both having diameter 1.0 mm) with increasing A/d:** (a) *LS* at $A/d = 0.5$, (b) *Convection* at $A/d = 1.5$, (c) *Convection* at $A/d = 3$, (d) *Gas* at $A/d = 4.5$, and (e) *Gas* at $A/d = 6$.

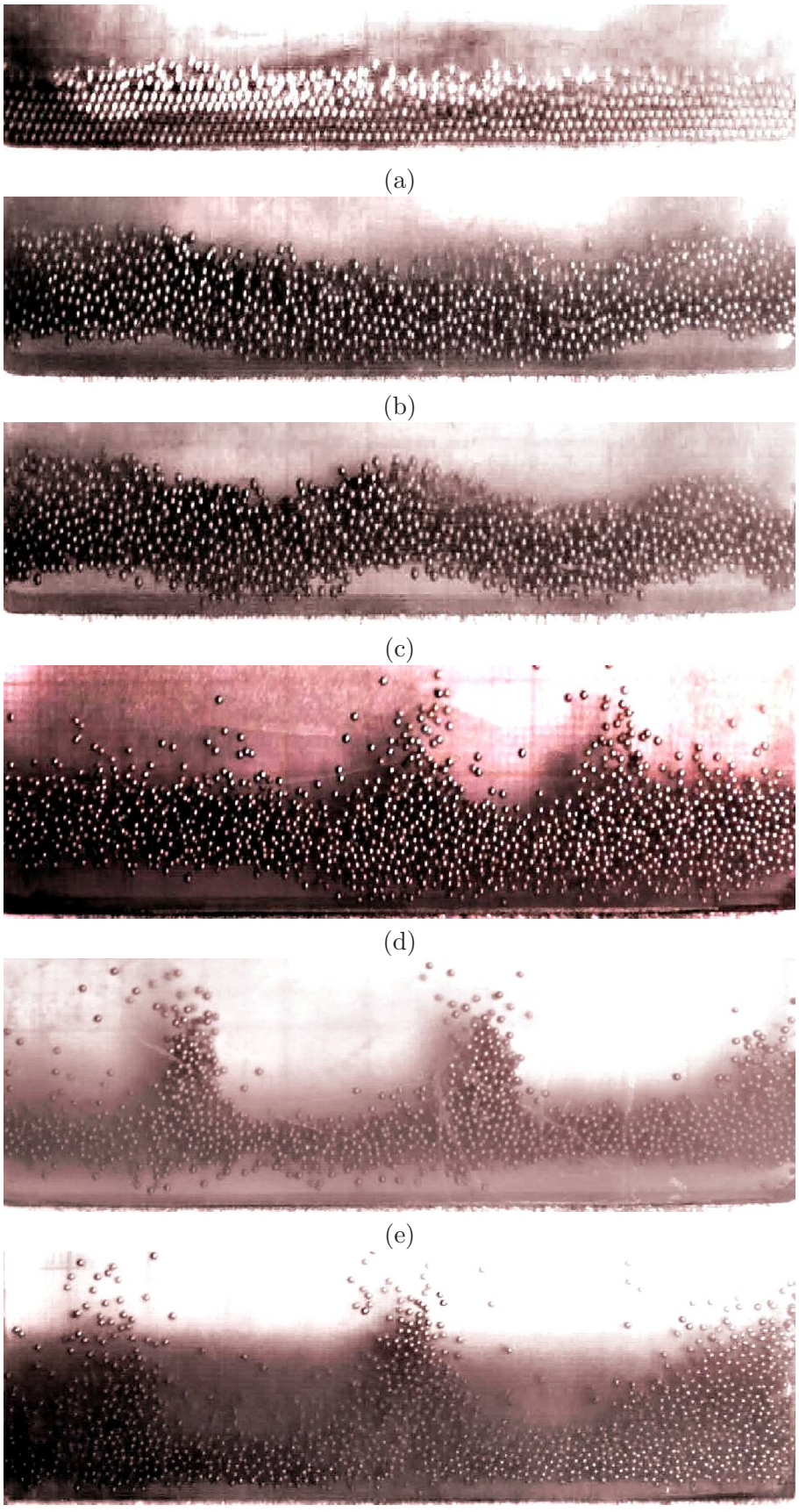

(a)

(b)

(c)

(d)

(e)

(f)

Figure 5.94: **Transition between various patterns at constant shaking intensity $\Gamma = 7$ in $F = F_s + F_b = 6$ layers of equimolar mixture of brass and steel particles (both having diameter 1.0 mm) with increasing A/d:** (a) *BB* at $A/d = 0.2$, (b) *UW* ($n = 2$ mode) at $A/d = 1$, (c) *UW* ($n = 4$ mode) at $A/d = 1.5$, (d) *Spikes* at $A/d = 2.5$, (e) *Spikes* at $A/d = 4.5$, and (f) *Spikes* at $A/d = 6$.

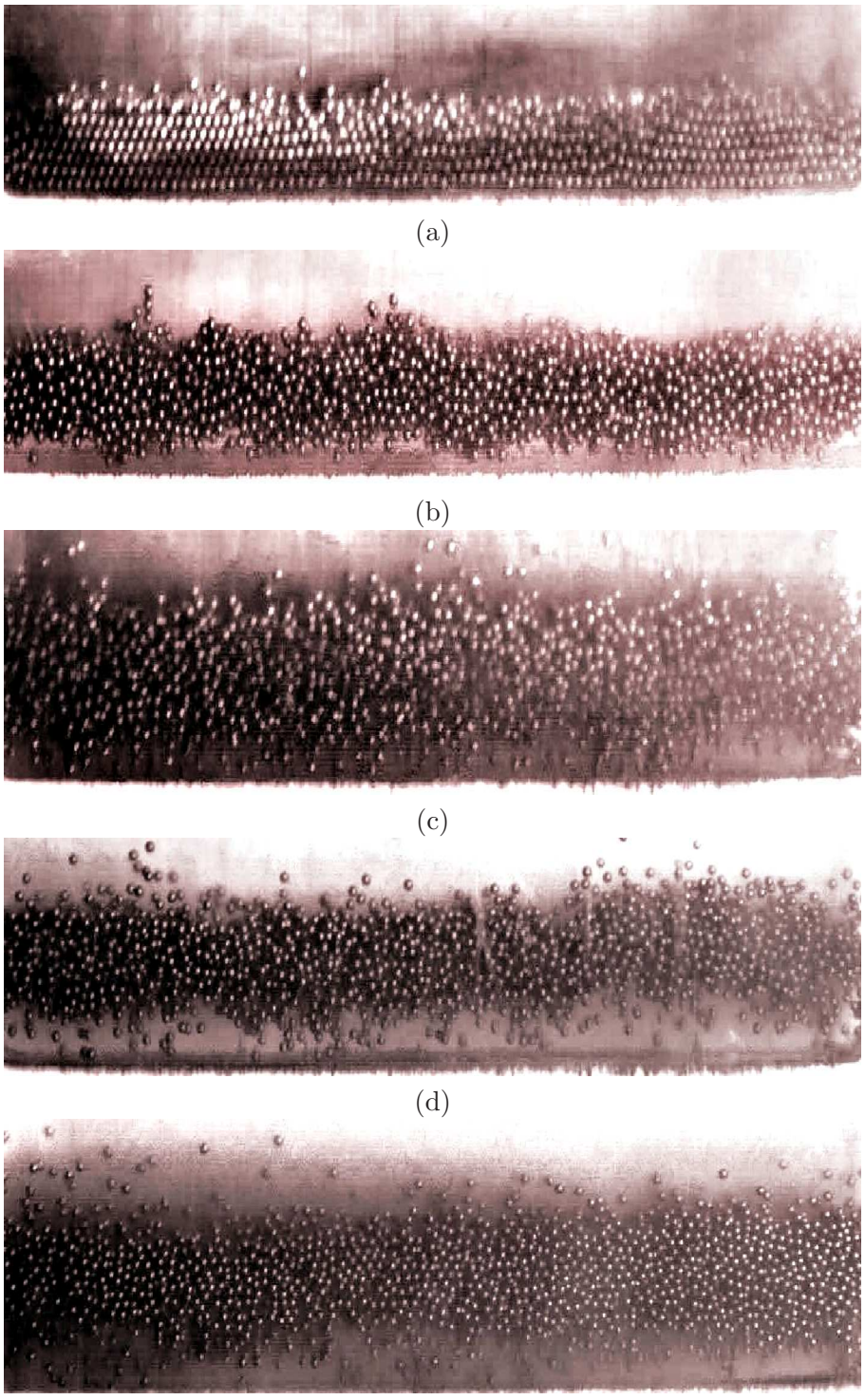

(a)

(b)

(c)

(d)

(e)

Figure 5.95: **Transition between various patterns at constant shaking intensity** $\Gamma = 25$ **in** $\boldsymbol{F = F_s + F_b = 6}$ **layers of equimolar mixture of brass and steel particles (both having diameter 1.0** $\boldsymbol{mm}$**) with increasing** $\boldsymbol{A/d}$**:** (a) BB at $A/d = 0.2$, (b) LS at $A/d = 1.5$, (c) LS at $A/d = 3$, (d) LS at $A/d = 4.5$, and (e) LS at $A/d = 6$.

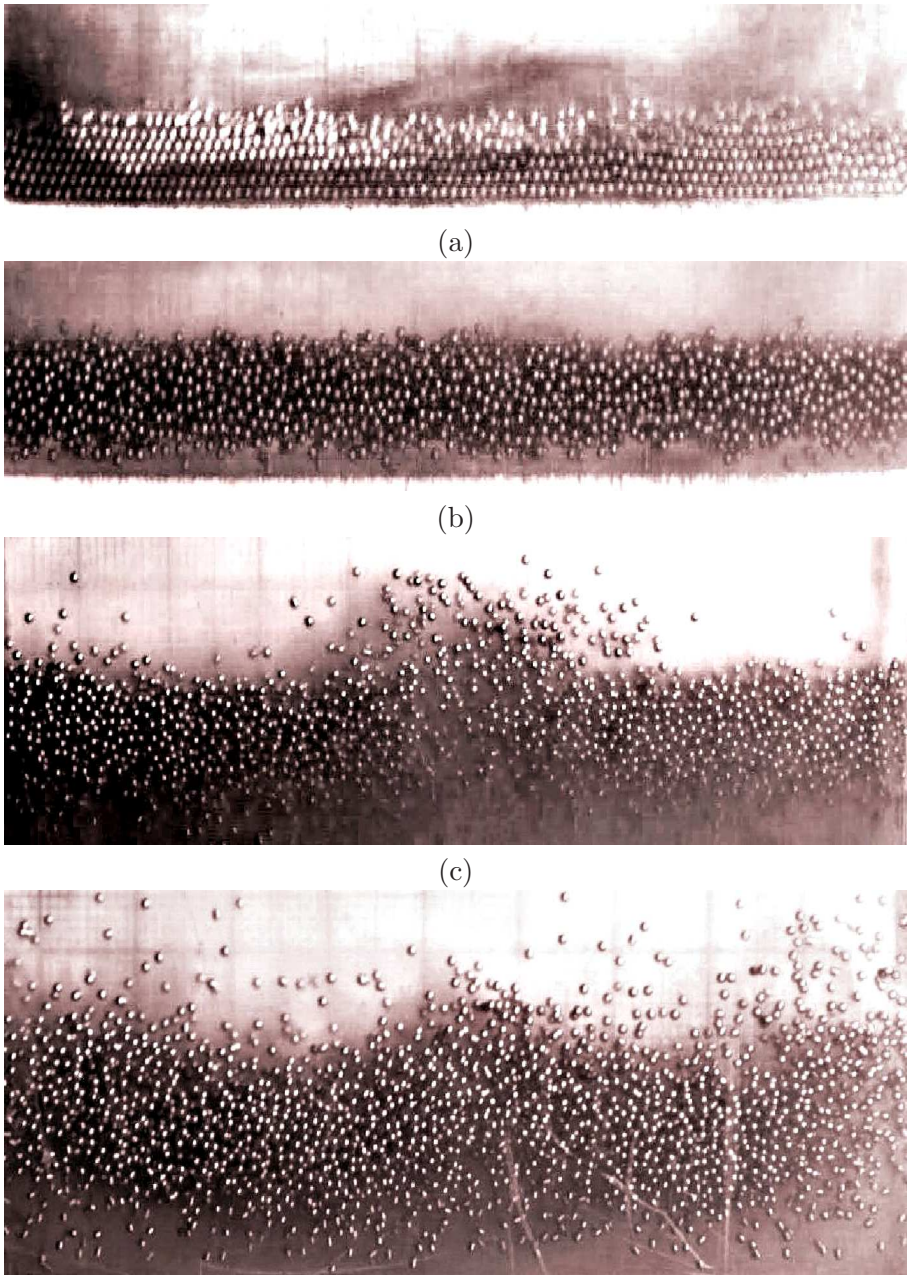

(a) (b) (c) (d)

Figure 5.96: **Transition at constant shaking intensity $\Gamma = 50$ in $F = F_s + F_b = 6$ layers of equimolar mixture of brass and steel particles (both having diameter 1.0 mm) with increasing A/d:** (a) *BB* at $A/d = 0.2$, (b) *LS* at $A/d = 1.5$, (c) *Convection* at $A/d = 4.5$, and (d) *Convection* at $A/d = 6$.

convection can be controlled by adding a very small amount (less than 5%) of heavier particles into a collection of lighter particles at the same energy input: the number of convection rolls decreased, leading to a "partial-convection" state in which a pair of counter-rotating rolls at one end of the container coexisted with a Leidenfrost state at the other end. Adding 50% heavier particles in the system suppresses the convection completely, giving birth to a complete Leidenfrost state (*LS*) spanning the whole length of the container.

We uncovered a dual dynamics of *Cluster+Gas* pattern: (i) a *stationary* cluster coexisting with a *Gas* for $1 \leq F \leq 3$ at lower shakings $5 < \Gamma < 28$ and (ii) an *Ratcheting/Oscillating* cluster coexisting with a *Gas* at higher shaking intensities $28 < \Gamma < 46$ and for filling depths $2 \leq F \leq 3$. The *stationary* cluster was born on either side of the container but once formed it retains its position over tens of thousands of shaking cycles. In contrast, *ratcheting/oscillating* cluster was found to drift from one side of the container to the other side.

Lastly, another interesting finding in shaken binary granular mixtures was the 'hysteretic' transition (downsweeping path bifurcates from the upsweeping one) from a 'complete' single-phase state to the 'partial' twin-phase states. The origin of such 'hysteresis' in the transition from *LS* to *LS+Convection* was identified by conducting experiments in an evacuated container at low vacuum levels. We found that the degree of hysteresis is maximum at atmospheric ambient pressure (P_{atm}) and suppresses completely at very low pressure settings. This phenomenon was explained by considering the theory of *viscous drag* experienced by two types of species constituting the mixture (Burtally *et al.* 2002).

Chapter 6

Conclusions and Future Work

6.1 Summary and Conclusions

We have carried out a detailed and systematic investigation of pattern formation dynamics in vertically shaken (i) quasi-two-dimensional and (ii) two-dimensional granular systems. A collection of spherical glass/steel/brass balls were held in a Heleshaw-type container of length $L/d \sim 100$, height $H/d > 100$ and depth $D/d \in (1.2, 5.5)$, with d being the diameter of a particle. This container was mounted on an Electromagnetic shaker and shaken harmonically via $y = A\sin(2\pi ft)$, where A is the amplitude of shaking and f is its frequency. In addition to the study of the patterned states in monodisperse systems of spherical glass/steel/brass balls (Chapters 3 and 4), a substantial amount of research has been focussed on the segregation dynamics and the pattern evolution in binary granular mixtures (Chapter 5).

The experimental results were presented for a wide range of (i) shaking intensities $\Gamma = A\omega^2/g \in (0, 55)$, (ii) particle loading or filling depths $F = h_0/d$ (where h_0 is the number of particle layers at rest), (iii) amplitude ratio $A/d \in (1, 6)$ and (iv) the relative number fraction ratio F_i/F of species i. Different types of patterns found in both monodisperse and bidisperse mixtures have been complied in phase diagrams on (i) the (Γ, F)-plane, (ii) the $(\Gamma, A/d)$-plane and (iii) the $(\Gamma, F_i/F)$-plane. In adiition to showing the raw images of various patterns, quantitative measurements have been made on (i) the coarse-grained velocity field via PIV (particle image velocimetry) (ii) the density and granular temperatures as well as the pair-correlation functions (for the case of a monolayer system) using particle tracking algorithms.

6.1.1 Patterns in monodisperse system

Most of the phenomena observed in the monodisperse granular system are characteristically similar to those reported by Eshuis *et al.* (2007). However, we found certain differences with the phase diagrams of Eshuis *et al.* (2007) and reported a new pattern (spikes) as well as a new route to convection from a gaseous state:

- We observed the emergence of a new type of subharmonic $(f/4)$ wave, called *Spikes*, which is absent in the phase diagrams of Eshuis *et al.* (2007) for the same monodisperse system. Moreover, we observed these *Spikes* even in binary granular mixtures. The 'Spikes patterns" correspond to an array of peaked structures along the length of the container were also reported by Sano *et al.* (1999) in a three-dimensional experimental setup.

- For lesser mumber of particle layers $F = h_0/d$, we observed a transition to the *Convection* regime from the gaseous phase whereas Eshuis *et al.* (2007) did not find such a transition. The related phase diagrams are shown in Figs. 6.1(a) and 6.1(b).

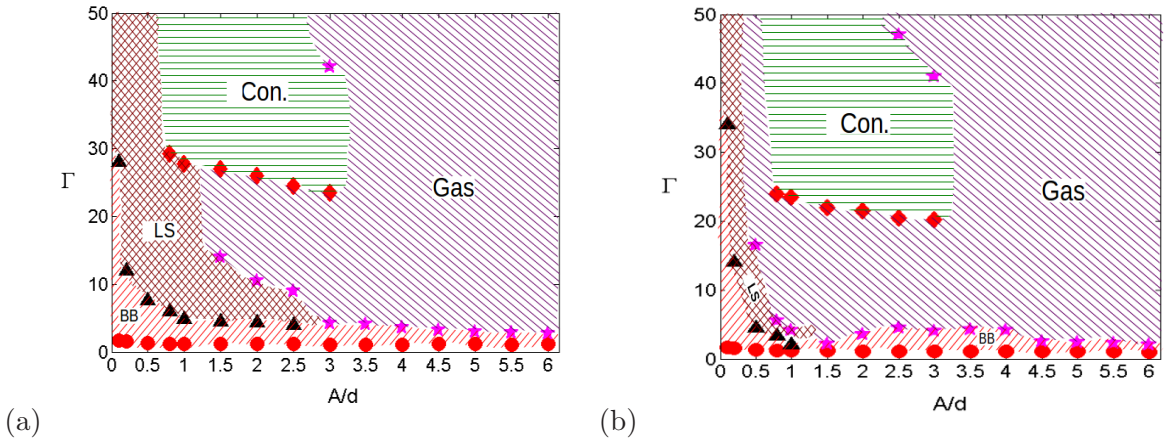

Figure 6.1: **Phase diagram on $(\Gamma, A/d)$-plane for $F = 3$ layers of 1.0 mm diameter particles confined in $L/d = 80$ box: (a) glass particles, and (b) steel particles.** The shaking intensity Γ has been increased at a constant shaking amplitude A/d via ramping frequency at a linear rate of 0.01 Hz/s.

- Eshuis *et al.* (2007) observed a transition to *Convection* from the *BB* regime which we did not find.

The qualitative nature of these patterns in the monodisperse system is independent of density of the particles used, although a variation in the onset value of Γ for the patterns is indeed observed in the phase diagrams. One remarkable characteristic of the convection which we observed in our system is that they are buoyancy-driven and occurs at strong shakings ($\Gamma > 25$) showing large density differences, similar to Ramírez *et al.* (2000) and Eshuis *et al.* (2007, 2010). This is in stark contrast with boundary-driven convection rolls observed at mild fluidization ($\Gamma < 5$) and induced by friction at two side walls (Clément & Rajchenbach 1991; Knight *et al.* 1993; Ehrichs *et al.* 1995; Aoki *et al.* 1996; Knight *et al.* 1996; Hsiau & Chen 2000; Wildman *et al.* 2001). Moreover, the number of convection rolls appearing in the system is found to be strongly dependent on the length of the container; the number decreases in shorter length container. This indeed suggests that a minimum horizontal length scale is associated with each convection roll and a particular length container can accommodate only a certain number of rolls at a given shaking intensity.

In addition to the shaking intensity Γ, the shaking amplitude A/d also played a crucial role in the fluidization of the particles leading to different patterns. For a given shaking intensity Γ and layer depth F, the higher shaking amplitude assisted the system to become fluidized states, such as *Gas* and *Convection*. The effects of the varying shaking amplitude on the dynamical patterns are clearly evident from the phase diagrams obtained on $(\Gamma, A/d)$-plane in Figs. 6.1(a) and 6.1(b).

6.1.2 Dynamics and Microstructure in a Monolayer System

In Chapter 4, we focused on studying the the unsteady dynamics and the microstructure of the well-celebrated 'density-inverted' *Leidenfrost State (LS)*. To accomplish this study, we performed experiments on the same two-dimensional Heleshaw-type container, with the depth of

the container (D) being slightly larger than the particle diameter ($D/d \sim 1.2$). Experiments have been carried out by considering various filling depths of 2.0 mm glass beads and $F = 12$ layers of 5.0 mm glass beads. In both case, we observed two phases, namely, the *Bouncing Bed (BB)* and the *Leidenfrost State (LS)* in a large parameter space in the $(\Gamma, A/d)$-plane.

The critical shaking intensity for the transition from *BB* to *LS* (Γ_{crit}) was found to have a power-law dependence on the particle loading depth ($F = h_0/d$) as well as on the shaking amplitude (A/d). The density and temperature profiles, obtained via particle tracking algorithms, have revealed a clear signature of the transition from the *BB* to the extreme density-inversion case of *LS*.

The study of the microstructure in the *LS* via radial distribution function (RDF) and radial-angular distribution function (RADF) helped to identify three distinct regions in *LS*: (i) the hexagonally packed compact *floating cluster*, (ii) the dilute gaseous *collisional layer* adjacent to the base of the vibrating container that acted as a cushion for the floating cluster and (iii) the *ballistic layer* consisting of fluidized particles on the top of clustered region. The anisotropy in the 'crysralline' packing of *BB* as well as in the 'floating cluster' of *LS* was found to decrease if one gradually increased the shaking amplitude (A/d) at a fixed shaking intensity Γ and vice versa.

Furthermore, we reported a novel unsteady behavior associated with the Leidenfrost state, wherein the height of the interface (that separates the floating cluster from the dilute gaseous region) as well as the top surface of the bed oscillated sinusoidally with time but with different amplitudes and a phase-lag. The oscillation frequencies closely matched the frequency of the shaker. Therefore, the granular LS is not a quasi-stationary state, rather it is a period-1 or f-wave. The amplitude difference and the phase-lag between the top-surface and interface motions are two distinguishing features of the "oscillatory" granular *Leidenfrost State*.

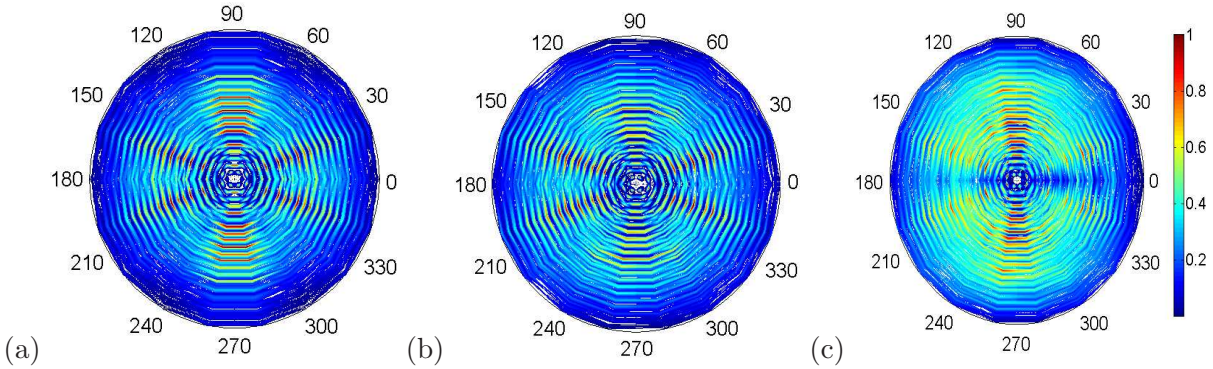

Figure 6.2: **Polar plots of radial angular distribution function (RADF)** for *BB* states with increasing A/d at constant shaking intensity Γ.

For the first time, the inception of *Convection* has also been reported in such a two-dimensional monolayer system by confining the beads in a longer length container. A phase diagram has been obtained (Fig. 4.23) that depicted the additional transition of *LS* to *Convection* having a pair of rolls which, with increasing shaking intensity Γ, became a one-roll convection state, and finally to a disordered gaseous state. To summarize, with increasing Γ, the sequence of bifurcations unfolded as follows: SB (solid bed) to BB (bouncing bed) to LS

(Leidenfrost state) to "2-roll Convection" to "1-roll Convection" to Gas.

6.1.3 Patterns and Segregation in Vibrated Binary Mixtures

The vertically shaken granular mixtures of equal sized, distinct density (large density ratio) particles have unfolded a diverse variety of patterns as detailed in Chapter 5. The most intriguing case is that of horizontal-segregation-driven 'phase-coexisting' patterns. These novel patterns display the coexistence of (i) sub-harmonic and synchronous states having different spatial and temporal orders and (ii) that of gas- and liquid-like states (both having the same temporal order but different spatial order), along with horizontal segregation, and (ii) a "partial" convection state that coexists with a Leidenfrost state (LS). For instance, an *UW* (undulatory wave) coexisting with a granular *Gas* is an example of a phase-coexisting pattern that has different spatial order (UW is in a liquid state and 'Gas' is spatially disordered) as well as different temporal symmetry (UW is a period-2 or f/2-wave, but the 'Gas' temporally disordered). On the other hand, both the *Cluster+Gas* and the *LS+Gas* have different spatial order but both being f-waves (i.e. synchronous with the excitation frequency) and hence have the same temporal symmetry. In summary, we have discovered an array of phase-coexisting patterns: (1) a granular gas coexisting with (1a) a subharmonic ($f/2$) undulatory wave (UW), (1b) a synchronous solid-like bouncing bed (BB), (1c) a static or an oscillating/ratcheting synchronous cluster and, (1d) a synchronous granular Leidenfrost state (LS), and (2) a synchronous LS coexisting with unsteady convection. In all these new states, the gaseous region is always found to be dominated with heavier particles, while the lighter particles-rich region exists in a *solid-like* or *liquid-like* state. Therefore, the origin of these phase-coexisting patterns is tied to the horizontal segregation of heavier and lighter particles, which, in turn, is tied to the "non-equipartition" of granular energy. To establish the validity of our claim, we performed experiments with two types of mixtures: (i) two different high density-ratio mixtures $\big[$steel-glass mixture ($\rho_s/\rho_g \approx 3.06$) and brass-glass mixture ($\rho_b/\rho_g \approx 3.46$)$\big]$ and (ii) a mixture with a small density-ratio $\big[$brass-steel ($\rho_b/\rho_s \approx 1.13$)$\big]$. We found that the mixtures with high-density disparity resulted in phase-separation while the mixture with slight density disparity behaved akin to the monodisperse system manifesting single phase patterns.

In addition to horizontal segregation we also observed vertical segregation (Brazil-nut segregation), however, it occured only in the case of BB states at low shakings. Although, this vertical segregation of two species in a vertically shaken binary granular mixture is well-known in literature (Brazil-nut segregation or reverse Brazil-nut segregation (Williams 1963; Rosato *et al.* 1987; Jullien *et al.* 1992; Duran *et al.* 1993; Dippel & Luding 1995; Shinbrot & Muzzio 1998; Hong *et al.* 2001)), our finding of horizontal segregation is indeed novel.

The variation of species number fraction in the mixture was found to influence the segregation dynamics dramatically, which in turn affected the onset/suppression of various types of patterns. In particular, the bidispersity of a mixture leads to patterns exhibiting phase separation, while, as the mixture approaches the limits of monodispersity ($F_i/F \to 0$ or 1), the binary mixture consisted of patterns with a single phase (gas or liquid or solid). Such characteristic features of patterns were ascertained from the examination of phase diagrams constructed on $(\Gamma, F_i/F)$-plane in Chapter 5.

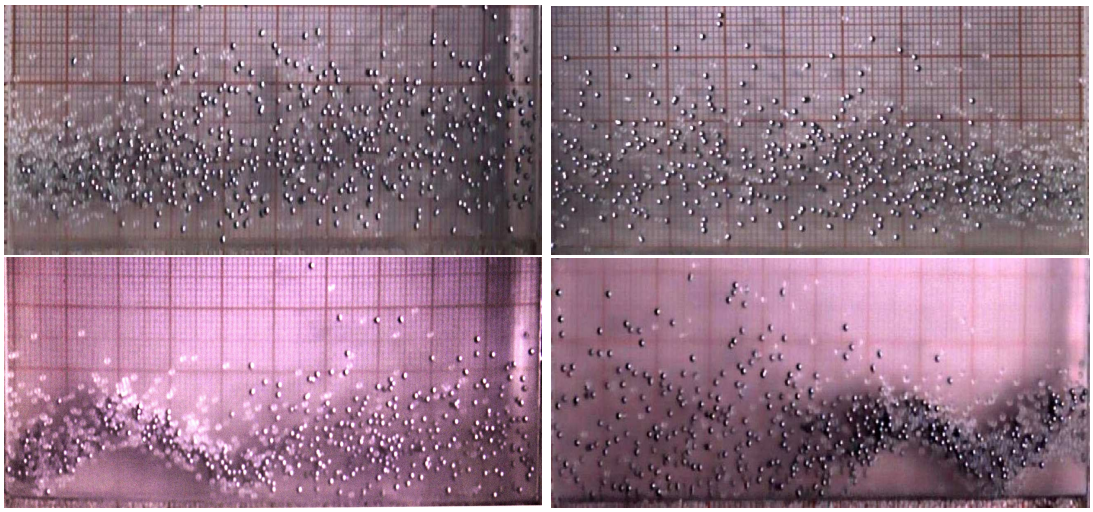

Figure 6.3: **Phase coexisting patterns**. Top row: *Gas+cluster*. Bottom row: UW+Gas

We discovered a simple recipe to control the buoyancy-driven convective motion in the shaken granular bed. We demonstrated this recipe in Chapter 5, wherein we showed that the convection can be controlled by adding a very small amount (less than 5%) of heavier particles into a collection of lighter particles at the same energy input: the number of convection rolls decreased, leading to a "partial-convection" state in which a pair of counter-rotating rolls at one end of the container coexisted with a Leidenfrost state at the other end. Adding 50% heavier particles in the system suppresses the convection completely, giving birth to a complete Leidenfrost state (LS) spanning the whole length of the container.

We uncovered a dual dynamics of *Cluster+Gas* pattern: (i) a *stationary* cluster coexisting with a *Gas* for $1 \leq F \leq 3$ at lower shakings $5 < \Gamma < 28$ and (ii) an *Ratcheting/Oscillating* cluster coexisting with a *Gas* at higher shaking intensities $28 < \Gamma < 46$ and for filling depths $2 \leq F \leq 3$. The *stationary* cluster was born on either side of the container but once formed it retains its position over tens of thousands of shaking cycles. In contrast, *ratcheting/oscillating* cluster was found to drift from one side of the container to the other side.

A closer inspection of the related movie of this *ratcheting* cluster revealed a more complicated *stick-slip-type* oscillatory motion: a cluster of glass-rich particles formed at one end of the container, grew over a period of time till it achieved a critical size, then started moving to the other end, the size of the cluster decreased upon a collision with the end-wall but it regrew again to its original size by accumulating particles, and finally started moving backward to its original end. Similar ratchet-type collective motion of particles has been found in a vertically vibrated setup with a 'saw-tooth' bottom plate (Farkas *et al.* 1999) as well as in 'compartmentalized' granular gas (Meer *et al.* 2004) which are, however, in stark contrast to our finding of spontaneous ratcheting motion in an unpartitioned box with an unbiased flat bottom plate. The normal restitution coefficient (and hence inelastic disspation) seems to be a key player for the onset of cluster and its mobility. We postulated a theory based on the competition the between differential dissipation rate ($e_n^1 \neq e_n^2$, where e_n^1 and e_n^2 are the normal restitution coefficients of two species in the binary mixture, respectively) and the shaking intensity Γ that might be responsible for such spontaneous ratcheting motion of the cluster through a granular gas.

Lastly, another interesting finding in shaken binary granular mixtures was the 'hysteretic' transition (downsweeping path bifurcates from the upsweeping one) from a 'complete' single-phase state to the 'partial' twin-phase states. The origin of such 'hysteresis' in the transition from *LS* to *LS+Convection* was identified by conducting experiments in an evacuated container at low vacuum levels. We found that the degree of hysteresis is maximum at atmospheric ambient pressure (P_{atm}) and suppresses completely at very low pressure settings. This phenomenon was explained by considering the theory of *viscous drag* experienced by two types of species constituting the mixture (Burtally *et al.* 2002).

6.2 Future Work

This thesis presented a comprehensive experimental investigation of pattern formation dynamics in harmonically shaken granular bed excited in vertical direction over a wide range of shaking intensities $\Gamma \in (0, 55)$. Despite probing a broad control parameter space in this research, the response of a set of control variables on the system still remains unexplored. In addition, our work poses several theoretical challanges for further research. The possible directions for the extension of this work on experimental, theoretical, and numerical grounds are summarized below.

- Within theroretical domain the following intriguing questions need to be addressed by conceiving an appropriate theoretical model. How does a "partial" undulatory wave survive with one end being in continual touch with a granular gas? What boundary condition one should use for "partial" undulatory waves? Does there exist a theory for granular mixtures that could unravel horizontally segregated states with different temporal and/or spatial symmetries? If so, can the partial (unsteady) convection state be explained as a bifurcation from the horizontally segregated Leidenfrost state?

- An immediate future work should focus on to fully validate the conjecture proposed for the driving mechanism of the ratcheting/oscillating cluster as well as to quantify numerically the role of energy non-equipartition and the related kinetics and dynamics of the horizontal-segregation-driven 'phase-coexisting' pattern formation scenario.

- In our experiments, the two side walls of the container have played a crucial role in fixing the boundary conditions for patterns, such as that of 'complete' undulatory wave and 'partial' undulatory wave, etc. We conjecture that the dynamics of the phase-coexisting patterns may change drastically, if one excludes the effect of side-walls. This can be achieved by carrying out experiments in an annular container. The annular cells have been used in past studies on surface waves in vertically vibrated monodisperse granular materials (Pak & Behringer 1993) and Brazil-nut effect observed with a large intruder (Chaiworn *et al.* 2010). But to our knowledge, the vibrated binary mixture problem of the present study has not been considered in an annular geometry.

- Our experimental work on binary granular mixtures focussed on same-size spherical particles of different densities. A natural augmentation of our work would be to investigate the pattern evolution and the segregation behavior in mixtures of unequal-sized particles

having the same or dissimilar densities. A study by Knight *et al.* (1993) has dealt with the rise of a single large glass bead through a vibrated cylindrical column of smaller particles; although they found that size separation arises from convective processes, none of the investigations has focussed on shaken binary mixtures constituting of distinct size particles and having comparable volume fractions of two species. Such type of study can be done in a quasi-two-dimensional box which can set a paradigm for further research.

- Another extension of the binary mixture problem would be to probe the segregation dynamics and the resulting pattern formation scenario in a vertically shaken *ternary* granular mixtures of different mechanical properties (size, density and/or restitution coefficient). Ternary mixtures represent the first step towards the understanding of the segregation in multicomponent mixtures, which are of considerable importance in industrial and natural settings, but unfortunately this problem has not received much attention from the granular community. The experimental investigation of the ternary mixture has been carried out to lesser extent. For example, Lecocq & Vandewalle (2000) studied stripes ordering in self-stratification, when a mixture of small, medium, and large grains was poured in vertical Hele-Shaw cell. Similarly, the segregation dynamics in ternary mixture has been studied in the cylindrical geometries, experimentally and numerically by Taberlet *et al.* (2006), and experimentally by Hajra & Khakhar (2011); Pereira & Cleary (2012). In any case, the segregation behavior and the pattern formation in externally vibrated ternary granular mixtures confined in a quasi-two-dimensional geometry still remains an open problem which needs to be focussed in future studies.

.

Appendix A

Raw Data for Phase Diagrams in Chapter 3

F	$SB \rightarrow BB$	$BB \rightarrow Gas$	$BB \rightarrow UW$	$BB \rightarrow Spikes$	$Spikes \rightarrow UW$	$Gas \rightarrow Con.$	$UW \rightarrow LS$	$LS \rightarrow Con$	$UW \rightarrow Gas$	$LS \rightarrow Gas$
2.5	1.48	5.5	-	-	-	-	-	-	-	-
3	1.52	10	-	-	-	-	-	-	-	-
3.5	1.55	-	5.6	-	-	29.5	-	-	11	-
4	1.58	-	5	-	-	30	12	-	-	24
4.5	1.61	-	5.2	-	-	-	13	32	-	-
5	1.63	-	5	-	-	-	12	34	-	-
6	1.65	-	-	5.7	8	-	12	47	-	-
6.5	1.67	-	-	6.2	8.1	-	14	-	-	-
7	1.68	-	-	6.1	8	-	13.8	-	-	-
7.5	1.69	-	-	6.2	8.2	-	13.7	-	-	-
8	1.72	-	-	6.3	8.3	-	14	-	-	-

Table A.1: **Raw Data for Γ_{crit} in Fig. 3.14(a)**

F	$SB \rightarrow BB$	$BB \rightarrow Gas$	$BB \rightarrow UW$	$BB \rightarrow Spikes$	$Spikes \rightarrow UW$	$Gas \rightarrow Con.$	$UW \rightarrow LS$	$LS \rightarrow Con$	$UW \rightarrow Gas$
2.5	1.48	5.5	-	-	-	-	-	-	-
3	1.5	7.5	-	-	-	-	-	-	-
3.5	1.52	-	5.73	-	-	23.37	-	-	10.86
4	1.55	-	5.32	-	-	30	-	-	17.4
4.5	1.56	-	5	-	-	-	15.6	32.6	-
5	1.58	-	4.8	-	-	-	17.4	35	-
6	1.65	-	5.3	-	-	-	18	45	-
6.5	1.67	-	6	-	-	-	18	46.4	-
7	1.7	-	7	-	-	-	14	-	-
7.5	1.71	-	-	7	8.5	-	16.5	-	-
8	1.72	-	-	7	9	-	18.4	-	-

Table A.2: **Raw Data for Γ_{crit} in Fig. 3.14(b)**

F	$SB \rightarrow BB$	$BB \rightarrow Gas$	$BB \rightarrow UW$	$BB \rightarrow Spikes$	$Spikes \rightarrow UW$	$UW \rightarrow LS$	$LS \rightarrow Con$
2.5	1.26	3.5	-	-	-	-	-
3	1.28	-	7.9	-	-	-	-
3.5	1.31	-	-	6.5	8.4	11	28.5
4	1.34	-	-	6.2	8.42	11.2	30
5	1.37	-	-	6.1	7.9	10.9	32.5
6	1.42	-	8	-	-	13.5	36
6.5	1.45	-	8.1	-	-	13	40
7	1.47	-	7.6	-	-	11.5	-
8	1.5	-	7.5	-	-	11	-

Table A.3: **Raw Data for Γ_{crit} in Fig. 3.19**

A/d	$SB \rightarrow BB$	$BB \rightarrow Gas$	$BB \rightarrow LS$	$LS \rightarrow Gas$	$Gas \rightarrow Con.$	$Con. \rightarrow Gas$
0.1	1.7	-	34	-	-	-
0.2	1.63	-	14	-	-	-
0.5	1.3	-	4.5	16.5	-	-
0.8	1.25	-	3.3	5.5	24	-
1	1.2	-	2	4.1	23.5	-
1.5	1.17	2.1	-	-	22	-
2	1.13	3.5	-	-	21.5	-
2.5	1.11	4.5	-	-	20.5	47
3	1.07	4	-	-	20.2	41
3.5	1.06	4.2	-	-	-	-
4	1.057	4.1	-	-	-	-
4.5	1.05	2.5	-	-	-	-
5	1.04	2.4	-	-	-	-
5.5	1.037	2.3	-	-	-	-
6	1.03	2	-	-	-	-

Table A.4: **Raw Data for Γ_{crit} in Fig. 3.29(a)**

A/d	$SB \rightarrow BB$	$BB \rightarrow LS$	$BB \rightarrow Spikes$	$Spikes \rightarrow UW$	$LS \rightarrow Con.$	$UW \rightarrow LS$	$BB \rightarrow UW$
0.1	2.65	-	-	-	-	-	-
0.2	2.55	-	-	-	-	-	-
0.5	1.92	12	-	-	-	-	-
0.8	1.77	10.05	-	-	-	-	-
1	1.29	10	-	-	-	-	-
1.5	1.28	9.7	-	-	45.7	-	-
2	1.29	-	-	-	32	9.2	7.48
2.5	1.28	-	-	-	31	9.3	7.66
3	1.2	-	6	8.2	30.5	10.9	-
3.5	1.21	-	6.05	7.57	29	11	-
4	1.23	-	5.95	7.88	27.5	10.9	-
4.5	1.25	-	6.1	8.3	26.5	11.5	-
5	1.24	-	6	7.88	26	11.3	-
5.5	1.22	-	5.9	8.47	25	11.5	-
6	1.21	-	5.92	8.6	24	11.2	-

Table A.5: **Raw Data for Γ_{crit} in Fig. 3.29(b)**

A/d	$SB \rightarrow BB$	$BB \rightarrow LS$	$LS \rightarrow Con.$	$BB \rightarrow Gas$	$LS \rightarrow Gas$	$Gas \rightarrow Con.$	$Con. \rightarrow Gas$
0.1	1.65	28	-	-	-	-	-
0.2	1.55	12	-	-	-	-	-
0.5	1.3	7.6	-	-	-	-	-
0.8	1.23	6	29.2	-	-	-	-
1	1.19	4.8	27.8	-	-	-	-
1.5	1.18	4.4	-	-	14	27	-
2	1.15	4.3	-	-	10.5	26	-
2.5	1.14	4	-	-	9	24.5	-
3	1.12	-	-	4.2	-	23.5	42
3.5	1.11	-	-	4.1	-	-	-
4	1.109	-	-	3.6	-	-	-
4.5	1.105	-	-	3.2	-	-	-
5	1.102	-	-	2.9	-	-	-
5.5	1.09	-	-	2.85	-	-	-
6	1.05	-	-	2.65	-	-	-

Table A.6: **Raw Data for Γ_{crit} in Fig. 3.39(a)**

A/d	$SB \rightarrow BB$	$BB \rightarrow UW$	$UW \rightarrow BB$	$BB \rightarrow Spikes$	$Spikes \rightarrow UW$	$UW \rightarrow LS$	$LS \rightarrow Con.$
0.1	2.6	-	-	-	-	-	-
0.2	2.5	4.4	12	-	-	-	-
0.5	2.4	4.6	-	-	-	13.8	-
0.8	1.78	5.3	-	-	-	13.5	-
1	1.54	6	-	-	-	11.5	-
1.5	1.5	6.3	-	-	-	9.7	-
2	1.38	6.25	-	-	-	9.66	43.6
2.5	1.34	6.4	-	-	-	9.6	33.5
3	1.28	6.3	-	-	-	10	30.5
3.5	1.25	4.79	-	-	-	11.2	27.5
4	1.23	-	-	5.9	7.66	11.4	26
4.5	1.21	-	-	5.8	8.3	12	25
5	1.19	-	-	5.4	7.9	11.5	24
5.5	1.16	-	-	5.2	8	11.8	23.6
6	1.14	-	-	5.5	7.9	12.2	23

Table A.7: **Raw Data for Γ_{crit} in Fig. 3.39(b)**

Appendix B

Raw Data for Phase Diagrams in Chapter 4

A/d	$SB \rightarrow BB$	$BB \rightarrow LS$
0.1	1.6	-
0.2	1.45	-
0.4	1.4	47
0.5	1.34	39
0.6	1.3	34.5
0.8	1.28	24.5
1	1.25	19
1.2	1.23	16
1.4	1.21	14.6
1.6	1.2	13.4
1.8	1.19	12.6
2	1.173	11.7
2.2	1.163	10.8
2.4	1.15	10.2
2.6	1.13	9.5
2.8	1.12	8.9
3	1.118	8.3

Table B.1: **Raw Data of Γ_{crit} in Fig. 4.1**

A/d	$F = 12, 5.0\ mm$	$\widehat{\Gamma}$	$\widetilde{\Gamma}$
0.1	48	5.517	8.0280
0.2	35	4.022	8.5552
0.4	20.5	2.356	8
0.6	13	1.494	9.0489
0.8	11	1.26	8.3143
1	8	0.919	9.1951
1.5	6	0.689	8.5599
1.8	4.8	0.5517	6.4009

A/d	$F = 15, 2.0\ mm$	$\widehat{\Gamma}$	$\widetilde{\Gamma}$
0.3	32.6	2.918	11.3684
0.4	25.3	2.265	11.3481
0.6	17.8	1.593	11.3842
0.8	13.8	1.235	11.3523
1	11.4	1.02	11.4
1.2	9.7	0.868	11.3777
1.4	8.5	0.761	11.4099
1.6	7.6	0.68	11.4662
1.8	6.8	0.608	11.3729
2	6.1	0.546	11.1874
2.2	5.7	0.51	11.363
2.3	5.5	0.49	11.3992
2.4	5.3	0.47	11.4015
2.6	5	0.447	11.5364
2.8	4.7	0.421	11.5707
3	1.12	0.1	11.7678

A/d	$F = 25, 2.0\ mm$	$\widehat{\Gamma}$	$\widetilde{\Gamma}$
0.4	47	2.266	21.0814
0.5	39	1.88	21.2649
0.6	34.5	1.66	22.0649
0.8	24.5	1.18	20.1544
1	19	0.916	19
1.2	16	0.77	18.7674
1.4	14.6	0.7039	19.5981
1.6	13.4	0.646	20.2167
1.8	12.6	0.607	21.0734
2	11.7	0.564	21.4579
2.2	10.8	0.5207	21.53
2.4	10.2	0.4918	21.9424
2.6	9.5	0.458	21.9192
2.8	8.9	0.429	21.9106
3	8.3	0.4	21.7050

A/d	$F = 35, 2.0\ mm$	$\widehat{\Gamma}$	$\widetilde{\Gamma}$
0.7	42.3	1.349	30.96
0.8	37.6	1.199	30.93
1	31	0.989	31
1.2	26.5	0.845	31.0835
1.4	23.2	0.74	31.1423
1.6	20.6	0.657	31.0794
1.8	18.6	0.593	31.1083
2	17	0.542	31.1781
2.2	15.6	0.497	31.0989
2.4	14.5	0.462	31.1927
2.6	13.5	0.43	31.1484
2.8	12.6	0.402	31.0194
3	11.9	0.379	31.1192

Table B.2: **Raw Data of Γ_{BB}^{LS}, $\widehat{\Gamma}$ and $\widetilde{\Gamma}$ for various data sets in Fig. 4.4**

A/d	$F = 50, 2.0\ mm$	$\widehat{\Gamma}$	$\widetilde{\Gamma}$
1	48.5	1	48.5
1.2	41.3	0.854	48.44
1.4	36	0.744	48.32
1.6	32	0.66	48.27
1.8	29	0.599	48.5
2	26.5	0.547	48.6
2.2	24.2	0.5	48.24
2.4	22.5	0.465	48.4
2.6	21	0.434	48.45
2.8	19.5	0.403	48
3	18.5	0.382	48.378

Table B.3: **Raw Data of Γ_{BB}^{LS}, $\widehat{\Gamma}$ and $\widetilde{\Gamma}$ for $F = 50$ layers of 2.0 mm diameter glass beads in Fig. 4.4**

A/d	$SB \rightarrow BB$	$BB \rightarrow LS$	$LS \rightarrow Con.(2-roll)$	$Con.(2-roll) \rightarrow Con.(1-roll)$	$Con.(1-roll) \rightarrow Gas$
1	1.5	12	44	-	-
1.5	1.45	9.5	39	-	-
2	1.38	7.5	37.1	-	-
2.4	1.33	6.5	37	47	-
3	1.3	5	36	44	-
3.5	1.28	3.85	35	43.4	54
4	1.25	3.15	35.5	43	52

Table B.4: **Raw Data of Γ_{crit} in Fig. 4.23**

Appendix C

Raw Data for Phase Diagrams in Chapter 5

F	SB to BB&Gas	SB to BB	BB&Gas to Gas&Clus.	Gas&Clus. to Gas	Gas&Clus. to Os.Clus.	BB&Gas to UW&Gas	BB to UW	UW&Gas to Gas&LS	UW to Gas&LS	UW to LS	LS to LS&Con.	UW to UW&Gas
1	1.4	-	2.2	5	-	-	-	-	-	-	-	-
1.5	1.42	-	4.2	23	-	-	-	-	-	-	-	-
2	1.45	-	5.5	36	23	-	-	-	-	-	-	-
2.5	1.46	-	5.75	37	26	-	-	-	-	-	-	-
3	1.5	-	-	46.4	29	5.07	-	11.23	-	-	-	-
3.5	1.54	-	-	-	-	4.5	-	13.63	-	-	-	-
4	-	1.55	-	-	-	-	4.83	11.23	-	-	-	8.67
4.5	-	1.56	-	-	-	-	5.9	12	-	-	-	8.4
5	-	1.568	-	-	-	-	5.89	15.65	-	-	-	12.13
5.5	-	1.569	-	-	-	-	7.86	-	12.6	-	-	-
6	-	1.6	-	-	-	-	7.97	-	-	13.95	53.4	-
6.5	-	1.62	-	-	-	-	7.78	-	-	11.6	44.9	-
7	-	1.65	-	-	-	-	8.22	-	-	12.36	-	-

F	SB to BB&Gas	SB to BB	BB&Gas to Gas&Clus.	Gas&Clus. to Gas	Gas&Clus. to Os.Clus.	BB&Gas to UW&Gas	BB to UW	UW&Gas to Gas&LS	UW to Gas&LS	UW to LS	LS to LS&Con.	UW to UW&Gas
1	1.45	-	2.6	9	-	-	-	-	-	-	-	-
1.5	1.454	-	4.2	23.5	-	-	-	-	-	-	-	-
2	1.458	-	5.5	34	23	-	-	-	-	-	-	-
2.5	1.46	-	5.7	27	20	-	-	-	-	-	-	-
3	1.5	-	-	40.6	28	4.83	-	10	-	-	-	-
3.5	1.56	-	-	-	-	7.55	-	15.2	-	-	-	-
4	-	1.565	-	-	-	-	4.78	10.15	-	-	-	7.85
4.5	-	1.57	-	-	-	-	4.6	10.7	-	-	-	7.9
5	-	1.574	-	-	-	-	4.5	-	10.86	-	-	-
5.5	-	1.58	-	-	-	-	4.46	-	11	-	-	-
6	-	1.59	-	-	-	-	4.45	-	-	12.75	46.1	-
6.5	-	1.62	-	-	-	-	4.26	-	-	12.36	48.6	-
7	-	1.64	-	-	-	-	4.68	-	-	14.78	-	-

Table C.1: **Top table: raw data for Γ_{crit} in Fig. 5.1(a). Bottom table: raw data for Γ_{crit} in Fig. 5.1(b).**

F	SB to BB&Gas	SB to BB	BB&Gas to Gas&Clus.	BB&Gas to UW&Gas	BB to UW	UW&Gas to Gas&LS	UW to Gas&LS	UW to LS	UW to UW&Gas	UW&Gas to Gas&Clus	LS to Gas&LS
2.5	1.46	-	5.75	-	-	-	-	-	-	-	-
2.75	1.48	-	7	-	-	-	-	-	-	-	-
2.8	1.49	-	-	4.9	-	-	-	-	-	8.5	-
2.9	1.494	-	-	5.1	-	-	-	-	-	9.8	-
3	1.5	-	-	5.07	-	11.23	-	-	-	-	-
3.25	1.52	-	-	4.6	-	12.5	-	-	-	-	-
3.5	1.54	-	-	4.5	-	13.63	-	-	-	-	-
3.65	1.543	-	-	6	-	12	-	-	-	-	-
3.75	-	1.545	-	-	4.9	11.4	-	-	8.6	-	-
4	-	1.55	-	-	4.83	11.23	-	-	8.67	-	-
4.25	-	1.554	-	-	5.4	11.6	-	-	8.2	-	-
4.5	-	1.56	-	-	5.9	12	-	-	8.4	-	-
4.6	-	1.562	-	-	5.87	12.3	-	-	9	-	-
4.7	-	1.563	-	-	5.8	12.7	-	-	9.6	-	-
4.75	-	1.564	-	-	5.84	13	-	-	10	-	-
4.9	-	1.566	-	-	5.8	14.3	-	-	11.1	-	-
5	-	1.567	-	-	5.89	15.65	-	-	12.13	-	-
5.1	-	1.5675	-	-	5.9	14	-	-	12.3	-	-
5.2	-	1.5678	-	-	5.92	-	12.4	-	-	-	-
5.25	-	1.568	-	-	5.95	-	12.5	-	-	-	-
5.5	-	1.569	-	-	7.86	-	12.6	-	-	-	-
5.6	-	1.574	-	5.89	7.95	-	-	12.7	-	-	15.1
5.75	-	1.58	-	-	8	-	-	12.8	-	-	18.5
6	-	1.6	-	-	7.97	-	-	13.95	-	-	-
6.5	-	1.62	-	-	7.78	-	-	11.6	-	-	-
7	-	1.65	-	-	8.22	-	-	12.36	-	-	-
7.5	-	1.66	-	-	8	-	-	11.6	-	-	-
8	-	1.68	-	-	7.78	-	-	10.7	-	-	-

Table C.2: **Raw data for Γ_{crit} in Fig. 5.3(a).**

F	SB to BB&Gas	SB to BB	BB&Gas to Gas&Clus.	BB&Gas to UW&Gas	BB to UW	UW&Gas to Gas&LS	UW to Gas&LS	UW to LS	UW to UW&Gas	UW&Gas to Gas&Clus	LS to Gas&LS
2.5	1.46	-	5.7	-	-	-	-	-	-	-	-
2.75	1.48	-	7.5	-	-	-	-	-	-	-	-
2.8	1.49	-	-	5	-	-	-	-	-	8.75	-
2.9	1.492	-	-	4.88	-	-	-	-	-	9.5	-
3	1.5	-	-	4.83	-	10	-	-	-	-	-
3.25	1.53	-	-	6.2	-	13	-	-	-	-	-
3.5	1.56	-	-	7.55	-	15.2	-	-	-	-	-
3.65	1.563	-	-	7.6	-	14	-	-	-	-	-
3.75	-	1.54	-	-	4.69	13.2	-	-	7.65	-	-
4	-	1.55	-	-	4.78	10.15	-	-	7.85	-	-
4.25	-	1.555	-	-	4.8	10.5	-	-	7.75	-	-
4.5	-	1.56	-	-	4.6	10.7	-	-	7.9	-	
4.6	-	1.562	-	-	4.64	10.65	-	-	8	-	-
4.7	-	1.563	-	-	4.6	10.68	-	-	8.1	-	-
4.75	-	1.564	-	-	4.7	-	10.76	-	-	-	-
4.9	-	1.566	-	-	4.6	-	10.8	-	-	-	-
5	-	1.567	-	-	4.5	-	10.86	-	-	-	-
5.1	-	1.5675	-	-	4.55	-	11	-	-	-	-
5.2	-	1.5678	-	-	4.5	-	10.9	-	-	-	-
5.25	-	1.568	-	-	4.6	-	10.96	-	-	-	-
5.5	-	1.569	-	-	4.46	-	11	-	-	-	-
5.6	-	1.574	-	-	4.6	-	-	11.9	-	-	17
5.75	-	1.58	-	-	4.7	-	-	12	-	-	-
6	-	1.59	-	-	4.45	-	-	12.75	-	-	-
6.5	-	1.62	-	-	4.26	-	-	12.36	-	-	-
7	-	1.64	-	-	4.68	-	-	14.78	-	-	-
7.5	-	1.66	-	-	4.7	-	-	13.4	-	-	-
8	-	1.69	-	-	4.73	-	-	11.97	-	-	-

Table C.3: **Raw data for Γ_{crit} in Fig. 5.3(b).**

F	Open Circles	Open Triangles	Open Diamonds	Closed Circles	Closed Triangles	Closed Diamonds
2.8	4.9	8.5	-	5	8.75	-
2.9	5.1	9.8	-	4.88	9.5	-
3	5.07	-	11.23	4.83	-	10
3.25	4.6	-	12.5	6.2	-	13
3.5	4.5	-	13.63	7.55	-	15.2
3.65	6	-	12	7.6	-	14
3.75	8.6	-	11.4	7.65	-	13.2
4	8.67	-	11.23	7.85	-	10.15
4.25	8.2	-	11.6	7.75	-	10.5
4.5	8.4	-	12	7.9	-	10.7
4.6	9	-	12.3	8	-	10.65
4.7	9.6	-	12.7	8.1	-	10.68
4.75	10	-	13	-	-	-
4.9	11.1	-	14.3	-	-	-
5	12.13	-	15.65	-	-	-
5.1	12.3	-	14	-	-	-

Table C.4: **Raw data for Γ_{crit} in Fig. 5.9.**

F	SB to BB & Gas	SB to BB	BB to BB &Gas	BB to Spikes	Spikes to UW	BB & Gas to UW	BB & Gas to UW & Gas	UW to UW& Gas	BB & Gas to Gas & Clus.	UW & Gas to Gas &Clus.	UW to LS	LS to LS & Gas	UW to LS& Gas	UW& Gas to LS& Gas	LS & Gas to Gas & Clus.
2.5	1.2	-	-	-	-	-	-	-	4.5	-	-	-	-	-	-
2.6	1.21	-	-	-	-	-	6.3	-	-	17	-	-	-	-	-
2.7	1.215	-	-	-	-	-	6.2	-	-	18	-	-	-	-	-
2.8	1.218	-	-	-	-	-	6.3	-	-	18.5	-	-	-	-	-
2.9	1.22	-	-	-	-	-	6.4	-	-	19.2	-	-	-	-	-
3	1.23	-	-	-	-	-	6.5	-	-	20	-	-	-	-	-
3.1	1.234	-	-	-	-	-	6.7	-	-	-	-	-	-	19	31
3.2	1.24	-	-	-	-	-	7	-	-	-	-	-	-	18	37
3.3	1.245	-	-	-	-	-	7.2	-	-	-	-	-	-	17.2	43
3.4	1.247	-	-	-	-	-	7.4	-	-	-	-	-	-	16.8	47
3.5		1.25	2.5	-	-	-	7.7	-	-	-	-	-	-	16.5	-
3.75	-	1.26	3.6	-	-	-	8.7	-	-	-	-	-	-	17.4	-
4	-	1.27	4.5	-	-	7.14	-	10	-	-	-	-	-	18.5	-
4.25	-	1.28	4.4	-	-	6.5	-	12	-	-	-	-	-	17.7	-
4.5	-	1.29	4.43	-	-	5.9	-	14.6	-	-	-	-	-	17	-
4.6	-	1.293	4.3	-	-	5.6	-	15	-	-	-	-	-	17.3	-
4.7	-	1.295	-	-	-	5.8	-	-	-	-	-	-	17.5	-	-
5	-	1.3	-	7	8	-	-	-	-	-	-	-	18	-	-
5.1	-	1.306	-	6.8	8	-	-	-	-	-	-	-	18.2	-	-
5.5	-	1.32	-	7	8.2	-	-	-	-	-	-	-	18.5	-	-
5.75	-	1.33	-	6.9	8.1	-	-	-	-	-	-	-	18.7	-	-
6	-	1.34	-	6.8	8.3	-	-	-	-	-	-	-	19	-	-
6.4	-	1.347	-	6.9	8.2	-	-	-	-	-	-	-	18.8	-	-
6.5	-	1.35	-	7	8.3	-	-	-	-	-	-	-	19	-	-
6.6	-	1.355	-	7.1	8.4	-	-	-	-	-	18.9	24	-	-	-
6.7	-	1.36	-	7	8.2	-	-	-	-	-	18.95	28	-	-	-
6.8	-	1.364	-	7.03	8.2	-	-	-	-	-	18.9	31.8	-	-	-
6.9	-	1.367	-	7.1	8.25	-	-	-	-	-	18.93	35.4	-	-	-
7	-	1.37	-	7.2	8.3	-	-	-	-	-	19	39	-	-	-
7.5	-	1.38	-	7	8.5	-	-	-	-	-	19	39	-	-	-
8	-	1.4	-	7.1	8.2	-	-	-	-	-	19.1	38	-	-	-
8.5	-	1.43	-	7.2	8.37	-	-	-	-	-	19.2	38	-	-	-
9	-	1.45	-	7.1	8.39	-	-	-	-	-	18.9	39	-	-	-
9.1	-	1.453	-	7.06	8.3	-	-	-	-	-	18.5	-	-	-	-
9.2	-	1.456	-	7	8.2	-	-	-	-	-	18.2	-	-	-	-
9.5	-	1.46	-	7	8.25	-	-	-	-	-	18.3	-	-	-	-
10	-	1.49	-	7.1	8.39	-	-	-	-	-	17.8	-	-	-	-

Table C.5: **Raw data for Γ_{crit} in Fig. 5.17(a).**

F	SB to BB & Gas	SB to BB	BB to BB &Gas	BB to UW	UW to Spikes	Spikes to UW	BB & Gas to UW & Gas	UW to UW& Gas	BB & Gas to Gas & Clus.	UW & Gas to Gas &Clus.	UW to LS	LS to LS & Gas	UW to LS& Gas	UW& Gas to LS& Gas	LS & Gas to Gas & Clus.
2.5	1.14	-	-	-	-	-	-	-	4.6	-	-	-	-	-	-
2.6	1.16	-	-	-	-	-	6	-	-	16	-	-	-	-	-
2.7	1.18	-	-	-	-	-	6.2	-	-	16.5	-	-	-	-	-
2.8	1.2	-	-	-	-	-	6.5	-	-	17	-	-	-	-	-
2.9	1.22	-	-	-	-	-	6.7	-	-	17.5	-	-	-	-	-
3	1.224	-	-	-	-	-	7	-	-	18	-	-	-	-	-
3.1	1.23	-	-	-	-	-	7.1	-	-	-	-	-	-	17.7	30.5
3.2	1.232	-	-	-	-	-	7.2	-	-	-	-	-	-	17.4	36.5
3.3	1.235	-	-	-	-	-	7.2	-	-	-	-	-	-	17.3	42
3.4	1.238	-	-	-	-	-	7.3	-	-	-	-	-	-	17.2	48
3.5	-	1.24	2	-	-	-	7.5	-	-	-	-	-	-	17.5	-
3.75	-	1.25	2.5	-	-	-	8.4	-	-	-	-	-	-	17.2	-
4	-	1.26	-	4.3	-	-	-	9.5	-	-	-	-	-	17	-
4.25	-	1.27	-	4.4	-	-	-	11.7	-	-	-	-	-	16.7	-
4.5	-	1.28	-	4.5	-	-	-	14	-	-	-	-	-	16.5	-
4.6	-	1.283	-	4.7	-	-	-	14.3	-	-	-	-	-	16.7	-
4.7	-	1.285	-	4.7	-	-	-	-	-	-	-	-	16.8	-	-
5	-	1.29	-	5.3	-	-	-	-	-	-	-	-	17	-	-
5.1	-	1.293	-	4.9	7	8	-	-	-	-	-	-	17.2	-	-
5.5	-	1.3	-	4.5	7.2	8	-	-	-	-	-	-	17.8	-	-
5.75	-	1.305	-	4.7	6.9	7.9	-	-	-	-	-	-	17.9	-	-
6	-	1.31	-	4.3	6.7	7.7	-	-	-	-	-	-	18	-	-
6.4	-	1.318	-	4.4	6.6	7.9	-	-	-	-	-	-	18.6	-	-
6.5	-	1.32	-	4.5	-	-	-	-	-	-	-	-	19.5	-	-
6.6	-	1.33	-	4.6	-	-	-	-	-	-	19	21.8	-	-	-
6.7	-	1.337	-	4.5	-	-	-	-	-	-	18.5	23.6	-	-	-
6.8	-	1.34	-	4.45	-	-	-	-	-	-	18	25.4	-	-	-
6.9	-	1.346	-	4.48	-	-	-	-	-	-	17.5	27.2	-	-	-
7	-	1.35	-	4.5	-	-	-	-	-	-	17	29	-	-	-
7.5	-	1.37	-	4.6	-	-	-	-	-	-	18	27	-	-	-
8	-	1.38	-	4.5	-	-	-	-	-	-	18.5	28	-	-	-
8.5	-	1.44	-	4.67	-	-	-	-	-	-	17.5	28.5	-	-	-
9	-	1.46	-	4.8	-	-	-	-	-	-	18	34	-	-	-
9.1	-	1.465	-	4.75	-	-	-	-	-	-	17.6	-	-	-	-
9.2	-	1.472	-	4.73	-	-	-	-	-	-	17.4	-	-	-	-
9.5	-	1.48	-	4.8	-	-	-	-	-	-	17.3	-	-	-	-
10	-	1.49	-	4.72	-	-	-	-	-	-	17.5	-	-	-	-

Table C.6: **Raw data for Γ_{crit} in Fig. 5.17(b).**

F	Closed Circles	Closed Triangles	Closed Diamonds	Open Circles	Open Triangles	Open Diamonds
2.6	6.3	17	-	6	16	-
2.7	6.2	18	-	6.2	16.5	-
2.8	6.3	18.5	-	6.5	17	-
2.9	6.4	19.2	-	6.7	17.5	-
3	6.5	20	-	7	18	-
3.1	6.7	-	19	7.1	-	17.7
3.2	7	-	18	7.2	-	17.4
3.3	7.2	-	17.2	7.2	-	17.3
3.4	7.4	-	16.8	7.3	-	17.2
3.5	7.7	-	16.5	7.5	-	17.5
3.75	8.7	-	17.4	8.4	-	17.2
4	10	-	18.5	9.5	-	17
4.25	12	-	17.7	11.7	-	16.7
4.5	14.6	-	17	14	-	16.5
4.6	15	-	17.3	14.3	-	16.7

Table C.7: **Raw data for Γ_{crit} in Fig. 5.17(c).**

F_s/F	LS → Con.	Gas & LS → LS & Con.	LS → Gas & LS	LS → LS & Con.
0	43	-	-	-
0.01	42.5	-	-	-
0.02	39	-	-	-
0.03	-	38.3	-	-
0.05	-	38	-	-
0.075	-	39	-	-
0.1	-	40	-	-
0.15	-	38	-	-
0.2	-	39	-	-
0.25	-	39	-	-
0.275	-	42	-	-
0.3	-	44	-	-
0.325	-	43.1	24	-
0.35	-	42	31	-
0.375	-	44	34.5	-
0.385	-	45	38.5	-
0.4	-	-	-	46
0.425	-	-	-	48
0.45	-	-	-	50
0.5	-	-	-	53.4

Table C.8: **Raw data for Γ_{crit} in Fig. 5.35.**

F_s/F	SB to BB	SB to BB & Gas	BB to BB & Gas	BB to Gas	BB to UW	BB & Gas to UW & Gas	UW to Gas	UW & Gas to LS & Gas	LS & Gas to Gas & Clus.	Gas & Clus. to Os. Clus.	Os. Clus. to Gas	Gas & Clus. to Gas
0	1.52	-	-	10	-	-	-	-	-	-	-	-
0.02	1.54	-	3.8	-	-	7.5	-	10.3	41	-	-	45.5
0.05	1.5	-	2.47	-	-	7.2	-	9.4	37	-	-	46
0.1	-	1.46	-	-	-	7.6	-	9.8	35	42	46.5	-
0.15	-	1.45	-	-	-	7.4	-	9.7	34	40.5	-	-
0.2	-	1.45	-	-	-	7.8	-	10	33	40	-	-
0.25	-	1.41	-	-	-	6.4	-	9.8	32	-	-	-
0.3	-	1.48	-	-	-	6.2	-	10.5	31	-	-	-
0.4	-	1.49	-	-	-	6.3	-	10	29.5	-	-	-
0.45	-	1.43	-	-	-	6.5	-	9.8	29.3	32	47.5	-
0.5	-	1.5	-	-	-	5.07	-	11.23	29	29	46.4	-
0.55	-	2.1	-	-	-	5.2	-	10.5	26.5	34	47	-
0.6	1.48	-	2	-	-	5.5	-	11.4	25	-	-	-
0.7	1.43	-	3.5	-	-	6.8	-	10.9	21	-	-	-
0.8	1.4	-	5.5	-	-	7.6	-	11	20.5	-	-	-
0.85	1.39	-	5.3	-	-	7.5	-	10.8	20	37	-	-
0.9	1.37	-	3.5	-	-	7.9	-	10.5	19	39	49	-
0.95	1.29	-	4.5	-	-	8.11	-	11.5	17	44	48	-
1	1.28	-	-	-	7.9	-	11	-	-	-	-	-

Table C.9: **Raw data of Γ_{crit} in Fig. 5.36(a).**

F_s/F	SB to BB	BB to UW	BB to Spikes	Spikes to UW	UW to LS	UW to LS & Gas	LS to LS & Gas	LS & Gas to LS & Con. (Up)	LS & Gas to LS & Con. (Down)	LS to Con. (Up)	LS to Con. (Down)	LS to LS& Con. (Up)	LS to LS& Con. (Down)
0	1.6	6	-	-	16	-	-	-	-	43	41	-	-
0.01	1.5	5	-	-	11.6	-	-	-	-	42.5	39	-	-
0.02	1.48	5	-	-	10.9	-	-	-	-	39	38	-	-
0.05	1.49	5.11	-	-	-	11.5	-	38	37	-	-	-	-
0.075	1.51	7.9	6.3	7.9	-	11	-	39	38	-	-	-	-
0.1	1.45	5.1	7.5	8.5	-	12.5	-	40	39	-	-	-	-
0.15	1.51	8	6	8	-	12	-	38	37	-	-	-	-
0.2	1.47	8	6.5	8	-	12.2	-	39	38	-	-	-	-
0.25	1.48	7.8	5.8	7.8	-	10.5	-	39	37	-	-	-	-
0.3	1.53	6	-	-	-	11	-	44	40	-	-	-	-
0.35	1.51	6.2	-	-	12	-	31	42	41	-	-	-	-
0.4	1.55	7.95	-	-	12	-	-	-	-	-	-	46	43
0.5	1.6	7.97	-	-	13.95	-	-	-	-	-	-	53.4	46.1
0.6	1.42	7.8	-	-	-	12.8	-	41	36	-	-	-	-
0.7	1.45	5.7	-	-	-	13	-	33.5	33	-	-	-	-
0.8	1.46	6	-	-	-	13.2	-	34	33	-	-	-	-
0.9	1.47	5.6	-	-	12.5	-	-	-	-	-	-	37	35.5
0.95	1.46	7	-	-	13.5		-	-	-	34	33	-	-
1	1.5	8	-	-	14	-	-	-	-	36	34	-	-

Table C.10: **Raw data of Γ_{crit} in Fig. 5.36(b.**

A/d	SB to BB	BB to UW	BB to Spikes	UW to LS	Spikes to UW	BB to LS	UW to BB	UW to Gas & LS	LS to Gas & LS	LS & Gas to LS & Con.
0.1	1.7	-	-	-	-	29	-	-	-	-
0.2	1.67	-	-	-	-	23	-	-	-	-
0.5	1.62	4.1	-	-	-	-	12.5	-	-	-
0.8	1.6	5.1	-	-	-	-	12.6	-	-	-
1	1.56	7.5	-	13.1	-	-	-	-	-	-
1.5	1.5	8	-	13.4	-	-	-	-	35.2	-
2	1.48	7.8	-	13.5	-	-	-	-	38	-
2.5	1.45	7.85	-	13.8	-	-	-	-	39.5	-
3	1.42	7.97	-	13.95	-	-	-	-	-	-
3.5	1.4	-	6.4	12	7.79	-	-	-	-	-
4	1.37	-	6.45	12.1	7.7	-	-	-	31	38.5
4.5	1.32	-	6.4	12.25	8	-	-	-	14.95	38
5	1.28	-	6.37	-	8.12	-	-	12.45	-	37
5.5	1.26	-	6.38	-	8.02	-	-	12.8	-	36
6	1.24	-	6.34	-	7.88	-	-	13.5	-	34.8

Table C.11: **Raw data for Γ_{crit} in Fig. 5.43(b).**

F_b/F	SB to BB	SB to BB & Gas	BB to Gas	BB & Gas to Gas & LS	BB & Gas to UW & Gas	BB to LS	UW & Gas to Gas & LS	Gas & LS to Gas & Clus.	LS to Gas	Gas to Con.	Gas & Clus. to Con.
0	1.52	-	10	-	-	-	-	-	-	-	-
0.05	1.4	-	3.8	-	-	-	-	-	-	-	-
0.1	-	1.38	-	6.5	-	-	-	17.5	-	-	-
0.2	-	1.33	-	7.5	-	-	-	16	-	-	-
0.3	-	1.31	-	8.5	-	-	-	15.8	-	-	-
0.4	-	1.3	-	10	-	-	-	15.3	-	-	-
0.5	-	1.32	-	-	6.7	-	11	15	-	-	-
0.6	-	1.3	-	-	6.4	-	11	15.2	-	-	44.7
0.7	-	1.27	-	-	6	-	10.95	15.3	-	-	44
0.8	-	1.24	-	-	5.5	-	10.9	15.5	-	-	42
0.9	1.22	-	-	-	-	5.5	-	-	12.2	26	-
1	1.14	-	-	-	-	5.8	-	-	12	25	-

Table C.12: **Raw data for Γ_{crit} in Fig. 5.53(a).**

F_b/F	SB to BB	BB to UW	BB to Spikes	Spikes to UW	UW to LS	UW to Gas &LS	Gas &LS to LS	LS to Gas &LS	Gas &LS to LS& Con. (Up)	Gas &LS to LS& Con. (Down)	LS to Con. (Up)	LS to Con. (Down)	LS& Con. to Con. (Up)	LS& Con. to Con. (Down)	LS to LS& Con. (Up)	LS to LS& Con. (Down)
0	1.65	-	5.7	8	-	-	-	-	-	-	43	41	-	-	-	-
0.01	1.45	-	5.3	7.5	-	-	-	-	-	-	44	43	-	-	-	-
0.02	1.4	5	-	-	-	-	-	-	-	-	-	-	44.5	43	-	-
0.05	1.38	5.1	-	-	-	11.5	13.2	29	36	34	-	-	51	50	-	-
0.1	1.36	5	-	-	-	10.5	13.8	28.5	38	36	-	-	-	-	-	-
0.2	1.37	5	-	-	-	11.5	14.3	28.7	37	35	-	-	-	-	-	-
0.3	1.38	5.1	-	-	-	12	14	30	35	34.5	-	-	-	-	-	-
0.4	1.4	5.4	-	-	-	11.2	14.1	31.8	33	32	-	-	-	-	-	-
0.45	1.38	5.3	-	-	-	11.5	14.8	-	-	-	-	-	-	-	34	33
0.5	1.35	-	6	7.5	-	11.4	14	-	-	-	-	-	-	-	41	40
0.55	1.35	-	6	7.6	13	-	-	-	-	-	-	-	-	-	46.3	44.5
0.6	1.36	-	5.7	7.58	12	-	-	-	-	-	-	-	-	-	51.4	48
0.65	1.35	5.5	-	-	12.9	-	-	31	42	40	-	-	-	-	-	-
0.7	1.34	-	5.6	7.45	12.5	-	-	25.5	39	37	-	-	-	-	-	-
0.8	1.38	-	6.1	7.84	12.8	-	-	29	38.5	36.5	-	-	-	-	-	-
0.9	1.3	-	5.9	7.69	11.2	-	-	32	38	35.5	-	-	-	-	-	-
0.95	1.35	-	5.9	7.69	12	-	-	-	-	-	-	-	-	-	-	-
1	1.22	-	6	7.7	11.5	-	-	-	-	-	-	-	-	-	-	-

Table C.13: **Raw data for Γ_{crit} in Fig. 5.53(b).**

A/d	SB to BB	SB to BB & Gas	BB to BB & Gas	BB & Gas to BB	BB to LS	BB to UW	UW to LS	BB & Gas to LS	LS to Gas & LS	BB & Gas to Gas & LS	BB & Gas to UW & Gas
0.1	1.7	-	-	-	7	-	-	-	39	-	-
0.2	1.6	-	-	-	9	-	-	-	16	-	-
0.3	1.56	-	-	-	9	-	-	-	19	-	-
0.5	1.5	-	-	-	-	4.5	8	-	15.5	-	-
0.8	-	1.68	-	3.5	-	5.4	7.8	-	10	-	-
1	-	1.55	-	-	-	-	-	4.2	8.2	-	-
1.5	-	1.3	-	-	-	-	-	-	-	6.5	-
2	-	1.32	-	-	-	-	-	-	-	-	5.3
2.5	-	1.3	-	-	-	-	-	-	-	-	5.1
3	-	1.32	-	-	-	-	-	-	-	-	6.7
3.25	1.35	-	3.14	-	-	-	-	-	-	-	-
3.5	-	-	-	-	-	-	-	-	-	-	6.9
4	1.32	-	3.1	-	-	-	-	-	-	-	6.7
4.5	1.29	-	1.8	-	-	-	-	-	-	-	7
5	1.28	-	1.85	-	-	-	-	-	-	-	6.45
5.5	1.265	-	2	-	-	-	-	-	-	-	-
6	1.25	-	2.6	-	-	-	-	-	-	-	-

A/d	Gas & LS to Gas & Clus.	BB & Gas to Gas & Clus.	UW & Gas to Gas & Clus.	Gas & Clus. to Gas	Gas & Clus. to Os. Clus.	Gas to Os. Clus.
0.1	-	-	-	-	-	-
0.2	-	-	-	-	-	-
0.3	-	-	-	-	-	-
0.5	-	-	-	-	-	-
0.8	-	-	-	-	-	-
1	46	-	-	-	-	-
1.5	32	-	-	-	-	-
2	22	-	-	-	-	-
2.5	12	-	-	-	-	-
3	15	-	-	-	-	-
3.25	-	11	-	-	34	-
3.5		-	11.5	-	38	-
4	-	-	11.8	-	30	-
4.5	-	-	12.3	20.5	-	28.5
5	-	-	11.9	22	-	29
5.5	-	6.5	-	24	-	32
6	-	6.4	-	26.8	-	36

Table C.14: **Raw data for Γ_{crit} in Fig. 5.64(a).**

A/d	SB to BB	BB to UW	BB to Spikes	Spikes to UW	UW to BB	UW to Gas & LS	Gas & LS to LS	UW to LS	BB to LS	LS to Con.	LS to LS & Con.
0.1	1.65	-	-	-	-	-	-	-	-	-	-
0.2	1.55	-	-	-	-	-	-	-	29	-	-
0.5	1.51	4.25	-	-	10.1	-	-	-	19.5	-	-
0.8	1.46	4.86	-	-	-	-	-	11.2	-	-	-
1	1.35	5.9	-	-	-	-	-	11.15	-	-	-
1.5	1.3	7.5	-	-	-	-	-	11.27	-	-	-
2	1.29	7.45	-	-	-	-	-	11.32	-	-	-
2.5	1.28	7.7	-	-	-	-	-	11.37	-	-	-
2.75	1.24	-	6.05	7.6	-	11.3	18	-	-	-	44.5
3	1.21	-	6	7.57	-	11.4	14	-	-	-	41
3.5	1.2	-	6	7.7	-	-	-	11.6	-	38	-
4	1.15	7.72	-	-	-	-	-	11.7	-	36	-
4.5	1.09	7.68	-	-	-	-	-	11.85	-	34.5	-
5	1.06	7.7	-	-	-	-	-	12.4	-	33.5	-
5.5	1.05	7.66	-	-	-	-	-	12.6	-	32.6	-
6	1.03	7.6	-	-	-	-	-	13	-	32	-

Table C.15: **Raw data for Γ_{crit} in Fig. 5.64(b).**

F	SB to BB	BB to UW	BB to Gas	BB to LS	BB to Spikes	UW to Spikes	Spikes to UW	UW to LS	LS to Gas	Gas to Con.	LS to Con.
2	1.2	-	2	-	-	-	-	-	-	-	-
2.5	1.23	-	2.6	-	-	-	-	-	-	-	-
3	1.24	-	-	6.5	-	-	-	-	11	24	-
3.5	1.27	-	-	6.2	-	-	-	-	16	29	-
4	1.28	5.9	-	-	-	-	-	9	-	-	30
5	1.31	5.5	-	-	-	-	-	9.5	-	-	30.4
5.5	1.33	5	-	-	-	6.5	8.45	10.2	-	-	32.5
6	1.36	4.5	-	-	-	6.4	8.1	10.7	-	-	42
6.5	1.38	-	-	-	6	-	7.6	11.5	-	-	-
7	1.4	-	-	-	6.3	-	7.5	11.4	-	-	-
8	1.42	-	-	-	6.4	-	7.3	12	-	-	-

Table C.16: **Raw data for Γ_{crit} in Fig. 5.73.**

F_b/F	SB to BB	BB to UW	BB to LS	UW to Gas	LS to Gas	Gas to Con.
0	1.28	7.9	-	11	-	-
0.025	1.26	8	-	11.2	-	-
0.05	1.25	7.95	-	11.5	-	26.5
0.1	1.2	-	5.9	-	12.1	24.8
0.2	1.15	-	6.2	-	11.7	24.5
0.3	1.17	-	6.3	-	11.4	24.3
0.4	1.21	-	6.4	-	11.2	24.15
0.5	1.24	-	6.5	-	11	24
0.6	1.2	-	6.2	-	11.3	24.2
0.7	1.17	-	6.1	-	11.5	24.5
0.8	1.15	-	5.95	-	11.6	24.7
0.9	1.16	-	5.9	-	11.8	24.9
1	1.14	-	5.8	-	12	25

F_b/F	SB to BB	BB to UW	UW to Spikes	BB to Spikes	Spikes to UW	UW to LS	LS to Con.
0	1.28	8	-	-	-	13.5	36
0.1	1.26	-	-	5.95	7.55	12.5	34.8
0.2	1.25	-	-	5.9	7.7	12.2	34.9
0.3	1.2	-	-	6.1	7.63	11.7	36.5
0.4	1.15	4.6	6.3	-	8.15	11.2	39
0.5	1.17	4.5	6.4	-	8.1	10.7	42
0.6	1.21	4.4	6.2	-	8.12	10.9	44
0.7	1.24	-	-	6.1	7.95	11	46
0.8	1.2	-	-	6	7.77	11.2	48
0.9	1.17	-	-	5.95	7.7	11.4	
1	1.15	-	-	6	7.7	11.5	

Table C.17: **Top table: raw data for Γ_{crit} in Fig. 5.81(a). Bottom table: raw data for Γ_{crit} in Fig. 5.81(b).**

A/d	SB to BB	BB to LS	BB to UW	BB to Gas	LS to Gas	Gas to Con.
0.1	2.4	28	-	-	-	-
0.2	1.85	19	-	-	-	-
0.3	1.8	9	-	-	-	-
0.5	1.78	-	4.7	-	-	-
0.8	1.51	-	4.4	-	44	-
1	1.43	-	4.6	-	43	-
1.5	1.35	-	4.5	-	26	38
2	1.26	4.6	-	-	21	29
2.5	1.23	5.2	-	-	14	26
3	1.21	6.5	-	-	11	24
3.5	1.2	-	-	4	-	22
4	1.17	-	-	3.5	-	24
4.5	1.1	-	-	2.5	-	-
5	1.09	-	-	2.2	-	-
5.5	1.08	-	-	2	-	-
6	1.07	-	-	1.98	-	-

A/d	SB to BB	BB to UW	BB to Spikes	UW to Spikes	Spikes to UW	UW to LS	LS to Con.
0.1	2.7	-	-	-	-	-	-
0.2	1.8	-	-	-	-	-	-
0.5	1.6	3.9	-	-	-	10.2	-
0.8	1.4	4.9	-	-	-	11.9	-
1	1.38	5.3	-	-	-	11.5	-
1.5	1.28	6	-	-	-	13.5	-
2	1.26	4.6	-	-	-	8	44
2.5	1.25	4.3	-	6	7.4	9.5	43
3	1.23	4.5	-	6.4	8.1	10.7	42
3.5	1.2	4.8	-	6.5	8.1	12	38
4	1.17	-	5.5	-	8.15	12.5	36
4.5	1.14	-	6.1	-	7.8	13	34
5	1.11	-	6.2	-	7.74	15	32
5.5	1.08	-	6	-	7.6	15.8	31.5
6	1.06	-	6	-	7.53	15	30

Table C.18: **Top table: raw data for Γ_{crit} in Fig. 5.89(a). Bottom table: raw data for Γ_{crit} in Fig. 5.89(b).**

References

Ahlers, G., Grossman, S. & Lohse, D. 2009 Heat transfer and large scale dynamics in turbulent rayleigh-bènard convection. *Review of Modern Physics* **81** (2), 503.

Alam, M. & Luding, S. 2002 How good is the equipartitionassumption for the transport properties of a granular mixture? *Gran. Matt.* **4**, 139.

Alam, M. & Nott, P. R. 1997 The influence of friction on the stability of unbounded granular shear flow. *J. Fluid Mech.* **343** (267).

Alam, M. & Nott, P. R. 1998 Stability of plane couette flow of a granular material. *J. Fluid Mech.* **377** (99).

Alam, M. & Shukla, P. 2013 Nonlinear stability, bifurcation and vortical patterns in three-dimensional granular plane couette flow. *J. Fluid. Mech.* **716**, 349–413.

Alam, M., Trujillo, L. & Hermann, H. J. 2006 Hydrodynamic theory for reverse brazil nut segregation and the non-monotonic ascension dynamics. *J. Stat. Phys.* **124**, 587.

Allen, M. P. & Tildesley, D. J. 1989 Computer simulation of liquids. *Oxford Science Publications* .

Alonso, M., Satoh, M. & Miyanami, K. 1991 Optimum combination of size ratio, density ratio and concentration to minimize free surface segregation. *Powder Technology* **68**, 145–152.

Andreotti, B. & Douady, S. 2001 Selection of velocity profile and flow depth in granular flows. *Phys. Rev. E* **63** (031305).

Ansari, M. I. H. & Alam, M. 2012 Patterns, segregation and hysteresis in vertically vibrated granular mixtures. *Bull. Am. Phys. Soc.* **57** (17), 358.

Ansari, M. I. H. & Alam, M. 2013 Patterns and velocity field in vertically vibrated granular materials. *AIP Conference Proceedings* **1542**, 775.

Aoki, K. M. & Akiyama, T. 1994 Control parameter in granular convection. *Phys. Rev. E* **58** (5629).

Aoki, K. M. & Akiyama, T. 1996 Spontaneous wave pattern formation in vibrated granular materials. *Phys. Rev. Lett.* **77**, 4166.

Aoki, K. M., Akiyama, T., Maki, Y. & Watanabe, T. 1996 Convective roll patterns in vertically vibrated beds of granules. *Phys. Rev. E* **54** (874).

Aranson, I. S. & Tsimring, L. S. 2006 Patterns and collective behavior in granular media: Theoretical concepts. *Rev. Mod. Phys.* **78** (641).

Armanini, A., Capart, H., Fraccarollo, L. & Larcher, M. 2005 Rheological stratification in experimental free-surface flows of granular-liquid mixtures. *J. Fluid. Mech.* **532**, 269–319.

Armanini, A., Fraccarollo, L. & Larcher, M. 2008 Liquid-granular channel flow dynamics. *Powder Technology* **182** (2), 218–227.

Dantec Dynamics A/S, D. 2012 Product information on adaptive correlation in dynamic studio. http://www.dantecdynamics.com.

Azanza, E., Chevoir, F. & Moucheront, P. 1999 Experimental study of collisional granular flows down an inclined plane. *J. Fluid. Mech.* **400**, 199–227.

Bachmann, D. 1940 Verfahrenstechnik Z.V.D.I. Beiheft. *Beiheft* (2), 43.

Bagnold, R. A. 1954 *The Physics of Blown Sand and Desert Dunes*. Methuen and Co., Ltd., London.

Bak, P., Tang, C. & Wiesenfeld, K. 1987 Self-organized criticality: an explanation of 1/f noise. *Phys. Rev. Lett.* **59**, 381–384.

Betat, A., Dury, C., Rehberg, I., Ristow, G., Cherer, M., Scroter, M. & Strassgurger, G. 1998 Formation of patterns in granular materials. *In: Evolution of spontaneous structures in dissipative continuous systems, Springer* .

Biswas, P., Sánchez, P., Swift, M. R. & King, P. J. 2003 Numerical simulation of air-driven granular separation. *Phys. Rev. E* **68** (050301 (R)).

Bizon, C., Shattuk, M. D. & Swift, J. B. 1999 Linear stability analysis of a vertically oscillated granular layer. *Phys. Rev. E* **60**, 7210.

Bizon, C., Shattuk, M. D., Swift, J. B., Mc Cormick, W. D. & Swinney, H. L. 1998 Patterns in 3d vertically oscillated granular layers: Simulation and experiment. *Phys. Rev. Lett.* **80**, 57.

Blair, D. L. & Kudrolli, A. 2003 Collision statistics of driven granular materials. *Phys. Rev. E* **67** (4), 041301.

Bodenschatz, E., Pesch, W. & Ahlers, G. 2000 Recent developments in rayleigh-bènard convection. *Annu. Rev. Fluid Mech.* **32**, 709.

Bogdan, T. V. 2006 Atom-atomic potentials and the correlation distribution functions for modeling liquid benzene by the molecular dynamics methods. *Russian Journal of Physical Chemistry* **80**, 14–20.

Bougie, J., Policht, V. & Pearce, J. K. 2012 Time dependence and density inversion in simulations of vertically oscillated granular layers. *Phys. Rev. E* **86** (020302(R)).

Bridgewater, J. 1976 Fundamental powder mixing mechanisms. *Powder Technology* **15**, 215–236.

Bridgewater, J. 1993 Mixing and segregation mechanisms in particle flow. *Gran. Matt., Springer-Verlag* pp. 161–195.

Bridgewater, J. 1995 Particle technology. *Chemical Engineering Science* **50**, 4081–4089.

Brilliantov, N. V. & Pöschel, T. 2004 *Kinetic Theory of Granular Gases*. Oxford University Press, Oxford, UK.

Brockbank, R., Huntley, J. & Ball, R. 1997 Contact force distribution beneath a three-dimensional granular pile. *J. Phys. II France* **7** (035506), 1521–1532.

Burtally, N., King, P. J. & Swift, M. R. 2002 Spontaneous air-driven separation in vertically vibrated fine granular mixtures. *Science* **295** (1877).

Burtally, N., King, P. J., Swift, M. R. & Leaper, M. 2003 Dynamical behaviour of fine granular glass/bronze mixtures under vertical vibration. *Gran. Matt.* **5** (57).

Campbell, C. S. 1990 Rapid granular flows. *Annu. Rev. Fluid Mech.* **22** (1), 57–90.

Cantelaube, F. & Bideau, D. 1995 Radial segregation in a 2d drum: an experimental analysis. *Europhys. Lett.* **30**, 133–138.

Capart, H., Fraccarollo, L., Guarino, L., Armanini, A. & Zech, Y. 2000 Granular temperature behaviour of loose bed debris-flows. *Debris-Flow Hazards Mitigation: Mechanics, Prediction, and Assessment* pp. 361–368.

Capart, H., Young, D. L. & Zech, Y. 2002 Voronoï imaging methods for the measurement of granular flows. *Exp. Fluids* **32** (1), 121.

Carrillo, A. J., Pöschel, T. & Salueña, C. 2008 Granular hydrodynamics and pattern formation in vertically oscillated granular disk layers. *J. Fluid Mech.* **597**, 119.

Chaiworn, P., Chung, F. F., Wang, C.-Y. & Liaw, S.-S. 2010 Brazil nut effect in annular containers. *Gran. Matt.* **13** (4), 379–384.

Chandrasekhar, S. 1961 Hydrodynamic and hydromagnetic stability. *Oxford University Press, Oxford, England.* .

Chapman, S. & Cowling, T. G. 1952 *The mathematical theory of non-uniform gases*. Cambridge University Press.

Chladni, E. F. F. 1787 Entdeckungen ueber die Theorie des Klanges .

Choo, K., Molteno, T. & Morris, S. 1997 Travelling granular segregation patterns in a long drum mixer. *Phys. Rev. Lett.* **79**, 2975–2978.

Clément, E., Duran, J. & Rajchenbach, J. 1992 Experimental study of heaping in a two-dimensional sand pile. *Phys. Rev. Lett.* **69**, 1189–1192.

Clément, E. & Labous, L. 2000 Pattern formation in a vibrated granular layer: The pattern selection issue. *Phys. Rev. E* **62**, 8314–8323.

Clément, E. & Rajchenbach, J. 1991 Fluidization of a bidimensional powder. *Europhys. Lett.* **16**, 133.

Clément, E., Vanel, L., Rajchenbach, J. & Duran, J. 1996 Pattern formation in a vibrated granular layer. *Phys. Rev. E* **53**, 2972.

Cordero, P., Ramírez, R. & Risso, D. 2003 Buoyancy driven convection and hysteresis in granular gases: Numerical solution. *Physica A* **327** (82).

Crocker, J. C. & Grier, D. 1996 Methods of digital video microscopy for colloidal studies. *J. Coll. Interface Sci.* **179**, 298–310.

Dantu, P. 1967 Etude expérimental d'un milieu pulvérulent. *Ann. Ponts Chauss* **4**, 193–202.

Deng, R. & Wang, C.-H. 2003 Particle image velocimetry study on the stripe formation in vertically vibrated granules. *Molecular Engineering of Biological and Chemical Systems (MEBCS), Singapore-MIT Alliance* .

Dippel, S. & Luding, S. 1995 Simulation on size segregation: geometrical effects in the absence of convection. *Journal de Physique I France* **7**, 1527–1537.

Dolgunin, V. N. & Ukolov, A. A. 1995 Segregation modeling of particle rapid gravity flow. *Powder Technology* **83**, 95–103.

Donald, M. B. & Roseman, B. 1962 Mixing and de-mixing of solid particles. part i. mechanisms in a horizontal drum mixer. *Br. Chem. Eng.* **7**, 749–753.

Douady, S., Fauve, S. & Laroche, C. 1989 Subharmonic instabilities and defects in a granular layer under vertical vibrations. *Europhys. Lett.* **8**, 621.

Drake, T. G. 1991 Granular flow: physical experiments and their implications for microstructural theories. *J. Fluid. Mech.* **225**, 121–152.

Duran, J. 2000 *Sands, Powders, and Grains: An Introduction to the Physics of Granular Materials*. Springer-Verlag, New York.

Duran, J., Rajchenbach, J. & Clément, E. 1993 Arching effect model for particle size segregation. *Phys. Rev. Lett.* **70**, 2431–2434.

Dury, C. M. & Ristow, G. H. 1997 Radial segregation in two-dimensional rotating drum. *J. Phys. France I* **7**, 737–745.

Edwards, W. S. & Fauve, S. 1994 Patterns and quasi-patterns in the faraday experiment. *J. Fluid Mech.* **278**, 123.

Eggers, J. 1999 Sand as maxwells demon. *Phys. Rev. Lett.* **83** (5322).

Ehrichs, E. E., Jaeger, H. M., Karczmar, G. S., Knight, J. B., Kuperman, V. Y. & Nagel, S. R. 1995 Granular convection observed by magnetic resonance imaging. *Science* **267** (1632).

Eshuis, P., Meer, D. V. D., Alam, M., van Gerner, H. J., Weele, K. V. D. & Lohse, D. 2010 Onset of convection in strongly shaken granular matter. *Phys. Rev. Lett.* **104** (038001).

Eshuis, P., Weele, K. V. D., Meer, D. V. D., Bos, R. & Lohse, D. 2007 Phase diagram of vertically shaken granular matter. *Physics of Fluids* **19** (123301).

Eshuis, P., Weele, K. V. D., Meer, D. V. D. & Lohse, D. 2005 Granular leidenfrost effect experiment and theory of floating particle clusters. *Phys. Rev. Lett.* **95** (258001).

Eskin, D. & Kalman, H. 2000 A numerical parametric study of size segregation in a rotating drum. *Chem. Eng. Proc.* **39**, 539–545.

Evesque, P. 1992 Shaking dry powders and grains. *Phys. Rev. E* **33** (4).

Fan, L. T., Chen, Y. & Lai, F. S. 1990 Recent developments in solids mixing. *Powder Technology* **61**, 255–287.

Faraday, M. 1831 On a peculiar class of acoustical figures and on certain forms assumed by groups of particles upon vibrating elastic surfaces. *Phil. Trans. R. Soc. London* **52**, 299–340.

Farkas, Z., Tegzes, P., Vukics, A. & Vicsek, T. 1999 Transitions in the horizontal transport of vertically vibrated granular layers. *Phys. Rev. E* **60** (7022).

Feitosa, K. & Menon, N. 2002 Breakdown of energy equipartition in a 2d binary vibrated granular gas. *Phys. Rev. Lett.* **88** (198301).

Fierro, A., Nicodemi, M. & Coniglio, A. 2003 'edwards' approach to horizontal and vertical segregation of hard spheres under gravity. *J. Phys.: Condensed Matter* **15**, S1095–1105.

Fiscina, J. E. & Cáceres, M. O. 2005 Fermi-like behavior of weakly vibrated granular matter. *Phys. Rev. Lett.* **95**, 108003.

Forterre, Y. & Pouliquen, O. 2008 Flows of dense granular media. *Annu. Rev. Fluid Mech.* **40**, 1–24.

Gallas, J. A. C., Herrmann, H. J. & Sokolowski, S. 1992 Convection cells in vibrating granular media. *Phys. Rev. Lett.* **69** (1371).

Garcimartin, A., Maza, D., Ilquimiche, J. L. & Zuriguel, I. 2002 Convective motion in a vibrated granular layer. *Phys. Rev. E* **65** (031303).

Garzó, V. & Dufty, J. W. 1999 Homogeneous cooling state for a granular mixture. *Phys. Rev. E* **60**, 5706.

Gayen, B. & Alam, M. 2008 Orientational correlation and velocity distributions in uniform shear flow of a dilute granular gas. *Phys. Rev. Lett.* **100**, 1–4.

Geng, J., Howell, D., Longhi, E., Behringer, R. P., Reydellet, G., Vanel, L., Clément, E. & Luding, S. 2001 Footprints in sand: The response of a granular material to local perturbations. *Phys. Rev. Lett.* **87** (035506).

Goddard, J. D. & Didwania, A. K. 2009 A fluid-like model of vibrated granular layers: Linear stability, kinks, and oscillons. *Mech. Mater.* **41**, 637–651.

Goldhirsch, I. 2003 Rapid granular flows. *Annu. Rev. Fluid Mech* **35**, 267–293.

Goldhirsch, I. & Zanetti, G. 1993 Clustering in- stability in dissipative gases. *Phys. Rev. Lett.* **70** (1619).

Gray, J. M. N. T. 2001 Granular flow in partially filled slowly rotating drums. *J. Fluid. Mech.* **441**, 1–29.

Gray, J. M. N. T. & Hutter, K. 1997 Pattern formation in granular avalanches. *Contin. Mech. and Thermodyn.* **9**, 341–345.

Gray, J. M. N. T., Tai, Y.-C. & Noelle, S. 2003 Shock waves, dead zones and particle-free regions in rapid granular free-surface flows. *J. Fluid. Mech.* **491**, 161–181.

Gutiérrez, G., Pozo, O., Reyes, L., Paredes, R., Drake, J. & Ott, E. 2004 Simple model for reverse buoyancy in a vibrated granular system. *Europhys. Lett.* **67** (369).

Haff, P. K. 1983 Grain flow as a fluid-mechanical phenomenon. *J. Fluid Mech.* **134**, 401–430.

Hajra, S. K. & Khakhar, D. V. 2011 Radial segregation of ternary granular mixtures in rotating cylinders. *Gran. Matt.* **13** (4), 475–486.

Harwood, C. F. 1977 Powder segregation due to vibration. *Powder Technol.* **16** (51-57).

Hayakawa, H. & Hong, D. C. 1997 Thermodynamic theory of weakly excited granular systems. *Phys. Rev. Lett.* **78** (14).

Hayakawa, H., Yue, S. & Hong, D. C. 1995 Hydrodynamic description of granular convection. *Phys. Rev. Lett.* **75** (2328).

He, X., Meerson, B. & Doolen, G. 2002 Hydrodynamics of thermal granular convection. *Phys. Rev. E* **65** (030301).

Henein, H., Brimacombe, J. K. & Watkinson, A. P. 1985 An experimental study of segregation in rotary kilns. *Metall. Trans. B* **16B**, 763–774.

Hill, K. M. & Kakalios, J. M. 1995 Reversible axial segregation of rotating granular media. *Phys. Rev. E* **52**, 4393–4400.

Hong, D. C., Quinn, P. V. & Luding, S. 2001 Reverse brazil nut problem: Competition between percolation and condensation. *Phys. Rev. Lett.* **86**, 3423–3426.

Hsiau, S. S. & Chen, C. H. 2000 Granular convection cells in a vertical shaker. *Powder Technol.* **111** (5210).

Hsiau, S. S. & Jang, H. W. 1998 Measurements of velocity fluctuations of granular materials in a shear cell. *Experimental Thermal and Fluid Science* **17** (3), 202–209.

Hsiau, S. S. & Shieh, Y. M. 2000 Effect of solid fraction on fluctuations and self- diffusion of sheared granular flows. *Chem. Eng. Sci.* **55** (11), 1969.

Hsiau, S. S. & Yu, H. Y. 1997 Segregation phenomena in a shaker. *Powder Technology* **93**, 83–88.

Iverson, R. M. 1997 The physics of debris flows. *Rev. Geophys.* **35**, 245–296.

Iwashita, K., Tarumi, Y., Casaverde, L., Uemura, D., Meguro, K. & Hakuno, M. 1988 Granular assembly simulation for ground collapse. *Micromechanics of Granular Material, Elsevier, Amsterdam* **33**, 125–132.

Jaeger, H. & Nagel, S. 1992 Physics of the granular state. *Science* **255**, 1523–1531.

Jaeger, H. M., Liu, C. & Nagel, S. R. 1989 Relaxation at the angle of repose. *Phys. Rev. Lett.* **62** (40).

Jaeger, H. M., Nagel, S. R. & Behringer, R. P. 1996*a* Granular solids, liquids and gases. *Review of Modern Physics* **68**, 1259–1273.

Jaeger, H. M., Nagel, S. R. & Behringer, R. P. 1996*b* The physics of granular material. *Physics Today* pp. 32–38.

Jain, N., Ottino, J. M. & Lueptow, R. M. 2002 An experimental study of the flowing granular layer in a rotating tumbler. *Phys. Fluids* **14**, 572–582.

Janssen, H. A. 1895 Experiments on grain pressure in silos. *Z. Ver. Dt. Ing.* **39**, 1045–1049.

Jenkins, J. T. & Richman, M. W. 1984 Grad's 13-moment system for a dense gas of inelastic spheres. *Archive of Rational Mechanics and Analysis* **87** (6825), 355–377.

Jenkins, J. T. & Savage, S. B. 1983 A theory for rapid flow of identical, smooth, nearly elastic spherical particles. *J. Fluid Mech.* **130**, 187–202.

Jenkins, J. T. & Yoon, D. K. 2002 Segregation in binary mixtures under gravity. *Phys. Rev. Lett.* **88** (194301).

Jullien, R., Meakin, P. & Pavlovitch, A. 1992 Three-dimensional model for particle-size segregation by shaking. *Phys. Rev. Lett.* **69**, 640–643.

Kadanoff, L. 1992 Built upon sand: theoretical ideas inspired by granular flows. *Rev. of Mod. Phys.* **71** (1), 435–444.

Khain, E. & Meerson, B. 2003 Onset of thermal convection in a horizontal layer of granular gas. *Phys. Rev. E* **67** (021306).

Khakhar, D. V., McCarthy, J. J. & Ottino, J. M. 1997 Radial segregation of granular materials in rotating cylinders. *Phys. Fluids* **9**, 3600–3614.

King, P., Lopez-Alcaraz, P., Pacheco-Martinez, H., Clement, C., Smith, A. & Swift, M. 2007 Instabilities in vertically vibrated fluid-grain systems. *Eur. Phys. J. E* **22** (219).

Knight, J. B., Ehrichs, E. E., Kuperman, V. Y., Flint, J. K., Jaeger, H. M. & Nagel, S. R. 1996 Experimental study of granular convection. *Phys. Rev. E* **54** (5726).

Knight, J. B., Jaeger, H. M. & Nagel, S. R. 1993 Vibration-induced size separation in granular media: The convection connection. *Phys. Rev. Lett.* **70** (3728).

Kroll, W. 1954 Fliesserscheinungen an Haufwerken in schwingenden Gefässen. *Chemie Ing. Techn.* **27** (1), 33–38.

Kudrolli, A. 2004 Size separation in vibrated granular matter. *Rep. on Prog. in Phys.* **67** (209).

Lan, Y. & Rosato, A. D. 1995*a* Macroscopic behavior of vibrating beds of smooth inelastic spheres. *Phys. Fluids* **7**, 1818–1831.

Lan, Y. & Rosato, A. D. 1995*b* Macroscopic behavior of vibrating beds of smooth inelastic spheres. *Phys. Fluids* **7**, 1818.

Lan, Y. & Rosato, A. D. 1997 Convection related phenomena in granular dynamics simulations of vibrated beds. *Phys. Fluids* **9**, 3615–3627.

Lang, G. F. & Snyder, D. 2001 Understanding the physics of electrodynamic shaker performance. *Dynamic Testing Reference Issue, Data Physics Corporation, California* .

Leaper, M. C., Smith, A. J., Swift, M. R., King, P. J., Webster, H. E., Miles, N. J. & Kingman, S. W. 2005 The behaviour of water-immersed glass-bronze particulate systems under vertical vibration. *Gran. Matt.* **7** (57).

Lecocq, N. & Vandewalle, N. 2000 Stripes ordering in self-stratification experiments of binary and ternary granular mixtures. *Phys. Rev. E* **62** (6).

Leidenfrost, J. G. 1756 De aquae communis nonnullis qualitatibus tractatus. *University of Duisburg, Germany* **50**, 4081–4089.

Liffman, K., Metcalfe, G. & Cleary, P. 1997 Granular convection and transport due to horizontal shaking. *Phys. Rev. Lett.* **79** (4574).

Liffman, K., Metcalfe, G. & Cleary, P. 2000 Convection due to horizontal shaking. *In: Powders and Grains, Balkema, Roterdam.* .

Liu, C. H., Jaeger, H. M. & Nagel, S. R. 1991 Finite-size effect in a sandpile. *Phys. Rev. A* **43**, 7091–7092.

Luding, S. 1997 a Surface waves and pattern formation in vibrated granular media. *Powders and Grains Balkema* p. 373.

Luding, S., Clément, E., Blumen, A., Rajchenbach, J. & Duran, J. 1994*a* The onset of convection in molecular dynamics simulations of grains. *Phys. Rev. E* **50** (R1762).

Luding, S., Clément, E., Blumen, A., Rajchenbach, J. & Duran, J. 1994*b* Studies of columns of beads under external vibrations. *Phys. Rev. E* **49**, 1634–1646.

Luding, S., Clément, E., Rajchenbach, J. & Duran, J. 1996 Simulations of pattern formation in vibrated granular media. *Europhys. Lett.* **36**, 247252.

Lueptow, R. M., Akonur, A. & Shinbrot, T. 2000 PIV for granular flows. *Exp. Fluids* **28**, 183–186.

Mandl, G. 1988 Mechanics of tectonic faulting : models and basic concepts. *Developments in structural geology, Elsevier Science Pub. Co. Amsterdam / New York* .

McNamara, S., Flekkoy, E. G. & Maloy, K. J. 2000 Grains and gas flow: Molecular dynamics with hydrodynamic interactions. *Phys. Rev. E* **61** (4054).

Medved, M., Dawson, D., Jaeger, H. M. & Nagel, S. R. 1999 Convection in horizontally vibrated granular material. *Chaos* **9** (691).

Medved, M., Jaeger, H. M. & Nagel, S. R. 2000 Modes of response in horizontally vibrated granular material. *Europhys. Lett.* **52** (66).

Meer, D. V. D., Reimann, P., Weele, K. V. D. & Lohse, D. 2004 Transitions in the horizontal transport of vertically vibrated granular layers. *Phys. Rev. Lett.* **92** (184301).

Meerson, B., Pöschel, T. & Bromberg, Y. 2003 Close-packed floating clusters: Granular hydrodynamics beyond the freezing point? *Phys. Rev. Lett.* **91** (024301).

Melo, F., Umbanhowar, P. B. & Swinney, H. L. 1994 Transition to parametric wave patterns in a vertically oscillated granular layer. *Phys. Rev. Lett.* **72**, 172.

Melo, F., Umbanhowar, P. B. & Swinney, H. L. 1995 Hexagons, kinks, and disorder in oscillated granular layers. *Phys. Rev. Lett.* **75**, 3838.

Metcalf, T. H., Knight, J. B. & Jaeger, H. M. 1997 Surface patterns in shallow beds of vibrated granular material. *Physica A* **236**, 202.

Metcalfe, G., Tennakoon, S. G. K., Kondic, L., Schaeffer, D. G. & Behringer, R. P. 2002 Granular friction, coulomb failure, and the fluid-solid transition for horizontally shaken granular materials. *Phys. Rev. E* **65** (031302).

Metha, A. & Luck, J. 1990 Novel temporal behavior of a nonlinear dynamical system: The completely inelastic bouncing ball. *Phys. Rev. Lett.* **65**, 393–396.

Miao, G., Huang, K., Yun, Y. & Wei, R. 2004 Active thermal convection in vibrofluidized granular systems. *Eur. Phys. J.* **B40** (301).

MiDi, G. 2004 On dense granular flows. *Eur. Phys. J. E* **14**, 341–365.

Miller, B., Ohern, C. & Behringer, R. P. 1996 Stress fluctuations for continuously sheared granular materials. *Phys. Rev. Lett.* **77** (15), 3110–3113.

Moakher, M., Shinbrot, T. & Muzzio, F. J. 2000 Experimentally validated computations of flow, mixing and segregation of non-cohesive grains in 3d tumbling blenders. *Powder Technology* **109**, 58–71.

Mobius, M. E., Cheng, X., Eshuis, P., Karczmar, G. S., Nagel, S. R. & Jaeger, H. M. 2005 Effect of air on granular size separation in a vibrated granular bed. *Phys. Rev. E* **72** (011304).

Möbius, M. E., Cheng, X., Karczmar, G. S., Nagel, S. R. & Jaeger, H. M. 2004 Intruders in the dust: air-driven granular size separation. *Phys. Rev. Lett.* **93** (198001).

Möbius, M. E., Lauderdale, B. E., Nagel, S. R. & Jaeger, H. M. 2001 Brazil nut effect: Size separation of granular particles. *Nature* **414** (270).

Mueth, D. M., Debregeas, G. F., Karczmar, G. S., Eng, P. J., Nagel, S. R. & Jaeger, H. M. 2000 Signatures of granular microstructure in dense shear flows. *Nature* **406** (6794), 385–389.

Mullin, T. 2000 Coarsening of self-organized clusters in binary mixtures of particles. *Phys. Rev. Lett.* **84** (20), 4741–4744.

Mullin, T. 2002 Mixing and de-mixing. *Science* **295** (1851).

Nakagawa, M. 1994 Axial segregation of granular flows in a horizontal rotating cylinder. *Chemical Engineering Science, Shorter communications* **49**, 2540–2544.

Natarajan, V. V. R., Hunt, M. L. & Taylor, E. D. 1995 Local measurements of velocity fluctuations and diffusion coefficients for a granular material flow. *J. Fluid. Mech.* **304**, 1–25.

Naylor, M. A., Swift, M. R. & King, P. J. 2003 Air-driven brazil nut effect. *Phys. Rev. E* **68** (012301).

Nedderman, R. & Laohakul, C. 1980 The thickness of the shear zone of flowing granular materials. *Powder Technology* **25**, 91–100.

Nityanand, N., Manley, B. & Henein, H. 1986 An analysis of radial segregation for di erent sized spherical solids in rotary cylinders. *Metall. Trans. B* **17B**, 247–257.

Ohtsuki, T. & Ohsawa, T. 2003 Hydrodynamics for convection in vibrating beds of cohesionless granular materials. *J. Phys. Soc. Jpn.* **72** (1963).

Olafsen, J. S. & Urbach, J. S. 1998 Clustering, order, and collapse in a driven granular monolayer. *Phys. Rev. Lett.* **81**, 4369–4372.

Ottino, J. M. & Khakhar, D. V. 2000 Mixing and segregation of granular materials. *Annu. Rev. Fluid Mech.* **32**, 55–91.

Ottino, J. M. & Khakhar, D. V. 2001 Fundamental research in heaping, mixing, and segregation of granular materials: challenges and perspectives. *Powder Technology* **121**, 117–122.

Painter, B. & Behringer, R. P. 2000 Substrate interactions, effects of symmetry breaking, and convection in a 2d horizontally shaken granular system. *Phys. Rev. Lett.* **85**, 3396–3399.

Pak, H., Doorn, E. V. & Behringer, R. P. 1995 Effects of ambient gases on granular materials under vertical vibration. *Phys. Rev. Lett.* **74** (14643).

Pak, H. K. & Behringer, R. P. 1993 Surface waves in vertically vibrated granular materials. *Phys. Rev. Lett.* **71** (1832).

Pereira, G. G. & Cleary, P. W. 2012 Multi-component granular segregation in a rotary classifier. *Ninth International Conference on CFD in the Minerals and Process Industries, CSIRO, Melbourne, Australia* .

Perng, A. T. H., Capart, H. & Chou, H. T. 2006 Granular configurations, motions, and correlations in slow uniform flows driven by an inclined conveyor belt. *Gran. Matt.* **8** (1), 5–17.

Pöschel, T. & Luding, S. 2001 Granular gases. *Springer-Verlag, Berlin Heidelberg, Germany* .

Pöschel, T. & Rosenkranz, D. 1998 *,in: A Perspective Look at Non-linear Media in Physics, Chemistry, and Biology*. Springer, Berlin.

Pöschel, T., Schwager, T. & Salueña, C. 2000 Onset of fluidization in vertically shaken granular material. *Phys. Rev. E* **62**, 1361.

Pouliquen, O. & Chevoir, F. 2002 Dense flows of dry granular material. *C. R. Physique* **3**, 163–175.

Prigozhin, L. & Kalman, H. 1998 Radial mixing and segregation of a binary mixture in a rotating drum: model and experiment. *Phys. Rev. E* **57**, 2073–2080.

Quere, D. 2013 Leidenfrost dynamics. *Annu. Rev. Fluid Mech.* **45**, 197.

Ramírez, R., Risso, D. & Cordero, P. 2000 Thermal convection in fluidized granular systems. *Phys. Rev. E* **85** (1230).

Renard, S., Schwager, T., Pöschel, T. & Salueña, C. 2001 Vertically shaken column of spheres. onset of fluidization. *Eur. Phys. J. E* **4**, 233.

Rericha, E., Bizon, C., Shattuck, M. & Swinney, H. L. 2002 Shocks in supersonic sand. *Phys. Rev. Lett.* **88** (014302), 355–377.

Reyes, L., Sánchez, I. & Gutiérrez, G. 2005 Air-driven reverse buoyancy. *Physica A* **358** (466).

Reynolds, O. 1885 On the dilatancy of media composed of rigid particles in contact, with experimental illustrations. *Phil. Mag. Series 5* **20**, 469–481.

Reynolds, O. 1886 Experiments showing dilatancy, a property of granular material, possibly connected with gravitation. *Proc. Royal Institution of Great Britain* **Read February 12**.

Rhodes, M. J. 1997 *Principles of Powder Technology*. John Wiley and Sons, Inc., USA.

Ristow, G. H. 1994 Particle mass segregation in a two-dimensional rotating drum. *Europhys. Lett.* **28**, 97–101.

Ristow, G. H. 1997 Critical exponents for granular phase transitions. *Europhys. Lett.* **40** (625).

Ristow, G. H. 2000 Pattern formation in granular materials. *Springer Tracts in Modern Physics* **64**.

Ristow, G. H., Strassburger, G. & Rehberg, I. 1997 Phase diagram and scaling of granular materials under horizontal vibrations. *Phys. Rev. Lett.* **79**, 833–836.

Rosato, A., Strandburg, K. J., Prinz, F. & Swendsen, R. H. 1987 Why the brazil nuts are on top: Size segregation of particulate matter by shaking. *Phys. Rev. Lett.* **58** (1038).

Rosenkranz, D. E. & Pöschel, T. 1997 Recurrent swelling of horizontally shaken granular material. *cond-mat* (9712108).

Rothman, D. H. 1990 Oscillons, spiral waves and stripes in a model of vibrated sand. *Phys. Rev. E* **57**, R1239–R1242.

Saitoh, K. & Hayakawa, H. 2007 Rheology of a granular gas under a plane shear. *Phys. Rev. E* **75** (021302).

Saitoh, K. & Hayakawa, H. 2011 Weakly nonlinear analysis of two dimensional sheared granular flow. *Gran. Matt.* **103** (697).

Salueña, C., Esipov, S. E. & Pöschel, T. 1997*a* Hydrodynamic fluctuations and averaging problems in dense granular flows. *Powders and Grains* pp. 341–344.

Salueña, C., Esipov, S. E. & Pöschel, T. 1997*b* Hydrodynamics of dense granular systems. *SPIE Proc.* **3045** (2).

Salueña, C., Esipov, S. E., Pöschel, T. & Simonian, S. 1998 Dissipative properties of granular ensembles. *SPIE Proc.* **3327**, 23.

Salueña, C. & Pöschel, T. 2000 Convection in horizontally shaken granular material. *Eur. Phys. J. E* **1**, 55–59.

Salueña, C., Pöschel, T. & Esipov, S. E. 1999 Dissipative properties of vibrated granular materials. *Phys. Rev. E* **59** (4422).

Sano, O. 2005 Dilatancy, buckling, and undulations on a vertically vibrating granular layer. *Phys. Rev. E* **72**, 051302.

Sano, O. 2010 Solid-fluid transition and the formation of ripples in vertically oscillated granular layers. *AIP Conf. Proc.* **121**, 254.

Sano, O., Ugawa, A. & Suzuki, K. 1999 Pattern formation on the vertically vibrated granular layer. *Forma* **14**, 321.

Savage, S. B. & Hutter, K. 1989 Finite mass of granular material down a rough incline. *J. Fluid. Mech.* **199**, 177–215.

Savage, S. B. & Jeffrey, D. J. 1981 The stress tensor in a granular flow at high shear rates. *J. Fluid Mech.* **110**, 255–272.

Sbalzarini, I. F. & Koumoutsakos, P. 2005 Feature point tracking and trajectory analysis for video imaging in cell biology. *J. Struct. Biol.* **151** (2), 182–195.

Scarano, F. & Riethmuller, R. L. 2000 Advances in iterative multigrid PIV image processing. *Exp. Fluids* **29**, S51–S60.

Seiden, G. & Thomas, P. J. 2011 Complexity, segregation, and pattern formation in rotating-drum flows. *Rev. Mod. Phys.* **83**, 1323–1365.

Shattuck, M. D., Bizon, C., Swift, J. B. & Swinney, H. L. 1999 Computational test of kinetic theory of granular media. *Physica A* **274**, 158–170.

Shinbrot, T. & Muzzio, F. J. 1998 Reverse buoyancy in shaken granular beds. *Phys. Rev. Lett.* **81** (4361).

Shinbrot, T. & Muzzio, F. J. 2000 Nonequilibrium patterns in granular mixing and segregation. *Physics Today* pp. 25–30.

Shinbrot, T. & Muzzio, F. J. 2001 Noise to order. *Nature* **410** (6825), 251–258.

Shukla, P. & Alam, M. 2009 Landau-type order parameter equation for shear banding in granular couette flow. *Phys. Rev. Lett.* **103** (103).

Shukla, P. & Alam, M. 2011*a* Nonlinear stability and patterns in granular plane couette flow: Hopf and pitchfork bifurcations, and evidence for resonance. *J. Fluid Mech.* **672** (147).

Shukla, P. & Alam, M. 2011*b* Weakly nonlinear theory of shear-banding instability in granular plane couette flow: analytical solution, comparison with numerics and bifurcation. *J. Fluid Mech.* **666** (204).

Shukla, P. & Alam, M. 2013 Nonlinear vorticity-banding instability in granular plane couette flow: higher-order landau coefficients, bistability and the bifurcation scenario. *J. Fluid. Mech.* **718**, 131–180.

Shukla, P., Ansari, M. I. H., Meer, D. V. D., Lohse, D. & Alam, M. 2014 Nonlinear instability and convection in a vertically vibrated granular bed. *J. Fluid Mech.* **761**, 123–167.

Spinewine, B., Capart, H., Larcher, M. & Zech, Y. 2003 Three-dimensional voronoï imaging methods for the measurement of near-wall particulate flows. *Exp. Fluids* **34** (2), 227.

Strassburger, G., Betat, A., Scherer, M. A. & Rehberg, I. 1996 Pattern formation by horizontal vibration of granular material. *Traffic and granular flow, World Scientific, Singapore* pp. 329–333.

Sunthar, P. & Kumaran, V. 2001 Characterization of the stationary states of a dilute vibrofluidized granular bed. *Phys. Rev. E* **64** (041303).

Taberlet, N., Newey, M., Richard, P. & Losert, W. 2006 On axial segregation in a tumbler: an experimental and numerical study. *J. Stat. Mech.* (P07013).

Taguchi, Y.-h. 1992 New origin of a convective motion: Elastically induced convection in granular materials. *Phys. Rev. Lett.* **69** (1367).

Tai, C. H. & Hsiau, S. S. 2004 Dynamic behaviors of powders in a vibrating bed. *Powder Technology* **139**, 221–232.

Tai, Y., Gray, J., Hutter, K. & Noelle, S. 2001 Flow of dense avalanches past obstructions. *Annal. Glac.* **32**, 281–284.

Talbot, J. & Viot, P. 2002 Wall-enhanced convection in vibrofluidized granular systems. *Phys. Rev. Lett.* **89** (064301).

Tan, M. L. & Goldhirsch, I. 1997 Intercluster interactions in rapid granular shear flows. *Phys. Fluids* **9** (856).

Tennakoon, S. G. K., Kondic, L. & Behringer, R. P. 1999 Onset of flow in a horizontally vibrated granular bed: Convection by horizontal shearing. *Europhys. Lett.* **45**, 470–475.

Terzaghi, K. 1943 *Theoretical Soil Mechanics*. John Wiley and Sons, Inc., USA.

Thomas, B. & Squires, A. M. 1998 Support for faraday's view of circulation in a fine-powder chladni heap. *Phys. Rev. Lett.* **81** (574).

Thomas, N. 2000 Reverse and intermediate segregation of large beads in dry granular media. *Phys. Rev. E* **62**, 961–974.

Trujillo, L., Alam, M. & Herrmann, H. J. 2003 Segregation in a fluidized binary granular mixture: Competition between buoyancy and geometric forces. *Europhys. Lett.* **64**, 190–196.

Tsimring, L. S. & Aranson, I. S. 1997 Localized and cellular patterns in a vibrated granular layer. *Phys. Rev. Lett.* **79**, 213–216.

Ugawa, A. & Sano, O. 2002 Dispersion relation of standing waves on a vertically oscillated thin granular layer. *Journal of the Physical Society of Japan* **71**, 2815.

Umbanhowar, P. B., Melo, F. & Swinney, H. L. 1996 Localised excitations in a vertically vibrated granular layer. *Nature* **382**, 793–796.

Umbanhowar, P. B. & Swinney, H. L. 2000 Wavelength scaling and square/stripe and grain mobility transitions in vertically oscillated granular layers. *Physica A* **288**, 344.

Vanel, L., Howell, D., Clark, D., Behringer, R. & Clément, R. 1999 Memories in sand: Experimental tests of construction history on stress distributions under sandpiles. *Phys. Rev. E* **60**, R5040–R5043.

Warr, S., Huntley, J. M. & Jacques, G. T. H. 1995 Fluidization of a two-dimensional granular system: Experimental study and scaling behaviour. *Phys. Rev. E* **52** (5), 5583–5595.

Wassgren, C. R., Brennen, C. E. & Hunt, M. L. 1996 Vertical vibration of a deep bed of granular material in a container. *J. Appl. Mech.* **63**, 712–719.

Wereley, S. T., Gui, L. & Meinhart, C. D. 2002 Advanced algorithms for microscale particle image velocimetry. *AIAA J.* **40** (6), 1047–1055.

Wildman, R. D. & Huntley, J. M. 2000 Novel method for measurements of granular temperature distributions in two-dimensional vibro-fluidised beds. *Powder Technology* **113**, 14–22.

Wildman, R. D., Huntley, J. M. & Hansen, J. P. 1999 Self-diffusion of grains in a two-dimensional vibrofluidized bed. *Phys. Rev. E* **60** (6), 7066–7075.

Wildman, R. D., Huntley, J. M. & Parker, D. J. 2001 Convection in highly fluidized three-dimensional granular beds. *Phys. Rev. Lett.* **86** (3304).

Williams, J. C. 1963 The segregation of powders and granular materials. *Fuel Soc.* **14**, 29–34.

Williams, J. C. 1976*a* Continuous mixing of solids, a review. *Powder Technol.* **15** (245).

Williams, J. C. 1976*b* The segregation of particulate materials. a review. *Powder Technology* **15**, 245–251.

Yan, X., Shi, Q., Hou, M., Lu, K. & Chan, C. K. 2003 Effects of air on the segregation of particles in a shaken granular bed. *Phys. Rev. Lett.* **91** (014302).

Yang, S. C. 2006 Density effect on mixing and segregation processes in a vibrated binary granular mixture. *Powder Technology* **164**, 65–74.

Zeilstra, C., van der Hoef, M. A. & Kuipers, J. A. M. 2006 Simulation study of air-induced segregation of equal-sized bronze and glass particles. *Phys. Rev. E* **74** (010302 (R)).

Zeilstra, C., van der Hoef, M. A. & Kuipers, J. A. M. 2008 Simulation of density segregation in vibrated beds. *Phys. Rev. E* **77** (031309).